LBL-4550
UC-2
TID-4500-R64

MATERIALS AND MOLECULAR RESEARCH DIVISION

Annual Report

1975

Lawrence Berkeley Laboratory
University of California
Berkeley, California

CONTENTS

3. Physical Properties

a. High Field Superconductivity
Milton R. Pickus, Principal Investigator

b. Microstructure and Mechanical Behavior of Ceramic Materials: Glass- and Ceramic-Metal Systems
Joseph A. Pask, Principal Investigator

c. High Temperature Reactions
Alan W. Searcy, Principal Investigator

d. Relation of Microstructure to Properties in Ceramics
Richard M. Fulrath, Principal Investigator

e. Structure and Properties of Carbon Materials and Composite Materials
Robert H. Bragg, Principal Investigator

GENERAL INTRODUCTION

David A. Shirley, Division Head
Rolf H. Muller, Assistant to the Division Head

This is the first annual report of the Materials and Molecular Research Division of the Lawrence Berkeley Laboratory. MMRD was formed late in the year--October, 1975--as part of a Laboratory reorganization. Elements of the Nuclear Chemistry Division and the Physics Division were added to the Inorganic Materials Research Division (IMRD), increasing its size by 55%. Division population as of the end of 1975 was: 47 principal investigators, 92 postdoctorals and other scientific personnel, 237 graduate students, and 67 technical, administrative and clerical support personnel for a total of 443. The total fiscal year 1976 operating budget for MMRD was $7,255,000. During calendar year 1975, 18 Ph.D, 3 Doctor of Engineering, and 22 M.S. degrees were awarded to MMRD students. One hundred and eighty-one journal articles were published by MMRD members during 1975.

The distinction of IMRD over the years and the effectiveness of its staff argued persuasively for retention of the IMRD administration structure and of Building 62 as Division Headquarters. Many important elements of MMRD are a direct outgrowth of IMRD: the strong materials science orientation, the interdisciplinary character, the annual review procedures, and this report, to name a few. We decided it best to issue this 1975 Report as an MMRD Annual Report, even though most of the work reported herein was in fact carried out in the separate components that were combined to form MMRD.

The Inorganic Materials Research Division was born in the post-Sputnik era, and its traditions and operating procedure reflected a strong academic basic-research orientation. The national attitude toward science was supportive and optimistic: basic research was fostered, and its growth was encouraged. The interdisciplinary character of IMRD, as well as its ability to combine the strengths of the Berkeley Campus and Lawrence Berkeley Laboratory, yielded many significant contributions to basic scientific knowledge and understanding. Nevertheless IMRD research had important--and at times dramatic--impact on the "real world" areas in which science affects the life of every citizen. It was unnecessary to stress these aspects of basic research, because they seemed to be widely appreciated.

Now the boundary conditions have changed. The Lawrence Berkeley Laboratory is funded by the Energy Research and Development Administration instead of the Atomic Energy Commission. The charter of ERDA is broader and its timetable is more demanding. It would be hard to imagine a greater scientific, technological, and social challenge than meeting America's energy needs during the last quarter of the twentieth century. Although the outcome is uncertain, this period is destined to mark a turning point in history. It is an exciting time to be alive and contributing to science and technology.

What are the implications for MMRD? Three conclusions can be drawn immediately:

1. The opportunities for basic research are greatly expanded by the broadened scope of ERDA's mission.

2. Applied science and engineering research opportunities abound in many areas that are both of importance to ERDA and covered by the expertise of MMRD investigators.

3. The diversity of ERDA, the breadth of MMRD, and the mood of the times necessitate investigators' taking more active roles than before in 'selling' their research ideas.

It is a pleasure to report that within the last few months MMRD investigators and staff have responded to these new challenges. Our investigators have made many trips to Washington, and almost every week someone in MMRD comes forth with a significant new research proposal for attacking a problem of interest to ERDA. It is particularly gratifying that a number of MMRD investigators are making serious studies of ERDA's most pressing problems, and are even helping to formulate ERDA programs. A continuing response of this nature will enable MMRD to play an increasingly important role in LBL and in ERDA.

The structure of MMRD includes some new features. A Divisional Council advises the Division Head on broad policy matters. The Council is represented by subject areas and its membership will rotate. Present members are Yuan Lee, Richard Marrus, Rolf Muller, Earl Parker, Alan Searcy, Y. Ron Shen, Gabor Somorjai, and Gareth Thomas. Most of the Division's basic research is conducted in the traditional format of a Principal Investigator, together with his assistants, attacking problems of a fundamental nature. To an increasing extent, however, another approach is emerging: that of a larger, more structured research group focusing its attention on specific applied research problems of particular relevance to ERDA. At this writing the

exact number and structure of these groups are not yet established, but several such groups are in their formative stages.

Among our Principal Investigators who have received awards and honors during 1975 were:

John Clarke and Y. Ron Shen were Miller Research Professors.

Marvin Cohen was Vice Chairman of the Solid State Division of the American Physical Society and will be Chairman in 1976.

John Conway was Chairman of the National Research Council/National Academy of Sciences Committee on Line Spectra.

Harold Johnston gave the U.C. Berkeley Gilbert N. Lewis Memorial Lecture on "Stratospheric Ozone and its Perturbation by Human Activities."

Yuan Lee was elected to the American Academy of Arts and Sciences.

William Miller received a John Simon Guggenheim Fellowship.

Joseph Pask was elected to the National Academy of Engineering.

Norman Phillips became dean of the College of Chemistry, July 1, 1975.

Alexander Pines was an Alfred P. Sloan Research Fellow.

Kenneth Pitzer was awarded the National Medal of Science--the U.S. Government's highest award for outstanding achievement in Science, Mathematics and Engineering.

David Shirley, in addition to being named an Associate Director of LBL and Division Head of MMRD, was chairman of the Division of Nuclear Chemistry and Technology of the American Chemical Society.

Gabor Somorjai was the Francis Clifford Phillips Lecturer, University of Pittsburg.

David Templeton was dean of the College of Chemistry until June 30, 1975.

Gareth Thomas is serving as Secretary-General of the International Federation of Electron Microscopy Society - 1974 through 1979.

Charles Tobias was selected as the first "BASF Renowned Scientist" Lecturer at Wayne State University, Detroit.

It is fitting and appropriate to finish this Introduction with a tribute to Professor Leo Brewer. MMRD embarks as a strong Division in large measure because of Leo Brewer's inspired leadership of IMRD over a fourteen-year period. His scientific leadership and administrative perspicacity, and most of all his system of values, provide a model for Division leadership that present and future administrations will do well to emulate.

David A. Shirley

A. METALLURGY AND CERAMICS

1. STRUCTURE OF MATERIALS

a. Microstructure, Properties and Alloy Design

Gareth Thomas, Principal Investigator

Structural Steels, Alloy Design

This program has been continuing with the objectives of producing high strength, tough, economical experimental steels by utilizing the martensitic transformation to obtain desirable microstructures. The principles and ideas behind the program have been described in previous reports. Applications involving energy considerations include (i) economy of materials selection, (ii) economy of processing, and (iii) development of superior properties for applications in the mining industry and for transportation. The program involves basic applications of phase transformations and microstructural analysis. The design ideas are directed towards achievement of properties through thermal processing alone (i.e., non-thermal-mechanical).

The following summarizes research work subsequent to that described in the 1974 annual report (*LBL-3530*). *I wish to acknowledge* continued support from industry for supplying (gratis) alloys designed to our specifications (especially Climax-Molybdenum Co., and Daido Steel Corp.).

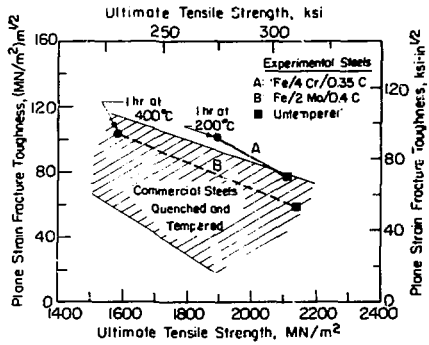

Fig. 1. Relationship between plane strain fracture toughness and ultimate tensile strength for two experimental ternary alloy steels developed recently. Note that the Fe/Cr/C steel has superior properties to the Fe/Mo/C steel and to other commercially available high strength steels, and 18Ni maraging alloys. Continuous films of stabilized interlath austenite could be identified in Fe/Cr/C steels whereas in Fe/Mo/C steels the amount, if any, was too small to be identified (Data from Refs. 1,2). (XBL 758-6866)

1. SIGNIFICANCE AND IDENTIFICATION OF RETAINED AUSTENITE IN STEELS

G. Thomas

Since the discovery of narrow films of untransformed austenite around martensite laths and packets by electron microscopy[1] it has become evident that this austenite, if thermally and mechanically stable, appears to convey improved K_{Ic} toughness (sharp notch) properties. This becomes evident by comparing the properties of experimental Fe/4Cr/0.35C,[1] Fe/2Mo/0.4C[2] steels and commercial steels[3] at the same strength levels, as shown in Fig. 1. It is evident that identification of retained austenite is a necessary and important aspect of research on steels. In the structural steels the retained austenite is severely deformed and in most cases the amount is so small that detection by x-ray analysis becomes impossible. However, sophisticated electron microscopic techniques involving carefui selected area diffraction, bright field and dark field imaging can unequivocally establish the presence of such small quantities of austenite.[4] Extremely useful morphological and microstructural information on the austenite can also be obtained from the electron metallography. Careful choice of orientation and dark field analysis is essential (Fig. 2) if austenite is to be uniquely identified and not confused with, e.g., carbides.

Figure 3 illustrates the systematic identification of retained austenite occurring at the lath boundaries of martensite. Commonly, the martensitic (α) laths in a packet occur in alternate $\langle 111\rangle_\alpha$ and $\langle 100\rangle_\alpha$ orientations. By tilting carefully, the thin films of austenite are brought into good diffracting condition whereby they appear light in the DF picture of Fig. 3(b). The diffraction pattern for the matrix and for the austenite correspond to a nonsymmetrical orientation and only $(002)_\gamma$ and $\{110\}_\alpha$ reflections are strongly excited. The DF picture [Fig. 3(b)] is obtained from $(002)_\gamma$ reflection whereby only the austenite reverses contrast. Also faint streaking in the diffraction pattern is discernible at $\{110\}_\alpha$, reflecting along a direction normal to the γ film, indicating that these films are indeed very thin. Often, however, the unequivocal identification of the austenite phase is complicated by the presence of reflections from auto-tempered carbides, from martensite substructure (twinning) and double diffraction. At 100 kV spherical aberration limits

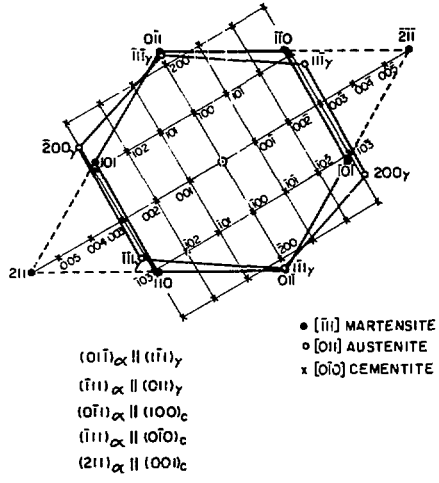

Fig. 2. Calculated electron diffraction pattern for martensite in [$\bar{1}$11] with retained austenite and Widmanstatten cementite. (XBL 758-6830)

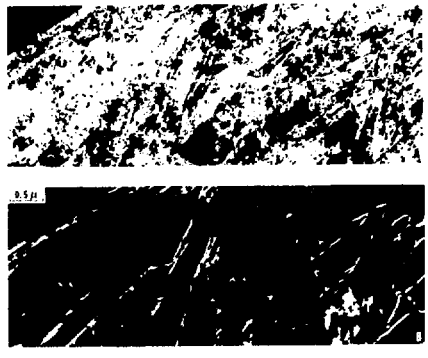

Fig. 3. Bright-field image (a) and dark field image (b) of an Fe/1Cr/1Mo/0.3C steel quenched from 870°C into ice water. Note that the interlath retained austenite films do not show good contrast in the bright field image, but are very clear in the (200)$_\gamma$ dark-field image. This is not always the case, but it serves to illustrate the importance of the proper dark field imaging. Courtesy Y.-L. Chen. (XBB 758-5825)

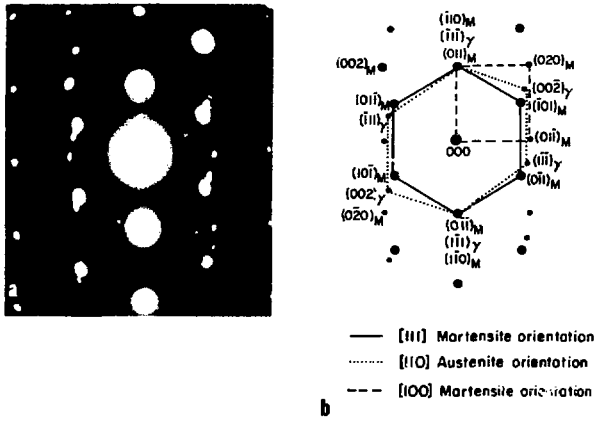

Fig. 4. The common orientation relationship observed between lath martensite and retained austenite in all the steels. The SAD pattern (a.) and the analysis (b.) show the Kurdjumov-Sachs orientation relationship viz., $[110]_\gamma \parallel [111]_M$, $(1\bar{1}1)_\gamma \parallel (1\bar{1}0)_M$ observed between bcc martensite and fcc γ. (XBB 755-3495)

SAD resolution to 2 μm, independent of the aperture size. The indexed SAD pattern of Fig. 4, which is obtained from a different area, clearly illustrates the most common orientation relationship (K-S) observed between α and γ (of Fig. 2).

Similar to earlier observations,[3] retained γ has also been identified conclusively in steels subjected to low temperature (~ 900°C) austenitizing treatments. In addition, extremely narrow interlath films of stabilized γ have been identified in Fe/0.5Mn/0.1C steel, which is quite surprising, since the occurrence of this phase in such low carbon steels has been overlooked by earlier investigators. Due to preferred orientation within a given martensite packet, x-ray analysis may not detect these small quantities, depending on prior γ grain size. While the amount of retained γ in a steel can vary with the heat treatment it received, its occurrence seems to be a rule rather than an exception, and its detection requires sophisticated electron metallography.[4]

1. J. McMahon and G. Thomas, Proc. Int. Conf. "Microstructure and Design of Alloys", Cambridge, Institute of Metals (London) 1, 180 (1973).
2. R. A. Clark and G. Thomas, Met. Trans. 6A, 969 (1975).
3. G. Y. Lai, W. E. Wood, R. A. Clark, V. F. Zackay and E. R. Parker, Met. Trans. 5, 1663 (1974).
4. B. V. N. Rao, J. Y. Koo and G. Thomas, Proc. EMSA 1975, p. 30 (Claitons Publishers, 1975), LBL-3771.

Fig. 1. Carbon in solution and martensite packet size are the two most important parameters influencing intergranular quench cracking in Fe/4Cr/0.4C steel, viz., an increase in either causes an increase in the transformation strains and the resultant impingement stresses of two growing martensitic packets. Conventional high temperature austenitization followed by quenching (Fig. A) invariably leads to intercrystalline cracking due to the large martensite packet size and the carbon being entirely in solution. After this treatment the steel failed prematurely at 200 ksi and at zero elongation. Conventional grain refinement, involving repeated austenitization and quenching (Fig. B) does not result in any significant improvement in mechanical properties since intergranular cracks produced during first quenching do not heal on subsequent heating. Although the transformation strains are reduced in the interrupted-quenched specimen (Fig. C), the intercrystalline cohesion remains poor because of the large martensite packet size. The specimen after this treatment does, however, yield plastically followed by failure at 270 ksi. When this specimen was re-austenitized at 900°C to refine the grain size (Fig. D), a substantial improvement in mechanical properties is achieved. A tensile strength of 335 ksi and a 6% elongation have been obtained. In this case, although the specimen retained most of the carbon in solution, the much reduced martensite packet size resulted in elimination of intergranular cracks. Courtesy of B. V. N. Rao. (XBB 757-5666)

2. HEAT TREATMENT, MICROSTRUCTURE AND MECHANICAL PROPERTIES OF EXPERIMENTAL HIGH STRENGTH Fe-4Cr-0.4C STEELS*

B. V. Narasimha Rao,† R. W. Miller‡ and G. Thomas

In a continuing program on alloy design of experimental structural steels,[1,2] the present investigation of the structure and properties of lower bainite and martensite of the simple ternary Fe-4Cr-0.4C steel is taken up since a similar martensitic alloy (but with a lower carbon content, viz., 0.35%) yielded superior mechanical properties even in the untempered condition.[3] The increase of carbon from 0.35 to 0.4% has the potential of economically raising the yield strength of the steel to 300 ksi, but the steel is then prone to embrittlement; hence the challenge is to eliminate such embrittlement.

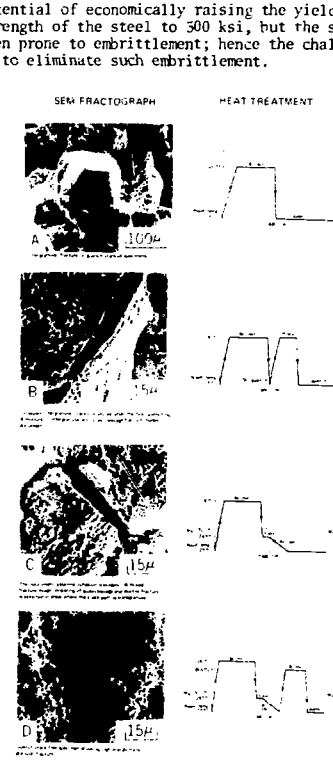

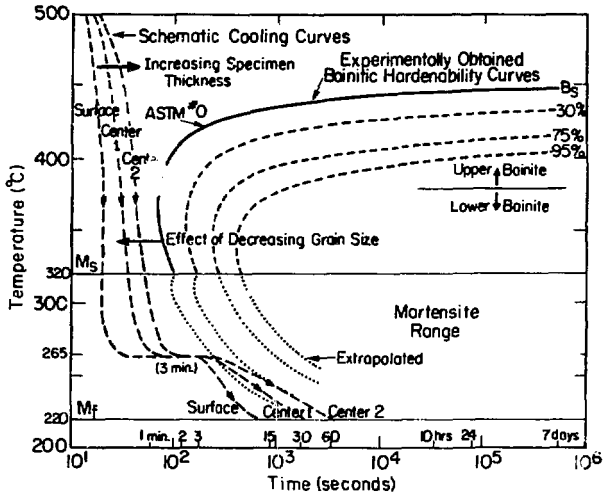

Fig. 2. Isothermal transformation diagram for the Fe-4Cr-0.4C steel. (XBL 7511-7577)

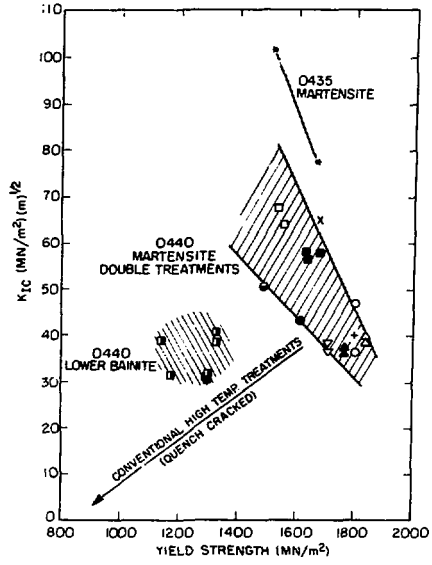

Fig. 3. Plot of plane strain fracture toughness vs. yield strength. (XBL 754-6180A)

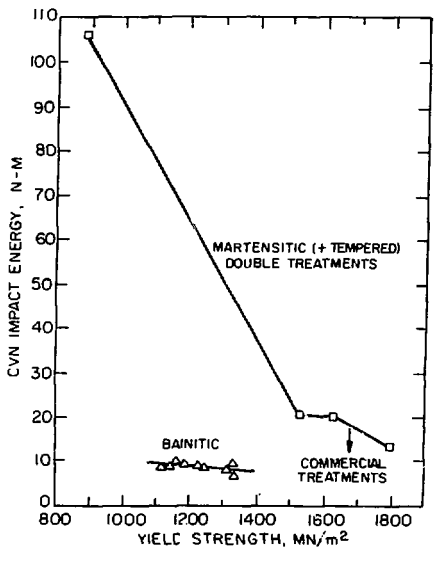

Fig. 4. Plot of Charpy impact energy vs. yield strength. (XBL 754-6181A)

Though a considerable amount of research in the past has been directed to the design and development of strong, tough new steels through often expensive adjustments in composition, comparatively little work has been done on the effective use of modifications in conventional heat treatment practices so as to produce desirable morphological and substructural features.

New double heat-treatments have been designed in order to avoid intergranular cracking in the as-quenched structures and to take advantage of both a higher austenitizing temperature and fine austenite grain size.[4] These treatments involve high temperature (1100°C) austenitizing during the first solution treatment followed by either interrupted quenching (Ms-Mf range) or isothermal transformation to produce lower bainite. Finally, the steels are given a 900°C grain refinement treatment. These treatments are illustrated in Fig. 1. Lower bainite was obtained by isothermally transforming austenite just above the Ms temperature (Fig. 2). Tempering after the martensitic and bainitic treatments was also done in an attempt to improve the toughness of the material.

The strength and toughness properties of as-quenched martensitic structures are somewhat superior while these properties of lower bainitic structures are comparable to those of a plain 0.4%C steel. After the multiple treatments, however, the quenched and tempered Fe/4Cr/0.4C steel is far superior to the bainitic one. These properties are summarized in Figs. 3 and 4.

*Invited paper for International Conference on Heat Treatment, Stratford, U.K. (May 1976), LBL-3982.

†M.S. Thesis (1975), LBL-3794.

‡R. W. Miller is now at Rockwell International, Materials Testing Division, Downey, California.

1. G. Thomas, Iron and Steel Int. 46, 451 (1973).
2. G. Thomas, LBL-4175.
3. J. McMahon and G. Thomas, Microstructure and Design of Alloys (Inst. of Metals, London) 1, 180 (1973).
4. B. V. N. Rao and G. Thomas, Mat. Sci. & Eng. 20, 195 (1975).

3. STRUCTURE AND MECHANICAL PROPERTIES OF EXPERIMENTAL Fe-1Cr-1Mo-0.25C ALLOYS WITH AND WITHOUT BORON*

Y. L. Chen†

A study of the microstructure and mechanical properties of martensitic steels with and without boron addition has been carried out because although boron has been known to be a very potent element in increasing the hardenability of steel, its effect on the structure and mechanical properties of martensitic steels is not clear. The results show that the as-quenched structures of both steels consist mainly of dislocated martensite. In the boron-free steel there are more lath boundary retained austenite films.

a. Conventional Treatments

The mechanical properties of these steels are shown in Figs. 1 and 2. The boron-treated steel shows higher strengths at all tempering temperatures but with lower Charpy V-notch impact energies. Both steels show tempered martensite embrittlement when tempered at 350°C for 1 hour, but the properties above 500°C tempering temperature are significantly different in the two steels. Above 500°C tempering temperature the boron-treated steel shows better strength but lower impact toughness. Transmission electron microscopy shows that in the 600°C tempered boron-treated steel, gross cementite particles precipitate at the lath boundaries, which are probably responsible for embrittlement. Thus although there is little difference in mechanical properties between steels with and without boron addition at high strength levels, the boron treated steel has substantially inferior impact toughness at lower strengths.

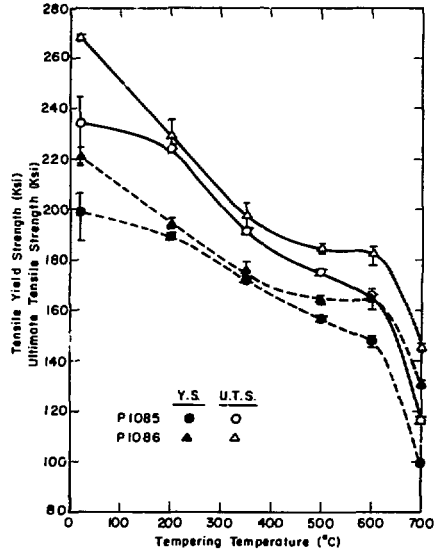

Fig. 1. Strength variation with tempering temperature. (XBL 749-7335)

b. Double Treatments

Figure 3 shows the strength-toughness characteristics of these experimental steels, both with and without boron compared to previous work on Fe/Mo/C steels.[1] As one of the alloy development

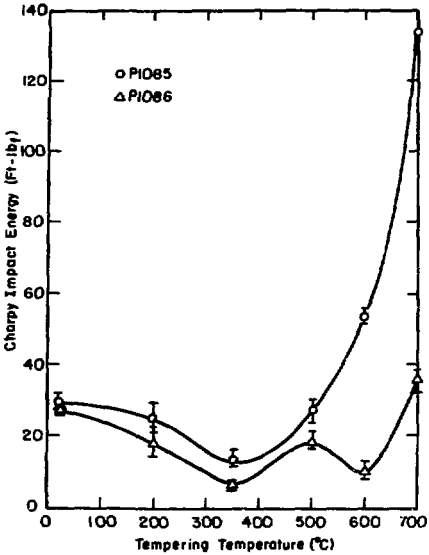

Fig. 2. Charpy impact energy variations with tempering temperature. (XBL 749-7537)

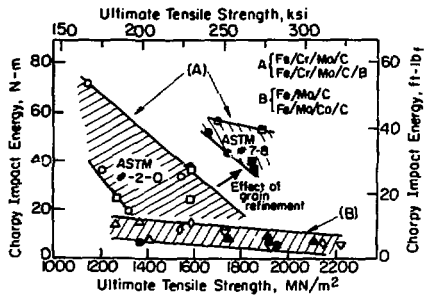

Fig. 3. Toughness-strength characteristics of the experimental steels. Also shows data from Fe-Mo-C alloys.[1] (XBL 758-6866)

programs in this research group, several experimental grain refinement treatments have been developed. In Fig. 4, a comparison of Charpy impact energy values of the experimental steels (grain refined) with several commercial high strength steels is shown. It is quite obvious that

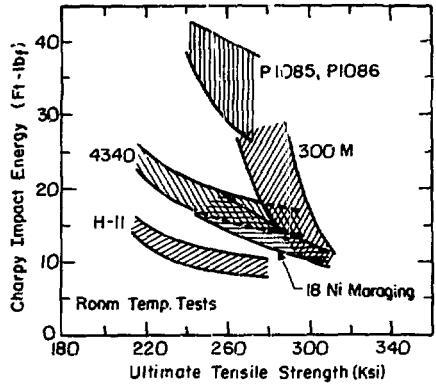

Fig. 4. Comparison of Charpy impact energy values of the experimental steel with several commercial high strength steels (data from AFML-TR-71-27). (XBL 7512-10,011)

the strength-toughness characteristics of the experimental steels are considerably better than the commercial high strength steels. These results are very encouraging for applications of HSLA steels.

---

*We acknowledge the Climax Molybdenum Corp. for supplying these alloys to our design specifications.

†Ph.D. Thesis, LBL Report # 5179.

1. R. A. Clark and G. Thomas, Met. Trans. 6A, 969 (1975).

4. THERMAL CYCLING TREATMENTS AND MICROSTRUCTURES FOR IMPROVED PROPERTIES OF Fe-0.12%C-0.5%Mn STEELS*†

J. Y. Koo‡ and G. Thomas

a. Summary

A non-standard heat-treating process has been investigated with the aim of improving the mechanical properties of low carbon Fe-0.12%C-0.5%Mn steels. The process consists of alternate thermal cycling in the γ range and two phase (α + γ) range with intermediate quenching so as to produce a microduplex fine-grained mixture of martensite and proeutectoid ferrite. Some retained austenite is also present. This heat-treatment cycle is illustrated in Fig. 1, and the microstructure is in Fig. 2. These structures were characterized using optical and transmission electron microscopy.

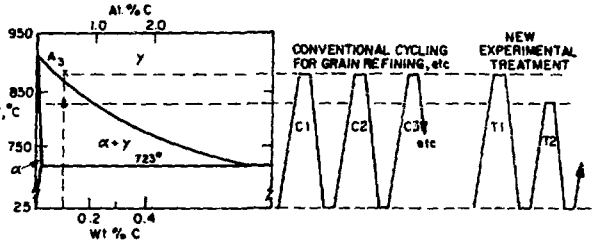

Fig. 1. Diagram showing principle of heat-treatment to produce martensite dispersions in ferrite the conventional grain refining cycling is also shown in comparison to that following two phase annealing.

(XBL 758-6925A)

Fig. 2. Electron micrograph showing dislocated martensite and ferrite in doubly treated "INNA" steel. Some heterogeneous precipitation occurs on dislocations in the ferrite especially after tempering.

(XBB 751-755)

The microduplex structures and the related tensile properties resulting from the heat treatment were compared with those from conventional and rapid heat treatment methods. The tensile properties of the microduplex structures are related to the volume fractions of ferrite and harder martensite phases as a composite, and the refined grain size. Considerable increases in strength are obtained as shown in Fig. 3. These results indicate the potential for utilizing these heat treatments for strengthening, in the finishing process, of steels useful in the transportation industry where weight savings and fuel savings are of prime significance.

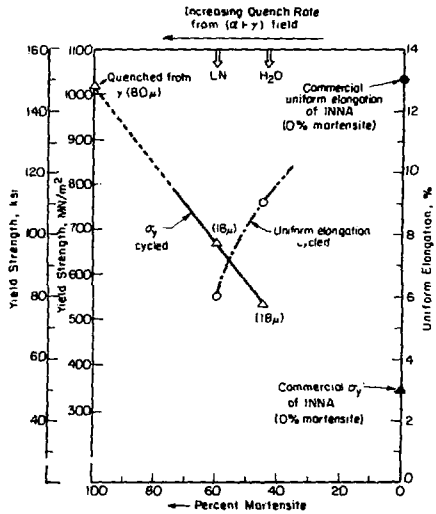

Fig. 3. Summary of mechanical properties of "INNA" steel showing influence of volume fraction of martensite and grain size.

(XBL 757-6818)

---

*We acknowledge Dr. D. J. Bailey of General Motors who provided the steels used in this research.

†Mat. Sci. and Eng. 24, 187 (1976).

‡M.S. Thesis (1975), LBL-3587.

5. PRECIPITATION OF TiC IN THERMALLY EMBRITTLED MARAGING STEELS*

E. Nes† and G. Thomas

It is shown that maraging steels can be embrittled by the precipitation of TiC during slow cooling and/or intermediate annealing in the austenite temperature range. It can also be especially problematic in castings. An important aspect in this embrittlement is the occurrence of discontinuous precipitation of TiC at the austenite grain boundaries, generating a cellular structure of large fern-leaf-like carbides. Within the austenite grains a non-uniform distribution of irregularly plate-shaped TiC particles are formed with {100} austenite habit orientation. Quenching to martensite prior to any intermediate anneals changes the carbide distribution upon subsequent annealing treatments into a fine dispersion of TiC particles. The embrittlement resulting from the various isothermal annealing treatments in the austenite temperature region could all be directly related to the carbide distribution in the prior austenite grain boundary region.

*E. Ness and G. Thomas, Met. Trans. 7A, 967 (1976).

†Permanent address: Central Institute for Industrial Research, Blindern, Oslo 3, Norway.

6. METALLOGRAPHY OF BAINITIC TRANSFORMATION IN SILICON-CONTAINING STEELS*

Der-hung Huang† and G. Thomas

The formation of carbide in lower bainite was studied in two silicon-containing carbon steels by transmission electron microscopy and diffraction techniques. Epsilon carbide was identified in the low temperature, isothermally transformed bainite structure. The crystallographic relationship between epsilon carbide and bainitic ferrite was found to follow the Jack orientation relationship, viz., $(0001)\varepsilon \parallel (011)\alpha$, $(10\bar{1}1)\varepsilon \parallel (10\bar{1})\alpha$. The cementite observed in lower bainite was in the shape of small platelets and obeyed the Isaichev orientation relationship with the bainitic ferrite, viz., $(010)c \parallel (1\bar{1}1)\alpha$, $(10\bar{3})c \parallel (011)\alpha$. Direct evidence showing the sequence of carbide formation from austenite in bainite has also been obtained and is illustrated in Fig. 1. Based on these observations and all the crystallographical features, it is strongly suggested that in silicon-containing steels, the bainitic carbide precipitated directly from austenite instead of from ferrite at the austenite/ferrite interface as has been proposed by Hehemann, Kinsman and Aaronson.[1] The uniformity of the carbide distribution is thus envisaged to be the outcome of precipitation at the austenite-ferrite interphase boundary.

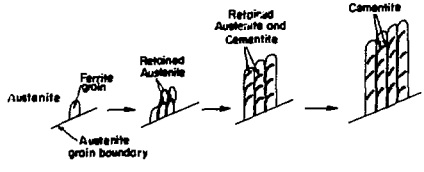

Fig. 1. Schematic drawing of bainite forming in silicon containing steel showing the nucleation of ferrite lath and a thin layer of carbon enriched austenite is retained in contact with the ferrite lath. The austenite subsequently decomposes into cementite and ferrite. In the absence of silicon the decomposition of retained austenite is very fast and the formation of retained austenite may be by-passed without being noticed. (XBL 752-5777)

*Submitted to Met. Trans.

†Ph.D. Thesis, LBL-3713.

1. R. F. Hehemann, K. R. Kinsman and H. I. Aaronson, Met. Trans. 3, 1077 (1972).

7. THE MICROSTRUCTURE OF NITRIDED Fe-0.3 Wt% Ti ALLOY ANNEALED AT 800°C*

D. H. Kirkwood† and G. Thomas

Iron-titanium specimens (containing 0.27 Wt% Ti) were nitrided at 600°C to form a fine precipitate within the grains, and subsequently were annealed at 800°C to promote precipitate coarsening. The microstructure was examined by electron microscopy, and precipitate size and coherency strain were measured as a function of aging time. In the very early stages of aging, a large coherency strain (~ 50%) is observed in the matrix around the small platelets lying on $\{100\}_\alpha$ planes which indicates that the precipitate is fcc TiN. The electron diffraction evidence supports this conclusion, and it is argued that TiN is also the initial product of nitriding. The disposition of platelets between the three possible orientations appears to be quite random in this alloy. Some preferred precipitation on dislocations is apparent but not on grain boundaries.

*D. H. Kirkwood and G. Thomas, Met. Trans. 7A, 764 (1976)

†Permanent address: Department of Metallurgy, Sheffield University, Sheffield, United Kingdom

8. THE MINIMIZATION OF ELASTIC STRAIN ENERGY AS A METHOD OF HABIT PLANE CALCULATION FOR SHEAR TRANSFORMATIONS*

D. R. Clarke

A new approach to the problem of calculating the habit planes of a transformed product phase has been developed. In essence it is to determine the

elastic strain energy generated during the transformation and then to find the orientation and shape of the product that minimizes the total energy. An important advantage of this approach is that it not only predicts the habit plane, but in doing so also determines the shape of the transformed phase and gives a numerical value to the strain energy accompanying the transformation.

The elastic strain energy is calculated by use of Eshelby's method for the solution of the transformation problem with the assumption that the transformed phase is ellipsoidal in shape. This elastic energy minimization is directly related to the phenomenological crystallographic theories. In the particular case of a transformation having an invariant shear plane, the elastic strain energy of an oblate spheroid is at a minimum when its long axes lie in the plane of invariant shear.

To demonstrate the application of the approach the habit planes of martensitic plates in In-20%Tl and Fe-31%Ni, which can be calculated by other methods, are alternatively determined by this method. In addition, for the first time, the habit plane for the martensitic transformation that occurs in oriented, bulk, high-density polyethylene has been calculated.

To illustrate the type of results created, Fig. 1 is included here. This is for the martensitic transformation in Fe-31%Ni of an oblate spheroidal plate of aspect ratio 0.05. The black dots mark the experimental mid-rib plane determinations made by Breedis and Wayman and the inverted triangles denotes the calculated position of minimum strain energy. The value of the elastic strain energy per unit volume at this point, which is close to 5, 13 and 18, is 8.9×10^{-2} μ, where μ is the shear modulus of the austenite. In addition, contours corresponding to 101% (solid line) and 105% (dashed line) of the minimum energy are also marked. These contours represent the angular range over which the habit plane would be found if energy perturbations of 1% and 5% above the mimimum energy value occurred during the formation of the phase. As can be seen from the figure, the scatter in the observed habit planes can be adequately described by energy fluctuations of less than 1% present during the formation of the martensitic plates. This

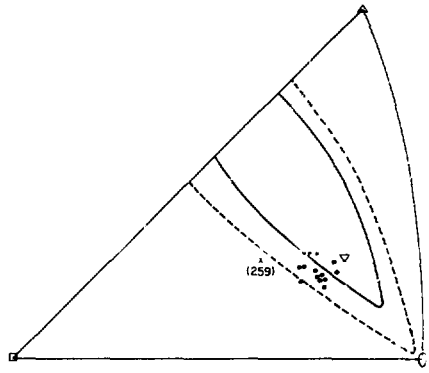

Fig. 1. Stereogram depicting the predicted habit plane (V-close to 5,13,18) and the 101% and 105% (dashed line) of minimum energy contours calculated for Fe-31%Ni using an aspect ratio of 0.05. Also shown (in dots) are the martensite mid-rib plane determinations made by Breedis and Wayman[1] on Fe-30.9%Ni and Fe-31.1%Ni specimens. (XBL 751-5436)

illustrates one of the advantages of the methodology; for the first time it is possible to make a quantitative estimate of the difference in strain energy corresponding to the various individual habit planes within a scatter of determinations.

It is a consequence of these calculations that for the transformations considered, the elastic strain energy is greater than the typical surface energies involved which suggests that the minimization of the strain energy term must dominate even at the earliest stages of the formation of the transformed phase.

---

* D. R. Clarke, Met. Trans. 7A, 723 (1976)

1. J. F. Breedis and C. M. Wayman, Trans. AIME, 224, 1128 (1962).

b. Ceramic Alloy Program

Gareth Thomas, Principal Investigator

A) FERRITES: HIGH VOLTAGE ELECTRON MICROSCOPE STUDIES OF CERAMIC FERRITES

It is now appreciated that the principal advantages of HVEM are 1) increased penetration, 2) increased resolution, 3) decrease in inelastic scattering (and thus bond-breaking damage), and 4) special effects due to multiple beam interactions, e.g., critical voltage, increased resolution of lattice defects using high order bright field imaging, etc. Some examples of applications have been reviewed recently.[1] The knock-on damage effect can be advantageous or not; its effect clearly limits the maximum voltage that can be used if knock-on damage is undesirable. As a result of these advantages we are now able to study difficult to thin and beam sensitive materials, e.g., ceramics and polymers. In our research emphasis is placed on studies of defects and phase transformations in ceramic ferrites.

We are interested in the ferrites because of their great commercial importance due to their unique magnetic and electronic properties. Both hard and soft ferrites are extensively used in manufacturing microwave device components, computer cores and permanent magnets. Ferrimagnetic oxides with spinel structure form an important class of the ferrites. Conventionally, grain size and porosity have been used for controlling properties in these materials, but it is very likely that heat treatments producing appropriate microstructures could lead to highly desirable properties. Thus the HVEM is essential to obtain basic structural information if progress is to be made in ceramics comparable to that in physical metallurgy. In a continuing program on microstructural characterization in these materials, studies of phase transformations such as ordering and precipitation reactions as well as analysis of defects have been carried out with particular emphasis to lithium ferrite ($LiFe_5O_8$) spinel. The results are given in the following.

1. PHASE TRANSITION STUDIES

a. Dynamic Studies of Order-Disorder in $LiFe_5O_8$ (1 MeV)

O. Van der Biest

Lithium ferrite ($LiFe_5O_8$) is a ferrimagnetic compound with some interesting technological properties.[2] Many of the properties of interest are influenced by the degree of order in the compound. The most important of these is the DC electrical resistivity which changes by several orders of magnitude upon ordering. Other properties such as the ferrimagnetic resonance line-width, the magneto-crystalline anisotropy constants and, for polycrystalline samples, the squareness of the hysteresis loop are all influenced to a lesser degree by the state of order.

In the disordered state the compound has the inverse spinel structure with a random mixture of $1Li^{+}$ and $3Fe^{3+}$ on the octahedral sites (space-group $Fd\bar{3}m$). Below 750°C the lithium ions and iron ions on the octahedral sites order and the space group symmetry is lowered to $P4_132$ ($P4_332$). The resulting domain structure has been described in detail by Van der Biest and Thomas.[3]

The kinetics of the ordering reactions have been studied in single crystals "in situ" in the hot stage of a HVEM. Annealing in the normal atmosphere of the microscope leads to a reduction of the compound in a way similar to that found for $CoFe_2O_4$.[4] In order to control the stoichiometry of the compound during the ordering reaction, it is necessary to maintain an oxygen atmosphere around the specimen, hence the use of a "environmental" cell is necessary. In this study the environmental cell designed by Swann[5] for the Imperial College HVEM was used. An oxygen pressure of 40 Torr was found to be high enough to prevent rapid reduction of the compound and low enough to have sufficient penetration and contrast in the images. Radiation damage definitely played a role during the experiments. Prolonged focusing of the beam (> 10 min) on one spot caused voids to nucleate and grow until holes were formed. It was also observed that the amount of damage was proportional to the time the specimen had spent above the ordering temperature. This suggests that the rate of damage is an order of magnitude larger in the disordered state for approximately the same temperature. The specimen was heated above Tc to about 770°C and then cooled as fast as the stage permits, to temperatures slightly below the ordering temperature (735°C-745°C). The changes in microstructure were followed in dark field with a superlattice spot. Images were recorded with a low light level TV system on video with a speed of 25 frames/sec. Figure 1 shows a disordering sequence. It can be seen that disordering starts at the anti-phase boundaries, which are replaced by a layer of disordered material. The domains subsequently shrink and disappear if heating is slow or the contrast may fade uniformly before the domains can disappear by shrinking. Figure 2 shows an ordering sequence. Individual domains can be seen nucleating and growing, until they impinge and form anti-phase domain boundaries.

The ordering reaction provides an example of the phase transformation with homogeneous nucleation and perfectly spherical growth. Studies of the nucleation rate as a function of undercooling indicate that the rate of nucleation follows the pattern predicted by the classical theory of homogeneous nucleation. Within a small range of undercooling, the nucleation rate increases by orders of magnitude. The growth rate of the domain is perfectly constant, until the domains touch one another. The growth rate as a function of undercooling was found to exhibit a maximum. This

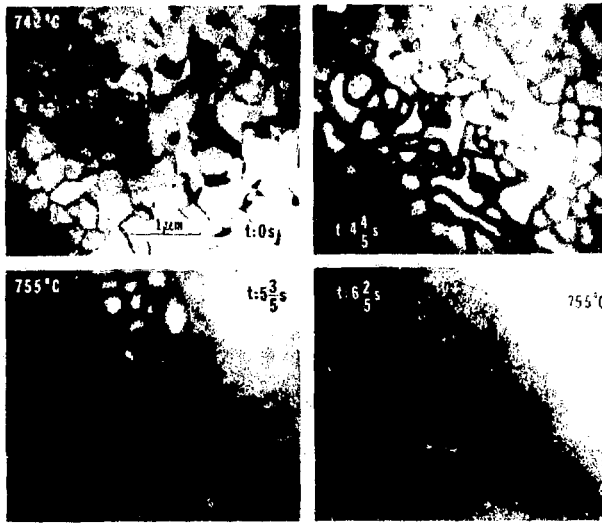

Fig. 1. Disordering sequence in situ at 1 MeV under 40 Torr oxygen pressure. Disordering nucleates at ABP's. Dark field image of 1/2 superlattice spot. (XBB 753-2230)

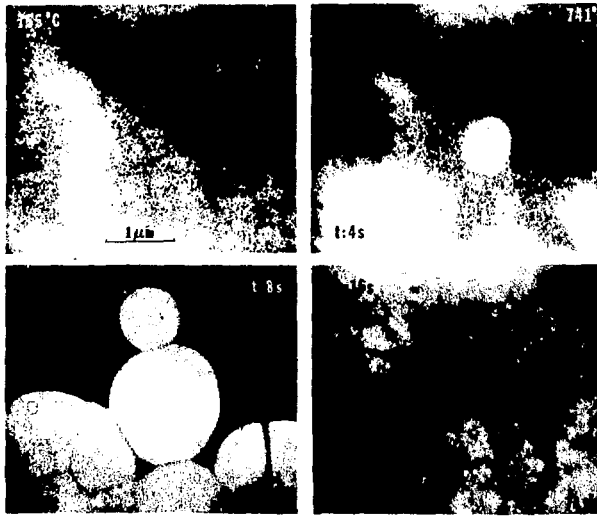

Fig. 2. Ordering sequence followed dynamically in situ at 1 MeV, as in Fig. 1. Dark field images of the 1/2 superlattice spot. (XBB 753-2231)

agrees with the theory of thermally-activated growth, where atomic processes at the interface are rate controlling. The mobility of the boundaries which form when two domains touch was immeasurable on the time scale of the experiments.

(We are indebted to Dr. P. R. Swann for the use of the 1 MeV microscope at Imperial College and Dr. E. P. Butler for help with these experiments. The National Science Foundation provided a travel grant to allow O. Van der Biest to use the Imperial College instrument.)

b. High Temperature Phase Transformation in $LiFe_5O_8$ (650 kV)

R. Mishra

In addition to the order-disorder phase transition at about 750°C in $LiFe_5O_8$, at higher temperature there occurs a precipitation reaction. This transformation was studied at 1200°C in air and in vacuum (10^{-5} Torr). Specimens for HVEM observation were prepared from the center of 15 mil thick heat-treated single crystal discs using the ion bombardment technique.

The microstructure for short annealing times consists of small octahedral precipitates dispersed in the spinel matrix as shown in Fig. 3a. The precipitate phase has been identified to be lithium ferrate ($LiFeO_2$) having a NaCl structure and lattice parameter 4.14 Å (a_{spinel} = 8.33 Å). Computations of interfacial energy and strain energy for these particles show that the most favorable shape would be an octahedron with {111} crystallographic planes as faces. In terms of the structure of the two phases, this amounts to the oxygen layers in the spinel and the precipitate being indistinguishable and the only difference is in the cation distribution in the interstices. For longer annealing times, these particles grow and become semicoherent (Fig. 3b), when their average size exceeds 2500 Å. The dislocations at the interfaces have Burgers vectors parallel to ⟨110⟩. Measurement of the separation between the interfacial dislocations give their magnitude to be 1/2⟨110⟩ for a lattice misfit of 0.6%. The $LiFeO_2$ phase has been observed to transform to a spinel phase for very long aging times. The available phase diagram on Li_2O - Fe_2O_3 system cannot explain this formation of $LiFeO_2$ from nearly stoichiometric $LiFe_5O_8$.

The formation of a glassy phase has been observed both in air and in vacuum. The glassy particles form very rapidly in vacuum-annealed specimens while they do not form in the air-annealed specimens until the $LiFeO_2$ phase has transformed back to spinel. Figure 4a is the microstructure obtained after prolonged annealing in air, and Fig. 4b shows preferential growth of the glassy phase at the $LiFe_5O_8$ - $LiFeO_2$ interface in vacuum. We believe that this phase is due to the presence of residual flux in the flux grown spinel single crystals.

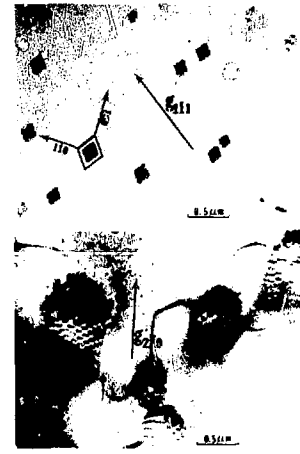

Fig. 3. a) Octahedral precipitates of $LiFeO_2$ in $LiFe_5O_8$, imaged near the (110) pole. b) Growing $LiFeO_2$ precipitates with semicoherent interfaces. (XBB 753-2454)

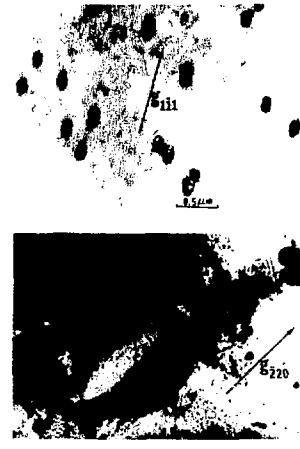

Fig. 4. a) Glassy particles dispersed in lithium spinel phase. b) Preferential growth of glassy phase at $LiFeO_2$-$LiFe_5O_8$ interface. Note the elongated $LiFeO_2$ particle morphology parallel to [220]. (XBB 757-5807)

2. STUDY OF THE DEFECTS (650 kV)

a. The Study of Stacking Faults in Nickel Ferrite

M. Kao

The ferrimagnetic $NiFe_2O_4$, with an inverse spinel structure possess a high Curie temperature (580°C) along with low dielectric loss[2] and is one of the commercial ferrites used in high speed computer memory units. Electron microscopy observation of some sintered fine grain polycrystalline $NiFe_2O_4$ samples has shown cation faults in most grains. Due to the very small grain sizes of many commercial ferrites, contrast analysis becomes difficult and tedious. However, analysis of a threefold junction shown in Fig. 1 is possible using ⟨131⟩, ⟨220⟩ and ⟨151⟩ sets of reflections in our 650 kV microscope due to our large angle double tilt stage. The results confirm that the faults are on {110} with 1/4⟨110⟩ fault vectors normal to the fault planes. This fault configuration is similar to that reported for $LiFe_5O_8$.[6] It may be noted that faults in {001} planes, reported for the normal spinel $MgAl_2O_4$ [9] have not been observed in any of these inverse spinels.

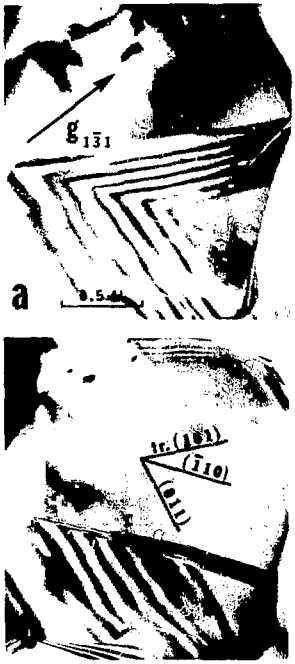

Fig. 1. Cation faults in polycrystalline nickel ferrite ($NiFe_2O_4$). The threefold fault junction is inside a grain. a) $g = 1\bar{3}1$, b) $g = \bar{1}3\bar{1}$.
(XBB 7511-8375)

b. Cation Faults in Lithium Ferrite: New Contrast Result

R. K. Mishra

In flux grown $LiFe_5O_8$ single crystals as well as sintered nickel ferrite polycrystal cation faults with $\alpha = \pm\pi$ have been observed, and have been characterized as {110}1/4⟨110⟩ growth faults.[6] Also, in our laboratory, faults with $\alpha = \pm\pi$ have been observed in sintered silicon carbide polycrystals. Special contrast effects occur for $\alpha = \pm 2\pi/3$ faulting in dark field images in $\pm g$ and $\pm 2g$, satisfied for systematic reflections and have already been described.[7] Similar imaging conditions can be used for rapid determination of the fault plane by identifying the top and bottom of the fault plane even when $\alpha = \pm\pi$. Figure 2a and 2b are D. F. pictures taken with g and -g, respectively, when 2g is excited. The computed fringe profiles for the two cases are shown in Figs. 2c and 2d. While the contrast difference in g and 2g is not very pronounced, the fringes in the -g and 2g condition show pronounced contrast corresponding to the bottom of the foil. The result has been confirmed by determining the actual fault plane from detailed contrast experiments.

c. Dissociated Dislocations and Stacking Fault Energy in $LiFe_5O_8$

R. K. Mishra

The multibeam dynamical interaction effect giving rise to increased resolution in B.F. images when a high order reflection in a systematic row is excited[7] has been used to resolve the partial dislocations in disordered lithium ferrite spinel. Figure 3 shows the B.F. micrograph along with a microdensitometer trace and the computed image profile for the two partials with $\alpha = 1/4\ 0\bar{1}1$. The dissociation can be represented as $1/2[011] = 1/4[011] + 1/4[011]$ on the $(01\bar{1})$ plane connected by a stacking fault 220 Å wide in the cation sublattice. The splitting here corresponds to a stacking fault energy of about 75 ergs/cm^2. Computation for inverse spinel gives a value of 80 ergs/cm^2 for lithium spinel.[8] This is the first time a stacking fault energy has been measured for an inverse spinel.

1. G. Thomas, Physical Aspects of Electron Microscopy and Microbeam Analysis, eds. B. M. Siegel and D. R. Beaman (1975), p. 81.
2. K.-H. Hellwege and A. M. Hellwege (eds.), Magnetic and Other Properties of Oxides and Related Compounds, Landolt-Bornstein Tables, III/4 (Springer-Verlag, 1970).
3. O. Van der Biest and G. Thomas, Acta. Cryst. A31, 70 (1975).
4. L. C. DeJonghe and G. Thomas, Mat. Sci. & Eng. 8, 259 (1971).
5. P. R. Swann, Electron Microscopy and Structure of Materials, eds. G. Thomas, R. Fulrath and R. Fisher (University of California Press, 1972), p. 878.

6. O. Van der Biest and G. Thomas, Phys. Stat. Solidi 24, 65 (1974).
7. L.J. Chen and G. Thomas, Phys. Stat. Solidi 25, 193 (1974).
8. R.K. Mishra, Ph.D. Thesis, in progress.
9. M.H. Lewis, Phil. Mag. 14, 1003 (1966).

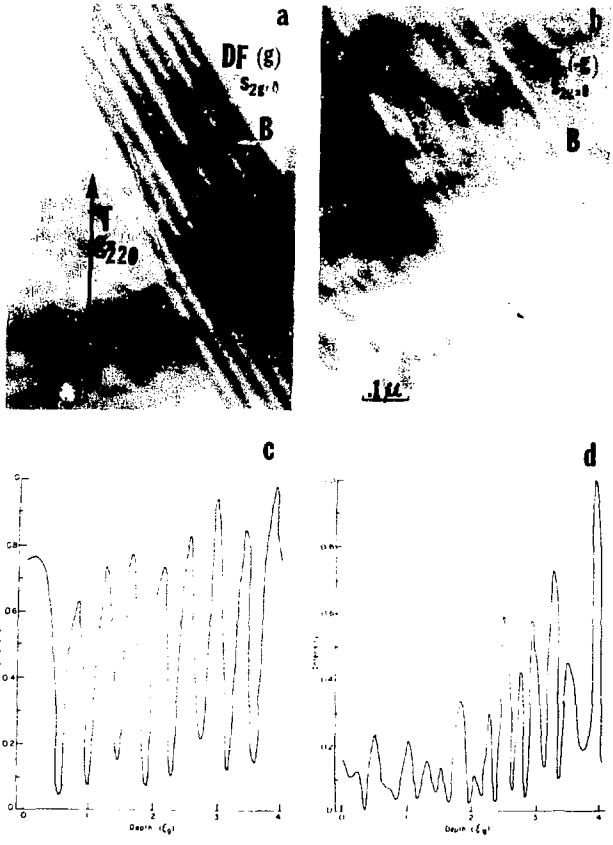

Fig. 2. D. F. image of cation faults in $LiFe_5O_8$, $s_{2g} = 0$; a) image of g, b) image of -g; c) and d) corresponding computed profiles (eight beam systematic (220)). (XBB 758-5878)

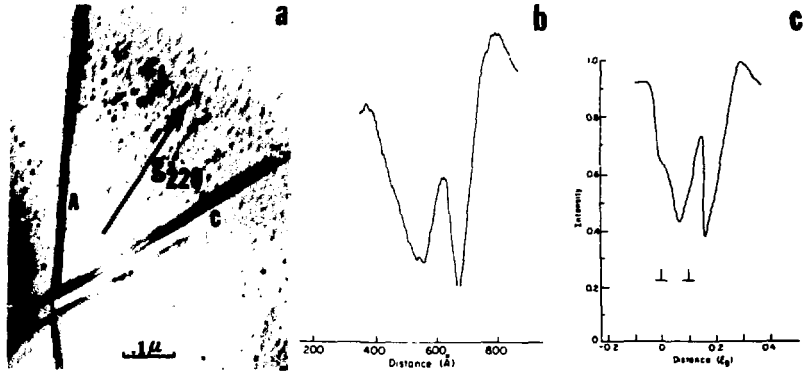

Fig. 3. a) Dissociated dislocations in $LiFe_5O_8$ imaged near (110) pole. b) Microdensitometer trace at A. c) Computed profile for 1/2[011] + 1/4[011] + 1/4[011]. (XBB 758-5877)

B) FERRITES: WORK IN PROGRESS AND FUTURE PLANS

O. Van der Biest and R. K. Mishra

a. Contrast in Non-Centrosymmetric Crystals

Computer programs for centrosymmetric crystals have been adapted to include non-centrosymmetry. The program has been applied to the problem of contrast between enantiomorphic domains under multibeam conditions (deviations from Friedel's law). The contrast is found to be very much thickness dependent. Influence of changes in orientation and choice of absorption parameter have also been investigated. Calculations on this project have been completed. The results now await a detailed interpretation. It will be possible to determine the structure absolutely, i.e., whether a particular domain is right or left handed.

b. Contrast of 1/6(111) Faults in Spinel

The nature of 1/6(111) faults in spinel is being investigated using contrast calculations. These calculations are now in progress.

c. Analysis of Kinetic Data Obtained by Hot Stage E.M. Studies

Detailed analysis of the hot stage data is in progress. Data on the growth rate of particles will be completed soon. Data on the nucleation rates are harder to obtain because of i) the uncertainty of the temperature, ii) the foil thickness is not accurately known for many sequences.

d. Surface Energy and Material Loss in Spinel

Material loss of spinel is a significant problem, e.g., in sintering: the anisotropy of this loss is being investigated in terms of the anisotropy of surface energy. This is the first time this problem has been studied in spinels.

C) REFRACTORY CARBIDES: TURBINE MATERIALS (WORK IN PROGRESS AND FUTURE PLANS)

F. Dizon and D. R. Clarke

a. Basis of Program, Objectives

Some desirable performance objectives for gas turbines used for power production include improved efficiency, lower initial cost, and extended engine life. These objectives are at present limited by the properties of super-alloys used in these turbines. These materials can be operated only at surface temperatures less than about 900°C unless cooling is used. The engine life of gas turbines is limited mainly by the poor corrosion-erosion resistance of these alloys when used at high temperatures. The susceptibility of super-alloys to impurities found in dirty residual fuels limits their fuel economy. The necessity for cooling increases the initial blade costs and decreases their power output.

Ceramics such as silicon nitride and silicon carbide overcome many of the limitations that the use of super-alloys imposes on the improved performance of gas turbines. Since ceramics have refractory properties, they can be used at surface temperatures exceeding 900°C without cooling. This is an important asset since it is known that engine efficiency increases with higher operating temperatures. Ceramics have superior corrosion-erosion resistance and are able to tolerate the contaminants found in residual fuels.

Unfortunately, ceramic parts cannot be substituted directly for parts which now use superalloys. The inherent brittleness of ceramics places doubt on their mechanical performance in these turbines. Additionally, more efficient and reproducible fabrication techniques need to be perfected for ceramics.

For silicon carbide one step towards its intended use in turbines has been made. The General Electric Company has invented a process which employs boron in the sintering of the cubic (β) form of silicon carbide. The addition of boron makes possible pressureless sintering with concurrent high densities. The reproducibility of this fabrication technique is thought to be satisfactory.

b. Summary of Research on βSiC

Research work so far has been concentrated on the analysis of line and planar defects in the GE β-silicon carbide in both its as-sintered and deformed states. The carbide has the sphalerite crystal structure and consists of two interpenetrating fcc sublattices, one of carbon atoms and the other of silicon atoms.

The sintered material is characterized by an extremely low density of dislocations of the type $b = a/2\langle 110 \rangle$, and in many grains, by a high density of stacking faults and micro-twins lying on the closely packed {111} planes. Although these faults appear visually to be arranged at random in any grain, the nonuniform intensity of the streaking through the {111} spot in the diffraction pattern indicates that some ordering of the faults does in fact occur. In addition, it is occasionally observed that some grains contain a high density of narrow twins, as in the dark field micrograph, Fig. 1.

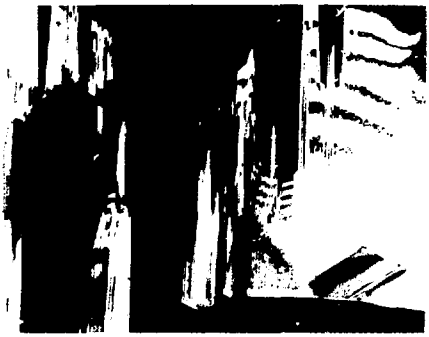

Fig. 1. Dark field electron micrograph. The light areas are regions that are crystallographically twinned with respect to the matrix (dark). (XBB 754-3138)

Fig. 2. Dark field electron micrograph of a broken fragment of silicon carbide showing a number of partially healed, secondary cracks stemming from the serrated fracture edge. (XBB 754-3148)

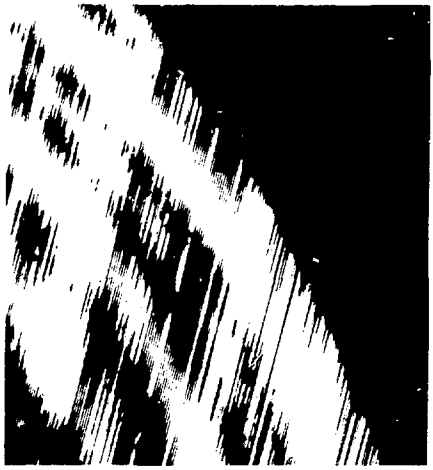

Fig. 3. High resolution electron micrograph of a complex faulted and twinned grain of cubic silicon carbide. Magnification calibration indicates that the coherent regions marked A are hexagonal (α) silicon carbide lying within the cubic material. (XBB 764-3196)

The defect structure of material deformed by breaking in bending is no different to the virgin sintered silicon carbide except close to the fracture edges. On occasions, limited plasticity takes place at these edges giving rise to high

densities of glide dislocations ($b = a/2\langle 110 \rangle$) lying parallel to the edge. In other instances (Fig. 2), the fracture edge is serrated and has associated with it a number of partially healed subsidiary cracks stemming from the serrations, but with few dislocations.

Although these characterizations have been carried out using conventional electron microscopy, lattice imaging will be utilized to interpret the complexities of the faulted regions and to confirm that regions such as A in Fig. 3 are indeed coherent hexagonal (α-SiC) laths within an otherwise cubic (β-SiC) grain.

(We are grateful to General Electric Co., Schenectady, New York, for supplying the SiC.)

c. Electron Microscopy

Gareth Thomas, Principal Investigator

1. HIGH RESOLUTION ELECTRON MICROSCOPY

G. Thomas

As reported in the 1974 Annual Report (LBL-3530) the availability of our two high-resolution microscopes (Siemens Elmiskop-102 and Philips EM-301) has enabled us to exploit the lattice imaging technique toward studies of coherent phase transitions, especially ordering (with emphasis on short range order) and spinodals. The method is particularly advantageous for studies of the initial stages of these transformtions.

The results of work on many ordering systems, e.g., Cu-Au, Au-Cr, Mg-Cd, confirm the microdomain model of short range order (s.r.o.) viz., that s.r.o. is physically described in terms of very small (~ 20 Å diameter) ordered domains in an essentially disordered matrix.[1-3] Also, as shown in LBL-3530, the lattice imaging technique enables the composition amplitudes of spinodally decomposed materials to be estimated from the lattice image spacings.

1. R. Sinclair and G. Thomas, J. Appl. Cryst. 8, 206 (1975).
2. R. Sinclair, K. Schneider and G. Thomas, Acta. Met. 23, 873 (1975).
3. J. Dutkiewicz and G. Thomas, Met. Trans. 6A, 1919 (1975); see following.

Fig. 1. A comparison of the lattice image taken with tilted illumination and (100) superlattice dark field of partially ordered Au_3Cr. Bright regions in the dark field micrograph correlate well with ordered domains visible in the lattice image. Only one domain marked "X" does not appear in the dark field micrograph. (XBB 751-788)

2. HIGH RESOLUTION STUDY OF ORDERING REACTIONS IN GOLD-CHROMIUM ALLOYS*

J. Dutkiewicz† and G. Thomas

The ordering reactions in Au_4Cr and Au_3Cr alloys have been investigated using high resolution dark field and lattice imaging techniques. It is shown, e.g. in Fig. 1, that there is good correlation between dark field imaging diffuse s.r.o. reflections and lattice imaging. The results strengthen our view of the microdomain concept of s.r.o. In all cases the ordered structures can be described in terms of compositional modulations as occur during spinodal decomposition. In alloys quenched from above the critical temperature s.r.o. microdomains of size 10-15 Å have been resolved with structures represented by modulations in composition along (420). After aging, the Au_4Cr alloys below T_c the Dl_a lro phase appears as ordered domains of size 50-100 Å showing composition modulations with wavelengths of 5d(531). These domains grow in size up to 500 Å, becoming finally the Dl_a fully ordered structure.

A new observation has been made in the Au_3Cr alloy, viz. that the lro structure is nonstoichiometric Ll_0 with $\lambda_{[001]} = 4$ Å. The transformation from s.r.o. in this alloy occurs with the formation of a transitional ordered phase (similar to DO_{22}), which can be described in terms of composition modulations along [001], with wavelengths equal to the c parameter (8 Å) of the DO_{22} structure.

Lattice imaging of the two variants of superlattice planes in ordered Au_3Cr enabled the atomic arrangement in the area of translational and rotational antiphase boundaries to be determined.

*Abstracted from Met. Trans. 6A, 1919 (1975), and LBL-3559.

†On one year leave from the Institute of Metallurgy, Polish Academy of Sciences, 30-059 Krakow, ul. Reymonta 25, Poland.

3. OPTICAL DIFFRACTION FROM LATTICE IMAGES OF ALLOYS*

R. Sinclair, R. Gronsky and G. Thomas

Optical diffraction patterns have been obtained from optimum lattice images of partially ordered

Cu_3Au and spinodally decomposed Au-Ni alloys. These diffraction results show excellent agreement with the corresponding portions of electron diffraction patterns, indicating that a direct correlation exists between the lattice images and the atomic lattices of the alloys studied. Since in electron microscopy the resolution limit for selected area diffraction is determined by spherical aberration of the objective lens and at 100 kV this is approximately 2 nm, the gain in localized information by optical analysis down to 10 Å is considerable.

A quantitative analysis of the spinodal and ordering transformations by combined lattice imaging and optical diffraction provides experimental detail on an extremely localized scale. Examples are shown in Figs. 1-3 for spinodal

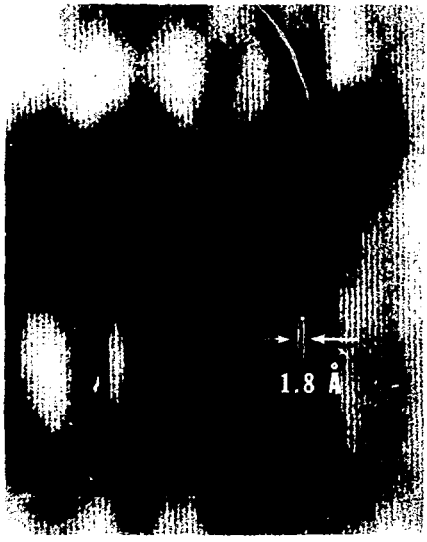

Fig. 1. Lattice image (positive print of the original plate) of spinodally decomposed Au-Ni. (XBB 757-5130)

transformations. All the results are in agreement with conventional experimental results and modern theories of phase transformations and illustrate an exciting new approach to gaining information about localized atomic mechanisms of phase transformations in alloys.

This research is supported by NSF.

*Acta. Met. (LBL-3970) (in press).

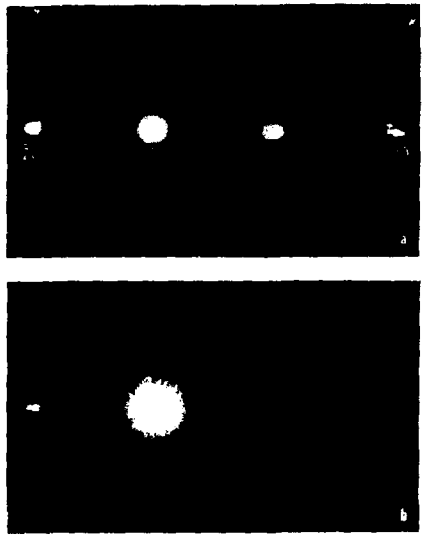

Fig. 2. Comparison of the electron diffraction pattern (a) from the decomposed Au-Ni specimen with the optical diffraction pattern (b) from the lattice image shown in Fig. 1. Satellites (s) about the fundamental (200) reflection (f) are arrowed. (XBB 757-5132A)

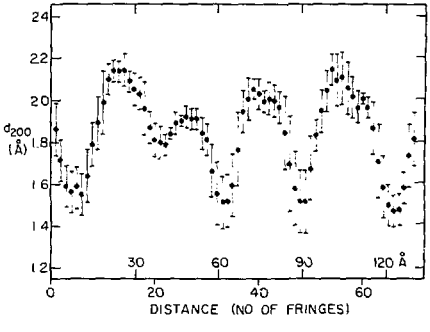

Fig. 3. Smoothed plot of fringe spacing with distance for Au-Ni as determined from a microdensitometer trace from the lattice image. (XBL 757-6648)

4. HIGH VOLTAGE ELECTRON MICROSCOPY: APPLICATION OF THE CRITICAL VOLTAGE EFFECT TO THE STUDY OF ORDERING IN ALLOYS*

R. Sinclair, M. J. Goringe† and G. Thomas

Calculated values have been obtained for the critical voltage (V_c) of several ordered alloys as a function of degree of long-range order (S). Most systems have a reflection showing a critical voltage within the range of our microscope (220-650 kV) but the variation with S is generally predicted to be very small. Experiments on Cu_3Au and Ni_4Mo further indicate that the critical voltage effect is not useful for obtaining new information about the early stages of ordering transformations.

Financial assistance from NSF is acknowledged by R.S. and G.T.

*Philosophical Magazine 32, 501 (1975).

†On leave from Department of Metallurgy and Science of Materials, University of Oxford, England.

5. THE ACCURATE MEASUREMENT OF THE ENERGY DEPENDENCE OF RADIATION DAMAGE RATES IN ORGANIC MATERIALS*

D. G. Howitt†

In electron microscopy and radiation damage studies in organic materials it is important to be able to make an accurate asessment of the rate at which the damage processes proceed.

Approximate values for these radiation damage rates have been calculated using solid state detectors in order to measure the appropriate beam current densities,[1] however, the strong intensity dependence of these devices and their susceptibility to radiation damage imposes large errors when any consistency in their efficiency is assumed.

A Faraday cup has been constructed (Fig. 1) which is capable of measuring currents down to 10^{-15} amperes cm^{-2} from the final image plane of an electron microscope, with an error of less than 1%. The cup, being positioned beneath the final viewing screen is therefore capable of distinguishing local incident intensities in the object plane.

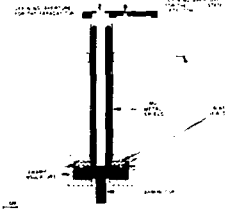

Fig. 1. Faraday cup. (XBL 763-652)

In assessing the beam current density at the specimen an overestimation can arise from electrons which are incident at the image plane but not derived from the associated object. This effect is most prevalent in high voltage microscopes and arises from the malalignment of lens apertures and the ability of secondary electrons, for example, those created on the walls of the microscope column, to reach the final image plane. The large operating range of the Faraday cup, however, facilitates the measurement of beam currents at very low magnifications where this effect is minimized.

In the measurement of radiation damage rates (see following abstract) the fading diffraction pattern technique is employed[2] and the determination of the end point can have a large degree of uncertainty associated with it, particularly at high voltages, when determined visually from the fluorescent screen. The Faraday cup can, however, when measuring high beam currents, sustain a rapid response to changes in intensity. Thus it may be utilized to monitor the decay of any Fourier component in the diffraction pattern to the intensity of the final background.

*EMSA Student Fellowship Award Paper 1975.

†M.S. Thesis, LBL-3180 (1975).

1. R. M. Glaeser, LBL-2164 (September 1973).
2. D. T. Grubb and G. W. Groves, Phil. Mag. 24, 815 (1971).

6. THE ENERGY DEPENDENCE OF RADIATION DAMAGE IN 1-VALINE*

D. G. Howitt, R. M. Glaeser, and G. Thomas

Experimental electron diffraction and microscopy results are described regarding the energy dependence of electron radiation damage in the aliphatic amino acid 1-valine. The critical exposure, defined as the electron flux necessary to destroy the crystallinity of a material, has been determined over a range of electron energy from 50 keV to 3 MeV. The results are shown in Fig. 1. In terms of the electron velocity, the results indicate a β^3 dependence rather than β^2 as predicted from stopping power theory. The results are used to estimate the applicability, especially with respect to potential resolution, of very high voltage electron microscopy in the study of beam sensitive organic materials, and indicate that a factor of two times improvement in resolution can be expected at 1 MeV compared to 100 keV.

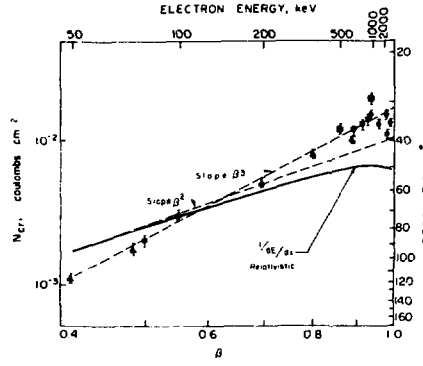

Fig. 1. The variation of the critical exposure N_{cr} with increasing electron energy. The relationship of β^3 in N_{cr} vs electron energy is obtained. (XBL 752-5710)

Some financial support from the National Institute of Health is gratefully acknowledged. We are particularly indebted to Professor G. Dupouy and Dr. B. Jouffrey for use of the Toulouse 3-MeV electron microscope.

*LBL-3958, submitted to J. Ultrastr. Res.

7. RESEARCH PLANS FOR CALENDAR YEAR 1976, ALLOY DESIGN

G. Thomas

a. Significance of Retained Austenite: Heat Treatment

M. Carlson, M.S. Thesis

In the high-strength, tough Fe/Cr/C martensitic steels, optimum heat treatments for heat properties involve annealing at 1000°C prior to the martensitic transformation. A systematic study of the effect of austentizing temperature, grain size, retained austenite martensite substructure and carbides on the strength and toughness (both K_{Ic} and Charpy) is underway.

b. Optimization of Tough, High Strength Fe/Cr/C Base Steels

B. V. N. Rao, Ph.D. Thesis

Experimental steels based on Fe/4Cr/0.3C with quaternary alloying additions (e.g., Mn, Ni, Ti) are being studied to optimize the yield strength and toughness by control of grain size, martensitic structure and to maintain stability of untransformed austenite. (We acknowledge Daido Steel Corp. for supplying the steels to our specifications.)

c. Steels for Transportation Applications

1. New Steels (J-Y. Koo, Ph.D. Thesis). Experimental low alloy steels based on the 1010 commercial type have been designed to exploit the two-phase ($\alpha+\gamma$) heat treatment and increase hardenability. The research program entails maximizing the role of martensite (morphology and distribution) to attain strength levels ~ 80,000 psi at acceptable ductilities. (We acknowledge Daido Steel Corp. for supplying the steels.)

2. Exploitation of Commercial 1010 and 1020 Steels (M. Young, M.S. Thesis). This is a continuation of J. Y. Koo's M.S. Thesis to explore the relation between strength and martensite volume fraction following two phase annealing and quenching.

d. Manipulation of Spinodal Transformations

1. CuNiFe (K. Kubarych, M.S. Thesis). Continuous cooling and step aging are underway to improve the strength and toughness of spinodal alloys utilizing the main strengthening mechanism viz. yield strength vs., $\Delta a/$ here Δa is the difference in lattice parameter between the coherent phases. Initial results indicate that 30% or more increase in strength with no sacrifice in ductility can be achieved compared to conventionally heat treated alloys.

2. Cu/29Ni/5Cr (C-K. Wu, M.S. Thesis). The relation between microstructure and mechanical properties is being established in this spinodal alloy system using conventional electron microscopy and high resolution lattice imaging to establish composition changes with heat treatment.

3. FeCrCo (M. Okada, Ph.D. Thesis). No systematic investigations appear to have been done on the relation between spinodal microstructure parameters (amplitude, wavelength, volume fraction) and magnetic properties. The goal is to achieve high coercivity (with good ductility for processing) by utilizing the spinodal transformation in FeCrCo alloys (e.g., (31Cr/23Co/46Fe)).

8. RESEARCH PLANS FOR CALENDAR YEAR 1976, RADIATION DAMAGE AND RELATED EFFECTS

a. Structural Defects in Fast Breeder Reactor and Controlled Thermonuclear Reactor Materials

K. H. Westmacott*

Tests of new alloy designs for application in advanced nuclear reactor systems are both costly and time-consuming, and sometimes impossible, in the actual reactor environment; consequently damage simulation methods are commonly employed. A new technique which offers several advantages over existing simulation methods is being investigated in a joint program with the Lawrence Berkeley Laboratory. The principal advantage of

the technique is that concurrent introduction of damage and inert gas atoms at a high (variable) rate is possible. Initial results will be compared with other simulation techniques and theoretical calculations to assess the potential of the method. The cooperation of the Lawrence Livermore Laboratory in the radiation experiments is gratefully acknowledged.

*On leave at LBL from Naval Weapons Center, China Lake Laboratories, 1975/76.

b. Short Range Order: Radiation Damage

U. Dahmen, Ph.D. Thesis (Fulbright Fellow)

Previous work on the s.r.o. state ("K" state) in Fe-Al alloys (G. Thomas and H. Warlimont, Met. Sci. J. 4, 47 (1970)) indicates that s.r.o. is very stable and ordered domains do not coarsen. This project explores this effect more deeply with a view towards establishing if s.r.o. is resistant to swelling under radiation conditions. The program involves an evaluation of s.r.o. in alloys up to 20%Al, and correlation with mechanical properties and irradiation damage by electrons (HVEM) and neutrons (reactor experiments).

9. 1975 PUBLICATIONS AND REPORTS

Gareth Thomas and Associates

Journals

1. O. Van der Biest and G. Thomas, Identification of Enantiomorphism in Crystals by Electron Microscopy, Acta. Cryst. A31, 70 (1975) (LBL-2773).

2. R. Sinclair and G. Thomas, Antiphase Domains and Superlattice Spot Splitting in Cu_3AuI, (Proc. Julich Conf.), J. Appl. Cryst. 8, 206-210 (1975) (LBL-2731).

3. G. Thomas, Some Applications at Berkeley and Possible Future Trends of HVEM, Electron Microscopy, Physical Aspects, B. Siegel and D. R. Beaman, eds., (J. Wiley & Sons, 1975), Chapter 7, 81-102. (LBL-2274).

4. K. Seshan, G. Thomas and L. J. Chen, Contrast and Resolution of Small Dislocation Loops in HVEM, Phys. Stat. Sol. (a) 28, 309-319 (1975) (LBL-1164).

5. R. Sinclair, K. Schneider and G. Thomas, Analysis of Ordering in Cu_3Au Utilizing Imaging Techniques, Acta. Met. 23 (1975) (LBL-3194).

6. G. Thomas, High Voltage E. M. Studies of Ceramic Ferrites, invited paper, Toulouse International Conf. on HVEM, Sept. 1-4, 1975 (LBL-4114).

7. G. Thomas, Utilization and Limitations of Phase Transformations and Microstructures in Alloy Design for Strength and Toughness, invited paper, Batelle Colloquium on Fundamental Aspects of Structural Alloy Design, 1975 (LBL-4175).

8. A. Rocher, R. Sinclair, and G. Thomas, Study of Atomic Scattering Factors from the Critical Voltage of Ordered Alloys — Application to Cu_3Au, Int'l. Conf. on HVEM, Toulouse, Sept. 1-4, 1975 (LBL-4563).

9. B. V. N. Rao and G. Thomas, Design of Fe/4Cr/0.4C Martensitic Steels Eliminating Quench Cracking, Mat. Sci. and Eng. 195-202 (1975) (LBL-3522).

10. J. Dutkiewicz and G. Thomas, High Resolution Study of Ordering Reactions in Gold-Chromium Alloys, Met. Trans. 6A, 1919-1928 (1975) (LBL-3559).

11. R. Sinclair, M. J. Goringe, and G. Thomas, Application of the Critical Voltage Effect to the Study of Ordering Alloys, Phil. Mag. 32, 3, 501-512 (1975) (LBL-3579).

12. O. Van der Biest, E. P. Butler and G. Thomas, Hot Stage HVEM Dynamic Studies of Order-Disorder Transitions in Lithium Ferrite, 33rd Annual EMSA Proceedings, Las Vegas, 1975, G. W. Bailey, ed., p. 36-37 (LBL-3762).

13. R. K. Mishra, Electron Microscopy of Early Stages of Precipitation in Lithium Ferrite ($LeFe_5O_8$) Spinel, 33rd Annual EMSA Proceedings, Las Vegas, 1975, G. W. Bailey, ed., p. 62-63 (LBL-3770).

14. B. V. N. Rao, J.-Y. Koo and G. Thomas, Electron Metallography Identification of Retained Austenite in Steels, 33rd Annual EMSA Proceedings, Las Vegas, 1975, G. W. Bailey, ed., p. 30-31 (LBL-3771).

15. R. Sinclair and J. Dutkiewicz, Lattice Image Studies of Ordered Alloys 33rd Annual EMSA Proceedings, Las Vegas, 1975, G. W. Bailey, ed., p. 10-11 (LBL-3781).

16. D. G. Howitt, R. M. Glaeser and G. Thomas, The Energy Dependence of Radiation Damage in l-Valine, 33rd Annual EMSA Proceedings, Las Vegas, 1975, G. W. Bailey, ed., p. 246-247 (LBL-3784).

17. R. Gronsky, M. Okada, R. Sinclair and G. Thomas, Lattice Imaging of Spinodal Alloys, 33rd Annual EMSA Proceedings, Las Vegas, 1975, G. W. Bailey, ed., p. 22-23 (LBL-3778).

18. D. G. Howitt, The Accurate Measurement of the Energy Dependence of Radiation Damage Rates in Organic Materials, 33rd Annual EMSA Proceedings, Las Vegas, 1975, G. W. Bailey, ed., p. 210-211 (LBL-3739).

19. R. Gronsky and G. Thomas, Discontinuous Coarsening of Spinodally Decomposed Cu-Ni-Fe Alloys, Acta. Met. 23, 1163-1171 (1975) (LBL-3523).

20. P. Rao and G. Thomas, Interstitial Order and Embrittlement in Ta-C Alloys, Acta. Met. 23, 309 (1975) (LBL-2570).

21. R. Clark and G. Thomas, Design of Strong, Tough Fe/Mo/C Martensitic Steels and the Effects of Cobalt, Met. Trans. 6A, (5) 969-979 (1975) (LBL-2504).

22. D. J. Rowcliffe and G. Thomas, Structure of Non-Stoichiometric TaC, Mat. Sci. and Eng. 18, 231 238 (1975) (LBL-2588).

23. R. H. Geiss, D. G. Howitt, and H. Arnel, Fresnel Diffraction and Lattice Plane Imaging in a Conventional S.T.E.M., 33rd Annual EMSA Proceedings, Las Vegas, 1975, G. W. Bailey, ed., p. 220-221, (LBL-4569).

LBL Reports

1. D. -H. Huang, Bainitic Transformations in Steels (Ph.D. Thesis), LBL-3713, July 1975.

2. J.-Y. Koo, Investigations of Heat Treatments for Improved Properties of Low Carbon Fe-0.12%C-0.5%Mn Steels (M.S. Thesis), LBL-3587, April 1975.

3. B. V. N. Rao, Improvement on Toughness Properties in Ultra-High Strength Fe/4Cr/0.4C Martensitic Steels (M.S. Thesis), LBL-3794, September 1975.

4. M. Von Heimendahl, G. Hubred, G. Thomas and D. W. Fuerstenau, A Transmission Electron Microscope Study of Deep Sea Manganese Nodules, (Deep Sea Research, in press), LBL-1496, March 1975.

5. O. Van der Biest and G. Thomas, Fundamentals of Electron Microscopy, Chapter in, Applications of Electron Microscopy in Mineralogy, H.-R. Wenk and G. Thomas, eds. (Springer-Verlag, Berlin, 1975), in press, LBL-3524, February 1975.

6. D. R. Clarke, Calculation of Habit Planes for Transformation by Minimization of Elastic Strain Energy (submitted to Met. Trans.), LBL-3573, August 1975.

7. E. Nes and G. Thomas, The Precipitation of TiC in Thermally Embrittled Maraging Steels (submitted to Met. Trans.), LBL-3927, August 1975.

8. D. H. Kirkwood and G. Thomas, The Microstructure of Nitrided Fe-0.3 wt% Ti Alloy, Annealed at 800°C (submitted to Met. Trans. A), LBL-3939, December 1975.

9. R. Sinclair, R. Gronsky and G. Thomas, Optical Diffraction from Lattice Images of Alloys (submitted to Acta. Met.), LBL-3970, August 1975.

10. J.-Y. Koo and G. Thomas, Thermal Cycling Treatments and Microstructures for Improved Properties of Fe-0.12%Mn Steels (submitted to Mat. Sci. and Eng.), LBL-3980, October 1975.

11. B. V. N. Rao, R. Miller and G. Thomas, Heat-Treatment, Microstructure and Mechanical Properties of Fe/4Cr/0.4C Steels (submitted to 16th Annual Int'l. Conf., England), LBL-3982, December 1975.

12. D. G. Howitt, G. Thomas and W. Toutolmin, A Comparison of the Measurment of Beam Current Densities in an E.M. Using a Faraday Cup and Solid State Detector (submitted to J.A.P.), LBL-3706, August 1975.

13. G. Thomas and D.-H. Huang, Metallography of Bainitic Transformations in Silicon Containing Steels (submitted to Met. Trans.), LBL-4519, December 1975.

14. K. H. Westmacott, The Origin and Nature of Multiple Loop Configurations in Quenched Aluminum and Aluminum Alloys (submitted to Phys. Stat. Solidi), LBL-4536, December 1975.

15. M. Bouchard and G. Thomas, Modulated Structures in Ordered (Cu-Mn)$_3$Al Alloys, (Acta. Met., in press), LBL-3719, May 1975.

16. O. Van der Biest and G. Thomas, The Order-Disorder Reaction in Lithium Ferrite, Chapter in Applications of Electron Microscopy in Mineralogy, H.-R. Wenk and G. Thomas, eds. (Springer-Verlag, Berlin, 1975), in press, LBL-3510, November 1974.

17. D. G. Howitt, The Measurement of Radiation Damage in Organic-Materials in the Range of Electron Energy Between 200 kV and 650 keV (M.S. Thesis), LBL-3180, February 1975.

d. Powder Metallurgy

Milton R. Pickus, Principal Investigator

1. THE TERBIUM-IRON PHASE DIAGRAM

M. P. Dariel, J. T. Holthuis and M. R. Pickus

The equilibrium phase diagrams of most rare-earth metal-iron binary systems have been reported. Notable exceptions are those of the bivalent rare-earth metals europium and ytterbium, and trivalent terbium. Some terbium-iron intermetallic compounds, particularly the Laves phase $TbFe_2$, have exceptionally interesting properties such as high magnetostriction, large magnetocrystalline anisotropy and a strong dependence of Young's modulus on an applied magnetic field (ΔE effect). In order to facilitate the development of technologically useful materials based on these compounds, it was deemed necessary to determine the terbium-iron diagram. The diagram shown in Fig. 1 was constructed from data acquired by means of metallographic, differential thermal analysis (DTA), x-ray diffraction and electron microprobe techniques.

The invariant temperature of the eutectic and of the four peritectic reactions were determined from the thermal arrests appearing on the heating curves. The solid solubility of iron in terbium is below the detection limit of the experimental techniques employed. The addition of terbium to iron slightly increases the $\alpha \rightarrow \gamma$ and decreases the $\gamma \rightarrow \delta$ transformation temperature. The rare-earth metals act as BCC stabilizers in iron. Electron microprobe and lattice parameter measurements indicate that the solid solubility of terbium in iron is below 0.1 at%.

Similar to the other heavy rare-earth (Gd to Lu)-iron systems, four intermetallic compounds occur in the Tb-Fe binary system. Structural data concerning these compounds are given in Table 1.

Table 1. Structural data for the Tb-Fe intermetallic compounds.

Compound	Crystal symmetry	Space group	Structure type	Lattice parameters (Å)
$TbFe_2$ (room temperature)	Rhombohedral	$R\bar{3}m$	distorted $MgCu_2$	a = 5.1896[a] c = 12.8214 (hex. axes)
$TbFe_3$	Rhombohedral	$R\bar{3}m$	$PuNi_3$	a = 5.139 ± 0.001 c = 24.610 ± 0.002 (hex. axes)
Tb_6Fe_{23}	Cubic	$Fm3m$	Th_6Mn_{23}	12.085 ± 0.002
Tb_2Fe_{17} (Tb-rich side)	Rhombohedral	$R\bar{3}m$	Th_2Zn_{17}	a = 8.504 ± 0.004 c = 12.413 ± 0.002 (hex. axes)
Tb_2Fe_{17} (Fe-rich side)	Hexagonal	$P6_3/mmc$	Th_2Ni_{17}	a = 8.472 ± 0.004 c = 8.321 ± 0.002

[a]Results taken from A. E. Dwight and C. W. Kimball, Acta Crystallogk. *B30* (1974) 2791.

Metallographic examination of iron-rich $TbFe_2$ samples, slowly cooled from 1100°C, indicated the presence of iron-rich precipitates in the $TbFe_2$ grains (Fig. 2). No such precipitates were observed in quenched samples, suggesting the presence of a homogeneity range at elevated temperatures, extending towards iron-rich compositions.

Contrary to some previous reports, the presence of the Tb_6Fe_{23} compound was definitely established.

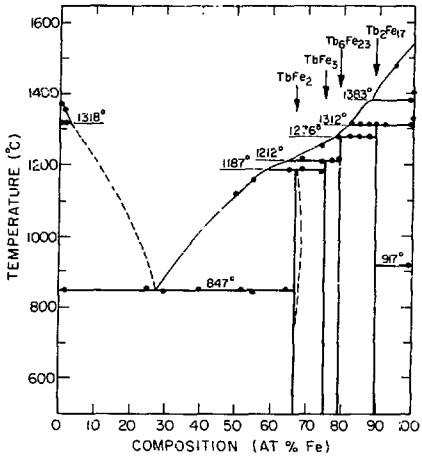

Fig. 1. The terbium-iron phase diagram. (XBL 755-6353)

Fig. 2. Two phase, 68 at% Fe alloy. Iron-rich precipitates in the $TbFe_2$ phase (on the left). Note their absence in the region abjacent to the $TbFe_2$-$TbFe_3$ phase boundary. (XBB 755-3922)

The nucleation of this compound is extremely sluggish, and lengthy anneals are necessary to reveal its presence.

Both structure types of the Tb_2Fe_{17} compound, namely the rhombohedral Th_2Zn_{17} and the hexagonal Th_2Ni_{17} are present in the Tb-Fe system (Fig. 3).

Fig. 3. Strongly twinned 89.5 at% Fe alloy, believed to be a mixture of the two structure variants of Tb_2Fe_{17}: Th_2Zn_{17} and Th_2Ni_{17} structure types. (XBB 755-3919)

The hexagonal type is found on the iron-rich side of the stoichiometric Tb_2Fe_{17} composition, in agreement with the observation that this structure is able to accommodate an excess of the smaller size component.

2. POWDER METALLURGICAL PROCESSING OF MAGNETOSTRICTIVE RARE-EARTH IRON LAVES COMPOUNDS

M. Malekzadeh, M. P. Dariel and M. R. Pickus

The pseudo-binary $Tb_{0.3}Dy_{0.7}Fe_2$ Laves compound exhibits magnetostriction to a degree that is higher by more than an order of magnitude than that of common magnetostrictive materials.[1] The exceedingly high magnetostriction and the relatively low magnetocrystalline anisotropy make this compound a potentially valuable material for magnetomechanical transducer applications. Like most intermetallic compounds the Laves phases are extremely brittle. The use of powder metallurgy techniques, therefore, seemed appropriate for processing magnetostrictive components in suitable shapes and sizes.

The alloys were prepared by arc melting weighed lumps of the components in a purified argon atmosphere. After homogenization at 900°C, the samples were crushed and then ground under toluene, using a steel container in a planetary mill. The milled powder was vacuum dried, packed into 8 mm diameter, 50 mm long, rubber tubing and isostatically compacted at 75,000 psi. The sintering parameters were investigated by varying time and temperature, and trying dynamic and static vacuum environments. A single phase Laves compound, containing about 20% residual porosity, was obtained by starting with an iron content of 65.3 at% and sintering at 1160°C for 10 hours.

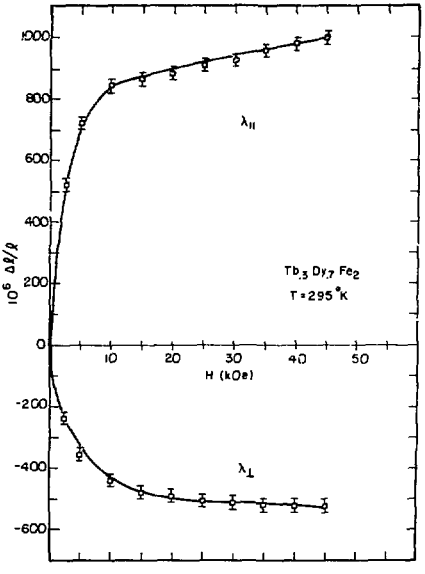

Fig. 1. Magnetic field dependence of the longitudinal ($\lambda_{\parallel}$) and transverse ($\lambda_{\perp}$) magnetostrictive strains in $Tb_{0.3}Dy_{0.7}Fe_2$.
(XBL 7511-9434)

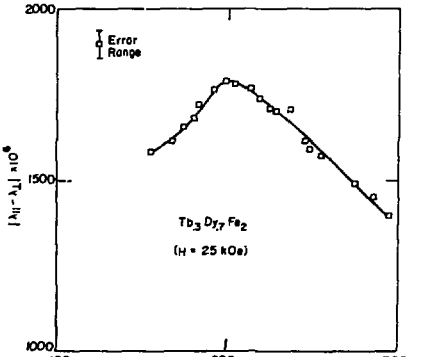

Fig. 2. Temperature dependence of the magnetostriction coefficient of $Tb_{0.3}Dy_{0.7}Fe_2$ at 25 kG.
(XBL 7511-9433)

Higher initial iron contents yielded samples containing varying amounts of additional phases.

The magnetostriction of the sintered samples was determined in a superconducting magnet at fields up to 45 kG, using the strain gauge technique. The longitudinal and transverse magnetostrictions were measured simultaneously by mounting two perpendicular gauges on the specimen surface. A special technique involving the use of a reference sample, was employed to compensate for temperature and magnetostrictive effects in the strain gauges.

The magnetic field dependence of the longitudinal and transverse magnetostrictions of a sintered $Tb_{0.3}Dy_{0.7}Fe_2$ sample is shown in Fig. 1. The temperature dependence of the magnetostrictive coefficient $|\lambda_{\parallel}-\lambda_{\perp}|$, shown in Fig. 2, was determined by carrying out two sets of measurements, one in the presence of an applied magnetic field of 25 kG, and the other without field. This procedure had to be followed in order to correct for the difference in the thermal expansion coefficient of the test sample and the adjacent reference sample.

Noteworthy is the aspect of curve $\lambda_{\parallel}$ in Fig. 1, suggesting that even at the highest applied field the magnetostriction is far from saturation. The density of the sintered material was only 80% of theoretical; further efforts are, therefore, necessary in order to eliminate the residual porosity and thereby increase the magnetoelastic force and energy density of the sintered compounds.

1. A. E. Clark, AIP Conf. Proc. 18, 1015 (1973).

3. OXYGEN-STABILIZED RARE-EARTH IRON INTERMETALLIC COMPOUNDS

M. P. Dariel, M. Malekzadeh and M. R. Pickus

In the course of the study of sintered pre-alloyed rare-earth iron powders, the presence of a previously unreported phase was observed. In an effort to identify the new compound, a systematic study in the Dy-Fe system was carried out. We were able to prepare a nearly single phase sample of this compound (called β-phase) and used powder diffraction spectra to determine its crystal structure.

On the basis of the composition ratio of the two components, corresponding to formula Dy_3Fe_8 and the x-ray data, we assigned the structure of the β-compound to space group $Im\bar{3}m$ (Int. Tab. No. 229) with four formula units per unit cell. No such compounds, however, have ever been reported in binary R-Fe systems and it seemed unlikely that they should have been overlooked. It was assumed, therefore, that the β-compounds had been stabilized by the presence of a ternary component.

Chemical analysis of the single phase Dy-Fe β-compound revealed the presence of approximately 1 at% oxygen. Crystal structure considerations

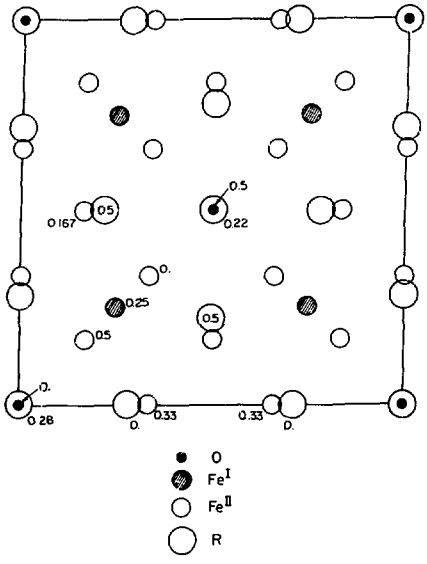

Fig. 1. Projection on the (001) plane of the proposed $R_{12}Fe_{32}O_2$ structure. (XBL 759-7328)

as well as the results of the chemical analysis suggest that the actual formula of the β-compound should be $Dy_{12}Fe_{32}O_2$, space group $Im\bar{3}m$ with the atoms distributed on the following sites (Fig. 1):

$$\begin{aligned} &2\ O \text{ in } \underline{a} \\ &\qquad (\lambda = 0.18) \\ &12\ Dy \text{ in } \underline{e} \\ &8\ Fe \text{ in } \underline{c} \\ &\qquad (\lambda = 0.667) \\ &24\ Fe^{I}_{II} \text{ in } \underline{h} \end{aligned}$$

An effort was made to determine the occurrence of the β-compounds in other R-Fe systems. The lattice parameters of the β-compounds that have been observed are shown in Table 1.

The best known ternary compounds are the rare-earth iron garnets ($R_3Fe_5O_{12}$) and orthoferrites ($RFeO_3$). Both series have a relatively high oxygen concentration and are non-metallic. In contrast, the β-compounds have a low oxygen concentration and a metallic luster.

All three groups of compounds — the rare-earth iron intermetallics, the garnets, and orthoferrites — have interesting magnetic properties on which are based a variety of practical applications. Since the β-compounds have a crystal structure that is different from that of any of these three groups, new magnetic structures can be expected.

Table 1. Lattice parameters of $R_{12}Fe_{32}O_2$ compounds.

R	a(Å)
Gd	8.919 + 0.002
Tb	8.885 + 0.002
Dy	8.8692 + 0.0005
Ho	8.8435 + 0.001
Er	8.815 + 0.002
Y	8.8832 + 0.0005

4. LIQUID PHASE SINTERING IN FERROUS SYSTEMS

John Klein and Milton R. Pickus

Most iron base components produced commercially by the powder metallurgy process contain an undesirable residual porosity of the order of 10%. Research on this problem was divided into two stages. The first, was an investigation of liquid phase sintering in the technologically important iron-carbon system. As reported last year, virtually fully dense alloys were obtained by a simple two-step procedure consisting of compaction and liquid phase sintering. However, in order to accomplish this at moderate temperatures (1175°C), the use of high carbon contents was necessary, resulting in a microstructure characterized by a continuous carbide network.

The second stage of this program, now in progress, is concerned with microstructure control and the application of liquid phase sintering to other ferrous systems. In an effort to eliminate the cementite network, ternary additions were made to the iron-graphite powder blend consisting of an element with a strong carbide-forming tendency. Preliminary experiments with titanium additions were disappointing. In contrast, the addition of tungsten was quite successful. For a powder composition of Fe: 20% W: 2.20% C, a density of 99.4% of theoretical was achieved by liquid phase sintering for 30 minutes at 1250°C. The microstructure (Fig. 1) shows fine angular grains of WC dispersed in a pearlitic matrix, along with an as yet unidentified phase. Another structure obtained with this system by changing the composition (Fe: 15% W: 2.34% C) and lowering the liquid phase sintering temperature to 1175°C — an attractive economic and energy saving feature — is shown in Fig. 2. The microstructure consists of WC grains and graphite nodules dispersed in a fine-grained ferritic matrix. The density of this sample is 99.0% of theoretical.

Some preliminary experiments were performed in the iron-boron system. The volume fraction of liquid phase at sintering temperature was varied

Fig. 1. Fe: 20% W: 2.20% C alloy liquid phase sintered for 30 minutes at 1250°C. Fine angular WC grains (1), in a pearlitic matrix (2), plus an unidentified phase (3). (XBB 7512-9221)

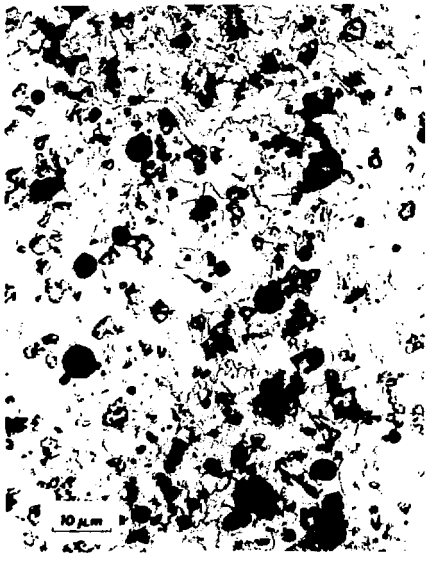

Fig. 2. Fe: 15% W: 2.34% C alloy liquid phase sintered for 30 minutes at 1175°C. WC grains and graphite nodules in a ferritic matrix.
(XBB 7512-9222)

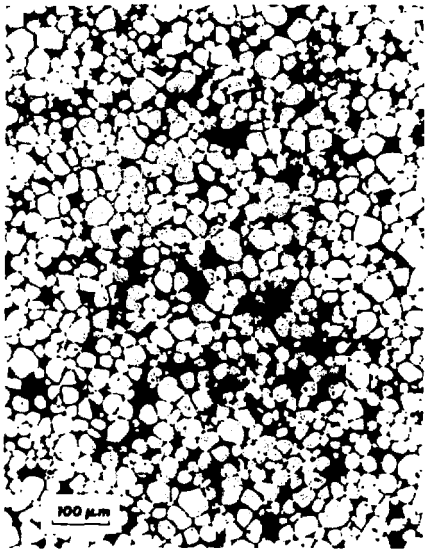

Fig. 3. Fe: 0.97% B alloy liquid phase sintered for 10 minutes at 1175°C. Rounded ferrite grains surrounded by a boron-rich network.
(XBB 7512-9220)

from 5 to 25%. With a boron content of 0.97%, resulting in a 25% volume fraction of liquid phase, a density of 99.2% of theoretical was obtained by sintering at 1175°C for only ten minutes. By increasing the sintering time to 30 minutes the density was increased to 99.4%. Figure 3 shows the microstructure of the sample sintered for 10 minutes. The structure consists of quite rounded ferrite grains surrounded by a boron-rich network.

5. Cu-Mn-Si ALLOYS FOR INFILTRATING IRON POWDER COMPACTS

Meng-Hsiu Chen, J. Ling-Fai Wang and Milton R. Pickus

Sintered iron compacts infiltrated with copper have nearly full density and improved tensile strength. The objective of this research is to develop better materials for use as infiltrants.

The copper-manganese-silicon system was selected as a promising one to investigate. A

composition was found that offered several attractive features. It has a melting point of ~ 780°C — about 200°C lower than that of copper, and exhibits excellent wetting characteristics with respect to iron. The prealloyed composition is very brittle and can be easily reduced to a fine powder. This offers the advantage that it can be used either as an infiltrant or as an additive to be blended with iron powder and thus provide a liquid phase during sintering.

Preliminary results indicate that this new material infiltrates iron compacts quite rapidly and that during the subsequent stage of liquid phase sintering, both silicon and manganese preferentially diffuse into the iron, leaving a ductile copper alloy to serve as a binder. The extensive solid solubilities of manganese and silicon in iron favor this type of preferential diffusion, which was confirmed by electron microanalysis.

With these favorable prognoses, it is planned to optimize the composition and volume fraction of the infiltrant and the sintering conditions, and then to evaluate the mechanical properties.

6. RESEARCH PLANS FOR CALENDAR YEAR 1976

Milton R. Pickus

Research on multiphase composites will concentrate on the nickel-titanium-silicon system. The program will be directed toward determining the thermal stability, the mechanical properties and the compatibility of several types of intermetallic phases (G,V,E,F, etc.) with a variety of matrices, both ferrous and non-ferrous. Special emphasis will be placed on the abrasion, erosion and friction related properties of the multiphase composites, since these properties have high relevance in new energy systems.

Further studies are planned on developing methods for controlling the microstructure of nearly full density iron base alloys produced by liquid phase sintering. The work on the iron-tungsten-carbon system has suggested other ways to modify the microstructure of high carbon alloys to obtain attractive properties. An immediate objective is to investigate procedures for eliminating continuous carbide networks by the preferential formation of spheroidized graphite induced by the use of innoculants and controlled furnace atmospheres. Such structures are expected to have markedly improved properties compared with conventional P/M steels.

The research on achieving full density iron alloys by the use of our newly developed Cu-Mn-Si infiltrating alloy will be centered on optimizing the composition of the infiltrant and the sintering parameters. The relationship between the added weight fraction of infiltrant, the sintered density and mechanical properties will be determined.

Our studies related to the rare-earth iron Laves compounds have shown that powder metallurgical techniques can be applied successfully to produce sintered samples with satisfactory static magnetostrictive properties. The first objective of our forthcoming program will be to improve the microstructure of the sintered compounds by eliminating the residual porosity. Efforts will be made to achieve this goal by hot-pressing the rare-earth iron pre-alloyed powder or, alternatively, by using liquid phase sintering. An increase in the concentration of the rare-earth component will indeed result in the presence of a liquid phase fraction at the sintering temperature. The resulting changes in microstructure will be correlated with magnetostrictive behavior. Trials will be made to produce more complex shaped sintered specimens, e.g., toroids.

The powder making facility we have under construction is now virtually complete. Studies will be undertaken to determine and control the process parameters that determine the characteristics of the powder produced.

7. 1975 PUBLICATIONS AND REPORTS

Milton R. Pickus and Associates

Journals

*1. M. P. Dariel, Solute Diffusion of Iron in the Light Rare-Earth Metals Cerium, Praseodymium and Neodymium, Acta Met. 23(4), 473 (1975).

*2. G. Dublon, M. P. Dariel and U. Atzmony, Ferrimagnetism in $SmFe_2$, Phys. Lett. A51(5), 298 (1975).

*3. U. Atzmony and M. P. Dariel, Spin Reorientation Studies in Cubic Laves Rare-Earth Iron Compounds, AIP Conf. Proc. 24, Magnetism and Magnetic Materials - 1974, p. 662 (1975).

*4. J. Ling-Fai Wang, J. L. Margrave and J. L. Franklin, Low Energy Electron Attachment to Gaseous Chromium Oxides, J. Inorg. Nucl. Chem. 37, 1107 (1975).

*5. S. L. Bennett, J. Ling-Fai Wang, J. L. Margrave and J. L. Franklin, High Temperature Negative Ions. The Enthalpies of Formation of Gaseous PbF_3 and SnF_3 from Low Energy Electron Impact Studies, High Temp. Sci. 7, 142 (1975).

LBL Reports

1. M. P. Dariel, J. Holthuis and M. R. Pickus, The Terbium-Iron Phase Diagram, (J. Less Common Metals - in press) LBL-3928, 1975.

2. U. Atzmony and M. P. Dariel, Non-Major Cubic Symmetry Axes of Easy Magnetism in Rare-Earth Iron Laves Compounds (submitted to Phys. Rev. B) LBL-4157, 1975.

3. M. P. Dariel, M. Malekzadeh and M. R. Pickus, Oxygen Stabilized Rare-Earth Iron Intermetallic Compounds (presented at the AIP Conf. Magnetism and Magnetic Materials, Philadelphia, December 1975) LBL-4105, 1975.

* not supported by MMRD.

2. MECHANICAL PROPERTIES

a. Theoretical Problems in Alloy Design

J. W. Morris, Jr., Principal Investigator

Introduction. The research to be reported here can be conveniently divided into two parts. The first part includes our theoretical research activities in fundamental metallurgy. During the past year this research has concentrated especially on the nature of microstructure and on the manner in which microstructural variables can be quantified and incorporated directly into the constitutive equations which determine material properties. The problem is being attacked from three different perspectives. The first, described under headings 1 and 2 below, includes an attempt to directly characterize the microstructures that might arise from simple nucleation and growth transformations in a prototypic simple solid. Both theoretical and computer simulation techniques are used. The object of the investigation is to define measurable parameters that characterize the relation between different poly-granular microstructures.

The second approach, reported under headings 3 to 5 below, has as its objective the direct determination of the structure-property relation for an idealized single crystal. The crystal is taken to be an ideal body containing a distribution of dislocations that may glide under an applied stress, and also containing a distribution of microstructural features that may act as barriers to dislocation glide, and which have prespecified properties. Using computer simulation and theoretical techniques, we then attempt to predict the mechanical equation of state of this crystal, hence predicting the rate of plastic deformation as a function of the temperature, the applied stress, and the nature and properties of the microstructural barriers. The result of the investigation is a precise specification of the mechanical equation of state of a simple prototype crystal.

The third approach, described under heading 6 below, involves a quasi-thermodynamic investigation of the mechanical equation of state of a simple solid. In this investigation we assume that insofar as its effect on the mechanical behavior of a material is concerned, the microstructure may be represented by a single structural variable. Incorporating this variable into a simple equation of state, we may investigate the formal properties of the equation of state and construct model constitutive equations that may be compared to empirical data on the behavior of real materials. These three theoretical approaches are, we believe, complimentary, and will together lead to new insight into the theory of the structure property relation in real materials.

The second major part of our research is concerned with the actual design of new engineering alloys to meet advanced requirements in the energy area. During the past year our research has included four specific alloy design projects together with supporting basic studies. The first of these, reported under headings 7 to 11, is a continuation of our research toward tough ferritic alloys for use at liquid helium temperature, the temperature encountered in a cool superconducting magnet and in other advanced cryogenic systems. During the past year our principal research effort has focused on reprocessing available cryogenic alloys, specifically the so-called "9Ni" cryogenic steel, to impart outstanding toughness in liquid helium. Basic research projects in support of this development include studies of ordering in iron nickel alloys, of passivation of iron nickel alloys, and studies of the role of retained austenite in controlling the ductile-brittle transition temperature of ferritic materials.

While this research has lead to a series of alloys that exhibit outstanding toughness in liquid helium, the alloys all contain high concentrations of nickel, and, would, as a consequence, be expensive in commercial practice. For this reason we have inaugurated a second alloy design project that has as its objective the development of nickel-free cryogenic alloys for use at temperatures such as the temperature of liquified natural gas at which large tonnages of cryogenic material are expected to be needed in the next few years. Our specific research is concentrated on the development of ferritic Fe-12Mn alloys for cryogenic use; this is reported under headings 12 and 13 below. Heading 12 describes the development of a new Fe-Mn cryogenic alloy that combines outstanding strength with excellent toughness at liquid nitrogen temperature. Heading 13 reports supporting basic research on microstructural control and on precipitation reactions that might prove useful in strengthening Fe-Mn alloys.

Our third alloy design project is directed toward the development of alloys of outstanding strength and toughness to meet advanced aerospace needs. This research, which is reported under headings 14 and 15 below, concentrated specifically on reprocessing commercial 250 grade maraging steel to impart exceptional toughness at strengths near 200 ksi yield. Under heading 14 we report a thermocycling procedure that appears successful in accomplishing this. Under heading 15 we discuss the role of retained austenite in the 250 grade maraging steel microstructure. Retained austenite is a mechanism that has often been

suggested as a device for improving the toughness of high strength steel, but in this instance turns out to be unsuccessful.

The fourth project below is a joint alloy design effort with Professor Gareth Thomas, and addresses the problem of designing very high strength, very high toughness austenitic alloys for use in retaining rings in large electrical generators. Initial research progress in this project is described under headings 16 and 17 below. Under heading 16 we report initial success in developing processing techniques for imparting exceptionally high strength to available Fe-Ni stainless steels. Under heading 17 we report the results of basic investigation that is oriented toward designing an alloy that can be thermally processed to exhibit outstanding toughness at strengths near the 200 ksi level, while remaining wholly austenitic at room temperature.

1. CHARACTERISTIC POLYGRANULAR MICROSTRUCTURES FROM SIMPLE NUCLEATION AND GROWTH TRANSFORMATIONS

John E. Sanchez and J. W. Morris, Jr.

The polygranular microstructure of a metal or ceramic is the product of the growth, impingement, and subsequent coarsening of individual grains. The grains may be nucleated, as in the case of a microstructure established through a phase transformation or recrystallization reaction, or preestablished, as in the case of a solid sintered from powder. The geometric characteristics of the microstructure, including those which have an important influence on subsequent physical properties, are hence a product of the process which brought the microstructure into being.

In this project we are investigating the various types of microstructures that may result from a simple, prototype nucleation and growth process with the objective of classifying the possible types of microstructure and identifying their geometric similarities and differences. We assume an initially homogeneous polygranular body that transforms by a nucleation and growth mechanism to yield a homogeneous product. Nuclei of the new phase are assumed to form either homogeneously in the bulk of the original phase or heterogeneously on one of the preferred sites (grain boundaries, grain edges, or grain corners) that exist in the initial phase. The expected frequency of nucleation per unit time is assumed constant for each type of site but varies with the type of the nucleation site, the thermodynamic driving force for the transformation, and the catalytic potency of the site according to relations given by classical nucleation theory. After nucleation the grains are assumed to grow at a constant, isotropic rate until they impinge on one another.

The dependence of the classical nucleation rate on thermodynamic variables is such that, except in rare circumstances, the transformation will be dominated by nuclei that form on a particular type of site (a result widely used in theories of the kinetics of phase transformations). The microstructure resulting from the transformation then depends on whether the dominant nucleation sites are "saturated" (consumed by nuclei or growing grains) before the transformation is essentially complete. The kinetic equations of nucleation are such that if "saturation" occurs at all, it may almost invariably be assumed to occur at the very beginning of the transformation.

Using these results, we are able to identify four distinct classes of microstructure. Specific microstructures within any class then bear a simple geometric relation to one another. The four classes are: (1) The Johnson-Mehl microstructure, the microstructure that arises from an unsaturated transformation irrespective of the dominant nucleation site. All Johnson-Mehl microstructures may be shown to be geometrically identical; they differ only through a scale factor which fixes the average grain size. (2) The cellular microstructure, arising from a saturated nucleation process at grain corners or on any set of discrete nucleation sites randomly distributed through the volume. These microstructures are also geometrically identical to within a scale factor which determines average grain size. (3) A microstructure consisting of columnar or lath-like grains arising from a saturated transformation dominated by grain boundary nucleation. (4) A microstructure consisting of platelike grains arising from a saturated transformation along grain edges. Individual microstructures within these latter two classes are not geometrically identical, but are simply related to one another.

We have also been able to establish simple rules to specify which of these characteristic microstructures will be established under particular transformation conditions.

2. COMPUTER SIMULATION OF MICROSTRUCTURE

Kim Walker Mahin and Kenton L. Hanson

Having identified classes of theoretically interesting microstructures, as described above,

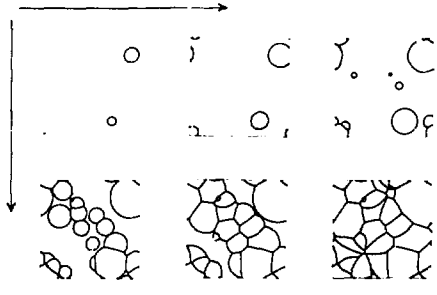

Fig. 1. Development of the Johnson-Mehl microstructure in a planar section through the transforming body. (XBL 757-6691)

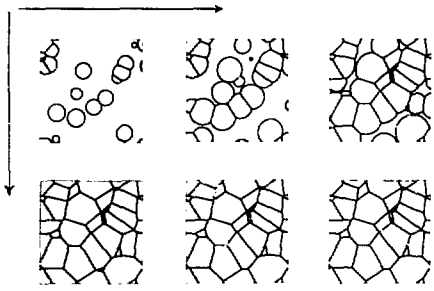

Fig. 2. Development of the cellular microstructure. (XBL 757-6694)

we are now employing computer simulation techniques to study and characterize those microstructures in some detail. To carry out these studies we have written a computer code that takes as input data a nucleation rate and a growth rate (which may be given as simple constants or in a wide range of functional forms) and generates the microstructure that will result from the transformation. The code will then examine selected planar sections, plotting the planar microstructures and measuring and plotting selected geometric information (such as histograms of area, side number, or junction angle). Research to date has concentrated on the Johnson-Mehl microstructure, shown in Fig. 1, and the cellular microstructure, shown in Fig. 2. We are in the process of establishing relevant histograms of the important geometric properties of those microstructures. An example, the histogram of cross-sectional areas of grains in a section through the Johnson-Mehl microstructure, is shown in Fig. 3.

In addition to permitting the geometric characterization of ideal microstructures, the code is capable of accepting the microstructure as input and providing a geometric characterization, a capability we hope to exploit in generating experimental data to compare to the theoretical.

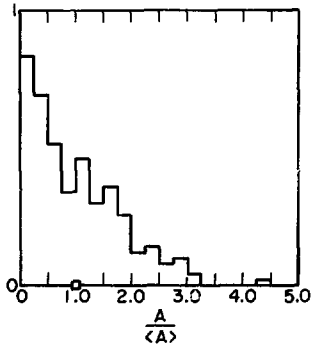

Fig. 3. Histogram of the cross-sectional area of grains in a planar section through the Johnson-Mehl microstructure. (XBL 761-2164)

3. DEFORMATION OF AN IDEALIZED SINGLE CRYSTAL CONTAINING IDENTICAL POINT BARRIERS TO DISLOCATION GLIDE

Sabri Altintas, Kenton Hanson and J. W. Morris, Jr.

Over the past several years we have been engaged in a combined computer simulation and theoretical study of the plastic deformation of idealized single crystal. The initial problem investigated was that of a crystal that deforms through the thermally-activated glide of dislocations, given that the crystal contains microstructural barriers that may impede the dislocation motion. The investigation was aimed at determining the critical resolved shear stress for dislocation glide at zero temperature and the velocity of thermally activated glide at finite temperature as a function of the applied stress and the nature and strength of the microstructural barriers to glide. During the past year our understanding of the glide dislocation through a field of random distributed identical point barriers was extended by the solution of two particular problems.

First, in earlier work we had derived and published theoretical expressions giving the critical resolved shear stress for dislocation glide through an array of like point barriers at zero temperature.[1] The derivation of the equations was such that the equations place an upper bound on the critical resolved shear stress in the limit as the array size approaches infinity. The theory was shown to be in reasonable agreement with computer simulation results. It accurately reproduced both the value of the critical resolved shear stress and the pertinent characteristics of the configuration of obstacles which determine the critical resolved shear stress over a range of conditions. However, the theory did slightly underestimate the critical resolved shear stress for dislocation glide in the limit of small obstacle strength. While it appears reasonable that this discrepency is due to the effect of the array size we felt it important to clarify the question by actually determining the variation of critical resolved shear stress with the array size. Carrying out this study required a significant revision in our computer simulation procedures, since it was necessary to devise a code to simulate glide through extremely large arrays in reasonable computer time. Such a code was written and used to generate the data shown in Fig. 1. In this figure the strength of the array is plotted as β, a number corresponding to the maximum dimensionless force exerted on the most stable configuration encountered by a dislocation in glide through the array at a fixed value of the applied stress. As can be seen from the figure, the parameter β increases with array size and appears to asymptote at a value very close to that predicted by the theory. For com-

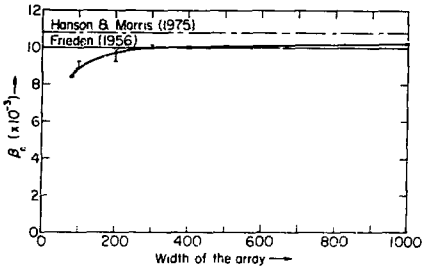

Fig. 1. The resistance to dislocation glide under a dimensionless stress of $\tau^* = 10^{-3}$ as a function of size of a square array of identical point barriers. (XBL 761-2169)

parison we have also included the limiting value of β as predicted by the "Friedel relation" commonly used in prior theoretical work. The large array code has also permitted us to conduct intensive studies on the geometric properties of significant configurations encountered in glide through very large arrays of obstacles.

The second major problem investigated during the past year is relevant to the theory of thermally activated glide through arrays of point obstacles. In earlier theoretical work[2] we had pointed out that the path followed by a dislocation in thermally activated glide through an array of point barriers will depend on the temperature as well as on the applied stress. This uncertainty in the glide path of the dislocation poses a significant problem in constructing a theory of thermally activated glide, since one must account for the variation of the glide path as well as for the variation in the velocity of glide along a given path. Our early computer simulation studies[3] suggested that this problem

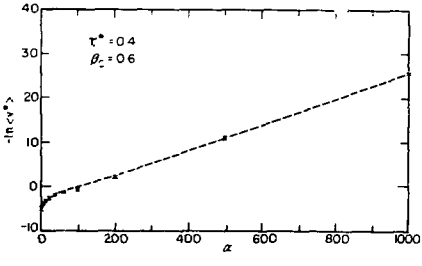

Fig. 2. Plot of velocity of thermally activated dislocation glide as a function of reciprocal temperature ($\alpha = 1/T^*$) through an array of identical obstacles of strength $\beta_a = 0.6$ at stress $\tau^* = 0.4$. The dashed line shows the velocity of glide along the "minimum single path. The bars represent computer simulation data permitting a statistical choice of glide path. (XBL 7410-7504)

might be avoidable. Since at higher temperature the difference in glide velocity among the various paths which the dislocation might follow becomes small, it may be possible to base a theory of thermally activated glide on the velocity for glide along the so-called minimum angle path, the path that is necessarily followed by the dislocation in glide through the array at very low temperature.

During the past year we studied this potentially useful approximation in more detail. The results are exhibited in Fig. 2. The bars in the figure represent the glide velocity as determined from a full statistical simulation of thermally activated glide at a given value of the stress and the obstacle strength. The solid line in the figure represents an estimate of the velocity of thermally activated glide based on the assumption that the dislocation follows the minimum angle path. As can be seen from the figure, the agreement between the two sets of data is quite good. Our current theoretical effort is hence focused on predicting the geometric properties of the obstacle configurations encountered along the minimum angle path in sufficient detail to write a theoretical prediction for the velocity of thermally activated glide as a function of temperature.

---

1. K. Hanson and J. W. Morris, Jr., J. Appl. Phys. 46, 953 (1975).
2. J. W. Morris, Jr. and D. H. Klahn, J. Appl. Phys. 44, 4882 (1973).
3. J. W. Morris, Jr. and D. H. Klahn, J. Appl. Phys. 45, 2027 (1974).

4. DEFORMATION OF AN IDEALIZED CRYSTAL CONTAINING MORE THAN ONE TYPE OF MICROSTRUCTURAL BARRIER

Kenton Hanson, Sabri Altintas, and J. W. Morris, Jr.

In glide through a real crystal a dislocation contributing to plastic deformation will generally encounter microstructural barriers of more than one distinct type. For example, in glide through a crystal containing both forest dislocations and small precipitate or solute atoms, both of these obstacles will contribute to the pinning force applied to a dislocation. In the most general case one would anticipate that the critical resolved shear stress for dislocation glide would be determined by some balance between the resistances of the various types of barriers that a dislocation might encounter. In research during the past year we found it possible to extend our theoretical solution for the critical resolved shear stress to predict the critical resolved shear stress when a distribution of obstacles of different types is present. The theory establishes an upper limit on the critical resolved shear stress. Subsequent computer simulation experiments have shown that as in the case of obstacles of a single type, the theory yields a good estimate of both the critical resolved shear stress and the geometric properties of the barrier configuration that determines the critical resolved shear stress. The fit between

theory and experiment is illustrated in Table 1, where we have selected ten example cases of arrays containing a mixture of relatively strong and relatively weak obstacles with the fraction of weak obstacles given by the number X_w. The experimental data listed in the table are taken from computer simulation experiments on arrays containing 1,200 points and are the mean values of the values actually obtained in experiments on ten such arrays. The results of a possibly more sensitive test of the accuracy of the theory are presented in Fig. 1 where we have compared the distribution of forces on the strength determining configuration in case number 7 of Table 1 with that predicted by the theory. As can be seen from the figure, the fit between theory and experiment is very good. In current research we are extending this treatment to construct a theory of a thermally activated dislocation glide through arrays containing distributions of distinct obstacle types.

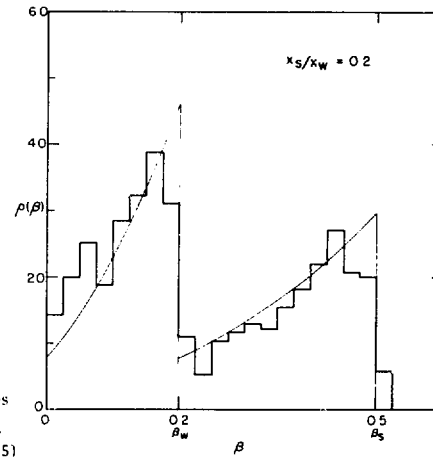

Fig. 1. The theoretical distribution of forces (β) applied to the strength-determining obstacles configuration in case 7 of Table 1 compared to an empirical histogram obtained through computer simulation. (XBL 7510-7475)

Table 1. Comparison between theory and computer simulation of the theoretical resolved shear stress for dislocation glide through an array of two types of point obstacles (of dimensionless β_s and β_w, with X_w the fraction of weaker obstacles). τ^* is the critical resolved shear stress in dimensionless form, c^w is the fraction of weak obstacles on the strength-determining configuration, and $\langle \ell \rangle$ is the mean segment length of this configuration.

Case	β_s	β_w	X_w	τ^*_{theory}	$\langle \tau \rangle_{exp}$	$\langle c^w \rangle_{theory}$	$\langle c^w \rangle_{exp}$	$\langle \ell \rangle_{theory}$	$\langle \ell \rangle_{exp}$
1	0.5	.2	.5	.240	.238	.13	.12	1.30	1.26
2	0.5	.05	.5	.231	.245	.020	.017	1.44	1.44
3	0.2	.05	.5	.057	.064	.064	.064	2.25	2.04
4	0.5	.2	.17	.299	.299	.030	.045	1.11	1.06
5	0.5	.05	.17	.297	.295	.0042	.0049	1.13	1.11
6	0.2	.05	.17	.073	.080	.014	.004	1.84	1.74
7	0.5	.2	.83	.157	.166	.40	.44	1.65	1.57
8	0.5	.05	.83	.135	.135	.088	.15	2.31	2.24
9	0.2	.05	.83	.035	.039	.24	.26	3.21	2.85

5. COMPUTER SIMULATION OF THE SIMULTANEOUS GLIDE OF SETS OF INTERACTING DISLOCATIONS THROUGH FIELDS OF MICROSTRUCTURAL BARRIERS*

Kenton Hanson

As further extension of the research on the plastic deformation of idealized crystals, we have begun computer simulation experiments on the simultaneous glide of sets of interacting dislocations through fields of microstructural barriers idealized as point obstacles. The construction of a computer simulation code capable of handling this more complicated problem in reasonable computational time posed a series of difficult problems, since the code must simultaneously account not only for the interaction of the dislocation with the obstacles it encounters but also for the interaction of segments of the dislocation with one another and with other dislocations in the array. Such a code has been written, and is now in use.

The initial problem investigated with the code is the critical resolved shear stress for the glide of a train of dislocations through an array of

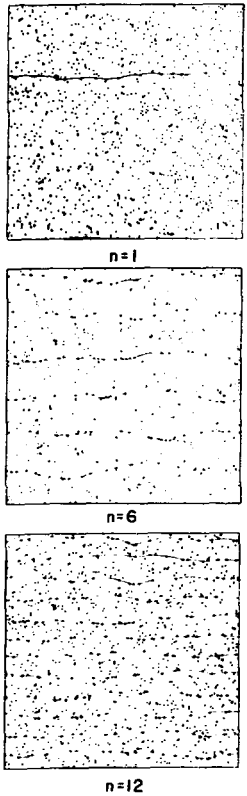

Fig. 1. The strength-determining configuration for the glide of interacting dislocations through are array of like obstacles of strength $\beta_c = 0.252$ in the fully periodic case. (XBL 761-2170)

like microstructural barriers. In these experiments we assume that a group of interacting dislocations is present within the array and further assume that the array is periodically repeated in all directions to produce a fully periodic infinite case. The code then computes the value of the stress necessary to cause the train of dislocations to become mechanically unstable, corresponding to the stress at which an infinite train of dislocations would move freely through the infinite periodic array. The critical configuration of dislocations, that is, the configuration assumed by the dislocations immediately prior to instability is shown in Fig. 1 for the case of one, six, and 12 dislocations within the array. An interesting feature of these configurations is their regularity.

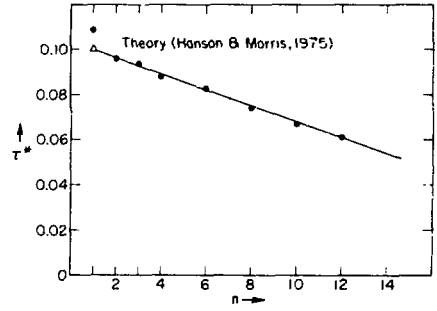

Fig. 2. The critical resolved shear stress for dislocation glide vs. the number of dislocations per array of 10^3 obstacles ($\beta_c = 0.252$) in the fully periodic case. (XBL 761-2167)

The dislocations in the critical configuration assume almost equispaced positions within the array; no "pile-up" is observed. The critical resolved shear stress for glide of the train of dislocations is plotted in Fig. 2 against the number of dislocat-ons present in the array. Two features of this plot are of interest. First, the critical resolved shear stress decreases rather slowly as dislocations are added to the array. In fact, when there are 12 dislocations present, the critical resolved shear stress for glide is fully 60% of the value for glide of a single dislocation through the array. Second, the decrement in the critical resolved shear stress per dislocaton added is virtually constant for the range of conditions studied in this simulation.

Computer simulation experiments over a wide range of conditions are now in progress. If the results of further research maintain the simplicity apparent in Figs. 1 and 2 then the construction of a rather general theory for the simultaneous glide of sets of interacting dislocations should be straightforward.

*Supported by the National Science Foundation under Grant No. DMR 75-08163.

6. RESEARCH ON THE MECHANICAL EQUATION OF STATE OF SIMPLE SOLIDS

M. C. H. Lee and J. W. Morris, Jr.

If the microstructure-property relation can be quantified, then it should prove possible to write an equation like Eq. (1) below (often referred to as the mechanical equation of state of solids).

$$\dot{\varepsilon} = \vec{\dot{\varepsilon}}\,(\sigma, \tau, n) \qquad (1)$$

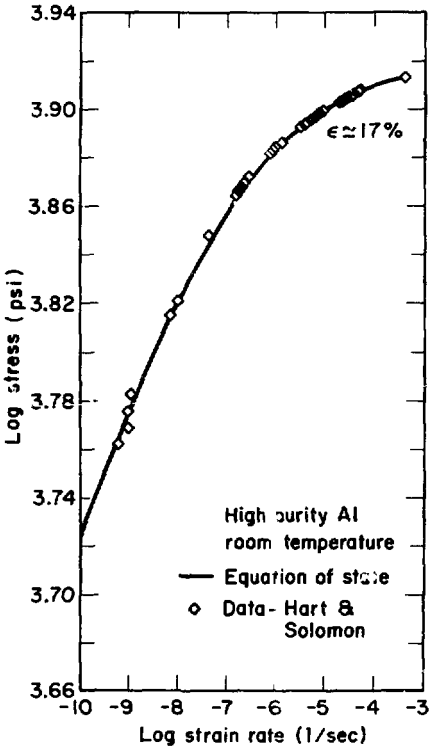

Fig. 1. Equation of state fit to the stress relation data of Hart and Solomon (Acta. Met. 21, 295 (1973)). (XBL 761-2165)

Equation (1) is written in uniaxial form and expresses the uniaxial strain rate as a function of the applied stress, the temperature, and a parameter or set of parameters which represent the effects of the microstructure.

Given the complexity of the microstructure of a real material, as discussed in the paragraphs above, there is no a priori reason to suspect that the parameter η can be written as a single parameter or even as a simple set of parameters in reasonably tractable form. One may nonetheless hope that simple forms for the microstructural parameter η may be found, at least for certain simple solids. In this case, the parameter η must represent either a scaling parameter that connects different topologically similar microstructures or an entropy-like variable that expresses the aggregate effect of a set of internal variables.

In the absence of detailed microstructural theory one may attempt to construct a model for the mechanical behavior of a solid by assuming the existence of a simple parameter and/or exploring the mathematical consequences of this assumption (in light of known experimental constraints) to determine plausible forms for the mechanical equation of state. This approach to the mechanical equation of state has received considerable attention in recent years from several investigators, in particular, E. W. Hart. There is, as a consequence, a mounting body of experimental evidence that the assumption of a rather simple microstructural parameter may be helpful in rationalizing experimental data on the mechanical behavior of many simple materials.

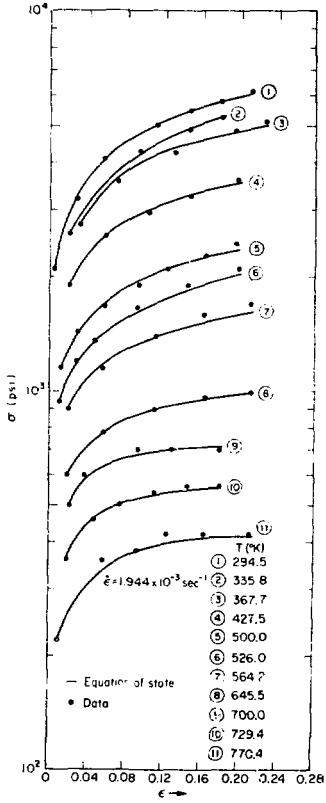

Fig. 2. Equation of state fit to the true-stress/true-strain tensile curves of high purity aluminum. Data from Trozera, Shirley and Dorn. (XBL 761-2166)

During the past year we inaugerated a theoretical investigation of the mechanical equation of state, under the constraint that we would like, insofar as possible, to maintain a model in which the effect of structure is represented by a single parameter. The model we are now studying has points of contact with the prior work of several investigators, and is based on two central assumptions. First, we assume that a steady state of mechanical deformation exists at all temperatures and that the sign and magnitude of the deviation from this steady state determines the rate of evolution of the current mechanical state. Second, we assume that the microstructure parameter, η, can be defined such that it relates to the plastic strain through an integrating factor. These assumptions allow the formulation of a set of constitutive equations which do a very good job of predicting the mechanical behavior of aluminum over a wide range of experimental conditions as illustrated in Figs. 1 and 2. Development of these equations and application to other materials is currently under way.

7. REPROCESSING COMMERCIAL CRYOGENIC STEEL FOR HIGH TOUGHNESS AT LIQUID HELIUM TEMPERATURE*

C. K. Syn and Sungho Jin

In the course of a research program on the development of ferritic cryogenic steels which has continued in this research group for several years, we were able to demonstrate the possibility of processing an Fe-12Ni-0.25Ti alloy to an extremely fine grain size. The alloy as processed has a remarkable combination of strength and toughness at liquid helium temperature. Specifically, it has a toughness estimated to be ~ 250 ksi $in^{1/2}$ at a yield strength ~ 200 ksi. These results show that the ductile-brittle transition temperature of a ferritic structural steel can be suppressed to below 4°K, and permit the specification of properly processed ferritic steels for structural use in liquid helium in advanced energy systems.

From the practical engineering point of view, however, the Fe-12Ni alloys employed are not now commercially available. As a consequence an engineer would have considerable difficulty procuring commercial ferritic cryogenic steel, unless he was prepared to order in large tonnage amounts. To overcome this problem we began research to reprocess commercially available nickel-bearing cryogenic steels to impart toughness at liquid helium temperature. The steel initially selected was the so-called 9Ni steel (of composition Fe-9Ni-1Mn-0.2C) which is a steel commonly used in cryogenic tankage. Previous research has shown that while 9Ni steel has a good combination of strength and toughness at liquid nitrogen temperature, it embrittles badly between liquid nitrogen temperature and liquid helium temperature and, hence, is not suitable for the use in liquid helium in its normal commercial treatment.

Commercial 9Ni steel was procured from the Nippon Steel Company and subjected to a grain refinement treatment similar to that used in the 12Ni alloy. The efficiency of the grain refinement process is apparent in the micrograph shown in Fig. 1. The final grain size of the 9Ni steel is approximately 1 μm. After grain refinement the alloy is tempered, both to temper carbides present in the microstructure and to introduce a fine distribution of retained austenite.

After processing the alloy was tested for its tensile and fracture toughness properties in both

MICROSTRUCTURE of 9Ni STEEL

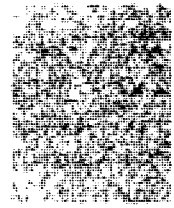

As Rec'd

C-R

C-R & Tempered

Fig. 1. Large grain size of ~ 10μ in the as-received condition was reduced to ~ 1μ through the thermal cycling. A slightly larger-looking grain size in the tempered condition is due to specimen variation rather than to grain growth during tempering. (XBB 758-5826)

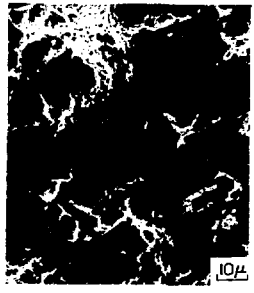

Fig. 2. The fracture made at liquid nitrogen and helium temperature (LNT and LHeT) changed from principally quasi-cleavage in the as-received condition to mixture of dominant dimple-rupture and quasi-cleavage in the grain-refined condition. (XBB 7512-9088)

Table 1. Cryogenic mechanical properties of 9Ni steel.

		Conventional (NNT)		Grain refined	
77K	YS	145	ksi	146	ksi
	K_{IC}	210	ksi$\sqrt{in}$	314	ksi$\sqrt{in}$
6K	YS	189	ksi	191	ksi
	K_{IC}	75	ksi$\sqrt{in}$	166	ksi$\sqrt{in}$

liquid nitrogen and liquid helium. The results are shown in Table 1. As can be seen from the table, the reprocessed alloy has been toughened considerably and exhibits an excellent combination of strength and toughness at temperatures near that of liquid helium. The improved toughness of the reprocessed alloy is also apparent in the fracture surface, Fig. 2. These results demonstrate that it is possible to reprocess commercially available cryogenic steels to have good toughness in liquid helium. While the properties of the reprocessed 9Ni steel are not as good as those obtained with the original 12Ni alloy, the cryogenic strength-toughness combination is favorable and the alloy should be suitable for all but the most demanding structural applications.

*Also supported by the Office of Naval Research under Contract N0014-75-C-0159.

8. INVESTIGATION OF Fe-Ni-Co-Mo ALLOYS FOR CRYOGENIC USE*

Bradley W. Whitaker and J. W. Morris, Jr.

Alloys of the maraging class have the favorable property that at room temperature they can be age-hardened to high strength levels without substantial loss of fracture toughness. For this reason we conducted an investigation of the potential of these alloys for cryogenic use in the hope that we might be able to age-harden to unusually high cryogenic strengths while maintaining good values of the fracture toughness. The alloys specifically investigated were low-interstructural alloys with compositions varying around a typical composition of Fe-12Ni-4Co-2Mo-0.05Ti. These alloys were processed and tested both in the as-quenched condition and after grain refining through a series of alternate treatments. The results of the investigation were less promising than had been hoped. The alloys showed a good combination of cryogenic strength and toughness in the as-grain refined condition; however, their properties were not markedly superior to those of the grain refined Fe-12Ni alloy without the addition of cobalt and Mo. On aging the alloys showed a deleterious trade-off between cryogenic strength and toughness. A slight increase in strength after aging led to a substantial decrease in cryogenic fracture toughness. Our conclusion was that these alloys are not suitable for use in the aged condition at temperatures of 77°K and below.

*Also supported by the Office of Naval Research under Contract N00019-75-C-0159.

9. ORDERING REACTIONS IN MARTENSITIC Fe-Ni ALLOYS*

Sheree Wen, G. Thomas and J. W. Morris, Jr.

The beneficial effect of nickel on the properties of martensitic steels is one of the most important and one of the least well understood facts of metallurgical science. As part of a general investigation of the specific role that nickel may play, we have been engaged in an investigation into possible ordering reactions in Fe-Ni martensities of intermediate nickel content. Our anticipation that alloys of composition near Fe-12Ni will show at least short range order is based on two considerations. First, it is well known that the equilibrium solubility of nickel in martensite is limited to approximately 7%. Hence, Fe-12Ni alloys contain a supersaturation of nickel at room temperature and one would expect this supersaturation to be locally relieved either through an ordering or a clustering reaction. On the other hand, it is known that iron-nickel alloys do order at higher nickel concentrations. The Ni_3Fe phase is well documented. There is additional experimental evidence for ordered phases for stoichiometric composition NiFe and Fe_3Ni. While these phases are based on the face-centered cubic γ structure, their existence suggests a tendency for ordering in Fe-Ni alloys.

Our search for ordered phases in Fe-12Ni martensite began with a careful microstructural survey using transmission electron microscopy. The initial stages of this investigation were not fruitful, at least in part because any possible ordered phases would yield defraction spots that would masked by the superlattice reflections from the oxide layer naturally present on Fe-Ni alloys at room temperature. While theoretical calculations suggest that more elaborate microscopy investigations using lattice imaging techniques might reveal ordered phases, these investigations are extremely difficult to carry out in the absence of a priori information on the structure of the ordered phases.

The experimental difficulties facing a transmission electron microscopy investigation, do not, however, pertain to an investigation using neutron diffraction. Since neutron diffraction is carried out on bulk specimens, it is not sensitive to surface contaminant phases. We therefore sought a cooperative program with the Oak Ridge National Laboratory to investigate the possibility of ordered phases in Fe-12Ni martensities. Neutron diffraction experiments conducted by Drs. Ray Carpenter and W. Koehler of the Oak Ridge Laboratory did produce evidence suggesting an ordered structure based on the BCC lattice in an Fe-12Ni martensite which had been aged for one month at intermediate temperature. The evidence, however, is not yet definitive and additional neutron diffraction experiments are currently underway at Oak Ridge. If the further neutron diffraction experiments substantiate the initial results then transmission electron microscope research will be conducted at Berkeley in an attempt to get a direct lattice image of the ordered phase and a consequent clear picture of the structure of this Fe-Ni order.

*Also supported by the Office of Naval Research under Contract No. N00019-75-C-0159.

10. LOW TEMPERATURE SURFACE OXIDATION OF Fe-12Ni ALLOYS*

Sheree Wen and J. W. Morris, Jr.

A passivating oxide layer is known to form rapidly on the surface of iron or iron alloys exposed to air at low temperature. The properties of this passivating layer largely control the low temperature oxidation and corrosion properties of steels. It is hence important that the nature of this passivating layer be well understood. The investigation conducted over the previous year principally involved a transmission electron microscopy examination of the thin oxide film formed on the surface of Fe-12Ni alloys on exposure to air at room temperature. Using high resolution microscopy the oxide particles of the film could be directly resolved and their structures and morphology characterized. The following conclusions were drawn from these characterization studies:

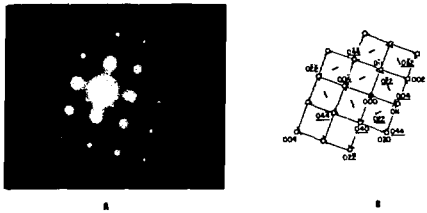

Fig. 1. Electron diffraction pattern from a $(100)_\alpha$ surface of an Fe-12Ni foil showing α diffraction spots and oxide spots. The interpretation of the diffraction pattern in terms of a Bain-related Fe_3O_4 oxide coating is drawn. (XBB 7512-9242)

1. A passivating oxide layer, principally Fe_3O_4, forms spontaneously on the surface of Fe-Ni alloys on exposure to air at room temperature.

2. The orientation relation between the oxide and the metal surface depends on surface orientation. The Bain relation is obeyed when the alloy surface is $(100)_\alpha$, while the Nishiyama-Wasserman relation is obeyed on other surfaces. The Bain related oxide on the $(100)_\alpha$ surface of the Fe-12Ni martensite is illustrated in Fig. 1, which shows the diffraction pattern obtained from a $(100)_\alpha$ surface together with its crystallographic interpretation in terms of a Bain-related oxide. The change of orientation of the surface is attributable to the need to accommodate the misfit strain between the oxide and the substrate.

3. The oxide layer consists of dispersed, small (approximately 20 Å in size) oriented particles rather than a continuous thin film. This observation is illustrated in Fig. 2 which shows individual oxide particles observed through dark field microscopy.

4. The size of the oxide particles and the density of their distribution is related to the crystal surface orientation and condition.

Fig. 2. Diffraction pattern and bright- and dark-field electron images showing discrete oxide particles on the foil surface. (XBB 752-1283)

*Also supported by the Office of Naval Research under Contract No. N00019-75-C-0159.

11. THE INFLUENCE OF RETAINED AUSTENITE ON THE PROPERTIES OF Fe-Ni CRYOGENIC STEELS*

C. K. Syn, Sungho Jin, and J. W. Morris, Jr.

The use of retained austenite has often been suggested as a means of improving the ductility and toughness of high strength ferritic steels. However, the introduction of retained austenite has given mixed results in practice. With specific reference to the cryogenic properties of ferritic alloys, any benefit attributable to austenite seems to depend on the nature of the alloy and whether the Charpy impact energy or the fracture toughness is used as a measure of alloy toughness. In light of these known ambiguities, we have begun research to clarify the effect of austenite.

The available data agrees on the beneficial effect of retained austenite on the ductile-brittle transition temperature as measured in the Charpy impact test. Retained austenite is intentionally introduced in the processing of both commercial 9Ni and 6Ni steels and is in both cases believed responsible for the good cryogenic properties obtained. Our own research[1] deomonstrated a substantial decrease in the ductile brittle transition temperature of Fe-8Ni-2Mn-0.25Ti alloy on introduction of a small addition (3-5%) of retained austenite and also found[1,2] that the introduction of retained austenite led to a substantial increase (of approximately 50%) in the Charpy impact energy measured above the ductile brittle transition temperature in both Fe-12Ni and Fe-8Ni alloys.

The effect of retained austenite on the fracture toughness is, however, less certain. Reports of spectacular improvement in K_{IC} on the introduction of retained austenite must be viewed with some caution because of interfering effects of the alloy yield strength. One must also distinguish between the effect of austenite on the ductile-brittle transition temperature and its effect on toughness measured above the ductile-brittle transition temperature. Prior work makes it clear that austenitizing treatments may be used to lower the DBTT as measured by the fracture toughness test. The effect is substantial in both commercial 9Ni and 6Ni cryogenic steels. The effect is also noticeable in our research 8Ni cryogenic steels, although the lowering of the ductile-brittle transition temperature as measured by the fracture toughness is substantially less than the lowering of the transition temperature as measured by the Charpy impact test. This result is illustrated in Fig. 1. The available data leads us to hypothesize that the beneficial effect of austenite is intimately connected with its mechanical stability.

In our research[3] on maraging steels, the austenite bearing alloys had comparitively higher toughness at the same strength level only when the austenite was mechanically stable. When the austenite was unstable the toughness was inferior to that of the martensitic structure. In tests at lower temperature, the toughness of the maraging steel showed a sharp comparative drop at a temperature near that of which the austenite

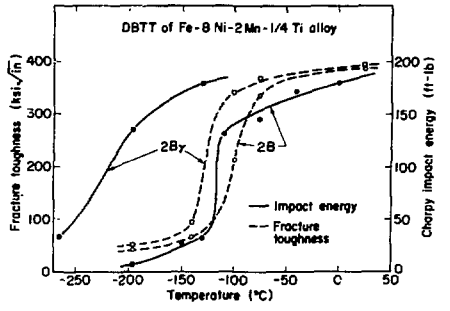

Fig. 1. The effect of retained austenite on the DBTT of an Fe-8Ni steel as measured by the Charpy impact and fractures toughness tests. Specimens 2b are as-grain refined. Specimens 2Br contain ~4% austenite introduced by tempering at 550°C. (XBL 761-2168)

first became mechanically unstable. Our research[1] on the effect of retained austenite on the grain refined Fe-12Ni alloy tested above the ductile-brittle transition temperature showed an apparent decrease in toughness. The austenite was again mechanically unstable under the test conditions.

Our tests on the Fe-8Ni cryogenic alloy (Fig. 1) suggest a relatively small decrease in the DBTT as measured by the fracture toughness. The austenite in this alloy is also mechanically unstable at cryogenic temperature. On the other hand, the austenite present in the 9Ni and 6Ni cryogenic steels, in which retained austenite is apparently beneficial, is stabilized by the presence of carbon. Comparative studies on the transformation of the retianed austenite in 9Ni steel on deformation at cryogenic temperature showed that only a small fraction transforms during extensive deformation. The beneficial effect of austenite on the Charpy impact energy may also be interpreted from the point of view of austenite stability, since it is expected that the mechanical transformation of austenite is suppressed in tests at high strain rates.

*Also supported by the Office of Naval Research under Contract No. N00019-75-C-0159.

1. S. Jin, S. K. Hwang and J. W. Morris, Jr., Met. Trans 6A, 1569 (1975).

2. S. K. Hwang, S. Jin, and J. W. Morris, Jr., Met. Trans. 6A, 2015 (1975).

3. S. Jin, D. H. Huang, and J. W. Morris, Jr., LBL-3936 (1975).

12. RESEARCH TOWARD Ni-FREE CRYOGENIC STEELS*

S. K. Hwang

While research in this laboratory and elsewhere has shown that Fe-Ni ferritic steels can be

Fig. 1. Fracture modes of Fe-12Mn-0.2Ti steels at -196°C A.S.; As-Solution treated Temp; Tempered at 500°C for 12 hours. C. W. & An.; Cold Worked 30% at room temperature and annealed at 600°C for 4 hours. (XBB 7510-7530)

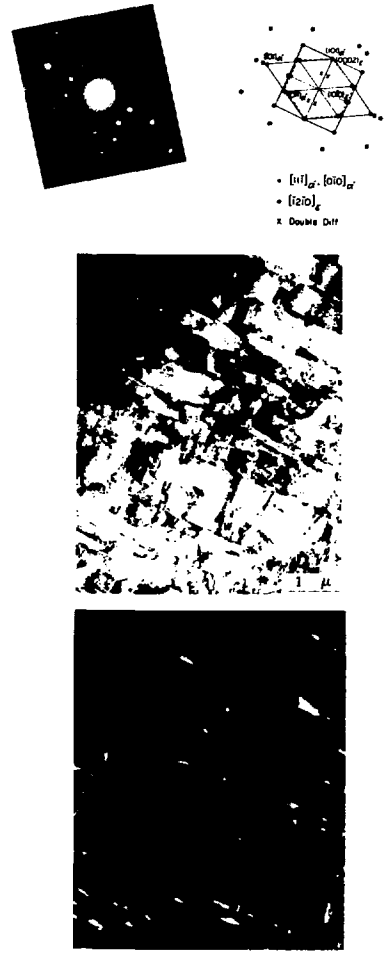

Fig. 2. TEM analysis of ε-martensites in Fe-12Mn-0.2Ti steels. The ε phase bounds the block-like α-martensite crystals. The orientation relationship between the two phases follows Kurdjumov-Sachs[1]. (XBB 7510-7954)

processed to have excellent strength/toughness combinations at cryogenic temperature, the high nickel content of these alloys has the consequence that they are commercially expensive. Since large tonnages of cryogenic structural steels are expected to be needed in the future for the transport and storage of liquified gases, a significant

Fig. 3. Grain refinement of Fe-12Mn-0.2Ti steel through room temperature deformation (~30%) followed by annealing at 600°C for 4 hours. (XBB 7510-7528)

level of industrial research is currently directed toward the development of cryogenic structural steels with lower nickel content. The bulk of this work emphasizes the partial replacement of nickel by manganese, a much less expensive alloying element.

Our current research in this project is directed toward the total replacement of nickel by manganese. To accomplish this we selected an initial alloy of Fe-12Mn and attempted to impart cryogenic toughness through processing treatments. We had initially hoped that this alloy could be grain-refined to high cryogenic toughness using the procedures developed for toughening Fe-Ni cryogenic steels. This approach was, however, unsuccessful for two reasons: First, as illustrated in Fig. 1, the Fe-Mn alloy shows significant grain boundary embrittlement in tests at cryogenic temperature; second, as illustrated in Fig. 2, the as-quenched Fe-12Mn alloy contains an admixture of hexagonal ε-martensite with the bcc α-martensite. The ε-martensite has an apparently deleterious effect on cryogenic strength, and also regenerates on thermal cycling, hence impeding grain refinement.

Two promising techniques for overcoming these problems were identified in research on Fe-12Mn. First, a tempering treatment at temperature near 550°C proved largely successful in suppressing grain boundary embrittlement at cryogenic temperature. This result was attributed to the introduction of austenite in the grain boundary during the tempering treatment. Second, the grain size of the alloy was successfully refined by a process involving cold work at room temperature followed by an anneal in the two-phase ($\alpha + \gamma$) range. The successful grain refinement is illustrated in Fig. 3. The beneficial effects of these treatments on the toughness of alloy are illustrated in Fig. 1 and in Table 1.

Even after processing, however, the cryogenic properties of the Fe-12Mn alloy are not as good as desired for cryogenic structural use. We therefore sought a chemical modification of the alloy to improve properties. While the chemistry of Fe-Mn alloys has not been well investigated, available metallurgical data on the Fe-Ni system suggested that Mo might be a useful addition to improve grain boundary properties. We therefore made and processed an Fe-12Mn-1Mo alloy.

Initial results with the Fe-12Mn-1Mo alloy are encouraging. As shown in Fig. 4, the Mo addition suppresses grain boundary embrittlement even in the as-quenched condition. After grain refinement

Fig. 4. Suppressed intergranular fracture at -196°C by the addition of 1Mo into Fe-12Mn-0.2Ti steel. Compare with Fig. 1. (XBB 7510-7534)

and tempering the alloy exhibits an excellent strength/toughness combination at liquid nitrogen temperature, as shown in Table 1. The alloy retains good toughness at 77°K a' a strength level 30 ~ 40 ksi above the strength of the 6Ni and 9Ni cryogenic steels in current use. These results suggest that wholly nickel-free steels can be processed for structural use at cryogenic temperature.

13. MICROSTRUCTURAL CONTROL IN Fe-Mn ALLOYS

S. K. Hwang and K. M. Chang*

The development of new Fe-Mn alloys of intermediate Mn content is made difficult by the complexity of the transformations shown by these alloys (in particular, the intrusion of hexagonal ε-martensite phase) and by the virtual absence of relevant prior metallurgical research. For this reason we initiated research on the control of phase transformations and microstructures in this alloy. We are particularly interested in finding techniques for suppressing the appearance of ε-martensite in Fe-12Mn alloys, and in identifying precipitation reactions which might be useful for strengthening austenitic Fe-Mn alloys of higher Mn content.

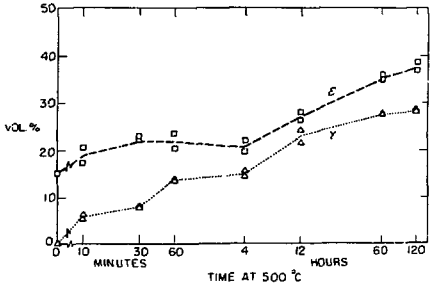

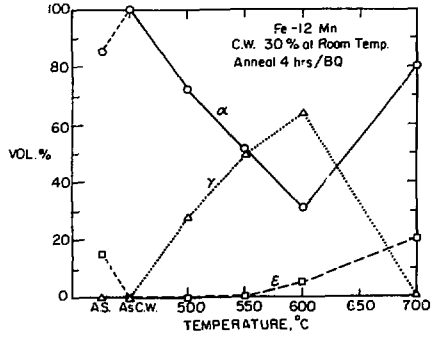

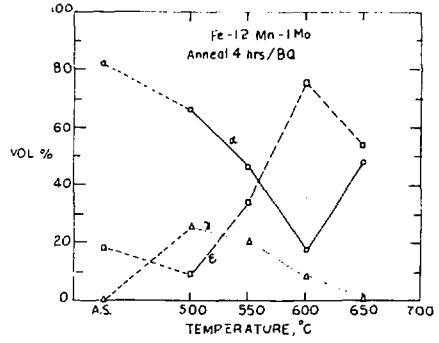

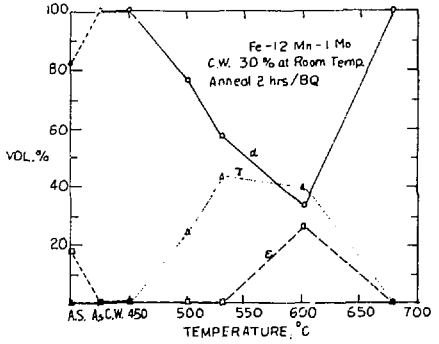

Fig. 1. Phase variations in the Fe-12Mn systems.
(a) Isothermal holding at 500°C. Fe-12Mn-0.2Ti (XBL 7510-7449)
(b) C. W. & Annealing Fe-12Mn-0.2Ti (XBL 7510-7448)
(c) Tempering at different temperatures (XBL 761-156)
(d) C. W. & Annealing Fe-12Mn-0.2Ti-Mo (XBL 761-157)

The intrusion of the ε-phase has been found to decrease after cold-work and on the introduction of Co and Mo alloying additions. The influence of the cold work and Mo addition on the phase distribution after amending is shown in Fig. 1. As can be seen from the figure, the addition of Mo causes a sharp minimum in the present ε as a function of annealing temperature near 500°C. The introduction of cold work suppresses the ε-phase for annealing temperatures less than ~550°C. This behavior can be interpreted on the basis of the mechanism of austenite reversions which associated transmission electron microgiaphic studies show to occur through a mechanization and growth process which initiates preferentially at the ε-phase.

The precipitation reactions currently under investigation involve the precipitation of Ti, V, Al, and Nb intermetallics, a group which, on the basis of work on Fe-Ni alloys and very limited data on Fe-Mn alloys, appears to include the most promising hardening agents. Initial studies have concentrated on precipitation in Fe-20Mn-1-5T, and have included the determination of the re-solution temperature, the characterization of precipitates involved in the aging process, and the determination of the aging response as a function of aging temperature.

*Also supported by the NASA Lewis Research Center under Grant NGR 05-003-526.

14. REPROCESSING 250 GRADE MARAGING STEEL TO HIGH TOUGHNESS*

S. Jin

The martensitic and the reverse-martensitic phase transformations occurring in alloy steels often produce tangles of dislocations of very high density (~ 10^{10} lines/cm^2), comparable to those of cold worked metals and alloys. This transformation-induced dislocation density not only increases the alloy strength significantly, but also provides uniformly distributed heterogeneous nucleation sites for precipitation of fine particles throughout the matrix. To maximize these benefits it may be desirable to further increase the dislocation density in the already dislocated martensite. Without employing plastic deformation, which is often undesirable in alloy processing, one may achieve higher dislocation density by use of second phase particles. As is well known from the theory of dispersion hardening, precipitate particles are very effective in causing dislocation multiplication during plastic flow. When the secondary shear in the martensitic and the reverse-martensitic phase transformations

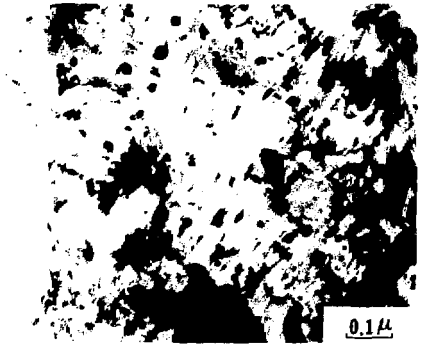

Fig. 1. Transmission electron micrograph of the maraged specimen (550°C/5 hr/Air Cool). (XBB 753-2512)

Fig. 2. Transmission electron micrograph. Maraged (550°C/5 hr/Air Cool), rapidly reverted to austenite in a salt bath (750°C/2.5 min.), and transformed to martensite by cooling to room temperature. (XBB 753-2185)

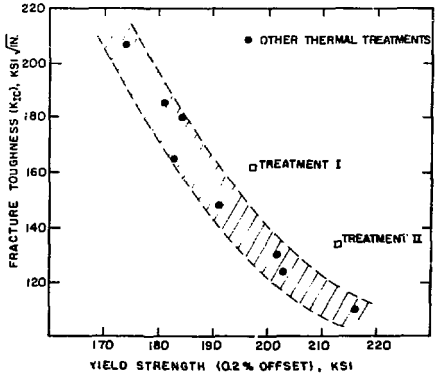

Fig. 3. Yield strengths and fracture toughnesses of rapidly transformed maraging steels. (Treatment I; Maraged (580°C/5 hr) + Rapidly austenized + Maraged (380°C/5 hr), Treatment II; Maraged (550°C/5 hr) + Rapidly austenized + Maraged (380°C/3 hr). (XBL 751-5604)

is accomplished by slip, the transformation may be regarded as a special type of plastic deformation. When such phase transformations occur in a matrix containing precipitates, the precipitates may serve as sources of interaction and multiplication of dislocations during phase transformation

(unless they are extremely fine and coherent with the matrix) resulting in a higher dislocation density.

Figures 1 and 2 show the change in dislocation density after the austenitic and martensitic phase transformations in a precipitate-decorated maraging steel. The precipitates in 250 grade maraging steel are mostly Ni_3Mo with some Ni_3Ti intermetallic compounds. A significant increase of dislocation density is clearly seen from the micrographs. Due to the interference of the high density of dislocatons, the precipitates in Fig. 2 are not very well resolved. A comparison of hardness data between these two microstructures indicate that the precipitates are mostly preserved during the phase transformations. In tensile tests the alloy shown in Fig. 2 exhibited an early departure from linearity in the stress-strain curve even though the ultimate tensile strength was close to the value of the simply maraged alloy, presumably representing the high mobility of un-pinned dislocations. An additional low temperature maraging has, therefore, been added to pin the fresh dislocations and increase the yield strength.

The mechanical properties of the processed maraging steel as illustrated in Fig. 3. The strength-toughness properties of the high-dislocaton-density maraging steels are superior to the values obtained by other heat treatments given to the same material.

15. THE INFLUENCE OF RETAINED AUSTENITE ON THE TOUGHNESS OF 250 GRADE MARAGING STEEL

S. Jin and D. Huang

A microduplex structure in a steel is a fine-scale two-phase mixture of austenite (γ) and martensite or ferrite (α). The microduplex structure is intriguing from the perspective of alloy design since it may offer a means for improving the toughness of high strength steels. A suitable distribution of relatively soft austenite in the ferrite matrix may serve to blunt a propagating crack, hence providing a higher resistence to fracture. Alternately, the stability of the austenite may be adjusted so that it transforms to martensite during deformation, hence incorporating the TRIP (Transformation Induced Plasticity) mechanism.

A simple two-step thermal processing technique was devised to impart a microduplex structure in a high strength 250-grade commercial maraging steel as shown in Fig. 1. A martensite grain size of approximately 1 μm was obtained with interspersed islands of retained austenite whose volume fraction and mechanical stability could be controlled by varying the thermal processing conditions. The microstructure and mechanical properties of the microduplex structure were compared to those of the alloy in the maraged, martensitic condition. Due to the presence of the austenite phase, the microduplex structure showed a much smaller temperature and strain rate dependence of deformation than the martensitic

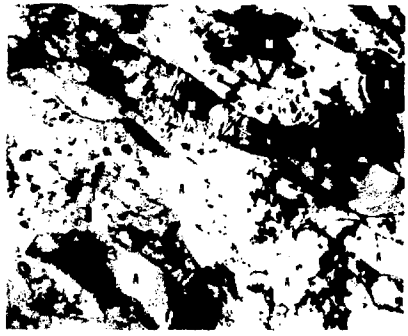

Fig. 1. High resolution electron micrograph of the microduplex alloy T8. The austenite phase is marked as A and the martensite as M. Note the distribution of precipitates and dislocations in each phase. (XBB 753-2152)

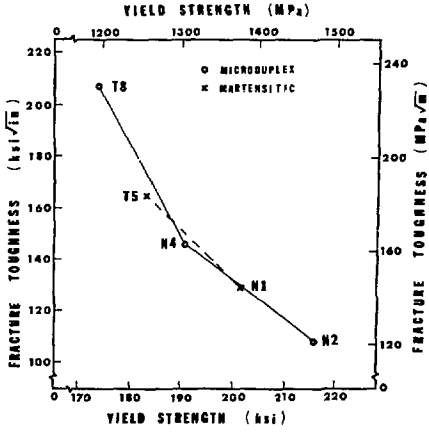

Fig. 2. Room temperature strength-toughness data for various alloys in Table IV. Microduplex alloys, N4 and N2, exhibit deformation-induced phase transformation at room temperature. (XBL 759-7294)

structure. A remarkable increase in uniform elongation was observed below the M_d temperature of retained austenite. The microduplex structure did not show any significant advantage in fracture toughness over the martensitic structure when compared at similar strength levels. (Table 1 and Fig. 2) By suitably adjusting austenitic stability a deformation-induced phase transformation (TRIP) of the retained austenite in the microduplex structure could be made to occur; however, the

Table 1. Room temperature mechanical properties of treated maraging steel.

	Specimen Number		Y.S.[a] (ksi)[e]	T.S. (ksi)[e]	Elong. (%)	R.A. (%)	$K_{Ic}(E)$[c] ($ksi\sqrt{in}$)[e]	$K_{Ic}(J)$[d] ($ksi\sqrt{in}$)[e]
Martensitic	T5	Aged 430°C/1 hr./AC	183	194	15.1	64.6	164	165
	N1	Aged 475°C/50 min./AC	202	220	14.4	61.2	129[b]	
Microduplex	N2	GR + Aged 475°C/3 hrs./AC	216	225	12.6	57.0	109[b]	
	N4	GR + Aged 550°C/2 hrs./AC	191	200	15.8	60.6	147	136
	T8	GR + Aged 550°C/5 hrs./AC (structure (e) in Table II)	174	182	19.5	63.0	207	200

GR: Grain Refined, AC: Air Cooling

[a] 0.2% offset yield strength.

[b] Valid plane-strain fracture toughness.

[c] Fracture toughness based on Equivalent Energy Method.

[d] Fracture toughness based on J-Integral Method.

[e] To convert to SI units, 1 ksi = 6.89 MPa and 1 $ksi\sqrt{in}$ = 1.09 $MPa\sqrt{m}$.

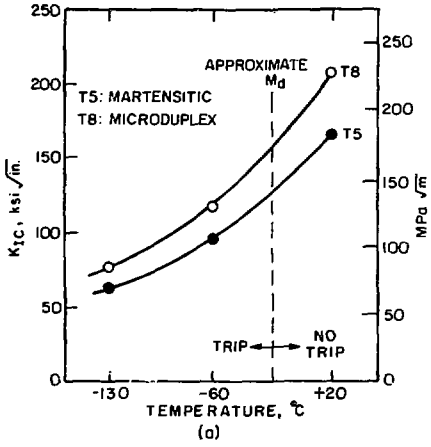

Fig. 3. Fracture toughness vs. test temperature. (Valid plane-strain fracture toughness at -60°C and at -130°C). (XBL 7512-9258)

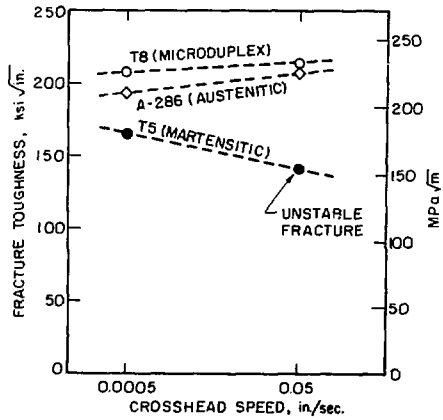

Fig. 4. Change of fracture toughness $K_{Ic}(E)$ with crosshead speed. (XBL 753-6008)

transformation did not lead to any evident increase in toughness (Fig. 3). The observed increase of fracture toughness at high strain rate in the microduplex alloy as well as in the austenitic alloy, A-286, was attributed to adiabatic heating near the crack tip during the fracture.

16. PHASE TRANSFORMATION AND STABILIZATION OF A HIGH STRENGTH AUSTENITE*

S. Jin, D. Huang, J. W. Morris, Jr. and G. Thomas

An investigation of the phase transformation and the austenite stabilization in a high strength austenite has been made. An Fe-29Ni-4.3Ti austenite age-hardened by $\gamma'(Ni_3Ti)$ precipitates showed a further increase of strength after martensitic and reverse martensitic phase transformations (Table 1). The strengthening of austenite through the phase transformations originates from the higher defect density and the fine substructure as shown in Figs. 1 and 2.

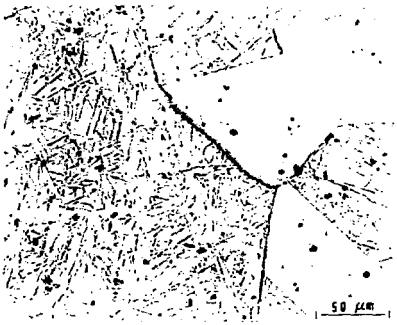

Fig. 1. Optical micrograph showing the "ghost-like" substructure after the ausaged and LN_2-cooled specimen is reverted to austenite.
(XBB 759-6731)

The stability control in precipitation-hardened high strength austenite becomes important especial ly when the martensitic and the reverse martensitic phase transformations are utilized to further strengthen the austenite. In such a case, the austenite stability should be low initially to allow martensitic transformations but should be restored to some extent after the reversion in order to maintain a reasonable austenite stability.

Fig. 2. Transmission electron micrograph of the dislocated austenite shown in Fig. 28. (a) Low magnification. Note the lath-like substructure and the high density of dislocations. (b) High magnification showing the γ' precipitates.
[(a) XBB 759-6631; (b) XBB 759-6630]

Table 1. Hardness of the Fe-29Ni-4.3Ti austenite.

Annealed	100% γ	$R_C \approx -15^a$ (R_A = 41)
Ausaged 750°C/30 min	100% γ	R_C = 35.3
Ausaged 750°C/30 min + Cooled to -196°C	70% α + 30% γ	R_C = 49.2
Ausaged 750°C/30 min + Cooled to -196°C + Reverted to austenite (800°C/30 sec)	100% γ	R_C = 41.0

[a] Invalid due to the extreme softness of annealed austenite.

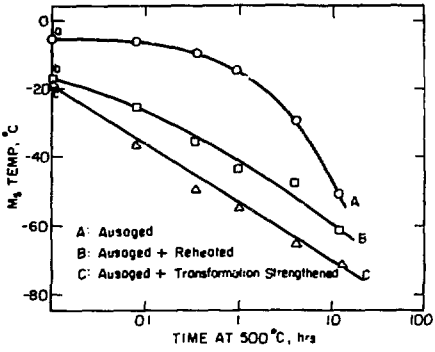

Fig. 3. Variation in M_S temperature of high strength austenite upon isothermal holding at 500°C. (part of XBL 759-7253; Top Fig. only)

The profound stabilization effect of fine coherent precipitates in Fe-Ni-Ti and Fe-Ni-Al systems is well known. The M_S temperature decreases during the early stage of precipitation in these alloys. But this effect is eliminated on further aging. By the time the precipitates grow sufficiently to provide a reasonable age hardening, the decrease of M_S that appeared at the early stage of ausaging is mostly erased and the M_S temperature continues to increase as the solute atoms are depleted from the matrix.

The present investigation demonstrates that the stability of ausaged austenite as well as ausaged and transformation-strengthened austenite was improved significantly through an isothermal treatment at 500°C, as shown in Fig. 3. The M_S temperature of the strengthened austenite was restored to nearly that of annealed austenite despite the decrease in solute content due to precipitation. The observed stabilization of high strength austenite as well as that of annealed austenite was attributed to the formation of G.P. zones or short-range order of less than ~ 10 Å in size based on the resistivity measurement.

*Research supported by the NASA Lewis Research Center under Contract No. NGR-05-003-526 and by the Electric Power Research Institute.

17. DEVELOPMENT OF A HIGH STRENGTH STABLE AUSTENITIC ALLOY*

S. Jin, D. Huang, G. Thomas and J. W. Morris, Jr.

The serious materials problems encountered in retaining rings for large electrical generator rotors have created a need for a high strength, high toughness, nonmagnetic steel. A desirable alloy would have a yield strength near 200 ksi with a fracture toughness above 130 ksi $\sqrt{in}$, and would be resistant to hydrogen embrittlement and stress corrosion cracking in service environments. Given that the best austenitic alloys in current use for retaining rings have yield strengths of only ~ 170 ksi (obtained by work hardening), the achievement of the desired properties will require a significant advance in the metallurgy of austenitic steels.

While our main research aim is to obtain a high strength austenite through thermal processing alone, an alternate way of achieving it through a simple mechanical deformation is also being sought. The preliminary data obtained in the present investigation demonstrates that a relatively simple combination of cold working and precipitation hardening is sufficient to achieve a 200 ksi yield strength in stable austenite. The chemical composition of the alloy studied is shown in Table 1. The cold rolling process of this alloy is fairly easy due to the extreme softness of annealed austenite. The alloy is further strengthened by the ausaging process. (Ni_3Ti precipitation).

Table 1. Chemical composition.

Fe	Ni	Cr	Ti	Mo	Al	V	B
Bal	27	6	3	1.3	0.2	0.3	0.01

Table 2. Tensile properties of high strength austenite.

Processing	Y.S. (ksi)	UTS (ksi)	Elong. (%)	R.A. (%)
CR + AA	190	202	9.3	38
CR + AA + RAA	197	209	10.5	44

CR: Cold Rolling 45 pct at room temp.
AA: Ausaging at 720°C for 4 hr.
RAA: Re-ausaging at 550°C for 12 hr.

The tensile properties of the processed high strength austenite are given in Table 2. The alloys in Table 2 are stable austenite and do not exhibit any deformation-induced phase transformation. The second ausaging treatment at lower temperature was introduced to maximize the use of alloying element for precipitation hardening. The solubility of nickel and titanium in this alloy system decreases as the temperature is lowered. An interesting observation is that not only the yield strength increases but the ductility also shows improvement after the additional low temperature precipitation. A further research is in progress to find out the nature of reactions and to improve the strength-toughness properties.

*Research supported by the Electric Power Research Institute.

18. RESEARCH PLANS FOR CALENDAR YEAR 1976

J. W. Morris, Jr.

During the coming year we plan to carry out the following work:

(1) We plan to complete the identification and geometric characterization of the microstructures arising from isotropic nucleation and growth transformations in simple solids. The research will then be extended to consider more realistic transformations, involving, for example, anisotropic growth. In corrollary work we plan research toward the optimal choice of parameters representing the microstructure for use in constitutive equations determining material properties.

(2) We plan to continue research toward a theory of plastic deformation through thermally activated dislocation glide. During the coming year this research will focus particularly on glide through mixtures of microstructural barriers and on the glide of interacting groups of dislocations, exploiting the potential of our new computer simulation codes.

(3) We plan to continue research on the mechanical equation of state of simple solids. During the coming year we specifically plan to refine and demonstrate the one-parameter equation of state we have successfully used for aluminum in uniaxial deformation, and hope to extend the equation to account for cyclic deformation and for static relaxation. The theoretical research will be supplemented by an experimental program to gather data needed to specify the empirical equation of state and to test its validity under new conditions.

(4) We plan to continue a cooperative search with the Oak Ridge National Laboratory for ordering reactions in Fe-Ni martensites. If the initial Oak Ridge data proves accurate, we will inaugurate lattice imaging studies to specify the nature of the order. We also plan to investigate alloys near Fe-30Ni, where an Fe_3Ni ordering has been reported in austenite.

(5) We plan to continue research to specify the effect of austenite on the toughness of high strength martensitic steels. We particularly plan to test the hypothesized connection between austenite stability and toughness through research on the strength-toughness properties of ferritic alloys having austenite additions of controlled stability.

(6) In alloy design research on Ni-alloy cryogenic steel we plan to interact with potential users of the alloys to explore specific applications in advanced energy systems. Essential corollary research may include processing studies to simplify alloy processing to lower manufacturing costs.

(7) We plan to continue the development of nickel-free cryogenic steels. In research during the coming year we specifically hope to eliminate the cold-work step now included in the processing of Fe-12Mn cryogenic steel while retaining properties competitive with Fe-9Ni steel at 77°K. We also hope to design a successful high strength austenitic Fe-Mn cryogenic steel.

(8) We plan to continue research on phase transformation kinetics and microstructural control in Fe-Mn alloys. During the coming year we hope to establish experimental control over the ε-martensite phase and determine the consequences of ε-martensite on cryogenic mechanical properties. We also hope to identify an efficient substitutional age-hardening system for austenitic Fe-Mn steels.

(9) We plan to continue research on the austenite reversion reaction as a means of achieving very high dislocation densities in un-worked materials. We hope to exploit this reaction in the design of high strength-high toughness austenitic steels.

(10) We plan to continue exploration of the double-aging treatment developed during the past year's research as a means for obtaining very high toughness in high strength stable austenitic steels. This research will begin with a determination of the strength-toughness characteristics of the high strength austenitic steels developed this fall.

19. 1975 PUBLICATIONS AND REPORTS

John W. Morris, Jr. and Associates

Journals and Books

1. D. H. Klahn and J. W. Morris, Jr., Characteristics of Dislocation Glide through a Random Array of Obstacles, in Rate Processes in Plastic Deformation, J. C. M. Li, ed., ASM (1975), pp.130-146 (LBL-1168).

2. F. A. Mohamed, K. L. Murty and J. W. Morris, Jr., Harper-Dorn Creep of Metals at High Temperature, in Rate Processes in Plastic Deformation, J. C. M. Li, ed., ASM (1975), pp. 459-478, (LBL-1158).

3. S. Jin, J. W. Morris, Jr. and V. F. Zackay, Grain Refinement through Thermal Cycling in an Fe-Ni-Ti Cryogenic Alloy, Met. Trans. 6A, 141 (1975) (LBL-2539).

4. K. Hanson and J. W. Morris, Jr., A Limiting Configuration in Dislocation Glide through a Random Array of Point Obstacles, J. Appl. Phys. 46, 983 (1975) (LBL-3160).

5. C. K. Syn, A. Ahmadieh and J. W. Morris, Jr., Elastic Solute-Dislocation Interaction in an Anistropic HCP Crystal, Phil. Mag. 31, 883 (1975) (LBL-3198).

6. S. Jin, B. Whitaker, J. W. Morris, Jr., and V. F. Zackay, Cryogenic Toughness through Microstructure Control in a Ferritic Fe-Ni-Ti Alloy,

Properties of Materials for Liquified Natural Gas Tankage, ASTM STP 579, 1975, pp. 348-360 (LBL-2756).

7. M. J. Schanfein, M. J. Yokota, V. F. Zackay, E. R. Parker and J. W. Morris, Jr., The Cryogenic Properties of Fe-Mn and Fe-Mn-Cr Alloys, Properties of Materials for Liquified Natural Gas Tankage, ASTM STP 579, 1975, pp. 361-378 (LBL-2764).

8. S. Jin, S. K. Hwang and J. W. Morris, Jr., Comparative Fracture Toughness of an Ultrafine-Grained Fe-Ni Alloy at Liquid Helium Temperature, Met. Trans. 6A, 1569 (1975) (LBL-3164).

9. K. Hanson, K. P. Walker and J. W. Morris, Jr., Computer Simulation of Microstructure, Proceedings of the 1975 Summer Computer Simulation Conference, Mich., San Francisco, 1975, pp. 415-416, (LBL-3554 Rev.).

10. K. Hanson and J. W. Morris, Jr., Estimation of the Critical Resolved Shear Stress for Dislocation Glide through a Random Mixture of Distinct Obstacles, J. Appl. Phys. 46, 2378 (1975) (LBL-3552).

11. S. Jin, S. K. Hwang and J. W. Morris, Jr., The Effect of Grain Size and Retained Austenite on the Ductile Brittle Transition Temperature of a Ti-Gettered Iron Alloy, Met. Trans. 6A, 1721 (1975) (LBL-3576).

12. S. K. Hwang, S. Jin and J. W. Morris, Jr., A Study of Retained Austenite in a Fine-Grained Fe-12Ni-0.2Ti Alloy, Met. Trans. 6A, 2015 (1975) (LBL-3714 Rev.).

13. C. K. Syn, A Ahmadieh and J. W. Morris, Jr., The Effect of Solute Atoms on the Motion of a Low Angle Tilt Boundary, Scripta Met. 9, 1255 (1975) (LBL-3735 Rev.).

Presentations

1. J. W. Morris, Jr., S. K. Hwang and Sheree Ken, Recent Contributions of Transmission Electron Microscopy to the Design of Tough Fe-Ni Steels, Joint Meeting, Louisiana and Texas Electron Microscopy Societies, New Orleans, Feb. 1975.

2. J. W. Morris, Jr. and S. Jin, The Design of Tough Ferritic Cryogenic Steels, Invited Paper, ASME Design Engineering Conference, New York, March, 1975.

3. Sheree Ken, J. W. Morris, Jr., and G. Thomas, Ordered Domains in Fe-Ni Martensites, TMS Spring Meeting, Toronto, May, 1975.

4. K. P. Walker, K. Hanson and J. W. Morris, Jr., Computer Simulation of the Johnson-Mehl Microstructure, TMS Spring Meeting, Toronto, May, 1975.

5. S. Altintas, K. Hanson and J. W. Morris, Jr., Computer Simulation of Plastic Deformation through Planar Glide in an Idealized Crystal, TMS-ASME Symposium on Micromechanical Modeling of Flow and Fracture, RPI, June, 1975.

6. K. P. Walker, K. Hanson and J. W. Morris, Jr., The Computer Simulation of Microstructure, Summer Computer Simulation Symposiu, San Francisco, July, 1975.

7. J. W. Morris, Jr., The Design of Tough Ferritic Cryogenic Steels, Tarrytown Research Center, Union Carbide Corp., August, 1975.

8. J. W. Morris, Jr., Research on the Nature of Microstructure, Scientific Laboratory, Ford Motor Co., October, 1975.

9. S. K. Hwang, S. Jin and J. W. Morris, Jr., Research Toward Ni-Free Cryogenic Steels, TMS-ASM Fall Meeting, Cincinnati, November, 1975.

LBL Reports

1. Sabri Altintas, Deformation Behavior of an Idealized Crystal (M.S. Thesis), LBL-3914, April 1975.

2. Kenton L. Hanson, Critical Resolved Shear Stress for Athermal Glide (Ph.D. Thesis), LBL-3923, May 1975.

3. S. Jin, D. Huang and J. W. Morris, Jr., Structure and Properties of a Microduplex Maraging Steel, LBL-3936, June 1975.

4. Bradley W. Whitaker, An Fe-12Ni-4Co-2Mo-0.05Ti Alloy for use at 77°K and Below, (M.S. Thesis), LBL-415., Sept. 1975.

5. S. Jin and D. H. Huang, Phase Transformation and Stabilization of a High Strength Austenite, LBL-4163, Sept. 1975.

b. Fundamentals of Alloy Design

Earl R. Parker and Victor F. Zackay, Principal Investigators

Introduction. In the past year, the program on alloy design has centered on five major aspects of alloy design, viz: (1) an attempt to derive by fundamental quantum mechanical methods the physical properties of metals (Shively); (2) the continuation of studies on the interactive efforts of alloying elements on the bainitic hardenability of steel (Llopis); (3) the structure-property relationships of ferritic (Bhat, Singh), austenitic (Haddick, Thompson, Clark), and quenched and tempered steels (Kohn, Horn, Bhat, Wylie, and Huang) as influenced by heat treatment, composition and microstructure; (4) the roles of environment, mean stress, and microstructure on the stress corrosion and fatigue crack propagation behavior of selected steels (Ritchie and Castro); and, (5) the fundamental and applied aspects of combined erosion and corrosion of metals (Levy, Kliest, McFadden, and Brass). Some recent accomplishments in several of the largest project areas (items 3, 4 and 5) are described below.

Research on the ferritic alloys, strengthened with dispersoids of intermetallic compounds (Laves phases) rather than the conventional alloy carbides, continues to show promise. The creep and creep rupture properties of these alloys are comparable to the better austenitic stainless steels at temperatures up to 650°C, and, recently, it has been shown that the high temperature (1100°C) treatment required to spheroidize the embrittling grain boundary film in these alloys may not be necessary in alloys containing W rather than Mo. In the former, the film is sufficiently discontinuous upon cooling from the solutionizing temperature to render the speroidizing heat treatment step unnecessary. Those alloys containing W appears to have comparable (or better) creep and creep rupture properties than their Mo-containing counterparts.

The energy-absorbing characteristics of alloys exhibiting a stress or strain-induced phase transformation were studied in binary and ternary alloys of the Fe-Mn system. Excellent combinations of tensile, impact, and ductile-to-brittle transition temperature properties were obtained, which suggests that these alloys may be potential candidates for mechanical energy absorbing devices.

The influence of Si and Al, and their combinations, on the mechanical properties of quenched and tempered and isothermally transformed steels was studied. A number of modified low-to-medium alloy commercial steels and several new promising laboratory-type alloys were evaluated. It is now clear that the extra silicon (1.5 to 3.0%) steels have significant technological promise in the ultra-high strength steel category. Especially promising are those having both Al and Si in their compositions. Steels of this type exhibit an unusually high resistance to tempering and have excellent toughness (70-80 ksi-in$^{1/2}$) at high tensile strengths (275-300 ksi).

In the past year, much progress was made in the construction of apparatus for the erosion and corrosion project as well as for the fatigue crack propagation project. Apparatus for these projects has been designed, built, and calibrated and is now being used to generate data.

1. THEORETICAL METALLURGICAL PHYSICS

John E. Shively

The purpose of this research is to understand the metallurgical properties of transition metals and their alloys in terms of the first principles theoretical framework of quantum physics. Instead of a model involving adjustable parameters, we propose a formulation that only uses fundamental physical constants of the material studied, e.g., the atomic masses and numbers of the atoms, the mass and charge of the electron, and the crystal composition and structure.

A method useful in understanding metallurgical properties is a new Hamiltonian formulation that transforms the electron Hamiltonian by a similarity transformation into a form more easily solved:

$$S^{-1} (H_o + V) S = H_o + W$$

This transformation preserves the eigenvalue spectrum as required and produces a new Hamiltonian to which perturbation theory can then be applied. A multiple scattering analysis of the transition operator constructed from this new Hamiltonian yields the total propagator in terms of the atomic scattering operators as an unrestricted summation

$$G^+ = G_o^+ + \sum_{n=1}^{\infty} \left[\sum_{\ell} \sum_{m=1}^{\infty} (-G_\ell^+ t_\ell)^m \right]^n G_o^+$$

The integrated density of states is given by the polar decomposition of this propagator as

$$N(E) = \frac{1}{\pi} \mathrm{Tr}\ \mathrm{Arg}\ [-G^+(E)]$$

from which the energy can be found by

$$E^{el} = \int E dN$$

The resulting equation for the total energy of the ions and electrons in a metal, derived to second order scattering, separates into two classes of terms: those dependent upon the lattice structure, and those dependent upon the total volume of the metal.

The significance of this separation into structure and volume terms can easily be demonstrated by

an examination of the parameter ν of elasticity theory: Poisson's ratio of lateral strain to longitudinal strain in simple tension or compression. The structure-dependent terms are effective central force interactions yielding elastic constants obeying the Cauchy relations which for cubic crystals imply

$$C_{12}^{str} = C_{44}^{str}, \text{ giving } \nu^{str} = 1/4$$

while the volume dependent terms contribute elastic constants with no resistance to shears

$$C_{11}^{vol} = C_{12}^{vol} \text{ and } C_{44}^{vol} = 0, \text{ giving } \nu^{vol} = 1/2$$

The Poisson ratio of a metal should then be an average of these two classes of contributions. Indeed, the harmonic mean of $\nu^{str} = 1/4$ and $\nu^{vol} = 1/2$ is $\nu^{metal} = 1/3$, in agreement with experiment for most metals.

As a quantitative test, the author has calculated the elastic constants for the transition metal Nb using this first principles theory. The results (in units of 10^{11} dynes/cm^2) were

Elastic Constant	Theory	Experiment
C_{11}	23.35	24.6
$C_{12} + 2C_{44}$	19.93	19.14

This initial success indicates that further properties of transition metals may be accurately calculated by this first principles theory.

---

1. John E. Shively, Unrestricted Summations for the Multiple Scattering Transition Operator and Propagator, LBL-3744, Feb. 1975.
2. John E. Shively, A New Density of States Formulation, LBL-3789, April 1975.

2. EFFECT OF THE ALLOYING ELEMENTS IN STEELS ON THE KINETICS OF THE AUSTENITE TO BAINITE TRANSFORMATION

Ana María Llopis

The purpose of this study was to investigate the effect of different alloying elements on the kinetics of the bainite reaction. Dilatometric studies on four Fe-C-X ternary systems, in particular, (X = Mo, Ni, Cr, Mn) were made. This technique allows the determination of the reaction start times for the isothermal decomposition of austenite in the bainite range. Another phase of the program was the extension of the investigation to include other combinations of these same alloying elements, such as Fe-C-Mo-Ni, Fe-C-Ni-Cr, and Fe-C-Ni-Cr-Mo.

Of the alloying elements studied, Mn, Ni, Cr (in order of effectiveness) shifted the start of the bainite reaction to longer times, increasing the bainite hardenability. The element, Mo, accelerated the bainite reaction. All of the alloying elements studied accelerated the austenite decomposition at isothermal transformation temperatures just above the Ms giving an S-like curve for the reaction start curve (see Fig. 1).

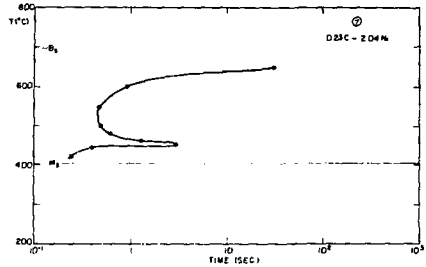

Fig. 1. Ex-start of the austenite to bainite transformation for Fe-C-Ni ternary system. (XBL 7512-9292)

All of the alloying elements lowered the temperature range of the bainite reaction, thereby promoting the formation of more lower bainite and, thereby, potentially increasing the fracture toughness of the alloys. Increasing amounts of the alloying elements in both the simple ternary and the more complex alloys had an additive effect in lowering the bainite reaction temperature. Combined additions had a multiplicative effect on the reaction start times for the isothermal decomposition of austenite, suggesting strong interaction effects. The combined addition Cr-Ni was six times more effective than the addition of Ni or Cr alone in moving the start curve for the bainite transformation to longer times. Similarly, the combined Mo-Ni and Mo-Cr alloys were more effective—by factors of 5 and 4 respectively—in delaying the start of the bainite transformation than were the same elements added separately; as a result, the bainite hardenability is increased.

3. LAVES-PHASE-STRENGTHENED FERRITIC ALLOYS FOR ELEVATED TEMPERATURE USE

M. S. Bhat

The effect of the lamellar and spheroidized microstructures on the creep and stress rupture behavior of Laves-phase strengthened (Fe/1Ta/7Cr/1/2Mo) alloys was determined. The alloy having the lamellar microstructure exhibited slightly better creep properties for shorter

rupture times (< 400 hr) at 1200°F (649°C) than the alloy heat treated to give a spheroidized structure. However, for times greater than about 400 hr, the alloy with the spheroidized microstructure appeared to be better. This behavior is shown in Fig. 1. Long exposure at 650°C could result in a breakdown of the lamellar structure thereby explaining the observed results. Finally, the creep properties, both in terms of creep rate and rupture time, are compared (Tables 1 and 2) to those of the commercially available ferritic and austenitic alloys. The potential of the Fe-Ta-Cr-Mo alloy is clearly evident from these tables.

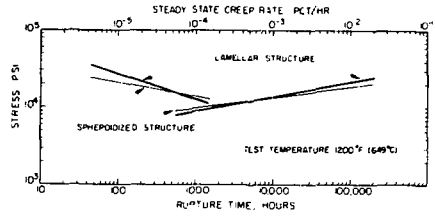

Fig. 1. Plot of stress vs rupture time and stress vs steady state creep rate for the spheroidized and lamellar structures.
(XBL 758-6997)

1. M. S. Bhat, Lawrence Berkeley Laboratory Report, LBL-2277, 1974.
2. Inorganic Materials Research Division Annual Report, LBL-3530, Lawrence Berkeley Laboratory, Berkeley, CA 94720, 1974, p. 147.

Table 1. 1000-Hour rupture stress and stress for a creep rate of 10^{-4} pct/hr for alloy Fe-Ta-Cr-Mo and some commercial ferritic and austenitic steels at a test temperature of 1100°F(593°C).

Alloy	1000 Hour Rupture Stress (psi)	Stress for a Creep Rate of 10^{-4} pct/hr (psi)
Fe-Ta-Cr-Mo (Spheroidized)	29,000	25,000
0.3C-1Cr-1Mo-0.25V Steel	36,000	*
0.15C-9Cr-1Mo Steel	14,100	6,300
403,410 Stainless Steel	10,000	4,200
Greek Ascaloy	22,000	*
422 Stainless Steel	33,800	19,000
304 Stainless Steel	22,600	11,500
304L Stainless Steel	23,000	9,700
309 Stainless Steel	28,000	11,600
310 Stainless Steel	25,000	13,000
316 Stainless Steel	33,000	18,200
316L Stainless Steel	26,900	14,100
321 Stainless Steel	29,500	17,000
347 Stainless Steel	34,000	23,000

*No values quoted for 1100°F.

The data for the ferritic steels were obtained mostly from reference 18, and those for the other steels from Engineers Guide to High Temperature Materials, F. J. Clauss, ed., (Addison and Wesley Pub. Co., Inc., Reading Massachusetts, 1971), Chapter 4, p. 86-128.

Table 2. 1000-Hour rupture stress and stress for a creep rate of 10^{-4} pct/hr for alloy Fe-Ta-Cr-Mo and some commercial ferritic and austenitic steels at a test temperature of 1200°F(649°C).

Alloy	1000 Hour Rupture Stress (psi)	Stress for a Creep Rate of 10^{-4} pst/hr (psi)
Fe-Ta-Cr-Mo (Spheroidized)	14,000	10,000
Fe-Ta-Cr-Mo (Lamellar)	13,000	9,000
0.3C-1Cr-1Mo-0.25V Steel	*	*
403,410 Stainless Steel	4,900	2,000
Greek Ascaloy	11,000	*
422 Stainless Steel	15,000	*
304 Stainless Steel	15,000	6,900
304L Stainless Steel	15,800	6,800
309 Stainless Steel	20,000	8,000
310 Stainless Steel	17,000	8,600
316 Stainless Steel	24,700	12,700
316L Stainless Steel	17,300	8,200
321 Stainless Steel	18,000	9,700
347 Stainless Steel	22,000	16,500

*No values quoted for 1200°F

The data for the ferritic steels were obtained mostly from reference 18, and those for the other steels from Engineers Glide to High Temperature Materials, F. . Clauss, ed., (Addison and Wesley Pub. Co., Inc., Reading, Massachusetts, 1971), Chapter 4, p. 86-128.

4. THE DESIGN OF A STRUCTURAL STEEL FOR USE IN COLD ENVIRONMENTS

Glenn Haddick

The results of this investigation have shown that new, lower cost TRIP steels (without chromium and nickel) could be made.

The iron-16 and 20% manganese binary alloys were selected for study because they exhibited the desired TRIP phenomena in a tension test[1] and possessed reasonable mechanical properties. Systematic additions of carbon and molybdenum were made to these two binary alloys and the resultant microstructure and mechanical properties were determined. The tensile test data and the Charpy V-notch data obtained are shown in Table 1.

In the 16% Mn alloys, the carbon additions predictably raised the strength and the DBTT (ductile to brittle transition temperature). Molybdenum was added to control the carbon content and, at the same time, add a network of dispersed particles. The molybdenum additions lowered the yield strength but increased the ductility and lowered the DBTT to pre-carbon levels. The yield strength of the 16%Mn-0.08%C-1.0Mo alloy was

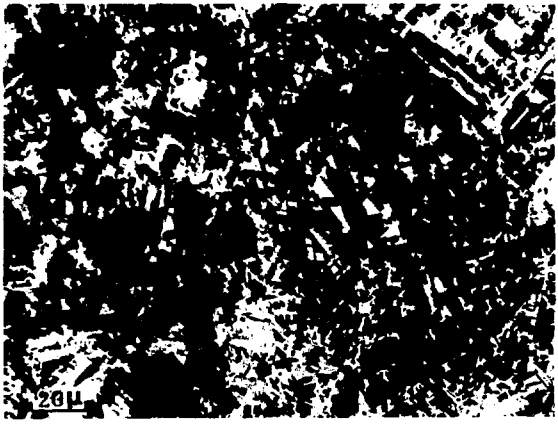

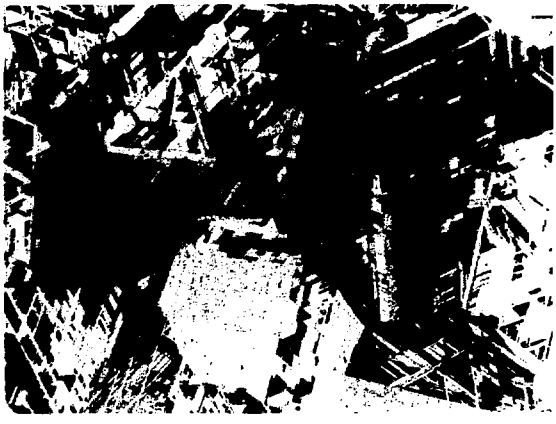

Fig. 1. (a) 16%Mn binary iron alloy, showing α-martensite (black lens shapes), ε-martensite (white), and austenite (gray). (500x)
(b) 16%M-0.08%C-1.0%Mo-iron alloy showing ε-martensite and austenite. (500x) (XBB 761-305)

Table 1. Mechanical Properties of Several Binary and Ternary Fe-Mn Alloys.

Alloy	TENSILE TEST: Tensile Properties Y.S., ksi	U.T.S., ksi	%El	R.A.	CHARPY V-NOTCH ENERGIES: Upper Shelf, ft-lb	Lower Shelf, ft-lb	DBTT* (°C)
16%Mn	30	101	30	71	130	27	-155
16%Mn - 0.05%C	50	122	38	73	125	42	-170
16%Mn - 0.13%C	60	175	28	20	93	6	-77
16%Mn - 0.08%C - 0.5%Mo	47	153	34	35	116	11	-155
16%Mn - 0.08%C - 1.0%Mo	46	150	46	51	120	11	-140
20%Mn	61	101	34	70	95	-	<-196
20Mn - 0.15%C	68	150	44	41	62	8	-105
20%Mn - 0.08%C - 0.5%Mo	71	140	43	37	93	15	-127
20%Mn - 0.08%C - 1.0%Mo	59	126	38	44	106	20	-141
AFTER THERMAL CYCLING							
16%Mn - 0.08% - 1.0%Mo	61	156	53	56			

*DBTT is defined as the temperature at one-half of the upper shelf energy value.

improved from 46 ksi to 61 ksi through a thermal cycling heat treatment[2,3] (see Fig. 1). The 20%Mn alloys performed in a similar manner.

Control of the TRIP process by carbon and molybdenum additions was shown to greatly improve the strength, ductility and energy absorption properties of the 16 and 20%Mn alloys (see Table 1).

1. M. J. Schanfein, The Cryogenic Properties of Fe-Mn and Fe-Mn-Cr Alloys (M.S. Thesis), LBL-2749, August 1974.
2. S. Jin, J. W. Morris, Jr., and V. F. Zackay, Grain Refinement Through Thermal Cycling in an Fe-Ni-Ti Cryogenic Alloy, Met. Trans. A 6A, 141 (1975).
3. Howard E. Adkins, Jr., Structure and Properties of TRIP Steels Processed by Deformation and Thermal Cycling (M.S. Thesis), LBL-1491, April 1973.

5. MECHANICAL PROPERTIES AND CORROSION BEHAVIOR OF Fe-Mn-Cr AND Fe-Mn-Cr-X ALLOYS

Larry Thompson

An investigation of the mechanical and corrosion behavior of Fe-Mn-Cr and Fe-Mn-Cr-X base alloys was carried out to establish promising austenitic alloy compositions that contained lower quantities of the alloying element, chromium.

Manganese concentrations in the Fe-Mn-Cr alloys investigated were varied between 14 and 20 w/o with Cr concentrations between 13 and 16 w/o. In the group of Fe-Mn-Cr alloys, a small addition of Al and Ti was made to remove from solid solution the interstitials (N and C). The best mechanical properties were obtained with the Fe-18 Mn-13 Cr alloys (see Table 1). In all cases, additions of

Table 1. Mechanical Properties of Several Ternary Fe-Mn-X Alloys.

Alloy Composition - %					Heat Treatment	Tensile Properties				
						Test Temperature	YS (ksi)	UTS (ksi)	%El.	Red. Area %
Mn	Cr	Si	Mo	N						
16	13			.134	900°C (2Hr) →Air Cool	23	46	121	69	77
					"	-196	94	152	25	17
16	13		2	.204	900°C (2Hr) →Ice Brine Quench	23	58	124	77	79
					"	-196	117	168	17	15
16	18		2	.180	900°C (2Hr) →Ice Brine Quench	23	79	116	61	59
					"	-196	128	187	19	17
16	18	1.5		.227	900°C (2Hr) →Air Cool	23	63	125	78	78
					"	-196	143	183	17	17
20	13	1.5		.130	900°C (2Hr) →Air Cool	23	50	109	72	80
					"	-196	98	181	47	24
18	13				900°C (2Hr) →Air Cool	23	44	92	58	82
					"	-196	53	161	60	71
	AISI 304 SS					23	35	85	50	70
	AISI 304L SS					23	28	75	50	-
	AISI 316 SS					23	40	90	50	-
	AISI 316L SS					23	32	75	50	-
	AISI 347 SS					23	40	97	45	

Cr greater than 13% were found to be detrimental to the overall mechanical properties.

The Fe-Mn-Cr-X alloys contained either 16 or 20 Mn with 13 and 18 Cr. Again, the best mechanical behavior was exhibited by the 13 Cr alloys in combination with 16 Mn. The alloying additions included a series with N, a series with Mo + N, a series with Si + N, and a series with Si + C, and a series with Mo. Nitrogen seemed to be the best alloying addition for high strength; those alloys that contained only a fourth alloying element without N showed less desirable mechanical properties.

Virtually all the alloys displayed a TRIP phenomenon (i.e., transformation induced plasticity) and phase transformations from the fcc (γ) phase to the hcp (ε) phase and to the bcc (α) phase. These transformations generally conferred uniform elongation and generally acceptable strength levels in the alloys studied. Enhancement of the ductility was most pronounced in those alloys containing N.

6. PROPERTIES, MICROSTRUCTURES, AND RADIATION RESISTANCE OF STAINLESS STEEL-GLASS COMPOSITE MATERIALS

Robert Clark

The object of this research was to develop a glass-in-metal composite material that would have a reduced tendency to swell under irradiation in a breeder type reactor environment. Since helium has a high solubility in certain glasses, a program was conducted to determine if a well dispersed compatible glass phase in a 316L stainless steel would inhibit swelling by the glass acting as a gettering agent for the He, thus preventing void nuclei stabilization. The mechanical properties and microstructures were characterized with particular attention paid to the effects of glass distribution. Transmission electron metallography established glass-metal interface characteristics.

The composites were successfully fabricated using powder metallurgy techniques. Figure 1

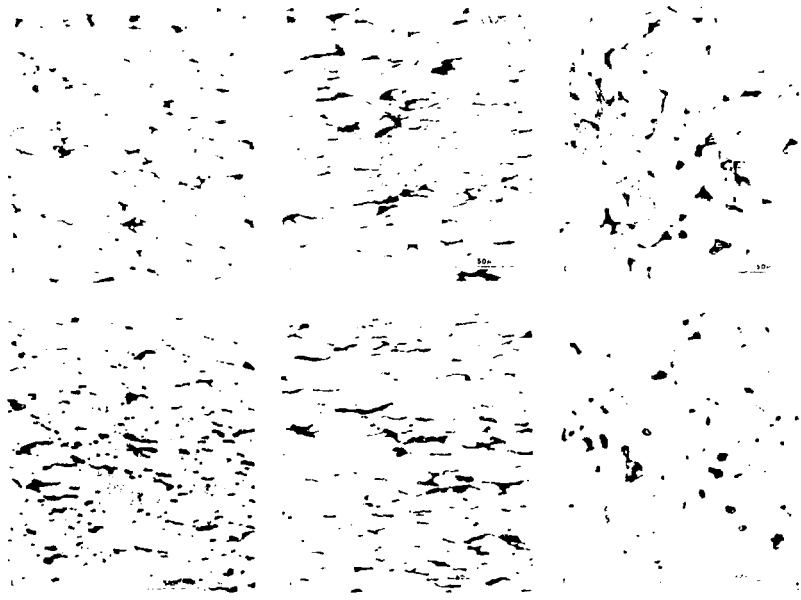

Fig. 1. Distribution of glass particles in the as-rolled and rolled and annealed condition of a stainless steel glass composite. (XBB 7510-7941)

shows the distribution of the glass particles in the 316LSS matrix in the as-rolled and rolled and annealed conditions. Particular attention was paid to the distribution of the glass particles and their effects on the materials behavior. Transmission electron micrography established glass-metal interface characteristics.

Tests of mechanical properties established that materials containing over 10 vol% glass can be readily fabricated. Incorporation of glass in the metal using p.m. techniques and subsequent thermo-mechanical treatments allowed a wide range of morphological distributions of a stable nonreactive phase to be established in situ after initial pressing and sintering. This program will conclude upon completion of the following tests now in progress: (1) creep tests, (2) high temperature tensile tests, and (3) swelling effects under 400 keV He^+ bombardment.

7. ISOTHERMAL TRANSFORMATIONS IN A "VASCO-MA" SECONDARY HARDENING STEEL

N. Kar

The usual way to obtain high strength in high C steels is by quenching to form martensite, followed by tempering to eliminate brittleness, while still maintaining high strength.

These high strength alloys, however, are associated with low toughness. Research by Thomas et al.[1,2] suggests that for steels with C content >0.4% a lower bainitic microstructure could give attractive properties. Honeycombe[3] suggests that secondary hardening may be pursued by an initial bainitic structure. In this project, transformations have been carried out to obtain martensitic, martensite plus lower bainite, and fully bainitic microstructures which have been tested untempered and tempered.

The steel being used is a commercial "Vasco MA" secondary hardening steel, which is well established as a tool steel. By modifying conventional heat treatment practices, different microstructural morphologies are being obtained, and it is hoped to obtain a correlation between microstructure and mechanical properties, using transmission electron microscopy.

The recommended austenitization treatment is found to leave undissolved carbides in austenite, a feature known to be associated with deleterious fracture properties.[4] As a basis for comparison, higher austenitizing temperature, with subsequent grain refinement, is being carried out prior to further transformations. The TTT diagram of the steel has been determined using the Theta dilatometer.

1. G. Thomas, Iron and Steel Intern. 46, 451 (1973).
2. S. K. Das and G. Thomas, Trans. ASM 62, 659 (1969).
3. R. W. K. Honeycombe, J. J. Irani, and H. J. Harding, High-Strength Materials (John Wiley & Sons, NY, 1965).
4. B. V. Narasimha Rao, Investigation of Ultra-High Strength Fe/4Cr/0.4C Martensitic Steels for Improved Toughness (M.S. Thesis), LBL-3794, June 1975.

8. HEAT TREATABLE ALLOY STEELS CONTAINING RETAINED AUSTENITE

G. Kohn

The objective of this study was to determine the effect of Si additions and variations of heat treatment on the amount and stability of retained austenite (Ret. γ) in a heat treatable AISI 4330 steel. Previous work[1] has indicated that the presence of retained austenite may enhance the fracture toughness of low alloy steels.

Silicon was chosen as a modifying element because it has been shown by Heheman[2] and Babu[3] that Si increases the amount of Ret. γ in isothermally transformed AISI 4300 type steels. It has also been shown that Si-modified AISI 4340, that is, 300 M, has improved toughness and better mechanical properties than the unmodified steels.

Isothermal transformations were conducted both above the M_S temperature (at 350°C) and below it (250°C, 200°C). From the results obtained, the following general conclusions can be made:

1. For isothermal transformations at 350°C:

a. Increasing the amount of Si increases the amount of retained austenite at room temperature following the isothermal treatment.

b. Increasing the amount of Si results also in a lowering of the yield strength.

c. The specimens in which the retained austenite was unstable upon loading in a tensile test had lower fracture toughness values. The probable reason for this is that the retained austenite is enriched in carbon and transforms (under load) to brittle martensite.

2. For isothermal transformations below the M_S:

a. Increasing the amount of Si increases the amount of Ret. γ, but the general level of Ret. γ is lower with the lower isothermal transformation temperature than the amount that occurs in the material transformed above the M_S temperature.

b. The strength level increases with the decreasing transformation temperature (compared to the 350°C transformed material) probably due to the presence of more martensitic phase in the as-heated treated material.

c. The carbon level in the Ret. γ is below 0.4 wt. pct. and, upon loading, it transforms to martensite which is not brittle. This results in increased fracture toughness over the material transformed at 350°C.

Figure 1, which is a summary of the mechanical properties vs the amount of Si for isothermal transformations at 250° (below the M_S), is representative of the data obtained in this program. Additional work will compare the behavior of the silicon modified steels to that of the standard AISI 4330 composition.

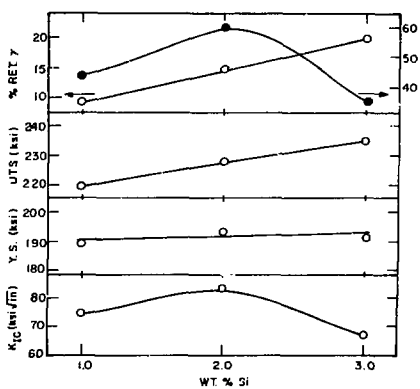

Fig. 1. AISI 4330 transformed at 250°C tempered at 400°C (1 hr). (XBL 762-6447)

1. G. Y. Lai, W. E. Wood, R. A. Clark, V. F. Zackay and E. R. Parker, The Effect of Austenitizing Temperature on the Amount of Retained Austenite in AISI Type 4340 Steel, LBL-2250, October 1973.
2. R. F. Hehemann, Phase Transformation (American Society for Metals, Ohio, 1970), p.397.
3. B. P. Babu, An Investigation of Bainite Transformation in Medium Carbon Low Alloy Steels (D. Eng. Thesis), LBL-2772, August 1974.

9. THE FRACTURE PROPERTIES OF A CONTINUOUSLY COOLED COMMERCIAL LOW ALLOY STEEL IN THICK SECTION

R. Horn

This investigation is aimed at establishing the relationship between microstructural features and fracture properties in a slow-cooled, commercial, silicon modified 4340 steel (300 M). Earlier work[1] showed that in this steel, slow cooling rates from the austenitizing temperature led to significant amounts of retained austenite as well as increased hardness over similarly heat treated 4340. This suggested possible application of 300 M as an air cooled, thick-section steel.

The investigation simulates thick-section, air-cooled material to determine the mechanical and fracture property dependence on microstructural features. Emphasis will be placed on the role of retained austenite in fracture and attempts will be made to isolate the effect of the austenite by using heat treatments subsequent to the slow cooling process. Initial work has been directed in four areas: (1) characterization of the air cooling process in steel; (2) determination of the response of the retained austenite to load and thermal treatment after cooling; (3) characterization of microstructures formed; and (4) determination of mechanical and fracture properties.

Numerical computing techniques were used to characterize the air cooling process. Heat transfer parameters were established by matching computer simulated rates with laboratory measured rates for two thickness. Figure 1 shows these rates for one thickness as they intersect the continuously cooling transformation curve for the steel of interest established in an earlier study.[1] The computer simulation also established that the edge-to-center temperature gradient in steel is insignificant up to large thicknesses, leading to a uniform microstructure throughout.

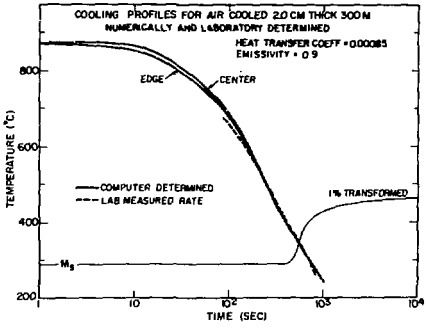

Fig. 1. Comparison of laboratory-determined and computer-simulated rates far air cooling 2.0-cm thick slab. (XBL 763-6603)

The response of the slow-cooled microstructures to uniaxial loading was determined. Magnetic saturation techniques were used to monitor the transformation of the retained austenite with stress. Figure 2 shows the characteristic stress-strain behavior as well as the behavior of the

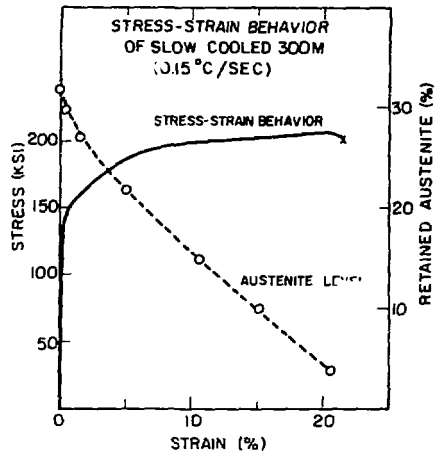

Fig. 2. Stress-strain behavior of slow-cooled 300M (austenite level shown as a function of strain). (XBL 763-6609)

retained austenite (cooled @ 0.15°C/sec). Significant transformation occurred in the uniform elongation region. Response to thermal treatment was different in that the austenite remained at essentially unchanged levels after post cooling thermal treatments up to 25°C. Microstructure characterization revealed that the austenite morphology was influenced by cooling rate. However, significant amounts of interlath austenite were usually found. This has been associated with good fracture properties in high strength materials.[2]

Future work will be concentrated in the areas of fracture property determination and microstructural characterization. Emphasis will be placed in investigating air-cooled microstructures found in slabs of specific thickness. Efforts will be made to isolate the role played by retained austenite in the mechanical properties of these steels.

---

1. IMRD Annual Report, LBL-3530, p. 163-165, April 1975.
2. G. Y. Lai, W. E. Wood, R. A. Clark, V. F. Zackay and E. R. Parker, Met. Trans. 5, 1663 (1974) (LBL-2250).

10. THE INFLUENCE OF Al AND Al-Si ADDITIONS ON THE MECHANICAL PROPERTIES OF LOW ALLOY ULTRA HIGH STRENGTH STEEL

M. S. Bhat

Low alloy heat treatable steels are used in applications where high stresses are encountered in service. The fracture toughness of these steels is not as high as that of the more expensive maraging steels. This research on VAR AISI 4340 low alloy steel has focused on improving its fracture toughness at high strength levels.

The approach used has been to utilize the effect of inexpensive alloying additions such as Al and Al+Si.

The M_s temperatures were determined using a dilatometer and ranged from 270° to 320°C. The austenitization temperatures as determined by dilatometry and optical metallography ranged from 900° to 1100°C. The tempering response of the modified steels was determined as a function of hardness and strength.

The variation in the yield and tensile strength with tempering temperature for the Al modified steels is shown in Fig. 1, and for the Al+Si modified steels in Fig. 2. Increasing the amounts

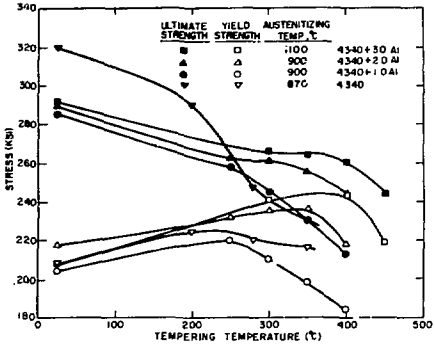

Fig. 1. Variation in tensile properties (0.2% offset yield and ultimate tensile strength) of AISI 4340 and 4340 + Al steels. (XBL 761-6113)

of Al and Al+Si raises both the yield and ultimate strengths following tempering. After an initial drop in ultimate strength with an increase in tempering temperature, a plateau appears; the plateau moves to higher temperatures with increasing amounts of Al and Al+Si. The yield strength increases to a peak value on tempering and decreases with higher tempering temperatures.

Compact tensi specimens were used to determine the resistance to crack initiation as a measure of fracture toughness. Figure 3 shows

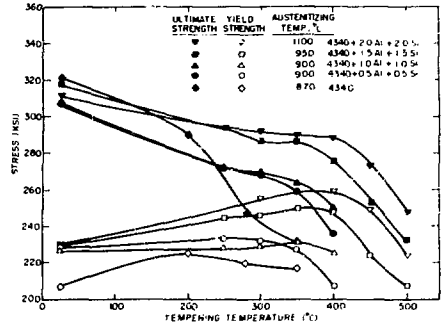

Fig. 2. Variation in tensile properties of AISI 4340 and 4340 + Al + Si steels. (XBL 761-6112)

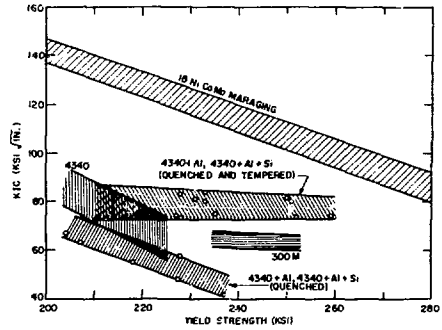

Fig. 3. Plot of plane strain fracture toughness K_{IC} vs yield strength for some commercial high strength steels and for the modified 4340 steels used in this investigation. (XBL 761-6105)

the fracture toughness K_{IC} as a function of yield strength between 210 and 260 ksi for the various modified steels. The variations of K_{IC} obtained with ultimate strengths ranging from 250 to 290 ksi are shown in Fig. 4. Also shown in Figs. 3 and 4 are the bands for the more expensive 18 NiCoMo maraging steels along with those of the unmodified AISI 4340 and 300 M steels. On the basis of both yield strength and ultimate strength, the bands for the steels used in the present investigation are located favorably, relative to the AISI 4340 and 300 M steels. The 18 NiCoMo maraging steel

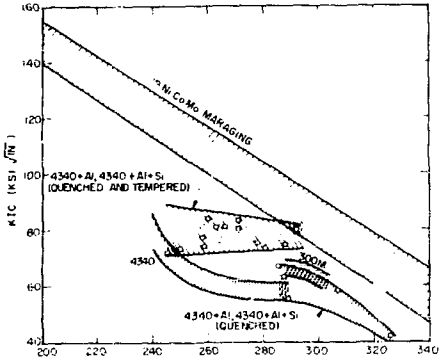

Fig. 4. Plot of K_{IC} vs tensile strength for some commercial high strength steels and for the modified 4340 steels. (XBL 761-6104)

band lies higher than that of the modified steels based on yield strength. However, based on ultimate strength (Fig. 4), the modified steel band is comparable to the 18 NiCoMo maraging steel band, especially at higher ultimate strengths.

11. THE EFFECT OF TEMPERING ON THE STRENGTH AND TOUGHNESS OF A SERIES OF Fe-Cr-Si-C ALLOYS

Edward A. Wylie

The mechanical properties of a series of high-strength Fe-Cr-C alloys with various silicon additions were determined for the as-quenched and the tempered conditions. Although silicon additions has been shown to improve the strength levels of high-strength steels in the as-quenched condition, its most important asset has been found to be its ability to delay the precipitation of cementite to higher temperatures during tempering. Silicon

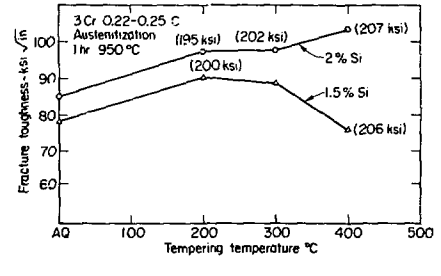

Fig. 1. Tensile properties of Fe-Cr-Si-C alloys. (XBL 764-2691)

does this through its effect on carbon activity, i.e., carbide precipitation kinetics. Thus, the ε carbide is stable to a higher tempering temperature. The tempered martensite embrittlement range is shifted to a higher temperature. This phenomenon is shown in Fig. 1 where data on the 2% Si alloy and the 1.5% Si alloys are presented. (The figures in parentheses in Fig. 1 represent the approximate yield strength of these alloys.

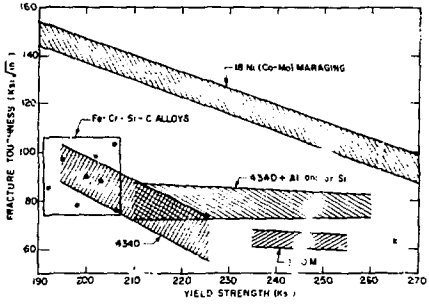

Fig. 2. Strength and toughness comparisons of experimental and commercial steels (XBL 761-6192)

The strength to toughness ratios (200 ksi yield strength to 100 ksi$\sqrt{in}$ fracture toughness) of these alloys allows them to be classified near the high strength-high toughness band the 18Ni maraging steels (alloy content approximately 30%) even though they are much leaner alloys (alloy content approximately 8%), (see Fig 2). An interesting feature of these alloys is that they contain neither nickel nor molybdenum, both of which are expensive and are almost invariably found in ultra high strength steels.

12. EFFECTS OF SILICON ON STRUCTURES AND PROPERTIES OF AISI 4320 LOW ALLOY STEEL

Jai-Song Huang

The effects of 2% silicon addition on the structures and properties of AISI 4320 steel were studied to determine to what extent the strength and toughness of lower carbon, weldable, low alloy steel could be increased. In quenched and tempered martensite, the silicon addition increases the temperature range in which ε carbide exists, delays the cementite precipitation and raises the retained austenite decomposition to higher temperature. The silicon addition increases the yield and ultimate tensile strength, but deteriorates the Charpy impact toughness except in the tempering range 200 ~ 300°C. This is mainly due to the occurrence of more internal twinning structure and more coarse or continuous carbide films precipitating along the martensite lath boundaries. Tempered martensite embrittlement is raised from about 200 ~ 300°C to about 350 ~ 500°C. Different embrittlement mechanisms are proposed for normal silicon and high silicon steels.

13. INVESTIGATION OF E52100 STEEL FOR IMPROVED TOUGHNESS

R. Kar

Commercial grade E52100 steel is a well known alloy in the ball bearing industry. This high carbon steel (1% C) is characterized by a high hardness in the tempered martensitic condition.

An investigated was initiated to determine whether the toughness of E52100 could be improved by use of techniques that had met with a reasonable measure of success in steels of lower carbon content.[1,2]

Commercial usage of E52100 involves initial austenitization at temperatures about 870-900°C resulting in incomplete dissolution of existing carbides. It is well known that a mixed microstructure consisting of undissolved carbides is deleterious to toughness, particularly if the carbide is present as a network at the original austenite grain boundary. For improved fracture toughness, it is therefore, necessary that all carbides go into solution during austenitization. Moreover, to decrease the tendency towards microcracking, grain refinement techniques are necessary.

Silicon addition to steels such as 4340 has shown increased resistance to softening during tempering of martensite,[3] and to extend the temperature range in which ε carbide precipitates. It is also known to retard the 500°F embrittlement of tempered martensite.[4]

It was decided to use these techniques to investigate whether their synergistic effect would improve the toughness in low temperature tempered martensite in E52100 steel. A study is also being made of the properties of lower bainitic structures obtained by isothermal holding in the bainitic temperature ranges of E52100 and its silicon variants; these properties of lower bainitic structures can then be compared with those of tempered martensite, since martensite in this system is predominantly twinned. Relevant sections of the T-T-T diagrams of E52100 and its silicon modifications, have been determined.

1. V. F. Zackay and E. R. Parker, LBL-2782, Lawrence Berkeley Laboratory, Berkeley, California (1974).
2. B. V. Narasimha Rao, Investigation of Ultra-High Strength Fe/4Cr/0.4C Martensitic Steels for Improved Toughness (M.S. Thesis), LBL-3794, June 1975.
3. C. J. Alstetter, M. Cohen and C. L. Averbach, Trans. ASM 55, 287 (1962).
4. G. R. Speich, W. C. Leslie, Met. Trans. 3, 1043 (1972).

14. THE INFLUENCE OF MICROSTRUCTURE, MEAN STRESS AND ENVIRONMENT ON FATIGUE CRACK PROPAGATION AND THRESHOLD BEHAVIOR IN HIGH STRENGTH STEELS

R. O. Ritchie

A program of research is being conducted to examine the growth of fatigue cracks in AISI 4340 and commercial Si-modified 4340 (300-M) steels in various environments; namely, laboratory air, water, and vacuum. The project will concentrate on fatigue crack propagation at very low stress intensities near the threshold stress intensity (below which cracks are not observed to propagate), where the growth rates are of the order of 10^{-6} mm/cycle and less. The research will examine how environment (principally the influence of water vapor) influences very low growth rates and values of the threshold stress intensity. The influence of material composition and microstructure (e.g., the effect of retained austenite in the as-quenched and quenched and tempered conditions) will also be specifically examined. Since material in service invariably contain residual stresses which can superimpose a static mean stress component on the applied alternating stress, the effect of mean stress (or maximum stress intensity K_{max}) is also being considered.

Tests are being conducted on fracture toughness-type CTS specimens, treated under load control at a frequency of 5-50 Hz (sine wave) in an electro-servo-hydraulic MTS testing machine. Growth rates are monitored using an electrical potential system,[1] where the potential difference generated across the test-piece notch face is monitored when a stabilized dc current is passed through the test-piece. Using this technique, changes in crack length can be measured to within 0.01 mm.

To date, tests have been completed on three microstructures, tested in laboratory air with controlled humidity at two mean stresses, namely stress ratios $R = K_{min}$, and $K_{max} = 0.05$ and 0.70. The heat treatments used and the resulting mechanical properties are shown in Table 1.

The values of the threshold stress intensities, below which no crack propagation is observed to occur, are shown in Table 2 for tests conducted at 50 Hz in laboratory air at a temperature of 23°C and relative humidity of 45%. The crack propagation data for these heat-treatments, in terms of the crack growth increment per cycle (da/dN) vs the alternating stress intensity (ΔK), are shown in Fig. 1. It can be seen from these data that, for the intermediate range of growth rates (typically 10^{-5}-10^{-3} mm/cycle), the crack propagation rate is largely insensitive to material, heat treatment and mean stress. At higher growth rates, approaching the stress intensity at failure (K_{Ic}), the growth rates are markedly mean-stress sensitive and propagation rates in 300-M exceed those in 4340. The latter results are consistent with the author's previous studies.[2]

Table 1. Mechanical properties of steels tested.

Material	Austenitizing Temp. (°C) Oil Quenched	Tempering Temp. (°C)	0.2% Proof Stress (MPa)	UTS (MPa)	Reduction in Area (%)	Elong. (%)	K_{Ic} (MPa$\sqrt{m}$)
4340	870	300	1497.2	1754.5	54.3	13.2	62.7
300-M	870	300	1737.2	2096.2	48.4	11.9	65.1
300-M	870	470	1496.6	1682.8	50.0	12.1	68.9

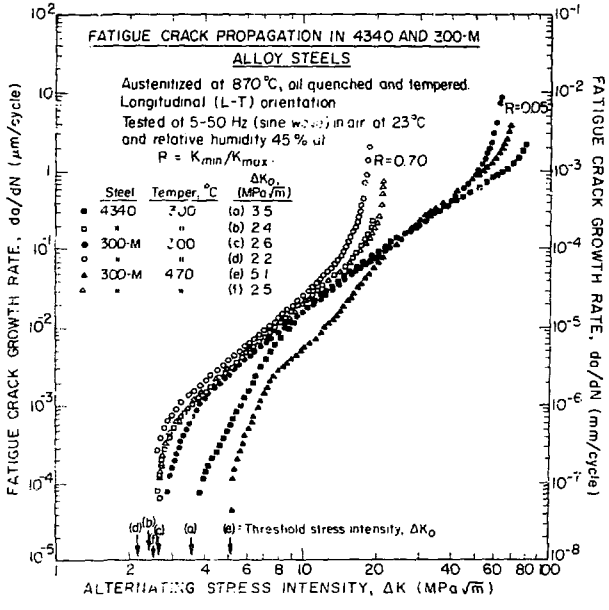

Fig. 1. Variation of fatigue crack growth rate (da/dN) with alternating stress intensity (ΔK) for alloy steels 4340 and 300-M, tested at stress ratios R=0.05 and 0.70. (XBL 762-6388)

At low growth rates ($\leq 10^{-6}$ mm/cycle), approaching the threshold stress intensity, propagation rates again become sensitive to material, heat-treatment, and mean stress. For the 300°C tempered condition, propagation rates are faster in 300-M than in 4340, but when 300-M is tempered to higher temperature (470°C), a marked reduction in growth rate can be observed. In all cases, growth at these low stress intensities is markedly mean-stress sensitive. As the stress ratio is increased from 0.05 to 0.70, increased propagation rates are always observed.

It is proposed to extend these studied to water and vacuum environments to determine the relative contributions to the growth rate from corrosion and mechanical fatigue cracking, with the ultimate aim of developing a model for the fatigue crack propagation mechanisms at low stress intensities.

1. R. O. Ritchie, et al., Int. J. Fracture Mechanics 7, 462 (1971).
2. R. O. Ritchie, J. F. Knott, Acta Met. 21, 639 (1973).

Table 2. Values of the maximum and alternating threshold stress intensities, K_{max_o} and K_o, at stress ratios of R = 0.05 and 0.70.

Material	Austenitizing Temp. (Oil Quench) (°C)	Tempering Temp. (°C)	Stress Ratio, R (K_{min}/K_{max})	ΔK_o (MPa$\sqrt{m}$)	K_{max_o} (MPa$\sqrt{m}$)
4340	870	300	0.05	3.8	4.0
			0.70	2.4	8.2
300-M	870	300	0.05	3.8	3.2
			0.70	2.3	7.7
300-M	870	470	0.05	5.1	5.4
			0.70	2.5	8.3

15. STRESS CORROSION CRACKING BEHAVIOR OF HIGH STRENGTH STEELS IN A WATER ENVIRONMENT

Mario H. Castro-Cedeno and R. O. Ritchie

A major limitation of materials in current usage is their mechanical behavior in the presence of an environment. Of particular importance is the phenomenon of stress corrosion cracking caused by the simultaneous action of an applied stress and an active environment. Commercial high strength steels, for example, can fail in water at stresses 1/3-1/4 of their failure stress in air. The purpose of this project is to examine the stress corrosion cracking behavior in distilled water of 4340 alloy steel, and compare this behavior with that of a commercial Si-modified 4340, 300-M. Previous results[1] have suggested that the addition of silicon to such high strength steels can markedly improve the stress corrosion cracking resistance by causing a reduction in stress corrosion crack propagation rates. It is planned to examine the influence of microstructure on the static growth rates in water, and compare these data with those obtained under cyclic conditions (i.e., fatigue crack growth) for the same materials and heat-treatments. (See section on Slow Fatigue Crack Growth by Ritchie in this volume.)

Stress corrosion crack growth rates are determined using fatigue-precracked, C.T.S. test-pieces stressed in distilled water under dead load conditions on cantilever bend rigs; the times to failure for particular initial stress intensities K_{Ii} are measured. Monitoring of crack length to determine propagation rates is achieved using displacement gages mounted on the notch face.

To date, two structures have been tested, namely 300-M, (austenitized at 870°C, oil quenched) tempered at 300°C and 470°C. Plots of initial stress intensity, K_{Ii} vs time to failure for both quenched and tempered conditions are shown in Fig. 1. From these plots, the stress intensity below which no stress corrosion cracking occurs,

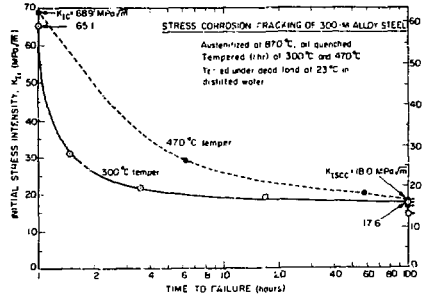

Fig. 1. Plots of time to failure versus initial stress intensity (K_I) for the stress corrosion cracking in water of 300-M steel, tempered at 300°C and 470°C. (XBL 762-6386)

K_{ISCC}, can be determined. It can be seen that tempering at the higher temperature (470°C), although improving the fatigue crack growth resistance at low stress intensities in air (see section by Ritchie in this volume), only marginally improves the value of K_{ISCC}.

Further testing will incorporate 4340 steel and isothermally transformed 300-M examine the influence of retained austenite on the growth of stress corrosion cracks. Further, testing with applied anodic/cathodic polarization potentials will be conducted together with extensive fractographic examination, with the sim or deducing a model for stress corrosion cracking in these materials.

1. C. S. Carter, Proc. ASM/WESTEC Conf., Los Angeles, Calif., March 1969.

16. THE FRACTURE TOUGHNESS OF HIGH STRENGTH Fe-Ni-Ti ALLOYS

Benjamin Francis

The fracture toughness of a series of Fe-Ni-Ti alloys was investigated to determine the thermal treatments that would preclude the precence of embrittling grain boundary precipitates in this low alloy family of maraging steels. The yield strengths of these alloys were in the range of 180-200 ksi. The iron alloys investigated were 12Ni-1Ti, 12Ni-2Ti, 16Ni-1Ti, 16Ni-1.5Ti, and 20Ni-1.5Ti. For the 16Ni alloys which had the best properties, it was found that excellent fracture toughness (K_{Ic} > 110 MPa$\sqrt{m}$) could be obtained if the age hardening temperature (550-600°C) was higher than that normally used for maraging steels (450-480°C) (see Table 1). If aging temperatures in the range of 450-500°C were used, severe grain boundary precipitation occurred and the alloys were brittle. Some evidence is presented which suggests that, at the higher aging temperatures, austenite forms very rapidly at the grain boundaries and greatly reduces the amount of boundary precipitate, thereby increasing the fracture toughness.

Table 1. Fracture for various aging temperatures.

Alloy (wt %)	Aging Temp.	R_c Hardness (y 200 ksi)	K_{Ic} (ksi$\sqrt{in}$) (23°C)	CVN (ft-lb) (23°C)
Fe-16Ni-1.5Ti	600°C	43	~114	27
	550°C	43	50	14
	450°C	43	-	3

17. EVALUATION OF TOUGHNESS IN AISI 4340 ALLOY STEEL AUSTENITIZED AT LOW AND HIGH TEMPERATURE*

R. O. Ritchie and B. Francis

Recent research[1] into the influence of austenitizing treatment on the mechanical properties of as-quenched AISI 4340 steel has shown that, compared to conventional austenitizing at 870°C, increasing the austenitizing temperature to 1200°C can raise the plane strain fracture toughness, K_{Ic}, by a factor of 2 without reduction in yield stress. However, concurrent with this improvement in K_{Ic}, there is an unexplained and perplexing reduction in Charpy impact energy. It was the purpose of this research[2] to offer an explanation of these contradictory toughness results reported for 4340 and other alloys, in the light of the basic differences between K_{Ic} and Charpy testing.

Uniaxial tensile, Charpy impact, fracture toughness (K_{Ic}) and dynamic fracture toughness (K_{Id}) tests were carried out on two heat-treated structures of 4340, namely (1) austenitized at 870°C and oil quenched (hereafter referred to as the 870°C structure) and (2) austenitized at 1200°C, held at 870°C and oil quenched (1200-870°C structure). The results obtained (Table 1) indicated that (a) the yield stress was unaffected by austenitizing treatment, (b) the 1200°C structure showed greater fracture toughness (K_{Ic}) and dynamic fracture toughness (K_{Id}); and (c) the 870°C structure showed greater Charpy impact energy, although the difference was small.

In the light of these data, and by examination of the fracture surfaces, it was concluded that the contradictory toughness results were independent of shear lip energy differences and independent of the marked difference in strain rate imposed by K_{Ic} and Charpy impact tests. The effect was attributed to the difference in notch root radius (ρ) of the stress concentrator introduced into the test-pieces: Charpy test-pieces contain a V-notch ($\rho \approx 0.25$ mm) whereas K_{Ic} test-pieces contain a fatigue precrack ($\rho \to 0$).

To determine how measured toughness varies with notch root radius for each austenitizing treatment, a series of notch-bend test-pieces was prepared with notch root radius ranging from a fatigue precrack to a 0.58 mm radius V-notch. The specimens were broken at room temperature in an instrumented Charpy machine, and the impact energy and "apparent" fracture toughness, K_A, measured in each case. In Fig. 1, the "apparent" fracture toughness, K_A, is plotted against the square root of the notch radius, $\rho^{1/2}$, for both microstructure. It can be seen that for small root radii ($\rho < 0.05$ mm) the toughness of the 1200-870°C structure exceeds that of the 870°C structure, whereas, at larger radii ($\rho > 0.05$ mm), the reverse is the case. Thus, it can be seen that, in fracture toughness tests, where $\rho \to 0$, the 1200-870°C structure will have the higher K_{Ic} value; but for Charpy tests, where $\rho = 0.25$ mm, the 870°C structure will fail at the larger K_A value, and thus show the larger impact energy.

An explanation for this behavior was deduced from the theory, developed by Tetelman and co-workers,[3,4] to account for the influence of notch root radius on toughness. They proposed that, for constant stress controlled fracture, the fracture toughness was given by

$$K_{Ic}(\text{or } K_{Ic}) \approx 2.9\, \sigma_y [\exp(\sigma_F/\sigma_y - 1) - 1]^{1/2}\, \rho_o^{1/2}$$

where σ_y is the yield stress, σ_F the critical fracture stress, and ρ_o the "effective" root radius; the root radius is related to the controlling microstructural feature (i.e., grain size, inclusion spacing, etc.).

In the present results (Fig. 1) the values of ρ_o for each microstructure were of the order of the prior austenite grain size. It was concluded that the structure obtained after austenitizing at 1200°C would show superior toughness for failure ahead of sharp cracks (i.e., in K_{Ic} and K_{Id}) tests due to its larger effective root radius for fracture. This was tentatively associated with the larger prior austenite grain size. The

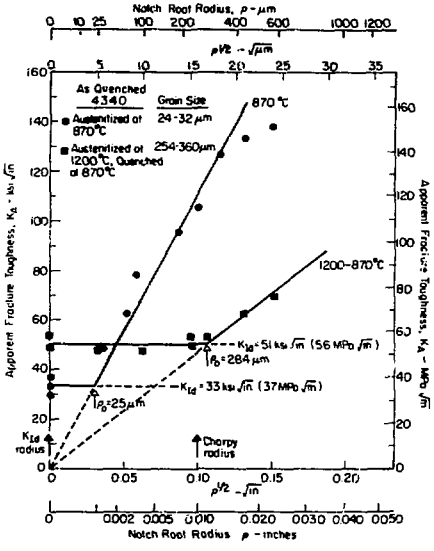

Fig. 1. The relationship between toughness, measured by the apparent dynamic fracture toughness (K_A) from instrumented Charpy tests, and notch root radius (ρ) in oil quenched AISI 4340, for the 1200-870°C and 870°C structures. ρ_o is the "limiting" root radius, K_{Id} the dynamic fracture toughness. (XBL 758-6995)

structure obtained after conventional austenitizing at 870°C, however, would show superior toughness for fracture ahead of rounded notches (i.e., in Charpy impact tests) due to its larger critical fracture stress for failure. This was associated with impurity element segregation to austenite grain boundaries during the high austenitizing treatment. A schematic representation of these fracture events is shown in Fig. 2; a more complete explanation can be found in Ref. 2.

Finally, it is suggested from this work that evaluation of material toughness for alloy design purposes should not be based solely on K_{IC} or Charpy impact energy values alone; an assessment from both sharp crack fracture toughness and rounded notch impact energy testing is required.

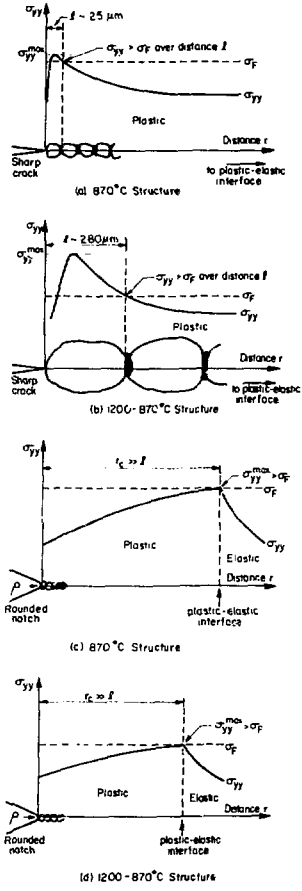

Fig. 2. Schematic representation of the distribution of tensile stress (σ_{yy}) at distance (r) ahead of stress concentrator at failure for (a) 870°C structure with sharp crack ($\rho < \rho_o$), (b) 1200-870°C with sharp crack, (c) 870°C structure with rounded notch ($\rho > \rho_o$), (d) 1200-870°C structure with rounded notch. Critical fracture event occurs when $\sigma_{yy} > \sigma_F$ over characteristic distance (ℓ) ahead of sharp crack, or when $\sigma_{yy}^{max} \geq \sigma_F$ at the plastic-elastic interface ($r_c \gg \ell$) ahead of rounded notch. Toughness of 1200-870°C structure is greater ahead of sharp crack because characteristic distance (ℓ) is larger; toughness of 870°C structure is greater ahead of rounded notch because fracture stress (σ_F) is larger. (XBL 758-6996)

---

*Abstracted from LBL-4125, September 1975

1. G. Y. Lai et al., Met. Trans. 5, 1663 (1974).
2. R. O. Ritchie et al., LBL-4125, (submitted to Met Trans.), Sept. 1975.
3. T. R. Wilshaw et al., Eng. Frac. Mech. 1, 191 (1968).
4. J. Malkin and A. S. Tetelman, ibid, 3, 151 (1971).

Table 1. Ambient temperature longitudial toughness properties for alloy AISI 4340 in the oil quenched condition.

Austenitizing Temperature, °C	Charpy V-notch Impact Energy		Plane Strain Fracture Toughness, K_{Ic}		Dynamic Fracture Toughness, K_{Id}	
	ft-lb	J	ksi$\sqrt{in}$	MPa$\sqrt{m}$	ksi$\sqrt{in}$	MPa$\sqrt{m}$
1200-870	5.4	7.32	63.8	70.1	54.2	59.6
	6.0	8.13	66.6	73.2	48.8	53.7
	5.0	6.78	61.2	67.2		
	2.0	2.71				
	6.0	8.13				
870	7.5	10.20	31.1	34.2	36.5	40.3
	6.1	8.27	39.0	42.9	30.0	33.0
	7.5	10.20	32.3	35.5	33.3	36.6

18. HIGH TEMPERATURE EROSION-CORROSION PROGRAM

A. Levy, D. Kleist, and D. McFadden

A potentially severe environment for metals and ceramics exists in several of the coal energy conversion systems that are currently under development. The coal gasification system and the direct coal fired turbine power plant both subject materials to high temperature erosion-corrosion by solid particle impingement in the presence of a highly reactive carrier gas with combined oxidation, sulfidation, carburization, and nitridation potential. The design of new materials that will be resistant to these environments for long service lives and that will utilize low amounts of critical, high cost alloying elements can best be undertaken when the mechanisms of degradation are well understood.

The separate determinations of erosion behavior and corrosion behavior of metals tested under conditions that simulate the applicable portions of the total environment in a coal gasification gasifier unit are now underway. Combined erosion-corrosion investigations will be integrated into the program upon the completion and checkout of a high temperature test device that will accurately simulate the particle flow and gas composition of a coal gasifier.

The initial work on erosion has been done using a room temperature limited blast tester. The identification of multiple mechanisms of erosion of commercially pure aluminum alloy impacted at room temperature by angular silicon carbide particles holds promise of markedly increasing the accuracy of erosion rate prediction. Equations in the literature are based on one or two mechanisms.[1-3] Six separate mechanisms can be defined analytically and the determination of the relative amount of each that can occur during an erosion exposure will be used to develop an integrated rate equation. Figure 1 shows SEM photographs of six active mechanisms of erosion.

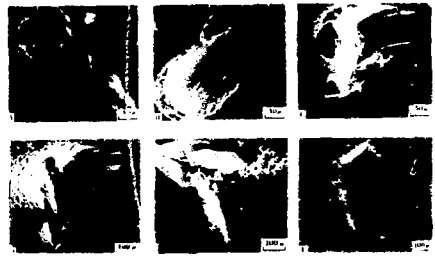

Fig. 1. Erosion craters. (XBB 761-582)

The conditions under which the impinging particles strike the surface of the material have a direct relationship to the amount of erosion that occurs. Figure 2 shows how the angle of erosion, α, affects the loss rate of material and what the prevelant mechanism is for several specific angles varies with impingement conditions.

In one-dimensional entrained particle, gas flow, a computer program has been developed that can predict particle velocities considering several active variables. Figure 3 shows how the calculated and experimental particle velocities vary with ΔP across the nozzle.

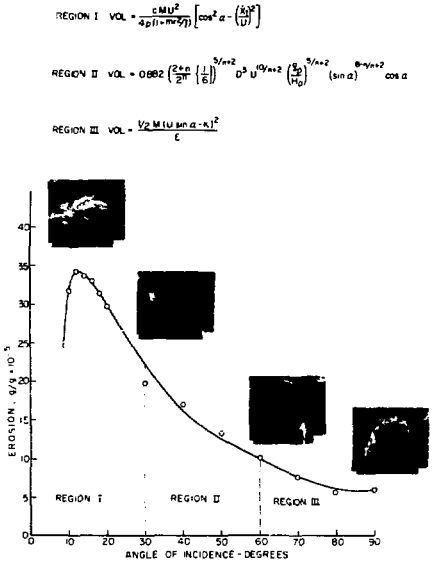

Fig. 2. Erosion rate vs. impingement angle. (XBB 761-589)

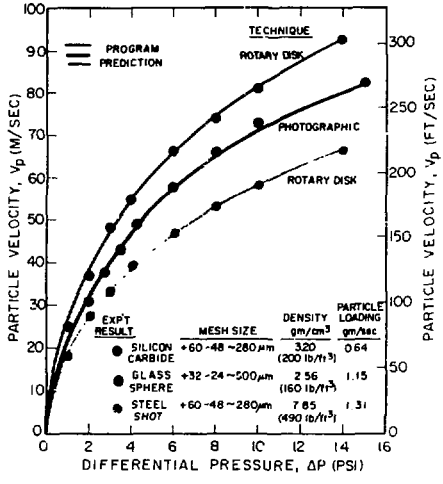

Fig. 3. Particle velocities. (BBC 751-626)

Figure 4 shows the high temperature erosion-corrosion test device. It is capable of directing high temperature solid particles entrained in gas mixtures that simulate exactly the compositions and flow rates that occur in coal gasifiers and coal-fired turbine power plants at target materials. Velocities to ~1,000 ft/sec, temperatures to 1000°F, and solids loadings up to 30 lb/100 acf can be maintained in certain combinations for time periods up to 10 hr duration between particle hopper reloadings.

1. J. H. Neilson and A. Gilchrist, Erosion by a Stream of Solid Particles, Wear 11, 111 (1968).
2. I. Finnie, Some Observations on the Erosion of Ductile Metals, Wear 19, 81 (1972).
3. G. P. Tilly, A Two Stage Mechanism of Ductile Erosion, Wear 23, 87 (1973).

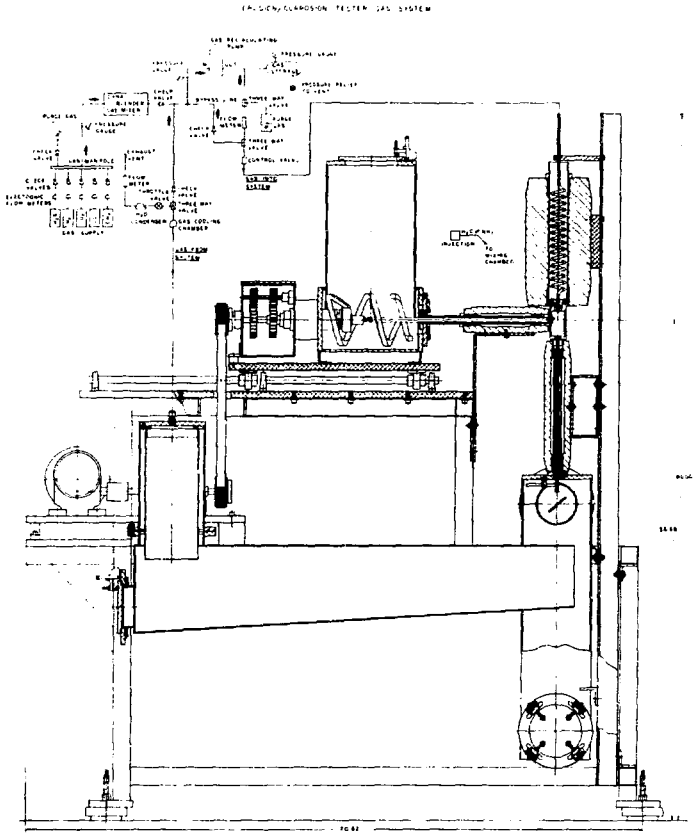

Fig. 4. Erosion-corrosion test device. (XBL 761-241)

19. RESEARCH PLANS FOR CALENDAR YEAR 1976

Victor F. Zackay and Earl R. Parker

We consider the long range studies of our group to be the building blocks of future alloys. These studies, which will be continued in the coming year, are concerned with: (1) the quantum mechanical efforts to describe quantitatively physical properties in terms of primary particles and energies; (2) the kinetic studies which are aimed at the elucidation of the interactive roles of alloying elements in the isothermal decomposition of the austenite of complex systems; (3) the fundamental and applied aspects of erosion and corrosion; and (4) the roles of stress, environment, and microstructure on the behavior of ferrous alloys.

The structure-property investigations of specific alloy systems will either be concluded at the appropriate time within the coming year, or, in some cases, continued with specific energy-related applications in mind. Several of the more promising technological applications of these systems are described below.

The ferritic alloys (based on intermetallic compound dispersoids) have been suggested for potential uses in: (1) cladding for breeder reactor fuel rods, (2) turbine blades for the temperature range of 550-650°C, (3) superheater tubes for boilers, and (4) components for coal gasification plants.

It has been suggested that the austenitic alloys based on the Fe-Mn system may be useful in energy absorbing devices; therefore, a research program involving both composition variation and thermo-mechanical processing will be initiated. Purpose of the program will be to optimize the mechanical properties of these alloys for their potential use in such devices.

Because of their hardness and toughness, the quenched and tempered, or alternatively, the isothermally transformed Si and Al alloys, may be used in tool bits for mining and tunnel boring equipment.

It is our hope that with the assistance of ERDA staff and the active support of energy-related industries that some of these alloys will eventually assume a useful place in technology.

20. 1975 PUBLICATIONS AND REPORTS

Victor F. Zackay, Earl R. Parker, and Associates

Journals

1. G. Sasaki and M. J. Yokota, Fracture Mode Determinations by SEM, Metallography 8, 265 (1975) (LBL-3120).

2. G. Sasaki and M. J. Yokota, Grain Size Versus Ductile Brittle Transition in an Fe-12% Ni Alloy, Met. Trans. 6A, 586 (1975) (LBL-2777).

3. M. J. Yokota and G. Y. Lai, Toughness of Lath Versus Plate Martensites, Met. Trans. 6A, 1832 (1975) (LBL-3144).

4. M. D. Bhandarkar, M. S. Bhat, V. F. Zackay and E. R. Parker, Structure and Elevated Temperature Properties of Carbon-Free Ferritic Alloys Strengthened by a Laves Phase, Met. Trans. 6A, 1281 (1975) (LBL-2273).

5. R. M. Horn, Influence of Heat Treatment on the Fatigue Crack Growth Rates of a Secondary Hardening Steel, Met. Trans. 6A, 1525 (1975) (LBL-2239).

6. M. J. Yokota, G. Sasaki and W. A. Horwood, Developing High Impact Toughness in Interstitial-Free Fe-Ni Alloys at Liquid Nitrogen Temperature, Materials Sci. & Eng. 19, 129 (1975) (LBL-2278).

7. G. Y. Lai, On High Fracture Toughness of Coarse-Grained AISI 4130 Steel, Materails Sci. & Eng. 19, 153 (1975) (LBL-2575).

8. G. Y. Lai, On the Precipitation of Epsilon-Carbide in Lower Bainite, Met. Trans. 6A, 1469 (1975) (LBL-2705).

9. E. R. Parker and V. F. Zackay, Microstructural Features Affecting Fracture Toughness of High Strength Steels, Engineering Fracture Mechanics 7, 371 (1975) (LBL-2771).

10. M. J. Schanfein, M. J. Yokota, V. F. Zackay, E. R. Parker, and J. W. Morris, Jr., Cryogenic Properties of Iron-Manganese and Iron-Manganese-Chromium Alloys, Properties of Materials for Liquefied Natural Gas Tankage, ASTM STP 579, Amer. Soc. for Testing and Materials, pp. 361-377 (1975) (LBL-2764).

11. S. Jin, B. Whitaker, J. W. Morris, Jr. and V. F. Zackay, Cryogenic Toughness Through Microstructural Control in Ferritic Fe-Ni-Ti Alloys, Properties of Materials for Liquefied Natural Gas Tankage, ASTM STP 579, Amer. Soc. for Testing and Materials, pp. 348-360 (1975) (LBL-2756).

12. E. R. Parker, Double Major Programs in Materials Science and Civil, Electrical and Mechanical Engineering at the University of California, Berkeley, Materials Science and Engineering 20, 205 (1975) (LBL-3935).

Paper Presented

1. V. F. Zackay, Fundamental Considerations in the Design of Ferrous Alloys, LBL-3595, Presented at the Specialists Meeting on "Alloy Design for Fatigue and Fracture Resistance", 40th Meeting of the Structures and Materials Panel, Brussels, Belgium, April 14-15, 1975.

LBL Reports

1. B. Francis, Homogenization of Ingots, LBL-2758, April, 1975.

2. B. Francis, Increasing the Fracture Toughness of Maraging Steel Type Alloy, LBL-3599, April, 1975.

3. J. Shively, A New Density of States Formulation, LBL-3798, April 1975.

4. K. Clark, Simplified Operations Manual for the Theta Dilatometers, LBL-3912, April, 1975.

5. J. Shively, Unrestricted Summations for the Multiple Scattering Transition Operator and Propagator, LBL-3744, Feb. 1975.

6. J. Wert, The Strain Energy of a Disk-shaped GP Zone, LBL-3174 Rev., May 1975.

7. G. Y. Lai, W. E. Wood, E. R. Parker and V. F. Zackay, Influence of Microstructural Features on Fracture Toughness of an Ultra-High Strength Steel, LBL-2236, April 1975.

8. David George Atteridge, An Investigation of the Structure and Properties of Iron-Manganese-Carbon Alloys, (D. Eng. Thesis) LBL-3574, May 1975.

9. R. H. Lamoreaux, Calculated Enthalpies of Transition at 0°K for Several Metallic Phase Transition, LBL-3711, May 1975.

10. Benjamin Francis, The Fracture Toughness of High Strength Fe-Ni-Ti Alloys, (Ph.D. Thesis) LBL-3124, May 1975.

11. R. O. Ritchie, B. Francis, and W. L. Server, Evaluation of Toughness in AISI 4340 Alloy Steel Austenitized at Low and High Temperatures, LBL-4125, Sept. 1975.

12. G. Y. Lai, V. F. Zackay and E. R. Parker, Enhancement of Fracture Toughness by Retained Austenite in 300M Steel, LBL-4513, Nov. 1975.

13. Stabinder Singh, Creep Rupture Properties of Laves Phase Strengthened Fe-Ta-Cr-W and Fe-Ta-Cr-W-Mo Alloys, (M.S. Thesis) LBL-4504, Dec. 1975.

14. Jai-Song Huang, Effects of Silicon on Structures and Properties of AISI 4320 Low Alloy Steels, (M.S. Thesis) LBL-4500, Dec. 1975.

15. Ana Maria Llopis, Effect of Alloying Elements in Steels on the Kinetics of the Austenite to Bainite Transformation, (M.S. Thesis) LBL-4555, Dec. 1975.

c. Relations Between Dislocations, Point Defects, and Properties of Metals

Jack Washburn, Principal Investigator

1. PREFERENTIAL CAPTURE OF INTERSTITIAL ATOMS BY DISLOCATIONS*

Thomas H. Kosel

The climb of dislocations due to preferential capture of interstitial atoms, which are produced in equal numbers with vacant lattice sites by the electron beam of a 650 kV electron microscope, has been studied in three Copper-Aluminum alloys of different stacking fault energy. It was found that dislocation segments remain on {111} planes during climb. The climb rate is a function of damage rate, temperature, stacking fault energy and distance of the dislocation from a foil surface but to a first approximation does not seem to depend on whether the dislocation is in nearly pure edge orientation or near pure screw orientation. The results suggest that under the conditions of these experiments climb rate is sometimes influenced by the rate of jog nucleation rather than being dependent only on the rate at which point defects migrate to the dislocation.

*This work has been partially supported by a grant from the General Electric Foundation.

2. STRUCTURE OF JOGS AND SMALL DISLOCATION LOOPS IN LOW STACKING FAULT ENERGY ALLOYS

Thomas Kosel

The shapes of small a/2 (110) loops and their orientation on the glide cyclinder have been calculated as a function of stress using a computer program that takes into account all the interaction energy terms for a finite number of short straight dislocation segments. The zero stress equilibrium orientation of the loop was found to be the pure edge position regardless of loop size. However small stresses can rotate a loop up to about 20° away from pure edge because the work necessary to rotate away from pure edge orientation on either the major or the minor axis only rises rapidly for angles greater than 20°.

3. THE MECHANISM OF JOG NUCLEATION ON WIDELY SPLIT DISLOCATIONS

Krishna Seshan and Thomas H. Kosel

Some preliminary calculations have been made based on Grilhe's[1] model for climb of split dislocations. Figure 1 shows three steps by which it is assumed a double jog is nucleated: first a cluster of interstitials forms in the region of hydrostatic tension below one of the partials, it is assumed to grow as a perfect 1/2 (110) loop

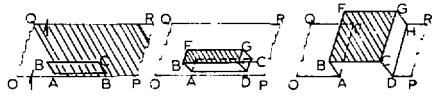

Fig. 1. Schematic model for jog nucleation on extended dislocations. (XBL 761-6302)

which lowers its energy by splitting on the two {111} planes that enclose its glide cylinder. At critical sizes and shapes the jog pair is formed by glide.

The effect of stacking fault energy, shape of the initial cluster, and of the angles between the burgers vectors of the partial dislocations and the directions of the lines is being studied using the same computer program as in report 2 above.

4. ON THE DISSOCIATION OF INTERSTITIAL FRANK LOOPS

Krishna Seshan

Our investigation of ion-implanted silicon[1,2] showed that most of the defects were hexagonal interstitial Frank loops. No triangular or tetrahedral defects were seen. Furthermore, in extensive studies of radiation damage in metals, interstitial tetrahedra have never been reported.

This should be explainable on the basis of the dislocation dissociation processes and the self energy of these defects (triangular and tetrahedral) relative to those that are observed. Therefore a study of the dissocition and the self energy of these defects has been started.[3] It has been found that interstitial Frank loops should dissociate to form obtuse angled, intrinsic faults. It appears to be easier to nucleate a simple shear (intrinsic) fault than a double shear extrinsic fault. Such an obtuse configuration would inhibit the formation of extrinsic or interstitial tetrahedra.

Calculations of the energy of these defects have been made using a program that computes the energy of interaction of straight dislocation segments. The sigificant results so for are:

(a) The configuration with obtuse splitting has a higher energy than the acute if $\gamma_{ext} = \gamma_{int}$ γ = (stacking fault energy).

(b) The mode of splitting of the hexagonal extrinsic Frank loop should depend on the ratio $\gamma_{ext}/\gamma_{int}$. For $\gamma_{int} \leq 0.8\ \gamma_{ext}$ obtuse splitting becomes favored.

It appears that the absence of tetrahedral defects can be satisfactorily explained on the basis of the above. The regions of stability of triangular and hexagonal defects are being investigated and the computation is being extended to other defects like the truncated tetrahedron, etc.

(We thank Drs. J. Grilhes and R. J. Giaboriaud for use of their programme.)

1. K. Seshan and J. Washburn, Phys. Stat. Sol. 26, 345 (1974).
2. K. Seshan and J. Washburn, Rad. Effects 26, 1-2, 31 (1975).
3. K. Seshan, J. Girilhe, and J. Washburn, Some Considerations in the Splitting of Frank Loops, Conf. on Fundamental Aspects of Radiation Damage, Gatlinburg, Tenn., Oct. 1975.

5. ION IMPLANTATION DAMAGE IN SILICON

Krishna Seshan

The characterization of secondary damage (damage left behind when the as-implanted damage or "primary damage" anneals) has been extended to doses above D_C, where a continuous amorphous layer is formed. The defects observed at these doses are not well characterized because they occur in very high densities and have been variously described as "microtwinned," "heavily faulted" with "small crystallites," etc.

Electron micrographs in weak beam contrast have shown that this seemingly complex microstructure is simply one with a very high density of stacking faults confined to a very narrow (3000 Å) buried region in the crystal. That this is so can be corroborated by the electron diffraction patterns.

A characterization of these stacking faults is being done from a simple model that assumes that the crystal regrows from many slightly misaligned remaining regions of good crystal. On the basis of this model it is expected that extrinsic and intrinsic stacking faults should both be present.

1. K. Seshan and J. Washburn, Some New Results in the Characterization of Defects in P^+ Implanted Silicon, Radiation Effects 26(1-2), 31 (1975).

6. DEVELOPMENT OF HETEROJUNCTION SOLAR CELLS

Terry Peterson and Barry Chin

A mixed crystal $Zn_yCd_{1-y}S$-Cu_xS solar cell has been shown to have important advantages compared to the ordinary CdS-Cu_xS heterojunction cell. The following is a summary of the results obtained so far.

(1) Expected Characteristics of Mixed Crystal Cells

A. Increased open-circuit voltage compared to CdS cell due to smaller electron affinity of Zn-containing crystal.

B. Slight increase in short-circuit current compared to CdS cell because better lattice parameter matching should yield lower density of mis-fit-accommodation dislocations, and hence, fewer interfacial recombination sites.

C. Improved resistance to long-term degradation arising from diffusion of copper into the n-type layer because of the lower diffusivity of copper in the mixed crystal compared to that in CdS.

D. Improved short-wavelength response of "back-wall" cells because of larger band gap of the mixed crystal compared to CdS.

(2) Results to Date on Mixed Crystal Cells

Characteristics A and D above have been directly verified in backwall cells made from a single crystal of nominally 25% ZnS. These results are reported in detail in LBL-3985. Characteristic C, the improved stability, is indirectly evidenced by the larger times required to form an opaque layer of Cu_xS in the Cu^{++} solution. The results of short-circuit current measurements were inconclusive with regard to the expected increase in mixed crystal cells.

Another part of this work has been the development of techniques for co-evaporation of Cu and S to form Cu_2S films. It is expected that a modification of this equipment can be used to grow epitaxial $Zn_yCd_{1-y}S$ on a GaAs substrate.

7. ON SATURATION OF RADIATION INDUCED SWELLING IN 316 STAINLESS STEEL

Arvind Srivastava

Solution annealed type 316 stainless steel was irradiated by 140 keV protons at 625°C to study its swelling behavior. The minimum and maximum fluence of protons at which samples were irradiated were about $2.25 \times 10^{19}/cm^2$ and $2 \times 10^{20}/cm^2$, respectively. The average dose rate was $8 \times 10^{14}/(cm^2\text{-sec})$. On the basis of theory the rate of displacement of atoms is expected to increase from 0.4×10^{-3}/sec at the surface of the sample to 2×10^{-3}/sec at about 6500 Å below the surface. The rate then decreases rapidly to zero at the end of proton range (~ 1 μm). The integrated swelling along the entire proton path produces a step between the irradiated and non-irradiated surfaces. The height of the step, a measure of the integrated swelling, was determined by a surface profilometer. Using the step-height data and the theoretical depth vs atom displacements, a swelling vs displacements per atom (dpa) curve was constructed (Fig. 1). There were three stages in the swelling regime. Stage I (dpa < 200) consisted of a rising rate of swelling,

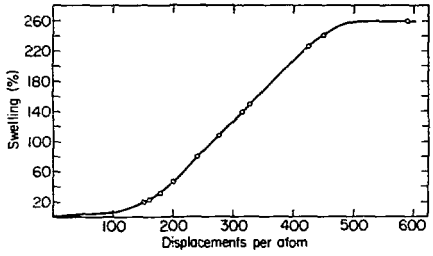

Fig. 1. Radiation induced swelling of 316 stainless steel at 625°C up to 500 displacements per atom.

(XBL 764-2687)

maximizing at about 0.75% per dpa. The rate of swelling apparently remained at this highest value during stage II (200 < dpa < 425). The magnitudes of swelling for 200 dpa and 425 dpa were about 50% and 230% respectively. Beyond 425 dpa the rate of swelling decreased. The observed results were explained on the basis of changes in dislocation density and void density during the irradiation.

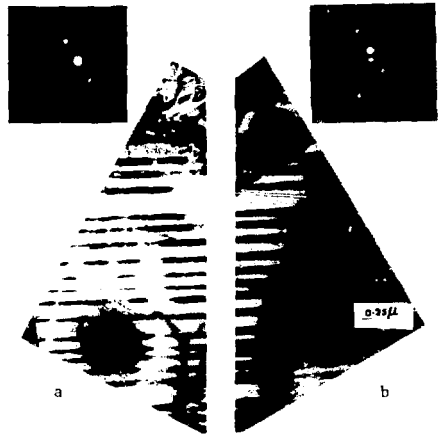

Fig. 1. Stress induced twin boundary migration in NiTi martensite a) before and b) after deformation. (see text for explanation) (XBB 761-248)

8. THE MECHANISM OF THE SHAPE MEMORY PHENOMENON IN NiTi*

Hani Mohammed

We have been investigating the mechanism of the shape memory effect in 50.3 at% Ni-Ti alloy which is associated with a reversible martensitic-type phase transformation (Ms ~ 55°C). A knowledge of the deformation modes, particularly in the early stages, is essential in order to explain this behavior. In a partially transformed material, it has been demonstrated that deformation in the early stages occurs by at least two modes: (i) stress-induced twin boundary migration within the martensite, and (ii) stress-induced growth of the most favorably oriented existing martensite plates in each grain.

Figure 1 shows bright-field transmission electron micrographs illustrating the first mode. The same area of Fig. 1 (a) was reobserved after the foil had been slightly bent outside the microscope at room temperature (the two images were printed such that they are mirror images and then were cut along the same line). Light optical micrographs of the surface of a tensile specimen (initially polished and unetched) during progressive straining at room temperature show the second mode. Surface relief effects associated with stress-induced growth of favorably oriented martensite plates are observed.

A further evidence for the above deformation modes was obtained from the observation that if a specimen was bent at room temperature and then

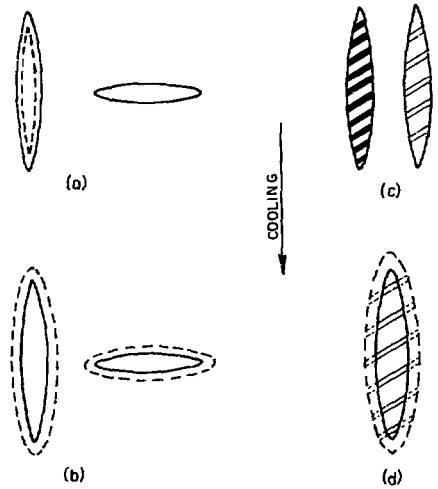

Fig. 2. Schematic illustration of the cause of spontaneous deformation of predeformed specimens during thermal martensite growth (see text).

(XBL 761-6208)

cooled further, thus causing additional martensite growth, it continued to bend spontaneously in the same direction. The effect of the initial bending and the reason that subsequent cooling should result in a further macroscopic strain is illustrated schematically in Fig. 2. Figure 2(a) shows a favorably and an unfavorably oriented martensite plate before (dashed lines) and after (solid lines) bending. Figure 2(b) shows their expected change in size after further cooling. Figure 2(c) shows twinned martensite plates (1) before, and (2) after bending, showing growth of one set of twins at the expense of the other. Figure 2(d) shows some growth of the martensite shown in (C-2) due to further cooling. Growth of plates that were preferentially enlarged by the initial bending and growth of those in which one set of twins had been widened at the expense of the other set should be expected to give rise to the observed spontaneous strain. Since the observed deformation modes are related to the transformation, it would be expected that the strain associated with these modes would be completely reversed when the martensite reverts by a shear mechanism to the high temperature phase during heating.

*This work was partially supported by the National Science Foundation.

9. ON THE IDENTIFICATION OF ASBESTOS PARTICLES FROM AIR SAMPLES

Krishna Seshan

Asbestos is a well established carcinogen and occurs as an air and water pollutant as isolated fibers about 1 um long and some thousands of angstroms in diameter.[1] Although they are ideally suited for morphological study in the transmission electron microscope (TEM),[2] there is much controversy as to whether they may be identified by electron diffraction data. Specifically Clarke and Rudd[3] have stated that lattice parameter measurements may be made using electron diffraction patterns whereas Skikne et al.[4] have reported that such diffraction data is unusable for simple fibres as their diffraction patterns are insensitive to tilts.

We have confirmed the observation of Skikne et al. and proposed a model to explain their results.[5] Further Skikne et al. have reported the occurrence of special periodicities in their diffraction patterns. It is our hypothesis that their results can be explained by pseudo symmetry present in amphiboles, periodic stacking faults and possibly polytypism. The latter two phenomena have been observed abundantly in other chain silicates such as wallastonite[6] and enstatite.[7]

Therefore we are now studying naturally occurring gunerite and tremolite in order to confirm this hypothesis. This work is a cooperative project with Professor H. B. Wenk of the Department of Geology and Geophysics.

1. J. J. Wessohowskii, R. Stanley, et al., Asbestos in the California Environment, Proc. Symposium on Adv. in Assessment of Health Effects of Environmental Pollution, Witto Conf., June (1974), Paris.
2. K. Seshan, Morphological Identification of Chrysotile Asbestos Fibres, AIHL Rpt. 179 Calif. State Dept. of Health.
3. R. L. Clarke and C. O. Rudd, Micron 5, 83 (1974).
4. M. I. Skikne, J. H. Talbot, R. E. G. Rendall, Env. Research 4, 141 (1971).
5. K. Seshan, On the Insensitivity to Fills of Amphibole Asbestos Fibres, LBL-Rept., (To be submitted to Micron).
6. H. R. Wenk, W. F. Muller, N. A. Liddell, P. P. Phakey, Polytypism in Wallastonite, in Electron Microscopy in Mineralogy, p. 324-31, Springer 1976.
7. S. Jijima, P. R. Buseck, High Reduction Electron Microscopy of Enstatite: Twinning, Psymorphism and Polytypism, Amer. Mineralyst 60, 758-70 (1975).

10. RESEARCH PLANS FOR CALENDAR YEAR 1976

Jack Washburn

Experimental and Theoretical Research on the Climb of Dislocations during Preferential Capture of Interstitial Atoms

This type of dislocation climb is the underlying cause of radiation-induced swelling of metals in the temperature range between one third and one half the absolute temperature of melting. The rates of climb for individual segments of dislocation line are being correlated using direct observation in the 650 kV electron microscope with the following parameters: 1) vacancy-interstitial pair production rate: This can be controlled by the beam current and accelerating voltage of the microscope. 2) Temperature: The experiments are performed on a special callibrated hot stage. 3) Orientation and length of the climbing segment: Climb of dislocation segments near screw orientation are being compared with those near edge orientation. 4) Stacking fault energy: The width of splitting of the dislocations is expected to affect the mechanism by which interstitial atoms are absorbed at the dislocation. 5) Accelerating voltage: The temperature dependence of the displacement threshold energy for production of a vacancy interstitial pair is not well known. Observation on dislocation climb provide a sensitive technique for studying this temperature dependence.

The experimental work is being carried on simultaneously with development of improved models for climb of split dislocations. Computer programs have been developed that make possible

computation of interaction energies for many close by segments of dislocations having any orientation and length.

High Fluence Radiation Induced Swelling Measurements

The swelling produced in stainless steels and special "low swelling" alloys is being measured using the proton beam of a Van de Graaff generator and the step height technique for doses much larger than can be studied by electron microscopy. Measurements have been made up to 500 displacements per atom which corresponds to swelling of more than 200%. Saturation effects are of particular interest for this wrok. On 316 stainless steel we have been able to carry our measurements to higher fluence than any previous work.

Ion Implantation Damage in Silicon

Previous work on characterization of rod and loop defects that form during 700°C to 800°C postimplantation annealing following low dose (2×10^{14} ions/cm^2) ion implantation with boron and phosphorous is being extended to study the nature of the so-called amorphous layer that results from higher doses. An ion implantation facility has recently become available to us on campus that will permit greater flexibility in the design of experiments and control of specimen temperature during implantation. The aim of the research will be an improved model for the recrystallization of amorphous zones and layers.

Solar Cell Research

Due to extremely encouraging results of preliminary experiments on $Zn_yCd_{1-y}S$-Cu_xS heterojunctions it is planned to produce thin mixed crystal layers of $Zn_yCd_{1-y}S$ by epitaxial growth on GaAs single crystal substrates. The aim of the research will be to find the optimum Zn to Cd ratio for solar cells based on this heterojunction and to make an estimate of obtainable efficiences and stability.

Characterization of Spectrally Selective Surface Coatings

Surface coatings that absorb visible light efficiently but absorb, and therefore reradiate long wavelength infrared light very poorly, are desirable for the collection of solar heat in photo-thermal collectors. Some surface coatings having these characteristics are commercially available, such as "black Chrome." We are starting a program aimed at correlating the visible and infrared performance of these surfaces with their microstructure by such means as surface topography, thickness of semiconducting oxide layer, nature of substrate.

11. 1975 PUBLICATIONS AND REPORTS

Jack Washburn and Associates

Journals

1. K. Seshan and J. Washburn, Some New Results in the Characterization of Defects in Phosphorous Ion-Implanted Silicon, Radiation Effects 26, 31 (1975) (LBL-2776).

2. K. W. Yeh, R. S. Muller, W.-K. Wu, and J. Washburn, Characterization of RF Sputtered ZnO Piezoelectric Films Using Transmission Electron Microscope, 33rd Ann. Proc. Electron Microscopy Soc. Amer., Las Vegas, Nevada, 1975, G. W. Bailey (ed.) (LBL-3775).

3. W.-K. Wu and J. Washburn, Boron Precipitates in Ion Implanted Silicon. "33rd Ann. Proc. Electron Microscopy Soc. Amer." Las Vegas, Nevada, 1975, G. W. Bailey (ed.) (LBL-3774).

4. W.-K. Wu and J. Washburn, Direct Observation of Radiation Induced Precipitation in High Voltage Electron Microscope, "33rd Ann. Proc. Electron microscopy Soc. Amer." Las Vegas, Nevada, 1975, G. W. Bailey (ed.) (LBL-3782).

5. H. A. Mohamed and J. Washburn, Mechanism of Solid State Pressure Welding, Welding Journal 54, 302s (1975) (LBL-3511).

Papers Presented

1. K. Seshan, J. Grilhe and J. Washburn, Some Considerations in the Splitting of Interstitial Frank Loops Formed by Irradiation, Intern. Conf. on Fundamental Aspects of Radiation Damage in Metals, Gatlinburg, TN, OCt. 1975.

2. W.-K. Wu, On Distinguishing between Small Vacancy and Interstitial Dislocation Loops using a Non-Conventional Weak Beam Dark Field Technique, 33rd Annual Proc. of the Electron Microscopy Soc. of Amer., Las Vegas, NV, Aug. 1975.

3. T. Kosel and J. Washburn, Climb of Prismatic Loops in Cu-Al Alloys During Irradiation in the HVEM, Intern. Conf. on Fundamental Aspects of Radiation Damage in Metal Gatlinburg, TN, Oct. 1975.

LBL Reports

1. Thomas Herbert Kosel, Irradiation Induced Dislocation Climb in Cu-Al Alloys of Different Stacking Fault Energies, (Ph.D. Thesis) LBL-3590, June 1975.

2. T. M. Peterson, Application of the Rigid-Band Model to the Enhancement/Quenching Effects in Heat-treated Cu_xS/CdS Heterojunctions, Phys. Stat. Sol., LBL-3751, March 1975.

3. Wei-Kuo Wu, Defects in Boron Ion Implanted Silicon, (Ph.D. Thesis), LBL-3758, May 1975.

4. Terry Michael Peterson, An Investigation of the $Cu_xS/Cd_{1-y}Zn_yS$ Heterojunction: A Potentially Low-Cost, High-Efficiency Photovoltaic Energy Converter, (Ph.D. Thesis), LBL-3985, Aug. 1975.

5. J. Grilhé, K. Seshan and J. Washburn, On the Possibility of Nucleating Loops with Burgers Vector ('DC') by the Clustering of Interstitials, Rad. Effects, LBL-3757, May 1975.

6. Krishna Seshan, Electron Microscopy Studies of Ion Implanted Silicon, (Ph. D. Thesis), LBL-2728, Nov. 1975.

7. Barry Lee Chin, An Investigation of the Cu_xS/Si Photovoltaic Cell, (M.S. Thesis), LBL-4553, Dec. 1975.

3. PHYSICAL PROPERTIES

a. High Field Superconductivity

Milton R. Pickus, Principal Investigator

1. SUPERCONDUCTIVE WIRES MADE BY THE INFILTRATION PROCESS

Kanithi Hemachalam and Milton R. Pickus

The infiltration process originally developed for producing a superconducting tape has been successfully adapted for the fabrication of multifilamentary wire. The wire process, which begins with isostatically compacting niobium powder, is shown schematically in Fig. 1. A comparison of the overall critical current density as a function of transverse magnetic field between this new wire (called MMRD wire for convenient reference) and commercial bronze-process wire is shown in Fig. 2. Both wires were tested under identical pulsed pulsed field conditions.

The MMRD wire with its monel cladding has a diameter of 0.013 in. It is a single core wire with a core diameter of 0.009 in. The size of the Nb_3Sn filaments varies from 1 to 2 μm. The wire, which has a critical temperature of 18.1°K, was reacted for 1 minute at 930°C.

The commercial bronze-process wire, which has a diameter of 0.012 in and contains more than 1000 cores, was made by repetitive wire bundling and mechanical deformation. It required a reaction time of 70 hours at 700°C. The Nb_3Sn layer thickness is 2 μm.

Bending tests performed on both wires indicate that MMRD wire suffers less degradation of current-carrying capacity for a given diameter bend. The bronze-process wire showed a 20% degradation after a 2.5 cm diameter bend. To produce the same degradation, MMRD wire had to be bent to a diameter of 1.5 cm.

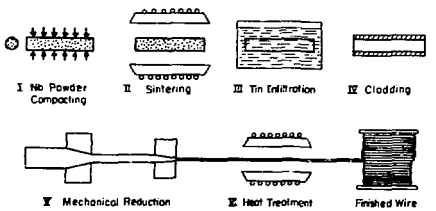

Fig. 1. Infiltration process for the fabrication of multifilamentary superconducting wire. (XBL 7510-7537)

It should be noted that the material represented by curve B of Fig. 2 has been intensively studied and optimized by many research groups, both in the United States and abroad. The new wire, on the other hand, which was produced by a comparatively simple and time-saving procedure, has not yet been fully optimized. By doping with zirconium and optimizing the cladding to core ratio, further improvements in current-carrying capacity are expected.

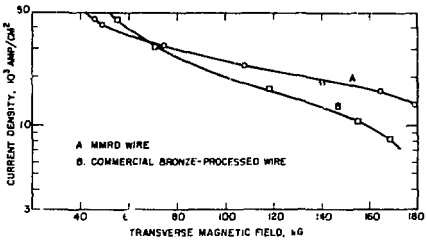

Fig. 2. Dependence of the overall critical current density on the magnetic field. (XBL 7511-9428)

2. PRELIMINARY STUDIES OF A NEW APPROACH TO HIGH FIELD SUPERCONDUCTORS BASED ON Nb_3Al

Robert Ciardella and Milton R. Pickus

There is at present no technologically satisfactory method for producing a superconducting wire or tape based on the A-15 compound, Nb_3Al. After an intensive study of the niobium-aluminum binary system, it was decided to investigate an approach based on the high temperature solid solubility of aluminum in niobium. According to the phase diagram shown in Fig. 1, this solubility increases with temperature to a maximum of about 23 at% at a temperature of approximately 1950°C. It may also be seen that at low temperatures the stable form for this composition is the desired A-15 compound. With these considerations in mind a new method of processing was devised which is shown schematically in Fig. 2.

The advantage of this method lies in its yielding an A-15 phase produced at temperatures less than 1000°C. This feature is of cardinal importance for current-carrying capacity. The A-15 phase has been characterized by x-ray diffraction, electron beam microprobe, metallography and critical temperature measurements. The T_c onset is 17.6°K. The current-carrying capacity has not yet been measured. However, it is expected to be quite high since the A-15 phase was formed at a low temperature. At the present stage of development, using high pressure helium as the quenching medium, the composition of the metastable

solid solution is limited to about 21 at% aluminum. This accounts for the T_c value being about 1°K lower than that of bulk samples. Even so, the value of T_c obtained is approximately 2°K higher than has thus far been reported for Nb_3Al made by other low temperature procedures.

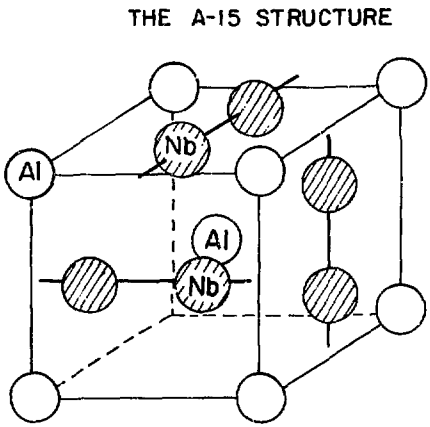

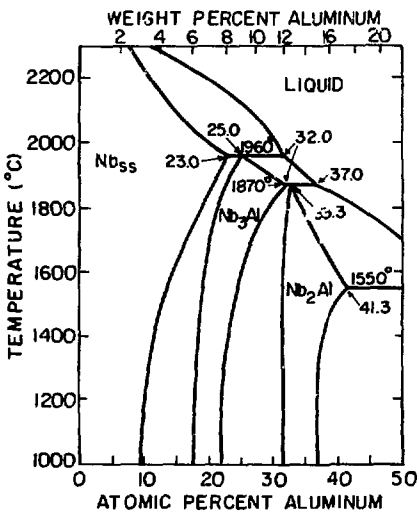

Fig. 1. Niobium-aluminum phase diagram.
(XBL 7511-7575)

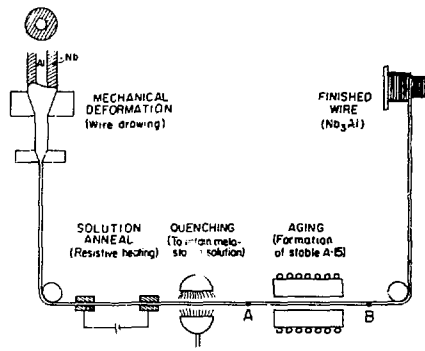

Fig. 2. Schematic diagram for the fabrication of Nb_3Al wire by the quench-anneal process.
(XBL 7511-7572)

3. DENSIFICATION STUDY OF A-15 COMPOUND POWDER

Dilip P. Modi and Milton R. Pickus

The objective of this investigation is to generate basic information on the response to heat and pressure of compacts made from A-15 compound powder, so that an assessment can be made of the feasibility of using such powders in the fabrication of practical superconductors. The compound $Nb_3(Al_{0.75}Ge_{0.25})$ was selected to initiate this study for two reasons: (1) it has better superconducting properties than any known A-15, with the exception of the metastable compound, Nb_3Ge; and (2) no technologically satisfactory method has yet been developed to produce superconducting tape or wire based on this compound.

The first part of the study involved the application of pressure and heat sequentially. The powder was prepared by pulverizing arc melted buttons. Small cylinders were isostatically compacted at a pressure of 60,000 psi and then sintered for one hour in a helium atmosphere at temperatures of 950°, 1150°, 1350°, and 1550°C. No densification occurred over the temperature range covered.

An attempt was then made to activate the densification process by the introduction of additives. Of those tried, copper was by far the most effective. Even with copper, however, it was not possible to achieve densities greater than 80% of theoretical.

Work is now in progress on applying heat and pressure simultaneously rather than sequentially. Densities of 95% of theoretical have already been achieved, without the use of additives. A

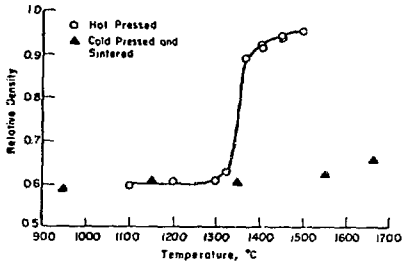

Fig. 1. Relative density as a function of temperature for compacts of Nb-Al-Ge A-15 powder. (XBL 7512-9464)

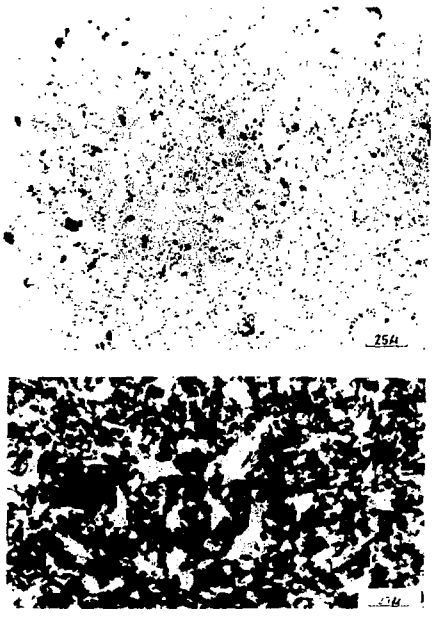

Fig. 2. Photomicrographs of densified compacts of Nb-Al-Ge A-15 powder. Upper: hot pressed at 1450°C. Lower: cold pressed and sintered at 1550°C. (XBB 7512-9219A)

comparison between the relative densities achieved by hot pressing and by cold pressing and sintering is shown in Fig. 1. Photomicrographs of samples cold pressed and sintered at 1550°C and hot pressed at 1450°C are shown in Fig. 2.

4. FORMATION OF THE Nb-Al-Ge A-15 COMPOUND BY REACTING THE ELEMENTAL COMPONENTS IN A SPECIAL CONFIGURATION

José J. Granda and Milton R. Pickus

This work involves another approach to generate data on the niobium-aluminum-germanium system that could be used to design a process for fabricating a superconducting wire. Niobium tubes were filled with a mixture of aluminum and germanium powders blended in a proportion corresponding to $Al_{0.75}Ge_{0.25}$. Form rolling was employed to consolidate the powder core. The composites were then reacted for various times over a range of temperatures to determine whether and in what manner the A-15 phase would form. In these preliminary studies, phase identification was based on the characteristic colors imparted by anodizing. It was found that both the morphology and the volume fraction of the phases formed varied markedly in the temperature range 1600°-

Fig. 1. Section through sample reacted for 4 minutes at 1800°C. Part of the niobium tube may be seen at the left. The A-15 phase occurs at the interface and as islands within the core. (XBB 7512-9145)

1800°C. The maximum amount of A-15 phase observed thus far was in a sample that was reacted for four minutes at 1800°C and then quenched. The microstructure is shown in Fig. 7. A critical temperature of 18°K was observed for this sample by inductive measurements. Optimization of thermal treatments is expected to raise this value substantially.

5. RESEARCH PLANS FOR CALENDAR YEAR 1976

Milton R. Pickus

Present results obtained with single core, multifilamentary wire produced by the infiltration process are very encouraging. We plan first to fully optimize the procedure, and then to characterize the wire as completely as possible so that a realistic assessment can be made of its potential value as a practical superconductor. The program will include doping with zirconium. This is expected to increase the current-carrying capacity of the wire substantially. Also planned is an extensive investigation of its mechanical behavior. Additionally, the ac losses characteristic of this type of wire will be determined by magnetization tests.

In regard to the new procedure we have developed for forming the A-15 phase of the niobium-aluminum system at temperatures below 1000°C, the first priority will be critical current density measurements. The data will be used to determine the optimum aging temperature. Preliminary experiments have shown that extensive twinning occurs in the mechanically deformed metastable solid solution, and that the twins are very effective nucleation sites for the formation of the A-15 phase. It is planned to determine whether these effects could be used to obtain a filamentary morphology without having to resort to the bundling of single core wires. We intend, also, to explore the possibility of using a more effective quench to increase the amount of aluminum retained in the metastable solid solution.

In the niobium-aluminum-germanium system, we believe that we have succeeded in synthesizing the A-15 compound by a diffusion reaction between a niobium sheath and an aluminum-germanium core. We plan to study the kinetics of formation of the various diffusion layers so that the growth rate of the A-15 phase can be optimized. The results of these studies will be used in designing a process for producing a multifilamentary $Nb_3(Al,Ge)$ superconductor.

In an alternative approach using precompounded $Nb_3(Al,Ge)$ powder, we have established that cold pressing followed by sintering is ineffective for achieving significant densification. Preliminary experiments with hot pressing on the other hand have resulted in densities approximately 95% of theoretical. Since we are interested in achieving maximum densities at the lowest possible temperature, we plan to continue these studies using hot isostatic compaction. With this procedure we should be able to use pressures at least an order of magnitude greater than is possible with hot pressing.

6. 1975 PUBLICATIONS AND REPORTS

Milton R. Pickus and Associates

Journal

1. K. Hemachalam and M. R. Pickus, Powder Approach for Multifilamentary Niobium-Tin Superconducting Wire, Appl. Phys. Lett. 27, 570 (1975).

LBL Reports

1. K. Hemachalam and M. R. Pickus, Niobium-Tin Superconducting Wire by the Infiltration Process, (submitted to J. Less Common Metals) LBL-4532, 1975.

2. Robert L. Ciardella, Design Parameters for Processing Flexible Nb_3Al High Field Superconducting Wires and Tape (M.S. Thesis) LBL-4174, 1975.

3. K. Hemachalam, Filamentary Niobium-Tin Superconductors Fabricated by Powder Metallurgy Approach, (D. Eng. Thesis) LBL-4181, 1975.

b. Microstructure and Mechanical Behavior of Ceramic Materials: Glass- and Ceramic-Metal Systems

Joseph A. Pask, Principal Investigator

A major objective of the research program deals with correlations of character (with emphasis on microstructures and nature of grain boundaries) with mechanical behavior and corrosion resistance at high temperatures, and with determining the factors that play a role in obtaining a ceramic material with a designed character. It involves studies on the mechanisms responsible for the mechanical behavior of single crystals, and on the application of such knowledge to the understanding of the behavior of polycrystalline ceramic materials. It also involves studies on the kinetics and mechanisms of solid state reactions, sintering, and distribution of phases in a multiphase system.

The compositions under study--mullite, alumina, forsterite, spinel, magnesia--are basic materials of industrial ceramics and refractories, and sintering is the basic method for their manufacture. The fundamental approach in these studies in terms of physical chemistry, solid state chemistry, and dislocation theory also makes the work relevant in that the determined principales should be applicable to other polycrystalline metal and ceramic materials, and composites.

A second objective of this program is concerned with structural, thermodynamic, and electrochemical studies of glass-metal and ceramic-metal systems. It involves studies related to wetting, bonding, and the nature of the interfaces between dissimilar phases; to the thermodynamics and kinetics of chemical reactions at such interfaces; and to the kinetics and mechanisms of dissolution and diffusion in glasses. A basic understanding of the nature of interfaces and the mechanisms of reactions at interfaces is critical in all materials.

1. STABLE AND METASTABLE EQUILIBRIA IN THE SYSTEM SiO_2-Al_2O_3*

İlhan A. Aksay† *and Joseph A. Pask*

Concentration profiles of Al_2O_3 in diffusion couples made from sapphire and fused silica were used to determine the stable equilibrium phase diagram of the system SiO_2-Al_2O_3 (Fig. 1). The intermediate compound mullite, $3Al_2O_3 \cdot 2SiO_2$, melts incongruently at 1828° ± 10°C; its stable solid-solution region ranges from 70.5 to 74.0 wt% Al_2O_3 below 1753°C and from 71.6 to 74.0 wt% at 1813°C. The microstructures of diffusion zones and heat-treated specimens also indicate the incongruency of mullite. Additional information is given for 3 metastable systems: SiO_2-Al_2O_3 in the absence of mullite, SiO_2—"ordered"-mullite in the absence of alumina, and SiO_2—"disordered"-mullite in the absence of alumina. Under metastable conditions, ordered mullite melts congruently at ~ 1880°C and its solid-solution range extends up to ~ 77 wt% Al_2O_3. The solid-solution range of disordered mullite extends to ~ 83 wt% Al_2O_3

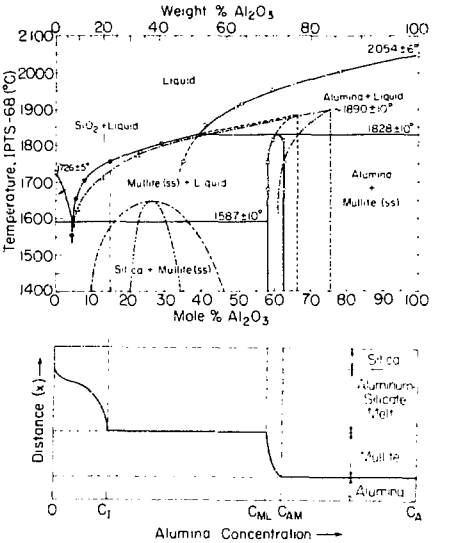

Fig. 1. Stable SiO_2-Al_2O_3 equilibrium phase diagram is shown by solid lines at top. Superimposed on stable equilibrium diagram are possible metastable phase diagrams for SiO_2-"ordered"-mullite and SiO_2-"disordered"-mullite systems. Immiscibility region is from Ref. 2 of Item 3. This feature is discussed in Item 3. Relation between concentration profile of a semi-infinite fused silica-Al_2O_3 diffusion couple and stable phase equilibrium diagram is drawn for 1753°C at bottom; C_A corresponds to 100% Al_2O_3. (XBL 7410-7523)

with an estimated congruent melting temperature of ~ 1900°C. The existence of metastable systems is associated with superheating of mullite above the incongruent melting temperature and with nucleation of alumina and mullite in supercooled aluminum-silicate liquids.

The SiO_2-Al_2O_3 binary system is of prime importance in ceramic technology because of the widespread use of these components in ceramic porcelains and insulators, refractories, and glass-ceramics.

---

*Abstract from J. Am. Ceram. Soc. 58 [11-12], 507-512 (1975).

†Present address: Department of Metallurgical Engineering, Middle East Technical University, Ankara, Turkey.

2. EFFECTS OF CaO ADDITIONS ON MULLITE PHASE EQUILIBRIA, SOLID SOLUTION AND GROWTH RATES

Victor F. Draper and Joseph A. Pask

In view of the recent revision of the Al_2O_3-SiO_2 stable phase diagram[1] (also, see Item 1), the question arises as to the true location of the mullite-corundum ($3Al_2O_3$·$2SiO_2$-Al_2O_3) phase boundary in the Al_2O_3-CaO-SiO_2 ternary system. The currently accepted boundary[2] was based on an earlier revision of the Al_2O_3-SiO_2 system.[3]

Aksay and Pask[1] have predicted a number of metastable phase diagrams within the Al_2O_3-SiO_2 system. Failure to take this metastability into account has led to misinterpretations of the location of the mullite-corundum boundary. They also showed that the stable mullite solid solution range could only be realized when mullite was grown by solid state reaction in the presence of alumina. This was accomplished using a diffusion couple technique between end components of fused silica and single crystal sapphire.

This diffusion couple technique is being utilized to yield information on the position of the mullite-corundum stable phase boundary in the Al_2O_3-CaO-SiO_2 ternary system. A number of compositions in the ternary system have been prepared for reaction with single crystal sapphire. Analyses of the experiments should yield the following information:

1) position of mullite-corundum stable phase boundary
2) temperature slope of the boundary
3) solid solution range of mullite in the presence of CaO

Additional experiments are being conducted to determine the extent of the metastable mullite (nominally $2Al_2O_3$·SiO_2) solid solution range in the binary Al_2O_3-SiO_2 system and in the ternary Al_2O_3-CaO-SiO_2 system and to determine the effect of CaO on the diffusional growth of mullite.

---

1. I. A. Aksay and J. A. Pask, J. Am. Cer. Soc. 58, [11-12] 507-512 (1975).
2. Phase Diagrams for Ceramists, Fig. 630, (1964). Publ: Am. Cer. Soc.
3. S. Aramaki and R. Roy, J. Am. Cer. Soc. 45, [5] 229 (1962).

3. METASTABILITY AND CRYSTALLIZATION IN THE SiO_2-Al_2O_3 SYSTEM

Subhash H. Risbud and Joseph A. Pask

The crystallization behavior and microstructure of glass-ceramic compositions can be significantly affected by prior liquid phase separation occurring either during cooling of the melt or reheating of the glass. Awareness of regions on the phase diagram that exhibit stable or metastable (subliquidus) immiscibility and their relation to the microstructure of crystallized melts and glasses is thus of value. The existence of immiscibility in the SiO_2-Al_2O_3 binary system[1] is therefore of great interest.

Experimental data presented by MacDowell and Beall[2] suggests the existence of phase separated structures in compositions between 7 and 55 mole alumina at a temperature of 1100°C with a consolute temperature of 1650°C. The metastable miscibility gap proposed by these authors has been questioned in phase equilibria studies by Aksay and Pask[1] and by observations on rapidly cooled glasses by Takamori and Roy.[3] Experimental difficulties in delineating immiscibility regions in the SiO_2-Al_2O_3 system include problems associated with quenching from high temperatures (about 2000°C) and the tendency of compositions greater than about 30 mole% alumina to crystallize readily. In view of these difficulties, a model based on regular solution thermodynamics has been used in this work along with the phase diagram data to estimate liquid-liquid immiscibility. The relationship of the calculated miscibility gaps to the microstructure of crystallized melts and glasses is then examined by experimental studies.

Thermodynamic data on activities, activity coefficients, and free energies of mixing were obtained for stable and metastable binary phase diagrams between silica, alumina, and mullite.[1] The procedures used required a knowledge of the heat of fusion and the position of the liquidus curve of the component under consideration. Such data for silica and alumina have been reported but the heat of fusion of mullite was not available. An estimate of the heat of fusion of mullite was made based on the principle that at a fixed composition the activity values of silica calculated from the silica and mullite liquidi should be the same. A heat of fusion of ~ 27,000 cals/mole for mullite was obtained by this estimation and used for the calculation of the thermodynamic data. The regions of immiscibility and spinodal curves resulting from the computations are shown in Fig. 1.

The calculated miscibility gap under the mullite liquidus extends from ~ 10 mole% to ~ 52 mole% alumina at a temperature of 1100°C. These limits closely match the compositions observed to be phase separated by MacDowell and Beall.[2] A representative composition within the immiscibility gap (~ 15 mole% Al_2O_3) was observed in the present study by direct transmission electron microscopy after quenching from above the liquidus. The resulting microstructure shows glass-in-glass phase separation (Fig. 2). The temperature of the consolute point calculated by the present approach, however, is ~ 1540°C. One of the limitations of the model used in this study[4] is that a narrower gap is predicted than is experimentally observed. The consolute temperature is, however, fairly accurately predicted. The calculations thus agree with the compositions suggested by MacDowell and Beall[2] but suggest that the consolute temperature should be ~ 1540°C.

A miscibility gap was calculated to be present under the alumina liquidus, but it is very difficult to verify experimentally. Its existence is, however, suggested by the considerable super-

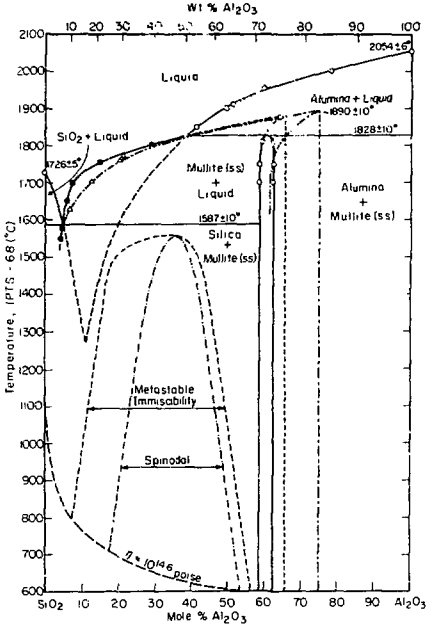

Fig. 1. Calculated miscibility gap is shown superimposed on the phase diagram of the SiO_2-Al_2O_3 system (Ref. 1). This replaces the miscibility gap proposed by Ref. 2 and shown in Fig. 1 of Item 1. (XBL 766-7008)

Fig. 2. Direct transmission electron micrograph of phase separation in an as-quenched 15 mole% alumina-85 mole% silica glass. Scale of phase separated glassy droplets (white) is ~ 350 Å. Diffraction pattern from the droplets shows diffuse halo characteristic of amorphous materials. (XBB 7510-7485)

cooling observed[5] in alumina-rich compositions prepared by laser spin melting. For example, a 73 wt% alumina composition was observed to undercool to a temperature of ~ 800°C before crystallization. This temperature is very close to the boundary of the miscibility gap calculated in the present work. Experimental evidence for immiscibility in alumina-rich compositions should be sought in rapidly cooled glasses between ~ 55 and 80 mole% alumina, after annealing for long times in the temperature range 600-850°C. In view of the problems in obtaining direct experimental data for locating immiscibility the present estimates may serve as at least a useful first approximation for workers studying phase separated structures and for those testing unusual glass-forming compositions by exotic quenching techniques.

In an attempt to experimentally correlate the calculated immiscibility with microstructural observations, melts of a number of compositions in the silica-alumina system were crystallized under controlled conditions in sealed molybdenum crucibles. The microstructure was affected by the heat treatment given the melt after it was homogenized at 2100°C for 30 to 40 minutes. As illustrated in Fig. 3, holding at temperatures of 1200°C and 1860°C does not cause significant

Fig. 3. Nomarski interference contrast micrographs illustrating the effect of a nucleation step on the microstructure of a 60 wt% alumina melt homogenized at 2100°C. The 1860 and 1200 microstructures are coarse while the 900 microstructure is fine. The latter received an annealing step within the miscibility gap (Fig. 1) prior to holding at 1750°C. (XBB 7510-7487)

variation in the microstructure. A prior nucleation step at 900°C followed by holding at 1750°C results in a finer microstructure. This suggests that a phase separation step which promotes nucleation is effective in developing a fine microstructure. Further work on crystallization behavior in melts and metastable reactions in powdered mixtures of silica and alumina is continuing.

1. I. A. Aksay and J. A. Pask, J. Amer. Cer. Soc. 54, [11-12], 507-512 (1975).
2. J. F. MacDowell and G. H. Beall, ibid, 52 [1], 17-25 (1969).
3. T. Takamori and R. Roy, ibid, 56 [12], 639-644 (1973).
4. R. H. Doremus, Glass Science, pp.57, John Wiley and Sons, New York, (1973).
5. R. A. Happe, Private Communication.

4. STUDIES ON CRYSTALLIZATION OF MULLITE*

Carolyn M. Kramer[†] and Joseph A. Pask

Aluminosilicate alkoxy powders were found to be intimate mixtures with some internal structure that form mullite at temperatures greater than 1200°C. Hot pressing techniques produced dense translucent mullite from amorphous alkoxy mullite powder. A temperature cycle of 1500°C/1/2-hr at 2930 kg/cm² developed 0.1 to 0.2 μm equiaxed mullite grains. Sintering at 1700°C/30-hr increased the grain size by an order of magnitude. The 80 powder that was hot pressed and annealed and the sintered 71.8% Al_2O_3 powder developed acicular grains that were attributed to the presence of a free siliceous phase. Course alkoxy powder granules are precursors to inhomogeneity and pores in the compacts.

The stable and metastable solid solutions of mullite were distinguished by plotting the lattice parameter a° vs wt% alumina. The pretreatments of the alkoxy powders when hot pressed and annealed changed the lattice parameters little compared to the scatter observed for arc fusion samples. Both the metastable and stable mullite had lattice parameters that increased with rising alumina content. Also V_c vs c° or a° indicated a general increase or positive slope. Additional studies are necessary to pinpoint the functional relations of x-ray parameters a° and c° with respect to V_c. Further work on the persistence of metastability in silicate systems and the sensitivity of mullite to heat treatments which change the crystallization of mullite is needed.

*Abstracted from LBL-3908

[†]Present address: Sandia Corp., Livermore, California

5. DETERMINATION OF PHASE DIAGRAMS USING DIFFUSION TECHNIQUES*

Joseph A. Pask and Ilhan A. Aksay

Semi-infinite diffusion couple arrangements between two condensed phases can be readily analyzed with the use of the electron beam microprobe analyzer to determine the composition profiles in the two end phases of the couple arrangement and in any intermediate phases that may grow between the end phases. When the reactions at the interfaces are diffusion controlled, chemical equilibrium exists at each interface and each interfacial composition then corresponds to either a liquidus or a solidus composition. These interfacial compositions, with the aid of microstructural observations, can be used in the construction of the stable and/or metastable equilibrium phase diagrams involving the end phases of the diffusion couple. This technique was applied to the study of phase equilibria in the SiO_2-Al_2O_3 system.

*Abstract from Mass Transport Phenomena in Ceramics, Materials Science Research, Vol. 9, edited by A. R. Cooper and A. H. Heuer, Plenum Publishing Corp., N.Y., 433-444 (1975).

[†]Present address: see Item 1.

6. THERMODYNAMICS AND KINETICS OF SINTERING*

Carl Hoge[†] and Joseph A. Pask

Thermodynamic approaches to sintering have received little theoretical or experimental investigation although a thorough understanding of thermodynamic factors is required to accurately understand and predict sintering phenomena. Since the basic driving force for sintering is the reduction in the total interfacial energy associated with changes in the surface and grain boundary areas of powder compacts, the differential of the free energy, δG, must remain negative for sintering to proceed. If δG becomes equal to zero, sintering ceases and possible endpoint densities less than theoretical will result.

A thermodynamic analysis of solid phase sintering for several geometric assemblages has been performed. In this analysis, the solid-vapor dihedral angle is related to critical ratios of γ_{ss}/γ_{sv} (i.e., grain boundary energy/surface energy) that determine endpoint densities for each packing array. The experimental dihedral angle in a sintering compact is also shown to influence the vacancy concentrations near internal and external interfaces, and to determine the thermodynamic driving force for densification.

Thermodynamic analyses of grain boundary motion indicate that pores pin planar grain boundaries and that a critical grain boundary curvature is necessary for grain boundaries to sweep past pores leaving them isolated and that this curvature is relatively independent of the dihedral angle for most solid phase sintering systems.

In order to compare theory with experiment, the sintering of MgO compacts was investigated. Results indicate that sintering rates are dependent upon the thermodynamic driving force for densification and that possible endpoint densities less than theoretical may be an inherent characteristic of MgO for certain packing arrays.

A thermodynamic analysis was also performed for liquid phase sintering systems forming zero and nonzero solid-liquid dihedral angles. Results indicate that critical ratios of γ_{sl}/γ_{lv} exist which are dependent on the magnitude of the dihedral angle for the system and on the volume fraction of liquid phase.

Additionally, kinetic analyses are performed using numerical integration techniques which enable a more accurate description of liquid phase sintering rates than have previously been discussed. These models are described in terms of particle size differences, in terms of magnitudes of dihedral angles, and in terms of volume of liquid phase in sintering compacts. From these analyses, densification parameters are related to time and to the initial particle sizes. The models are

then discussed in terms of existing experimental data.

*Abstracted from LBL-3116, LBL-3546, and LBL-3563.

†Present address: Bendix Research Labs., Bendix Center, Southfield, Michigan.

7. KINETICS AND MECHANISMS OF SINGLE PHASE SOLID STATE SINTERING*

Boon Wong† and Joseph A. Pask

Sintering kinetic models based on rate controlling mass transport mechanisms, unified macroscopic viscous flow, and microscopic vacancy diffusion concepts were used to develop equations for both the intermediate and final stages of sintering. Experimental sintering studies on both undoped and CaO doped MgO powder compacts in static air and flowing water vapor atmospheres were performed in the temperature range between 1280°C and 1600°C. Corresponding microstructural changes of sintered specimens during sintering were examined with a scanning electron microscope.

Sintering kinetic data obtained were subsequently analyzed in terms of the appropriate proposed models. The rate controlling step for sintering in air was bulk diffusion due to the driving force to eliminate the surface reverse curvature resulting from neck formation. The rate controlling step for sintering in flowing water vapor was grain boundary diffusion due to the maintenance of a small nonequilibrium dihedral angle because of rapid surface diffusion.

*Abstracted from LBL-3957

†Present address: Department of Materials Science and Engineering, Virginia Polytechnic Institute & State University, Blacksburg, Virginia.

8. HIGH TEMPERATURE DEFORMATION OF SINGLE CRYSTAL AND POLYCRYSTALLINE MgO*

Philip C. Dokko and Joseph A. Pask

This investigation was directed toward understanding of the roles of plastic anisotropy, grain boundary and diffusional processes in deformation of MgO at elevated temperatures. Both single crystals (undoped crystals in ⟨100⟩, ⟨110⟩, and ⟨111⟩ orientations and Ni-doped crystals in ⟨100⟩ orientation) and fully dense polycrystals (with grain sizes ranging from 4 to 160 μm) were deformed in compression under stress-strain and creep testing conditions (thus covering strain rates differing by 4 orders of magnitudes) at 1200°C (0.48 T_m) and 1400°C (0.55 T_m). In general, no polycrystals were harder than a ⟨111⟩ crystal, nor softer than a ⟨100⟩ crystal, which represented dislocation glide on the more difficult and the less difficult slip planes, respectively.

Grain size dependence of yield stresses (Fig. 1) indicated that yielding of medium-grained or coarse-grained specimens involved stress concentrations due to pileup of dislocations at grain boundaries. There was, however, evidence of intergranular separation at the yielding stages. The effect of grain boundary nature, per se, was also indicated by the variability of the yield stress for the same grain size as a function of prior heat treatment. On the other hand, yielding of fine-grained specimens (< 15 μm) involved accomodation by dislocation climb.

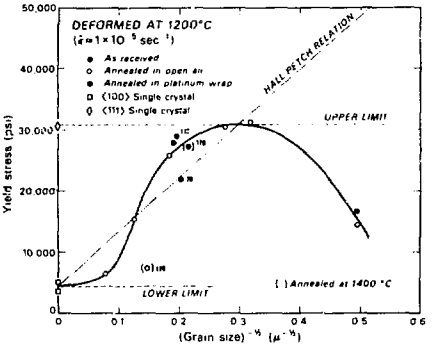

Fig. 1. Grain size-dependence of yield stress (the numbers equal annealing periods in hours).
(XBL 755-4886)

As shown in Fig. 2, fine-grained specimens were more ductile than medium-grained specimens, all of which yielded at the same stress as an ⟨111⟩

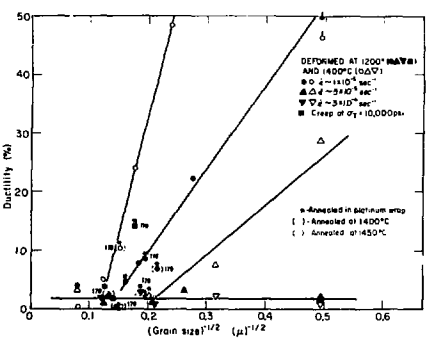

Fig. 2. Ductilities as a function of grain size at different temperatures and strain rates (the numbers equal annealing periods in hours).
(XBL 755-4974 A)

single crystal. Since all five slip systems would have been activated, the failure to realize a large ductility in the latter specimens was attributed primarily to plastic anisotropy. In view of the ability to deform after the loss of transparency, intergranular separation was considered as a mode of accommodation, although it was accompanied by weakening effects.

Steady flow stresses or steady creep rates were essentially independent of grain size as long as a dislocation mechanism was operative. Polycrystals tended to behave like a (111) crystal as temperature was increased and strain rate was decreased. Fine-grained specimens exhibited a strain rate sensitivity and were deformed by the Coble type of diffusional mechanism when crept under low stresses at 1400°C.

*Abstracted from LBL-3979.

9. EFFECT OF PROCESSING ON MICROSTRUCTURE AND MECHANICAL BEHAVIOR OF MgO*

Truett B. Sweeting+ and Joseph A. Pask

Specimens of polycrystalline MgO were fabricated from two powders by hot pressing in graphite or alumina dies, followed by annealing in air, vacuum, or within the graphite die in vacuum. Character parameters affected were density, grain size, and visual appearance which was considered to be dependent on grain boundary structure. Correlations of the character or microstructure of the specimens were made with their mechanical behavior in compression at a constant strain rate at 1200°C. Specimens made from the purer powder showed higher ductility when annealed in air. The formation of a boundary liquid phase with the other type of powder tended to eliminate the effect of the processing variables. All of these specimens had a lower yield stress and less ductility.

*Abstracted from LBL-3700

+Present address: New York State College of Ceramics, Alfred, N.Y.

10. EFFECT OF Cr_2O_3 ON SINTERING AND MECHANICAL BEHAVIOR OF MgO

Nicholas Cassens, Jr. and Joseph A. Pask

With increasing demands for higher temperature refractories to improve efficiencies in modern steelmaking, it becomes very important to understand the effects of additives on the character of refractories and their mechanical behavior. Additions of Cr_2O_3 are used in MgO refractories to improve strength and slag corrosion resistance. However, results are sometimes erratic and improvements are marginal.

Studies have been started to determine the effect of Cr_2O_3 additions on MgO. Two commercially available calcined MgO powders of 99+% and 95% purity will be used. In the fabrication of specimens factors being explored are agglomeration, mixing, pressing, and sintering under reducing and oxidizing atmospheres. Questions of particular concern with respect to the use of Cr_2O_3 are its vaporization during sintering, spinel formation, and solid solution.

11. MICROSTRUCTURE ANALYSIS AND STRESS-STRAIN BEHAVIOR OF A MODEL REFRACTORY SYSTEM MgO-$CaMgSiO_4$*

William E. Snowden+ and Joseph A. Pask

A model system was developed to study the effect of the presence of a boundary phase on the high temperature mechanical behavior of MgO materials. Specimens of polycrystalline MgO containing up to 15% of a silicate phase equivalent to $CaMgSiO_4$ were fabricated by hot pressing or by hot pressing and annealing techniques. Phase diagram analysis and x-ray diffraction indicated the presence of CMS and suggested in addition the presence of an amorphous phase in the boundary material.

The high temperature stress-strain behavior of these specimens was studied in compression over the temperature range 1200-1400°C. Behavior was found to be strongly dependent on the degree of continuity of the boundary phase. At 1200°C the stress-strain behavior was concluded to be controlled by the relatively rigid boundary phase, while at 1400°C deformation was controlled by the boundary phase only when the MgO grain-grain contact area was low.

*Abstracted from J. Am. Ceram. Soc. 58 311-314 (1975), and LBL-3507 Rev. (Partially supported by a Grant-in-Aid from the Refractories Division, Kaiser Aluminum & Chemical Corp., Pleasanton, CA.

+Present address: Corning Glass Works, Corning, N.Y.

12. CREEP BEHAVIOR OF A MODEL REFRACTORY SYSTEM MgO-$CaMgSiO_4$*

William E. Snowden+ and Joseph A. Pask

The high temperature creep behavior of MgO containing ~ 5% CMS and a glassy phase distributed along MgO grain boundaries was studied in the range 1200-1450°C. Although uncertainty in the shear modulus of this composite system precluded comparison of observed strain rates with pre-

dictions of various models as is customary in analysis of creep data, realistic values for the stress exponent n and activation energy Q were obtained. These results indicated a change in the predominant mechanism controlling creep, consistent with microstructure observations of deformed specimens.

At 1200°C deformation was concluded to be controlled by a dislocation mechanism in the MgO framework, with n = 3.6 and Q = 194 kcal/mol. At higher temperatures creep was controlled by viscous deformation of the boundary region, with n ≈ 1; values for Q greater than 200 kcal/mol were measured. An increase in Q with temperature indicated that two or more mechanisms were contributing to creep simultaneously.

*Abstract from LBL-4122.

†Present address: Corning Glass Works, Corning, N.Y.

13. REACTIONS AND WETTING BEHAVIOR IN THE MOLTEN ALUMINUM — FUSED SILICA SYSTEM*

Chisato Marumo† and Joseph A. Pask

The sessile drop technique was used to study the wetting behavior of fused silica by molten aluminum in the temperature range 800°C to 1000°C, and provided the specimens for the reaction studies.

Contact angle between fused silica and molten aluminum decreased down to 90° mainly due to the contribution of the free energy of the reaction

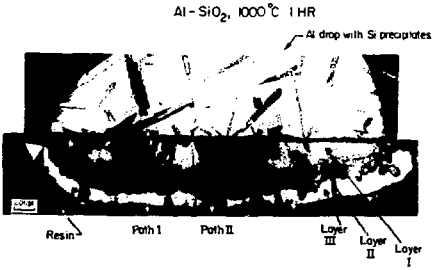

Fig. 1. Appearance at room temperature of cross-section of sessile drop of aluminum on fused silica after heating at 1000°C for 1 hour in vacuum. (XBB 759-6822)

(-)Δg to the solid-liquid interfacial tension γ_{sl} and due to the change of the surface tension γ_{lv} of molten aluminum which dissolves silicon as a result of the reaction. Below 90° the periphery of the drop was in contact with the intermediate reaction layer.

Three reaction layers, I (adjoining the drop), II, III (adjoining SiO_2) were formed. The main reaction layer I-b at 800°C is identical to layer I-a at 900°C; and the thin layer at 800°C is identical to layers II-a and III-a at 900°C. Using an Al drop saturated with Si at 800°C, two reaction layers II-c and III-c were formed; a layer equivalent to I-a and I-b was not present. A cross-section of a specimen heated at 1000°C for 1 hour is shown in Fig. 1.

At the test temperature layer I is assumed to be AlO which is stabilized by forming a solid solution with SiO and Al_2O, and layer III is assumed to form a spinel type structure $(xAlO(1-x)SiO)Al_2O_3$ which is also stabilized by solid solution. Reactions then proceed by counterdiffusion of Al ions and Si ions through the reaction layers. On cooling to room temperature the reaction products dissociate to form crystalline Al_2O_3, Al and Si.

*Abstracted from LBL-4123. Partially supported by a Grant-in-Aid from Kanebo, Ltd., Osaka, Japan.

†Present address: Kanebo Research Center, Kanebo, Ltd., Osaka, Japan.

14. SODIUM BORATE GLASSES AND PLATINUM OR GOLD WETTING AND REACTIONS*

Glenn A. Holmquist and Joseph A. Pask

Sessile drop experiments were conducted to analyze the wetting characteristics of molten B_2O_3 and sodium borate glass on platinum and gold. For both platinum and gold in the absence of carbonaceous gases, the contact angle was small (6 ± 3°) and invarient over the ambient pressure range of 10^{-4} torr to one atmosphere (dry air) at temperatures of 700 to 1000°C. Adsorption of carbon at the metal surface decreased the solid-vapor surface energy and increased the contact angle on platinum to 68 ± 2°, as shown in Fig. 1,

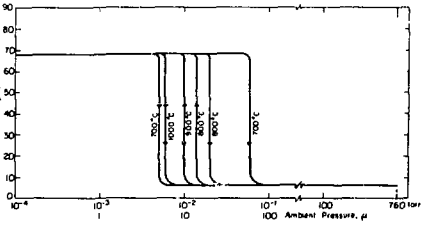

Fig. 1. Contact angle vs ambient air pressure for B_2O_3 glass on platinum at 700°, 800°, 900° and 1000°C. (XBL 754-6192)

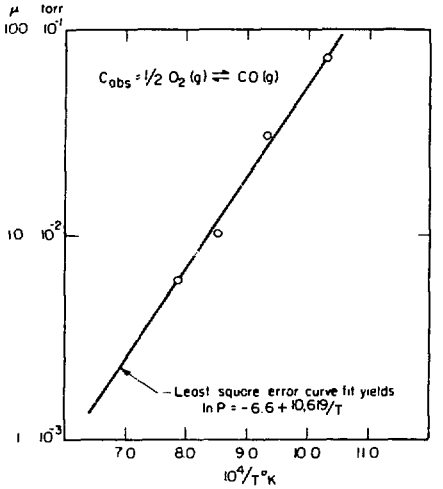

Fig. 2. Critical pressure vs 1/T for data in Fig. 1. (XBL 754-6194)

and on gold to 48 ± 2°. The carbon was removed by oxidation. On increasing the ambient pressure the angle dropped at a sharply defined critical pressure. On decreasing the pressure, a hysteresis effect was noted. The hysteresis is believed to be due to the slow kinetics of carbon adsorption. The temperature dependence of the critical pressure for oxidation of the adsorbed carbon on platinum with increasing pressure is shown in Fig. 2. For gold this data could not be accurately measured.

Controlled atmosphere experiments were conducted in a fused silica tube furnace. For experiments designed for carbon contamination of the platinum cleaned surfaces, the cold traps were not activated, allowing the organic vapor evolved from the vacuum hose coupled with some backstreaming from the diffusion pump to enter the chamber.

When sodium borate glass was equilibrated with moist ambient air and remelted it spread on either substrate. Also, anhydrous molten glass absorbed water and spread on platinum when it was exposed to moist air. Such spreading is the result of the reduction of the interfacial energy due to an interfacial reaction.[1] Development of adherence was associated with spreading. The bonding between the glass and the substrate indicates the development of equilibrium compositions at the interface due to the interfacial reactions.[2] The reaction products are the oxides or hydroxides of the substrate metals formed by reactions with the hydroxyl anions in the glass.

Thermodynamic data for the platinum and gold compounds are not available. Further experimental work is necessary to ascertain which reaction products occur. Whichever the reaction product, the formation of and saturation of the interface with a compound of the substrate is consistent with the theory that the interface has to be saturated with a compound that is mutually soluble in both the metal and the glass.[2] It is postulated that this requirement for equilibrium compositions at the interface has been realized because of the low solubilities of platinum and gold compounds in the glasses.

---

*Abstracted from LBL-3905 and LBL-3967. Partially supported by a Grant-in-Aid from Corning Glass Co., Corning, N.Y.

1. I. A. Aksay, C. M. Hoge and J. A. Pask, J. Phys. Chem. 78, 1178-1183 (1974).
2. J. A. Pask and R. M. Fulrath, J. Am. Ceram. Soc. 45 [12] 592-596 (1962).

15. RESEARCH PLANS FOR CALENDAR YEAR 1976

Joseph A. Pask

(a) Microstructure Development

The need of low cost refractories for furnaces used in coal gasification and other high temperature processes has regenerated interest in materials containing mullite, nominally with a composition of $3Al_2O_3 \cdot 2SiO_2$. Despite the fact that SiO_2 and Al_2O_3 are the most abundant oxides in the earth's crust, detailed knowledge of the SiO_2-Al_2O_3 system and its compounds is lacking. Design and realization of microstructures requires understanding of nucleation and growth phenomena of mullite and alumina in aluminum silicate melts, and information on solid solution ranges of metastable mullite and on the effect of additions of other oxides on solid solution ranges and growth rates of mullite. Such studies have been undertaken. Developed principles should also be applicable to other systems.

(b) Mechanical Behavior

A class of refractories that are used extensively in high temperature furnaces having basic corrosive conditions are based on magnesia. MgO materials also have other potential industrial applications. Cr_2O_3 additions have been used extensively to improve their properties, but their basic functional behavior is not known. Studies are being undertaken to determine the role that Cr_2O_3 additions to MgO play both in modifying grain boundaries and in affecting mechanical behavior at elevated temperatures.

(c) Refractories for Coal Gasification Processes

This group has received support from the National Science Foundation for a project entitled "Structure, Strength and Corrosive Resistance of Aluminum Silicate Materials". Actual activity was started during the last quarter of 1974. A project objective is to evaluate the capability of mullite and mullite-containing compositions to

potentially resist corrosion and erosion environmental conditions encountered in coal gasification processes. The specific research program is divided into two parts: high temperature mechanical behavior, and corrosion resistance to H_2-containing atmospheres. Single crystal information will be utilized to evaluate behavior of polycrystalline mullite, and mullite compositions or "bodies" containing a second phase consisting of glass or predominately glass. This information will be used to design microstructures with improved properties.

(d) Nature of Interfaces

Interfaces between ceramics (glass or crystalline) and metals are critical in determining the behavior of composites, protective coatings, thin and thick films in electronic devices, and electrical lead-throughs. Studies are being undertaken to aid in the understanding of amorphous semiconductor device behavior. Metal ion diffusion (Al^{3+} and Au^{+}) in the chalcogenide glass series As_2S_3, As_2Se_3, As_2Se_2Te and As_2SeTe_2, and the effect of the variation of the charge of the diffusing ion will be investigated. A factor that will be considered is the interfacial introduction of the diffusing ion into the diffusion media.

16. 1975 PUBLICATIONS AND REPORTS

Joseph A. Pask and Associates

Journals and Books

1. Joseph A. Pask, Ceramic Processing--Characterization of Starting Materials, in Processing, Kinetics and Properties of Electronic and Magnetic Ceramics, U.S. - Japan Seminar in Basic Science of Ceramics, Hakone, Japan, June 23-27, 1975, 229-236 (1975).

2. William E. Snowden and Joseph A. Pask, Microstructure Analysis and Stress-Strain Behavior of a Model Refractory System MgO-$CaMgSiO_4$, J. Am. Ceram. Soc. 58, 311-314, (1975) (LBL-3507 Rev.).

3. Joseph A. Pask and İlhan A. Aksay, Determination of Phase Diagrams Using Diffusion Techniques, in Mass Transport Phenomena in Ceramics, Materials Science Research, Vol. 9., edited by A. R. Cooper, and A. H. Heuer, Plenum Publishing Corp., N.Y., 433-444 (1975) (LBL-2299).

4. İlhan A. Aksay and Joseph A. Pask, Stable and Metastable Equilibria in the SiO_2-Al_2O_3 System, J. Am. Ceram. Soc. 58, 507-512, (1975) (LBL-2747).

Invited Talks

1. Joseph A. Pask, Thermodynamic Aspects of Solid State Sintering, University Conference on Ceramic Science, University of Notre Dame, Notre Dame, Indiana, May 25-28, 1975.

2. Joseph A. Pask, Visiting Professor of Ceramic Engineering, Tokyo Institute of Technology, sponsored by Japan Society for Promotion of Science, June 15-July 12, 1975.

3. Joseph A. Pask, Member, U.S.-Japan Seminar on Basic Science of Ceramics, Hakone, Japan, June 23-27, 1975.

4. Joseph A. Pask, Visiting Scientist, Center of Nuclear Studies at Saclay, French Atomic Energy Commission, October 15-December 12, 1975.

LBL Reports

1. Carl E. Hoge, Thermodynamics and Kinetics of Sintering, (Ph.D. Thesis) LBL-3116, January 1975.

2. Truett B. Sweeting and Joseph A. Pask, Effect of Processing on Microstructure and Mechanical Behavior of Magnesium Oxide, LBL-3700, January 1975.

3. Glenn A. Holmquist, Effect of Ambient Atmosphere on the Wetting of Platinum and Gold by Borate Glass, (M.S. Thesis), LBL-3905, May 1975.

4. Joseph A. Pask and Carl E. Hoge, Thermodynamic Aspects of Solid State Sintering, LBL-3563, June 1975.

5. Carolyn M. Kramer, Experiments on the Crystallization of Mullite, (M.S. Thesis), LBL-3908, June 1975.

6. Boon Wong, Kinetics and Mechanisms of Single Phase Solid State Sintering, (Ph.D. Thesis), LBL-3957, August 1975.

7. William E. Snowden and Joseph A. Pask, Creep Behavior of a Model Refractory System MgO-$CaMgSiO_4$, LBL-4122, August 1975.

8. Chisato Marumo, Reactions and Wetting Behavior in the Molten Aluminum--Fused Silica System, (M.S. Thesis), LBL-4123, August 1975.

9. Carl E. Hoge and Joseph A. Pask, Thermodynamic Considerations of Solid State Sintering, LBL-3546 Rev., September 1975.

10. Glenn A. Holmquist and Joseph A. Pask, Sodium Borate Glasses and Platinum or Gold-Wetting and Reactions, LBL-3967, September 1975.

11. Subhash H. Risbud and Joseph A. Pask, Thermodynamically Estimated Immiscibility in the SiO_2-Al_2O_3 System, LBL-4190, October 1975.

12. Chung P. Dokko, High-Temperature Deformation of MgO, (D. Eng. Thesis), LBL-3979, November 1975.

c. High Temperature Reactions

Alan W. Searcy, Principal Investigator

Introduction. Research by this group is now centered in two related, but independently important, areas of research:

1. The kinetics and thermodynamics of endothermic decomposition reactions, with particular current emphasis on carbonate and sulfate decompositions. These reactions are the principal sources of lime, magnesia, and barium oxide for industry. The reverse of sulfate decompositions can be used to remove sulfur trioxide or sulfur dioxide plus oxygen from combustion products.

2. The chemistry of gas and vapor transport through porous solids. Equilibrated reactive flow, which was predicted and then demonstrated under this program in 1974, has been shown to be a phenomenon of scientific value when physical or chemical properties of individual constituents of complex gas or vapor mixtures are desired. Preliminary evidence suggests that high temperature preferential surface diffusion through porous solids may prove a valuable new means for commercial separation of gases and vapors.

To further these studies, two of our existing pieces of apparatus were modified during 1975 to serve new functions, and a new apparatus was constructed for measurement of static carbon dioxide or sulfur trioxide.

1. THE KINETICS OF VAPORIZATION OF II-VI SEMICONDUCTORS

Alan W. Searcy and David J. Meschi

The II-VI semiconductors are of major interest to the electronic industry and their vaporization kinetics has been the subject of considerable recent study. These solids characteristically vaporize by reactions of the form

$$MY\ (s) \rightarrow M\ (g) + 1/2\ Y_2(g) \qquad (1)$$

where M is zinc or cadmium and Y is oxygen, sulfur, selenium, or telurium. Theoretical analyses of reaction (1) have been made by Somorjai and coworkers, by Hirth, Munir, and coworkers, and by Searcy, Meschi and coworkers, but none of these models has satisfactorily explained all the experimental observations. We have now developed a modification of our earlier model that appears to do so.

The critical feature of the new model is the evaluation of the two chemical components of the reaction in the self-adsorption layer in terms of their activities in the surface. It is shown that for one component the activities in these two regions will be essentially the same during steady state vaporization, while for the other component the activity in the self-adsorption layer will be reduced from the equilibrium value. Recognition that the rate limiting process is desorption of the gaseous products with one of the products at the reduced activity leads to prediction of kinetic behavior in agreement with the known apparent activation entropies and enthalpies, background pressure dependence, and other experimental observations.

2. EQUILIBRATED FLOW OF SODIUM CHLORIDE VAPOR AND OF LITHIUM FLUORIDE VAPOR THROUGH NICKEL POWDER BEDS

Pirooz Mohazzabi and Alan W. Searcy

Weight loss and mass spectrometer measurements have been made of the effect of approximately 2 mm thick layers of nickel powder on the total mass flux and on the molecular compositions of sodium chloride vapor and on lithium fluoride vapor. Diameters of the pores through the bed of lightly sintered powder were estimated to average about 50μ and the porosity was of the order of 50%.

The beds reduced the total mass fluxes of both vapors by a factor of 2×10^{-2}, with an uncertainty factor of about 3. These mass flux reductions are of the order predicted from the porosity on the assumption of Knudson flow, 3×10^{-2}, also with an uncertainty of a factor of 2 or 3.

Mass spectrometer peaks which arise from vapor dimer molecules were reduced in intensity at least an order of magnitude more than were peaks from monomers. From these peak intensities, from the relative cross sections measured under equilibrium conditions, and from the total mass fluxes measured through the barriers, values of $(P_{monomer})^2/(P_{dimer})$ were calculated for the exit vapors. For sodium chloride vapor 2.7×10^{-4} was calculated compared to the accepted equilibrium value 3.9×10^{-4}, and for lithium fluoride 3.4×10^{-5} was calculated compared to the accepted value 2.7×10^{-5}. Equilibrated Knudsen flow, therefore, characterizes both of these halide vapors through the nickel powder beds.

3. SOME EFFECTS OF MULTIPLE BARRIERS ON THE FLOW OF VAPORS

David J. Meschi, Tushar K. Basu and Alan W. Searcy

In investigations of the flow of gases and vapors through porous media it is important to establish whether an orifice in a lid placed in contact with a porous disc satisfactorily defines the area of the disc which is effective in transmitting gases. Results obtained for the effect of alumina barriers on the decomposition of calcite seemed to indicate that an area of the barrier larger than the area of the orifice was transmitting significant fluxes of carbon dioxide.

To study this effect we undertook a series of experiments using sodium chloride, which is known to be an equilibrium source of vapor. Calcium carbonate is not an equilibrium source of carbon dioxide. Previous experiments have shown that NaCl vapors pass through porous alumina by Knudsen flow.[1]

The NaCl was placed in a Knudsen cell that had a 0.2 mm thick porous disc placed immediately below the lid. The disc, of 44% porosity, was similar to those described previously.[1] Runs were made at 1137°K using orifices with diameters of 0.4, 0.6, 1, 3, 4.7, and 10 mm. The quantities vaporized were measured by means of weight loss. Figure 1 shows the flux densities plotted against orifice diameters as open circles. There is a strong dependence of the flux density on orifice diameter, with the smallest orifice showing a value two orders of magnitude greater than the largest.

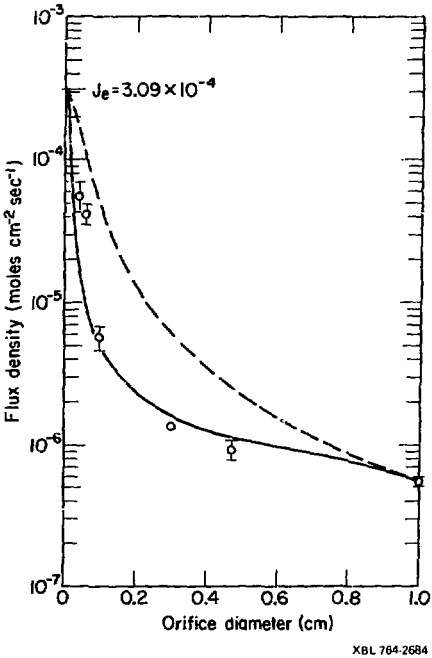

Fig. 1. NaCl flux density as a function of orifice diameter. (XBL 764-2684)

An attempt was made to explain this behavior on the basis of a simple model in which it was assumed that the porous disc divides the cell into two chambers: a lower one consisting of the cell space containing the sample, and an upper chamber formed by the narrow gap between the lid and porous disc. The flux density of the material escaping from the cell would then be given by the following relation:

$$J = \frac{f_d}{f_d + f_o(1-f_d)} \, J_o$$

Here J is the escaping flux density, J_o is the equilibrium flux density in the lower chamber, f_d is the transmission coefficient of the disc, and f_o is the transmission coefficient of the orifice, defined as the ratio of the orifice area to the cross-sectional area of the cell.

The dashed line in Fig. 1 shows the model to be qualitatively correct.

A more realistic model assumes that a pressure gradient exists along the radial direction in the narrow gap between the lid and porous disc. Vapor molecules which pass through the portion of the disc under the lid must diffuse via the gas phase to the orifice in order to escape. Solution of the equation for a gap of 20μ between the lid and disc gives the solid line of Fig. 1. The good agreement with the experimental points supports the thesis that the transport process involves the passage of vapor through the whole of the porous disc; as a consequence, the vapor that escapes directly through the orifice is augmented by vapor that diffuses to the orifice from the region between the lid and the disc.

1. P. Mohazzabi and A. W. Searcy, J. Chem. Phys. 61, 4358 (1974).

4. THE EFFECT OF POROUS BARRIERS ON VAPOR TRANSPORT

Chinhong Chen and Alan W. Searcy

Mohazzabi and Searcy[1] found that the ratio of monomer to dimer molecules in NaCl and LiF vapors can be markedly increased by effusion through porous barriers. The effect of porous barriers is here applied to study the vaporization of cuprous iodide and silver chloride. Cuprous iodide is of interest because appearance potential data[2] suggested the possibility that an unusual molecule, Cu_4I_3, might be a neutral species in the vapor. Silver chloride is of interest because existing data[3] indicated that Ag_3Cl_3 differs from any other known inorganic vapor molecules in having a temperature-dependent mass spectrometer fragmentation pattern.

One Knudsen effusion run and three independent Al_2O_3 porous-barrier runs were made at about 720°C. The first barrier run, showed much higher total fluxes than those found with sodium chloride in similar barriers and showed non-equilibrium among different vapor species. In this run, silver

chloride vapor species did not equilibrate in the aluminum oxide surfaces of the porous solid and the polymers passed through the barrier by surface diffusion more readily than did the monomer. The fact that the ion intensity ratio of $Ag_3Cl_2^+$ to $Ag_3Cl_3^+$ was independent of the change in the ion intensity ratio of the monomer to the trimer indicates that Ag_3Cl_2 is a fragment ion of Ag_3Cl_3; therefore, Ag_3Cl_3 must have a temperature dependent mass spectrometer fragmentation pattern, as was reported earlier.[3]

The second and third barrier runs gave very different results. Although the ion intensities of the monomers are comparable to those found in the first barrier run, none of the polymers was present at detectable levels and mass fluxes were reduced to about 1/40th that in the first run.

These latter results are of a kind expected from previous studies with sodium chloride[1] and lithium fluoride. The extent of surface diffusion must be strongly influenced by changes in surface impurities or by other as yet unidentified system variables. Efforts are being made to reproduce the first run because selective surface diffusion is of considerable theoretical and possibly practical interest.

Effusions of CuI at temperatures of about 450°C from a Knudsen orifice, through a Cu-powder layer, and through an Al_2O_3 porous layer have been successively studied. The ion intensity ratios of monomer to dimer or trimer species are the same for both the Cu powder and the Al_2O_3 even though the total fluxes are reduced by a factor of 200 by the barriers. This result is consistent with the observation[2] that fragmentation of the trimer is the principal source of $Cu_2I_2^+$ and CuI^+ ions.

1. P. Mohazzabi and A. W. Searcy, J. Chem. Phys. 61, 4358 (1974).
2. T. E. Joyce and E. J. Rolinski, J. Phys. Chem. 76, 2310 (1972).
3. L. C. Wagner and R. T. Grimley, J. Phys. Chem. 76, 2819 (1972).

5. THE EFFECT OF PRODUCT GAS PRESSURE ON THE RATE OF DECOMPOSITION REACTIONS

Taghi Darroudi and Alan W. Searcy

It has always been supposed that the net rate of decomposition reactions would decrease linearly with the product gas pressure as the gas pressure increases from zero to the equilibrium dissociation pressure. Searcy and Beruto[1] have shown, however, that the rate limiting step of the decomposition reaction may be one involving the solid reaction product. If such is the case, the net flux may decrease much more rapidly with product gas pressures at low pressures than would be expected from the linear prediction, and be relatively insensitive to product gas pressures near the equilibrium value.

We began in the summer of 1975 to modify and test an apparatus for measurement of decomposition rates under controlled pressure of the product gas. The studies are being conducted in a new system in which weight changes of single crystals or powders can be followed continuously in either a static atmosphere or in an atmosphere maintained at a steady value by a balance of leak and pumping.

At the end of the year the apparatus had been calibrated and tested by obtaining vacuum measurements of decomposition rates for calcite ($CaCO_3$) and barium carbonate; the rates are in good agreement with those obtained previously with other apparatuses. Measurements of barium carbonate decomposition rates in the presence of background CO_2 were found to be obscured by a reaction of carbon dioxide with tantalum in the system. The tantalum is being replaced by tungsten for future studies.

1. A. W. Searcy and D. Beruto, J. Phys. Chem. 80, 425 (1976).

6. THE SOLUTION CHEMISTRY OF SOLID INORGANIC COMPOUNDS

Rama Shukla and Alan W. Searcy

It is known that partial molal thermodynamic properties and transport properties in any binary phase must be functions of composition, but few experimental studies of the functional relations have been reported for solid phases of narrow composition limits. As a result, solid phases with composition ranges that are too narrow to measure by ordinary analytical techniques are usually treated as having chemical properties that are independent of composition. A recent study in our laboratory[1] of gallium sesquisulfide demonstrates that the composition dependence for partial molal properties in phases of narrow composition ranges can differ in unexpected manners from those of familiar solutions.

During 1975 we constructed and completed preliminary tests with an apparatus for measurement of partial pressure variations and rates of partial pressure change in phases of narrow composition ranges. The kinetic measurements will be directed toward determining if the relatively high rates of decomposition which have been reported for early stages of some decomposition reactions may sometimes result from diffusion of the gaseous product from the interior of the reactant phase rather than from surface degassing, as has been supposed. At the end of the year we succeeded in measuring the release and reabsorption of carbon dioxide by calcite.

1. James A. Roberts, Jr. (Ph.D. Thesis) LBL-2507, Feb., 1974.

7. RESEARCH PLANS FOR CALENDAR YEAR 1976

Alan W. Searcy

The effect of background pressures of carbon dioxide gas on the rate of decomposition of barium carbonate will be measured as a function of temperature. Such measurements will later be extended to a second of the carbonates or to one of the sulfates for which we have already measured decomposition rates in vacuum. Similar measurements on calcium carbonate are being made in a collaborative study at the University of Genoa under the direction of Dario Beruto. In that study particular emphasis is being placed on the influence of carbon dioxide pressure on the formation of the metastable form of calcium oxide, which was identified by Beruto and Searcy as a product of vacuum decomposition of calcite. The data from these experimental studies will be compared to a new theory by Searcy and Beruto. The new theory predicts that, depending on the nature of the rate limiting chemical step, some decomposition reactions will have rates which are much more sensitive to product gas pressures than others.

A torsion-Langmuir and supporting torsion effusion study of the kinetics of decomposition of magnesium carbonate in vacuum will be carried out. Existing kinetic data for magnesium carbonate are conflicting, and equilibrium decomposition pressures are somewhat uncertain. The structure, particle size, and porosity of the magnesia produced will be characterized because of their probable importance in affecting the reactivity of the magnesia in later appplications.

An effort will be made to prepare anhydrous aluminum sulfate that has negligible porosity; it will be prepared from its hydrate. We will investigate with the mass spectrometer the fluxes of SO_3 and SO_2 produced by decomposing the anhydrous sulfate in vacuum. The decomposition of aluminum sulfate is theoretically interesting because, under equilibrium conditions SO_3 and SO_2 fluxes should be nearly equal, but work in this laboratory on barium and strontium sulfate decomposition kinetics and especially unpublished studies by Hildenbrand and Cubicciotti at Stanford Research Institute on magnesium sulfate and calcium sulfate imply that SO_2 vaporization from high density pellets of aluminum sulfate may be almost totally surpressed in vacuum. Particular attention will be given to characterizing the aluminum oxide product. Because the decomposition of aluminum sulfate occurs in two steps, both of which occur at relatively low temperatures, the aluminum oxide produced probably is of exceptionally small particle size. It is formed in a metestable, and therefore reactive modification.

Theoretical and experimental studies of the kinetics of transport of gases and vapors through porous barriers will complement the studies of the kinetics of decomposition reactions. A mass spectrometer has been modified to permit studies of the effect of porous barriers on gases and on gas mixtures of known compositions over a much greater temperature range than has previously been studied. Permeabilities will be measured for barriers formed from a variety of materials, eg. alumina, zeolites, nickel metal, and carbons, to gases and vapors that are prototype for substances that would be encountered in coal gasification. In regard to the latter, permeabilities will be measured for aliphatic and aromatic hydrocarbons, sulfur dioxide, hydrogen sulfide, carbon dioxide, and water. It is hoped that selecitve surface diffusion through porous solids will provide a practical means for separating relatively polar molecules such as sulfur dioxide and hydrogen sulfide from less polar and non-polar gas molecules.

The apparatus that has been used for studies of the deflection of gas molecules which have unpaired electrons will be modified, if funds are available, for studies of the non-steady state transport of gases and vapors through porous barriers. Pending this modification, the apparatus is being applied to generating SeS gas from a metal sulfide plus metal selenide reaction in order to measure properties of SeS. This substance has never been observed, but can be shown on theoretical grounds to be the probable carrier of selenium impurities from many metal sulfides when they are decomposed in vacuum.

8. 1975 PUBLICATIONS AND REPORTS

Alan W. Searcy and Associates

Journals

1. Alfred Buchler and David J. Meschi, The Magnetic Moment of Se_2, J. Chem. Phys. 63, 3586 (1975) (LBL-3761).

LBL Reports

1. Pirooz Mohazzabi and A. W. Searcy, The Kinetics and Thermodynamics of Decomposition to Barium Sulfate, LBL-3773, April 1975.

2. Pirooz Mohazzabi and Alan W. Searcy, The Effect of Porous Barriers on the Molecular Composition and Total Flux of a Reactive Gas Mixture, LBL-4120, Aug. 1975.

3. T. K. Basu and A. W. Searcy, The Kinetics and Thermodynamics of Decomposition of Barium Carbonate, LBL-4150, Aug. 1975.

4. Sheldon Chil Pin Lim, The Effect of a Porous Layer on the Kinetics of Decomposition of Calcite (M.S. Thesis) LBL-3578, Jan. 1975.

5. Pirooz Mohazzabi, The Effect of Porous Barriers on the Molecular Compositions of Reactive Gas Mixtures, (Ph.D. Thesis) LBL-3565, Feb. 1975.

d. Relation of Microstructure to Properties in Ceramics

Richard M. Fulrath, Principal Investigator

Introduction. The physical, chemical, and mechanical properties of ceramic materials are determined by the composition and processing of the material. Unlike many metals which can be treated thermally, mechanically or by combinations of both to significantly change their properties, the properties of processed ceramic materials are essentially unchanged by these processes. Therefore, to optimize the properties of existing ceramics and develop new materials for technological systems generated by raw material and energy shortages research related to processing and the relation of processing to properties is essential to the progress of ceramic science.

This research effort is divided into three areas; first, studies of densification of powder compacts (sintering) with and without the presence of a liquid phase using the MMRD-developed capabilities in hot stage scanning electron microscopy. Second, processing studies of important piezoelectric ceramic materials which find many applications in electronic devices, and thirdly, research in the microstructure developed in processing of thick films used for conductors and resistors in electronic circuits. Thick films are a significant user of precious metals.

1. SOLID STATE SINTERING STUDIES

David N. K. Wang and Richard M. Fulrath

Solid state sintering of powder compacts is an important processing step in the production of refractory ceramic materials. Linde-A alumina doped with a small amount of magnesium oxide (0.1 - 0.25% wt) has been one of the most widely used materials in studying solid state sintering kinetics. Coble[1] and Bruch[2] studied MgO doped Al_2O_3 for the later stages of the sintering process. Jorgensen[3] also studied the effect of MgO dopant on the sintering kinetics of Al_2O_3. These previous studies have concentrated on the use of isothermal techniques. A complete analysis of sintering kinetics is unattainable due to uncertainties in the change of density of the compact with temperature and time in the initial heating period. The present work uses a constant heating rate technique to monitor the complete densification kinetics including the change of density and densification rate with temperature and time from the start to the completion of the sintering process.

Powder compacts made by cold pressing submicron Linde-A Al_2O_3 undoped and doped with 0.1 wt% of MgO were used. The compacts having an initial density of 40% of the theoretical density were heated in the hot stage of a scanning electron microscope at various heating rates. The scanning electron fractograph of the green compact taken at different magnifications are shown in Fig. 1. Agglomerates of about 20 μm in diameter resulting from the standard powder processing and forming techniques

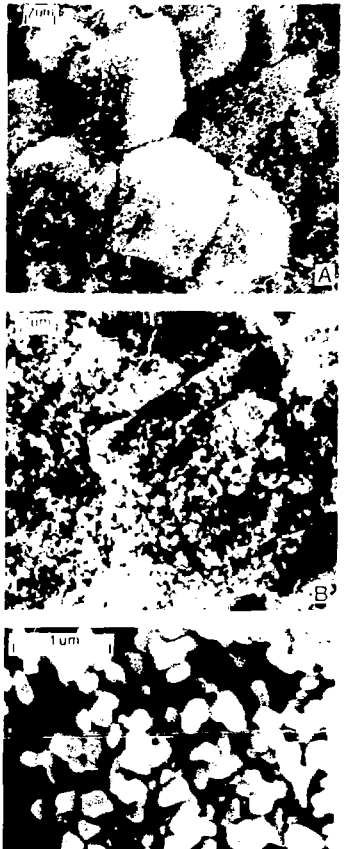

Fig. 1. Scanning electron fractographs of the pre-fired alumina powder compact with an initial density of 40% of the theoretical density at various magnifications. (XBB 7510-7852)

are shown in Fig. 1a. Higher magnifications are shown in Figs. 1b and 1c. Figure 1c shows that in spite of the presence of those large agglomerates in the powder compact there are numerous small clusters formed by several individual particles. These variations in the initial particle packing and the associated complexities commonly present in the powder compact make an oversimplified theory

inapplicable to describe the sintering behavior. Experimental results obtained during last year[4] have shown that the densification rate in accordance with the change of density of the compact during the sintering process can be divided into two parts. In the first part, i.e., below a critical density of about 73%, the densification rate is not a function of density or heating rate but a function of temperature only. In the second part, i.e., from 73% density to nearly theoretical density, the densification rate is not only a function of temperature but also a function of density. It was found that the sintering rate followed an exponential change of temperature with an effective activation energy of 57 kcal/mole. Therefore, the densification rate of the process can be described by the following relationship regardless of the detailed mass transport mechanisms and structural change of the compact:

$$\frac{d\rho}{dt} \propto \exp(-\frac{Q}{RT})\ \rho^m/kT$$

where $d\rho/dt$ and ρ are the densification rate and density at any temperature respectively, Q is the effective activation energy for the sintering process, m is a constant, R is the gas constant, and T is the sintering temperature (°K) at which $d\rho/dt$ and ρ are determined. With the effective activation energy being determined, which is 57 kcal/mole, one is able to obtain the time dependence of the process. This has been done in Fig. 2 by plotting $\ln d\rho/dt/\exp(-Q/RT)$ versus ρ for the results obtained during last year. The curve in this figure is composed of all data points calculated either from the constant rate of heating region or from the following isothermal sintering. Figure 3 shows, in accordance with the change of the porosity of the compact, the sintering process

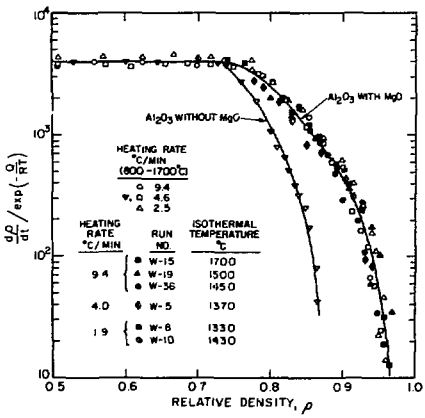

Fig. 2. Plot of $\ln \frac{d\rho}{dt}/\exp(-\frac{Q}{RT})$ versus ρ for both MgO doped and undoped Al_2O_3 computed by using Q equivalent to 57 kcal/mole. (XBL 746-6548A)

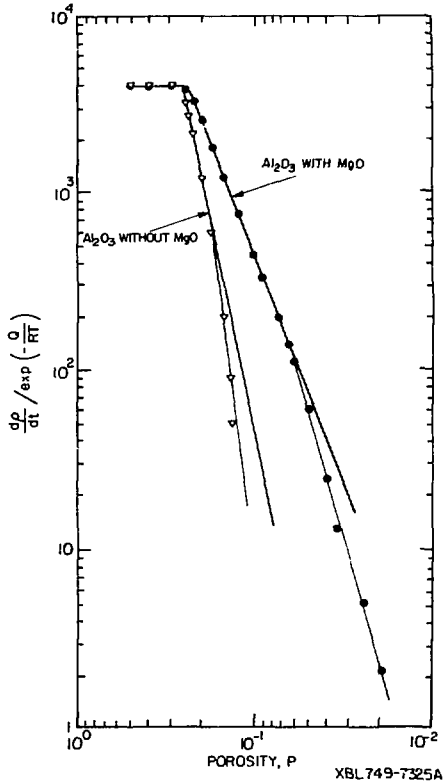

Fig. 3. Plot of $\ln \frac{d\rho}{dt}/\exp(-\frac{Q}{RT})$ versus $\ln p$ for both MgO doped and undoped Al_2O_3. ($p = 1-\rho$) (XBL 749-7325A)

of both MgO doped and undoped Al_2O_3 can be divided into three stages after an initial change of density from 40% to 50% of the theoretical density. Analysis of the data has shown the following empirical equation to be applicable:

$$\frac{1}{p^n} - \frac{1}{p_i^n} = K \exp(-\frac{Q}{RT})(t - t_i)$$

where p is the fractional porosity after sintering, t is the sintering time, p_i and t_i are the porosity and time at the beginning of each of the stages, T is the isothermal sintering temperature, n and K are constants changing with the change of

stage, and Q is the effective activation energy for the process. This equation has been tested by using Coble,[1] Jorgensen[3] and Bruchs'[2] data. A logarithmic plot of those data according to the equation has been made and are shown in Figs. 4-7. Lines with slopes equal to one have been drawn for each set of data. This indicates the time dependence of the sintering process deduced from a nonisothermal study in the present work can precisely describe the behavior of the process at an isothermal sintering temperature.

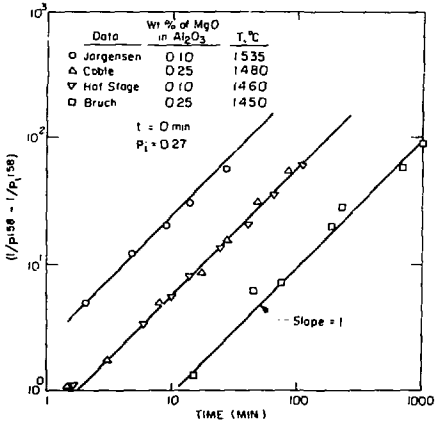

Fig. 4. Densification data by previous investigators for Linde-A alumina with MgO dopant (Refs. 1, 2,3). (XBL 7511-7649)

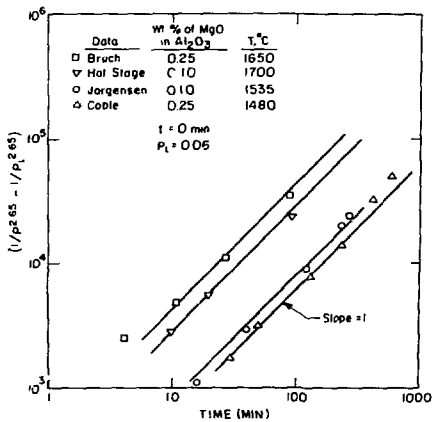

Fig. 5. Densification data by previous investigators for Linde-A alumina with MgO dopant (Refs. 1, 2,3). (XBL 7511-7647)

1. R. L. Coble, J. Appl. Phys. 32(5), 793-99 (1961).
2. C. A. Bruch, Bull. Am. Ceram. Soc. 41(12), 799-806 (1962).
3. P. J. Jorgensen, J. Amer. Ceram. Soc. 48(4) 207-210 (1965).
4. D. N. Wang and R. M. Fulrath, LBL-3530, 203-205 (1974).

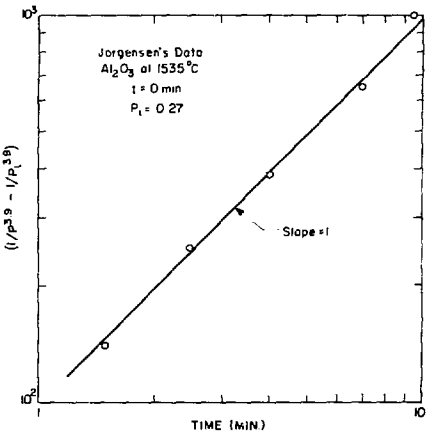

Fig. 6. Densification data by Jorgensen for Linde-A alumina (Ref. 3). (XBL 7511-7648)

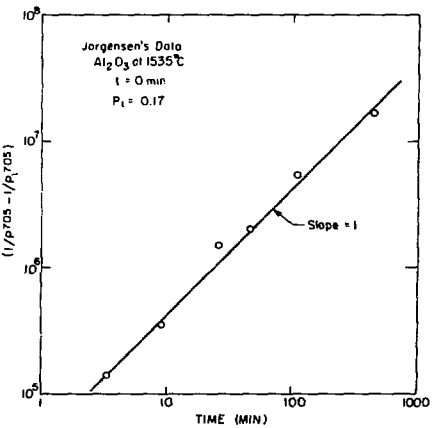

Fig. 7. Densification data by Jorgensen for Linde-A alumina (Ref. 3). (XBL 7511-9400)

2. SINTERING OF URANIUM DIOXIDE BY HOT STAGE SCANNING ELECTRON MICROSCOPY

Daniel J. Miller and Richard M. Fulrath

Uranium dioxide is fuel material in the majority of nuclear power reactors in operation today. UO_2 is incorporated into the reactor in the form of pellets, produced by the densification of powder compacts. The efficiency and stability of these UO_2 pellets in reactor environments is intimately dependent on the microstructure developed during this densification process. A full understanding of the sintering process of uranium dioxide is mandated by these considerations and the economics of optimizing this important processing step.

The hot stage of the scanning electron microscope has proven to be a powerful tool in studying the sintering of alumina.[1] This technique is now being used to study the densification of uranium dioxide powder compacts. The primary objective of this study is to obtain the sintering kinetics from the initial compact density to nearly theoretical density.

Specimens were supplied by the General Electric Company, Vallecitos, California. A submicron uranium dioxide powder, O/U ratio 2.15-2.20, was uniaxially pressed to 50% TD (theoretical density) with no binder. Sintering kinetics of these compacts were correlated to linear shrinkage measurements taken under varied constant heating rates and isothermal heat treatments. Linear shrinkage was measured from the changes in separation distance of Al_2O_3 microspheres on the surface of the compact, constantly monitored using time-lapsed photography.

Figure 1 shows the change in relative density, calculated from linear shrinkage data, as a function of heating rate and temperature. When densification rate is determined from the data of Fig. 1 and plotted as a function of density, an interesting observation can be made as seen in Fig. 2. The densification rates goes through a maximum at approximately the same density of 66% TD independent of heating rate. This observation of a density critical to sintering kinetics has also been observed for Al_2O_3 powder compacts[1] and is further evidence of the necessity of considering microstructure development in the densification process.

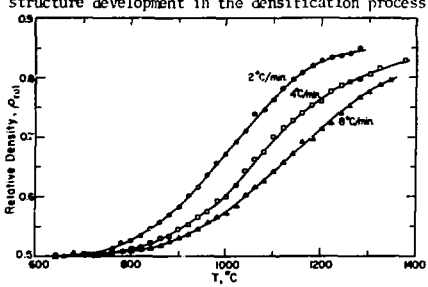

Fig. 1. The relative density changes of UO_2 powder compacts as a function of heating rate and temperature. (XBL 759-7379)

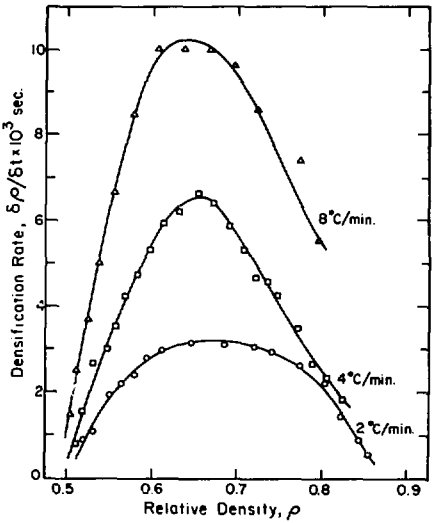

Fig. 2. Densification rate as a function of heating rate and relative density for UO_2 powder compacts. (XBL 759-7380)

A problem encountered in obtaining data to nearly theoretical density under constant heating rate conditions was the evolution of a gaseous uranium bearing species at temperatures above 1300°C. The evolution of this gas, previously reported for non-stoichiometric UO_2 in a similar vacuum environment,[2] resulted in the movement of the alumina microspheres on the surface of the compact. Shrinkage measurements at these higher temperatures, were therefore, not possible. Recent experiments using constant heating rates to 1000°C accompanied by isothermal temperature holds indicates densities near theoretical can be obtained. The effects of deviation from stoichiometry on sintering and densification profiles to nearly theoretical densities will be the next focus of analysis. This data will assist in developing a better theory of sintering of uranium dioxide.

1. D. N. K. Wang and R. M. Fulrath, LBL-3530, p. 203-205 (May 1975).
2. A. T. Chapman and R. E. Meadows, J. Am. Ceram. Soc. 47(12), 614-621 (1964).

3. MICROSTRUCTURE DEVELOPMENT IN CONDUCTING THICK FILMS

V. K. Nagesh and Richard M. Fulrath

Conducting or resistive thick films are conventionally a mixture of a metal or oxide powder com-

bined with powdered glass which when suspended in an organic vehicle can be printed (painting or screen printed) onto a ceramic substrate and subsequently fired to bond the film to the substrate and develop the required electrical properties. Because the firing is usually in an oxidizing atmosphere the conducting films use a precious metal (Ag, Au, Pt, or combinations of these metals with Pd). The film thickness is usually on the order of a few mils[1] which distinguish them from thin films (<1 μm).

Thick film circuits are widely used in hybrid integrated circuits, TV components, computer components, etc., and are a significant user of precious metals because present commercial thick film conductor compositions use about 70 wt% metal in the solids composition. This research was undertaken to provide a better understanding of the microstructure development and the electronic conduction process in thick films with the aim at reducing the precious metal content while still maintaining suitable electrical conduction.

Because the glass component of the conductor system performs two functions in a thick film conductor system, 1) bonding the film to the ceramic substrate, and 2) holding the metallic particles together in the film, it was obvious that the microstructure of the metal-glass system is important in developing a good conductor. The obvious structure for minimum metal content while still retaining electrical conductivity is one in which the metal forms a continuous film around each glass particle.

In view of the above, research was directed to attaining the optimum microstructure by concentrating on the glass phase of a thick film conductor system. A simple glass composition consisting of PbO, B_2O_3, and SiO_2 which matched the thermal expansion of the Al_2O_3 substrate material was used as the base glass. The glass composition was melted then crushed to a particle size fraction between 20 and 44 μm. The glass particles were then mixed with a silver resinate to give the required weight per cent silver metal after decomposition of the metal-organic. Some glass particles were given a prior chemical treatment in HCl before contacting with the silver resinate. In this chemical treatment it was found that the reaction:

$$Pb^{++}(\text{solid soln. in glass}) + 2H^{+}(\text{acid}) \rightarrow$$

$$2H^{+}(\text{solid soln. in glass}) + Pb^{++}(\text{in acid soln.})$$

took place. Subsequent reaction with the silver resinate caused the reaction:

$$H^{+}(\text{solid soln. in glass}) + Ag^{+}(\text{in resinate}) \rightarrow$$

$$Ag^{+}(\text{solid soln. in glass}) + H^{+}(\text{in resinate}).$$

Therefore, this chemical pretreatment placed silver metal ions on the activated glass surface, which on firing should form a continuous interconnected silver metal film around each glass particle and lead to maximum conduction with minimum silver content. Figure 1 shows the microstructure of a thick film with 25 wt% silver - 75 wt% glass formed by using a chemical pretreatment for the glass phase. Figure 2 shows the same system under identical processing conditions but without chemically activating the glass phase. This method of produc-

Fig. 1. Microstructure of a thick film conductor containing 25 wt% Ag fired at 600 C for 8 minutes using an activated glass. (XBB 7510-7537)

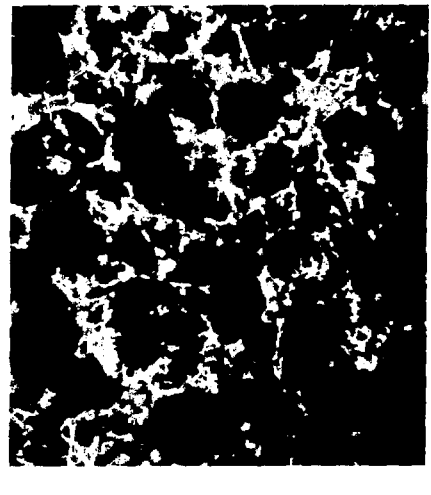

Fig. 2. Microstructure of a thick film conductor identical to Fig. 1 except that a nonactivated glass was used. (XBB 7510-7536)

Table 1. Sheet resistivities of conducting thick films.

Silver metal content (wt%)	Surface treatment (45 sec)	Firing Temp. (°C)	Firing Time (min)	Sheet resistivity (mΩ/□)
40	0.25 N HCl	550	8	44
	0.25 N HCl	575	14	32
30	0.01 N HCl	500	20	80
	0.01 N HCl	500	30	120
	0.01 N HCl	600	8	85
	0.01 N HCl	640	8	70
	0.01 N HCl	700	8	80
25	0.01 N HCl	500	8	160
	0.01 N HCl	600	8	165
	0.01 N HCl	700	8	160
20	0.01 N HCl	500	30	230

ing optimum microstructures was largely developed through previous research in glass to metal bonding conducted in this laboratory.[2]

Typical sheet resistivities developed with this process are given in Table 1. In all systems using the same glass and identical processing techniques except for the surface activation there was no measurable conduction.

1. T. M. Place, Proceedings of the First Thick Film Symposium, ISHM, p.12-19 (1967).
2. J. A. Pask and R. M. Fulrath, J. Am. Ceram. Soc. 45(12), 592 (1962).

4. ELECTRICAL CONDUCTIVITY IN LEAD ZIRCONATE-TITANATE CERAMICS

Jiunn-Jye Dih and Richard M. Fulrath

Lead zirconate-titanate (PZT) is an important ceramic material widely used for piezoelectric devices. Electrical conductivity is an important physical property in piezoelectric applications. Compositions that are too conductive are difficult to pole, tend to overheat in high power applications and have undesirably high dielectric loss. The mechanism of electrical conductivity in PZT has not been clearly defined. The energy band structure of PZT has not been described. The major problem in defining the electrical properties of PZT is the difficulty in controlling the sample composition during sintering. It is well known that PZT loses PbO at high temperature. In this laboratory, a packing powder technique has been developed to control the material loss during firing. The purpose of this study was to determine the actual mechanism of electrical conduction in polycrystalline PZT with better defined composition. The effects of dopents and temperature on electrical conduction behavior have been determined.

In this research, a PZT composition of $Pb(Zr_{0.5}Ti_{0.5})O_3$ was prepared from chemical compounds. The raw materials used for the principle constituents were lead oxide powder, zirconium tetra-butoxide liquid and titanium tetra-butoxide liquid. Scandium oxide and niobium oxide powders were used as dopent materials. It has been established that Nb^{+5} and Sc^{+3} substitute for $(Ti,Zr)^{+4}$ and create lead vacancies and oxygen vacancies respectively. A flow chart outlining the procedure of powder preparation is shown in Fig. 1. After cold pressing, the pellets were sintered at 1200°C for 16 hours. All the pellets were buried deep in a packing powder that would provide a known PbO vapor pressure to control material loss from the sample during sintering. Density of the undoped and niobium doped samples were above 98% theoretical density after firing and that of scandium doped samples achieved 95%. X-ray diffraction of each sample showed typical PZT patterns.

DC bulk resistivity was measured by using a guard ring method. Sputtered gold electrodes were used to ensure intimate contact. The contact resistance was found to be negligible. Most of the measurements were conducted in the temperature range 150-500°C. Thermoelectric power measurements were also performed to determine the type of charge carrier contributing to the conduction process.

The influence of dopents and temperature on the resistivity of PZT is shown in Fig. 2. The resistivity always decreases with increasing temperature and follows the simple theoretical expression for semiconductor behavior; $\rho = \rho_0 \exp(E/RT)$, where ρ is the resistivity, ρ_0 is a constant, E is the activation energy, k is the Boltzmann constant, and T is the absolute temperature. It has been reported that the electrical conduction in $PZ_{0.5}T_{0.5}$ is almost entirely electronic. Measurements of the thermoelectric voltage showed that hole conduction (p-type semiconductor) dominated in all the samples. It suggests that electrical conduction in PZT is due to lead vacancies.

The effect of the intrinsic nonstoichiometric on electric conductivity is shown in Fig. 3. Two samples were sintered in 1 atm oxygen with different packing powders, i.e., PZ + Z and PZT + Z + T. The PbO activity of PZ +Z is higher than that of PZT + Z + T. Therefore, lowering the lead oxide activity, at a fixed oxygen pressure, will increase the lead vacancy concentration. It was found that the resistivity decreased with an increased lead vacancy concentration formed by using a low activity packing powder. Consequently, the electrical conductivity of undoped PZT is due to lead vacancies.

The lead vacancy concentration increases with increasing Nb_2O_5 content in the system. However, the experimental results showed that the conductivity drops while more and more Nb_2O_5 was added. This is explained as a compensation effect. Nb^{+5} ions in the matrix can serve as donors of electrons which can decrease the hole concentration due to the law of mass action. For scandium doped samples, the resistivity drops with increasing amounts of scandium because the Sc^{+3} can act as an electron acceptor and increase the hole concentration. The activation energy which can be correlated with the

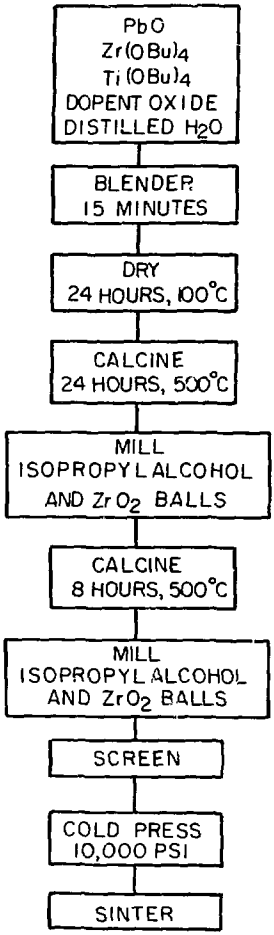

Fig. 1. Sample fabrication flow sheet for chemically prepared PZT samples. (XBL 759-7355)

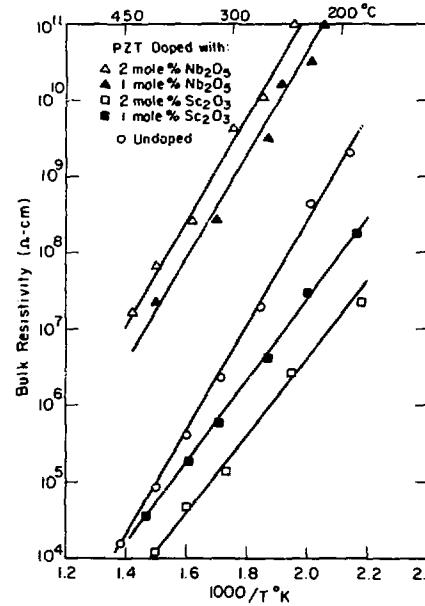

Fig. 2. Resistivity of doped and undoped PZT as a function of temperature. (XBL 759-7360)

ionization energy was plotted against the amount of dopents as shown in Fig. 4. Nb doped and undoped PZT has the same activation energy of 1.41 eV. This indicates that their conduction mechanism is *the same; hole migration associated with lead vacancies.* The activation energy for the scandium doped samples is only 1.1 eV. Therefore, electrical conduction in Sc doped samples cannot be due to lead vacancies. It is probably due to Sc^{+3} ions severing as acceptors and increasing the charge carrier concentration.

The effects of ball milling impurities on the electrical conductivity of PZT were investigated and are shown in Fig. 5. There is a clear difference between the activation energies of the two samples prepared from powders ground by different milling media (alumina balls and zirconia balls). The activation energy is 1.05 eV for the sample using alumina balls as the grinding medium and 1.41 eV for the sample using zirconia balls. It is suggested that an Al^{+3} impurity ion from the milling media goes into solid solution in PZT and acts as an acceptor giving lower bulk resistivity and a lower activation energy similar to Sc^{+3}.

In studying the electrical conductivity of PZT over the temperature range 150~800°C, the activation energy above 650°C was found to be 3.6 eV. It is suggested that at temperatures higher than 650°C, intrinsic conduction prevails in PZT.

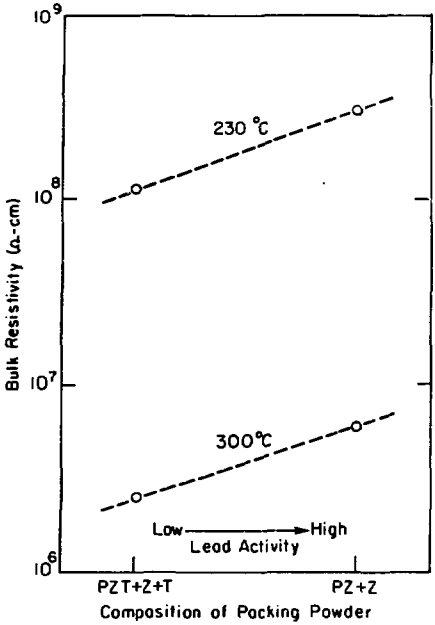

Fig. 3. Dependence of lead activity on the resistivity of PZT. (XBL 7510-7481)

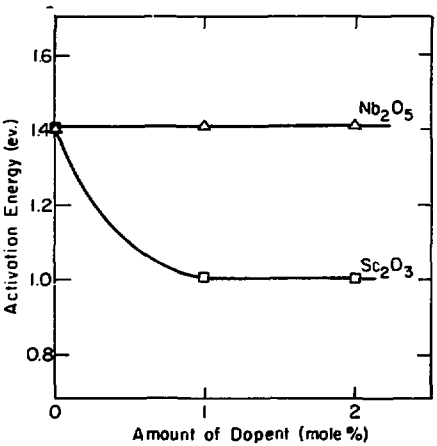

Fig. 4. Dependence of the activation energy for the conduction process on dopent content. (XBL 759-7366)

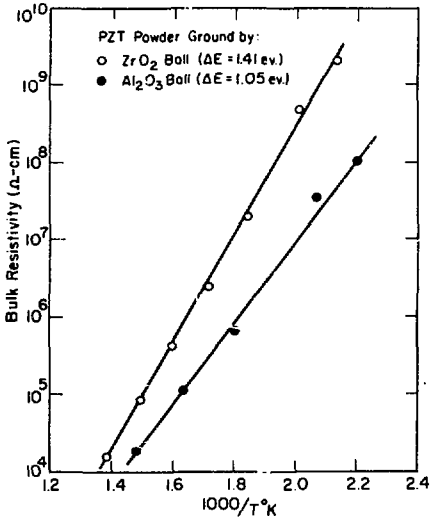

Fig. 5. Effect of ball milling impurities on the electrical resistivity of PZT. (XBL 759-7363)

5. KINETICS OF PEROVSKITE COMPOUND FORMATION IN THE PbO-TiO_2-ZrO_2 SYSTEM

Sudhir S. Chandratreya and Richard M. Fulrath

The literature on PZT ceramics is replete with reports relating the electrical properties of the ceramic to its composition. It is now widely accepted that the processing of the ceramics determines to a significant extent its electrical properties like dielectric constant, dielectric energy loss and the coupling coefficient. Thus the quest for an ideal high permitivity ceramic like PZT reduces to the search of a proper process for manufacture.

One of the first steps involved in the processing of PZT is the synthesis of the compound itself. This is done by heating the reactant oxide powders of PbO, ZrO_2, and TiO_2 to a temperature high enough to yield the perovskite compound. This process is called calcination. Product powder is then ground, compacted, and sintered to obtain a dense ceramic body. Unfortunately, most of the work reported on the properties of PZT has been conducted with little understanding of the calcination process. It has been assumed that calcining temperatures anywhere between 800°C to 1000°C and calcining times from a few minutes to several hours is enough to give uniform fully reacted powder ready for sintering. Robinson and Joyce[1] were the first to report that even at very high temperatures, as much as 3 mole % of the participating oxides may remain unreacted. Robinson and Luff[2] simultaneously reported that

any unreacted PbO and, in particular, ZrO_2 can severely deteriorate the dielectric constant, the coupling coefficient and consequently the energy efficiency of the ceramics. It has been reported that in sintering of PZT, the final density is largely determined by the temperature of the calcination process.[3,4]

Noting that from the point of view of sinterability as well as electrical properties, calcination is an important process step in which the present study was undertaken to characterize the process. For this one must investigate the reactions taking place between various component oxides and devise simple methods of monitoring them. In the current investigations, various techniques like Differential Thermal Analysis (DTA), Dilatometric Expansion and X-ray Analysis were used.

Five compositions were selected from the pseudo-binary phase diagram of $PbTiO_3$-$PbZrO_3$ system. They are as follows:

Composition	Mole % PbO	Mole % TiO_2	Mole % ZrO_2
1	50	17.5	32.5
2	50	25.0	25.0
3	50	32.5	17.5
4	50	50.0	--
5	50	--	50.0

Raw materials used were all of high purity and known crystalline form. They were crushed to the micron size range and were then mixed intimately in the required proportions. The powder mixtures were hydrostatically pressed to 30,000 psi when required by the experiments.

Initially, DTA was conducted using Al_2O_3 as the standard. Results are shown in Fig. 1 for the compositions 2, 4 and 5. It was observed that the mixture of PbO and TiO_2 reacts at 450°C exothermically while the mixture of PbO and ZrO reacts at a much higher temperature of 700°C endothermically. The reaction products on x-ray analysis proved to be $PbTiO_3$ (PT) and $PbZrO_3$ (PZ) respectively. The mixture of PbO, TiO_2 and ZrO_2 shows two peaks similar to those above at the same temperatures. The product was again a mixture of PZ and PZ without any trace of PZT. The same results were obtained for rutile (TiO_2) as for anatase (TiO_2).

For dilatometry, isostatically pressed samples in the shape of cylindrical slugs 1 in. long and 1/4 in. diameter were used. The temperature was raised at various rates (190°C/hr, 260°C/hr, 340°C/hr, and 490°C/hr) while the linear expansion was plotted directly against temperature as shown in Fig. 2. It is seen that the mixture of PbO + TiO_2 starts reacting at 450°C as indicated by the sharp expansion peak. Similarly a mixture of PbO and ZrO_2 has an expansion peak starting at 710°C. The mixture of PbO, TiO_2 and ZrO_2 behaves like two separate mixtures of PbO + TiO_2 and PbO + ZrO_2 were reacting independent of each other, resulting in two peaks. The beginning of both the

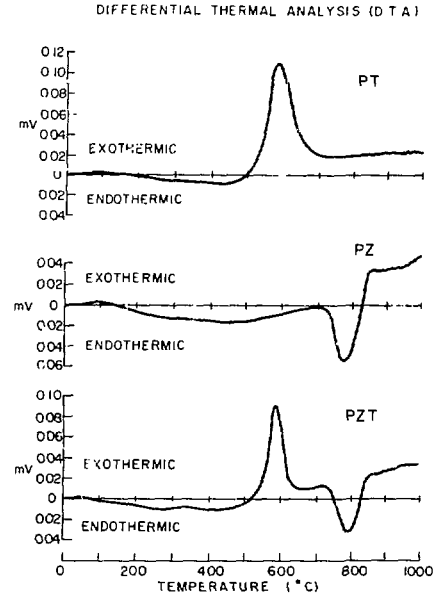

Fig. 1. Differential thermal analysis of mixtures of PbO, TiO_2 and ZrO_2. (XBL 756-6525)

peaks is at the same temperatures as seen in DTA experiments. Results were invariant with change in heating rate or ZrO_2:TiO_2 ratio in the mixtures.

To identify the various phases formed during the course of reaction, samples were taken to various temperatures above reaction-starting-temperature and suddenly quenched. Resulting sample was subjected to x-ray analysis. In the case of the PbO + TiO_2 mixture, only PT was observed above 600°C even at fast heating rate. On the other hand, reaction between PbO and ZrO_2 giving PZ was seen to be incomplete even at temperatures as high as 1000°C with the slowest heating rate. The ternary mixtures show both PT and PZ along with unreacted oxides but no trace of PZT. This finding though directly contradictory to the one reported by Matsuo and Sasaki[5] earlier, is in agreement with the work of Ohno, Takahasi and Tsubouchi.[6]

On the basis of the above experiments it is clear that even at higher temperatures perovskite PZT solid solution may not form. PZ and PT form independently of each other and in totally different temperature ranges. Such partially reacted powder containing PZ and PT but no PZT when used for sintering will give a ceramic body with two phases instead of one. This is because counter-diffusion of Zr^{+4} and Ti^{+4} to give PZT during sintering is expected to be very slow and difficult. A two

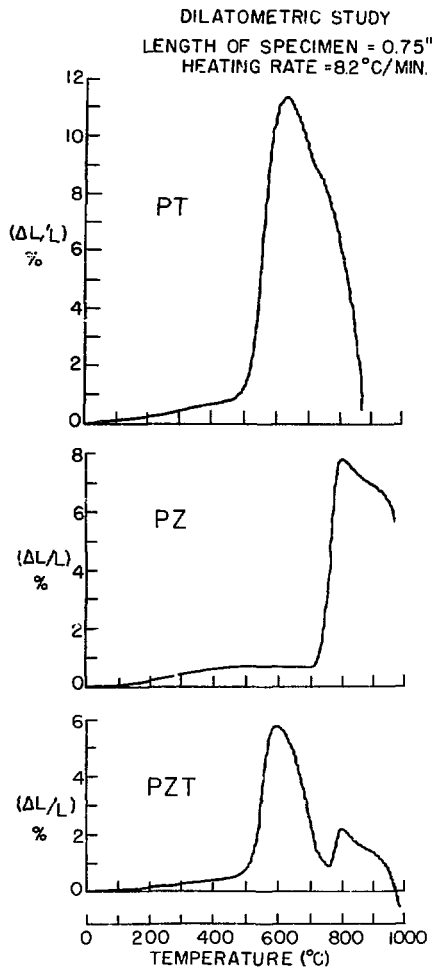

Fig. 2. Dilatometric study of mixtures of PbO, TiO_2 and ZrO_2. (XBL 756-6424)

phase system will result in poor sinterability and electrical properties. Endothermic formation of PZ in contrast to exothermic formation of PT, though chemical properties of ZrO_2 and TiO_2 are similar, is of interest. This could lead to difference in the rate controlling mechanisms operative in PZ and PT formation.

1. A. E. Robinson and T. A. Joyce, Trans. Brit. Ceram. Soc. 61(2), 85-93 (1962).
2. A. E. Robinson and D. Luff, Trans. Brit. Ceram. Soc. 61(2), 94-103 (1962).
3. H. Iwasaki, Jap. J. Appl. Phys. 4(3), 190 (1965).
4. D. A. Buckner and P. D. Wilcox, Bull. Am. Ceram. Soc. 51(3), 218 (1972).
5. Y. Matsuo and H. Sasaki, J. Am. Ceram. Soc. 48, (6), 289 (1965).
6. T. Ohno, M. Takahashi, N. Tsubouchi, J. Jap. Soc. Powder & Powder Met. 20, 154 (1973).

6. FRACTURE STRENGTH OF POROUS POLYCRYSTALLINE CERMAICS

Dipak R. Biswas and Richard M. Fulrath

Most ceramic materials even after firing are left with some amount of porosity. This porosity reduces the mechanical strength considerably and is extremely important in the use of ceramics as structural materials. However, over the past few years, a number of studies[1] have been performed relating the fracture strength with porosity and general relationships are beginning to emerge. In the previous work the effect of size and shape of pores on the fracture strength was not considered. Therefore, an attempt has been made to perform a systematic study of fracture strength of a highly dense, well-characterized polycrystalline ceramic containing controlled amounts of pores of different sizes and shapes.

The material used in this study was lead zirconate-titanate (PZT) ceramic. The samples were fine-grained (2-5μ) polycrystalline ceramics in which the grain size is controlled by doping with one mole percent Nb_2O_5. The advantage of using this material is that specimens are easy to fabricate with good reproducibility and control of grain size from batch to batch. It was found that the addition of 5.5 wt% excess PbO enhances the ease of fabricating this material by sintering, and densities over 99% of the theoretical value can be obtained without difficulty. Spherical and acicular pores were introduced into the specimen using organic materials mixed with the PZT powder prior to sintering.

The composition of the PZT-Nb doped ceramic (PNZT) was $Pb_{0.99}\square_{0.01}(Zr_{0.52}Ti_{0.46}Nb_{0.02})O_3$, where □ is the Pb-vacancy. The raw powders of PbO, ZrO, TiO and Nb O were milled in a vibratory energy mill for 4 hours using isopropyl alcohol as a liquid medium, then dried and calcined at 850°C for 4 hours. The calcined powders were then mixed with 5.5 wt% excess PbO and milled again for 4 hours using isopropyl alcohol and polyvinyl alcohol (as a binder) in water and then air dried. The controlled amount of porosity was introduced by doping with organic powders of controlled size and shape. The proper amount of PNZT-organic powders were cold pressed to 1.5 in. diameter and 0.2 in. thick pellets. They were dried at 250°C for 12

hours to decompose the organic material and finally sintered at 1200°C for 3 hours in a $PbZrO_3$ + ZrO_2 packing powder and at 1 atm. pressure of oxygen in order to prevent PbO loss from the specimen. The distribution of pores and grain sizes is shown in Fig. 1 and Fig. 2. Specimens were cut from the sintered discs using a diamond saw. The nominal dimensions were 0.05 in. thick and 0.2 in. wide. The specimens were tested in a four-point bending machine with a distance between supports of 0.75 in. and a distance between the center loading points of 0.25 in. Actual dimensions varied slightly; exact values were used in calculating the fracture strength.

The effect of spherical and acicular porosity on the fracture strength is shown in Fig. 3. The strength decreases continuously with increase in porosity and then levels off. The grain size was very small compared to the pore size. The strength in the acicular pores, however, does show a rapid decrease with low porosity. This is probably due to the higher stress concentrations for acicular

Fig. 1. Micrograph of controlled porosity in a PNZT matrix, a) 4.65 v/o spherical pores, 60-75μ and, b) 4.65 v/o acicular pores, 110-150μ.
(XBL 7512-9061)

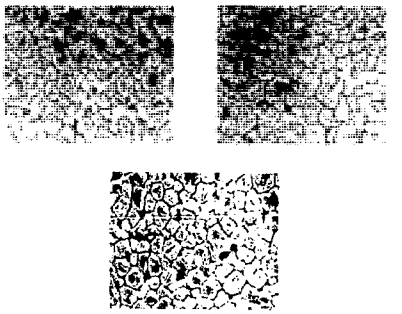

Fig. 2. Micrographs of a typical microstructure showing the distribution of grains.
(XBL 7510-7489)

pores because the aspect ratio gives the pore an effective size larger than that of an equivalent spherical pore.

Considering the effect of stress concentration in general, on the average strength of brittle solids subjected to a tensile stress, it is always less than would be expected from the theoretical stress concentration factor. This observation can be explained qualitatively by noting that the brittle materials contain a distribution of inherent flaws of varying severity. It is quite clear from Fig. 3 that the strength of porous

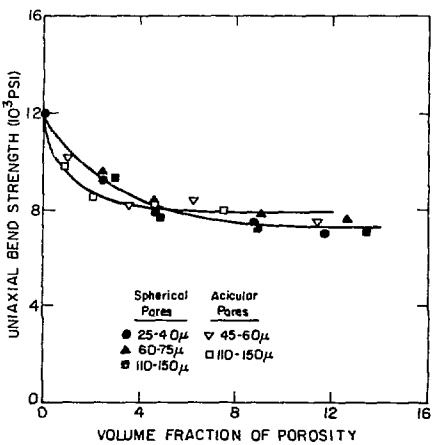

Fig. 3. Plot of the uniaxial bend strength against volume fraction of porosity (spherical and acicular pores) when the pore sizes are much larger than the grain size in a polycrystalline matrix.
(XBL 7512-10,007)

ceramics cannot be predicted by dividing the strength of zero porosity material by the effective stress concentration factor. For this reason, we turn to the Weibull probabilitic approach to brittle strength which allows us to consider the effect of the stressed volume, as well as the stress level, on the probability of failure. The Weibull[2] analysis is based on the assumption that a large number of inherent flaws exist throughout the stressed volume. The present investigating material, with its very fine grain size relative to the pore size, is probably very close to this ideal.

Varder and Finnie[3] applied Weibull's probabilistic approac to predict the strength of brittle solids and showed that reasonable prediction can be made for medium strength of a ceramic containing porosity up to about 10%. The analytical solution for the medium strength against percent porosity is shown in Fig. 4. To minimize computation, the median strength is used in bending tests rather than the mean. Since the specimen, having the same volume and value of Q (defined in Fig. 4) is unchanged, the ordinate in Fig. 4 may be used directly to estimate the effect of porosity on the median strength. Figure 5 shows the experimental results from Fig. 3 and the prediction based on the Weibull approach. Also shown in Fig. 5 is the prediction for relative strength obtained by considering only the decrease in cross-sectional area and that obtained by combining the stress concentration factor with the decrease in cross-sectional area due to pores.

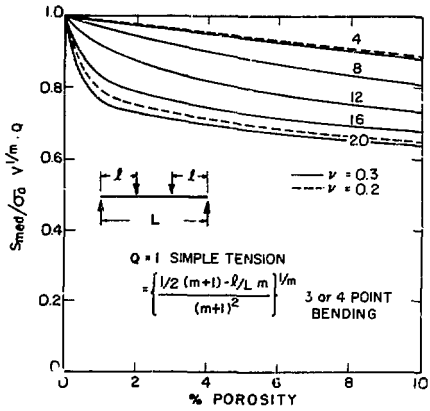

Fig. 4. Predicted variation of median strength as a function of porosity for values of the Weibull parameter m shown on curves. V is the total volume of material containing pores loaded by a nominal stress S. (XBL 7512-9462)

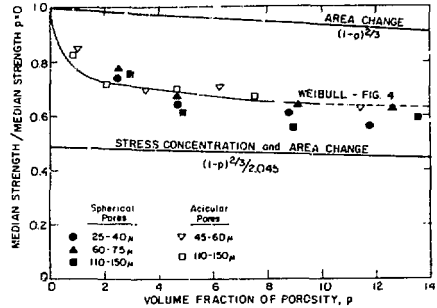

Fig. 5. Predicted and observed ratio of median strength with porosity to median strength with zero porosity. The prediction of Fig. 4 is extrapolated for values over 10% porosity. (XBL 7512-9463)

These results show that the effect of porosity on bending strength is predicted quite well by the Weibull approach. Other approaches which might be considered based on stress concentration factors or effective cross-sectional area are completely inadequate when the pore size is much larger than the grain size of a polycrystalline ceramic. Weibull's analysis predicts that only the total porosity and not the pore diameter will control the strength.

---

1. J. E. Baily and N. A. Hill, Proc. Brit. Ceram. Soc. 15, 15-35 (1970).
2. W. Weibull, Invetenskakad. Hanal. 151, Stockholm (1939).
3. O. Vardar and I. Finnie, Dept. of Mechanical Engineering, U. C. Berkeley, private communication.

7. VARIATIONS IN THE FERRAELECTRIC AND PIEZOELECTRIC PROPERTIES OF LEAD ZIRCONATE TITANATE CERAMICS WITH Cr_2O_3 ADDITIONS

John F. Dullea, Jr. and Richard M. Fulrath

Piezoelectricity is the reversible conversion of electrical to mechanical energy by straining the lattice of a polarized crystal. Polycrystalline ferroelectric lead zirconate titanate (PZT) can be made piezoelectric by creating a preferred orientation of the spontaneously polarized domains within each grain. The efficiency in energy conversion, as measured by the planar coupling coefficient, kp, will be determined by the effectiveness of this poling. Domain realignment will be influenced greatly by defect structure which can be extrinsically altered by the addition of doping oxides. Several such oxides have been studied. Takahashi[1] studied the effects of Cr_2O_3 on the electrical properties of $Pb(Zr_{.52}Ti_{.48})O_3$ and found a strong dependence of kp on the poling temperature and the amount of Cr_2O_3 added as shown in Fig. 1. The lack

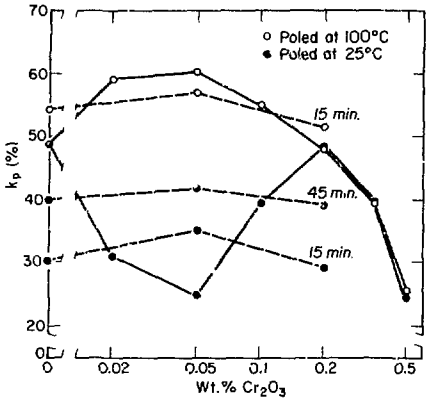

Fig. 1. Variation of the planar coupling coefficient, kp, with Cr_2O_3 added in $Pb(Zr_{.52},Ti_{.48})O_3$. (XBL 761-2163)

of material characterization suggested a more comprehensive study was needed to define the effects of Cr_2O_3 on the electrical properties of PZT because of the influence such factors as grain size, density, and crystal structure have on the electrical properties.

Single phase $Pb(Zr_{.52},Ti_{.48})O_3$ was prepared from high purity (≥ 99.9%) reagent grade powders. Cr_2O_3 was added in two concentrations; 0.05 wt%, and 0.20 wt%. The valence of Cr in Cr_2O_3 is +3 and its ionic radius is 0.68 A, indicating its solution on B sites in the PZT perovskite structure and generating oxygen vacancies. The stoichiometric modifications would be;

$$Pb(Zr_{.52},Ti_{.48})O_3 + 0.05 \text{ wt\% } Cr_2O_3 \rightarrow$$

$$Pb[(Zr_{.52},Ti_{.48})_{.9978}Cr_{.0022}]\ O_{2.9989}\square_{.0011}$$

and

$$Pb(Zr_{.52},Ti_{.48})O_3 + 0.20 \text{ wt\% } Cr_2O_3 \rightarrow$$

$$Pb[(Zr_{.52},Ti_{.48})_{.9912}Cr_{.0088}]\ O_{2.9956}\square_{.0044}$$

where □ denotes vacancies. The appropriate weights of powders were mixed with distilled water for 24 hours in a rubber lined ball mill using Teflon balls, dried thoroughly, and calcined at 850°C for 4 hours. The calcined powder was milled with distilled water for 4 hours in a polyurethane lined vibratory mill using high density ZrO_2 balls. Before milling, 1 wt% excess PbO was added to enhance sintering, and 0.5 wt% polyvinyl alcohol was added as a pressing aid. After drying, the powder was sized (-200 mesh) and pressed at 10,000 psi into 5 gram 1-in. diameter discs that were sintered in a lead zirconate +1 wt% excess zirconia packing powder for 16 hours at 1200°C. This packing powder was chosen because previous studies in this laboratory indicated it would give a single phase material of controlled stoichiometry.

The 0.05 wt% Cr_2O_3 modified PZT showed the highest density (99.9%) and finest grain size (6.2 μm). The 0.20 wt% Cr_2O_3 modified PZT showed the lowest density and an intermediate grain size. Grain growth was most extensive in the unmodified PZT. This would suggest a solute segration to the grain boundaries causing a reduced grain boundary mobility.[2] The grain growth inhibition exhibited by the 0.05 wt% Cr_2O_3 modified PZT, relative to the 0.05 wt% Cr_2O_3 modified PZT is similar to that reported by Atkin[3] and Fulrath doping with Nb^{+5}, a lead vacancy generator, relative to Al^{+3}, an oxygen vacancy generator, and suggests the solution of Cr as Cr^{+6} in the lower dopant level. Ferroelectric behavior of the 0.05 wt% Cr_2O_3 modified PZT also indicated this probability.

The domain structure within the grains is shown in Fig. 2. As Cr_2O_3 is added the domain structure changes from one of entirely 180° domains in the unmodified material (Fig. 2a) to one of primarily

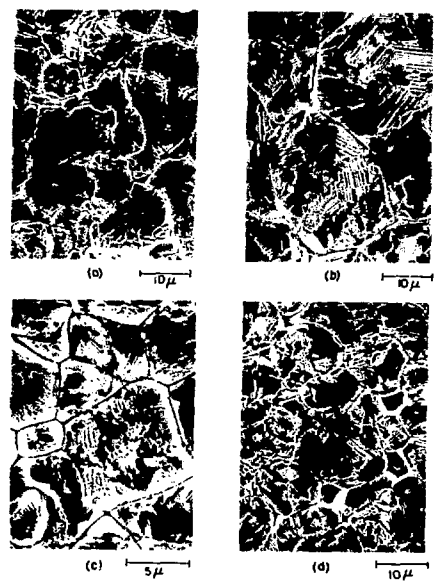

Fig. 2. Microstructures of unpoled PZT ceramics; a) unmodified, b) unmodified sintered by an alternate procedure, c) 0.05 wt% Cr_2O_3 modified PZT, d) 0.20 wt% Cr_2O_3 modified PZT. (XBB 7512-9041)

90° domains in the 0.2 wt% modified PZT, similar to doping with Al^{+3}.[3] This indicates the influence of oxygen vacancies on the formation of domains on spontaneous polarization. The ferroelectric properties of the materials indicated a domain wall pinning by the oxygen vacancies was operative.

Samples were electroded with a 1000 Å thick gold sputtered on the surface, and poled in a high dielectric silicone oil at 3 kV/mm for 15 and 45 minutes at 100°C. Values of kp were determined by the resonance method 24 hours after poling in accordance with I.R.E. Standards.[4] The variation in kp with the amount of Cr_2O_3 added and the poling time and temperature as determined in this study are also shown in Fig. 1 (dashed lines). The difference in the dependence of kp and the amount of Cr_2O_3 in the earlier study was found to be a result of poor stoichiometry control during sintering. The effect was confirmed by sintering undoped samples by the method used by Takahashi.[1] The average grain size was increased and the number of 90° domains increased greatly as observed by comparing Fig. 2b to 2a. The decrease in kp in a PbO deficient composition is significant[5] as in the samples sintered by the procedure used in the earlier study.

The poling time and temperature dependence of kp results from the pinning of domain walls by oxgyen vacancies and the low vacancy diffusion which is increased by poling at 100°C. Poling and switching characteristics also exemplified these effects.

In summary, the dependence of kp on the amount of Cr_2O_3 added to an unmodified PZT composition results from the bivalent solution of chromium, and the poling time and temperature dependence is due to a vacancy pinning of domain walls.

1. Marao Takahashi, Jap. J. Appl. Phys. 31(1), 189 (1970).
2. P. J. Jorgensen, J. Am. Ceram. Soc. 48(4), 207 (1965).
3. R. B. Atkin and R. M. Fulrath, ibid 54(5), 265 (1971).
4. Proc. I.R.E. 49(7), 1161 (1961).
5. A. H. Webster, T. B. Weston and N.R.H. Bright, J. Am. Ceram. Soc. 50(9), 490 (1967).

8. RESEARCH PLANS FOR CALENDAR YEAR 1976

Richard M. Fulrath

The study of densification of powder compacts using the MMRD-developed hot stage scanning electron microscopy facility has been one of the most successful techniques for sintering studies. This work will be expanded into other systems of technological importance while continuing the work already started on Al_2O_3, UO_2, and TiC-Ni. Studies on microstructure development in thick film conducting systems with the aim of reducing precious metal content and development of systems that do not use precious metals will be pursued.

Research on the kinetics of perovskite compound formation with the aim of producing better piezoelectric ceramics will be continued along with studies to determine the equilibrium PbO vapor pressure in the $PbO-Al_2O_3$ system. This latter effort is important because Al_2O_3 refractories are extensively used in processing lead titinate zirconate ceramics.

It is anticipated that during 1976 the present programs on the effect of pore size and shape on the strength of polycrystalline ceramics and electrical conductivity in lithium ferrite and lead zirconate titinate will be completed.

9. 1975 PUBLICATIONS AND REPORTS

Richard M. Fulrath and Associates

Journals

1. D. R. Biswas and R. M. Fulrath, Strength and Fracture in Glass Matrix Composites, J. Am. Ceram. Soc. 58, 526 (1975) (LBL-3915).

2. G. Bandyopadhyay and R. M. Fulrath, Effect of NiO and $NiFe_2O_4$ Dopants on the Processing and Properties of Lithium Ferrite Spinel, Bull. Am. Ceram. Soc. 54, 506 (1975)(LBL-2255).

3. L. Froschauer and R. M. Fulrath, Direct Observation of Liquid Phase Sintering in the System Iron-Copper, J. Material Sci. 10, 2146 (1975) (LBL-2270).

Papers Presented

1. R. M. Fulrath, Sintering Ceramics, Lawrence Livermore Laboratory, April 1, 1975.

2. R. M. Fulrath, Processing of Ceramics in the Lead Zirconate Titinate System, U.S. Japan Seminar on Basic Science of Ceramics, Hakone, Japan, June 23-27, 1975.

3. R. M. Fulrath, Recent Developments in Sintering Reactive and Non-reactive Aluminum Oxide, Basic Science Division Meeting, Japan Ceramic Society, Tokyo, June 28, 1975.

4. R. M. Fulrath, Sintering, Northern California Section American Ceramic Society Education Seminar, Berkeley, September 10, 1975.

5. R. M. Fulrath, Sintering, University at Notre Dame, September 30, 1975.

6. D. R. Biswas, Thermal Energy Storage Using Sodium Sulfate Decahydrate and Water, 1975 International Solar Energy Congress, Los Angeles, July 28-August 1, 1975.

7. Papers presented at the 28th Pacific Coast Regional Meeting of the Am. Ceram. Soc., Seattle, October 29-31, 1975.

7a. D. R. Biswas and R. M. Fulrath, Fracture Strength of Porous PZT Polycrystalline Ceramics.

7b. S. S. Chandratreya and R. M. Fulrath, Reaction Kinetics in the Formation of Compounds in the $PbO-ZrO_2-TiO_2$ System.

7c. J. J. Dih and R. M. Fulrath, Electrical Conductivity in Lead Zirconate Titanate Ceramics.

7d. D. J. Miller and R. M. Fulrath, Sintering of Uranium Dioxide by Hot Stage Scanning Electron Microscopy.

7e. V. K. Nagesh and R. M. Fulrath, Microstructure and Electrical Properties of Glass-Metal Composites.

7f. N. K. Wang and R. M. Fulrath, SEM Hot Stage Sintering.

8. R. M. Fulrath, Hot Stage Scanning Electron Microscopy, Lawrence Livermore Laboratory, December 8, 1975.

LBL Reports

1. D. R. Biswas and R. M. Fulrath, Strength and Fracture in Glass Matrix Composites, LBL-3915, May 1975.

2. D. R. Biswas, Thermal Energy Storage Using Sodium Sulfate Decahydrate and Water, LBL-3998, July 1975.

3. J. J. Dih and R. M. Fulrath, Electrical Conductivity in $LiFe_3O_8$, LBL-4151, September 1975.

4. L. Froschauer and R. M. Fulrath, Direct Observation of Liquid Phase Sintering in the System Tungsten Carbide-Cobalt, J. Material Sci. (LBL-3189)

e. Structure and Properties of Carbon Materials and Composite Materials

Robert H. Bragg, Principal Investigator

1. ELECTRICAL PROPERTIES OF GLASSY CARBON

Ram Saxena and Robert H. Bragg

Studies have been made of a series of glassy carbon (GC) samples heat treated at various temperatures above 1000°C in increments of 100°C for two hours at each temperature. For all isochronals $\ln\sigma$ is linear versus 1/T in the high temperature range, 200 - 300°K, with an activation energy of about 2 - 4 MeV. At the lowest temperatures $\ln\sigma$ is linear versus $1/T^{1/4}$, in agreement with Mott's theories.[1] The slope and intercept of the linear region of the $\ln\sigma$ versus 1/T plots show little change with heat treatment temperature (HTT), although our x-ray studies[2] show that the structure does change to a measurable extent, in agreement with a recent ESR[3] study in which localized and conduction electrons of comparable densities were observed at all HTT's studied. The microstructural basis of the localized states is difficult to ascertain for lower HTT material because of the extreme disorder present in the material. At higher HTT the two likely candidates are voids and crystallite boundaries where we believe that the carbon atoms are tetrahedrally bonded.[4] As yet no attempt has been made to introduce void characteristics into our model.

The magnetoresistance $\Delta\rho/\rho$ increases with magnetic field at a given temperature, increases as the measurement temperature T is lowered (Fig. 1), and follows a power law $\Delta\rho/\rho \propto H^n$. Some trends

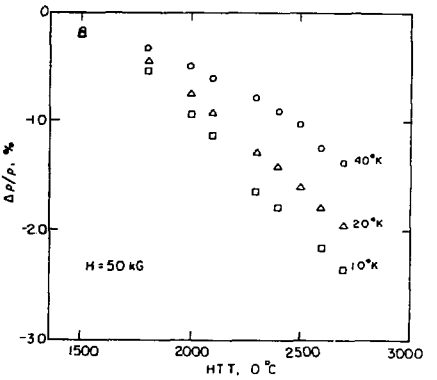

Fig. 1. Magnetoresistance of glassy carbons heat treated two hours. Magnetic field is 50 KG.
(XBL 761-6277)

in the HTT − T dependence of the exponent n are as follows:

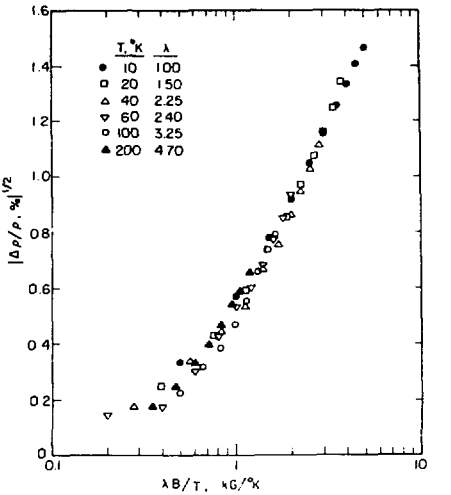

Fig. 2. Magnetoresistance of GC plotted according to Delhaes, λ adjustable. (XBL 761-6278)

1) At a given HTT, n is close to 1 at the lowest temperature and increases toward 2 as the temperature is raised to room temperature.

2) At a given T in the 2000 - 2800°C HTT range, n decreases with increasing HTT. In the HTT range 1000 - 2000°C, not enough samples have been studied to ascertain the trends in n.

The complete interpretation of negative magnetoresistance awaits theoretical understanding of the proposed mechanisms;[5,6] more than one are likely to be operative in GC. Some important considerations are:

1) With the small crystallite size (~ 100 Å) in GC the mean free path of conduction electrons is most likely limited by boundary scattering. In a simplified calculation this mechanism has been shown[7] to give negative magnetoresistance with $\Delta\rho/\rho \propto H^2$.

2) Following Delhaes *et al*[6] we have plotted $|\Delta\rho/\rho|^{1/2}$ versus $\ln \lambda B/T$ (λ-adjustable parameter)

and the result is shown in Fig. 2. This could be made to agree with Toyozawa's model of negative magnetoresistance, where free carriers are scattered by localized states.

3) Mott[8] has suggested that a localized state would tend to order the surrounding spins, thus increasing the hopping activation energy. A magnetic field would tend to destroy this order giving rise to negative $\Delta\rho/\rho$. "Details of this mechanism have not been worked out, but we believe it may be most important in low-temperature conduction in amorphous materials" (Mott p. 182). We are currently investigating the temperature ranges of applicability of these mechanisms to GC.

Reliable Hall effect measurements could not be made for all samples because of the extremely small signals involved. Where possible they showed saturation with magnetic field and little temperature dependence. The values obtained for the number of carriers from the simple expression R = 1/ne were of the same order of magnitude as reported in the ESR[5] work on GC.

1. N. F. Mott, Electronic Processes in Non-Crystalline Materials, Oxford Press (1971).
2. R. Saxena and R. H. Bragg, IMRL Annual Report for 1974 (LBL-3530), p.178.
3. S. Orzeszko and K. T. Yang, Carbon 12, 493 (1974).
4. R. Saxena and R. H. Bragg, K-Emission, Carbon 12, 210 (1974).
5. S. K. Das, Metallurgical Engineering, Ph.D. Thesis, University of Michigan (1974).
6. For a list, see Delhaes et al, Phil. Mag. 29, 130 (1974).
7. S. Fugita, Carbon 6, 746 (1968).
8. Same as Ref. 1, p. 182.

2. X-RAY STUDIES AND KINETICS OF ORDERING GLASSY CARBON

Sudhangshu Bose, Ram Saxena and Robert H. Bragg

Mr. Bose has joined the group and is following up on the work on x-ray characterization begun by R. Saxena and R. H. Bragg. This work involves the determination of the kinetics of ordering in glassy carbon (GC) by accurate measurement of the temperature dependence of the kinetics of the interlayer spacing, d_{002}. While the experimental data are relatively easy to obtain and can be interpreted without ambiguity in the case of graphitizing carbons such as pyrolytic graphite (PG), the situation is very different for glassy carbon. This problem is well illustrated by the data in Fig. 1, which compares the diffraction patterns of artificial graphite, a highly oriented PG, and GC which has been heat treated to 1000°C. Clearly in GC the accurate location of the 002 maximum is difficult, and the 004 maximum is so weak as to be observable only with very tedious measurements.

Strong intensity below the 002 maximum has been ascribed by many workers to "unorganized carbon", but as yet it has not been satisfactorily explained.

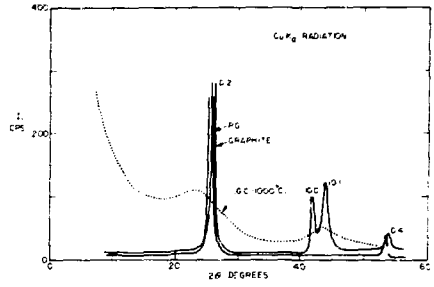

Fig. 1. Diffraction patterns of graphite, pyrolitic graphite (PG), and glassy carbon (GC). (CuKα radiation). (XBL 761-6279)

This intensity decreases with increasing heat treatment temperature, as shown in Fig. 2, but the excess intensity does not justify an explanation in terms of independent scattering by N carbon atoms. It was felt by our group that the excess intensity was due to double Bragg diffraction, and preliminary experiments appeared to support this explanation.

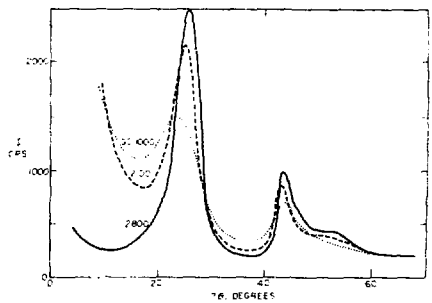

Fig. 2. Diffraction patterns of GC heated one hour at various temperatures (CuKα radiation). (XBL 761-6280)

However, more extensive experiments and some order-of-magnitude calculations have eliminated this possibility. By reducing the thickness of the specimen in an x-ray measurement, the relative magnitude of the component of doubly diffracted radiation should be reduced, but, as shown in Fig. 3, no such reduction is found.

It is now clear that the excess intensity is due to the small angle scattering from the voids in GC. Analysis of the experiments in reflection and transmission show that in reflection, the effective irradiated volume varies as $1/\sin\theta$, and this would accentuate the apparent small angle scattering, whereas in transmission the irradiated volume varies as $1/\cos\theta$, which diminishes the importance of the small angle component.

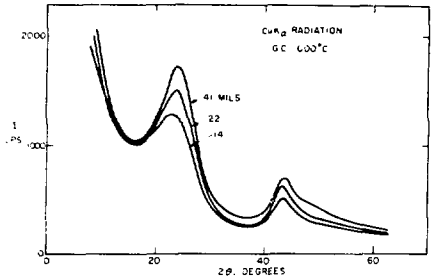

Fig. 3. Diffraction patterns of GC from specimens of different thickensses (CuKα radiation)
(XBL 761-6281)

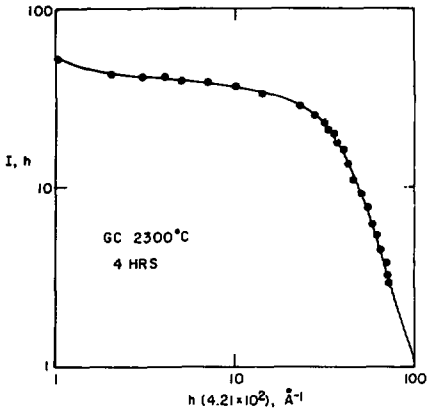

Fig. 4. Typical small angle scattering data obtained Bonse-Hart small angle scattering apparatus (CuKα$_1$ radiation). (XBL 761-6282)

It is known that the general features of accurate small angle x-ray scattering data are as shown in Fig. 4, and data obtained in transmission with a conventional diffractometer should be similar at small angles. Data obtained in reflection and transmission using a GE XRD-3 diffractometer are shown in Fig. 5. Ideally they would superimpose when corrected by factors of sinθ and cosθ for reflection and transmission respectively. This discrepancy has finally been traced to the divergence of the incident beam, and when this is suitably reduced, data such as in Fig. 6 are obtained.

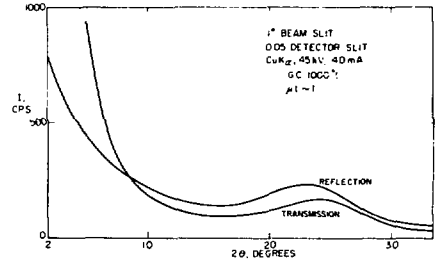

Fig. 5. Diffraction data for glassy carbon taken in reflection and transmission (CuKα radiation). (XBL 761-6283)

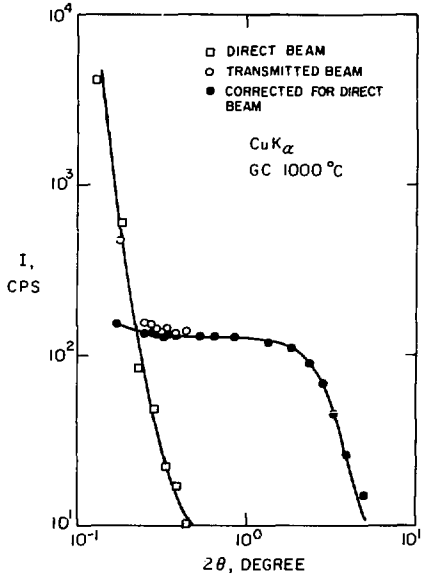

Fig. 6. Diffraction data obtained in transmission using fine collimation ahead of detector (CuKα radiation). (XBL 761-6284)

An important finding is that in the reflection data the intensity maximum is displaced to smaller 2θ, which leads to an overestimate of d_{002}, but data taken in transmission are relatively unaffected.

A detailed quantitative demonstration of this explanation has been started, and its implications are already being used.

3. SMALL ANGLE SCATTERING BY GLASSY CARBON AND PYROLYTIC GRAPHITE

Sudhangshu Bose and Robert H. Bragg

A calculation to predict the small angle scattering from a dilute dispersion of non-randomly oriented ellipsoids of revolution[1] was made to facilitate the analysis of the pore structure of carbon materials. Pyrolytic graphite (PG) provides a nearly ideal experimental vehicle to test the validity of the calculation. The calculation predicts that for ellipsoids of axes 2a, 2a and 2b having a fixed common orientation γ between the axis of symmetry and the normal to the direct beam and the plane of observation, the scattering is equivalent to that of a "Guinier sphere" whose radius is $H = (a^2\sin^2\gamma + b^2\cos^2\gamma)^{1/2}$. H is determined from the slope of *Guinier* plots of ln scattered intensity versus h^2 ($h = 4\pi/\lambda \sin\theta$).

Measurements were made on specimens cut as shown in Fig. 1 from a specially prepared block of pyrolytic graphite, about 2.5 cm thick, supplied

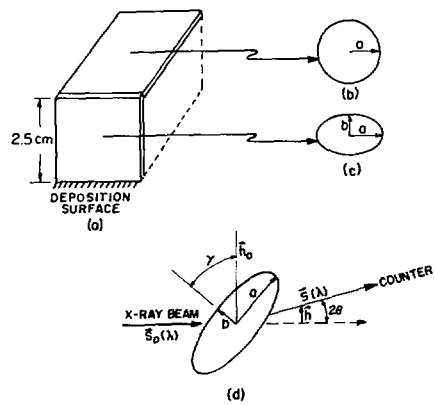

Fig. 1. a) Block of pyrolytic graphite, b) Voids project as circles, c) Voids project as ellipses, d) Geometry of voids in scattering measurements. (XBL 761-6285)

by Pfizer, Inc. The mode of preparation suggests that the common axis of rotation b will be normal to the deposition surface, and hence the scattering from a specimen cut parallel to it should be independent of the angle of rotation. This is confirmed by the data of Fig. 2.

Typical data obtained for the Guinier region are shown in Fig. 3 which show that the scattering is anisotropic, i.e., a function of γ. The observed γ dependence of H is shown in Fig. 4 along with the calculated least square best fit curve for 2a = 228A, and 2b = 152A. The agreement between theory and experiment is considered satisfactory.

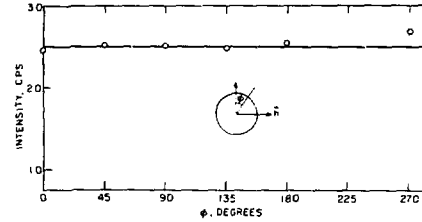

Fig. 2. Isotropic scattering from specimen cut parallel to the dependence surface; h = constant. (XBL 761-6286)

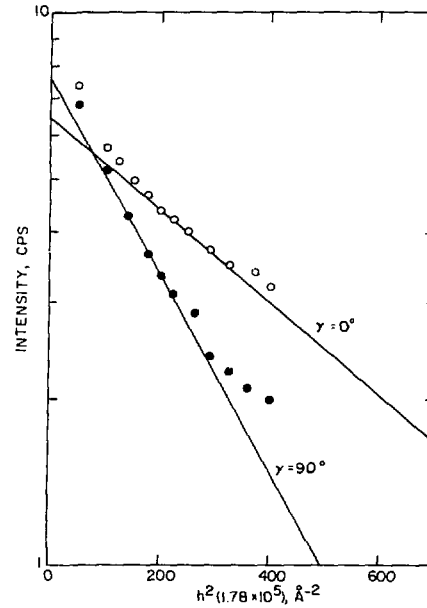

Fig. 3. Typical Guinier plots for oriented pyrolytic graphite. (XBL 761-6287)

The experimental data in Fig. 4 are based upon "edge-on" views of the ellipses, but a direct measurement of 2a was also made from the specimen used to obtain Fig. 2. Results obtained for this orientation in which the ellipses are projected as circles of radius a gave a value 2a = 214A, in good agreement with the result obtained for $\gamma = 90°$ in Fig. 4.

The foregoing affords strong confirmation of the model and the calculation. A second major

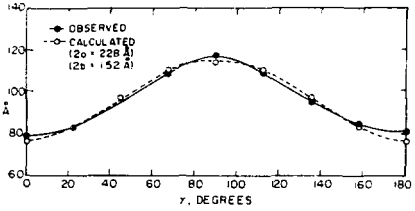

Fig. 4. Dependence of "Guinier Sphere" radius on orientation. (XBL 761-6288)

prediction is that in the Porod region curves of ln intensity versus ln h should be linear and have ordinates proportional to H^{-4}. Figure 5 shows typical data, which are in qualitative agreement, but the precision of the present data is inadequate for a quantitative comparison of H^{-4} versus γ.

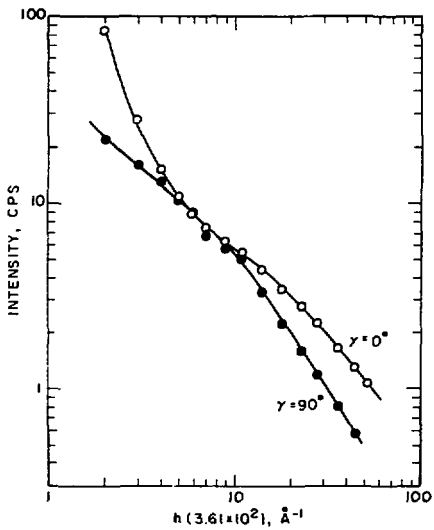

Fig. 5. Typical Porod plots for oriented pyrolytic graphite. (XBL 761-6289)

These results make available a much improved theory for interpreting the scattering from oriented non-spherical "particles" in solids. In our work the "particles" are the voids in carbons and graphites such as those in fibers, pyrolytic graphite, and plastically deformed glassy carbon. However, the present results do not prove that the voids in PG are ellipsoidal; in fact the microstructural evidence suggests that they are probably better approximated by half ellipsoids of dimensions 2a, 2a and b, and it is possible that the scattering from circular discs of radius a, 2a and thickness 2b would also fit the predicted dependence of H on γ reasonably well. This can be expected intuitively since *any* reasonable volume of revolution can be approximated by an ellipsoidal of revolution.

There is an additional internal check possible for consistency beyond that afforded by verification of the expected H^{-4} dependence of the intensity upon γ in the Porod region. The theory for a monodisperse system predicts an ordinate on the intensity axis at h = 0 which can be used to calculate the total volume of voids. On the other hand, the void volume can be determined experimentally from density measurements. Thus to complete the characterization it is also necessary to use the scattering data to predict the observed void volume to ensure internal and external consistency of the data.

---

1. F. M. Hamzeh and R. H. Bragg, J. Appl. Phys. 45, 3189 (1974); LBL-1874 (August 1973).

4. ELECTRICAL RESISTIVITY OF Al-$CuAl_2$ EUTECTIC

Kwaku Danso and Robert H. Bragg.

In a previous report[1] studies were reported on the electrical resistivity versus time of directionally solidified Al-5.7 Cu(α) and Al-$CuAl_2$(θ) alloys, which had been solution heat treated and aged at 25°C, 150°C, and 315°C. In all cases the resistivity versus time curves of each showed a maximum indicating that the Al-5.7 Cu alloy phase in the lamellar eutectic microstructures ages independently of the adjoining θ phase. However, the overaged α alloys showed the expected θ precipitates on {100} Al planes at optical magnifications whereas there was no clear indication of oriented precipitates in the α-phase of the eutectic. Initial attempts at electron microscopic observation of oriented precipitates in the eutectic alloy at any stage of the precipitation were unsuccessful. Thus there is a question whether or not the microstructures of the Al-5.7 Cu alloy are identical whether grown and aged separately or between lamellae of θ in the eutectic alloy. A second difficulty with interpreting the resistivity data in terms of any theory of composite materials is the absence of any information on the resistivity of $CuAl_2$(θ). Since this material has a tetragonal unit cell, it is necessary to know the resistivity in the a and c directions to permit any comparison with a theory of the properties of composite materials.

Because the resistivity of the aligned eutectic depends upon both the microstructure of the lamellae and the crystallographic orientations within phases, it is necessary to determine both. Unfortunately, it appears to be necessary to do this for each specimen measured. There is considerable confusion in the literature concerning the crystallographic relationships that occur in growth of the eutectic.

The most reliable seems to be that reported by Cantor and Chadwick,[2] which are as shown in the table below.

Interphase orientation relationship	Growth direction	Interface facets
{111} Al // {211} $CuAl_2$	varies	within ±8° from
<110> Al // <210> $CuAl_2$		{111} Al, {211} $CuAl_2$

The growth direction was reported as variable, but was usually between <321> Al, <211> Al, and <310> Al. This variability does not appear to have been the subject of a systematic investigation but seems likely to be associated with kinetic factors of the growth process and anisotropy in the interfacial energies. However, the one approximate determination made in this work indicating <100> is almost certainly in error.

With the solidification apparatus used in the initial phases of this work it was not possible to obtain temperature gradients, G, at the solid-liquid interface greater than about 30°C/cm. However, when the work on the Al-Si eutectic was begun, a special chiller (Fig. 1) was designed by Dr. Stefan Justi with which gradients to 80°C/cm are obtainable.

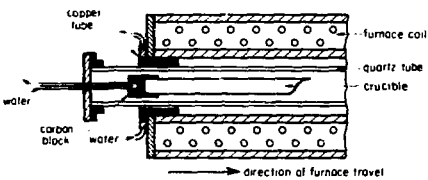

Fig. 1. Solidification apparatus (detail of the cooling end). (XBL 7512-9251)

A set of ingots consisting of two Al-5.7 wt% Cu alloys, three Al-33.15 wt% Cu alloys, and two Al-33.30 wt% Cu alloys have been directionally frozen at 4.7 cm/hr using the revised apparatus. All of the latter five ingots appear to have well aligned eutectic microstructures although they differ slightly in chemical composition. Auxiliary experiments with melted buttons showed that the eutectic composition is closer to Al-33.30 wt% Cu than to Al-33.15 wt% Cu, but possibly during the normal one-pass freezing the composition changes so that most of the frozen ingot has the eutectic composition in either case. A single crystal of $CuAl_2$ has been obtained from Professor A. S. Yue, UCLA, for resistivity measurements. This crystal will provide resistivity data for $CuAl_2$ from which, with the existing data for the α and θ alloys, a comparison of theory with experiment can be made.

1. Kwaku A. Danso, Electrical Resistivity Studies of Unidirectionally Solidified Al-$CuAl_2$ Eutectic Alloy, LBL-3547 (M.S. Thesis, 1974).

2. B. Cantor and G. A. Chadwick, J. Crys. Growth 25, 12 (1974).

5. UNIDIRECTIONAL SOLIDIFICATION OF Al-Si EUTECTIC*

Stefan Justi+ and Robert H. Bragg

Al-Si alloys were unidirectionally frozen at rate R between 0.1 and 47 cm/hr in a horizontal resistance heated furnace where the temperature gradient G, ahead of the liquid solid interface was kept fairly constant at about 78°C/cm. Typical optical micrographs such as shown in Fig. 1 indicate

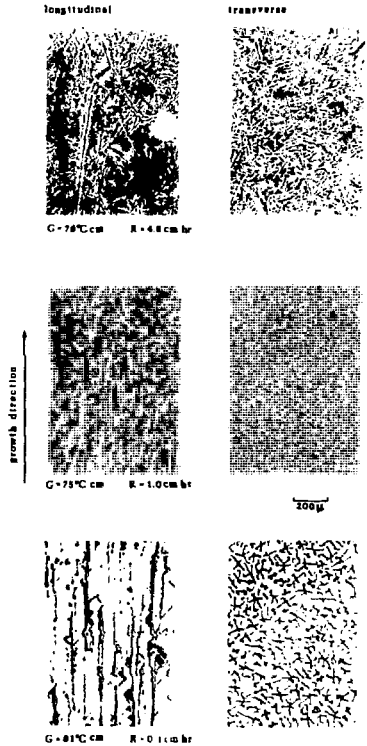

Fig. 1. Optical micrographs of unidirectionally solidified Al-Si eutectic grown at different growth rates. (XBB 761-16)

a definite alignment of the fibrous Si phase at lower growth rates. At growth rates greater than about 5.0 cm/hr the microstructure is irregular and similar to that of chill-cast material, but some preferential orientation of the Si rods parallel to the growth direction can still be observed.

Figure 2 shows a diagram of the solidification experiments in which the lines are drawn according to the classification of Day and Hellawell.[1] According to these authors, the part of the diagram to the right of about R = 1.0 cm/hr represents the breakdown of the planar solid-liquid interface during solidification. The present results show that the division is not sharp; preferential alignment persists up to about R = 5.0 cm/hr.

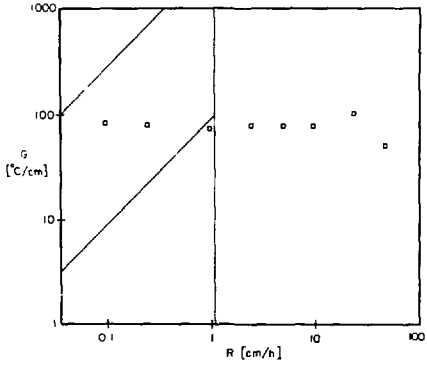

Fig. 2. Diagram of Al-Si unidirectional solidification experiments. (XBL 7512-9498)

Previous workers have shown that for this system an interdendritic spacing, λ, of the Si fibers follows a law closely approximated by $\lambda^2 R$ = constant, at least for growth rates above about the 1.0 cm/hr. If λ plays the role of grain size in this system, and the yield strength or hardness is plotted versus $\lambda^{-1/2}$, or alternatively $R^{1/4}$, then a straight line should be obtained. Vickers hardness tests (HV1) were made on surfaces in three orthogonal directions as shown in Fig. 3. The results are shown in Fig. 4 in which each point is the mean of 18 measurements. There appears to be a linear relationship and a slight orientation dependence, up to about 5.0 cm/hr, but at higher rates the hardness increases only slightly, and there is no indication of an orientation dependence.

The point for R = 0.25 cm/hr appears anomalous, and the micrographs for this alloy show a transverse banding phenomenon which has been reported by other investigators. Since banding was not observed for higher or lower growth rates it is unrepresentative. The slightly higher hardness is explained as due to an excess of Si in these bands.

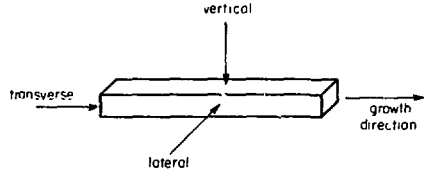

Fig. 3. Orientation directions for hardness measurements. (XBL 7512-9253)

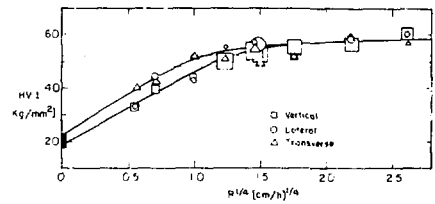

Fig. 4. Vicker's hardness HV1 vs growth rate, $R^{1/4}$. (XBL 7512-9499)

The solid bar at R = 0 indicates the range of hardness of the 1100 Al alloy whose chemical composition, and presumably mechanical properties are those of the Al matrix. The data appear to extrapolate into this region, and this suggests that even when frozen at the slowest rates, for which an aligned, coarse grained microstructure is obtained, the hardness of the eutectic will be essentially that of the matrix phase alone. There is no indication of fiber composite strengthening.

The dashed lines in Fig. 4 indicate the range of hardness values obtained from chill cast eutectic alloys. It appears that a higher hardness is obtained by directional solidification. Examination of the microstructures of the chill cast alloy showed regions of Al dendrites which was not characteristic of the directionally frozen alloys. These dendrite should impart a softening to the alloy and could explain the apparently anomalously lower hardness. The results suggest, however, that without additions of impurities for grain refinement the hardness of Al-Si alloys can be increased by directional solidification under controlled conditions.

*This work is presented more completely in LBL-4560 and has been submitted for publication in Trans AIME.

†Dr. Justi is a Max Kade Postdoctoral Research Fellow on leave from the Technical University of West Berlin.

1. M. G. Day and A. H. Hellawell, Proc. Roy. Soc. A 305, 473 (1968).

6. YIELD STRENGTH OF DIRECTIONALLY SOLIDIFIED Al-Si EUTECTIC

Danny G. Morrow and Robert H. Bragg

The effect of directional solidification on the yield strength and microstructure of the Al-Si eutectec has been investigated. Eutectic alloys (Al-12.7 wt% Si) were directionally frozen through a temperature gradient of about 80°C/cm at rates, R, between 0.097 and 47 cm/hr. The microstructures and crystallographic relationships were characterized using optical microscopy and transmission Laue x-ray photography. As found by Day and Hellawell,[1] for freezing rates lower than approximately 1.0 cm/hr, the Si crystals exhibited a <100> fibre texture within a matrix of polycrystalline Al (see title 5 above and Fig. 1). At higher growth rates irregular microstructures similar to those of the as-cast alloy were found. Transmission Laue photographs show concentric Debye rings (Fig. 2) due to the fine dispersion of multiple twinned {111} Si crystals in a matrix of polycrystalline Al.

Linear transverse measurements of the optical micrographs showed that the "interdendritic" spacing λ between Si fibres obeyed a $\lambda^2 R$ = constant dependence for R greater than 1.0 cm/hr (Fig. 3) but at slower growth rates this dependence is not found. In the lower growth rate region transverse bands rich in Si are observed, as reported by Day and Hellawell.[1] But as yet no correlation between band spacing and growth rate has been made.

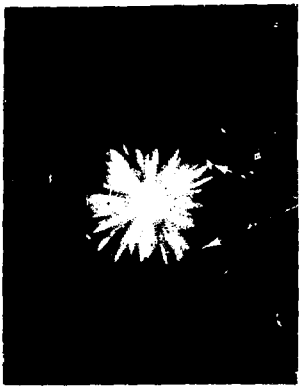

(a) R = 0.25 cm/hr
Arcs result from <100> fiber texture of {111} crystals.

Arcs

Growth Direction

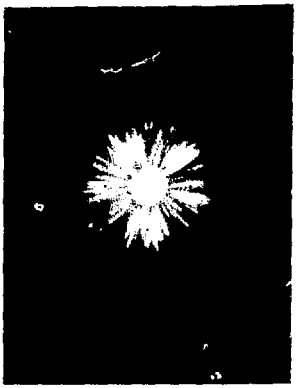

(b) R = 0.97 cm/hr

Fig. 1. Transmission Laue photographs for low growth rates (Ni filtered CuKa radiation). XBB 7512-9073

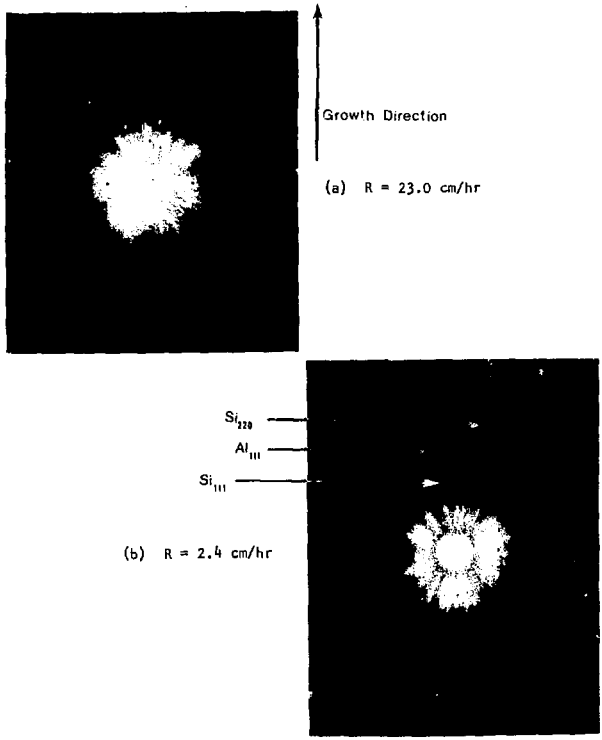

Fig. 2. Transmission Laue photographs for R greater than 1.0 cm/hr (Ni filtered Cuka radiation. (XBB 7512-9074)

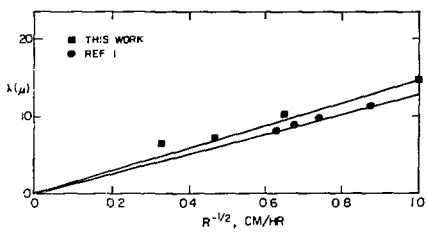

Fig. 3. "Interdendritic" spacing from linear traverse measurements. (XBL 761-6290)

Tensile tests were made using specimens fabricated parallel to the growth direction according to ASTM-E8-69. Data on the 0.2% offset yield strength was obtained from these tests and plotted versus $R^{1/4}$ (Fig. 4). For R greater than about 1.0 cm/hr, Fig. 4 shows that the yield strength is proportional to $R^{1/4}$. Using the above relationship between R and λ, it follows that

$$\sigma_{y.s.} \propto \lambda^{-1/2} .$$

So, for the higher growth rates a Hall-Petch type relationship exists between the yield strength and the distance between the brittle Si crystals. However, contrary to the results implied by the hardness data obtained by Justi and Bragg (see 5 above) the maximum yield strength obtained is below that of chill cast material. This reduction in yield strength from the as-cast alloy is most probably due to the greater ease of crack propagation along the {111} cleavage faces of the Si crystals due to a crystal size larger than in the as-cast material. In the lower growth rate region, where aligned microstructures are obtained, the yield strength

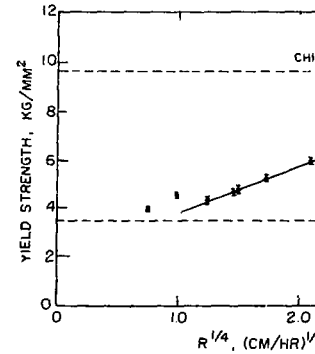

Fig. 4. Dependence of yield strength on growth rate. (XBL 761-6291)

is relatively insensitive to growth rates and is only slightly higher than that of the Al matrix alone. Examination of the fracture surfaces in this region shows flat transverse fractures at the interfaces of the Si-rich instability bands.

For microstructures aligned in a regular manner, a yield strength independent of growth rate would be expected.[2] Also, since Si has a much higher modulus of elasticity than Al, a yield strength higher than that of the matrix, essentially 1100 Al, would be expected. Present results indicate that aligned fiber composite strengthening is not obtained due to the presence of the brittle Si bands lying normal to the growth direction.

1. M. G. Day and A. H. Hellawell, Proc. Roy. Soc. A. 305, 473 (1968).
2. H. Bibring, Proc. of Conference on In-Situ Composites 3, 12-15 (1975).

7. RESEARCH PLANS FOR CALENDAR YEAR 1976

Robert H. Bragg

The work on the kinetics of changes in electrical properties of heat treated glassy carbon (GC) will be completed by mid-1976, by Ram Saxena, and will be extended by Showchia Ho to the effect of neutron irradiation on GC in order to clarify the mechanisms responsible for negative magnetoresistance. Auxiliary measurements on oriented pyrolytic graphite (PG) irradiated under similar conditions will be made.

The x-ray studies of the kinetics of ordering using d_{002} will also be completed by mid-1976. The explanation of non-organized carbon is being treated as a separate project, by S. Bose, but enough is known so that the d_{002} kinetic data can be analyzed quantitatively. Small angle scattering will be obtained by S. Bose from the entire series of specimens used in the studies of electrical properties and will be used in the first systematic study of the kinetics of void growth in GC. A small furnace will be designed and built for short time heat treatments at high temperatures (> 1000°C). The experimental test of the equations derived to characterize the orientation dependence of scattering by anisotropic voids in materials will be completed.

The work on the electrical properties of directionally solidified Al-$CuAl_2$ eutectic, begun by K. Danso (LBL-3547), will be continued by D. Baker who will investigate the directional dependence of the thermal expansion of the α and θ phases, and the eutectic. A series of alloys will be grown at different rates to determine if the interlamellar spacing, λ, plays a role in the electrical and thermal properties. The dialatometric investigation is the major new thrust in our research program for 1976.

The work on the microstructure of directionally solidified Al-Si eutectic will be completed by Dr. Stefan Justi (Max Kade Postdoctoral Fellow), but work on tensile properties will be continued by D. Morrow, to determine if the oriented microstructures obtained at low growth rates have the expected high elastic modulus. We will also begin tensile property measurements on the directionally solidified Al-$CuAl_2$ eutectic. Professor R. H. Bragg will be on sabbatical (in residence) during the period April - June 1976.

8. 1975 PUBLICATIONS AND REPORTS

R. H. Bragg and Associates

LBL Reports

1. Kwaku A. Danso, Electrical Resistivity of Unidirectionally Solidified Al-$CuAl_2$ Eutectic Alloy, M.S. Thesis. LBL-3547.

2. Stefan Justi and Robert H. Bragg, Microstructure and Hardness of Directionally Solidified Al-Si Eutectic, (submitted for publication in Trans. AIME). LBL-4560.

Papers Presented

1. S. Justi and R. H. Bragg, Unidirectional Solidification of Al-Si Eutectic, Third American Conf. on Crystal Growth, Stanford University, July 1975.

2. R. H. Bragg and R. Saxena, Electrical Properties of Glassy Carbon, 12th Biennial Conf. on Carbon, Pittsburgh, August 1975.

3. M. M. Biswal, S. Bose and R. H. Bragg, Void Growth in Glassy Carbon, 12th Biennial Conf. on Carbon, Pittsburgh, August 1975.

4. S. Bose, R. H. Bragg and R. Saxena, Explanation of "Disordered" Carbon in Glassy Carbon, American Ceramic Society 28th Pacific Regional and Nuclear Division Meeting, Seattle, October 1975.

B. SOLID STATE PHYSICS

1. EXPERIMENTAL RESEARCH

a. Far Infrared Spectroscopy

Paul L. Richards, Principal Investigator

1. FAR INFRARED SPECTRA OF LIQUID ELECTRON-HOLE DROPS IN GERMANIUM

Richard L. Aurbach, Lawrence Eaves, Carsen D. Jeffreys, Robert S. Markiewicz, and Paul L. Richards.

Droplets of electron-hole liquid are known to condense in He-temperature Ge that is optically pumped with band gap radiation. This new form of matter is being actively studied in many laboratories. In unstressed samples, a cloud of small (α) droplets is formed having a radiative decay lifetime of ~40 μs. In nonuniformly stressed Ge a potential well can be created in which a single large (γ) drop is formed. These γ-drops can have radii as large as 400 μm and radiative lifetimes as long as 400 μs.

The far infrared attenuation in both α and γ drops over the frequency range from 25 to 200 cm^{-1} with a variety of stress orientations is shown in Fig. 1. Because of the remarkable similarity of all of these curves, it was necessary to verify that γ-drops had been formed. This was done in three different ways. The γ-drops were photographed before and after the far infrared spectra were measured using an infrared vidicon which was sensitive to the recombination radiation. The

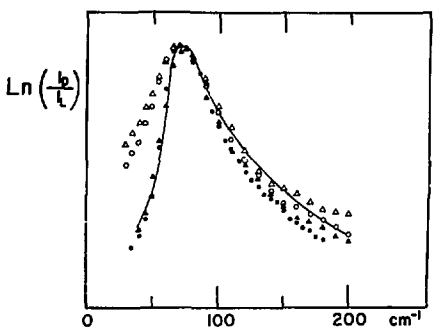

Fig. 1. The ratio of the transmitted intensity with (I_L) and without (I_D) optical pumping plotted as a function of frequency. The open symbols are for γ-drops formed in Ge stressed with T ∥ (110). The closed symbols are for T ∥ (100). Two levels of pump power are shown in each case. The solid line is the spectrum of α-drops in unstressed Ge. (XBL 761-1234)

recombination lifetimes were measured and microwave Alfven-wave resonances were observed in the same stress conditions used for the far infrared experiments.

Calculations based on Mie scattering theory in the small drop limit show that the peak of the far infrared spectrum for α-drops is at $\omega_p/\sqrt{3}$, where ω_p is the plasma frequency. A similar calculation carried out in the large drop limit of the Mie theory shows that the peak is close to ω_p for γ-drops. The spectra in Fig. 1 are therefore in agreement with a result deduced from other experiments, that the plasma density in the γ-drops is a factor ~ 4 smaller than in the α-drops. The calculations show good agreement with the measured spectra of the γ-drops.

2. A MEASUREMENT OF THE SPECTRUM OF THE COSMIC BACKGROUND RADIATION

David P. Woody, Norman S. Nishioka and Paul L. Richards

We have made the first accurate direct measurement of the submillimeter spectrum of the cosmic background radiation (CBR). The frequency range of our measurement includes ~ 70% of the radiant energy in the universe. Previous ground-based measurements at frequencies below ~ 3 cm^{-1} support the idea that the CBR is isotropic and has a characteristic temperature of ~ 3K. The peak in a 3K blackbody curve occurs at ~ 6 cm^{-1}, and thus the Wien part of the spectrum lies in the submillimeter range where the atmospheric emission precludes a direct ground-based measurement of the CBR. We used a balloon-borne liquid-helium-cooled spectrophotometer to measure the spectrum in the frequency range from 3 to 30 cm^{-1}.

The instrument features a germanium bolometric detector, a polarizing interferometer for Fourier spectroscopy, and a cooled conical antenna. The development and characterization of the instrument are described in the 1973 IMRD Annual Report.

The data for our measurement were obtained during a successful balloon flight from Palestine, Texas on July 24, 1974. A description of the flight and a preliminary data analysis are given in the 1974 IMRD Annual Report.

The experiment consisted of measuring the night sky emission spectrum at an altitude of 39 km and correcting for the emission from the residual atmosphere and other sources of contaminating radiation. The atmospheric radiation is dominated

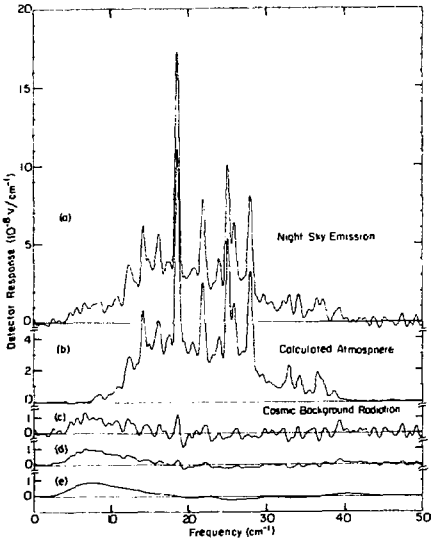

Fig. 1. (a) Night sky emission spectrum; (b) calculated best fit atmospheric spectrum; (c,d and e) CBR spectrum (residual of (a) - (b)) at three different resolutions. (XBL 759-7305)

by the line emission from H_2O, O_2, and O_3 molecules. We developed a model for the atmosphere that had only two free parameters for the concentrations of H_2O and O_3. The concentration of O_2 was determined from its known mixing ratio in the atmosphere. Figures 1(a) and (b) show the observed night sky emission spectrum and the calculated atmospheric emission respectively. The residual, which is shown in Figs. 1(c), (d) and (e) at three different resolutions, is the CBR.

Our flight data also allowed us to determine the continuum radiation contributed by earthshine diffracted into our antenna and emitted by the instrument itself. This required a model for the antenna pattern valid for large off-axis angles. We calculated a theoretical antenna pattern, using a technique based on geometrical optics, which also includes diffraction effects. The calculated antenna pattern shown in Fig. 2 is in excellent agreement with the experimental data over the angular range from 0 to 1 radian. This is the first time a broadband submillimeter antenna has been successfully measured and analyzed at large off-axis angles.

The CBR spectrum deduced from our observations is shown in Fig. 3. The error limits include detector noise, measured limits on continuum contamination and possible errors in the atmospheric emission model. This establishes the CBR spectrum in the frequency range from 4 to 17 cm^{-1}

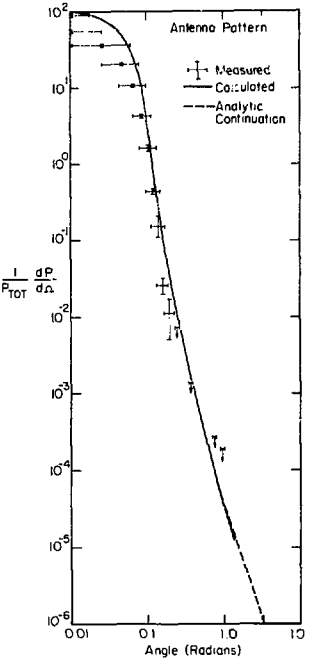

Fig. 2. Theoretical and measured antenna pattern. (XBL 757-6730)

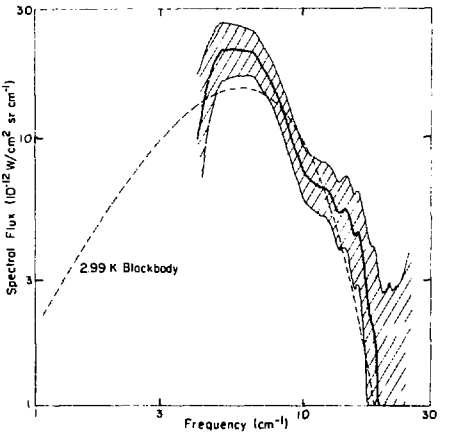

Fig. 3. CBR spectrum with 95% confidence limits. (XBL 759-7300)

and clearly shows that it follows the Planck curve for a ~ 3K blackbody at frequencies beyond the peak. Our results yield a temperature for the blackbody of $2.99^{+.07}_{-.14}$ K.

Several changes to the apparatus have been made to improve the measurements. A composite bolometer has been fabricated which will increase our sensitivity by nearly an order of magnitude. This will allow us to obtain higher resolution spectra and thus improve our modeling of the atmospheric emission. The system has also been improved by the use of Winston light cones to define the geometrical optics beam and the addition of a flared horn to further decrease the diffraction sidelobes. These improvements will allow us to greatly reduce the error limits in our measurement. A new balloon flight is planned for the spring of 1976.

Using the improved apparatus it should be possible to detect stratospheric constituents at the level of 10^8 molecules/cm^3. Plans are being made to test this capability to see if molecular species of importance to the catalysis of stratospheric O_3 can be detected in this way.

This program is being carried out in collaboration with the Berkeley Space Sciences Laboratory and has received support from NASA.

3. DEVELOPMENT OF PURIFICATION METHODS FOR HIGH PURITY GERMANIUM

Eugene E. Haller, William L. Hansen and Paul L. Richards

Far infrared photothermal ionization spectra of ultrapure Ge are being measured on a routine basis. These spectra provide detailed information on residual ionized impurities at the level of ~ 10^8 atoms/cm^3. The technique used is described in detail in the 1974 IMRD Annual Report.

The information gained from these studies has been used to identify non-segregating compounds of B and Al which are difficult to remove from Ge by the usual techniques. Information about residual impurities obtained from photothermal ionization spectroscopy and electrical measurements has permitted the development of techniques to consistently purify Ge to the 10^{10} atoms/cm^3 range. This Ge is used primarily for radiation detectors.

4. FAR INFRARED SEMICONDUCTING BOLOMETER DETECTORS

Norman S. Nishioka and Paul L. Richards

The use of heavily doped semiconductors as low temperature (T ≈ 1.5K) far infrared bolometer detectors has been common for many years. However, poor far infrared absorptivity and excess current-dependent noise have prevented these detectors from reaching the theoretical limits of sensitivity. We have initiated a detector development program whose major goal is to improve the sensitivity of semiconducting bolometers.

In spite of the detrimental effects of excess noise and low absorptivity, semiconducting bolometers are popular for several reasons. Primary among these are 1) the required electronics consist of a low noise preamplifier and a bias battery that are straightforward to construct and operate, 2) the dynamic range is large, often being in excess of 10^7, and 3) it is unconditionally thermally stable, that is, its thermal feedback is such that thermal runaway is impossible.

Conventional semiconducting bolometers require the semiconductor to act as both the infrared absorber and the temperature sensing element. Our approach has been to separate these two functions. Figure 1 shows how these "composite" bolometers are assembled. They consist of a thin sapphire substrate coated with a bismuth film of ~ 200 Ω/□ resistance as the infrared absorber and a ~ 1 × 1 × 0.2 mm slice of gallium-doped germanium as the temperature sensing element. The bismuth coated sapphire provides a far-infrared absorption of ~ 50%. The doped germanium thermometer is glued to the sapphire substrate, which is suspended from a brass ring by four nylon threads. These threads provide a robust vibration-free mounting for the detector. Electrical contact to the thermometer is made via a pair of wires soldered to opposite ends of the germanium. These wires also provide the dominant thermal conductance to the heat sink. Adjusting the size and composition of these wires allows us to alter the thermal conductance to the bolometer.

Computer simulations of bolometer performance indicate a complicated relation between the optimum bolometer parameters and the amount of infrared background power loading present. Using these calculations as a guide we are now in the

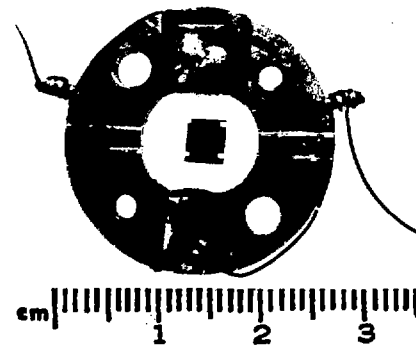

Fig. 1. Composite far infrared bolometer with a semiconducting thermometer. (XBB 7512-9203)

process of constructing bolometers whose performance is optimized for the background loading present in several different experiments. In many cases, the theoretical limits of sensitivity have been achieved.

In addition, our computer calculations imply that a significant improvement in sensitivity can be acquired by using liquid ^{3}He instead of liquid ^{4}He as the coolant. We have recently begun a program to optimize the performance of these bolometers at the lower temperature (T ~ 0.3K) provided by liquid ^{3}He.

5. FAR INFRARED SUPERCONDUCTING BOLOMETER DETECTORS

John Clarke, Gary I. Hoffer, Paul L. Richards, and Nan-Hsiung Yeh

A continuing program of development of composite far infrared bolometer detectors with superconducting thermometers has yielded a five-fold increase in sensitivity since our last annual report. The noise in a bolometer which uses a superconducting Al thin film transition edge thermometer operated at 1.5K has been reduced to the fundamental Johnson noise limit. This gives a bolometer noise equivalent-power of NEP = 10^{-15} W/$\sqrt{\text{Hz}}$ which is the best ever reported for a ^{4}He-temperature bolometer. Although they are not as fully developed or as easy to use, these bolometers are more sensitive than the composite bolometers with Ge thermometers described above.

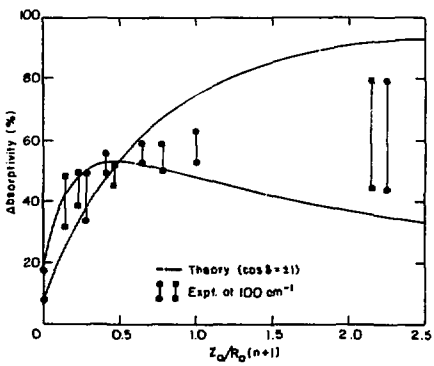

Fig. 1. Theoretical absorptivity of a composite bolometer plotted as a function of the ratio of the free space impedance Z_0 to the product $R_\square(n+1)$, where $R_\square$ is the film resistance and n is the index of refraction of the substrate. The lines give the values of absorptivity at the maxima and the minima of the interference pattern. The length of the bars gives the measured values of the same quantity. (XBL 756-6571)

The absorbing element used in our composite far infrared bolometers is a conducting film of Bi on a substrate of Al_2O_3. The far infrared absorptivity of this structure has been evaluated experimentally and theoretically. The absorption is an oscillatory function of frequency for most values of resistance per square of the Bi film because of interference effects in the Al_2O_3 substrate. The maxima and minima of the interference pattern are plotted in Fig. 1 as a function of the normalized conductance of the film. These results show that a frequency independent absorption of 50% and a peak absorption of ~ 90% in a narrow frequency internal can be achieved with these composite bolometer structures.

These bolometer detectors will be used in our measurements of the cosmic background radiation described above and the sky survey described below. If the balloon flights are successful, these bolometers will be used in the first two infrared astronomical satellites: the large Space Telescope and the Infrared Explorer Satellite.

6. FAR INFRARED SKY SURVEY*

Stephen E. McBride, Norman S. Nishioka, Paul L. Richards and David P. Woody

Astronomy at far infrared frequencies is still in its infancy. One important reason for this lack of progress is the lack of sensitive far infrared detectors. The development of the new bolometers described above now makes very exciting astronomy possible. The next logical step in the development of far infrared astronomy is to survey the sky to see what sources can be found.

We are constructing the one-meter Cassegrain balloon telescope shown in Fig. 1 to survey the northern hemisphere in seven frequency bands between 10 and 1000 cm^{-1}. The limiting flux sensitivity will be a few flux units (1 f.u. = 10^{-20} W/m^2 Hz), which is orders of magnitude more sensitive than previous surveys. The angular resolution will be 11 arc min.

Unusual features of the telescope include the use of diamond-machined metal optics (which were developed at the Lawrence Livermore Laboratory for the laser fusion program), Winston light concentrators (developed at the Argonne National Laboratory for particle detectors), and the composite bolometer detectors developed in our group. Great care has been taken to minimize the infrared background radiation falling in the detectors, and to discriminate against all telluric signal sources.

The design of the telescope is complete and fabrication is well advanced. The first balloon flight is expected in mid-1976.

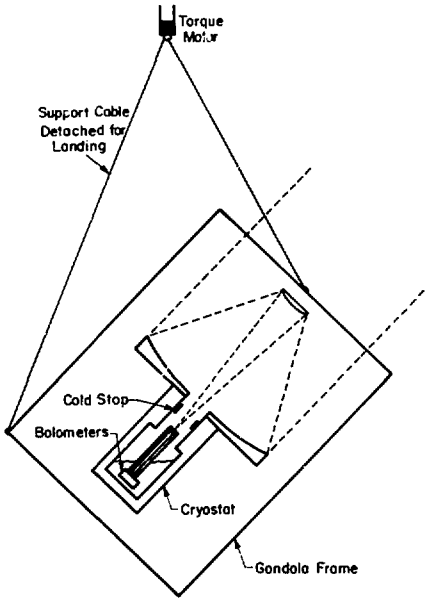

Fig. 1. Schematic diagram of the one meter Cassegrain balloon telescope. The telescope will be suspended at 45° to the zenith from a balloon at an altitude of ~ 100,000 ft. The rotation of the telescope at ~ 2 rpm combined with the rotation of the earth provides a scan of the northern sky in 24 hours of observing time.
(XBL 7510-7473)

*This project is partially supported by a grant from the Director of the LBL.

7. SURFACE MAGNETIC RESONANCE IN MnF_2

Robert B. Bailey and Paul L. Richards

A sensitive magnetic resonance spectrometer employing a 100-kg superconducting solenoid has been constructed in an attempt to detect surface spin states in the widely studied antiferromagnet MnF_2.

In zero field the bulk antiferromagnetic resonance (AFMR) frequency of 8.7 cm^{-1} is determined by the anisotropy and by nearest neighbor exchange interactions in the crystal. Surface spins experience smaller exchange forces and should have lower resonant frequencies. A simple theoretical model predicts that the collective surface excitations split off from the bulk mode by as much as 2.5 cm^{-1}. These surface modes should have penetration depths averaging five atomic layers and involve approximately 4×10^{15} spins per cm^2 of surface area. There has as yet been no experimental verification of surface spin states in any material.

Three different spectroscopic techniques have been used to study the MnF_2 spectrum. Fourier spectroscopy has been limited by the power available at 8.7 cm^{-1} from broadband thermal sources and by detector sensitivity. Antiferromagnetic resonances with a minimum of 6×10^{17} spins and linewidths less than the 0.1 cm^{-1} instrumental resolution were observable in the frequency range 6-9 cm^{-1}. Single crystals showed only the bulk resonance while a powder sample ground from the same crystal and with an effective surface area of 3000 cm^2 showed four additional modes between 7.4 cm^{-1} and 8.3 cm^{-1}. Some of these modes have the intensity expected of surface states. Positive identification can be made only on single crystal smaples where one surface at a time can be studied.

Bulk and surface spin wave modes in MnF_2 should both be split linearly with a g-factor of two in magnetic fields applied parallel to the c-axis of single crystal. We have studied the low frequency branch using field-swept microwave resonance techniques at 10 GHz and 150 GHz. At 150 GHz simple transmission measurements were capable of detecting 2×10^{14} spins in the bulk AFMR mode whose linewidth was 300 gauss. No additional resonances could be identified, suggesting that the surface modes are either substantially broadened, they penetrate fewer than five layers, or they lie very close to the bulk mode and cannot be distinguished from it.

At 10 GHz a bridge sepctrometer has been built with an AFMR sensitivity of 2×10^{12} spins for the measured bulk linewidth of 100 gauss. Operation of a superheterodyne bridge spectrometer at high microwave power levels, in fields up to 100 kg, and at modulation levels of several hundred gauss, places extreme demands on the mechanical stability of the microwave components and the frequency stability of the klystrons. The required spectrometer performance has nearly been achieved. Its sensitivity will be sufficient to detect surface modes penetrating only one atomic layer if their linewidths are no larger than a kilogauss.

8. ELECTRON SURFACE STATES IN LIQUID HELIUM

David K. Lambert and Paul L. Richards

A project has been initiated to study electrons trapped at the surface of liquid helium by a combination of electrostatic "image" attraction and short range "exchange" repulsion. Microwave studies of this system by others have yielded many new effects. These include the observation of transitions between the Stark-shifted energy levels, and electron cyclotron resonance.

By extending these measurements to higher frequencies we expect to be able to study the

surface plasma at higher densities so as to observe interaction effects, and to extend the measurements to other materials such as superfluid helium films, liquid and solid H_2 and liquid Ne.

9. SPECTROSCOPIC APPARATUS FOR THE INFRARED

Robert B. Bailey, James L. Bonomo, Ted S. C. Chang, Eugene E. Haller, David K. Lambert and Paul L. Richards

The tools available for infrared spectroscopy are being upgraded in several significant ways. 1) A new far infrared polarizing interferometer with a limiting resolution of 0.05 cm^{-1} has been constructed and is now ready for use in the frequency range from 3 to 100 cm^{-1}. 2) A far infrared molecular waveguide laser that is pumped from a well stabilized CO_2 laser is nearing completion. When finished this system will provide coherent monochromatic radiation at hundreds of far infrared frequencies. 3) A commercial near infrared Fourier spectrometer has been purchased from the BOCOM Corporation. This instrument will make possible high throughput Fourier spectroscopy at all infrared frequencies, with a limiting resolution of 0.07 cm^{-1}. An optical system has been designed for the interferometer that will allow it to be used for a wide variety of chemical and solid state physics problems.

10. JOSEPHSON EFFECT MILLIMETER WAVE RECEIVERS*

John C. Claassen, Paul L. Richards, Tak-Ming Shen, and Yuan Taur

The usefulness of superconducting Josephson junctions for low noise receivers of coherent millimeter wave radiation is being explored. Results of the program to date include: 1) the construction of a millimeter wave heterodyne mixer with the lowest noise yet achieved (T_m = 54°K at 36 GHz), 2) preliminary evaluation of a similar mixer at 140 GHz, and 3) operation of a Josephson junction parametric amplifier at 36 GHz with a gain of 12 dB. In each of these devices, the active element is a single point contact Josephson junction. Projects have been initiated to evaluate the performance of series arrays of thin film microbridges and also thin film superconducting bolometers as active elements in heterodyne mixers.

*This program is totally supported by the Office of Naval Research.

11. RESEARCH PLANS FOR CALENDAR YEAR 1976

Paul L. Richards

Semiconductor Physics. The investigations of electron-hole drops in Ge will be extended to include magnetic field effects and a search for surface plasmons on the γ drops. Photothermal ionization spectroscopy of ultrapure Ge will continue.

Infrared Astrophysics and Bolometer Development. The improved cosmic background experiment will be flown to search for deviations from the black body spectrum. The sky survey telescope will be flown for the first time and the first survey data analyzed. These flights will test the suitability of our new composite bolometer detectors for use in infrared satellites. Work will proceed on the development of optimized composite bolometers for operation at ^{3}He temperatures.

Resonance Spectroscopy. The new magnetic resonance spectrometer will be used to press the search for magnetic surface modes in MnF_2. The new polarizing interferometer and the CO_2 pumped molecular laser will be used to observe resonance effects of electrons trapped on the surface of liquid He.

Millimeter Wave Mixer Development. The point contact mixer at 140 GHz and the array Dayem bridge mixer at 36 GHz will be evaluated. Exploration of thermal mixers will continue.

Infrared Spectroscopy. The new BOCOM Fourier spectrometer will permit a number of new projects to be initiated in collaboration with campus and LBL groups. The first of these will be ATR spectroscopy of surface films related to pollution studies, the arc spectra of molecules of interest to high temperature chemistry, and the near infrared absorption in ultrapure Ge.

12. 1975 PUBLICATIONS AND REPORTS

Paul L. Richards and Associates

Journals

1. P. W. Anderson and P. L. Richards, Comment on "Search for the AC Josephson Effect in Liquid He", Phys. Rev. B 11, 2702 (1975) (LBL-2569).

*2. J. H. Claassen, Y. Taur, and P. L. Richards, Noise in Josephson Effect mm-Wave Mixers, IEEE Trans. Magnetics 11, 798 (1975).

*†3. J. H. Claassen, Y. Taur, and P. L. Richards, Noise in Josephson Point Contacts With and Without RF Bias, Appl. Phys. Letters 25, 759 (1974).

*4. Y. Taur and P. L. Richards, Relaxation Oscillations in Point Contact Josephson Junctions, J. Appl. Phys. 46, 1793 (1975).

5. D. P. Woody, J. C. Mather, N. S. Nishioka, and P. L. Richards, A Balloon-Based Measurement of the Cosmic Background Radiation, Bull. Am. Phys. Soc. (Ser. II) 20, 18 (1975) (LBL-3519).

6. W. E. Tennant, R. B. Bailey, and P. L. Richards, Magnetism and Magnetic Materials - 1974, AIP Conference Proceedings 24, 170 (1975).

7. R. L. Aurbach and P. L. Richards, Dynamic Jahn-Teller Effect in Mn^{3+}:Al_2O_3, Bull. Am. Phys. Soc. (Ser. II) 20, 435 (1975) (LBL-3581).

*8. P. L. Richards, High Frequency Josephson Devices, Bull. Am. Phys. Soc. (Ser. II) 20, 478 (1975).

9. P. L. Richards, A Measurement of the Spectrum of the Sub-Millimeter Cosmic Blackbody Radiation, Bull. Am. Phys. Soc. (Ser. II) 20, 540 (1975) (LBL-3701).

10. D. P. Woody, J. C. Mather, N. S. Nichioka, and P. L. Richards, A Measurement of the Spectrum of the Sub-millimeter Cosmic Background, Phys. Rev. Letters 34, 1036 (1975) (LBL-3588).

*11. P. L. Richards, J. H. Claassen, and Y. Taur, Josephson Effect MM-Wave Receivers, Low Temperature Physics - LT14, Krusius and Vuorio, eds. (North Holland/Elsevier, New York, 1975) V.4, p.238.

12. R. L. Aurbach and P. L. Richards, Far Infrared EPR of Al_2O_3:Mn^{3+} and γ-Irradiated Ruby, Phys. Rev. B 12, 2588 (1975) (LBL-3723).

13. J. Clarke, G. I. Hoffer, P. L. Richards, and N-H. Yeh, A Superconducting Transition Edge Bolometer, Low Temperature Physics - LT14, Krusius and Vuorio, eds. (North Holland/Elsevier, New York, 1975) V.4, p.226 (LBL-3906).

LBL and Other Reports

1. D. P. Woody, J. C. Mather, N. S. Nichioka, and P. L. Richards, A Comment on "Spectrum of the Cosmic Background Radiation Between 3 mm and 800 μm," LBL-3572, Dec. 1975.

**2. P. L. Richards and A. Yariv, Antenna Structures for Infrared Diodes, 1975 Materials Research Council Report.

3. P. L. Richards, Far Infrared Applications of a Large Millimeter Wave Telescope, LBL-3983, July 1975.

4. D. P. Woody, J. C. Mather, N. S. Nishioka, and P. L. Richards, Measurement of the Spectrum of the Submillimeter Cosmic Background, LBL-3588 (To be published in Proceedings of the International Conference on Infrared Physics).

5. Richard Lawrence Aurbach, Far Infrared Spectroscopy of Solids: I. Impurity States in Al_2O_3. II. Electron-Hole Droplets in Ge, (Ph.D. Thesis), LBL-4102, Sept. 1975.

6. David Paul Woody, An Observation of the Sub-millimeter Cosmic Background Spectrum, (Ph.D. Thesis), LBL-4188, Nov. 1975.

*Sponsored by the Office of Naval Research.
**Sponsored by the Advanced Research Projects Agency.
†Not previously listed.

b. Experimental Solid State Physics and Quantum Electronics

Y. Ron Shen, Principal Investigator

1. STUDY OF SELF-FOCUSING OF LIGHT

Eric G. Hanson* and Y. Ron Shen

Self-focusing of light in Kerr liquids has been extensively investigated, and the behavior in both the transient and steady state limits is now well understood. In the quasi-steady-state limit, the focusing behavior has been explained in detail by the moving focal spot model.[1] In the extreme transient limit, the effects are well explained by dynamic trapping.[2] In the intermediate range, detailed numerical calculations have been made. However, no experiments have yet been made to quantitatively check these predictions.

We have made a detailed investigation of the behavior of self-focusing in this intermediate range where the optical Kerr relaxation time is comparable to the laser pulse length. We have used a mixture of a nematic liquid crystal and a normal liquid as our Kerr liquid sample. This sample has a relaxation time which is significantly longer than response time of our photodiode and streak camera detectors. This insures that we can resolve the detailed time dependence of the focusing behavior. Furthermore, in this liquid the relaxation time varies strongly with sample temperature--from more than 4 times to less than 1/15 as long as our 20-nsec, single-mode laser pulse. This allows us to investigate the whole intermediate range, from the nearly transient limit to the nearly steady-state limit. We can do this without changing the sample or the optical imaging system, so we can quantitatively compare the behavior with different relaxation times.

With a long relaxation time, we see a smooth

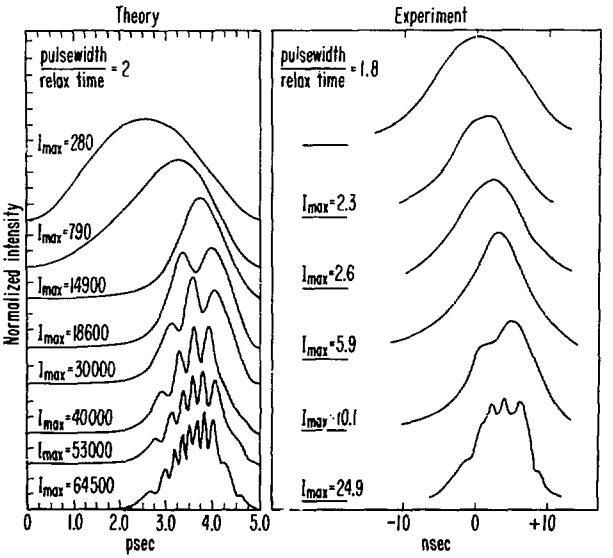

Fig. 1. Comparison between theory and experiment of the on-axis intensity pulses of the self-focused beam at various peak intensities I_{max}.
(XBL 764-2699)

horn-shaped pulse. In the intermediate range, we see a horn-shaped pulse containing fast intensity oscillations. These results are in good agreement with the predictions of numerical calculations (Fig. 1). In the short relaxation time limit, we see much more abrupt focusing, as expected for a moving focal region.

*Partially supported by the National Science Foundation.

1. M. M. T. Loy and Y. R. Shen, Phys. Rev. Lett. 22, 994 (1969); 25, 1333 (1970).
2. George K. L. Wang and Y. R. Shen, Phys. Rev. Lett. 32, 527 (1974).

2. NONLINEAR OPTICAL STUDY OF PRETRANSITIONAL BEHAVIOR OF NEMATIC COMPOUNDS*

Eric G. Hanson and Y. Ron Shen

We have shown by nonlinear optical measurements that liquid crystalline materials in their isotropic phase can have a large optical Kerr constant with a long relaxation time. Such characteristics result from the pretransitional behavior of the materials. The measurements provide a stringent test on the Landau phase transition model for liquid crystals. From these measurements, together with measurements on latent heat and anistropy in refractive indices, one can deduce values for a large number of characteristic material parameters aside from the measured ones. In order to understand how molecular structure affects the characteristics of liquid crystals, one would like to know these parameters for a group of compounds in a homologous series. We have made the first attempt to find these parameters from our nonlinear optical measurements for a homologous series; partial results are shown in Table 1.

*Partially supported by the National Science Foundation.

3. THEORETICAL INVESTIGATION OF NONLINEAR EXCITATION OF SURFACE POLARITONS

Francesco De Martini and Y. Ron Shen

Surface polaritons in solids have recently become a subject of great interest. These surface waves are usually studied optically by the attenuated total reflection method or by spontaneous Raman scattering. One would expect, however, that they could also be studied by nonlinear optical means. We have shown that by optically mixing two laser beams one can indeed generate surface polaritons in solids. In addition, we have worked out the first theory of nonlinear excitation of surface polaritons. This theory can be extended to other problems related to the interaction of surface and bulk waves and, therefore, is the basis of all calculations of nonlinear optics involving surface waves.

The nonlinearly excited surface waves can be detected either by the prism coupling method or by coherent light scattering. We have estimated in that GaP a surface polariton wave of about 1 W at 380 cm^{-1} can be generated by two 2 × 2-mm^2 dye laser beams of 40 kW each. A 40-kW probe beam can then yield a coherent scattering signal of 2 × 10^{-7} W. We have also made numerical estimates of the nonlinear excitation of surface exciton-polaritons and surface plasmons. In all cases, experiment appears to be feasible.

Table 1. Critical transition temperatures T_c, orientational relaxation times τ, and nonlinear susceptibilities $\chi_Q^{(5)}$ for various nematic liquid crystalline compounds.

Compound	R	T_c(°C)	$\tau(T - T_c)$ (10^{-8} sec-°K)	$\chi_Q^{(5)}(T - T_c)$ (10^{-10} su-°K)
C_4H_9- (C_6H_4) - CH:N - (C_6H_4) -R	CH_3	41.7	67	13.2
	C_2H_5	67.6	21	7.8
	CH_3	130.7	8.5	15
RO - (C_6H_4) - N_2O - (C_6H_4)-OR	C_2H_5	161.0	7.5	10.2
	C_5H_{11}	115.0	25	5.6
	C_6H_{13}	126.0	15	4.7
	C_7H_{15}	121.3	15	5.4

4. LASER TECHNOLOGY

Arnold J. Schmidt and Y. Ron Shen

a. Simultaneous Two-Wavelength Output of a Dye Laser

For a number of applications, such as difference frequency generation, two-photon spectroscopy, and excited-state spectroscopy, two tunable lasers are required. When both wavelengths are obtainable from the same lasing dye, however, a number of systems exist that can be used to generate two frequencies in one laser. We want to present a new method, which is extremely simple and easy to operate, of generating two frequencies.

Figure 1 shows the setup used. The N_2-laser pumped dye laser is of the usual design, consisting of a partial mirror, a transversely pumped dye cell, a telescope, and a grating. We place a rectangular glass wedge between the beam-expanding telescope and the grating; the wedge is placed in such a way that it intersects only the lower half of the beam. The angle of incidence is then different for the upper and lower half of the grating and the dye laser can operate on two wavelengths simultaneously.

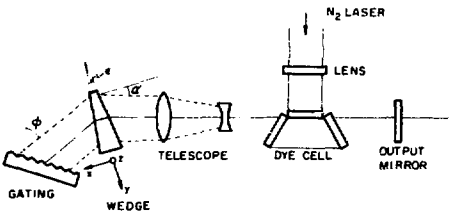

Fig. 1. Schematic diagram of the setup. (XBL 753-5998)

b. Generation of a Single Tunable Ultrashort Light Pulse

Single tunable ultrashort light pulses of high power are useful in a large number of scientific and technical applications. Such pulses are typically generated in one of two ways: (1) the mode-locked output of a Nd- or ruby laser, if necessary its second harmonic, pumps a dye laser of matching cavity length; or (2) a flashlamp-pumped, dye laser is passively mode-locked. One or more dye laser amplifiers usually are used to obtain appreciable powers. If the use of a single pulse is desired, a laser-triggered spark gap is commonly used to select one pulse from the train. In any case, the generation of such a pulse is a multistage operation and keeping its performance at an optimum is troublesome.

We constructed a system that can generate single, high power, tunable picosecond-pulses in a simple and convenient way. The pulse train from a mode-locked, flashlamp-pumped, dye laser is sent through a dye laser amplifier; the amplifier is pumped by a N_2-laser. The pulse length of an N_2 laser is typically a few nanoseconds and the fluorescence lifetime of laser dyes is of the same order, or less. Therefore, the amplifier has gain only for a few nanoseconds. One can then arrange the relative timing of the N_2-laser pulse with respect to the mode-locked train so that only one pulse in the train gets amplified.

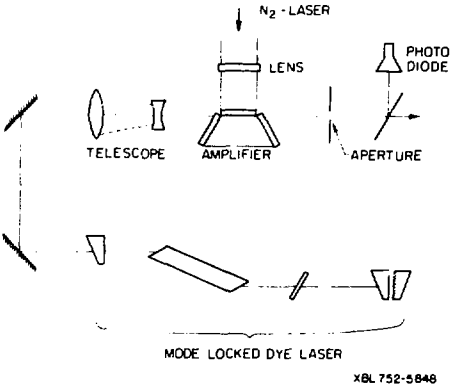

Fig. 2. Experimental setup for generation of a single tunable picosecond pulse.

Figure 2 shows details of the setup used. With an input mode-locked train of 2.5 J per pulse, we have obtain a single-pulse output of 100 J from the amplifier. The N_2-laser-pumped amplifier normally had an output of 300 J in the oscillator mode.

5. NONLINEAR OPTICAL STUDIES WITH FLASHPUMP TUNABLE DYE LASER

Robert W. Smith and Y. Ron Shen

Optical processes in solids have received a great deal of attention over the last decade since the advent of the laser, and especially with the recent development of the tunable dye laser. The dye laser offers us a tunable source with a highly directional beam, narrow bandwidth, and high average power which can be used to probe both linear and nonlinear optical processes. Our efforts this year have been directed toward acquiring these useful experimental tools.

Our particular interests have been in obtaining a high average power flashlamp-pumped dye laser (FL laser). From experience we know this type of dye laser can be easily tuned from 450 nm to 640 nm using various organic dyes. The FL laser can also be frequency-doubled or used as a pump for a parametric oscillator, thus extending to near

uv and near ir frequencies. The desired characteristics of the visible FL laser are: (1) pulse width of 1 μsec; (2) pulse energy of 50 mJ (narrow band); and (3) repetition rate of 10-20 pps. Such a laser then has a peak power of 50 kW and an average power of about 500 mW.

In order to obtain such an FL laser system and to acquire a thorough knowledge of its operation and construction, built our own. We carefully examined the commercially available units of Chromatix and Zeiss-Lambda Physik and modeled ours after theirs. At present our system is operational but not optimized. We will continue to develop the laser while we begin to use it in the following experiments.

The immediate use for the laser will be in an experiment dealing with the nonlinear coupling-to-surface polaritons in CdS; the experiment is to be performed with D. Bethune. Another possible experiment for the coming year is to look for induced absorption in CuO_2 at helium temperatures. This type of experiment will require two synchronized laser pulses at different frequencies. The generation of two such pulses is now being investigated. Beyond this, there is the possibility of using an FL laser to do Raman scattering in the blue region of the spectrum. In conclusion, the high average power FL laser is opening up many experimental possibilities for us.

6. INSTRUMENTATION OF N_2-LASER-PUMPED DYE LASER SYSTEM

Alex Jacobson and Y. Ron Shen

1. Pulsed N_2 Laser

We have spent a great deal of time on the design of the N_2 laser. Good nitrogen lasers are available commercially but duplicating them is of interest from the point of view of saving money and of developing the technological know-how of high speed gas discharge lasers.

We at first underestimated the difficulties involved because it is quite easy to build a 1.5-mJ, 200-kW laser operating at around 5 Hz. However much experience has shown that this class of simple lasers is not of much use experimentally. We have upgraded our technical effort to duplicate and then modify the most powerful commercial units.

a. Series Gas Discharge N_2 Laser. This system is essentially the same as the Molectron uV-1000 N_2 laser system. It should deliver 1 mW, 10-nsec pulses at 25 Hz, and 250 mW average power at 50 Hz. The laser tube is made of two aluminum bars with embedded stainless steel knife edge electrodes. Epoxy fiberglass is used for insulating top and bottom walls. The output window is a λ/10 quartz flat and the mirror is a λ/4 uV enhanced mirror. The tube is fed by a 100-cable transmission line that acts as a low-inductance dumping capacitor of c=0.05 μF, and Z = 148 ohms. The system is designed to be dc charged to 30 kV routinely. A water-cooled, three-electrode spark gap discharges a 0.09 μF capacitor into the transmission line to the laser tube. The gap electrodes are made of a machinable tungsten-nickel alloy. The gap can be pressurized from 0-50 psig and the electrode spacing is adjustable.

The design is based on the Molectron UV-1000 design of Woodward and Sasselt. It differs only in that (1) the laser tube is watercooled, (2) we use a 0.09-μF, 50-kV capacitor which has perhaps more inductance than their 0.05-uF, 30-kV one, and (3) we use a spark gap rather than an HY5 or HY3202 thyratron.

b. Traveling Wave Discharge N_2-Laser System. This system can produce 300-400 mW at 60 Hz and 1 mW peak power at lower rep rates. Based on the design of Fitzsimmons, the principal feature is an extremely compact, very low inductance capacitor used also as a transmission line. It is in a sandwiched parallel plate configuration using mylar as the insulator, oil as a corona arresting agent, and mechanical compression to maintain a uniform geometry. The value of the storage capacitor is 0.05 uF with an impedance of 0.04 ohms; the value of the transmission line impedance is 0.053 ohms. The matching of the storage capacitor impedance to the transmission line and the low value of the impedance enables the system to run at a voltage below 20 kV.

The system uses a two-electrode, water-cooled, pressurized copper spark gap. It is ac-resonantly charged and the laser pulses at suhmultiples of the line frequency chosen by an ic-controlled SCR in the primary of the high voltage transformer.

The laser tube is water cooled, the copper cooling tubes being the electrodes themselves. The N_2 gas is transversely flowed through small holes above and below the electrodes from low flow impedance input and output manifolds. The laser tube is electrostatically shielded from the ground planes running above and below it.

2. Dye Laser System

Using a preliminary N_2 laser, oscillator-amplifier systems of the design of Wallenstein and Hansch, and of Lawler, Fitzsimmons, and Anderson can be built. With suitable narrowing optics it should be possible to produce two 25-kW beams with bandwidths of 0.001 A or less in this way. Other multiple beam arrangements are possible. By using amplifiers, 5% total conversion efficiency should be possible in the narrowest bandwidths. The system will be even more versatile if the mirror can be removed from the N_2 laser without loss of power or beam quality.

Future Plans

With the advent of powerful tunable lasers we should be able to study tunable uv and ir generation, stimulated electronic Raman scattering, forbidden susceptibilities arising from quadrupole transition, and the effects related to excitation to high Rydberg and continuum states.

7. MEASUREMENT OF DISPERSION OF NONLINEAR OPTICAL SUSCEPTIBILITIES OF InAs, InSb, AND GaAs IN THE VISIBLE REGION

Don Bethune, Arnold J. Schmidt, and Y. Ron Shen

Many experimental and theoretical studies have been made recently of the dispersion of nonlinear susceptibilities of semiconductors, since there is the possibility of obtaining detailed information about their electronic structure from these studies. In the case of second harmonic generation, this can be seen from the theoretical expression of the second-order nonlinear susceptibility

$$\chi^{(2)}(2\omega) = C \int_{B.Z.} d^3k \sum_{vcc'} \frac{P_{vc}P_{cc'}P_{c'v}}{(E_{cv}-\hbar 2\omega)(E_{c'v}-\hbar\omega)}$$

A peak of $\chi^{(2)}$ corresponds, for example, to resonance of ω, or 2ω, or both with critical point transitions.

Using a flash-pumped dye laser (1-μsec pulse, 2-kw peak power) to produce reflected second harmonic light, we have measured $\chi^{(2)}_{(2\omega)}$ for three semiconductors (InAs, InSb, GaAs) between 2.0 and 2.7 eV, where all three crystals absorb strongly at both ω and 2ω. The results of these measurements are shown in Figs. 1-3, together with the values recently calculated from the empirical pseudopotential model by Fong and Shen,[1] and the linear susceptibilities previously measured for these crystals.

The observed structures can be related to some extent to large joint densities of states identified before in reflectivity measurements. Agreement with the computed values of Fong and Shen[1] is fair.

From our work, we realize that there are a number of difficulties with measurements of this type. The fact that both ω and 2ω are in the absorption region limits the overall conversion efficiency to very small values. On the other hand, using a fundamental laser beam of higher power or tighter focusing would cause local sample heating and surface damage. The low conversion results in small signals with large statistical fluctuations. The signal was also found to depend strongly on the laser mode structure. A high-power laser pulse with stable, single transverse mode, incident on a large sample area is probably

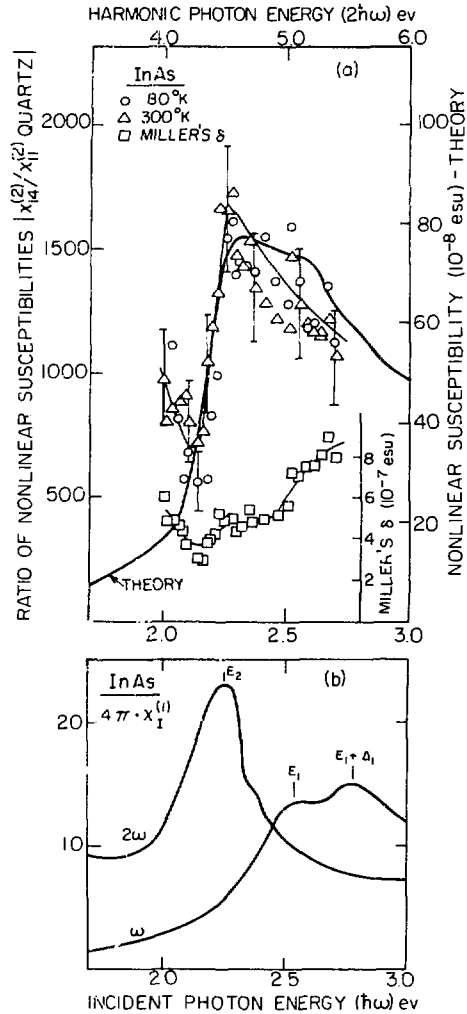

Fig. 1. (a) Experimental values of ratio of nonlinear susceptibilities $|\chi_{14}^{(2)}(\text{InAs})/\chi_{11}^{(2)}(\text{quartz})|$ at 80 and 300 K. The light curve is a rough fit to the data, and the heavier curve is the theoretical calculation of Fong and Shen (Ref. 25). Also shown are the values of Miller's Δ derived from the experimental data and the linear constants. (b) The imaginary dielectric constants $\varepsilon_I(\omega) = 4\pi\chi_I^{(1)}(\omega)$ and $\varepsilon_I(2\omega) = 4\pi\chi_I^{(1)}(2\omega)$ for InAs. The features corresponding to the E_1 and E_2 peaks are indicated.

(XBL 751-5528)

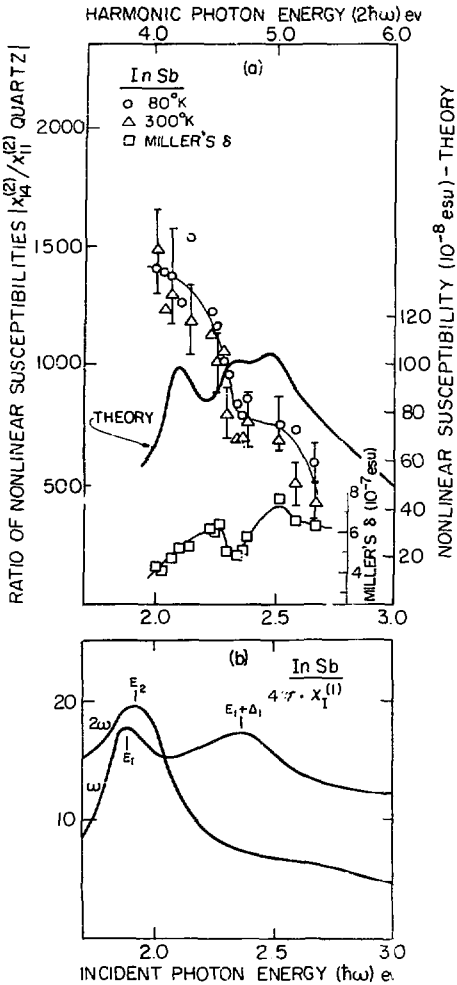

Fig. 2. (a) Experimental values of ratio of nonlinear susceptibilities $|\chi_{14}^{(2)}(\text{InSb})/\chi_{11}^{(2)}(\text{quartz})|$ at 80 and 300. The light curve is a rough fit to the data, and the heavier curve is the theoretical calculation of Fong and Shen (Ref. 25). Also shown are the values of Miller's Δ derived from the experimental data and the linear constants. (b) The imaginary dielectric constants $\epsilon_I(\omega) = 4\pi\chi_I^{(1)}(\omega)$ and $\epsilon_I(2\omega) = 4\pi\chi_I^{(1)}(2\omega)$ for InSb. The feature corresponding to the E_1 and E_2 peaks are indicated.

(XBL 751-5521)

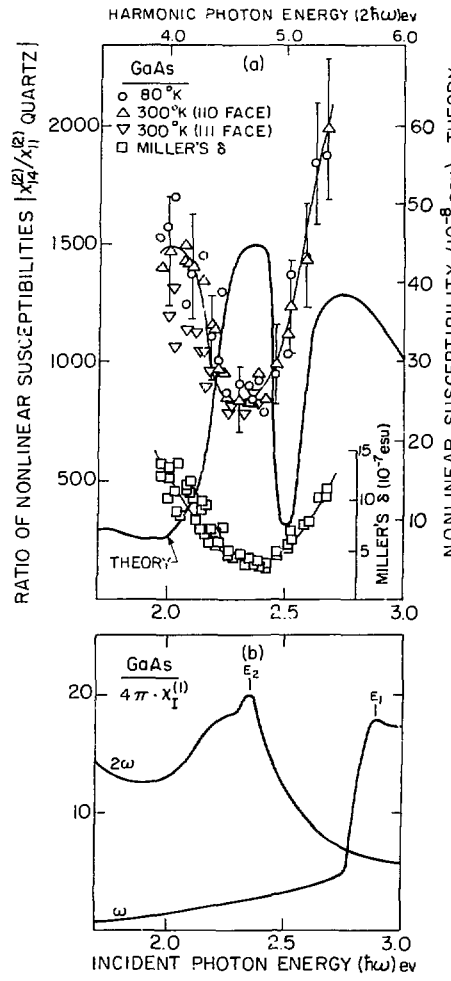

Fig. 3. (a) Experimental values of ratio of nonlinear susceptibilities $|\chi_{14}^{(2)}(\text{GaAs})/\chi_{11}^{(2)}(\text{quartz})|$ at 80 and 300 K. The light curve is a rough fit to the data, and the heavier curve is the theoretical calculation of Fong and Shen (Ref. 25). Also shown are the values of Miller's Δ derived from the experimental data and the linear constants. (b) The imaginary dielectric constants $\epsilon_I(\omega) = 4\pi\chi_I^{(1)}(\omega)$ and $\epsilon_I(2\omega) = 4\pi\chi_I^{(1)}(2\omega)$ for GaAs. The features corresponding to the E_1 and E_2 peaks are indicated.

(XBL 751-5530)

necessary for accurate and reliable measurements. Single picosecond laser pulses are preferable to avoid the effects of sample heating.

1. C. Y. Fong and Y. R. Shen, Phys. Rev. B12, 2325 (1975).

8. THEORETICAL STUDY OF DISPERSION OF NONLINEAR OPTICAL SUSCEPTIBILITIES OF SEMICONDUCTORS

Ching Y. Fong and Y. Ron Shen

Experimental results on dispersion of nonlinear optical susceptibilities $\chi^{(2)}$ of semiconductors have become available recently with the advent of tunable lasers. It is possible to correlate the structures in $\chi^{(2)}$ with the band structure effect.

The microscopic expression of $\chi^{(2)}$ can be obtained easily from the second-order perturbation theory. However, no realistic calculation of $\chi^{(2)}(2\omega)$ for a solid has ever appeared in the literature! The major difficulties come from the lack of detailed information about the band structure and the transition matrix elements. Recently, empirical pseudopotential band calculations have been very successful in reproducing the experimental linear reflectivities of solids, in particular the IV and III - V semiconductors.[16,17] The resulting band structure and momentum (transition) matrix elements can then be used for calculations of other properties. We have made calculations of $|\chi_{14}^{(2)}(2\omega)|$ with $0.05 \leq \hbar\omega \leq 3.0$ eV for GaAs, InAs, and InSb using the energies and the transition matrix elements directly obtained from the empirical pseudopotential band calculations. These results represent the most realistic treatment on the dispersion of $|\chi_{14}^{(2)}(2\omega)|$ up to now. As an example, we show in Fig. 1 the calculated $|\chi_{14}^{(2)}(2\omega)|$ of InAs in comparison with the experimental results.

9. EXCITATION OF DOMAIN PATTERN BY ACOUSTIC WAVES IN A NEMATIC FILM*

Ken Miyano and Y. Ron Shen

Study of acoustic wave propagation in a liquid crystal film is interesting in its own right as well as for its potential device applications. With sufficiently intense acoustic wave excitation, we have observed a domain pattern of induced molecular reorientation in a nematic film, as shown in Fig. 1a.

We prepared the liquid crystal film homeotropically aligned (optical axis perpendicular to the surface) between two glass plates. An interdigital surface wave transducer with a fundamental frequency of 12.3 MHz was evaporated on a Y-cut quartz plate. The surface wave generated by the transducer on the quartz plate was transferred to a glass plate through a water coupler and then propagated into the nematic film. The sound velocity in the film was measured by a Raman-Nath type diffraction measurement as a function of the film thickness (19 ~ 65 μm). Three modes were found in this thickness range. They agree with the theoretical prediction assuming the nematic liquid crystal was an isotropic low viscosity fluid.

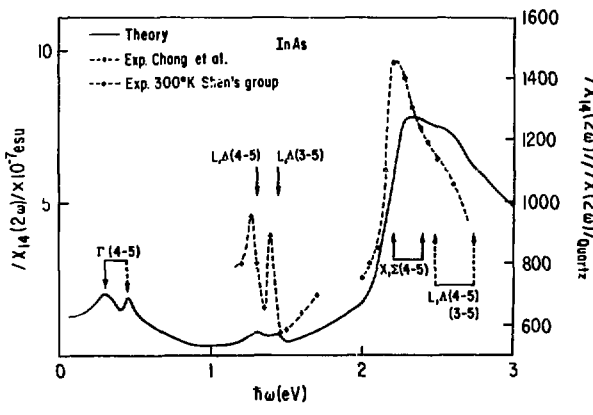

Fig. 1. Comparison of $|\chi_{14}^{(2)}(2\omega)|$ of InAs with available experimental data. (XBL 764-1167)

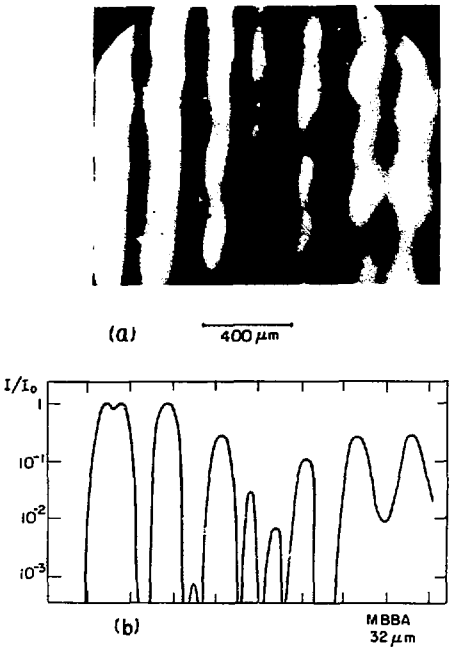

Fig. 1. (a) Stripes observed under crossed polarizers at the feeding edge. MBBA is homeotropically aligned and 32 μm thick. The polarizer axes are at 45° with respect to the stripes. (b) Model calculat-on of the transmission coefficient I/I_0 for (a). (XBB 751-8140)

A semi-periodic stripe pattern was observed (Fig. 1a) when the film was examined under crossed-polarizer microscope. The sound propagation direction was perpendicular to the stripes and the axes of the polaroids were at 45° with respect to the stripes. The domain pattern was apparently due to semi-periodic optical birefringence induced by the acoustic wave. Flow vortices were observed in the film and therefore flow reorientation of molecules is believed to be the cause of the induced birefringence. We calculated (1) acoustic streaming produced by the mixing of the propagating acoustic modes with their measured characteristics, (2) the molecular reorientation induced by the streaming, and (3) the transmission of light as a function of distance. The calculated result (shown in Fig. 1b) agrees very well with the experimental observation in Fig. 1a.

*Partially supported by a grant from the National Science Foundation.

10. WAVELENGTH MODULATION SPECTROSCOPY

Stanley E. Kohn, Jean-Paul Voitchovsky, Jean Camassel, and Y. Ron Shen

The Wavelength Modulation apparatus has been used in an extensive study of the optical properties of layer compounds. From a theoretical viewpoint, these compounds are of interest because of their apparent two dimensional nature. From an applied viewpoint, they are of interest because of observed Ovishinsky-type switching effects. Our interest has been focused on the GaS-GaSe alloy system. Together with the Solid State Theory group, we have made an extensive study of the electronic and optical properties of the GaS_xSe_{1-x} alloy system.

The layer structure of GaSe (and of GaS) is formed by a chain of four atoms: Se-Ga-Ga-Se (or S-Ga-Ga-S). The binding between the layers, that is, between the Se (S) atoms is probably due to van der Waals interaction. The binding is so weak that the crystals can frequently be cleaved by peeling off layers with Scotch tape.

The derivative reflectivity of GaSe and the theoretical spectrum calculated by M. Schlüter and M. L. Cohen, are shown in Fig. 1. The peaks have been labeled either G, GS, or S. Experimentally, we can divide the various structures into the following three classes on the basis of the magnitude of the energy shift of the structure with alloy composition: (1) type G structures, which have a small shift in energy (less than 10 MeV) as the composition is changed from GaS to GaSe; (2) type S structures, which have a large energy shift (about 700 MeV); and (3) Type GS structures, which have an intermediate shift (about 400 MeV). Theoretically, the transitions in the Brillouin Zone can be divided into these same three classes on the basis of the origin of the transition. Type G transitions originate primarily from states associated with the Ga-Ga bond. Since the Ga-Ga bond should be little affected by the alloy composition, these transitions should have a very small energy shift. Transitions labeled type S are determined predominantly by states localized around the anion, and those labeled type GS correspond to mixed anion character.

During the past year, progress has been made toward extending the wavelength modulation equipment to operate in the vacuum ultraviolet region of the spectrum from 1000 to 2000 Å. This region is of great interest because most II-VI and I-VII compounds have most of their valence to conduction band transitions in this wavelength region. To date, very little high-resolution, modulated optical spectroscopy work has been done in the vacuum ultraviolet. To extend our apparatus to work in this region, it is necessary to construct a large vacuum system for the optical system, and to build a small, high-power continuum light source in the vacuum uv. The light source has been built by designing a special water-cooled, deuterium lamp with a lithium fluoride window. This lamp has promise of being one of the most intense, compact, continuous light sources in this spectral region.

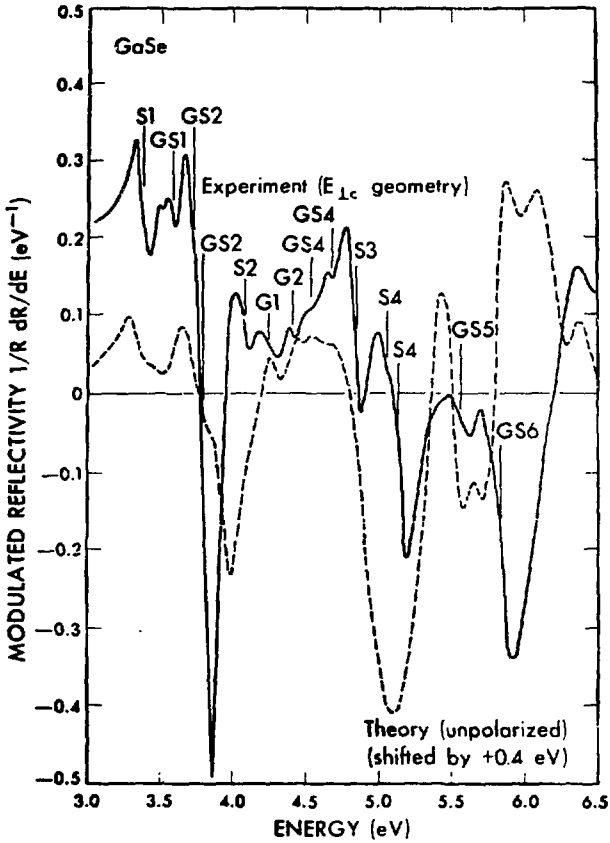

Fig. 1. Experimental derivative spectrum (full line) and theoretical derivative spectrum (broken line) of GaSe. (XBL 764-1168)

11. STUDY OF PHOTOLUMINESCENCE IN Cu_2O

Yves Petroff, Peter Y. Yu, Y. Ron Shen, and Nabil M. Amer

We have studied the photoluminescence spectrum of Cu_2O using a tunable dye laser. We found that most of the luminescence peaks can be identified as due to recombination of the 1s yellow exciton of Cu_2O or its phonon replica. These phonon replicas showed asymmetric broadening with increase in temperature. A few of the lines showed very strong temperature dependence disappearing rapidly at high temperature. The origins of these lines are still a matter of speculation. The luminescence excitation spectrum of Cu_2O is also presented and interpreted.

We have studied the problem of distinction between RRS and hot luminescence by investigating the temperature dependence of the lineshape of the Γ_{12}^{-} (110 cm^{-1}) mode when excited at the 1s yellow exciton. We found that above 4°K, the mode appeared to have a narrow symmetric line superimposed on a broader asymmetric base. The asymmetric part is typical of a phonon-assisted

luminescence line while the symmetric part is mainly due to RRS.

We have found two sharp luminescence lines at 198 and 200 cm^{-1} below the 1s yellow exciton line. These lines disappeared above 3°K. Their positions suggest that they are due to emission of $\Gamma_{12}^- + \Gamma_{25}^+$ and $2\Gamma_{12}^-$ phonons respectively in the recombination of the 1s yellow exciton, but such luminescence processes are not allowed by symmetry. The luminescence (and/or RRS) was quite efficient when the laser excitation was at resonance with the 1s yellow exciton. Their intensities varied superlinearly with the laser intensity and saturated quickly. We believe that these lines are due to emission of $\Gamma_{12}^- + \Gamma_{25}^+$ and $2\Gamma_{12}^-$ phonons respectively in the recombination of a weakly trapped 1s yellow exciton.

12. RESONANT RAMAN STUDIES IN Cu_2O NEAR THE PHONON-ASSISTED EXCITONIC ABSORPTION EDGE

Peter Y. Yu and Y. Ron Shen

Resonant Raman scattering in Cu_2O has been studied at low temperature in the vicinity of its phonon-assisted 1s yellow excitonic absorption edges using a cw continuously tunable dye laser. The multiphonon Raman modes which show resonance enhancement in this region are the following: $\Gamma_{12}^- + P$ (where P is an odd-parity optical phonon); $2\Gamma_{12}^- + P$ (where P is an acoustic or odd-parity optical phonon); $2\Gamma_{12}^- + 2LA$; and $4\Gamma_{12}^-$. The Raman cross sections of these modes have been calculated using perturbation theory. To explain the dispersion in the experimental cross section it was found necessary to introduce a wave-vector-dependent damping constant for the 1s yellow exciton. A simple model proposed earlier by Yu, Shen, Petroff, and Falirov was used to calculate this damping constant. Our result showed that the damping is predominantly due to intraband scattering via the longitudinal acoustic (LA) phonon. Good agreement was found between experiment and theory. Our results also indicate that the resonant three- and four-phonon Raman processes in Cu_2O in this region involve cascading of the photoexcited 1s yellow exciton with emission of phonon(s). The Raman frequencies of some of the modes of Cu_2O were found to depend on the incident laser frequency. The behavior of these dispersive Raman modes was found to be well explained within the above model and enabled us to determine directly the effective mass of the 1s exciton to be $(3.0 \pm 0.2)m_0$ (where m_0 is the free mass of the electron), as previously reported. Relative magnitudes of various 1s exciton-phonon interactions have also been obtained from our result.

13. RESONANT RAMAN SCATTERING AND FLUORESCENCE IN ANTIFERROMAGNETIC MnF_2

Nabil M. Amer, Tai C. Chiang, and Y. Ron Shen

We have made the first investigation of resonant Raman scattering and resonant fluorescence in a magnetically ordered crystal: MnF_2 in its antiferromagnetic phase. The experiment was done by using a dye laser to excite the crystal around two sharp excitonic absorption lines and their magnon sidebands. As expected, the two-magnon line showed a resonance enhancement at the magnon sidebands but not at the exciton lines, while the phonon modes would show resonance enhancement only at the exciton lines. Physically, the two-magnon resonant Raman process can be considered as a process in which a magnon-assisted absorption to the magnon sideband is immediately followed by a magnon-assisted emission. This indicates that for a given excitation frequency ω_ℓ, only those magnons whose frequencies $\omega_m(\vec{k})$ satisfy the relation

$$\omega_\ell = \omega_{ex}(\vec{k}) + \omega_m(-\vec{k}) = \omega_s + \omega_m(\vec{k}) + \omega_m(-\vec{k})$$

are being scattered in the resonant Raman process, where ω_{ex} and ω_s are the frequencies of the exciton and the scattered radiation respectively. Since the dispersion of $\omega_m(\vec{k})$ is appreciable, the above equation suggests that the observed Raman shift $\omega_\ell - \omega_s$ should vary with ω_ℓ. This is indeed what we have found experimentally. In the region where ω_ℓ is at resonance with two magnon sidebands simultaneously, we have even observed two two-magnon lines for the above reason. The resonant scattering mechanism described here is clearly different from the nonresonant two-magnon scattering mechanism described earlier by other.[1] A simple approximate derivation shows that, for a given ω_ℓ, the two-magnon resonant Raman cross-section is connected with the corresponding nonresonant one by:

$$\sigma_R \propto (d\sigma_{NR}/d\omega_s)(\omega_\ell - \omega_s = 2\omega_\ell - 2\omega_{ex}) .$$

This agrees quite well with the experimental data. Our resonant fluorescence results suggest that the excited excitons have in fact reached thermal equilibrium before they are radiatively recombined.

---

1. P. A. Fleury and R. Loudon, Phys. Rev. 166, 514 (1968).

14. RESONANT RAMAN SCATTERING IN SbSI NEAR THE ABSORPTION EDGE

Nabil M. Amer, Yves Petroff, Y. Ron Shen, and Peter Y. Yu

In the literature there exists a controversy about the nature of the fundamental absorption edge. Some authors believe it is due to phonon-assisted indirect transitions;[1] others think it is due to strong interaction between electrons and ~ 210 cm^{-1} phonons at the direct gap.[2] We have performed studies of resonant Raman scattering (RRS) around the absorption edge. We expected that if the gap is indirect only the appropriate two-phonon modes will show resonant enhancement, while if the gap is direct all allowed phonon modes will show resonant enhancement. Our results with the sample at liquid nitrogen tempera-

ture indicate that the latter is true. We have studied RRS with different polarization combinations for incident and scattered radiation and compared our results with the simple RRS theory at a direct gap.

We have also investigated RRS in SbSI below and above the ferroelectric phase transition. We found no obvious change in the RRS of any phonon mode. This suggests that the nature of the fundamental gap remains essentially unchanged at the phase transition, since otherwise some phonon modes would show different resonant enhancement behavior. The results are consistent with the band structure calculations which show that the top valence band and the bottom conduction band mainly come from the p band of I and the s band of Sb, respectively. In the phase transition, the S and Sb atoms are displaced but not the I atoms, and the band ordering around the gap remains the same. In the paraelectric phase, the soft mode shows a somewhat stronger resonant enhancement.

1. E. I. Gerzanich, Sov. Phys.-Solid State 9, 2358 (1968); V. M. Fridkin, E. I. Gerzanich, I. I. Groshik, and V. A. Lyakhovitskaya, JETP Lett. 4, 139 (1966).
2. A. Kh. Zeinally, A. M. Mamedov, and Sh. M. Efendiev, Sov. Phys.--Semiconductors 7, 271 (1973); H. Kamimura, S. M. Shapiro, and M. Balkanski, Phys. Lett. 33A, 277 (1970).

15. STUDY OF RESONANT RAMAN SCATTERING IN GaS_xSe_{1-x} MIXED CRYSTALS

Jean Camassel, Tai C. Chiang, Y. Ron Shen, Jean-Paul Voitchovsky, and Nabil M. Amer

Resonant Raman scattering (RRS) around exitonic transitions in solids has been a subject of extensive investigations in recent years. Among various semiconductors, the layer compounds GaS_xSe_{1-x} seem to be particularly worth studying. They have direct as well as indirect exciton states. For sulfur concentration $x \leq 0.3$, the exciton states at liquid nitrogen temperature lie within the tuning range of a Rhodamine GG, Rhodamine 110, and Coumarine 6 dye lasers. This makes the RRS measurements relatively easy. We have studied the resonant enhancement of the various phonon modes in these crystals as a function of sulfur concentration. In particular, RRS up to four phonons in pure GaSe and RRS up to two phonons in the mixed crystals have been observed. We find the dispersion of the RRS is dominated by resonances with the exciton states and the results can be explained quite satisfactorily by a simple cascade theory.

16. RESEARCH PLANS FOR CALENDAR YEAR 1976

Y. Ron Shen

We shall continue our study on self-focusing of light. After completion of the measurements on self-focusing from the steady-state to the transient limit, we will shift our emphasis to the polarization dependence of self-focusing and will start working on self-focusing in active media. The latter problem is important for understanding high-power beam propagation in a laser amplifier. We shall explore the possibility of using liquid crystals as an optical pulse shaper or mode-locker in laser applications. Using tunable dye lasers, we shall try to excite surface polaritons in solids and evaluate the potential of using this method for surface study. We shall continue our laser development and apply the pulsed tunable lasers to problems on nonlinear excitations in solids and nonlinear optical spectroscopy in general. We plan to extend our optical derivative spectroscopy technique to the far uv region where the optical properties of solids are generally more complicated and more interesting. The possibility of using the technique to study surface contamination and interface properties will also be explored. Our program on resonant Raman scattering and fluorescence will also be continued with more emphasis on magnetic crystal and semiconductors, and on nonlinear optical scattering. A new program on study of laser interaction with molecular beams will be initiated in collaboration with Yuan T. Lee's group. Emphasis will be on the understanding of the multiphoton molecular dissociation process applied to isotope separation.

17. 1975 PUBLICATIONS AND REPORTS

Y. Ron Shen and Associates

Journals and Books

1. Y. R. Shen, Stimulated Raman Scattering, in "Light Scattering in Solids", edited by M. Cardona, (Springer-Verlag, Berlin, 1975) (LBL-2709).

2. Y. R. Shen, Self-Focusing of Light: Review of Experimental Results and Physical Interpretations, Prog. in Quan. Elec. 4, 1 (1975) (LBL-2703).

3. N. M. Amer, Y. S. Lin, and Y. R. Shen, The Temperature Dependence of Rayleigh-Wing Scattering from Liquid Crystalline p-Methoxy-Benzylidene-p-n-Butylaniline, Sol. St. Comm. 16, 1157 (1975) (LBL-2529 Rev.).

4. N. M. Amer, T. C. Chiang, and Y. R. Shen, Two-Magnon Resonant Raman Scattering in MnF_2, Phys. Rev. Lett. 34, 1454 (1975) (LBL-3747).

5. D. Bethune, A. J. Schmidt, and Y. R. Shen, Dispersion of Nonlinear Optical Susceptibilities of InAs, InSb, and GaAs in the Visible Region, Phys. Rev. B11, 3867 (1975) (LBL-3585).

6. A. Mysyowicz, A. J. Schmidt, P. Robrish, H. Rosen, and Y. R. Shen, Luminescence of CdS Generated by High-Intensity Excitation Below the Bandgap, Sol. St. Comm. 17, 523 (1975) (LBL-3544)

7. A. J. Schmidt, Generation of a Single Tunable Ultraviolet Light Pulse, Optics Comm. 14, 287 (1975) (LBL-3731).

8. P. Y. Yu and Y. R. Shen, Resonance Raman Studies in Cu_2O: 1. The Phonon-Assisted 1s Yellow Excitonic Absorption Edge, Phys. Rev. B12, 1377 (1975) (LBL-3901).

9. A. J. Schmidt, Simultaneous Two Wavelength Output of an N_2 Pumped Dye Laser, Optics Comm. 14, 294 (1975) (LBL-3765).

10. Y. Petroff, P. Y. Yu, and Y. R. Shen, Study of Photoluminescence in Cu_2O, Phys. Rev. B12, 2488 (1975) (LBL-3709).

11. C. Y. Fong and Y. R. Shen, Theoretical Studies of the Dispersion of the Nonlinear Optical Susceptibilities in GaAs, InAs, and InSb, Phys. Rev. B12, 2325 (1975) (LBL-3783).

12. J. Camassel, D. Auvergne, and H. Mathieu, Temperature Dependence of the Band Gap and Comparison with the Threshold Frequency of Pure GaAs Lasers, J. Appl. Phys. 46, 2683 (1975) (LBL-3557).

Conferences

1. D. Bethune, A. J. Schmidt and Y. R. Shen, Dispersion of Nonlinear Optical Susceptibilities of InAs, InSb, and GaAs, Deutsche Physikalische Gesellschaft E. V., (Sept. 1, 1975) in München, LBL-3730 Abstract.

2. A. J. Schmidt, Generation of a Single Tunable Ultrashort Light Pulse, Deutsche Physikalische Gesellschaft E. V., (Sept 1, 1975) in München, LBL-3731 Abstract.

3. A. Mysyrowicz, A. J. Schmidt, Y. R. Shen, P. Robrish, and H. Rosen, Luminescence of CdS Generated by a Tunable Dye Laser, 1975 International Conference on Luminescence, (Sept. 1, 1975) in Tokyo, Japan, LBL-3909 Abstract.

4. N. M. Amer, T. C. Chiang, and Y. R. Shen, Resonant Raman Scattering and Fluorescence in Antiferromagnetic MnF_2, Third International Conference on Light Scattering in Solids (July 1975) in Brazil, LBL-3760 Abstract.

5. P. Y. Yu, N. M. Amer, Y. Petroff, and Y. R. Shen, Resonant Raman Scattering in SbSI Near the Absorption Edge, Third International Conference on Light Scattering in Solids (July 1975) in Campines, Brazil, LBL-3779 Abstract.

6. Y. Petroff, C. Carillon, N. M. Amer, and Y. R. Shen, Some Aspects of Resonant Raman Scattering and Luminescence in Cu_2O, Third International Conference on Light Scattering in Solids, (July 1975), in Campines, Brazil, LBL-3772 Abstract.

LBL Reports

1. J. Camassel and D. Auvergne, Temperature Dependence of the Fundamental Edge of Germanium and Zincblende Type Semiconductors, LBL-3553.

2. Y. R. Shen, Comment on Resonant Scattering or Absorption Followed by Emission, LBL-3577.

3. K. Miyano and Y. R. Shen, Domain Pattern Excited by Surface Acoustic Waves in a Nematic Film, LBL-4155.

4. J. A. Stokes, Effects of Uniaxial Stress on the E_0' Peaks in the Derivative Reflectivity of GaAs, LBL-3707.

5. J. Camassel, T. C. Chiang, Y. R. Shen, J. P. Voitchovsky, and N. M. Amer, Multiphonon Resonant Raman Scattering in GaSe, LBL-4522.

6. F. DeMartini and Y. R. Shen, Nonlinear Excitation of Surface Polaritons, LBL-4511.

7. Y. R. Shen, Nonlinear Optics in One-Dimensional Periodic Medium, LBL-4180.

8. Y. R. Shen, Nonlinear Optical Study of Pretransitional Behavior in Liquid Crystalline Materials, LBL-4178.

9. M. Schluter, J. Camassel, S. Kohn, J. P. Voitchovsky, Y. R. Shen, and M. L. Cohen, Optical Properties of GaSe and $GaS_x Se_{1-x}$ Mixed Crystals, LBL-4184.

10. Y. R. Shen, Recent Advances in Nonlinear Optics, LBL-3792.

11. N. M. Amer, P. Y. Yu, Y. Petroff, and Y. R. Shen, Resonant Raman Scattering in SbSI Near the Absorption Edge, LBL-3779.

12. Y. R. Shen, Resonant Raman Scattering Near Excitonic Transitions, LBL-4170.

13. Y. R. Shen, Some Fundamental Aspects of Nonlinear Optics, LBL-4179.

c. Research on Superconductors and Superconducting Devices

John Clarke, Principal Investigator

1. 1/f NOISE IN METAL FILMS

John Clarke and Richard F. Voss

The accuracy of most measurements at low frequencies is limited by "flicker noise" - noise whose power spectrum varies approximately as 1/f, where f is the frequency. Thus an understanding of the physical origins of 1/f noise is not only of theoretical interest but is of great practical importance. We have made considerable progress in understanding the mechanism of the noise in metal films, and we can make quantitative predictions of its magnitude. The theoretical model is quite general, and we have to be able to apply suitable modifications of it to other systems.

Our theory assumes that the noise arises from equilibrium temperature fluctuations in the film. These fluctuations in turn produce resistance fluctuations provided that the temperature coefficient of resistance, $\beta = (1/R)dR/dT$ is non-zero. When a steady current is passed along the film, the resistance fluctuations give rise to voltage fluctuations or "1/f noise". The mean square voltage fluctuation is thus given by

$$\langle(\Delta V)^2\rangle = \int S_V(f)df = \beta^2\bar{V}^2\langle(\Delta T)^2\rangle = \beta^2\bar{V}^2k_BT^2/C_V ,$$

where $\bar{V}$ is the mean voltage across the film, C_V is the heat capacity of the film, and $S_V(f)$ is the power spectrum of the voltage fluctuations. The dependence of $S_V(f)$ on β^2, $\bar{V}^2$ and C_V has been experimentally demonstrated. The transport of heat in the film obeys a diffusion equation, which introduces a frequency dependent correlation length $\lambda(f) \approx (D/f)^{1/2}$ where D is the thermal diffusivity. As a consequence, the noise should be spatially correlated over distances of order $\lambda(f) \sim 1$ mm at 1 Hz. This spatial correlation has been experimentally observed, and has the predicted form. Finally, by introducing a 1/f region into $S_V(f)$ with appropriate cut-offs at low and high frequencies, we can predict the absolute magnitude of the voltage noise power spectrum:

$$S_V(f) \approx \frac{\bar{V}^2\beta^2k_BT^2}{C_V[3 + 2\ell n(\ell_1/\ell_3)]f} , \qquad (1)$$

where ℓ_1 and ℓ_3 are the maximum and minimum dimensions of the sample. Equation (1) is in excellent agreement with the measured power spectra of a large number of metal samples.

We have also investigated both theoretically and experimentally the nature of the temperature fluctuations. In the usual Brownian motion treatment, the fluctuations are temporally and spatially uncorrelated; however, this model does not produce a 1/f power spectrum. We have found that a model in which the fluctuations are spatially correlated can produce a 1/f power spectrum of the appropriate magnitude. The two types of fluctuations can be experimentally distinguished by applying either a delta function or a step function of power to the sample and measuring the resulting change in resistance with time. The Fourier transforms of the responses to the delta and step functions are the power spectra for the uncorrelated and correlated cases respectively. In Fig. 1 we plot $\log_{10}S(f)$ versus $\log_{10}(f)$ for the measured noise, the step function response, and the delta function response. The delta function response is quite different from the measured power spectrum, while the step function response is in excellent agreement with the measured power spectrum, with no fitted parameters.

The implications of this measurement are being investigated, and the extension of the fluctuation model to other systems is being studied.

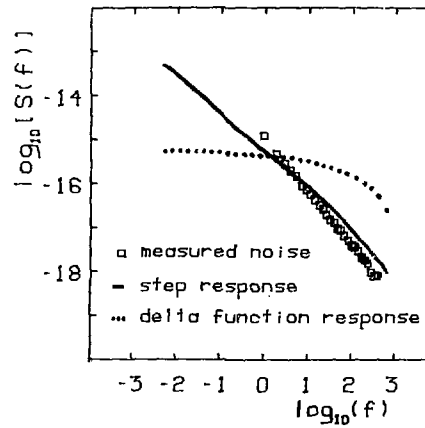

Fig. 1. S(f) from cosine transform of temperature response to delta function (----) and step function (——). The measured power spectrum is also shown (□). (XBL 758-6842)

2. 1/f NOISE IN AN EQUILIBRIUM SYSTEM

John Clarke and Richard F. Voss

In the past decade, a number of theories of 1/f noise have implied that the noise is a non-equilibrium phenomenon. Thus one theory suggests that the heating of the sample by the current passing through it gives rise to the noise, while another suggests that the current produces a turbulence in the electron gas that generates the noise. On the other hand, our theory of 1/f noise is an equilibrium theory. The noise is generated by the fluctuations that occur in a system in thermal equilibrium. In the usual current-biased measurement the current probes these equilibrium fluctuations but in no way generates them. It is therefore of great importance to distinguish

between these two types of theory. We have performed an experiment that clearly indicates that 1/f noise is an equilibrium phenomenon. Thus any theory that is inherently non-equilibrium is incorrect.

The experiment measures the fluctuations in the mean square Johnson noise voltage of a tiny bridge of InSb. In an equilibrium model, the resistance R of the bridge should fluctuate with a 1/f power spectrum whether or not a current flows through it. If this hypothesis is correct, the mean square voltage $\langle \bar{V}^2 \rangle = 4k_B TR\delta f$ should also exhibit a 1/f spectrum even in the absence of a current (δf is the bandwidth). In our experiment, the 1/f power spectrum was first measured in the usual way by passing a current through the sample. The normalized spectrum $S_V(f)/\bar{V}^2$ is shown as a continuous line in Fig. 1. The current was then turned off. The Johnson noise was amplified, passed through a band pass filter, and squared. The power spectrum of the squared voltage is shown as a series of open squares in Fig. 1. The agreement between the two curves at low frequencies is excellent. As a check on the measurement apparatus, the bridge was replaced by a large metal film resistor (of the same resistance) in which the fluctuations should be quite negligible. The resultant power spectrum was white down to 10^{-2} Hz.

Similar results were obtained with a thin metal film. These experiments convincingly demonstrate that 1/f noise is an equilibrium effect.

3. 1/f NOISE IN THIN FILMS AT THE SUPERCONDUCTING TRANSITION

John Clarke and Thomas Y. Hsiang

In order to further test the validity of our thermal fluctuation model of 1/f noise, we have measured the power spectra of voltage fluctuations in current-biased films at the superconducting transition. These experiments enable us to make large variations in the relevant parameters. The results lend very strong support to the thermal fluctuation theory.

We first investigated the power spectra of tin films evaporated on glass slides. The samples were mounted in a vacuum can immersed in liquid helium. The power spectra were always 1/f. According to the theory, the power spectra $S_V(f)$ should be proportional to $\beta^2\bar{V}^2/\Omega$, where Ω is the sample volume. We show in Fig. 1(a) the dependence of $S_V(f)$ on $(dR/dT)^2$; and in Fig. 1(c) the dependence of $S_V(f)$ on $\bar{V}^2$. The value of dR/dT was varied by

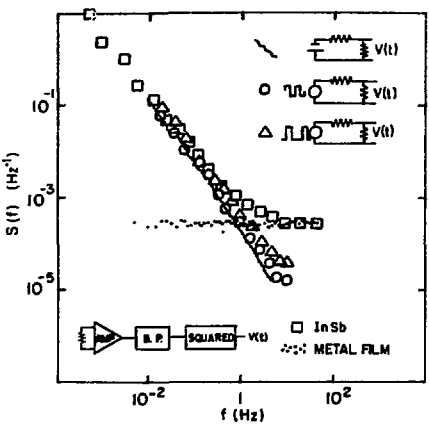

Fig. 1. InSb bridge: $S_V(f)/\bar{V}^2$ using dc bias (——); Johnson noise measurement, $S_p(f)/P^2$ (□). (XBL 755-6349)

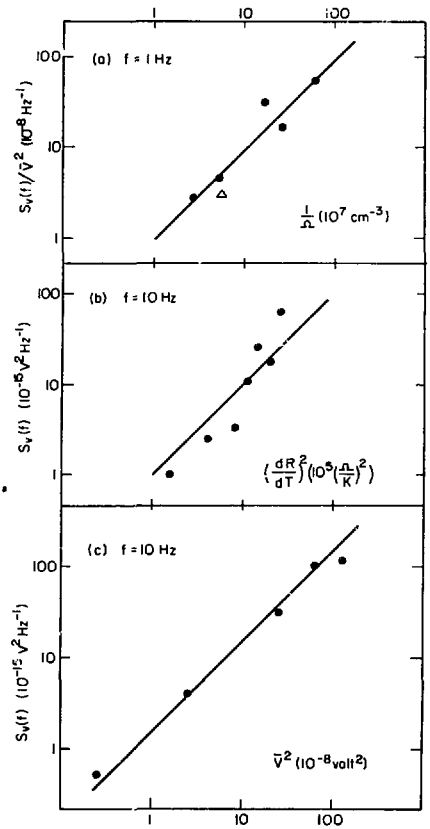

Fig. 1. a) $S_V(1)/\bar{V}^2$ versus Ω^{-1};
b) $S_V(10)$ versus $(dR/dT)^2$;
c) $S_V(10)$ versus $\bar{V}^2$. (XBL 751-5427A)

biasing the films at different points on the superconducting transition curve or by applying a magnetic field. The scaling of $S_V(f)$ with $\beta^2\tilde{V}^2/\Omega$ is in good agreement with theory. We next made samples in which a 50 Å film of aluminum was deposited on the substrate prior to the tin evaporation. The aluminum greatly enhanced the thermal coupling between the film and the substrate. As a result the power spectra flattened at low frequencies: the heat conduction is no longer predominantly along the film but rather between the substrate and the film. It can be shown that as a result the spectrum will flatten at low frequencies, and the observed flattening further supports the diffusion mechanism.

The thermal origin of the noise was further demonstrated by the observation of spatial correlation in the noise. The correlation observed for samples without (○) and with (●) an aluminum underlay is shown in Fig. 2, and is in excellent agreement with our expectations.

In the absence of the underlay, the observed spectrum is quantitatively predicted by $S_V(f) = \tilde{V}^2\beta^2 k_B T^2/C_V[5 + 2\ln(\ell_1/\ell_3)]f$. This is a very convincing demonstration of the validity of this expression. When a tin film is cooled from room temperature to the mid-point of the superconducting transition, the value of $S_V(f)$ increases by about 9 orders of magnitude, yet at each temperature is accurately predicted by the theory.

We have demonstrated the validity of the thermal diffusion model of 1/f noise at low temperatures. This work has already resulted in the development of a very sensitive superconducting bolometer.

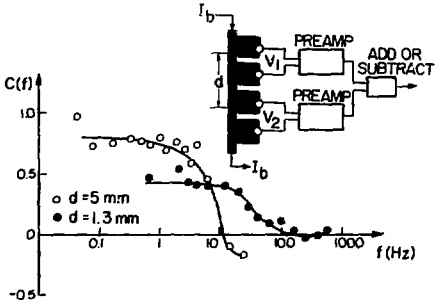

Fig. 2. C(f) versus f for tin films without (○) and with (●) aluminum underlay. Inset shows experimental configuration. (XBL 751-5428A)

4. POWER SPECTRA OF FLUCTUATIONS OF PARTICLES IN BROWNIAN MOTION

John Clarke and Richard F. Voss

Brownian motion has been extensively studied both theoretically and experimentally. However, relatively little attention has been paid until recently to the question of number fluctuations. We have experimentally studied the fluctuations of the number of particles in a small volume by direct measurement of the power spectrum. The results are in good agreement with theory.

In our experiment, a solution of polystyrene spheres in Brownian motion was confined between two microscope slides and illuminated with a collimated beam of laser light. The fluctuations in the intensity of the scattered light were measured with a photomultiplier, and their power spectrum taken. Two typical normalized power spectra $S_I(f)/\bar{I}^2$ ($\bar{I}$ is the average scattered intensity as shown in Fig. 1. In Fig. 1(b), the slope is -3/2 over five decades of frequency, and the magnitude is as predicted by the theory of Brownian motion. In Fig. 1(a), the scattering volume has been reduced by about four orders of magnitude. The relative power spectrum is therefore larger by the same factor. In addition, the spectrum flattens at frequencies below about 10^{-2} Hz. This flattening is also predicted by the theory.

These results represent the first detailed experimental verification of the number fluctuations predicted by Brownian motion theory. It is very important to realize that the spectrum is *not*

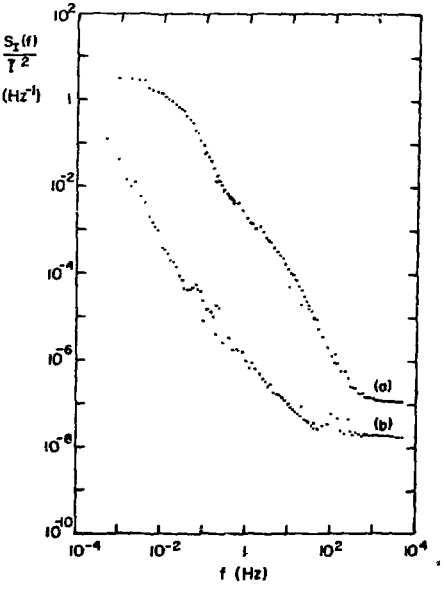

Fig. 1. Power spectrum $S_I(f)/\bar{I}^2$ for light scattered from two volumes of different sizes: In (a) the volume is about 10^4 times smaller than in (b). (XBL 751-5679)

1/f over any sizeable range of frequencies. This result graphically demonstrates that the usual theory of Brownian motion, in which the fluctuations are uncorrelated in space and time, cannot account for 1/f noise in solids.

5. IMPROVEMENTS IN dc SQUIDS*

John Clarke, Wolfgang M. Goubau and Mark B. Ketchen

The use of Superconducting Quantum Interference Devices (SQUIDS) for the detection of extremely small changes in magnetic field is currently of interest in certain areas of medical and geophysical research. We have made further improvements in the sensitivity and long term stability of our thin film tunnel junction dc SQUID that make it the most sensitive presently available. The problems of low frequency noise and long term drift are of particular concern in geophysical applications. We have also studied the most efficient ways to couple signals to the SQUID via coupling coils.

In many applications, it is desirable to couple the signal to the SQUID by means of a coil wound on to the SQUID, and we have analyzed in considerable detail the various parameters involved. As a result, we have been able to achieve very efficient coupling. A convenient way to characterize the sensitivity of a SQUID is in terms of the parameter $\langle \phi_N^2 \rangle / 2\alpha^2 L$, where $\langle \phi_N^2 \rangle$ is the mean square flux noise of the SQUID per $\sqrt{Hz}$, α is the coupling coefficient between the coil and the SQUID, and L is the SQUID inductance. The parameter $\langle \phi_N^2 \rangle / 2\alpha^2 L$ represents the energy resolution of the SQUID per unit bandwidth, and takes into account the coupling efficiency of the coil and SQUID. In Fig. 1 we plot the noise power spectrum of a typical SQUID. The left-hand axis is labeled in terms of $\langle \phi_N^2 \rangle$ in units of ϕ_0^2, and the right-hand axis is labeled in units of $\langle \phi_N^2 \rangle / 2\alpha^2 L$. In the white noise region, the rms noise is 3.5×10^{-5} ϕ_0 $Hz^{-1/2}$ or 8×10^{-30} J/Hz. The noise is limited by Johnson noise in the SQUID. This energy resolution is the best reported for any type of SQUID. At frequencies below 10^{-2} Hz, the power spectrum is approximately 1/f. The 1/f noise is significantly lower than that reported in other devices.

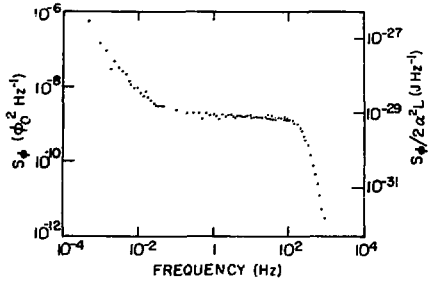

Fig. 1. Power spectrum of SQUID. (XBL 7511-9432)

The long term drift of the device over a period of 20 h is shown in Fig. 2. The drift is about 2×10^{-5} ϕ_0 h^{-1}, significantly less than other reported values.

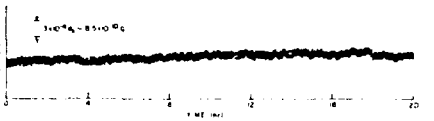

Fig. 2. Long term drift of SQUID. (XBL 753-6016)

*Work supported in part by the U.S.G.S.

6. GEOPHYSICAL MEASUREMENTS WITH SQUIDS*

John Clarke, Thomas Gamble and Wolfgang M. Goubau

We have constructed, calibrated, and field-tested a 3-axis magnetometer. Three SQUIDS are mounted orthogonally in a lightweight portable fiberglass cryostat, with the electronics mounted on the top (Fig. 1). The design of the electronics has been optimized to give a dynamic range of $\pm 10^{-3}$ G, a frequency response of 0-5 kHz, and a slewing rate of 3×10^{-2} G sec^{-1}.

In collaboration with Professor H. G. Morrison and his students we have used the magnetometer to record magneto-telluric data at numerous sites of geothermal exploration in Grass Valley, Nevada. In these measurements, we simultaneously record orthogonal components of the natural fluctuations in the magnetic and electric fields at the earth's surface. These fluctuations originate in the magnetosphere. From the data we obtain a measure of the electrical conductivity of the ground below the surface. The probing depth is the skin depth at the frequency of the radiation, typically 5 km at 0.1 Hz. By searching for layers of anomalously

Fig. 1. 3-axis SQUID magnetometer in use in the field. (CBB 7512-9227)

high conductivity we hope to locate sources of geothermal activity. Preliminary analysis of our data suggests that such layers can be readily detected. Thus this technique may become an important tool in locating geothermal sources.

We also used our magnetometer in conjunction with a commercial SQUID to investigate gradient fluctuations in the earth's magnetic field. The two cryostats were placed 170 m apart and the two outputs subtracted to give the difference between the field fluctuations at the two locations. We measured the fluctuations between 0.03 Hz and 3 Hz. A sample of the gradient fluctuations is shown in Fig. 2. The rms fluctuation of the subtracted signal was about 4×10^{-8} G, corresponding to a gradient of 2.4×10^{-12} G cm^{-1}. Most of the gradient fluctuations were at frequencies between 0.1 and 0.2 Hz. This gradient measurement appears to be the most sensitive yet made with such a short baseline.

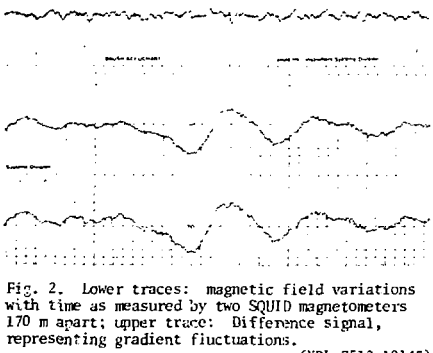

Fig. 2. Lower traces: magnetic field variations with time as measured by two SQUID magnetometers 170 m apart; upper trace: Difference signal, representing gradient fluctuations.
(XBL 7512-10145)

*Work supported in part by the U.S.G.S.

7. THEORY OF THE dc SQUID

John Clarke and Claudia Tesche

The dc SQUID is a very sensitive detector of magnetic fields. In order to optimize its sensitivity, a detailed knowledge of its operation and noise limitations is necessary. Since neither the theory of operation nor the noise limitations have previously been analyzed in detail, we have undertaken such a study.

The dc SQUID consists of two Josephson junctions mounted on a superconducting ring. When the junctions are biased at a non-zero voltage by a dc current, the critical current of the junctions and hence the average voltage across them are periodic in the flux applied to the SQUID, with period ϕ_0. A set of differential equations has been developed describing the time development of the circulating current j around the SQUID and the voltage v across the SQUID as functions of SQUID inductance L, resistance R, critical current I_c, bias current I_b, and applied flux ϕ_a. The self-induced flux generated by the circulating current was explicitly included. These equations cannot be solved analytically; the LBL 7600 computer was used to compute the average circulating current $\langle j \rangle$ and average voltage $\langle v \rangle$ for various values of the SQUID parameters. From these results we computed the critical current and current-voltage characteristics for the SQUID as a function of applied flux. The variation of critical current with applied flux for several values of LI_c/ϕ_0 is shown in Fig. 1.

We have made preliminary calculations of the effects of Johnson noise in the junctions on the SQUID by using a Gaussian random number generator to produce a step approximation to Johnson noise. The accuracy of this procedure was checked by first applying it to a single resistively shunted junction. The noise-rounded current-voltage characteristics were in good agreement with analytical results. The noise rounding of the SQUID characteristics was then computed. The final step will be the calculation of the noise power spectrum of the voltage fluctuations across the SQUID as a function of ϕ and $\langle v \rangle$. From these results and a knowledge of $\partial\langle v \rangle/\partial\phi$ as a function of $\langle v \rangle$ we will be able to compute the optimum operating conditions for the SQUID.

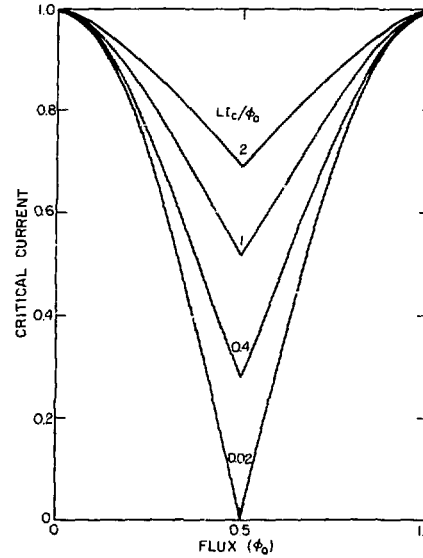

Fig. 1. dc SQUID: critical current versus applied flux for several values of LI_c/ϕ_0. (XBL 761-6115)

8. FABRICATION OF Nb-Nb JOSEPHSON TUNNEL JUNCTIONS

John Clarke and Gilbert Hawkins

For some applications of the Josephson effect, for example to SQUIDS and to standards of emf, it is highly desirable to use tunnel junctions that can be stored and thermally cycled over long periods of time, and that are mechanically very durable. Junctions made from niobium would meet these requirements, but in the past have proved difficult to fabricate because of the formation of microshorts between the niobium films. We have developed a new technique for simply and reproducibly making Nb-Nb junctions. Our junctions have been stored for periods of up to a year and recycled up to 50 times without significant deterioration.

A film of niobium, typically 200 Å thick and 200 μm wide is first sputtered onto a glass substrate. The film is thermally oxidized, and a very thin film of copper (8 - 20 Å thick) evaporated over the oxide. A cross strip of niobium completes the junction. For reasons that are not completely understood, the copper film prevents the formation of microshorts between the two niobium electrodes. The critical current of these junctions is a strong function of oxidation time and temperature and of copper thickness, and is reproducible to ± 20%. The variation of critical current with copper thickness is shown in Fig. 1.

These junctions have proved virtually indestructible. We propose to incorporate them in future SQUIDS.

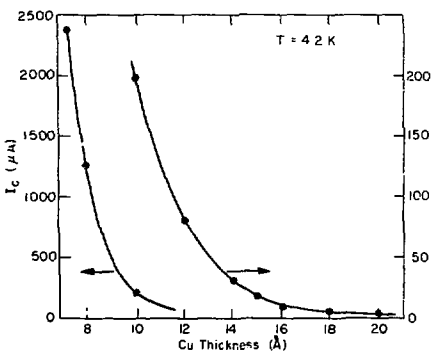

Fig. 1. Critical current versus copper thickness for an oxidation of 5 min at 125°C. (XBL 758-6915)

9. SUPERCONDUCTING FAR INFRARED BOLOMETERS

John Clarke, Gary I. Hoffer, Paul L. Richards and Nan-Hsiung Yeh

Many measurements of broadband far infrared radiation in astrophysics and in the laboratory are limited by detector noise. It is therefore important to develop improved bolometers for these applications. We have developed a superconducting bolometer with a figure of merit $D^* = (\text{area})^{1/2}/\text{NEP}$ of about 10^{14} cm W^{-1} $Hz^{1/2}$. This represents an order of magnitude improvement over the best semiconducting bolometers.

Figure 1 shows the construction of the bolometer. The temperature sensing element is an aluminum film evaporated onto a sapphire substrate. A bismuth strip is used as a heater to calibrate the bolometer. Two indium-coated nylon threads are pressed onto indium films evaporated on the corners of the substrate to provide mechanical support and electrical connection to the aluminum and bismuth films. A thin film of bismuth evaporated on the back of the substrate is used as a far infrared absorber. The substrate is connected via the nylon threads to a large copper ring, the whole assembly being mounted in a vacuum can. The aluminum film forms one arm of a low temperature Wheatstone bridge operated at 1 kHz. The output voltage from the bridge is matched with a cooled transformer to a room temperature preamplifier. The signal is then lock-in detected. The output from the lock-in is fed into a heater mounted on the copper ring to maintain its temperature near the mid-point of the aluminum transition.

Current (usually at frequencies of 1 to 10 Hz) is applied to the heater, and the resulting change in the temperature of the bolometer is detected as a change in the output of the lock-in. The

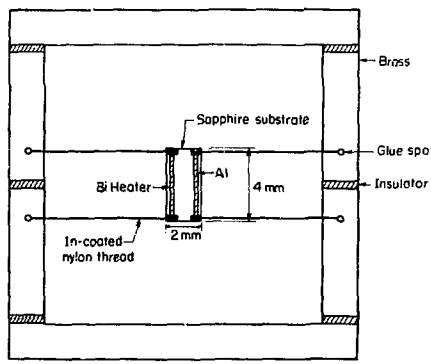

Fig. 1. Superconducting bolometer. (XBL 757-6819)

best NEP achieved so far is about 3×10^{-15} WHz$^{-1/2}$, corresponding to a D* of 9×10^{13} cm W^{-1} Hz$^{1/2}$. The response time is 50 ms. The NEP is close to the limit set by intrinsic thermal fluctuations in the bolometer. Further improvements may decrease the NEP by a factor of 2 or 3, and reduce the response time to 10 ms. In a separate series of experiments we have made careful measurements of the absorption of the bismuth film. We find an absorptivity of approximately 50% over a range from 10 to 300 cm^{-1}.

10. RESISTANCE OF SUPERCONDUCTOR-NORMAL METAL-SUPERCONDUCTOR SANDWICHES

John Clarke and M. L. Rappaport

Using a SQUID voltmeter, we have measured the resistances of superconductor-normal metal-superconductor (SNS) sandwiches from 20 mK to the transition temperature (T_c) of the superconductor in our dilution refrigerator. The resistance increases rapidly with temperature near T_c, and decreases as the temperature is lowered below about 1K. These results provide two pieces of information.

Near T_c, many of the normal electrons (quasiparticles) in the normal metal have energies higher than the energy gap, Δ, of the superconductor. These quasiparticles are thus able to propagate into the superconductor. When a current is passed through the SNS sandwich, it is carried dissipatively by the quasiparticles into the superconductor: this dissipation gives rise to the observed increase in resistance as the temperature is raised towards T_c. As the quasiparticle current flows into the superconductor, it is converted into a supercurrent over a characteristic length

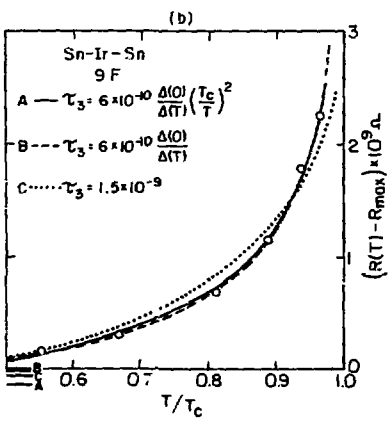

Fig. 1. Resistance of Sn-Ir-Sn sandwich versus reduced temperature: Experiment (o); theory (----). (XBL 7511-7584)

$\lambda_3 = (\ell v_f \tau_3)^{1/2}$, where ℓ and v_f are the mean free path and fermi velocity of the superconductor, and τ_3 is the "branch relaxation" time. From the increase in resistance, one can deduce a value for λ_3 and hence for τ_3. In Fig. 1 we show the change in resistance with temperature measured experimentally, compared with several theoretical models. An excellent fit is obtained with $\tau_3 = 6\times10^{-10}\Delta(0)/\Delta(T)$. This time is within a factor of two of the value found previously by a quite different technique. This measurement of τ_3 is important for two reasons. First, it enables one to calculate the dissipation in a superconductor when there is an electric current carried by quasiparticles. Second, one can relate τ_3 to the recombination time of the quasiparticles.

A superconducting energy gap is induced into the normal metal by the superconductors. As the temperature is lowered, a non-zero energy gap propagates further into the normal metal, and as a result, the resistance drops. The fall-off in this resistance is related to the BCS parameter N(0)V of the normal metal. We have now collected a considerable amount of data on this change in resistance, and we are in the process of analyzing it to obtain estimates of N(0)V in copper, silver, gold, and rhodium.

11. RESEARCH ON SEMICONDUCTORS

R. Dalven

Research carried out in 1975 was theoretical in nature and was primarily concerned with two problems. The first was the question of the parity assignments at the L point of the band structure of the lead salt semiconductors. The second was an investigation of possible experiments to realize and detect the three-dimensional Wigner electron lattice in solids.

Concerning the first problem, it is well known that the band edges in the lead salt semiconductors PbS, PbSe, and PbTe are at the L point. It has also been generally agreed that the conduction band (CB) edge is an L_6^- state and the valence band (VB) edge is an L_6^+ state. A recent paper by Glosser et al (PRL 33, 1027 (1974)) has suggested that these parity assignments are incorrect. My work examined this suggestion in the light of interband momentum matrix elements calculated by M. Schluter. It was concluded that the values of these matrix elements support the Glosser scheme of parity assignments. However, it is quite clear that further optical experimental studies, especially on PbS and PbSe, by means other than electro reflectance, are necessary before the presently accepted parity assignments at L can be called into question.

The second problem investigated was the Wigner electron lattice in solids. It was proposed by Wigner that, as the electron concentration in a solid became smaller, the electrons would become localized in space and form a bcc lattice. Possible means of experimentally realizing and detecting this lattice have been examined. It was concluded that very pure germanium, doped with

antimony may offer the possibility of obtaining extrinsic electron densities low enough to form the Wigner lattice. It also proposed that Brillouin scattering of photons by the LA and TA modes of vibration of the electron lattice offers a possible method of experimental detection. This is because the scattering spectrum of the electron lattice is anticipated to include structure not found in the spectrum of the electron gas of the same density.

12. RESEARCH PLANS FOR CALENDAR YEAR 1976

John Clarke and Associates

Our work on 1/f noise will first be directed to a theoretical and microscopic understanding of the correlated temperature fluctuations that produce the noise in metals. We will make low temperature measurements of 1/f noise in paramagnetic salts in which temperature fluctuations produce fluctuations in magnetic susceptibility. We also propose to measure the 1/f noise in superconducting microbridges. These devices have important device applications, and a study of their low frequency noise is urgently needed. We plan to study noise in semiconductors: we will measure the noise in specially fabricated FETS in which four terminal measurements of the noise are possible, and also study the noise in single crystal semiconductors. It is hoped that a microscopic picture of 1/f noise in semiconductors will emerge from this work.

We plan to continue the magnetotelluric measurements using our dc SQUID magnetometers. By using the very high sensitivity and low drift inherent in these devices we will be able to extend our measurements down to 10^{-4} Hz, and thus probe the conductivity of the earth's crust down to distances of as much as 50 km. Much of the work will be carried out at geothermal sites in Nevada, to correlate our measurements with known values of conductivity. We also plan to investigate magnetic field gradient fluctuations in regions of high inhomogeneity, for example, along earthquake fault lines. The intense, changing pressures along a fault line are known to produce local magnetic field fluctuations via the piezomagnetic effect. It would be of great interest to see whether or not there are detectable gradient fluctuations. The observation of such effects may have important implications in earthquake prediction.

We will construct and test a thin film gradiometer in which a dc SQUID is an integral part of the device. The complete gradiometer will be constructed by a series of evaporations on a single optically polished substrate. As a result, the gradiometer should be very stable and maintain its balance indefinitely. Superconducting devices for the measurement of magnetic field gradients have important applications in medical physics and geophysics.

Work on the theory of operation of dc SQUIDS and on their noise limitations will be completed. The results of this work will enable us to optimize the sensitivity of these devices.

The development of superconducting far infrared bolometers will continue, and should be completed in the coming year. We hope to be able to exploit the very high sensitivity of these devices both in laboratory far infrared measurements, and in far infrared astronomy.

We will continue research on non-equilibrium processes in superconductors, aimed at a better understanding of quasiparticle dissipation and relaxation processes. Experimental work on the resistance of SNS sandwiches is now complete, and we hope to complete the theoretical analysis of the data in the near future. From the data near T_c we will extract values for the quasiparticle branch relaxation and recombintaion times in tin and lead. From the low temperature data we will obtain values for the BCS parameter N(0)V in copper, silver, gold, and rhodium. A new experiment will be started to explore the effects of monochromatic phonons on superconducting quasiparticle tunnel junctions. The phonon frequency will lie below the energy gap frequency of the superconductor. According to a theory of Eliashberg, the phonons should enhance the energy gap and hence the transition temperature of the superconductor. We will test this theory by making tunneling measurements of the energy gap as a function of phonon intensity and frequency. We expect this experiment to give considerable insight into non-equilibrium effects in superconductors.

13. 1975 PUBLICATIONS AND REPORTS

John Clarke and Associates

Journals

1. Richard Dalven, A Course in Applied Solid State Physics, Am. J. Phys. 43, (4) 364 (1975) (LBL-2784).

2. J. Clarke, W. M. Goubau and M. B. Ketchen, A Reliable DC Squid Made with Tunnel Junctions, IEEE Trans. on Magnetics 11, 724 (1975) (LBL-3191).

3. J. Clarke and T. Y. Hsiang, Low Frequency Noise in Superconducting Sn Films at the Transition Temperature, IEEE Trans. on Magnetics 11, 845 (1975)(LBL-3188).

4. J. Clarke and G. Hawkins, IEEE Trans. on Magnetics 11, 841 (1975) (LBL-3182).

5. J. Clarke, Josephson Junction Devices, Advances in Cryogenic Engineering, Vol. 20 Ed. K. D. Timmerhaus, Plenum Publishing Corp., 1975 (LBL-3528).

6. J. Clarke and T. Y. Hsiang, Low Frequency Noise in Tin Film at the Superconducting Transition, Phys. Rev. Letters 34, (9) 1217 (1975)(LBL-3702).

7. J. Clarke, W. M. Goubau and M. B. Ketchen, A Thin-Film DC SQUID with Low Noise and Drift, Applied Physics Letters 27, (3) 155 (1975) (LBL-3797).

8. Richard Dalven, Parity Assignments at L in the Lead Salt Semiconductors, Phys. Rev. Letters 35, (1) 66 (1975) (LBL-3900).

9. R. F. Voss, Comments on "A Simple Model for the 1/f-Type Power Spectrum" by M. Agu, Phys. Letters 53A, 277 (1975) (LBL-3911).

LBL Reports

1. J. Clarke and T. Y. Hsiang, Low Frequency Noise in Tin and Lead Films at the Superconducting Transition, LBL-4535, Nov. 1975.

2. R. Voss and J. Clarke, Amplitude Fluctuation of Johnson Noise in Semiconductors and Discontinuous Metal Films: 1/f Noise in An Equilibrium System, Fourth International Conference on Physical Aspects of Noise in Solid State Devices, Sept. 9-11 1975, Noordwijarhout, The Netherlands, LBL-3592.

3. J. Clarke and G. Hawkins, Low Frequency Noise in Josephson Junctions, Fourth International Conference on Physical Aspects of Noise in Solid State Devices, Sept. 9-11, 1975, Noordwijarhout, The Netherlands, LBL-3593.

4. Richard F. Voss and John Clarke, 1/F Noise in Music and Speech, LBL-3959, June 1975.

5. Gary Irl Hoffer, Superconducting Junction Bolometers (Ph.D. Thesis), LBL-3759, August 1975.

6. Richard Dalven, Proposed Experiment to Realize and Detect the Three Dimensional Wigner Lattice, J. of Physics and Chemistry of Solids, LBL-4131, Sept. 1975.

7. Richard Dalven, Connection Between the Dispersion Relation, Surfaces of Constant Energy, and Energy Bands in Solids, LBL-3907, Sept. 1975.

8. G. Hawkins and J. Clarke, Nb-Nb Thin Film Josephson Junctions, LBL-4113, Sept. 1975.

9. R. Dalven, Possible Light Scattering Experiment to Detect the Three Dimensional Wigner Lattice, LBL-3937, Aug. 1975.

10. R. F. Voss and J. Clarke, 1/f Noise: Equilibrium Temperature and Resistance Fluctuations, LBL-4109 Rev., Aug. 1975.

11. R. F. Voss and J. Clarke, 1/f Noise from Systems in Thermal Equilibrium, LBL-3969, June 1975.

12. R. F. Voss and J. Clarke, 1/f Noise in Music: Music From 1/f Noise, Perspectives in New Music, LBL-4117, Aug. 1975.

13. Richard Voss, 1/f Noise: Diffusive Systems and Music, (Ph.D. Thesis) LBL-4109, Nov. 1975.

14. John Clarke, The Application of Josephson Junctions to computer Storage and Logic Elements to Magnetic Measurements, 21st Ann. Conf. of Magnetism and Magnetic Materials in Philadelphia, PA, Dec. 9-12, 1975, LBL-4548.

2. THEORETICAL RESEARCH

a. Theoretical Solid State Studies

Marvin L. Cohen, Principal Investigator

Introduction. We used the empirical pseudopotential method (EPM) to calculate various electronic properties of a variety of materials. The method was extended to include localized configurations such as surfaces, vacancies, and interfaces. This latter development added a new dimension to our calculational abilities. (All work jointly funded with NSF.)

1. METHOD FOR LOCALIZED CONFIGURATIONS*

Marvin L. Cohen

We have developed a new method using pseudopotentials in a self-consistent manner to describe localized configurations. The method has been applied to an Si_2 molecule, metal and semiconductor surfaces, an Si vacancy, a step on an Si surface, and metal-semiconductor interfaces. The surface and interface calculations will be discussed separately.

The standard pseudopotential approach to bulk properties of solids is difficult to extend to surface studies because of the necessity for periodicity. In an attempt to circumvent this problem, we construct large cells which are repeated periodically. The large cells contain the configuration we are interested in and the electronic structure is treated self-consistently using Hartree potentials (obtained using Poisson's equation) and Slater exchange potentials. For example, in the case of the diatomic molecule the structure is repeated infinitely and the charge density is calculated self-consistently to produce the energy spectrum and charge density for the molecules. This method, which is based on a plane-wave expansion, gives results that are accurate and agree quite well with Hartree-Fock calculations.

The method was applied to a vacancy in Si. Three different structural models for the neutral vacancy were considered. Vacancy states were found to exist in the Si thermal gap for each structure. The character of these states is predominantly dangling-bond and p-like localized on the four atoms surrounding the vacancy.

This new method can also be used to study impurities, finite change of atoms, adsorbates, and other localized configurations.

*This work is described in Journal (23) and LBL Reports (8,10) listed at the end of this section.

2. SURFACE STATES ON SOLIDS*

Marvin L. Cohen

The method described above was used to calculate the electronic structure Si(111) surface models (Figs. 1-3). The results for (1×1) unreconstructed, relaxed, and unrelaxed structures compare well with earlier calculations. A fully self-consistent calculation was then carried out for Haneman's (2×1) reconstructed surface model. This was the first calculation of this type and important experimental results can be understood using this model. In particular, results of the calculations bear on experiments measuring electron spin-resonance, infrared absorption measurements, photoemission measurements, and angular-dependent photoemission measurements.

The method was then applied to study the electronic structure of the (111) surface of aluminum. Surface states were identified and the work function calculated. The behavior of the total charge density and the potential near the surface were computed and displayed. Self-consistency was found to be of crucial importance.

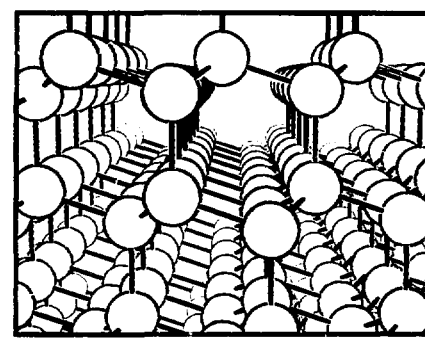

Fig. 1. Perspective view of the Si crystal structure projected on a (110) plane. The [111] direction is vertical. The (111) surface is obtained by cutting the vertical bonds in a horizontal plane.

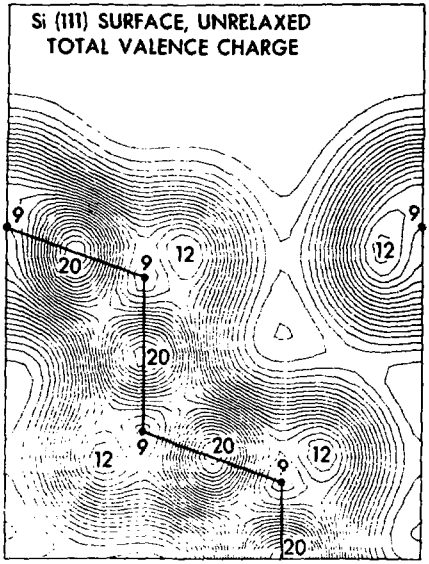

Fig. 2. Total valence charge distribution for an unrelaxed Si(111) surface (for geometry see Fig. 1). The plotting area starts in the vacuum and extends 4-1/2 atomic layers into the crystal. The atomic positions and bond directions are indicated by dots and heavy lines respectively. The smoothing out of the charge around the cut dangling-bond charge and the "valley" which extends from the surface into the bulk (along which impurities probably migrate) is clearly displayed. (XBL 758-6950)

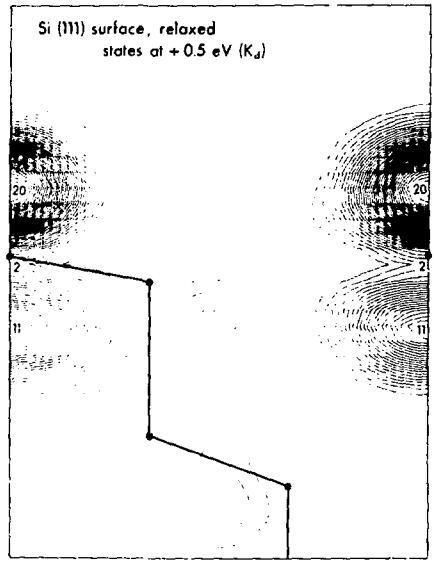

Fig. 3. Charge density plot to illustrate a surface state configuration. This state corresponds to a dangling-bondstate on Si(111) for a relaxed but nonreconstructed model.

(XBL 758-6968)

The electronic structures of III-V and II-VI zincblende semiconductors were studied. Early calculations by our group using the tight-binding method were found to be quite helpful and indicated where surface states exist in these materials. However, charge density calculations and self-consistency are not possible using standard tight binding schemes. Using our new method we were able to compute the total valence charge densities and charge densities for individual states for both GaAs and ZnSe which served as prototypes for the III-V and II-VI semiconductors. A local density of states was also calculated for anion and cation surfaces.

The surface calculations on diamond and zincblende semiconductors and on metals using our new technique are among the most extensive available. They provide details related to the local density of states at the surface, and the charge density of the various surface states. It has even been possible to compute the surface states near a step on the (111) surface of silicon. This calculation yielded new edge-states which are responsible for added structure in the surface density of states. This structure appears to agree well with recent photoemission measurements.

*This work is described in Journals (5,6,14,15,21, 23) and LBL Reports (2,4,5,10) listed at the end of this section.

3. METAL-SEMICONDUCTOR INTERFACES*

Marvin L. Cohen

The electronic structure of a jellium-Si interface is calculated with an assumed jellium density corresponding to aluminum and self-consistent Si pseudopotentials. This model of the metal-semiconductor interface was explored using the techniques described above. The calculation was done self-consistently and the Schottky barrier height was calculated in excellent agreement with experiment. It was found that all previous theories of Schottky barriers were incomplete. The state involved in pinning the Fermi level in the Schottky barrier is composed of the tails of the wavefunctions coming from the metal component of the junction. These tails concentrate their charge on the dangling-bond silicon states that would be present if the interface were Si-vacuum. We called these states metal-induced gap states (MIGS). We have computed the total charge density for the metal semiconductor interface and have also calculated the charge densities of the (MIGS) states. We also find interface states at -8.5 eV relative to the top of the Si valence band edge.

*This work is described in Journal (18) and LBL Report (6) listed at the end of this section.

4. NARROW GAP IV-VI SEMICONDUCTORS*

Marvin L. Cohen

We have done a series of calculations on the electronic structure and properties of PbSe and PbTe. These calculations involve the use of the empirical pseudopotential method (EPM) and included nonlocal corrections. Band structures, densities of states, effective masses, optical constants, charge densities, and pressure and temperature coefficients of band edges were all computed. The theoretical results were compared successfully in most cases with experiment. Some new interesting features of these calculations include the following. It was necessary to use nonlocal corrections to obtain agreement with optical data over an energy range from 0 to 26 eV. In analyzing the synchrotron radiation studies (18-20 eV) it was discovered that a shift of 0.8 eV between photoemission and reflectivity studies existed. The calculation of the temperature dependence of energy levels in these materials revealed the necessity of using both Brooks-Yu and Fan formulations. The Fan contributions included intravalley and intervalley scattering.

Generally the results of our detailed investigations of these materials revealed some interesting features and provided a theoretical picture of the electronic structure to explain the interesting physical properties of these materials which have been used for basic research and device applications.

*This work is described in Journals (3,4,12,16,17, 22) listed at the end of this section.

5. AMORPHOUS TETRAHEDRAL SYSTEMS*

Marvin L. Cohen

We continued our work on amorphous semiconductors. Emphasis was given to an attempt to understand the role of short range order and short range disorder in tetrahedral materials. We approached the problem using two methods that we developed in the past. One method was to use the EPM and tight-binding models to solve complex crystalline systems. The complex nature of these systems was related to the features expected in the amorphous semiconductors. Another method was the "Cluster-Bethe-Lattice" approach. The electronic structure and optical properties of homopolar and heteropolar systems were studied. In addition to tetrahedral semiconductors, amorphous Se and Te were also analyzed.

*This work is described in Journals (1,10,11) and LBL Report (3) listed at the end of this section.

6. ELECTRONIC STRUCTURE OF CHAIN AND LAYER MATERIALS, AND OF THE SUPERCONDUCTING POLYMER $(SN)_x$*

Marvin L. Cohen

The electronic structure of chain and layer materials, $(SN)_x$, and the electronic structure of trigonal and amorphous Se and Te were investigated using the EPM. Charge density calculations and simple tight-binding models allowed interpretation of the photoemission experiments on these materials.

For Se and Te, estimates of interchain bonding strengths were made using the charge density calculations. The EPM results along with model calculations allowed an analysis of the effects of bond angle variations on chains and the presence of 6- and 8-fold rings of bonds. The relation between density of states structure and charge density was explored. The results allowed an identification of photoemission spectra with particular interchain and intrachain bonding states.

The layer compounds GaSe and GaS and mixed crystals of these compounds were studied experimentally and theoretically. The experimental work was done by Professor Shen's group. The theoretical analysis involved calculations of the band structure, reflectivity, and modulated reflectivity of these materials. The main structures in the optical response functions were identified in terms of their location in k-space and their atomic character. For example, the main structures in the optical spectra of GaSe were found to result from excitations of the Ga-Ga bond and from atomic s-like transitions between nonbonding Se p- and s-states. The alloy spectra can be decomposed into three classes of transitions which exhibit zero, intermediate, and strong energy shifts with anion alloying. This observation can be explained

theoretically using charge concentration analysis of optical transitions.

The polymer $(SN)_x$ is of interest because of its superconducting behavior. Using the EPM scheme we have calculated the band structure, density of states, Fermi surface, and optical spectrum. Using the results of our calculations we have estimated the electron-phonon coupling constant and have analyzed the observed increase of the superconducting transition temperature with pressure. The assumption of an electron-phonon mechanism for superconductivity in $(SN)_x$ is consistent with our results. Our calculations indicate that this material is probably a standard BCS superconductor, and it differs from other superconducting materials in that the electrons at the Fermi surface are predominantly p-like.

*This work is described in Journals (1,7,19) and LBL Reports (7,10) listed at the end of this section.

7. ELECTRONIC STRUCTURE: LOCAL FIELDS IN Si, CHARGE DENSITIES IN NOBLE METALS, TIGHT BINDING PARAMETERS FOR SEMICONDUCTORS, AND CHARGE DENSITIES IN SEMICONDUCTORS*

Marvin L. Cohen

The question of the role of local fields on the optical spectra of semiconductors has arisen in the literature many times. In order to estimate the effects of local fields we calculated the dielectric function of silicon for zero wavevector as a function of frequency. Contrary to recent calculations on diamond, local fields corrections do not shift the prominent peak positions. In addition to analyzing the optical spectrum of silicon, the calculated dielectric function was used to compute the energy loss spectra. Agreement with measured energy loss spectra is significantly better when local field effects are included.

We used our pseudopotential techniques to calculate the energy band structure of copper and silver, and the resultant wavefunctions were used to compute the charge density for these materials. The results illustrate the interesting features of d-electrons. In both silver and copper the total charge density for the occupied conduction band resembles a muffin-tin configuration.

Using the tight-binding method, the valence band structure and densities of states of C, Si, Ge, GaAs, and ZnSe were calculated. Very good agreement was obtained with other calculations when all nearest and one-second-nearest neighbor interactions were included. The effects of the various interactions on the density of states were explored. Because of the success of our tight-binding model in producing valence band structures close to those computed using the EPM, these models have been used extensively to explore the bonding nature and surface states in diamond and zincblende semiconductors.

Our previous success in determining the electronic charge density of silicon was extended to zincblende semiconductors. Recent x-ray data on InSb allows an assessment of the valence charge density provided by our calculations. It was found that our recent nonlocal pseudopotential calculations yielded good agreement with the x-ray results, and the nonlocal calculations were far superior to the calculations done without using the nonlocal potentials.

*This work is described in Journals (2,8,9,13) and LBL Reports (1,10) listed at the end of this section.

8. RESEARCH PLANS FOR CALENDAR YEAR 1976

Marvin L. Cohen

We plan to extend our calculations of surface and interface states. In particular we will explore the role of ionicity in the properties of Schottky barriers. We also plan to examine the role of metal overlayers on semiconductor surfaces using realistic pseudopotentials for the metal. More detailed properties of semiconductor surfaces will be computed. We also plan to examine the properties of surface states on transition metals.

Adsorbates on semiconductors, such as hydrogen on Si, will be explored. Recent experiments indicate some interesting properties. We will also continue to study layer compounds, diamond and zincblende semiconductors, and other semiconductors such as AgCl and BiI_3. We plan to explore the role of electron-hole interactions on the d-core levels and III-V semiconductors by comparing our calculated one-electron spectra with results measured experimentally using synchrotron radiation.

Other plans involve studies of the bulk properties and superconducting properties of transition metals and studies of the electronic structure of molecules.

9. 1975 PUBLICATIONS AND REPORTS

Marvin L. Cohen and Associates

Journals

1. J. D. Joannopoulos, M. Schlüter, and M. L. Cohen, Electronic Densities of States of Amorphous and Trigonal Se and Te, 12th International Conference on the Physics of Semiconductors, Stuttgart, Fed. Rep. Germany, (1974) p. 1304 (LBL-2790).

2. S. G. Louie, J. R. Chelikowsky, and M. L. Cohen, Local Field Effects in the Optical Spectrum of Silicon, Phys. Rev. Letters 34, 155 (1975) (LBL-3539).

3. G. Martinez, M. Schlüter, and M. L. Cohen, The Electronic Structure of PbSe and PbTe, I. Band Structure, Densities of States and Effective Masses, Phys. Rev. B11, 651 (1975) (LBL-3536).

4. G. Martinez, M. Schlüter, and M. L. Cohen, The Electronic Structure of PbSe and PbTe, II. Optical Properties, Phys. Rev. B11, 660 (1975) (LBL-3537).

5. D. J. Chadi and M. L. Cohen, Intrinsic (111) Surface States of Ge, GaAs and ZnSe, Phys. Rev. B11, 732 (1975) (LBL-3534).

6. D. J. Chadi and M. L. Cohen, Tight-Binding Calculations of (111) Surface Densities of States of Ge and GaAs, Solid State Comm. 16, 691 (1975) (LBL-3132).

7. J. D. Joannopoulos, M. Schlüter, and M. L. Cohen, The Electronic Structure of Trigonal and Amorphous Se and Te, Phys. Rev. B11, 2186 (1975) (LBL-3130).

8. D. J. Chadi and M. L. Cohen, Tight-Binding Calculations of the Valence Bands of Diamond and Zincblende Crystals, Phys. Stat. Solidi (b) 68, 405 (1975) (LBL-3128).

9. C. Y. Fong, J. P. Walter, and M. L. Cohen, Comparison of Band Structures and Charge Distributions of Copper and Silver, Phys. Rev. B11, 2759 (1975) (LBL-3535).

10. F. Yndurain and J. D. Joannopoulos, The "Cluster-Bethe-Lattice" Method: The Electronic Density of States of Heteropolar Systems, Phys. Rev. B11, 2957 (1975) (LBL-3567).

11. J. D. Joannopoulos and F. Yndurain, Moments and Averages of the Electronic Density of States of Amorphous and Crystalline Homopolar Solids, Physics Lett. 51A, 79 (1975) (LBL-3570).

12. M. Schlüter, G. Martinez, and M. L. Cohen, Electronic Charge Densities in PbSe and PbTe, Phys. Rev. B11, 3808 (1975) (LBL-3569).

13. C. Y. Fong, D. J. Chadi, and M. L. Cohen, An Alternate Form of the Non-Local p-Potential in the Empirical Pseudopotential Method, Phys. Rev. B11, 4063 (1975). Erratum Phys. Rev. B12, 4584 (1975) (LBL-3540).

14. M. Schlüter, J. R. Chelikowsky, S. G. Louie, and M. L. Cohen, Self-Consistent Pseudopotential Calculations on Si (111) Unreconstructed and (2×1) Reconstructed Surfaces, Phys. Rev. Lett. 34, 1385 (1975) (LBL-3767).

15. M. Schlüter, J. R. Chelikowsky, and M. L. Cohen, The Electronic Configuration of Si (111) (2×1) Reconstructed Surfaces, Phys. Lett. 53A, 217 (1975) (LBL-3943).

16. G. Martinez, M. Schlüter, R. Pinchaux, P. Thiry, D. Dagneaux, Y. Petroff, and M. L. Cohen, Synchrotron Radiation Measurements and Calculation of Core - to Conduction Level Transitions in Lead Chalcogenides, Solid State Comm. 17, 5 (1975) (LBL-3538).

17. M. Schlüter, G. Martinez, and M. L. Cohen, Pressure and Temperature Dependence of Electronic Energy Levels in PbSe and PbTe, Phys. Rev. B12, 650 (1975) (LBL-3568).

18. S. G. Louie and M. L. Cohen, Self-Consistent Pseudopotential Calculation for a Metal-Semiconductor Interface, Phys. Rev. Lett. 35, 866 (1975). Erratum PRL 36, 173 (1976).

19. M. Schlüter, J. R. Chelikowsky, and M. L. Cohen, Electronic Properties of Polymeric Sulfur Nitride, Phys. Rev. Lett. 35, 869 (1975). Erratum PRL 36, 452 (1976).

20. J. R. Chelikowsky, M. Schluter, S. G. Louie, and M. L. Cohen, Self-Consistent Pseudopotential Calculation for the (111) Surface of Aluminum, Solid State Comm. 17, 1103 (1975) (LBL-3768).

21. M. Schlüter, J. R. Chelikowsky, S. G. Louie, and M. L. Cohen, Self-Consistent Pseudopotential Calculations for Si(111) Surfaces: Unreconstructed (1×1) and Reconstructed (2×1) Model Structures, Phys. Rev. B12, 4200 (1975) (LBL-3944).

22. G. Martinez, M. L. Cohen, and M. Schlüter, Energy-Level Parities at L in PbTe, Phys. Rev. Lett. 35, 1746 (1975)

23. M. L. Cohen, M. Schlüter, J. R. Chelikowsky, and S. G. Louie, Self-Consistent Pseudopotential Method for Localized Configurations: Molecules, Phys. Rev. B12 5575 (1975) (LBL-3766).

LBL Reports

1. J. R. Chelikowsky and M. L. Cohen, Pseudopotential Valence Charge Densities in Homopolar and Heteropolar Semiconductors, Phys. Rev. Lett. (in press)

2. J. R. Chelikowsky and M. L. Cohen, (110) Surface States in III-V and II-VI Semiconductors, Phys. Rev. (in press)

3. J. D. Joannopoulos and M. L. Cohen, Theory of Short Range Order and Disorder in Tetrahedrally Bonded Semiconductors, Academic Press (in press)

4. M. Schlüter and M. L. Cohen, Local Density of States for a Relaxed Si(111) Surface, Dec. 1975.

5. M. Schlüter, K. M. Ho and M. L. Cohen, Electronic States at Step Surface, Aug. 1975

6. S. G. Louie and M. L. Cohen, Electronic Structure of a Metal-Semiconductor Interface, Phys. Rev. (in press).

7. M. Schlüter, J. Camassel, S. Kohn, J. P. Voitchovsky, Y. R. Shen and M. L. Cohen, Optical Properties of GaSe and GaS_xSe_{1-x} Mixed Crystals, Phys. Rev. (in press) (LBL-4184).

8. S. G. Louie, M. Schlüter, J. R. Chelikowsky and M. L. Cohen, Self-Consistent Electronic States for Reconstructed Si Vacancy Model, Phys. Rev. (in press).

9. S. G. Louie, J. R. Chelikowsky and M. L. Cohen, Ionicity and the Theory of Schottky Barriers, Dec. 1975.

10. J. R. Chelikowsky, The Electronic Structure of Molecules Solids and Solid Surfaces, (Ph.D. Thesis) LBL-3962, Sept. 1975.

C. MATERIALS CHEMISTRY

1. CHEMICAL STRUCTURE

a. High Pressure Chemistry

George Jura, Principal Investigator

1. HIGH PRESSURE CHEMISTRY

K. Y. Kim and George Jura

The purpose of these experiments is the determination of the heat capacity of metals and alloys as a function of temperature and pressure. It also should be possible to determine a quantity that is proportional to the heat conductivity of the surrounding medium as a function of temperature and pressure. In the past we have developed electronic methods using a constant current pulse for the above determinations. Enticingly reasonable results have been obtained in the past over a limited range, but there has never been the feeling that they could be given unequivical trust.

To this last end, the apparatus and theory were reexamined, and both were found to be lacking. The results had to have more precision than we had in the past to be certain that the simple theory was not applicable.

The electronics of the constant current pulse and the switching circuit were redesigned and rebuilt. The result of the electronic changes has been to greatly increase the accuracy of the results. The average deviation of the results from a two parameter equation that relates the EMF vs time has been decreased by a factor of 5. The circuitry has also been modified so that a single individual rather than two can perform a heat capacity experiment.

The increase in accuracy of the experiments has led to a necessity for improvement in the theory used to treat the data. If the sample is in vacuo or surrounded by as much as 1 atm of inert gas, the simple theory used in the past is satisfactory. However, when the method is used to study the heat capacity under high pressure, then the simple theory is no longer applicable. In the past, the data were never sufficiently good to show that a more sophisticated theory is required.

The simple theory states that at zero time,

$$dE/dt = I^3 R_o R'/C_p$$

where E is the voltage, t the time, I the current, R_o the resistance of the sample before the start of the pulse, R' the temperature coefficient of resistance. From the above equation, it is evident that a plot of dE/dt vs I^3 should go through the origin. This condition is satisfied when the sample is not under pressure. When the sample is pressurized, there is a linear relationship between dE/dt and I^3, but this line does not go through the origin. At the present time, we can show that what we observe is qualitatively correct, but we have not as yet been able to write a quantitative correction so that we can compute the heat capacity and the heat conductivity of the surrounding medium, which is what we are trying to do. Progress is being made. At the present time, we are redetermining the quantity R', so that we can be sure of our calculated results. This will be done better than we have in the past. At the present time, it appears that when a couple of minor problems are solved, we will be able to do what we started out to do.

b. Low Temperature Properties of Solids

Norman E. Phillips, Principal Investigator

1. HEAT CAPACITY OF fcc Tl-Pb-Bi ALLOYS

F. Hermans, J. D. Boyer and Norman E. Phillips

In recent years considerable attention has been directed to the relation between the superconducting critical temperature of a metal and its normal-state electronic properties and phonon spectrum. Most of the work in this area has been discussed in terms of a relation[1] developed by McMillan. McMillan[1] also noted that for a number of transition metals the electron-phonon interaction parameter λ seemed to be determined by an average phonon frequency and was largely independent of electronic properties. There have been several theoretical justifications of this correlation, and it has been used in a number of cases to predict or to rationalize trends in T_c. In this context, the fcc alloys of Tl and Bi with Pb are of particular interest because (1) the relevant average phonon frequency is insensitive to composition,[2] but T_c increases by a factor of 4 as the electron/atom ratio, z, changes from 3.2 to 4.4, and (2) extensive electron-tunneling and neutron-scattering data have defined the phonon dispersion curves and the electron-phonon coupling in unusual detail. The available heat capacity data,[3] however, are confined to the dilute alloy region ($3.9 < z < 4.1$) and are not sufficiently precise to detect the change in slope of the density of states vs z that would be expected on the basis of the λ vs z data. To correct these shortcomings we have undertaken new measurements of the heat capacity of these alloys throughout the region of stability of the fcc phase. The measurements will permit an unusually detailed comparison of band structure calculations with experiment, and will also be of interest in determining the extent to which the low-temperature lattice heat capacity reflects the features of the phonon spectrum that are important for superconductivity.

To date, pure Pb and six binary alloys with $3.91 < z < 4.12$ have been studied. There is a well defined discontinuity of slope in γ vs z at pure lead that, when compared with recent tunneling data for λ vs z, is consistent with the rigid band model. It is also in approximate agreement with the calculated[4] density of states at the Fermi surface, but not with the derivative of that quantity with respect to z. The peak in the average phonon frequency observed in tunneling experiments is at least qualitatively reflected in the T^3 term of the lattice heat capacity, but the data obtained so far do not permit a quantitative comparison.

1. W. L. McMillan, Phys. Rev. 167, 331 (1968).
2. R. C. Dynes and J. M. Rowell, Phys. Rev. B11, 1884 (1975).
3. L. C. Clune and B. A. Green, Phys. Rev. B1, 1459 (1970).
4. J. R. Anderson and A. V. Gold, Phys. Rev. A139 1459 (1965).

2. HEAT CAPACITY OF He II

Brent S. Krusor and Norman E. Phillips

Several years ago temperature scale errors were discovered in the thermometer that was used for our earlier measurements on various phases of ^{4}He. Most of those data were published with corrections to the derived thermodynamic properties for the change in temperature scale, but for the He II data it seemed worthwhile to correct the raw heat capacity data and repeat the later steps in data analysis. The first steps in this project have now been completed: The heat capacity data have been corrected and refit to expressions for the sum of phonon and roton heat capacities in the low-temperature region. No qualitative changes in the interpretation of the data are suggested--in particular the conclusion about anomalous phonon dispersion is unchanged--but a troublesome discrepancy between sound velocity measurements and the calorimetric Debye temperature has been eliminated.

Progress in the way of extending new measurements to lower temperatures has been delayed by problems with design of the cell valve and by effort devoted to rechecking our temperature scale in the region below 1K.

3. HEAT CAPACITY OF ^{150}Nd

William E. Fogle and Norman E. Phillips

Following the discovery that the large linear term in the heat capacity of β-Ce was magnetic field dependent, it seemed interesting to test the field dependence of other rare earth metals in which large "electronic" heat capacities had been observed. A sample of ^{150}Nd was obtained (to minimize the hyperfine heat capacity which tends to obscure the linear term) and studied in magnetic fields to 38 kOe. These results were reported in our 1973 Annual Report, but measurements in higher fields were prevented by the deterioration of the high-field superconducting solenoid. Since then a new solenoid has been obtained and the measurements have been extended to 65 kOe. The data have not yet been completely analyzed, but it is clear that the heat capacity decreases approximately linearly with increasing field in the region below 1K and in fields to 65 kOe. This further supports the idea that the linear term is not electronic in origin.

4. PROGRESS ON EXPERIMENTS BELOW 50 mK

Gary E. Brodale, Erwin W. Hornung, William E. Fogle, and Norman E. Phillips

The earlier improvements in still design and increases in the capacity of the heat exchangers have improved the dilution refrigerator so that

it now operates in steady state to 12 mK and to 8 mK in the one-shot mode. A dc, SQUID-based susceptibility thermometer has been made and partially tested. It uses cerium magnesium nitrate as the magnetic material, and should therefore give a good approximation to the thermodynamic temperature scale in the region accessible with the dilution refrigerator. Apparatus for experiments on ^{3}He in the temperature region down to 1.5 mK has been partially designed and built.

5. RESEARCH PLANS FOR CALENDAR YEAR 1976

Norman E. Phillips and Associates

The study of Tl-Pb-Bi alloys will be extended to lower and to higher electron concentrations, and to "pseudo-Pb" alloys ($Tl_xPb_{1-2x}Bi_x$). The data will permit an unusually rigorous test of band structure calculations and will determine the influence of scattering centers on the low-frequency part of the phonon spectrum.

The re-analysis of the old heat capacity data on liquid ^{4}He will be completed to obtain the entropy and various derived quantities as functions of volume and temperature. New measurements, to approximately 0.1K, will be made in the new apparatus to obtain a more accurate characterization of the anomalous phonon dispersion.

The design of high-pressure cells for low-temperature calorimetry will be reconsidered with the aim of improving our capability for such measurements.

Several changes in plans for the dilution-refrigerator apparatus have been made. Various problems with dc and low-frequency ac nuclear susceptibility measurements have led us to substitute cerium magnesium nitrate (CMN, for a metal containing magnetic nuclei in the SQUID-based susceptibility thermometer to be used in heat capacity measurements to 12 mK. We regard this substitution as temporary, but the best way to obtain the necessary sensitivity and low-power dissipation in a reasonable time. The plans to measure Kapitza resistances between ^{3}He and magnetic alloys have been abandoned in favor of proceeding immediately to experiments on ^{3}He in the region down to approximately 1.5 mK. These temperatures will be reached by two-stage adiabatic demagnetization of CMN from 12 mK. This will permit the attainment of 1.5 mK with a relatively large ^{3}He/CMN ratio. The first goal will be the determination of the heat capacity of ^{3}He in the normal state as a function of pressure and temperature. The data will be important as an independent test of spin-fluctuation effects, and in extending earlier measurements to lower temperatures and additional pressures. Preliminary data on the superfluid phases will also be obtained. Another by-product of the measurements will be the heat capacity of powdered CMN and an independent determination of the T^*-T relation.

6. 1975 PUBLICATIONS AND REPORTS

Norman E. Phillips and Associates

Journals

1. M. Wun and Norman E. Phillips, Low Temperature Specific Heat of Apiezon N Grease, Cryogenics, 36 (1975) (LBL-3185).

2. S. D. Bader, N. E. Phillips, M. B. Maple, and C. A. Luengo, Heat Capacity of the Superconducting Kondo System $(LaCe)Al_2$, Solid State Commun. 16, 1265 (1975)(LBL-2744).

3. M. T. Hirvonen, T. E. Katila, K. J. Riski, M. A. Teplov, B. N. Malkin, N. E. Phillips, and Marilyn Wun, Magnetic Ordering in Terbium Ethyl Sulphate, Phys. Rev. B 11, 4652 (1975) (LBL-3750).

4. S. D. Bader, Norman E. Phillips, and E. S. Fisher, Low Temperature Heat Capacity of α-Uranium and its Relation to the Pressure Dependence of T_c, Phys. Rev. B 12, 4929 (1975) (LBL-3705).

LBL Report

1. J. K. Hoffer, W. R. Gardner, C. G. Waterfield, and N. E. Phillips, Thermodynamic Properties of ^{4}He. II. The bcc Phase and the P-T and V-T Phase Diagrams Below 2K, LBL-4116 (Aug. 1975).

Paper Presented

1. S. D. Bader, W. E. Fogle, Norman E. Phillips, M. B. Maple, and C. A. Luengo, Quatriene Conference Internationale de Thermodynamique Chimique, Montpelier, Aug. 1975 (LBL-3755).

c. Mass and Charge Transport

Charles W. Tobias, Principal Investigator

1. FUNDAMENTAL STUDIES OF TRANSPORT PROCESSES IN ELECTROCHEMICAL REACTORS

a. Studies of the Events Occurring at Gas-Evolving Electrodes

Ronald A. Putt and Charles W. Tobias

The physical events associated with the evolution of hydrogen and oxygen at electrode surfaces in concentrated sulfuric acid and potassium hydroxide solutions have been observed, and recorded by flash photography (Fig. 1). A special technique for photographing the electrode surface shortly after current initiation (13-300 msec) provided a view unobstructed by rising gas bubbles (Fig. 2). Bubble growth rate, number density, and maximum bubble size data were obtained for gas generation rates in the range 3.5-14 cm^3/cm^2 min, corresponding to current densities for hydrogen evolution of 0.5-2 A/cm. The velocity of the rising gas emulsion and degree of gas bubble coalescence within it were also observed.

The growth characteristics of bubbles depend strongly on the electrolyte composition, being different for hydrogen and oxygen in the same electrolyte. In the range studied, increasing the gas generation rate does not change the character of the events, only the rate of their occurrance. Bubble growth before separation involves repeated sequences of coalescences.

Comparison of estimates of the sizes that bubbles should reach under equilibrium growth conditions with those observed reveals that separation is controlled by the dynamics of bubble interactions.

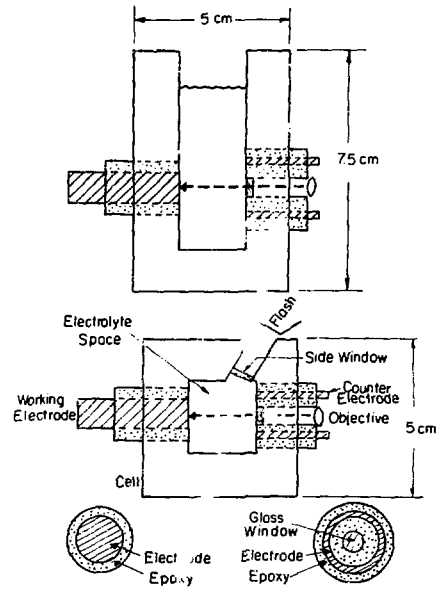

Fig. 1. Incipient bubble growth cell and electrode construction. (XBL 759-7091)

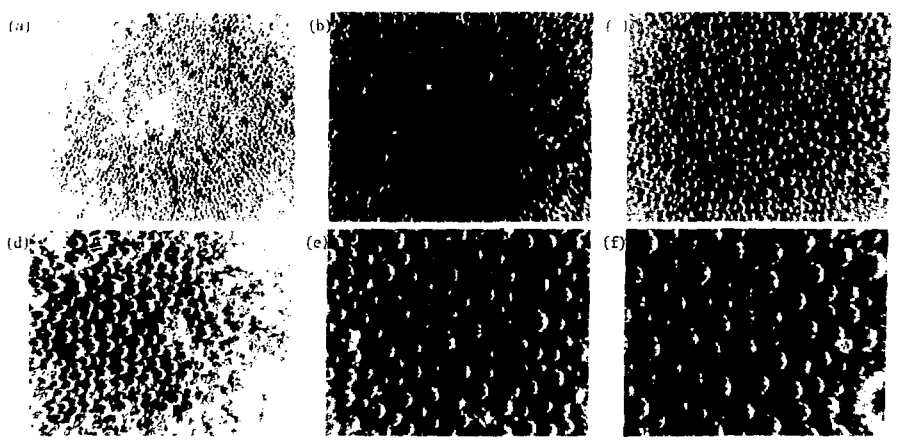

Fig. 2. Incipient bubble growth photographic sequence: hydrogen bubbles in 5M electrolyte, 7cm^3/cm^2 min (magnification 45×) arrows point to coalescing bubbles. (XBL 758-6370)

Altering the surface condition of the electrode showed that the microscopic roughness of a planar electrode has little effect on the character of gas evolution. The electrolyte velocity generated by the rising gas bubble stream is primarily a function of gas generation rate and is not overly dependent on the character of gas evolution. An extreme sweeping action, or "scavenging effect", of gas bubbles rising along the electrode surface occurs extensively in sulfuric acid electrolyte.

---

1. R. A. Putt and C. W. Tobias, Physical Processes in Electrolytic Gas Evolution, IMRP Annual Report for 1974, LBL-3530, April 1975, p. 37.
2. R. A. Putt, Studies of the Events Occurring at Gas-Evolving Electrodes (M.S. Thesis, University of California), LBL-3989, Oct. 1975.

b. Current Distribution in Electrochemical Machining

James B. Riggs, Rolf H. Muller and Charles W. Tobias

In the present state of electrochemical machining (ECM) technology, which is particularly effective in the shaping of high strength alloys, "trial and error" procedure is required for the design of the tool piece (cathode) shape that will yield the desired metal removal in the workpiece. A mathematical model for ECM is being developed that will determine the proper tool piece geometry. This model is based upon a numerical solution of Laplace's equation[1] with the boundary conditions determined by the solution conductivity and the surface overpotential. The conductivity is modeled as a function of temperature, electrolyte concentration, and electrolyte gas content. The surface overpotential will be modeled considering the effects of reaction and activation overpotential and the effect of resistive films on the electrode surfaces.[2]

To advance the development of the theoretical model, experimental anode profiles obtained by anodic dissolution using a tube shaped cathode (Fig. 1), are compared to calculated profiles.

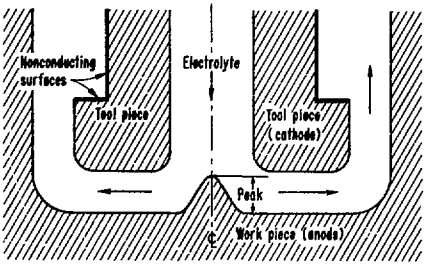

Fig. 1. Cross section of workpiece and tool piece for "pipe shaped" tool piece used for hole sinking. Arrows indicate flow of electrolyte. (XBL 764-2690)

Figures 2 and 3 show the effect of tool piece feed rate and of applied voltage on the peak height (Fig. 1) in the cutting of copper using KNO_3 electrolyte. The calculated points were obtained assuming no current-dependent surface overpotential. The deviation between calculated and

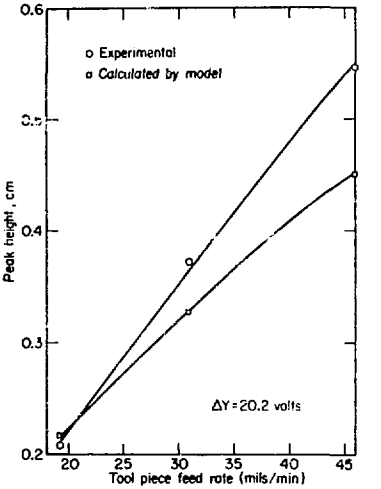

Fig. 2. Effect of tool piece feed rate on peak height. (XBL 764-2688)

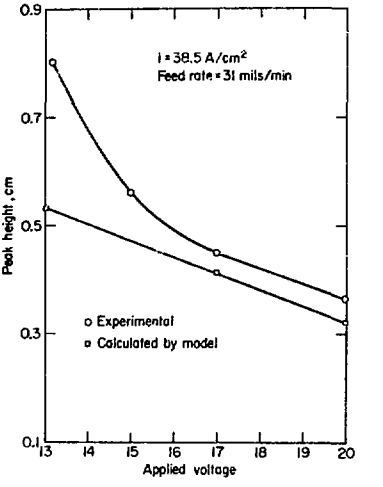

Fig. 3. Effect of applied voltage on peak height. (XBL 764-2695)

experimental curves is in part explained by the formation of a resistive film observed on the cathode surface.

---

1. R. N. Fleck, D. N. Hanson and C. W. Tobias, Numerical Evaluation of Current Distribution in Electrochemical Systems, UCRL-11612, Sept. 1964.
2. Kimio Kinoshita, Studies on the Anodic Dissolution of Copper at High Current Densities (Ph.D. Thesis, University of California, Berkeley), UCRL-19051, Sept. 1969.

c. Mass Transport and Current Distribution on Rough Electrodes in Channel Flow

Uziel Landau, Andrew Kindler and Charles W. Tobias

Correlation of limiting current data obtained in the electrodeposition of copper in the turbulent regime shows that the entrance section, X_e is independent of the Schmidt number:[1]

$$X_e/d_h = 756\ Re^{-0.57}$$

where d_h is the hydraulic diameter. In this section (Fig. 1) the local transport rates are best represented by

$$Sh_x = 0.067\ Re^{0.75} Sc^{1/3} (d_h/x)^{0.3} .$$

At flow rates exceeding the critical transition Reynolds number the mass transport rates for rough surfaces become approximately proportional to the Re number:

$$Sh_L = 0.0039\ Re^{1.06} Sc^{1/2} (e/d_h)^{0.21}$$

where e is the height of the roughness element. The dependence of the transition Re numbers and of the rate increases on the Sc number indicates that the relative height of the roughness elements to the diffusion layer thickness (rather than to the hydrodynamic boundary layer thickness) is the dominant parameter.

Extensive corrosion of metal parts, loss of good electric contacts, air leaks, and deposits of organic impurities required part by part overhauling of the channel flow apparatus, which was in continuous use over the past seven years.[2,3]

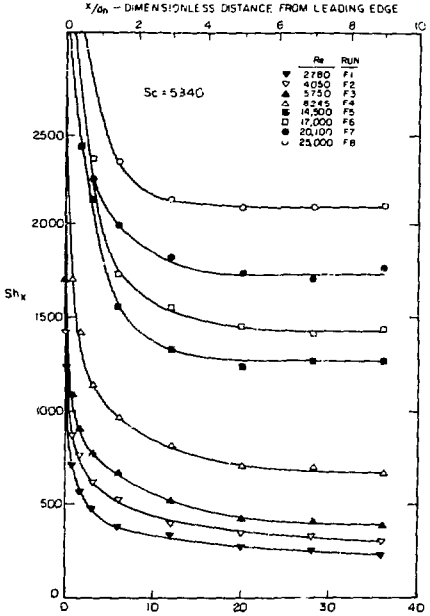

Fig. 1. Distribution of local mass transport rates along the electrode in turbulent flow. (XBL 744-6012)

---

1. Uziel Landau and Charles W. Tobias, Distribution of Mass Transport Rates Along Parallel Plane Electrodes in Forced Convection, 1974 IMRD Annual Report, LBL-3530, April, 1975, p.35.
2. Jan Selman and Charles W. Tobias, Current and Potential Distribution in Forced and Free Convective Mass Transfer at Plane Electrodes, IMRD Annual Report 1965, Feb. 1966, p.46.
3. Uziel Landau and Charles W. Tobias, Flow Circuit for Ionic Mass Transfer Studies at High Flow Rates, IMRD Annual Report 1970, April, 1971, p.35.

2. ELECTROCHEMISTRY IN NONAQUEOUS SOLVENTS

a. An Ambient Temperature Process for Reduction of Potassium Metal

Radoslav Atanasoski, Henry Law and Charles W. Tobias

The effectiveness of a simplified method for electrolyte preparation, and the achievement of high current efficiencies, indicate that a process for the recovery of potassium metal from solutions of its salts in propylene carbonate may be economically attractive. Cyclic voltametry appears to offer a convenient means for monitoring impurity concentrations in the electrolyte.

The tedious and complicated electrolyte purification procedure[1] employed so far has been simplified by the use of potassium tetrachloraluminate, $KAlCl_4$, synthesized in this laboratory.[2] The salt $KAlCl_4$ dissolves readily in propylene carbonate and has a saturation concentration of 1.6 M at 25°C. Large quantities of electrolyte can now be prepared in a straightforward manner. Prolonged electrolysis at a temperature (70-85°C) slightly higher than the melting temperature of

the potassium demonstrates the electrolyte is stable. The good quality of molten potassium deposit is shown in Fig. 1.

Fig. 1. Deposit of potassium on platinum in liquid form: ~85°C; 0.2-2.0 mA/cm²; duration of electrolysis -- 3 days. (XBB 763-2974)

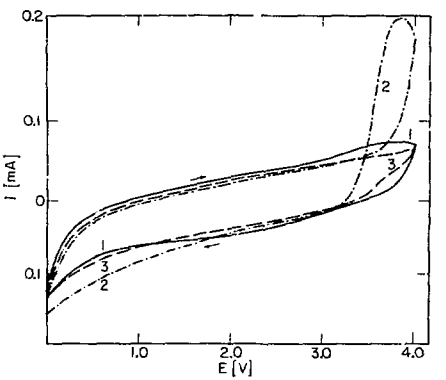

Fig. 2. The effect of the addition of 1 ppm H_2O in 0.1 M $KAlCl_4$ in propylene carbonate: working electrode, stainless steel cylinder, diameter 0.74 cm, 1 cm²; counterelectrode, potassium deposited on platinum screen; reference electrode, potassium in the same solution; scanning rate, 25.6 mV/sec. Cyclic voltammogram
#1 ——— before the addition of water.
#2 —•— 7th cycle after adding 1 ppm of water
#3 ------ 25th cycle after the addition of water
(XBL 764-2697)

For any practical process, it is imperative that one be able to monitor the impurity concentration. Cyclic voltammetry was found to be an excellent technique for water determination in the 0.1 to 1 ppm range. The effect of the addition of 1 ppm water to the electrolyte is shown by the voltammograms in Fig. 2. Comparison of curves 1 and 2 demonstrates that the water content is far below 1 ppm. Curve 3 illustrates the self-cleaning aspect of this cyclic process.

The current efficiency for the potassium deposition has been found to be greater than 95%. Since it was not possible to remove the potassium covered cathode from the electrolyte without leaving some loose particles of potassium behind, it is believed that the cause of the deviation from 100% current efficiency is mechanical loss of potassium rather than any side reaction.

---

1. Oscar Chacon, Cathodic Reduction of Potassium in Propylene Carbonate Electrolytes (M.S. Thesis, University of California, Berkeley), LBL-3542, 1974.
2. J. Kendall, et al., J. Am. Chem. Soc. 45, 963-996 (1923).

3. EVALUATION OF NEW ELECTROCHEMICAL PROCESSES

a. Hybrid Electrolysis-Thermal Cycle for Hydrogen Generation

David H. Munger, Rolf H. Muller and Charles W. Tobias

A search for a practical hybrid electrolysis-thermal cycle for the generation of hydrogen has been undertaken. Of particular interest is an anodic process in which a solid metal oxide is formed at potentials lower than that required for oxygen evolution.[1,2] The oxide is removed from the electrolytic cell and the anode substrate is subsequently regenerated by thermal dissociation. The anodic reaction involves either a metal/metal-oxide couple or a lower/higher oxide couple The thermal reduction phase is thus described as

$$M_rO_s \triangleq M_rO_{s-x} + x/2\ O_2 \quad \text{(e.g., } PbO_2 \rightarrow PbO + 1/2\ O_2\text{)}.$$

Following establishing favorable equilibrium behavior, the kinetics of the anodic process is of greatest importance. After a favorable kinetic behavior is demonstrated, the investigation will turn to the other features relevant to the chosen process. These include oxide coherence (minimize degradation of substrate upon cycling), oxide layer thickness (maximization of oxide to substrate weight ratio), oxide layer conductivity (ionic and electronic), and thermal reduction parameters.

The objective of this research is to define a scheme that improves the energy efficiency of hydrogen production by the reduction of electrode overpotentials, reduction of cell ohmic drop accomplished by the elimination of customary separation diaphrams, etc.), and by improved use of reactor heat by waste heat utilization.

1. J. W. Diggle, Ed., Oxides and Oxide Films, Marcel Dekker, Inc., New York, Volume 1, 1972.
2. L. Young, Anodic Oxide Films, Academic Press, New York, 1961.

4. RESEARCH PLANS FOR CALENDAR YEAR 1976

Charles W. Tobias

Research on the fundamentals of *transport phenomena in electrochemical reactors* will be focused on the elucidation of the dynamics of formation of metallic and of gas phases at electrode surfaces *in high rate processes:*

a) Experimental prototype cutting of metal profiles by anodic dissolution (ECM) under broad ranges of current densities, solution compositions and flow rates, will serve to evolve a practical theoretical model by which cathode geometries appropriate *for obtaining predetermined anode shapes* may be designed.

b) The surface memory effect will be modeled, and experimentally tested to establish methods for the prediction of micro- and macro-geometries of electroformed (thick) metallic deposits.

c) Experiments will be initiated for the *determination of supersaturation at gas evolving electrodes* under conditions characteristic of practical electrolysis, *to advance* new approaches in the design of *more efficient electrolytic gas generation equipment.*

The project directed toward *innovations in electrochemical synthesis and energy conversion,* involving energetic reactants or products (e.g., alkali metals) in propylene carbonate as ionizing solvent will be continued in the following directions:

a) Solvent stability studies will be conducted *exploring the range of possible reactions at the positive electrode.* Specifically the use of sacrificial metals (e.g., Al, Mg) and of halogen electrodes (Cl_2,Br_2) will be evaluated *for use in electrowinning and in galvanic cells.*

b) Thermodynamic and kinetic criteria of the *separation of alkali metals* by selective reduction *from solutions of their mixed salts* will be examined.

Exploratory work on an *electrolysis-thermal hybrid cycle for the efficient production of hydrogen* will be completed. Two reaction schemes will be evaluated:

a) Oxidation of a lower-to-higher metal oxide in a cell where hydrogen is evolved at the cathode, followed by thermal dissociation of the higher metal oxide to the lower oxide and oxygen, etc.

b) Oxidation of a metal in an electrochemical cell, followed by chemical reduction of the oxide at medium high temperature (e.g., by carbon monoxide).

5. 1975 PUBLICATIONS AND REPORTS

Charles W. Tobias and Associates

Journals

1. F. R. McLarnon, R. H. Muller and C. W. Tobias, Light-Deflection Errors in the Interferometry of Electrochemical Mass Transfe. Boundary Layers, J. Electrochem. Soc. 122, 59-64 (1975) (LBL-2240 Rev.).

2. Jacob Jorné and Charles W. Tobias, Thermodynamic Properties of the Alkali Metals in Aluminum Chloride-Propylene Carbonate Solution, J. Electrochem. Soc. 122, 624-632 (1975) (LBL-1111 Rev. 4).

3. J. E. A. John, C. W. Tobias et al., Emissions Control of Engine Systems, Consultant Report to the Comm. on Moter Vehicle Emissions, Commission on Sociotechnical Systems National Research Council, (Sept., 1974)(Published by EPA).

4. F. R. McLarnon, R. H. Muller and C. W. Tobias, Derivation of One-Dimensional Refractive-Index Profiles from Interferograms, J. of the Optical Soc. of Amer. 9, 1011-1018 (1975)(LBL-3141).

5. J. Jorné and C. W. Tobias, Electrodeposition of the Alkali Metals from Propylene Carbonate, J. Appl. Electrochem. 5, 279 (1975)(LBL-1111 Rev. 6).

6. F. R. McLarnon, R. H. Muller and C. W. Tobias, Reflection Effects in Interferometry, Applied Optics 14, 2468 (1975) (LBL-3140).

7. J. W. Bjerklie, E. J. Cairns, C. W. Tobias and D. G. Wilson, An Evaluation of Alternative Power Sources for Low Emission Automobiles, Automative Engineering, SAE 750930, Oct. 1975.

8. J. R. Selman and C. W. Tobias, Unsteady State Effects in Limiting Current Measurements, J. Electroanal. Chem. 65, 67-85 (1975)(LBL-20557 Rev.).

9. J. Jorné and C. W. Tobias, Potential Differences between the Alkali Metals and their Amalgams 122, 1485 (1975)(LBL-1111 Rev. 5).

Papers Presented and Invited Lectures

*1. C. W. Tobias, Trends in Electrochemical Technology, Lockheed Palo Alto Research Laboratory, March 6, 1975.

*2. C. W. Tobias, Electrolysis at Very High Rates, University of Wisconsin, Madison, April 23, 1975.

3. J. F. Cooper, R. H. Muller, C. W. Tobias, Periodic Phenomena during the High Current Density Dissolution of Copper, 147th Meeting of The Electrochemical Society, Toronto, Canada, May 12, 1975.

*4. C. W. Tobias, Instruction in Electrochemical Engineering at Berkeley, 147th Meeting of The Electrochemical Society, Toronto, Canada, May 14, 1975.

*5. C. W. Tobias, Corrosion, and Instruction in Electrochemical Engineering at Berkeley, University of Veszprem, September 11, 1975.

*6. C. W. Tobias, Incentives and Prospects for the Electric Automobile, Hungarian Academy of Sciences, Budapest, Hungary, September 16, 1975.

*7. C. W. Tobias, Chemical Engineering Education at Berkeley, University of Technical Sciences, Budapest, Hungary, September 17, 1975.

*8. C. W. Tobias, Mass Transfer and Current Distribution in Electrochemical Systems, Hungarian Chemical Society, Budapest, Hungary, September 18, 1975.

9. C. W. Tobias, Cathodic Reduction of Potassium in Propylene Carbonate, 26th Meeting of the International Society of Electrochemistry, Baden, Austria, September 25, 1975.

10. J. Jorné and C. W. Tobias, Electrodeposition of the Alkali Metals in Propylene Carbonate, 26th Meeting of the International Society of Electrochemistry, Baden, Austria, September 25, 1975.

*11. C. W. Tobias, The Future of Electrochemical Engineering, the first BASF Renowned Scientist Lecture, Wayne State University, Detroit, Michigan, December 3, 1975.

LBL Reports

1. John Frederick Cooper, Periodic Phenomena in the High Current Density Anodic Dissolution of Copper (Ph.D. Thesis, University of California, Berkeley), LBL-2730, April 1975.

2. Ronald Alan Putt, Studies of the Events Occurring at Gas-Evolving Electrodes (M.S. Thesis, University of California), LBL-3989, Oct. 1975.

3. J. R. Selman and C. W. Tobias, The Limiting-Current Technique in Mass-Transfer Measurements, UCRL-20557 Rev. 1.

2. HIGH TEMPERATURE AND SURFACE CHEMISTRY

a. High Temperature Chemistry

Leo Brewer, Principal Investigator

1. THERMODYNAMIC PROPERTIES OF THIRD AND FOURTH GROUP TRANSITION METALS WITH PLATINUM GROUP METALS

Gary L. Bullard and David A. Goodman

A high temperature, solid electrolyte cell is being used to measure the variation of the Gibbs energy with concentration for the tantalum-iridium system. It is hoped the results will allow improvement of bonding models based on utilization of low-energy bonding orbitals. The solid-electrolyte presently in use is made of a ZrO_2-CaO solid solution. Work is in progress to include electrolytes based on HfO_2 and ThO_2.

2. APPLICATIONS OF REGULAR SOLUTION THEORY TO METALLIC SOLUTIONS

Robert H. Lamoreaux

Regular solution calculations are being tested against experimental data for metallic alloys in which acid-base interactions producing strongly negative deviations from ideality are expected to be small. The effects of size disparity, deviation from the geometric mean assumption, and the use of bonding energy of the valence state rather than that of the ground state for characterizing the cohesive energy are being tested. Procedures for estimating the thermal expansivities of liquid metals and the solubilities of inert gases in liquid metals are being developed.

3. THERMODYNAMIC EVALUATION AND COMPILATION OF METAL ALLOY SYSTEMS

Leo Brewer, Ralph R. Hultgren and Robert H. Lamoreaux

A bibliography of publications on the thermodynamics of metallic binary and ternary systems is being maintained. The compilation of thermodynamic properties of molybdenum and its compounds and the diffusion characteristics of molybdenum alloys is nearly completed.* Work is continuing on the thermodynamic properties of the alloys systems of the lanthanide and actinide elements and binary and ternary alloys of iron.

*Partially supported by the International Atomic Energy Agency.

4. MATRIX SPECTRA OF OXIDES OF CALCIUM*

Walter D. Duley, John Ling-Fai Wang and Lester Andrews

The study of some of the specimens formed when Ca is deposited together with N_2O, O, O_2, and O_3 in rare gas or nitrogen matrices at liquid hydrogen temperatures has essentially been completed. One paper has been published, a second paper has been submitted for publication, and a third manuscript is almost complete.

*Supported in part by N.S.F.

5. RESEARCH PLANS FOR CALENDAR YEAR 1976

Leo Brewer

The work on matrix isolation of oxide species of calcium will be essentially terminated with the completion of the last manuscript summarizing the work done. If resources allow, a few isotopic experiments will be carried out to test some points not completely resolved.

With the high temperature CaO-ZrO_2 electrolyte cell in operation, measurements of the activity of tantalum in iridium-rich alloys are expected to be completed this year. The extension of the electrolyte to HfO_2 and ThO_2 based solid solutions will allow measurements for more highly reduced alloys with extensions to other alloys of third and fourth group transition metals with the platinum group metals that can help improve our understanding of the bonding of these strongly interacting metals.

If funds permit, the evaluation and compilation program for thermodynamic data and phase diagrams of metals will be expanded. The molybdenum manuscript should be completed early in the year and progress on the other compilation should accelerate and be extended to additional new materials that should be of value in development of new energy processes.

6. 1975 PUBLICATIONS AND REPORTS

Leo Brewer and Associates

Journals

1. Leo Brewer, National Academy of Sciences Report on the Conference on Thermodynamics and

National Energy Problems, Washington, D.C., 1974: Plenary Lecture and Discussion, pp. 8-24, Summary of Conclusions and Recommendations (with F. D. Rossini and E. F. Westrum, Jr.), pp. iv-xiv; Discussion, pp. 19-24, 53, 59, 301, 328-9, and 338-62; editing of Section VI, Energy Storage and Solar Energy.

2. Leo Brewer, Stability of Silicon Monoxide, J. Chem. Educ. 10, 686 (1975).

3. Leo Brewer (with F. D. Rossini, A. Ferri, F. S. Johnson, R. H. Miller, J. M. English, I. Glassman, S. S. Penner, and R. A. Rudey), National Academy of Sciences Report on Environmental Impact of Stratospheric Flight, 1975, Chapter 6, Nitrogen Oxide Emissions and Engine Design and Operation, pp. 66-73; Chapter 7, Climate and Aircraft Fuels, pp. 74-76; Appendix J, Detailed Report on Engines and Fuels, pp. 257-290.

4. Lester Andrews, Vibronic Spectra of the Ozonide Ion in the Matrix-Isolated $M^+O_3^-$ Species, J. Chem. Phys. 63, 4465 (1975).

LBL Reports

1. Lester Andrews, Ultraviolet Absorption Studies of the Alkali Metal Atom-Oxygen Molecule Matrix Reaction, submitted to J. Phys. Chem. (LBL-4164).

2. Leo Brewer, The Cohesive Energies of the Elements, (LBL-3720).

3. Robert H. Lamoreaux, Calculated Enthalpies of Transition at 0°K for Several Metallic Phase Transition, submitted to J. Solid State Chem. (LBL-3711).

4. Lester Andrews, Optical Spectra of the Dibromide and Diiodide Ions in the Matrix-Isolated $M^+Br_2^-$ and $M^+I_2^-$ Species, submitted to J. of Amer. Chem. Soc. (LBL-3997).

5. Lester Andrews, Optical Spectra of the Difluoride, Dichloride, and Trichloride Ions in the Matrix-Isolated $M^+F_2^-$, $M^+Cl_2^-$, and $M^+Cl_3^-$ Species, submitted to J. of Amer. Chem. Soc. (LBL-4111).

b. Nuclear Technology Problems

Donald F. Olander, Principal Investigator

1. REACTION OF ATOMIC HYDROGEN WITH PYROLYTIC GRAPHITE

M. Balooch* and D. R. Olander

Over one hundred years have elapsed since Berthollet[1] first investigated the thermodynamics of the carbon-hydrogen system, and four decades have passed since Barrer's[2] classic kinetic study of this system appeared.[3] The voluminous literature on this subject since these early investigations has been reviewed in a separate document.[3] Recently, the graphite-hydrogen reaction has assumed an important role in several energy production technologies, in particular production of inexpensive heating gas by coal gasification, and graphite corrosion in the high temperature gas cooled reactor and of first wall liners in the controlled thermonuclear reactor.

All previous studies of the carbon-hydrogen reaction have been of the conventional chemical kinetic type, in which hydrogen gas at pressures ranging from a few torr to tens of atmospheres is passed over a sample of carbon held at temperatures between 600 and 2600°C. Usually the sole measure of the reaction rate is sample weight loss, although occasionally the quenched gases are analyzed for methane, acethlene and higher hydrocarbons. The specimens are in the form of tubes, bulk shapes, fine filaments, or powders in a packed bed. The types of carbon range from amorphous to graphitic. Even among the graphites, the reaction kinetics are quite sensitive to the purity and degree of crystallinity of the sample. It is not surprising that the apparent reaction rate constant obtained from these data differ by as much as five orders of magnitude at the same temperature. There is no established mechanism of the reaction.

In the present investigation, the reaction specimens are high-temperature annealed pyrolytic graphite in either the basal or prism plane orientations. The molecular beam-mass spectrometric techniques described in Ref. 4 are employed in the kinetic studies. The molecular form of hydrogen is very unreactive towards graphite; the inertness of H_2 is due to the very low probability of dissociative adsorption of the diatomic molecule on graphite surfaces. To render the reaction detectable in the molecular beam system, atomic hydrogen is used as the reactant gas. Thermal dissociation of H_2 prior to striking the graphite target greatly increases the sticking probability but does not influence the course of the subsequent surface reactions which ultimately lead to gaseous hydrocarbon products. The variation of reaction product yield (both the signal amplitude and its phase lag) is monitored as a function of beam intensity, surface temperature and modulation frequency.

The temperature dependence of the reaction is shown in Fig. 1. At temperatures up to 800°K, methane is the sole product. Acetylene is observed at temperatures above 1000°K. Between 800 and 1000°K, no carbon gasification occurs; the surface acts only to recombine H atoms to form H_2. The data are analyzed in terms of the model shown in Table 1. Methane is formed by sequential addition of H atoms to CH_n (n = 0,1,2,3) and acetylene is formed by surface combination of two CH groups. Solution and diffusion of H atoms in the graphite lattice are important steps in the process. The agreement between the model and the molecular beam data is very good.

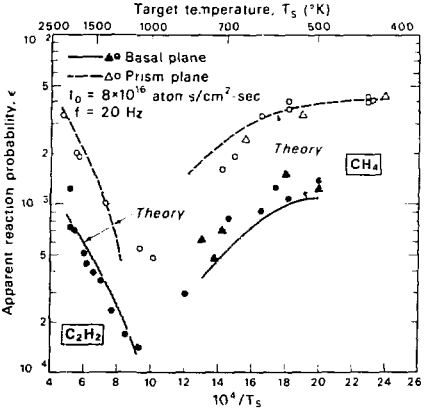

Fig. 1. Temperature dependence of the reaction probabilities for methane and acetylene.
(XBL 755-4920)

Table 1. H atom-Graphite Reaction Model.

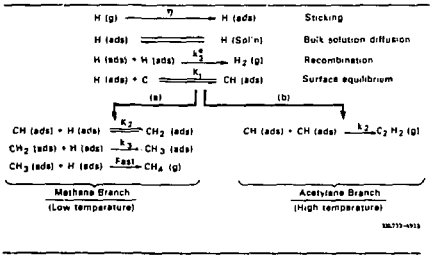

The model predictions are compared to previous high pressure (1 atm H_2) carbon gasification rates determined in conventional kinetic experiments in Fig. 2. The solid curves and the symbols represent previous data as summarized in Ref. 3. The dashed curves are the predictions of the present model (Table 1) with η' = sticking probability of molecular hydrogen as a parameter. The significance of the comparison shown in Fig. 2 is two-fold. First, the mechanism determined by the low pressure (5×10^{-4} torr) molecular beam experiment using atomic hydrogen as reactant can be extrapolated to predict gasification rates at H_2 pressures which are six orders of magnitude larger without any adjustments of the model. Second, the fact that $\eta' = 0$ is adequate to fit the older data substantiates the model proposed by Clarke and Fox,[5] who attributed all reaction to the dissociated fraction of the reactant hydrogen gas.

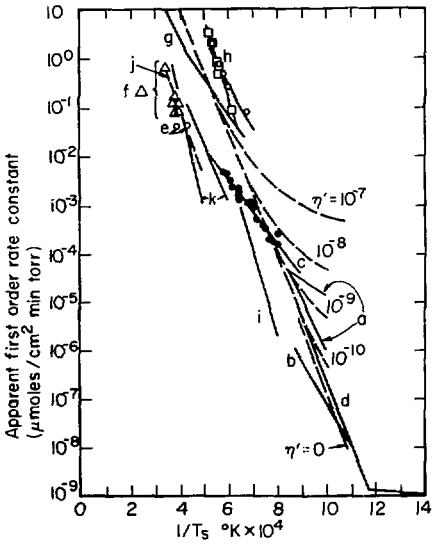

Fig. 2. High pressure kinetics of the carbon-hydrogen reaction. Dashed lines: extrapolation of model based on molecular beam data to H_2 pressures of 1 atm for various H_2 sticking probabilities; solid lines and points: data from investigations summarized in Ref. 3. (XBL 727-4404)

In most reaction systems, extrapolation of a reaction model determined by low pressure molecular beam methods by six orders of magnitude in reactant gas pressure would be unsuccessful because the low pressure model would not be able to foresee coverage effects which become important at high pressures. However, because of the very low sticking probability of molecular hydrogen, the H atom coverages of the surface calculated from the model for p_{H_2} = 1 atm are found to be of the same order of those in the molecular beam experiment, namely < 0.1% of a monolayer.

---

*Present address: Department of Mechanical Engineering, Aryā-Mehr University of Technology, Teheran, Iran.

1. M. Bertholet, Ann. Chim. Phys. 67, 52 (1963).
2. R. M. Barrer and E. K. Rideal, Proc. Roy. Soc. 149A, 231 (1935).
3. R. A. Krakowski and D. R. Olander, Lawrence Berkeley Laboratory Report UCRL-19149 (1970).
4. R. H. Jones, D. R. Olander, W. J. Siekhaus, and J. A. Schwarz, J. Vac. Sci. Technology 9, 1429 (1972).
5. J. T. Clarke and B. R. Fox, J. Chem. Phys. 46, 827 (1967).

2. ANALYSIS OF NONLINEAR REACTIONS IN MODULATED MOLECULAR BEAM-SURFACE EXPERIMENTS*

Alan Ullman† and D. R. Olander

An approximate method of analyzing nonlinear reaction models in modulated molecular beam surface kinetic studies is developed. The exact method for treating nonlinear surface mechanisms[1] is tedious and almost always requires computer analysis. The proposed approximate method is a simple extension of the Fourier expansion technique valid for linear surface reactions[2]; it quickly provides analytical expressions for the phase lag and amplitude of the reaction product for any type of nonlinear surface mechanism, which greatly facilitates comparison of theory and experiment.

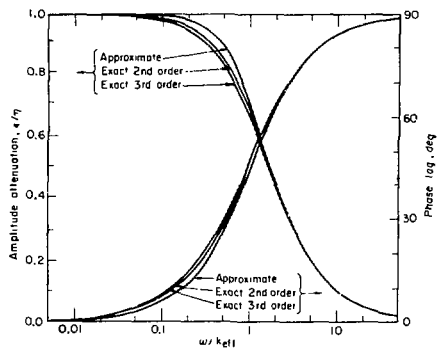

Fig. 1. Phase lag and amplitude attenuation for first, second and third order reaction kinetics. The curve labelled "approximate" corresponds to the exact first order solution and to the linearized results for higher order reactions.

(XBL 757-4475)

The approximate and exact methods are compared for a number of prototypical surface reactions which include coverage-dependent adsorption and reaction kinetics of order greater than unity. Figure 1 shows the good agreement between the approximate method and the exact solution for the reaction:

$$A_2(g) \rightarrow 2A(ads)$$

followed by

$$\text{surface atom} + mA(ads) \rightarrow \text{Product}$$

where m = 2 or 3, representing second and third order kinetics, respectively. Except for certain extreme forms of coverage-dependent adsorption, the approximate method provides a good representation of the exact solution. The errors increase as the nonlinearities become stronger. Fortunately, when the discrepancy between the two methods is substantial, the reaction product signal is so highly demodulated that reliable experimental data usually data usually cannot be obtained in these regions anyway.

---

*Abstracted from LBL-4130, to be published in Int. J. Chem. Kinetics.

†Present address: Energy and Kinetics Department, School of Engineering and Applied Sciences, University of California, Los Angeles, Calif.

1. D. R. Olander, in "The Structure and Chemistry of Solid Surfaces", G. A. Somorjai, Ed., p. 45-51, Wiley, New York (1969).
2. R. H. Jones, D. R. Olander, W. J. Siekhaus and J. A. Schwarz, J. Vac. Sci. & Technol. 9, 1492 (1972).

3. TWO-UP, ONE-DOWN IDEAL CASCADES FOR ISOTOPE SEPARATION*

Donald R. Olander

Ideal cascades for isotope separation are usually constructed so that the heads stream from a stage furnishes part of the feed to the next stage up and the tails stream from the stage is fed to the adjacent lower stage. This symmetric arrangment is satisfactory if the separative power of the individual separating units of which the cascade consists is independent of the cut at which they are operated. However, some separating units operate more efficiently at a cut considerably less than one-half than they do at a cut in the neighborhood of one-half. The gas centrifuge is an example of an isotope separation device that exhibits this preference. Operation of these units in a cascade can be improved by carrying the enriched stream from each stage two stages forward instead of one stage forward. This modification permits each separative unit to operate at a lower cut than the one that would be required of it in a conventional cascade, yet maintains the condition of no-mixing of streams of different composition. The "two-up, one-down" ideal cascade has been briefly mentioned in the literature, but no detailed analysis has been reported. The purpose of this study was to provide such an analysis.

A schematic of a two-up, one-down ideal cascade is shown in Fig. 1. Each separating unit in the cascade operates at the same throughput and cut; the heads and tails flow rates from each stage are permitted to vary in a manner which insures that the two streams which provide the feed to a

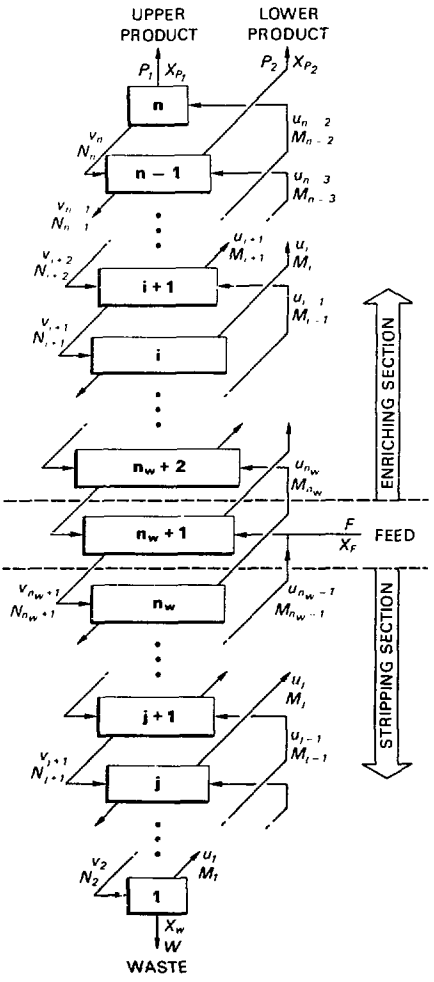

Fig. 1. Interstage flows in a two-up, one-down ideal cascade. (XBL 754-4843)

stage have the same composition. The required variation of interstage flows with height in the cascade is accomplished by joining the appropriate number of separating units in parallel at each stage. Application of the theory to ideal cascades composed of separating units which exhibit high separative power at low cuts shows that the two-ups, one-down configuration provides the same performance as does the symmetric cascade but requires fewer units to do so. Since the cost of isotope separation is directly proportional to the number of separating units in the cascade, the economics of uranium enrichment may be substantially improved by the nonconventional cascade design.

*Abstracted from LBL-4103, to be published in Nuclear Technology.

4. DESIGN OF IDEAL CASCADES OF GAS CENTRIFUGES WITH VARIABLE SEPARATION FACTORS*

D. R. Olander

As far as is known, all cascades for uranium isotope separation are designed with all separating units operated in exactly the same manner. When the separation factor (or the separative power) does not vary with stage number, the characteristics of the ideal cascade may be obtained from the theory developed by Cohen.[1] However, we show in this study that it is possible to construct ideal (i.e., non-mixing) cascades in which the separation factor varies from stage to stage. For certain types of separating units, the performance of this "variable-α" ideal cascade is superior to that of the conventional "constant-α" ideal cascade.

In order to attain the non-mixing condition at each point in the cascade where streams join, each separating unit in a constant-α cascade must be operated symmetrically.[2] In symmetric operation, the heads separation factor α is equal to the tails separation factor β. In a variable-α ideal cascade, on the other hand, the no-mixing requirement imposes different constraints on the asymmetries of the units in adjacent stages.

The ability of a centrifuge to perform as an isotope separator is described by the dependence of its separative power on all experimentally controllable variables. The latter may be divided into two classes: internal parameters and operating parameters. The distinction between the two classes is as follows: changing an internal parameter affects only the product and waste compositions but does not alter the feed, product or waste flow rates. Change of an operating variable disrupts both the flows and compositions of the streams leaving the centrifuge. The two operating variables are the cut θ and the throughput L. Among the internal parameters are the temperature differences across the end caps of the rotor and the design and position of any scoops inside the rotor. The geometry (height and radius) and peripheral speed of the rotor are not considered to be controllable variables. The rotor is always driven close to its strength or stability limit; there is no reason to do otherwise.

Theory and experiment give the separative power as a function of all controllable parameters of the centrifuge, or by a function of the general form:

$$\delta U(L, \theta, \text{internal variables})$$

The centrifuge performs most efficiently when the internal variables are adjusted (at each combination of L and θ) so that the separative power is a maximum. The optimized separative power is therefore a function only of the operating variables L and θ. Alternatively α and β may replace L and θ as independent variables.

Using an asterisk to denote optimization with respect to all internal variables, the function $\delta U^*(\alpha,\beta)$ is called the performance function of the centrifuge. Provided all of the internal variables have been considered in the optimization process, the isotope separating capability of the centrifuge is completely defined by the performance function.

If the condition of symmetry (α=β) is imposed upon the centrifuge because it is to be employed in a constant-α ideal cascade, δU^* is a function of L only. However, for the variable-α cascade, the restriction α = β does not apply and knowledge of the complete (i.e., two-dimensional) performance function must be used in cascade analysis.

The contour plot of Fig. 1 shows the performance function for this type of centrifuge. The separative power in the region of symmetric

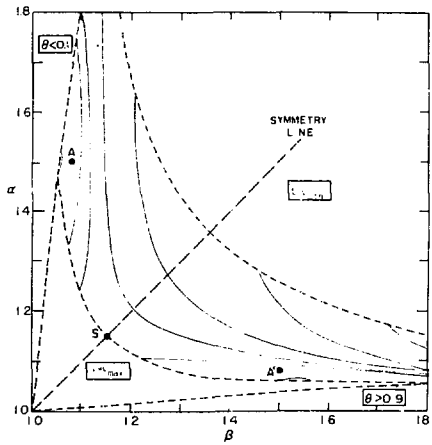

Fig. 1. Performance function for a gas centrifuge with a minimum in the internal flow near the midplane. The small segments of contour lines near points A and A' represent the largest values of δU^*. (XBL 7412-7628)

operation (i.e., along the 45° line where $\alpha = \beta$) is lower than on the heights on either side. Consequently, a variable-α cascade whose stage operating points oscillate between A and A' in Fig. 1 shows better performance (by about 5%) than the best constant-α cascade (which is at point S). This calculation demonstrates that for at least one type of performance function, cascades should be constructed with variable rather than constant separation factors at each stage. Determination of the performance function of a particular centrifuge (i.e., one of specified roter geometry and peripheral speed) either theoretically or experimentally is a tedious job, primarily because of the necessity of optimizing the performance function with respect to all internal variables which can affect the gas circulation inside the rotor. The cost of obtaining the performance function $\delta U^*(\alpha,\beta)$ must be justified in terms of the potential benefits of more efficient cascade performance. The savings of ~ 5% found for the hypothetical centrifuge in this study can be translated into a cost saving in the following way. The annual separative work capacity which will be required in the United States in the next 50 years has been estimated to be between 100 and 400 million SWU/yr, depending upon the date of introduction of LMFBRs. The specific cost of plants constructed in this time period will probably be between $130 and $200 per SWU/yr capacity. Thus, the investment in isotope separation plants up to the year 2020 will be between 13 and 80 billion dollars. If all of this capacity is in the form of centrifuges, a 5% improvement in efficiency represents a saving of between 0.6 and 4 million dollars. There appears to be ample incentive to justify exploring all proposed centrifuge designs for the possibility of cost reduction by use in ideal cascade with variable separation factors.

*Abstracted from LBL-3551 Rev., To be published in Nucl. Sci. & Eng.

1. K. P. Cohen, "The Theory of Isotope Separation as Applied to the Large Scale Production of U-235", McGraw-Hill, New York (1951).
2. This requirement assumes that the heads and tails streams from a stage are fed to the adjacent upper and lower stages, respectively. If the heads or tails streams are allowed to bypass adjacent stages, ideal, constant-α cascades can be constructed using a single type of asymmetrically oerated separating unit. This type of design is analyzed in the preceding summary.

5. EQUIPMENT DEVELOPMENT FOR HIGH TEMPERATURE STUDIES OF UO_2

R. Yang, K. Kim and D. R. Olander

The chemical behavior of uranium dioxide at high temperatures (1500-3000°K) is important to the successful performance of nuclear fuel elements. As a basis for conducting high temperature studies of UO_2, two specialized pieces of equipment have been developed and constructed.

The oxygen-to-metal ratio significantly affects all of the high temperature chemical properties of UO_2. Figure 1 shows the layout of the UO_2 stoichiometry control and measurement apparatus. The equipment is designed to permit preparation of urania specimens of known oxygen-to-metal ratios. The specimen is supported from the arm of an electrobalance inside a tungsten crucible which is placed in a vacuum resistance furnace. The oxygen potential of the system (which controls the O/U ratio of the specimen) is established by a water vapor-hydrogen gas mixture which flows over the specimen. The H_2O/H_2 ratio of the gas is determined by analysis by an on-line mass spectrometer. The weight gain or loss of the sample as recorded by the electrobalance determines the O/U ratio. The equipment will be used to prepare specimens of UO_{2-x} for experiments investigating 1) the reaction of H atoms with

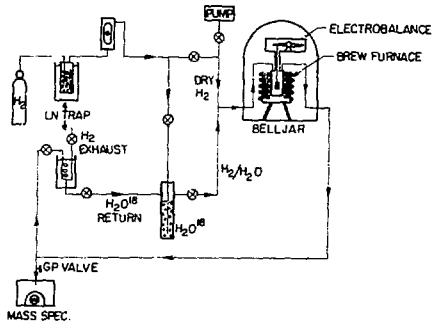

Fig. 1. Apparatus for control and measurement of the stoichiometry of UO_2. (XBL 7511-7613)

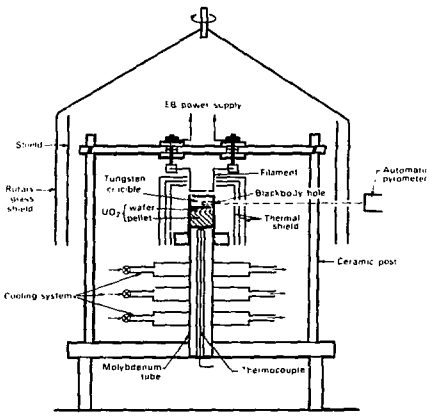

Fig. 2. Temperature gradient furnace. (XBL 7511-9157)

UO_2, 2) laser vaporization of UO_2, 3) thermal gradient migration of metallic inclusions in UO_2, and 4) oxygen self diffusion in UO_2 by a diffusion couple consisting of UO_2^{18} and UO_2^{16} wafers.

Figure 2 shows the design of a temperature gradient furnace in which experiments investigating the redistribution of fuel constituents (oxygen, heavy metals and fission products) can be conducted. The specimen of UO_2 is contained in a tungsten crucible which is closed at the top to avoid UO_2 loss by vaporization. The top of the crucible is heated by electron bombardment and the bottom temperature of the specimen is controlled by a cooled molybdenum rod. The upper temperature is measured by an automatic optical pyrometer and the bottom temperature by a W/W-Re thermocouple. The furnace is capable of producing a temperature gradient of 1500 °K/cm at a maximum temperture of 3000°K.

6. RESEARCH PLANS FOR CALENDAR YEAR 1976

Donald R. Olander

The migration of metallic fission product precipitates up the temperature gradient in nuclear fuel elements will be investigated using the temperature gradient furnace. The fission product inclusions will be simulated by tungsten particles.

The stoichiometry control apparatus will be used to prepare wafers of $U^{18}O_2$ and $U^{16}O_2$ for measuring the self diffusion coefficient of oxygen in this ceramic. This transport property is important in assessing the extent of oxygen redistribution in nuclear fuel elements.

The laser pulsing apparatus will be used to measure the vapor pressure of UO_2 up to ~ 5000°K. In addition to the experimental work, a major computational effort is required to properly interpret the vaporization rate in terms of the vapor pressure. The high temperature vapor pressure of UO_2 is important in analysis of nuclear fuel meltdown accidents.

The reaction of modulated beams of atomic hydrogen with UO_2 and several candidate insulator materials for fusion reactors (Al_2O_3, SiC) will be studied. The stability of insulators in a hydrogen-rich plasma evironment is important to the successful functioning of a controlled thermonuclear reactor.

The radiation-enhanced corrosion of graphite by trace impurities (H_2O, CO_2) in the coolant stream of the high temperature gas cooled reactor will be investigated using the Van de Graaff accelerator. In addition, the homogeneous radiolysis of the water gas shift reaction will be studied.

7. 1976 PUBLICATIONS AND REPORTS

Donald R. Olander and Associates

Journals

1. R. A. Olstad and D. R. Olander, Evaporation of Solids by Laser Pulses. I-Iron, J. Appl. Phys. 46, 1499 (1975) (LBL-3167).

2. R. A. Olstad and D. R. Olander, Evaporation of Solids by Laser Pulses, II--Zirconium Hydride, J. Appl. Phys. 46, 1509 (1975) (LBL-3168).

3. R. Yang, J. Hovingh, E. LeBorgne and D. R. Olander, Diffusion of Lanthanum in Liquid Uranium, High Temp. Sci. 7, 55 (1975)(LBL-2534 Rev.).

4. C. B. Kerkdijk, C. Smits, and D. R. Olander, The Shape of Doppler-Broadened Spectral Lines Produced by Light Atom Reflection from Metals, I--Theory, Surf. Sci. 49, 28 (1975).

5. C. B. Kerkdijk, C. M. Smits, F. W. Saris, and D. R. Olander, The Shape of Doppler-Broadened Spectral Lines Produced by Light Atom Reflection from Metals, II--Experimental - Protons on Copper, Surf. Sci. 49, 45 (1975).

6. S. Guarro and D. R. Olander, Actinide Redistribution due to Pore Migration in hypostoichiometric Mixed-Oxide Fuel Pins, J. Nucl. Mat. 57, 136 (1975) (LBL-3196).

7. M. Balooch and D. R. Olander, Reactions of Modulated Molecular Beams with Pyroltic Graphite. III Hydrogen, J. Chem. Phys. 63, 4772 (1975) (LBL-4146).

Presented Papers and Lectures

1. D. R. Olander, Perspectives on Nuclear Power, Environment & Energy Section of the Commonwealth Club of California, Nov. 3, 1975, San Franscisco.

2. D. R. Olander, Nuclear Power, Northern Calif. Geological Soc., Oct. 15, 1975, San Franscisco.

3. D. R. Olander, Laser Vaporization of Solids, Amer. Chem. Soc., Chicago, Aug. 27, 1975.

4. D. R. Olander, Hydrogen Attack of Fusion Reactor First Walls made of Graphite, American Nuclear Society Winter Meeting, Nov. 19, 1975, San Franscisco.

5. V. Kruger, The Kinetics of Radiolytic Gas Phase Reactions by Modulated Molecular Beam Mass Spectrometry, 23rd Annual Conf. on Mass Spectrometry, Houston, Texas, May 30, 1975.

6. D. R. Olander, Evaporation of Solids by Laser Pulses, 23rd Conf. on Mass Spectrometry, Houston, Texas, May 30, 1975.

7. A. Machiels, The Reaction of Fluorine and Uranium Dioxide Investigated by Modulated Molecular Beam Mass Spectrometry, California Catalysis Society, Los Angeles, Nov. 7, 1975.

8. A. Ullman, H_2O - D_2O Isotope Exchange on Pyrolytic Graphite, California Catalysis Society, Los Angeles, Nov. 7, 1975.

LBL Reports

1. A. Ullman and D. R. Olander, Analysis of Nonlinear Reactions in Modulated Molecular Beam-Surface Experiments, LBL-4130, Aug. 1975.

2. V. R. Kruger and D. R. Olander, Oxygen Radiolysis by Modulated Molecular Beam Mass Spectrometry, LBL-2727 Rev., Aug. 1975.

3. D. R. Olander, Two-Up, One-Down Ideal Cascades for Isotope Separation, LBL-4103, Aug. 1975.

4. D. R. Olander, Design of Ideal Cascades of Gas Centrifuges with Variable Separation, LBL-3551 Rev., Sept. 1975.

c. Crystallization Kinetics

Lee F. Donaghey, Principal Investigator

Introduction. This research program is concerned with the characterization of chemically reactive processes useful in the preparation of solid-state materials for energy conversion application. Of particular interest are processes for preparing crystalline films and coatings, such as chemical vapor deposition, reactive sputtering and liquid phase epitaxy. The program utilizes the coordinated contributions of the following subprograms: (1) The thermodynamic properties of inorganic compounds and solid solutions are studied by high temperature electrochemical cells using solid electrolytes. (2) The reaction kinetics of plasma, vapor and liquid phase growth processes are explored through reaction rate studies. (3) Heteroepitaxial crystalline layers and films are characterized by diffraction, electronic and optical methods to deduce the influence of process variables on physical properties. (4) The transport processes and energetics of these processes are studied analytically and by computer simulation. These subprograms are coordinated to deduce the influence of process variables on structural and electronic defects, and to provide a comprehensive basis for industrial process design.

1. THERMODYNAMIC STUDIES

T. J. Anderson and L. F. Donaghey

Solid state electrochemical techniques were utilized for the study of some thermodynamic and kinetic properties of Group III and V semiconducting materials.

The sesquioxides of Ga and In are important in semiconductor processing and In_2O_3 is used as a thick film resistor.[1] The Gibbs energies of forming the Group III sesquioxides were directly measured with a solid state galvanic cell employing calcia-stabilized zirconia as the solid electrolyte. This cell can be schematically represented as;

$$Pt|C|M^{III}, M_2^{III}O_3||CSZ||CO, CO_2|Pt \qquad (1)$$

where M^{III} is the Group III metal. A reference oxygen activity was established from the high temperature equilibrium of CO and CO_2. Analysis of the developed cell potential measurements produced the following expressions for the formation free energies:

$$\Delta G_f^o(\beta\text{-}Ga_2O_3) = -265,300(\pm 150) + 82.47(\pm 0.16)\ T \quad \text{kcal/mole}$$

$$\Delta G_f^o(In_2O_3) = -223,160(\pm 140) + 79.47(\pm 0.12)\ T \quad \text{kcal/mole}$$

Comparison was made to other reported free energies by a third law calculation with the data of this investigation proving to be the most consistent.

Solid state electrochemical cells were employed to measure gallium activities in Ga-Sb liquid alloys. A survey of the available literature indicated gallium activities ranging from moderately positive to strongly negative deviations from Raoults law. The results of this investigation showed moderate negative deviations from ideality in the composition range $0.059 \leq x_{Ga} \leq 0.855$. From the temperature dependence of the measured activities, partial molar enthalpies and entropies were calculated; these are within experimental error, in agreement with calorimetric data[2,3] to calculate the liquidus temperature of the Ga-Sb system: the results were in excellent agreement with measured liquidus temperatures. The effect of short-range ordering was also investigated.

Coulometric titration techniques were used to investigate the solubility and diffusivity of oxygen in liquid indium. Dissolved atomic oxygen was found to follow Henry's law and a saturation solubility of $x_o^{sat} = 3.3\times10^{-5}$ was determined at 908°K. From a galvanostatic response of an indium electrode, an oxygen diffusivity of 2.2×10^{-6} cm sec^{-1} was found, in good agreement with a previous study.[4]

The application of CaF_2 as a solid electrolyte to the study of Group III-and V materials has several advantages over the oxide electrolyte, in that electrodes containing Al can be used, lower working temperatures are accessible, and rapid response allows solid solutions to be investigated. In view of these, several experimental galvanic cell configurations using CaF_2 are under study.

An inert gas purifier was constructed and characterized. The purifying device was designed specifically to remove oxygen and consisted of a two stage process, using a molecular sieve as an initial bulk getter and than hot Ti sponge to obtain the final purity. A CSZ monitoring galvanic cell was used to characterize the purifier performance. As an example of its capability, Ar flowing at a rate of 60 cc/min was purified to

5.4×10^{-39} atm partial pressure of oxygen with the purifier operated at a temperature of 670°K.

1. J. H. W. Dewit, J. Solid State Chem. 8, 142 (1973).
2. B. Predel, and D. E. Stein, J. Less Common Metals 24, 391 (1971).
3. A. Yazawa, T. Kawashima and K. Itagaki, J. Japan Inst-Metals 32, 1788 (1968).
4. K. A. Klinedinst, and D. A. Stevenson, J. Electrochem. Soc. 120, 304 (1973).

2. VAPOR PHASE ETCHING KINETICS OF GaP

C. Figueroa and L. F. Donaghey

The kinetics of vapor phase etching of GaP in H_2-PH_3-NH_3-HCl gaseous mixtures is under study by thermogravimetric analysis to determine the mechanisms and characteristics of vapor phase etching, and to determine conditions for optimum surface preparation prior to epitaxial growth.

Mechanisms for nitrogen incorporation into gallium phosphide, GaP, during vapor phase growth were studied. It is proposed that the anomalous solubility is governed by relatively strong adsorption of ammonia molecules on selective surface sites.[1] It is shown that nitrogen already in the bulk solid attracts electrons from the adjacent surface gallium atoms which make these particular gallium atoms slightly more positive relative to other surface gallium atoms. The ammonia molecule (NH_3) would therefore have a longer residence time on these selective sites and a greater probability of nitrogen incorporation. The proposed model allows several phenomena to be supported by existing experimental evidence.[1,2] In particular, by increasing the ammonia partial pressure, the larger ammonia surface coverage decreases the epitaxial growth rate. Also, the magnitude of nitrogen incorporation into gallium phosphide during vapor phase growth varies almost linearly with ammonia partial pressure.

Vapor phase etching of (100)+(111) gallium phosphide substrates using HCl-H_2-PH_3 gas mixtures is currently under study with both doped and undoped gallium phosphide samples. The optimal conditions for processing smooth surfaces suitable for vapor phase epitaxy is one objective of the study.

1. G. B. Stringfellow, M. E. Weiner and R. A. Burmeister, J. Electronic Materials 4, 362 (1975).
2. B. W. Hessels, J. Electrochem. Soc. 122, 402 (1975).

3. REACTIVE SPUTTERING OF Ti-C-N COMPOUNDS

R. Gentile and L. F. Donaghey

Ti-C-N compounds have potential use as refractories in coal gasification reactor, where erosion-corrosion problems occurs under severe conditions (700-2000°K; 6-100 atm).[1] Reactive sputtering is a way to produce a study of phases in this system that could occur by diffusion of the gases through a Ti-N refractory. On the other hand, the sputtering parameters needed to produce a film of given composition and structure from reactive sputtering with various reactive gases should be of interest, and are under study toward the further development of this process.[2]

The reactive sputtering of Ti in a nitrogen-argon or NH_3-Ar rf plasma is under study to determine the threshold for target oxidation, and similarities to the previous study for TiO_2.[3] Similar behavior of TiO_2 and TiN at lower partial pressure of reactive gas are expected.[4] The study of the reactive sputter deposition of TiC is also planned. The reactive sputtering of Ti in NH_3, CH_4, Ar plasmas will enable us to study the physical properties of different phases and compositions of films in the Ti-C-N system.

1. A. M. Hall, Material Engineering 80(1), 16 (1974).
2. L. M. Reiber, Le Vide 28, 168, 242 (1973).
3. K. G. Geraghty, LBL-2788.
4. D. Gerstenberg, Ann. Physik 11, 354 (1963).

4. HETEROEPITAXIAL GROWTH OF GaAs FOR SOLAR CELL APPLICATION

A. Lin, R. deBernardy and L. F. Donaghey

The GaAs solar cell is considered one of the attractive solar energy converters for terrestrial application, because of its high efficiency, lack of thermal degradation and relative insensitivity to temperature as compared to cells made from narrower band gap semiconductors. The use of heteroepitaxial GaAs film on a suitable cheap substrate appear to be a promising approach for the fabrication of stable, high efficiency and yet economical solar cells.

For heteroepitaxial growth, it is important to have the growth reaction free of any etching species, such as halides, to prevent contamination by elements from the substrate. Also, a method by which the film can be grown at low temperature is also essential for heteroepitaxial growth, since, most readily available low-cost substrates have a thermal expansion coefficient differing from that of GaAs. Based on these facts, the thermal decomposition of trimethyl gallium $Ga(CH_3)_3$ (TMG) and arsine AsH_3 in a H_2 gas flow system was chosen for the chemical vapor deposition of GaAs.[1]

The growth apparatus constructed in this study is shown in Fig. 1. It consists principally of a water-cooled vertical quartz reactor, a pyrolytic graphite pedestal which can be inductively heated, glass bubblers containing the liquid metal-organic compounds, appropriate flowmeters for monitoring gases and stainless steel tubings and joints. TMG is transfered by bubbling H_2 through the TMG container.

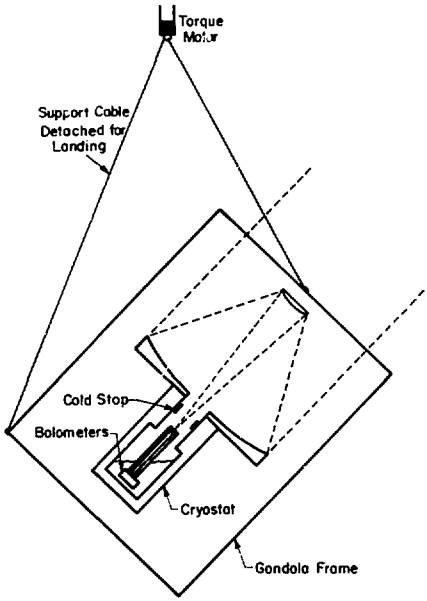

Fig. 1. Schematic diagram of the one meter Cassegrain balloon telescope. The telescope will be suspended at 45° to the zenith from a balloon at an altitude of ~ 100,000 ft. The rotation of the telescope at ~ 2 rpm combined with the rotation of the earth provides a scan of the northern sky in 24 hours of observing time.
(XBL 7510-7473)

*This project is partially supported by a grant from the Director of the LBL.

7. SURFACE MAGNETIC RESONANCE IN MnF_2

Robert B. Bailey and Paul L. Richards

A sensitive magnetic resonance spectrometer employing a 100-kg superconducting solenoid has been constructed in an attempt to detect surface spin states in the widely studied antiferromagnet MnF_2.

In zero field the bulk antiferromagnetic resonance (AFMR) frequency of 8.7 cm^{-1} is determined by the anisotropy and by nearest neighbor exchange interactions in the crystal. Surface spins experience smaller exchange forces and should have lower resonant frequencies. A simple theoretical model predicts that the collective surface excitations split off from the bulk mode by as much as 2.5 cm^{-1}. These surface modes should have penetration depths averaging five atomic layers and involve approximately 4×10^{15} spins per cm^2 of surface area. There has as yet been no experimental verification of surface spin states in any material.

Three different spectroscopic techniques have been used to study the MnF_2 spectrum. Fourier spectroscopy has been limited by the power available at 8.7 cm^{-1} from broadband thermal sources and by detector sensitivity. Antiferromagnetic resonances with a minimum of 6×10^{17} spins and linewidths less than the 0.1 cm^{-1} instrumental resolution were observable in the frequency range 6-9 cm^{-1}. Single crystals showed only the bulk resonance while a powder sample ground from the same crystal and with an effective surface area of 3000 cm^2 showed four additional modes between 7.4 cm^{-1} and 8.3 cm^{-1}. Some of these modes have the intensity expected of surface states. Positive identification can be made only on single crystal smaples where one surface at a time can be studied.

Bulk and surface spin wave modes in MnF_2 should both be split linearly with a g-factor of two in magnetic fields applied parallel to the c-axis of single crystal. We have studied the low frequency branch using field-swept microwave resonance techniques at 10 GHz and 150 GHz. At 150 GHz simple transmission measurements were capable of detecting 2×10^{14} spins in the bulk AFMR mode whose linewidth was 300 gauss. No additional resonances could be identified, suggesting that the surface modes are either substantially broadened, they penetrate fewer than five layers, or they lie very close to the bulk mode and cannot be distinguished from it.

At 10 GHz a bridge sepctrometer has been built with an AFMR sensitivity of 2×10^{12} spins for the measured bulk linewidth of 100 gauss. Operation of a superheterodyne bridge spectrometer at high microwave power levels, in fields up to 100 kg, and at modulation levels of several hundred gauss, places extreme demands on the mechanical stability of the microwave components and the frequency stability of the klystrons. The required spectrometer performance has nearly been achieved. Its sensitivity will be sufficient to detect surface modes penetrating only one atomic layer if their linewidths are no larger than a kilogauss.

8. ELECTRON SURFACE STATES IN LIQUID HELIUM

David K. Lambert and Paul L. Richards

A project has been initiated to study electrons trapped at the surface of liquid helium by a combination of electrostatic "image" attraction and short range "exchange" repulsion. Microwave studies of this system by others have yielded many new effects. These include the observation of transitions between the Stark-shifted energy levels, and electron cyclotron resonance.

By extending these measurements to higher frequencies we expect to be able to study the

5. MODELING OF A VERTICAL CYLINDER REACTOR FOR CHEMICAL VAPOR DEPOSITION OF SILICON

C. W. Manke and L. F. Donaghey

Heat, momentum and mass transfer in vertical cylinder reactors was studied both analytically and experimentally to develop a reactor design thats maximizes the chemical efficiency and deposition rate uniformity of silicon from H_2-$SiCl_4$ reactant mixtures. The growth rate of silicon is shown to vary with the square root of temperature. Thus, considerations of heat transfer in the reactor are essential to the development of models for the deposition rate profile. Contrary to models that have been published in the literature,[2,3] the results indicate that temperature is increasing over most of the susceptor length at typical flow velocities as shown in Fig. 1. The growth rate distributions predicted by this work differ significantly from those predicted by fully developed temperature growth rate models as shown in Fig. 1. A comparison of experimental data with the predicted rates indicates that the methods developed in this

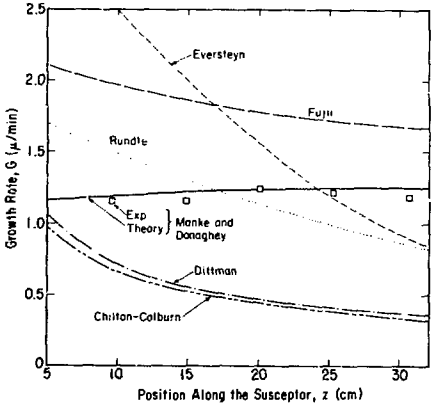

Fig. 1. Silicon epitaxial growth rates predicted by several models compared with experimental data. (XBL 764-952a)

work give a much better description of growth rate variation in the vertical cylinder reactor than do models based on a fully developed temperature distribution.

6. PROCESS CONTROL APPLICATIONS OF MICROCOMPUTERS

D. Jacobs and L. F. Donaghey

Microcomputer-based systems and control algorithms are being studied to devise methods for controlling important chemical processes, such as chemical vapor deposition and diffusion at high temperature. An initial study of thermal control has already been reported by Seim.[1]

In the broad sense we are exploring the possibilities of using a microcomputer system as the single controller of several control loops with a high degree of accuracy, despite its computational limitations and restricted memory capacity.

The experimental system was built around the Intel 8080 microprocessor. With this system a finite time setting deadbeat controller was implemented to achieve, i.e., ripple free thermal response with no over-shoot of a tube furnace. Takahashi[2] states that the use of this method is limited to systems whose dynamic parameters are completely known. In practice, however, this requirement is not readily achievable. We have identified the plant parameters by an interactive, on-line model-reference adaptive system (MRAS) that recomputes the control parameters until complete identification has been achieved. This process compensates for the error introduced by considering the plant as a linear system. The MRAS algorithm that was found applicable to thermal control preblems is a series-parallel type.

Simulations on the CDC 6400 suggest that very good results can be obtained by the above method. Theory does not yield a general solution for this problem, however, and a new dead-beat compensator must be computed for each new set-point since the latter is dependent upon the number of saturated control steps; this is not possible in practice.

An original method of power control has been designed and tested in the course of the project. This controllable power source is used for studies of thermal control. The power control is obtained by analog and digital circuitry, eliminating the need for a digital-to-analog converter at the computer output.

---

1. T. Seim, Technical Report BMWL 1975, Battelle, Nov. 1973.
2. T. Takahashi, et al., Control and Dynamic Systems (Addison-Wesley, 1970).

7. RESEARCH PLANS FOR CALENDAR YEAR 1976

Lee F. Donaghey

The control of heterogeneous nucleation and growth of GaAs on thin film and bulk substrates of metals and insulators will be studied with the objective of improving the grain size in polycrystalline GaAs for low-cost solar cell applications. Theoretical analyses of the effects of thermal cycling and process rate transitions will be initiated to predict methods of grain size enhancement in polycrystalline GaAs layers.

The emission spectra of reactive sputtering plasmas will be studied to determine plasma species formed during the reactive sputtering of

titanium by gaseous mixtures of argon, oxygen, methane and nitrogen. The application of optical measurements to monitor transient target oxidation phenomena will be explored. Methods of preparing titanium compounds with controlled stoichiometries will be explored.

Study of the systematics of the thermodynamic properties of compound semiconductor solid solutions will be undertaken to develop methods of tieline prediction in multi-component systems. Solid-state electrochemical studies will utilize CaF_2 electrolytes for determining activity coefficients in selected alloys useful in electro-optical devices.

Manuscripts are in preparation on the following topics: critical and transport properties of volatile silicon compounds; divergent x-ray studies of liquid phase epitaxial III-IV heterostructures; divergent x-ray studies of (111) GaAs and (111) InP substrates and homoepitaxial layers; analysis of transport processes in vertical cylinder epitaxy reactors; vapor phase etching kinetics of (100) GaAs in $HCl-H_2$; anomalous diffusion in transition metal sulfide electrodes; direct digital control algorithms for thermal process control by microcomputers.

8. 1975 PUBLICATIONS AND REPORTS

Lee F. Donaghey and Associates

Journals

1. Lee F. Donaghey and R. H. Bissinger, Characterization of GaAs Substrates and Epitaxial $GaAs_{1-x}P_x$ Layers by Divergent X-Ray Beam Diffraction, J. Electronic Materials 4, 131-158 (1975)(LBL-1872).

2. Lee F. Donaghey, Critical Path Planning of Graduate Research, Chemical Engineering Education 9, 192-195, 203 (1975) (LBL-4155).

3. Lee F. Donaghey and Steven R. Styer, Vapor Pressure of Zn and As during Closed-System Zn Diffusion into GaAs from a $ZnAs_2$ Source, Mat. Res. Bull. 10, 1297-1304 (1975)(LBL-4134).

Papers Presented

1. L. F. Donaghey, Chemical Effects of Alloying Elements in Nickel-Base Alloys for Dentistry, Dental Laboratory Conf., San Francisco, CA, January 24-25, 1975.

2. L. F. Donaghey, Studies of Physical and Reactive Sputtering, Annual Review Symposium of the Materials and Molecular Research Division of the Lawrence Berkeley Laboratory, Feb. 4, 1975.

3. L. F. Donaghey, Superalloy-Ceramic Systems for Dental Prosthetics, 110th Midwinter Meeting, Chicago Dental Soc., Chicago, Ill., Feb. 14-15, 1975.

4. L. F. Donaghey, Technology and Commercial Potential for Photoemissive Solar Cells, Energy and Environment Seminar, University of California, Berkeley, CA, Feb. 26, 1975.

5. L. F. Donaghey, Welcoming Remarks and Introduction, Third Annual Electronic Materials Symposium, Palo Alto, CA, March 20, 1975.

6. L. F. Donaghey, Recent Developments in Chemical Processing of Electronic Materials, Solid State Seminar, University of California, Berkeley, CA, April 9, 1975.

7. L. F. Donaghey, Processing of Electro-Optical and Magneto-Optical Films, Department of Chemical Engineering, University College London, England, Sept. 15, 1975

8. L. F. Donaghey, Solid-State Electrochemical Studies Related to the Processing of III-V Semiconducting Compounds, Department of Metallurgy and Materials Science, School of Mines, Imperial College of Science and Technology, London, England, Sept. 16, 1975.

9. L. F. Donaghey, High Voltage Electron Microscopy of Phase Transformations in Steels, File Radiation Chemistry Division, AERE Harwell, Didcot, Berkshire, England, Sept. 18, 1975.

10. L. F. Donaghey and Steven R. Styer, Monitoring of Vapor Pressures of Group II and V Elements During Vapor Phase Crystal Growth, Fifth Intern. Conf. on Chemical Vapor Deposition, Conference Center, Fulmer Grange, Stoke Poges, Buckinghamshire, England, Sept. 22, 1975.

11. L. F. Donaghey and Kenneth G. Geraghty, Kinetics of the Reactive Sputter Deposition of Titanium Oxides, Fifth Intern. Conf. on Chemical Vapor Deposition, Conference Center, Fulmer Grange, Stoke Poges, Buckinghamshire, England, Sept. 25, 1975.

12. L. F. Donaghey, Vapor Phase Etching and Growth of III-V Compounds, Allan Clark Research Division, Plessey Co. Ltd., Caswell, Towcester, England, Sept. 26, 1975.

LBL Reports

1. L. F. Donaghey, Process Monitoring with an 8008 Microprocessor, LBL-3947, Aug. 1975.

2. S. R. Styer and L. F. Donaghey, Determination of the Width of the GaAs+$ZnAs_2$ Two Phase Region in the Ga-As-Zn System by Optical Absorption Spectroscopy, LBL-3973, July 1975.

3. K. G. Geraghty and L. F. Donaghey, Kinetics of the Reactive Sputter Deposition of TiO_X Phases, LBL-3974, 1975.

4. S. R. Styer and L. F. Donaghey, Monitoring of Group II and V Elements in Vapor Phase Crystal Growth Processes by Optical Absorption Spectroscopy, LBL-3975, 1975.

5. K. K. Rubin, G. M. Bobba and L. F. Donaghey, Application of Control Flags in Microcomputer Programming, LBL-3981, July 1975.

6. R. Pong and L. F. Donaghey, Thermodynamic Studies of Ga-In Liquid Alloys by Solid-State Electrochemistry with Oxide Electrolytes, LBL-4107, 1975.

7. K. G. Geraghty and L. F. Donaghey, Effect of Target Oxidation on Reactive Sputtering Rates of Titanium in Argon-Oxygen Plasmas, LBL-4110, Aug. 1975.

8. T. J. Anderson and L. F. Donaghey, Solid-State Electrochemical Study of the Free-Energy of Formation of β-Gallium Sesquioxide Using a Calcia-Stabilized Zirconia Electrolyte, LBL-4128, Aug. 1975.

9. L. F. Donaghey, Microcomputer Systems for Chemical Process Control, LBL-4129, Aug. 1975.

10. T. J. Anderson and L. F. Donaghey, Solid-State Electrochemical Study of the Free Energy of Formation of Indium Sesquioxide, LBL-4137, Aug. 1975.

11. G. M. Bobba and L. F. Donaghey, A Microcomputer System for Real-Time Monitoring and Control of Gas Chromatography, LBL-4138, Sept. 1975.

12. G. M. Bobba and L. F. Donaghey, A Microcomputer System for Analysis and Control of Multiple Gas Chromatographs, LBL-4139, 1975

13. G. M. Bobba and L. F. Donaghey, Microcomputer System Interfaces for Process Monitoring and Control Applications, LBL-4140, Dec. 1975.

14. G. M. Bobba and L. F. Donaghey, A Real-Time Clock for Process Monitoring and Control with 8-bit Microcomputers, LBL-4141, Dec. 1975.

15. G. M. Bobba and L. F. Donaghey, Improved Floating-Point Mathematical Subroutines for Intel 8008 and 8080-based Microcomputers, LBL-4143, Dec. 1975.

16. T. J. Anderson and L. F. Donaghey, Solid-State Electrochemical Study of Ga-Sb Liquid Alloys, LBL-4153, Sept. 1975.

17. T. J. Anderson and L. F. Donaghey, Determination of the Solubility of Oxygen in Liquid Indium, LBL-4577, Dec. 1975.

18. Timothy James Anderson, Thermodynamic and Kinetic Studies of Some Group III and Group V Elements and Alloys by Solid State Electrochemical Techniques, (M.S. Thesis) LBL-4148, Oct. 1975.

19. Raymond Pong, Thermodynamic Studies of Ga-In, Ga-Sb and Ga-In-Sb Liquid Alloys by Solid State Electrochemistry with Oxide Electrolytes, (M.S. Thesis) LBL-2785, April 1975.

20. Steven Roy Styer, Optical Absorption Study of Phase Equilibria in the Ga-As-Zn and Ga-As-Cd Systems with Application to Design of Diffusion Processes, (M.S. Thesis) LBL-3586, June 1975.

d. Electrochemical Phase Boundaries

Rolf Muller, Principal Investigator

1. OPTICAL STUDIES OF ELECTROCHEMICAL INTERFACES

a. Ellipsometry of Boundary Layers

Craig G. Smith and Rolf H. Muller

Electrochemical reactions, such as those involved in the charging and discharging of battery cells, are accompanied by ionic transport in the solution. The resulting change in the electrolyte composition at the electrode can greatly affect the electrode reaction. The experimental determination of interfacial concentrations is therefore of continuing interest.

Ellipsometry has been established as a new technique for the observation of boundary layers. This technique complements that of light interference, in that it is usually not sensitive to the geometrical extent of the region of changed concentration, but depends only on the concentration difference between bulk fluid and interface.

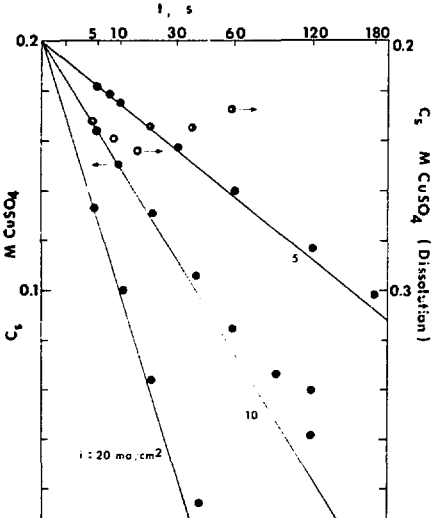

Fig. 1. Determination of interfacial concentration by ellipsometry. Horizontal Cu electrode facing down. ● Deposition from 0.2M $CuSO_4$, ○ ◑ dissolution into 0.2M $CuSO_4$. Solid curves expected from Sand equation[4] with $D = 5 \times 10^{-6}$ cm^2/s, $t_+ = 0.385$. (XBL 7510 7440)

The optical effect of boundary layers, which are optically inhomogeneous, can be computed by use of models that employ a large number of homogeneous layers. Under typical transport conditions, the effect of electrochemical mass transport boundary layers on ellipsometer measurements can, however, be represented by a much simpler model.[1,2] This model is based on the light deflection in the boundary layer and the resultant change in the angle of incidence at the electrode surface.

Experiments have been conducted with the dissolution and deposition of copper. The use of (111) and (100) single crystal faces as electrodes has reduced changes in surface roughness during experiments. A current interruption technique, in combination with our fast self-compensating ellipsometer,[3] has further facilitated the isolation of boundary layer effects. Experimental results for the interfacial concentration during metal deposition and dissolution on an electrode facing down agree well with theoretical expectations in the absence of convection and deviate from theory after convection sets in (Fig. 1).

The interpretation of in situ measurements of solid electrochemical surface layers can be improved by considering boundary layer effects.

---

1. R. H. Muller and C. G. Smith, Ellipsometry of Mass-Transport Boundary Layers, 3rd Int. Conf. on Ellipsometry, Sept., 1975. Proceedings to be published in Surface Science (LBL-3929, Sept. 1975)
2. C. G. Smith, Effect of Mass-Transport Boundary Layers on the Ellipsometry of Surfaces (M.S. Thesis) (LBL-3905, December 1975).
3. H. J. Mathieu, D. E. McClure, and R. H. Muller, Rev. Sci. Instrum. 45, 789 (1974).
4. H. J. S. Sand, Phil. Mag. 1(6), 45 (1901).

b. Ellipsometry of Anodic Films

Craig G. Smith and Rolf H. Muller

Ellipsometer measurements of a growing oxide film in the anodic dissolution of Cu in 0.1M $CuSO_4$ are shown Fig. 1. Up to point P1 the observations closely follow computations for a homogeneous film of refractive index 2.45 - i 0.60. Transport theory indicates that near this point the interfacial concentration of $CuSO_4$ reaches its solubility limit. Independent evidence for the formation of compact and porous oxide layers under different conditions is shown in Fig. 2.

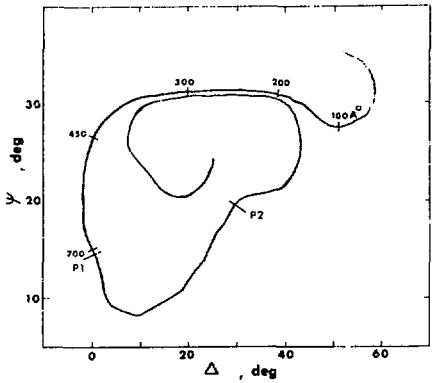

Fig. 1. Variation of Δ and ψ for Cu dissolution in 0.1 M $CuSO_4$ accompanied by oxide film growth. Convective diffusion with Re = 600 corresponding to an average linear flow velocity $\bar{u}$ = 8.7 cm/s. Film thickness indicated along curve. Electrode area 3.2 cm^2. Current density varies from 140 to 175 mA/cm^2. (XBL 7510-7441)

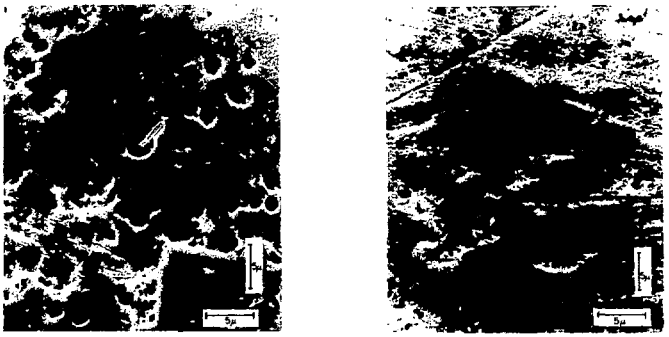

Fig. 2. Scanning-electron micrograph of compact and porous copper oxide films grown in 1 M $NaClO_3$, under different electrode current densities and electrolyte flow rates. (XBB 7410-7016)

c. Automatic Ellipsometers*

Rolf H. Muller

Operating principles and capabilities of presently built automatic ellipsometers have been reviewed. The instruments have been classified according to their optical principles of operation. The principal categories are compensating and non-compensating operation. Previously proposed criteria for comparing the performance of automatic ellipsometers[1] have been uniformly applied. Compensating instruments provide best accuracy, and non-compensating instruments show fastest response.

*Abstract of invited paper, 3rd Int. Conf. on Ellipsometry, Sept. 1975. Proceedings to be published in Surface Science (LBL-3930, Sept 1975).

1. R. H. Muller and H. J. Mathieu, Appl. Opt. 13, 2212 (1974).

d. Thin Electrolyte Films

Michael L. Sand and Rolf H. Muller

The dynamic behavior of thin electrolyte films, which occur on gas electrodes and in corrosion processes on metal surfaces, has been studied by the photographic observation of interference colors.[1] The drainage of films with thicknesses of the order of 1μ from polished vertical metal surfaces has been found to be much slower than predicted by theory (Fig. 1). Efforts to eliminate particulate impurities as a possible cause of the deviation are in progress.

The computed series of interference colors has been compared with observations, using cryolite films on chromium and aluminum near the optimum angle of incidence. Good agreement has confirmed the validity of the colorimetric computations (Fig. 2).

1. M. L. Sand, Light Interference in Electrolyte Films on Metals (M.S. thesis), LBL-3589, June 1975.

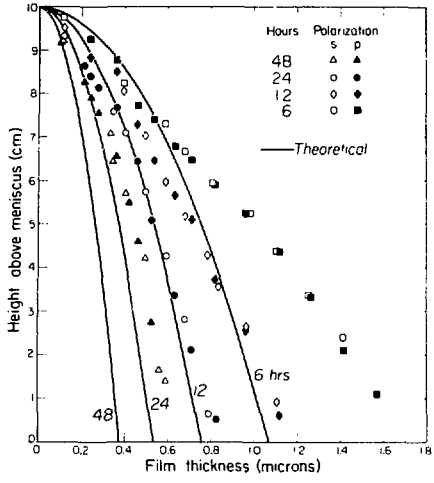

Fig. 1. Film thickness profiles of 9.2N aqueous potassium hydroxide during drainage from a vertical platinum electrode. Thicknesses derived from interference colors of polarized light.

(XBL 756-5148)

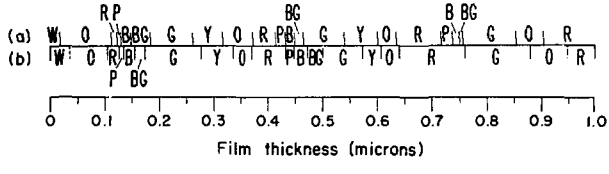

Fig. 2. Comparison between (a) calculated and (b) observed color series with color transitions occurring at film thicknesses determined by ellipsometry. Cryolite film (refractive index = 1.34) on chromium substrate (refractive index = 2.23-1.23i), angle of incidence 72°, S-polarized light (3200°K tungsten). (XBL 761-2132)

e. Laser Velocimetry

Calvin F. Chew and Rolf H. Muller

A laser Doppler velocimeter has been constructed to provide direct evidence of the three-dimensional flow fields in electrochemical boundary layers under combined forced and natural convection; the existence of such fields has been inferred from interferometer observations. The instrument samples an unusually small liquid volume (50 μ diameter) and can operate in either the differential or reference mode (Figs. 1 and 2).

Experiments have confirmed the theoretically expected optimum size of light-scattering particles to be 0.5-1 μ. The effect of light deflection due to the presence of refractive index gradients has been analyzed theoretically in order to correct for the geometrical displacement of the observed volume element.

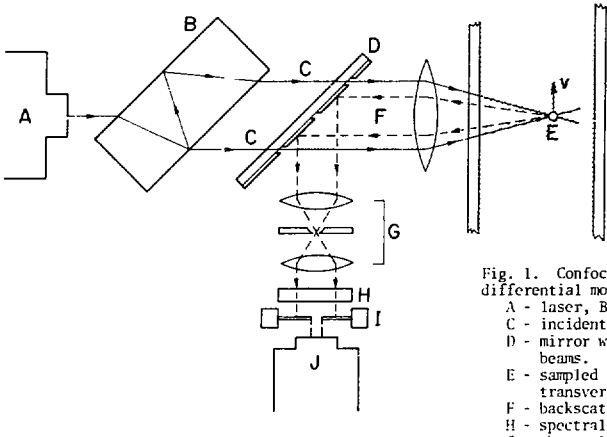

Fig. 1. Confocal backscatter laser velocimeter, differential mode.
A - laser, B - beam splitter,
C - incident light beams,
D - mirror with transparent areas for incident beams.
E - sampled volume element with measured transverse velocity component v
F - backscattered light, G - spacial filter
H - spectral filter, I - iris diaphragm,
J - photomultiplier (XBL 762-2196)

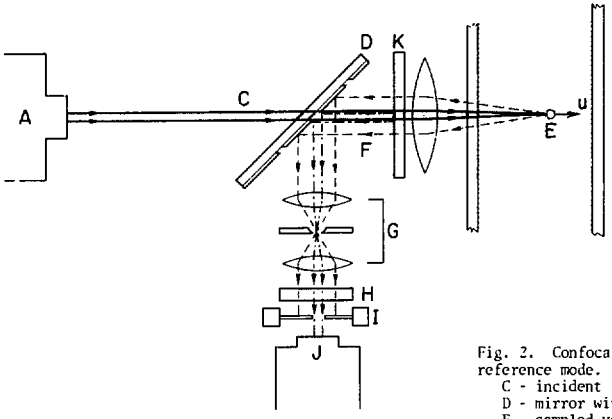

Fig. 2. Confocal backscatter laser velocimeter, reference mode.
C - incident light beam,
D - mirror with transparent center area
E - sampled volume element with measured longitudinal velocity component u
K - beam splitter
other parts as in Fig. 1. (XBL 762-2197)

2. RESEARCH PLANS FOR CALENDAR YEAR 1976

Rolf H. Muller

The determination of interfacial concentration at working electrodes by ellipsometry will be extended to cover a wider range of flow velocities and, thus, establish the limits of the applicability of the technique. Of particular interest are boundary layers that are too thin for observation by interferometry or that possess extremely high concentration gradients, where the simplified optical analysis should no longer be valid.

The in situ characterization of solid surface layers by ellipsometry, under consideration of boundary layer effects, will be directed towards quantitative porosity determinations in combination with scanning electron microscopy.

The role of particulate impurities and residual surface roughness in the behavior of thin electrolyte films on metals will be investigated as a model for catalyzed gas electrode surfaces.

Laser velocimetry will be employed for the elucidation of the complex flow fields present under combined forced and natural convection.

Experiments will be conducted to identify the critical parameters needed for the theoretical prediction of shapes resulting from high-rate anodic metal dissolution. (see section II.C.1.c with C. W. Tobias).

3. 1975 PUBLICATIONS AND REPORTS

Rolf H. Muller and Associates

Journals and Books

1. F. R. McLarnon, R. H. Muller, and C. W. Tobias, Light-Deflection Errors in the Interferometry of Electrochemical Mass Transfer Boundary Layers, J. Electrochem. Soc. 122, 59-64 (1975).

2. F. R. McLarnon, R. H. Muller, and C. W. Tobias, Discussion of Light-Deflection Errors in the Interferometry of Electrochemical Mass Transfer Boundary Layers, J. Electrochem. Soc. 122, 1636-37 (1975).

3. Rolf H. Muller, Electrochemical Aspects of the Hydrogen Economy, Proc. Cornell Int. Symposium and Workshop on the Hydrogen Economy, Aug. 20-22, 1973, S. Linke, ed., Cornell University, April 1975, pp. 345-49.

4. F. R. McLarnon, R. H. Muller, and C. W. Tobias, Derivation of One-Dimensional Refractive-Index Profiles from Interferograms, J. Opt. Soc. Am. 65, 1011-18 (1975).

5. F. R. McLarnon, R. H. Muller, and C. W. Tobias, Reflection Effects in Interferometry, Appl. Opt. 14, 2468-72 (1975).

Presented Papers

1. J. F. Cooper, R. H. Muller, and C. W. Tobias, Periodic Phenomena during the High Current Density Anodic Dissolution of Copper, Electrochem. Soc., Toronto, Ont., May 12, 1975 (Abstract 67).

2. Rolf H. Muller, Present Status of Automatic Ellipsometers, invited paper, Third Internatl. Conf. on Ellipsometry, University of Nebraska, Lincoln, Nebr. Sept. 23, 1975.

3. Rolf H. Muller and Craig G. Smith, Ellipsometry of Mass-Transport Boundary Layers, Third Internatl. Conf. on Ellipsometry, University of Nebraska, Lincoln, Nebr., Sept. 25, 1975.

LBL Reports

1. Rolf H. Muller, Present Status of Automatic Ellipsometers, LBL-3950, Sept. 1975.

2. Rolf H. Muller and Craig G. Smith, Ellipsometry of Mass-Transport Boundary Layers, LBL-3929, Sept. 1975.

3. John F. Cooper, Periodic Phenomena in the High-Current Density Dissolution of Copper (Ph.D. Thesis) LBL-2750, April 1975.

4. Michael L. Sand, Light Interference in Electrolyte Films on Metals (M.S. Thesis) LBL-3585, June 1975.

5. Craig G. Smith, Effect of Mass Transfer Boundary Layers on the Ellipsometry of Surfaces (M.S. Thesis) LBL-3903, Dec. 1975.

6. Rolf H. Muller, Meeting Report, Third Internatl. Conf. on Ellipsometry, University of Nebraska, Lincoln, Nebr., Sept. 22-25, 1975, LBL-4501, Oct. 1975.

e. Solid State and Surface Reactions

Gabor A. Somorjai, Principal Investigator

1. SURFACE STRUCTURE AND CHEMISORPTION BY LOW ENERGY ELECTRON DIFFRACTION

a. The Surface Structure and Bonding of Acetylene to the Pt(111) Surface*

Larry L. Kesmodel, Peter C. Stair, and G. A. Somorjai

The first determination of the bonding geometry of a molecule on a surface, acetylene on the platinum (111) surface, was carried out by analysis of low energy electron diffraction (LEED) intensity-voltage (I-V) profiles for the Pt(111)-(2×2)-C_2H_2 structure. A well-ordered C_2H_2 overlayer was obtained at low gas exposures (~1 Langmuir), and the LEED beam intensities were measured by a recently developed photographic technique[1] at several incident beam angles for energies of 10-200 eV. The surface structure analysis was carried out by comparing calculated I-V profiles for a large number of models of the Pt-C_2H_2 geometry to the experimental results. The model calculations employed a computer program[2] that takes full account of multiple electron scattering and provides for calculation of several overlayer geometries with little increase in computation time over a single-geometry calculation.

The local bonding geometries considered in this calculation are shown in Fig. 1. We conclude that acetylene is chemisorbed with the molecule centered on a triangular site (C2) at a perpendicular distance of 1.95±0.10 Å above the topmost plane of platinum atoms. The carbon atoms are equivalent by symmetry and relevant C-Pt distances are 2.25 and 2.56 Å. It is interesting to note that this same bonding geometry is exhibited in trinuclear metal-alkyne clusters; moreover, the average C-Pt distance we find (2.42±0.1 Å) is similar to that (2.22 Å) determined for the $Os_3(CO)_{10}(C_2Ph_2)$ cluster, the osmium covalent radius being only 0.04 Å shorter than that of platinum. Our results argue against popular notions of acetylene adsorption on transition metal surfaces that propose either an acetylene π complex coordinated to a single metal atom or a di-σ complex in which each of the two carbon atoms forms a σ-bond with a different metal atom.

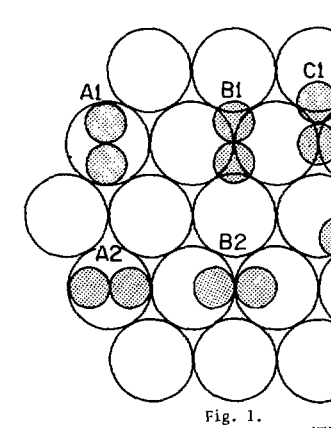

Fig. 1.

XBL 7512-10,012)

*Abstracted from LBL-4572 (submitted to Physical Review letters).

1. P. C. Stair, T. J. Kaminska, L. L. Kesmodel, and G. A. Somorjai, Phys. Rev. B 11, 623 (1975) (LBL-3149).
2. Program constructed by L. L. Kesmodel (MMRD-LBL) in collaboration with R. C. Baetzold (Eastman Kodak).

b. Low-Energy Electron Diffraction from Vapor-Deposited Phthalocyanine Crystals

J. Buchholz and G. A. Somorjai

The surface structure of epitaxially grown films of copper-, iron-, and metal-free phthalocyanines has been studied using low-energy electron diffraction (LEED). These materials are deposited in ultrahigh vacuum onto Cu(111) and Cu(100) single crystal substrates by heating the phthalocyanines to about 300°C to yield sufficient vapor pressure to produce a molecular beam. The structure of the deposited film is monitored continuously by LEED, allowing observation of both the initial monolayer and the final thick layer deposit.

The orientation of the initial layer of phthalocyanine is dependent on the symmetry of the substrate. On a Cu(100) surface the three phthalocyanines grow into identical structures with the initial layer consisting of molecules oriented with the molecular plane parallel to the substrate. The thick layer of the phthalocyanines on Cu(100) maintains the same surface unit mesh as the first layer, the surface apparently consisting of one molecule per unit mesh, oriented parallel to the surface. This is unlike any plane in the bulk crystal structure of phthalocyanine indicating either a rearrangement of the surface or the growth of a film with a new crystal structure. The bonding of the first layer to the substrate is stronger than the intermolecular bonding in the bulk crystal as indicated by thermal desorption results. The independence of the structures on the central metal atom of the phthalocyanines means that the substrate-phthalocyanine bonding is primarily through the phthalocyanine ligand.

The various phthalocyanines deposit on the Cu(111) substrate in a somewhat different fashion. The molecule is again oriented parallel to the substrate in the first layer but its detailed azimuthal orientation depends on the central metal atom. The metal-free phthalocyanine, bonding

through the phthalocyanine ligand, observes 6-fold rotational symmetry of the Cu(111) substrate rather than the true 3-fold symmetry as indicated by the structures for the metal phthalocyanines. The central metal atom thus interacts with surface orbitals exhibiting 3-fold rotational symmetry, such as the substrate d-orhitals. In the thick layer structures on Cu(111) the exposed surface plane is the same as on Cu(100) except that the surface is not parallel to the substrate but inclined at an angle of about 11°.

These results for large molecules, such as the phthalocyanines, suggest the possibility of studying other large molecules such as the biologically important porphyrins and polymeric molecules. At present, work is in progress studying several amino acids.

c. The Surface Structure of Vapor Grown Molecular Crystals

L. Firment and G. A. Somorjai

Organic solids are materials of practical, theoretical, and biological importance. Many of their properties are surface related: reactivity, adhesion, vaporization. Yet there has been no data on the molecular arrangement at molecular surfaces, data necessary for the understanding of these phenomena. Low energy electron diffraction (LEED) is the best available technique for obtaining surface crystallographic data; however, its application to molecular materials is not straightforward. Molecular solids are insulators and subject to radiation damage by the probe electrons. These difficulties have been overcome, and surface crystallographic data on ice and naphthalene have been reported.[1] LEED studies of molecular solids have continued with observation of a series of organic materials. By correlating LEED data from a range of materials, generalizations about surface structures of molecular materials and the limitations of the technique can be made.

The experiments are performed by condensing the vapors of the molecular material onto a cold platinum (111) single crystal surface in an ultrahigh vacuum chamber, and observing LEED patterns during film growth. Thin films (10^2-10^3Å) have sufficient conductivity to prevent surface charging. Rapid photography of the diffraction pattern minimized radiation damage. Of eight molecular materials studied to date, only one, acetic acid, would not grow epitaxially on the platinum substrate with sufficient crystallinity for observation of the diffraction pattern. This method allows study of the film at each stage of growth, from clean substrate, through the monolayer, to thick film.

The naphthalene (001), ice I_c(111) (or I(0001)), trioxane (0001), and cyclohexane (001) crystal surfaces have been observed at 100-200K and 10^{-7} torr. These surfaces are unreconstructed; that is, the geometry at the surface is identical to the arrangement in the bulk of the molecular crystal. Diffraction patterns from surfaces of benzene, n-octane, and methanol have been observed, but the data have not been interpreted in terms of the expected bulk crystal structures. Further examination of these surfaces is in progress.

The crystallinity and orientations of the grown films have been found to depend strongly on substrate preparation, but in a manner characteristic for each molecule. In several cases an atomically clean surface was necessary for best growth; in others a prepared ordered monolayer was necessary. The aromatic samples and ice are better conductors than the aliphatic samples, but all could be observed at thicknesses of several hundred Angstroms.

Other molecular surfaces will be explored and their behavior correlated. The metal single crystal substrate will be varied to study its effect on growth of a crystalline molecular film.

---

1. L. E. Firment and G. A. Somorjai, J. Chem. Phys. 63, 1037 (1975).

d. The Atomic Structure and Stability of Stepped Platinum Surfaces

D. Blakely and G. A. Somorjai

A series of Pt single crystals has been studied by LEED and Auger electron spectroscopy (AES) to determine the equilibrium structure of the surfaces of the crystals. The single crystals have been cut to expose surfaces representative of all possible planes, and are related to these planes by the symmetry of the fcc lattice. The equilibrium structure of the crystal surface is directly related to the surface free energy, or surface tension, of the crystal. The equilibrium structure may be (1) monatomic height steps separating low Miller-Index terrace planes, (2) multiple height steps, two or three atoms high, separating the terraces, or (3) a hill and valley structure consisting of pairs of low Miller Index planes (the surface still appears as a staircase, but not on an atomic scale).

To our knowledge the stability has been determined for the first time on known clean surfaces, as evidenced by AES. The stability has also been determined for crystals with known impurities, oxygen or carbon, on their surfaces. The atomically clean surfaces of Pt exhibit the largest region of stability of the monatomic height step configuration. The surfaces vicinal to the (111) plane and between the (111) and (001) planes are stable in a monatomic height step structure. Near the (011) plane and between the (011) and (001) planes either a hill and valley structure or double height steps are stable. When heated in an oxygen ambient, the surfaces become unstable. Near the (001) plane, as little as 0.01 monolayers of oxygen cause the formation of a hill and valley structure composed of (001) and (113) and/or (012) planes, and near the (111) plane, the steps become multiple height. Near the (011) plane, the steps are already unstable and no further changes result from either oxygen or carbon adsorption. Graphitic carbon of the (001) vicinal surfaces induces the formation of a hill and valley structure similar to that formed by oxygen. On

the (111) plane vicinal surfaces between the (112) and (445) surfaces 1/n between Pt(S)-[15(111)×(001)] and Pt(S)-[9(111)×(001)] 1/n a monolayer of graphitic carbon causes the formation of a hill and valley structure consisting of the (112) and (445) planes and not the low Miller Index plane, (111). The (445) plane is stabilized from the coincidence of the Pt and graphite lattices at a nine Pt atom terrace width.

Some conclusions about the surface tension anisotropy, or γ-plot, may be reached from these observations. There is evidence for a double change in the curvature of the γ-plot for clean Pt in the region near the (112) surface; this is not expected from theories unless there is a cusp in the γ-plot at the (112) plane at the high temperature (1200K) of the equilibration. (At absolute zero there is a cusp at every plane that has rational Miller indices.) There are apparently cusps at high temperature at the (112), (113), (012), and (255) poles as well as at the low index poles, (111), (001), and (011), from the faceting behavior of the surfaces. These cusps are deepened by a small amount of oxygen or carbon, and hill and valley structures are formed.

e. Surface Crystallography of Hydrocarbons on the Pt(111) Crystal Surface

P. C. Stair and G. A. Somorjai

The knowledge of the detailed atomic structure of hydrocarbons adsorbed on a platinum surface is necessary for a complete understanding of platinum's role in hydrocarbon catalysis. The structure of a hydrocarbon adsorbed in an ordered overlayer on a well defined single crystal platinum surface may be obtained from an analysis of the diffraction beam intensities in a low energy electron diffraction (LEED) experiment. In order to determine that the necessary beam intensities were obtained, a photographic method of measurement was developed. This method has been used to determine the LEED intensities from ordered overlayers of acetylene ($HC{\equiv}CH$), ethylene ($H_2C{=}CH_2$), propylene ($H_3C\text{-}CH\text{-}CH_2$), and methylacetylene ($H_3C\text{-}C{\equiv}CH$) on a Pt(111) single crystal surface. Intensity measurements are in progress for benzene and naphthalene on the Pt(111) surface, and measurements from the Pt(100) surface are planned for the near future.

f. Chemisorption of O_2, H_2, CO, C_2H_2, C_2H_4, C_6H_6, C_2H_{12}, and C_7H_{16} on Iridium Crystal Surfaces

B. E. Nieuwenhuys and G. A. Somorjai

Adsorption of various gases was studied on two different iridium surfaces, viz. the atomically densely packed (111) surface and a stepped (high Miller) surface consisting of (111) type terraces separated by (100) like steps. The gases used were hydrogen, oxygen, carbon monoxide, ethylene, acetylene, cyclohexane, benzene, and n-heptane. Auger electron spectroscopy and thermal desorption were used besides low energy electron diffraction.

The principal aim of this study was to investigate the influence of the surface structure on the adsorption of these gases and to compare this influence with that found previously on similar surfaces of platinum.

It appears that both hydrogen and oxygen are more strongly bound on steps than on (111) type sites. Ordering of CO molecules, just as on platinum, is more difficult on the stepped Ir plane than on the smooth Ir(111) plane. From the results it can be concluded that C-H bond breaking occurs more easily on Ir than on Pt. The influence of the surface structure in this process is marked. On both metals C-H bond breaking occurs easier on stepped surfaces than on the (111) surfaces.

g. The Chemisorption of Oxygen, Water, and Selected Hydrocarbons on the (111) and Stepped Gold Surfaces

M. A. Chesters and G. A. Somorjai

The dissociative chemisorption of oxygen and water is reported on both (111) and [6(111)×(100)] crystal faces of gold. The oxide formation becomes rapid above 500°C at pressures of about 10^{-6} torr. The resulting gold oxide is bound strongly. It is similar in structure to the corresponding sulphide and is stable on both surfaces to 800°C in vacuum. Ethylene, cyclohexene, n-heptane, and benzene did not chemisorb on gold under low pressure conditions on either the (111) or on the stepped gold surface; however, napthhalene exhibited dissociative chemisorption on both types of surfaces. Hydrocarbon fragments are bound strongly to the gold surface but the activation energy for dissociative adsorption of light hydrocarbon molecules appears to be high.

h. The Thorium(100) Crystal Face. A Study of Its Cleaning, Surface Structures, and Interaction with Oxygen and Carbon Monoxide

T. N. Taylor, C. A. Colmenares, R. L. Smith, and G. A. Somorjai

The cleaned Th(100) crystal face was studied by low energy electron diffraction (LEED) and Auger electron spectroscopy (AES). The various thorium Auger transitions have been identified and assigned. Chemisorption of oxygen and CO was monitored by LEED, AES, and work function change (WFC) measurements. The work function of thorium was found to decrease with the chemisorption of oxygen and CO. Continued oxygen adsorption leads to its dissolution in the bulk and subsequent oxide formation at the surface. The oxide may be ordered by heating it to 1000K; heating to higher temperatures leads to dissolution of the oxide by oxygen diffusion into the bulk. The data suggest dissociative chemisorption of CO on the studied (100) surface.

i. Calculations of Structure and Charge Density of Stepped Surfaces

Yvonne W. Tsang, Larry L. Kesmodel, Leo M. Falicov, and G. A. Somorjai

Surfaces of crystal characterized by high Miller indices consist of terraces of low-index planes separated by steps that are often one atom in

height. Chemisorption and chemical reaction studies on metal and semiconductor surfaces have indicated that atomic steps play a key role in enhancing these processes. We considered three aspects of a theoretical, solid-state physics approach to the question of why atoms in steps behave in a fundamentally different way from atoms on low-index planes; these are outlined below.

1. Lattice structure calculations on stepped surfaces.[1] We investigated the simple question of the actual position of atoms in stepped surfaces of Ar, a noble-gas solid, and NaCl, an alkali halide, by means of pair potentials and polarizabilities. Negligible surface relaxation was found for Ar stepped surfaces. In the case of NaCl, polarization effects accounted for surface buckling and surface atom displacements on the order of 5-10% of the atomic step height.

Electronic Potential in a Metal Close to a Surface Edge.[2] We obtained an approximate solution of the Schrödinger-Hartree-Poisson equations for a 90° metallic wedge chosen to simulate the behavior of a free-electron gas confined to a step-like geometry. The results indicate that in the presence of geometrical irregularities the Friedel oscillations of the electron gas get markedly enhanced, producing fairly large effects in the neighborhood of such imperfections. This may result in reoccupation of d-orbitals of atoms in steps together with charge transfer to or from the bulk.

Steric Properties of Transition-Metal Ions on Stepped Surfaces.[3] Simplified model calculations of the steric properties of the transition-metal ions in various crystalline geometries on stepped surfaces have been carried out by applying the point-charge ionic model of crystal field theory to determine level splittings of the d-orbitals at terrace and step sites. The s-electrons are assumed to be free conduction electrons while the d-electrons are treated as localized and atomic-like. The results indicate considerably different steric properties of atoms in step sites as opposed to terrace sites.

These results taken together with Fermi level-density-of-states considerations give a consistent picture of available experimental data on the catalytic properties of Pt and Au stepped surfaces.

1. Y. W. Tsang and L. M. Falicov, Phys. Rev. B 12, 2441 (1975) (LBL-3904).
2. L. L. Kesmodel and L. M. Falicov, Solid State Comm. 16, 1201 (1975).
3. Y. W. Tsang and L. M. Falicov, J. Phys. C: Solid State Phys. (to be published).

2. ELECTRON SPECTROSCOPY STUDIES OF ALLOY SURFACES AND ADSORBATES

a. Surface Compositions of the Silver-Gold and Gold-Tin Systems

S. Overbury and G. A. Somorjai

Throughout the last year we continued to examine the surface composition of binary alloys.[1] The surface phase diagram of the Au-Ag binary alloy system was studied by use of Auger electron spectroscopy.[2] The intensities of principal Auger peaks over a wide range of electron energies were obtained as a function of alloy bulk composition for the clean equilibrated alloy surfaces. Their ratios were compared with intensity ratios calculated for a surface showing no surface segregation, and for a surface obeying the regular solution model[3] (which predicts silver surface segregation). The experimental results give evidence for enrichment of the surface with silver, but to an extent less than predicted by the regular solution model.

Recently an improved Auger electron spectrometer was assembled that uses a cylindrical mirror-type electrostatic analyzer capable of greater resolution and improved signal-to-noise ratios. This faster analyzer, coupled with a new precision manipulator, makes surface analysis faster and more accurate. This spectrometer is currently being used to determine the Au-Sn surface phase diagram. A bulk two-phase region of this system is being studied to look for preferential nucleation of a surface active phase at the surface. For this system, tin might be expected to segregate to the surface to relieve lattice strain and to lower the surface energy.

1. S. H. Overbury, P. A. Bertrand, and G. A. Somorjai, Chem. Rev. 75(5), 547 (1975).
2. S. H. Overbury and G. A. Somorjai, Surface Sci., to be published.
3. Presented at the Discussions of Faraday Soc. on Elect. Spect. of Solids and Surfaces, G. A. Somorjai and S. H. Overbury, Vancouver, Canada, July 15-17, 1975.

3. HETEROGENEOUS CATALYSIS BY METALS

a. The Dehydrogenation and Hydrogenolysis of Cyclohexane and Cyclohexene on Stepped (High Miller Index) Platinum Surfaces

D. W. Blakely and G. A. Somorjai

The dehydrogenation and hydrogenolysis of cyclohexane and cyclohexene were studied on

platinum single crystal surfaces of varying atomic surface structure at low pressures (10^{-6} torr) in the temperature range of 300-725K. The quantitative reaction rates were monitored by a mass spectrometer, and the surface structure and surface composition were determined by low-energy electron diffraction and Auger electron spectroscopy. Atomic steps have been identified as the active sites for C-H and H-H bond breaking processes. The dependence of the dehydrogenation and hydrogenolysis rates on the platinum surface structure revealed kinks in the steps as active sites for C-C bond scission in addition to their ability for breaking C-H and H-H bonds. The active catalyst surface was covered with a carbonaceous overlayer, which was ordered or disordered. The properties of this overlayer influence significantly both the rate and the product distribution of the catalytic reactions. An expanded classification of structure-sensitive reactions is suggested.

b. Studies of Hydrocarbon Reactions on Pt Crystal Surfaces at High Pressures

R. K. Herz, W. E. Petersen, and G. A. Somorjai

Kinetic studies of the reactions of n-heptane and cyclohexane have been completed on a Pt(111) platinum single crystal surface and on a stepped Pt(s)-[6(111)×(100)] surface at atmospheric pressure reaction conditions. The reaction rates and product selectivities obtained agree with data in the literature for supported platinum catalysts.

The data in this work at high reactant pressures can be compared with results obtained by D. W. Blakely (of this research group) at low ($\sim 10^{-8}$ torr) pressures. The stepped catalytic surface is more active than the flat surface in both pressure ranges. The selectivity in the cyclohexane reaction shifts towards benzene at the high pressures as hydrogenolysis is suppressed.

Auger analysis of the crystals after reaction at either pressure condition shows the presence of surface carbon. The amount of the carbonaceous overlayer present is relatively insensitive to total pressure, but increases with the hydrocarbon to hydrogen ratio and the catalyst temperature. This overlayer affects both the activity of the surface and the product distribution.

Since the carbonaceous overlayer on the catalyst is always present in varying amounts during a hydrocarbon reaction, reaction rates at different reactant pressures and crystal temperatures must be compared when the amount of carbon on the catalyst surface is the same. For these dehydrocyclization and dehydrogenation reactions, it is interesting to note that the order with respect to hydrogen is observed to be negative when the effect of the surface overlayer is taken into account.

Carbonaceous overlayers deposited at these high pressures on single crystals appear to be irreversibly adsorbed, while layers deposited at low pressures are somewhat reversibly adsorbed. This behavior, and the fact that product distributions change greatly between high and low pressure, suggest that carbonaceous specie of several type are always present on a catalyst surface during hydrocarbon reactions. These species affect the activities of the various surface sites of a catalyst in a complex manner dependent upon hydrocarbon type and pressure, hydrogen pressure, hydrogen-to-hydrocarbon ratio, and catalyst temperature, and may themselves be catalytically active.

c. The Effect of Gold on Hydrogenolysis, Isomerization, and Dehydrocyclization Reactions on Polycrystalline Platinum and Iridium Foils

D. I. Hagen and G. A. Somorjai

The effect of the addition of gold to polycrystalline platinum and iridium foil samples on the initial reaction rates for the hydrogenolysis of propane, isobutane and n-heptane, the isomerization of isobutane, and the dehydrocyclization of n-heptane to toluene has been studied. These studies were carried out on samples of area ~1 cm^2 cleaned and maintained under UHV conditions and in a 5:1 hydrogen to hydrocarbon ambient at a total pressure in the 10^{-4} torr range. Mass spectroscopy was used to monitor the reactions in a temperature range of 100°C to 500°C. The platinum-gold and iridium-gold samples were prepared by evaporating several monolayers of gold on the cleaned surfaces and annealing in vacuum until the desired surface concentration of gold was obtained as determined by Auger electron spectroscopy. The nature of the resulting surfaces was further studied by chemisorption of carbon monoxide.

The rates of hydrogenolysis and isomerization on the pure platinum and iridium surfaces were found to be within a factor of 5 of the corresponding rates measured by others at higher pressures (48 Torr-1 atmosphere); this suggests that the hydrogen to hydrocarbon ratio is more important to the rates than absolute pressure. Absolute pressure was found to play a more important role in dehydrocyclization where a two order of magnitude difference in the rate on platinum was observed between the low pressure studies described in this paper and the high pressure studies carried out by others. Platinum was found in general to be more active for hydrogenolysis and isomerization while iridium was the more active for dehydrocyclization. Time dependent poisoning of the rates, the existence of a rate maximum as a function of temperature, and the predominance of low molecular weight hydrogenolysis products are attributed to the lower hydrogen pressures used in this work.

The addition of gold to the platinum and iridium surfaces decreases the rates for all reactions studied. An approximately linear decrease in isomerization rate as a function of gold coverage was observed while hydrogenolysis and dehydrocyclization decreased in a similar fashion with each other and much more rapidly than isomerization. Thus the selectivity for isomerization as compared to hydrogenolysis is increased with increasing gold coverage while little change is expected for dehydrocyclization. These results coupled with differences in the

time-dependent poisoning of the various reactions suggest that the surface sites responsible for isomerization are different from those for hydrogenolysis and dehydrocyclization.

4. COAL CONVERSION CATALYSIS

a. High-Pressure, Low-Pressure Studies of the Carbon Monoxide-Hydrogen Reaction on Transition Metal Surfaces

Brett A. Sexton and G. A. Somorjai

The CO-H_2 reaction on transition metals is an important method of synthesizing organic fuels (alkanes, alkenes and alcohols). The normal synthesis conditions on industrial catalysts range from 1-100 atm pressure and temperatures up to 500°C. In order to study this reaction on well defined transition metal surfaces, an apparatus has been constructed which incorporates a high pressure isolation cell into the usual UHV apparatus. This enables the circulation of gases over the sample at pressures up to 100 atm, and analysis of the reaction products with gas chromatography. After reaction the sample is exposed to vacuum and analysed with Auger spectroscopy, LEED, and thermal desorption. Low pressure catalysis (10^{-4}-10^{-8} Torr) can also be studied, with the mass spectrometer as detector. A feature of this apparatus is a manipulator which allows 180° rotation of the sample and direct-current heating. This is necessary in the cleaning and analysis of the sample surface.

Preliminary studies on the surfaces of iron, cobalt, and rhodium at 1 atm pressure have shown that they are catalytically active in the range 200-500°C and C_1-C_5 species are formed. The relative activities are in the order Fe > Co > Rh. At lower pressures, (10^{-4} Torr) no products were detectable. The life of the catalyst sample in the high pressure chamber is shortened by the transfer of sulphur impurity from the stainless steel walls. Auger electron spectroscopy studies indicated that the active, methane-producing rhodium surface is covered with a monolayer of carbonaceous residue.

Studies are presently underway to investigate the influence of pressure, temperature, gas composition, and surface composition on the reaction on Fe, Co, Rh, and Ru foils. These studies will be extended to include surface structure information on single crystals over the next 12 months.

5. MOLECULAR BEAM-SURFACE INTERACTIONS

a. The H_2-D_2 Exchange Reaction on Stepped Platinum Surfaces

R. Gale, M. Salmeron, S. Ceyer, and G. A. Somorjai

Our molecular beam-surface scattering apparatus has been modified to permit investigation of chemical reactions in which the reacting species reside on the surface for relatively long times (10^{-1}-1 sec). Experimental results indicate that many surface chemical reactions take place in this time scale.

We have extended the studies of the H_2-D_2 exchange reaction to lower beam modulation frequencies, with the expected increase in reaction probability. Utilizing this enhanced signal level, we have investigated the dependence of the hydrogen-deuterium exchange reaction on the orientation of the step edges to the incoming beam on a Pt(S)-[5(111) x (111)] single crystal surface. At high temperatures, the exchange is most favorable when the open edge of the step is perpendicular to the incident beam. The reaction probability decreases as the step edges become more parallel and reaches a minimum when the step edges are antiperpendicular; that is, the step edges are perpendicular, but with the open edge of the step directed away from the incoming beam. The production of HD varies by a factor of two as the step edges range from perpendicular to antiperpendicular to the incident molecular beam.

The dependence of HD formation on the angle of incidence of the molecular beam was also examined at high surface temperatures. With the step edges perpendicular to the incident beam, increase of HD production was found as the angle of incidence became more grazing toward the open edge of the steps. The formation of HD decreases as the angle of incidence becomes more grazing away from the open edge of the step. The exchange reaches a maximum when the angle of incidence is ~20° from the macroscopic surface normal, essentially the bisector of the angle between the terrace and step.

This study was carried out at high surface temperatures, ~1300°K. Future studies will be made as a function of beam and surface temperatures to further investigate the mechanism of this H-H bond breaking reaction.

b. Scattering of Thermal Helium Beam From High Miller Index (Stepped) Platinum Crystal Surfaces

S. Ceyer, R. Gale, S. Bernasek, and G. A. Somorjai

Helium beams generated by a 300K source were scattered from single crystal platinum surfaces. The angular distribution of the scattered beam was monitored as a function of azimuthal angle ϕ and incident angle θ. The effect of the presence of atomic steps on the angular distribution of scattered helium atoms was studied on a crystal surface composed of terraces that were on the average five atoms in width separated by steps of monatomic height. Rainbow scattering is observed when the step edges are oriented perpendicular to the incident beam direction, indicating strong modulation of the angular distribution by the periodic step potential. Only specular scattering is observed when the incident beam impinges on the crystal along the step edges, which indicates minimal effects of the presence of steps on the scattering distribution. These results as well as the absence of

diffraction are in good agreement with previous theoretical calculations.

c. Molecular Beam Studies of Exothermic Surface Chemical Reactions

R. Gale, S. Ceyer, W. Siekhaus, and G. A. Somorjai

A molecular beam apparatus has been developed which will enable us to not only measure the angular distribution of products of chemical reactions on well-characterized surfaces, but also to determine the translational energy distribution of reactants and products, with an improved signal-to-noise ratio. We utilize two atomic or molecular beams as reactants impinging on the surface. The detector, a quadrupole mass spectrometer, is mounted in a rotatable chamber inside the ultra high vacuum system. The ultra high vacuum system, which is equipped with two stages of differential pumping, is used to further reduce background noise. The velocity distribution can be determined by modulation of the signal to the mass spectrometer with a cross correlation chopper, which, due to its slightly greater than 50% on-time, provides a higher signal level and improved signal-to-noise ratio compared with conventional single-shot, time-of-flight techniques. Such a chopper can also be used to modulate one of the incident beams for investigation of the kinetics and mechanisms of surface chemical reactions.

Our primary area of interest is that of exothermic reactions to determine the energy partitioning into the kinetic energy of the product. The recombination of a hydrogen atom with a deuterium atom on a platinum surface will be the first system to be investigated. Further studies will involve the reactions of hydrogen atoms with adsorbed molecules.

6. SOLAR CELL RESEARCH

The objective of this research is to accelerate the development of economical photovoltaic solar energy conversion. The problem areas investigated in this work are those where the application of recently developed surface science techniques either promise improvement in the production of the raw material (silicon) and of the cell (thin polycrystalline films with large grains) or allow determination of the phenomena that determine lifetime and efficiency of polycrystalline solar cells (impurity segregation, effect of surface structure and impurities on electronic states.).

a. The Effect of Surface Structure and Impurities on Electronic Surface States

Yip Wah Chung, Wigbert Siekhaus, and Wei-Jen Lo

Electron loss spectroscopy was used to determine the electronic surface states of the Si(111) surface as a function of surface order and surface impurities. Surface order was determined by LEED and varied by temperature treatment or argon ion bombardment. Impurities deposited onto the surface under UHV conditions were acetylene, oxygen, and aluminum.

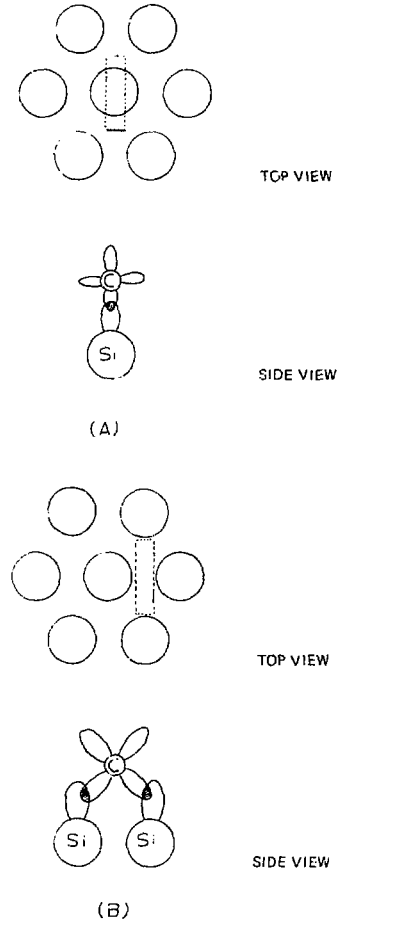

Fig. 1. Models of acetylene orientation on the silicon surface. (a) The acetylene molecule sits on the top of the silicon surface atom. (b) The acetylene molecule sits in a bridge position between two silicon surface atoms.

(XBL 7512-10067)

Acetylene and oxygen were adsorbed on both the disordered and ordered silicon surfaces of (111) orientation. The ELS data suggest that electrons in the silicon-oxygen chemisorption bond are more tightly bound on the disordered than on the silicon(111) surface with a (7×7) surface structure.

The adsorption of acetylene produces two electron loss peaks (7.0 and 8.4 eV, respectively) on the disordered silicon surface. In the Si(111)-(7×7) surface acetylene adsorption gives rise to only one strong electron loss peak at 7.3 eV and a weak shoulder at 8.4 eV. In addition, the dangling bond state transition of Si is completely removed on the disordered surface by the adsorption of 0.25 monolayer of C_2H_2; it is still present on the Si(111)-(7×7) surface even after saturation. These results indicate that the adsorption of acetylene on the Si(111)-(7×7) surface takes place on preferred sites, arising mainly as a result of the overlap between the silicon surface dangling bond orbitals and the π orbitals of the C_2H_2 molecules. They support the conclusion that on the (111)-(7×7) surface the acetylene molecule predominantly sits between two silicon atoms in a bridge position (Fig. 1b). On the disordered surface, however, most of the adsorbed acetylene molecules are located on top of the silicon surface atoms (Fig. 1a).

The adsorption of aluminum on the (111) silicon surface introduces changes in the ELS spectrum wheich show that the interaction of Al with Si is strongly dependent on the Si surface temperature. At temperatures below 300°C and a coverage of about 0.5 monolayer the adsorbed Al is uniformly distributed over the surface, and the ELS and LEED data show that a Al-Si surface phase (α-Si(111)-7-Al) is formed. At temperatures above 600°C and a coverage between 0.5 and 1 monolayer a different Al-Si surface phase is formed (γ-Si(111)-7-Al), as shown by the observed changes in the ELS spectrum and the LEED pattern. Further, it is observed that under this condition Al coalesces on the Si surface as evidenced by the appearance of strong Al bulk and surface plasmons. The results show that the ELS technique can be used to study the initial stages in the formation of a metal-semiconductor contact which is of utmost importance in Schottky-barrier type devices.

Electron loss spectroscopy does not generally determine the absolute location of or the electron population in electronic states. We therefore want to complement it with UV photoelectron spectroscopy and have designed and are building a high intensity UV light source, differentially pumped, to retain UHV conditions at the target during electron loss as well as photoelectron spectroscopy.

b. Impurity Segregation

Tom Kaminska and W. Siekhaus

During the past year we have examined polycrystalline silicon fracture characteristics and Auger analyzed some of these surfaces after fracture in ultra high vacuum to determine impurity segregation onto grain boundaries. To make possible better examination of the samples after fracture we have built a new pumping station and installed a Scanning Auger Microprobe with secondary electron detection capability.

Our intent in examining polycrystalline silicon fracture surfaces was to determine if impurities do in fact segregate to grain boundaries as suggested by some authors.[1] If the experiment is to succeed the silicon must fracture along the grain boundary. We therefore tried fracturing polycrystalline silicon in the following four ways: (1) shear fracture at room temperature, (2) shear fracture at liquid nitrogen temperature, (3) thermal stress, and (4) rapid bending at elevated temperature. The resulting surfaces were examined with a scanning electron microscope. All surfaces appeared to give predominately transgranular fracture as indicated in the accompanying typical micrograph. Point Auger analysis of such surfaces did not indicate the presence of impurities even when the doping level was as high as 10^{19}.

It is possible, however, that some small percentage of the fracture surface is intergranular and that only by good fortune would a point-by-point analysis land on such an intergranular surface. We therefore built the new pumping station and installed the Scanning Auger Microprobe. This instrument gives a physical image as well as an image of the impurity distribution of the fractured surface. We now have a spacial resolution capability of 1 μ and an analytical capability of 1 part in 1000. This will enable us to look in situ at fracture surfaces, pick out likely looking fracture regions, and Auger analyze them to look for evidence of segregation. We will be pursuing this course of research in the future.

In addition to the above approach, we will, in the next year, add two additional efforts. For the first, we have prepared one series of arsenic and one series of boron-doped, silicon single crystal samples. Boron and arsenic represent opposite segregation tendencies according to theories of segregation based on heats of sublimation.[2] The doped silicon wafers will be cleaned in ultra high vacuum and annealed to establish an equilibrium surface concentration which will be Auger analyzed. This will permit a check on the segregation theory. Electron loss spectra will also be employed to study the surface states resulting from impurity segregation and to determine surface crystallinity.

Our second approach will involve diffusing materials such as nickel into polycrystalline silicon. Nickel rapidly diffuses in silicon especially along grain boundaries, and because it has low solubility it will tend to remain in the grain boundary region. The presence of nickel may weaken the grain boundary so a larger percentage of intergranular fracture will occur. These surfaces can be Auger analyzed using the nickel as an indicator of an intergranular region.

1. M. E. Cowher and T. O. Sedwick, J. Electrochem.

Soc., Solid State Science and Technology, 11, 1565-1659 (1972).
2. S. H. Overbury, P. A. Bertrand, and G. A. Somorjai, The Surface Composition of Binary Systems, Predictions of Surface Phase Diagram of Solid Solutions, LBL-2746, May 1974.

c. Catalysis of Chemical Vapor Deposition (CVD)

Chin An Chang, W. Siekhaus, and John McLure

Both the deposition rate and the activation energy of Si-CVD processes are strongly affected by impurities present at the silicon surface. In general, a p-type dopant impurity increases the deposition rate while a n-type dopant decreases the deposition rate. Since both SiH_4 and $SiCl_4$ are tetrahedral molecules carrying a slight negative excess charge on the hydrogen atoms, it is tempting to propose, that the p-dopant forms a charge-layer at the surface which attracts such molecules whereas n-dopants form a repulsive layer. Table 1 shows that a prediction of this proposed model, that is, the reduction of the deposition rate of diamond from CH_4, a molecule with a slight positive excess charge on the hydrogen in the presence of B_2H_6, is verified by the literature cited.

To test the predicted influence of surface charges induced by electric fields on the deposition rate in silicon CVD processes, a CVD reactor was modified such that external electric fields of variable strength and polarity can be applied during deposition.

Table 1. Predicted and observed dopant gas effects on the deposition rates of silicon and carbon chemical vapors.*

	SiH_4	$SiCl_4$	CH_4	CCl_4
Bonding Characters	Si^+-H^-	Si^+-Cl^-	C^--H^+	C^+-Cl^-
B_2H_6	I	I	D	D
	I[a]	I[a]	D	
PH_3	D	D	I	I
	D[a]			
AsH_3	D	D	I	D
	D[a]			

*I and D indicate an increase and decrease, respectively, in deposition rate. The first row for each dopant gas is for the predicted effects, the second row for the observed effects.

[a]F. A. Cotton and G. Wilkinson, Advanced Inorganic Chemistry, Second Ed., John Wiley and Sons, New York. (1966), p. 466.

7. PRODUCTION OF SYNTHETIC FUELS BY PHOTON ASSISTED CATALYZED REACTIONS

J. Kleckner and G. Somorjai

Photon assisted catalysis is another direction of research in catalysis science for the production of synthetic fuels. Many reactions like the dissociation of water ($H_2O = H_2 + 1/2\ O_2$) or photosynthesis ($CO_2 + H_2O \rightarrow$ hydrocarbons) require large energy inputs and are thermodynamically prohibited. If energy can be provided by sunlight, however, and efficiently utilized in the course of these reactions, hydrogen and hydrocarbons may be produced. Research is being carried out at LBL to study the feasibility of photocatalysis of these thermodynamically unfavorable reactions. Surfaces of metals and oxides are prepared and the various reactions are studied in the presence of light. The light excites electrons in the solid surface which are then trapped by the adsorbed molecules. The modified adsorbed species may react with other adsorbates to form the desired products. If successful, photocatalysis may play an important role in synthetic fuel production.

8. RESEARCH PLANS FOR CALENDAR YEAR 1976

G. A. Somorjai

We shall attempt to synthesize new metal catalyst systems by controlled deposition of bimetallic alloys. We shall make use of substrates with stepped surfaces for this purpose.

The mechanism of prototype hydrocarbon reactions, dehydrogenation, hydrogenolysis, isomerization and dehydrocyclization will be studied on iridium, rhodium, and palladium surfaces and will be correlated with that on platinum.

The surface crystallography of hydrocarbon molecules on Pt(111) and Rh(100) surfaces will be explored.

We shall initiate studies of chemical reactions (polymerization, gas-surface reactions) on organic crystal surfaces.

We shall explore the reaction mechanism of the CO/H_2 reaction to produce hydrocarbons on rhodium, cobalt, and iron surfaces.

We shall study the photocatalytic dissociation of water on oxide surfaces to produce hydrogen.

Studies of alloy surfaces will be extended to include Pd-Au, Pd-Ag, and Pd-Cu systems that are of catalytic importance.

The reduction of nitrogen oxides (NO_x) to dinitrogen (N_2) will be studied on platinum surfaces.

9. 1975 PUBLICATIONS AND REPORTS

G. A. Somorjai and Associates

Journals

1. J. L. Gland, K. Baron, and G. A. Somorjai, Low-Energy Electron Diffraction, Work Function Change and Mass Spectrometric Studies of Chemisorption and Dehydrogenation of Cyclohexane, Cyclohexene, and 1,3-Cyclohexadiene on the Pt(111) Surface, J. of Catalysis 36, 305 (1975) (LBL-2768).

2. S. H. Overbury, P. A. Bertrand, and G. A. Somorjai, The Surface Composition of Binary Systems. Prediction of Surface Phase Diagrams of Solid Solutions, Chem. Revs. 75, 547 (1975) (LBL-2746).

3. S. L. Bernasek and G. A. Somorjai, Molecular Beam Study of the Mechanism of Catalyzed H_2-D_2 Exchange on Platinum Single Crystal Surfaces, J. Chem. Phys. 62, 3149 (1975) (LBL-3115).

4. S. L. Bernasek and G. A. Somorjai, Small Molecule Reactions on Stepped Single Crystal Platinum Surfaces, Proceedings of the Surface Science Conference, Rolla, Mo., Surf. Sci. 48, 20 (1975) (LBL-2759).

5. M. A. Chesters and G. A. Somorjai, The Structure of Surfaces, Ann. Rev. Mat. Sci. 418 pp. Annual Revs. Inc., 1975, R. A. Higgins, ed. (LBL-3187).

6. L. L. Kesmodel and G. A. Somorjai, Structure Determination of the Platinum (111) Crystal Face by Low-Energy Electron Diffraction, Phys. Rev. B 11, 630 (1975) (LBL-3148).

7. P. C. Stair, T. J. Kaminska, L. L. Kesmodel, and G. A. Somorjai, A New Rapid and Accurate Method to Measure Low-Energy Electron Diffraction Beam Intensities. The Intensities from the Clean Pt(111) Crystal Face, Phys. Rev. B 11, 623 (1975) (LBL-3149).

8. S. L. Bernasek and G. A. Somorjai, Scattering of Helium and Deuterium from Single Crystal Pt(111) Compared from Two Different Laboratories, J. Vacuum Sci. and Tech. Letter 12(2), 655 (1975).

9. L. E. Firment and G. A. Somorjai, Low Energy Electron Diffraction (LEED) Studies of Molecular Crystals: The Surface Structures of Vapor Grown Ice and Napththalene, J. Chem. Phys. 63, 1037 (1975) (LBL-3558).

10. S. L. Bernasek and G. A. Somorjai, Molecular Beam Scattering from Solid Surfaces, Prog. in Surf. Sci. 5, 377 (1975) (LBL-2591).

11. M. A. Chesters and G. A. Somorjai, The Chemisorption of Oxygen, Water, and Selected Hydrocarbons on the (111) and Stepped Gold Surfaces, Surface Sci. 52, 21 (1975) (LBL-3741).

12. Y. W. Tsang and L. M. Falicov, Calculation of the Lattice Structure on Stepped Surfaces of Ar and NaCl, Phys. Rev. B 12, 2441 (1975) (LBL-3904).

13. Chin-An Chang and Wigbert J. Siekhaus, Auger Analysis of Silicon Thin Films Deposited on Carbon at High Temperature, J. Applied Phys. 46(8), 3402 (1975) (LBL-3186).

14. Chin-An Chang, Wigbert J. Siekhaus, Thomas Kaminska, and Donald Tai-Chan Huo, Enhanced Crystallinity of Silicon Film Deposited at Low Temperature, Applied Phys. Letters 26(4), 178 (1975) (LBL-3165).

Talks

1. G. A. Somorjai, Reactive Scattering of Molecular Beams from Platinum Surfaces, Stanford University, Palo Alto, CA, January 29, 1975.

2. G. A. Somorjai, Surface Science of "New" Materials Studies of Organic, Iron, Thorium and Alloy Surfaces, California Institute of Technology, Pasadena, Calif., Feb. 12, 1975.

3. G. A. Somorjai, The Atomic Structure and Reactivity of Metal Surfaces, Lehigh University, Bethlehem, Pa., February 19, 1975.

4. G. A. Somorjai, Studies of Metal, Alloy and Organic Surfaces on the Atomic Scale, University of Pittsburgh, Pittsburgh, Pa., March 19, 1975.

5. G. A. Somorjai, Catalysis of Hydrocarbons by Platinum Crystal Surfaces at High and Low Pressures, University of Pittsburgh, Pittsburgh, Pa., March 20, 1975.

6. G. A. Somorjai, The Structure and Reactivity of Metal Surfaces, University of Pennsylvania, Philadelphia, Pa., April 9, 1975.

7. G. A. Somorjai, Catalysis by Platinum Single Crystals, Pennsylvania State University, University Park, Pa., April 10, 1975.

8. G. A. Somorjai, Catalysis of Hydrocarbons by Platinum, Iowa State University, Ames, Iowa, April 14, 1975.

9. G. A. Somorjai, Surface Studies of Alloys and Organic Crystal Surfaces, Iowa State University, Ames, Iowa, April 14, 1975.

10. G. A. Somorjai, Recent Advances in the Physics and Chemistry of Surfaces. Argonne Natl. Labs., Chicago, Ill., May 17, 1975.

11. G. A. Somorjai, Studies of Hydrocarbon Catalysis on Platinum Crystal Surfaces of High and at Low Pressures, Gordon Conference on Catalysis, June 16, 1975.

12. G. A. Somorjai, Inorganic Surface Chemistry on the Atomic Scale, Gordon Conference on Inorganic Chemistry, New Hampshire, Aug. 6, 1975.

13. G. A. Somorjai, Surface Structure Analysis of Organic Adsorbates on the Pt(111) Crystal Face, ACS Meeting, Chicago, Ill., Division of Colloid and Surface Chemistry.

14. G. A. Somorjai, Surface Crystallography in 1975 and the Directions of Research for the Future, Chairman, Structure of Surfaces Section, 10th Intern. Congress of Crystallography, Amsterdam, Holland, Aug. 12, 1975.

15. G. A. Somorjai, Catalysis of Organic Reactions on Metal Surfaces, University of California, Santa Cruz, Calif., Oct. 15, 1975.

16. G. A. Somorjai, Mechanisms of Catalyzed Hydrocarbons and Hydrogen on Metal Surfaces, University of California, San Diego, Calif., Oct. 27, 1975.

17. G. A. Somorjai, Science of Metal Catalysis, ASC lecture tour of the Northwest, Corvallis, Oregon; Tacoma, Washington; Moscow, Idaho. Solar Energy Conversion by Surface Science, Spokane, Washington; Pulman, Washington, Oct. 20-27.

18. G. A. Somorjai, The Structure and Chemistry of High Miller Index Surfaces, Stanford University, Palo Alto, Calif. Nov. 15, 1975.

19. G. A. Somorjai, Correlation Between Structure and Catalytic Activity, First Chemical Congress of the North American Continent, American Chemical Society, Mexico City, Mexico, Dec. 1, 1975.

LBL Reports

1. D. I. Hagen and G. A. Somorjai, Catalysis of Hydrocarbons on Platinum Iridium and Their Alloys with Gold, LBL-3438, Feb. 1975.

2. S. H. Overbury and G. A. Somorjai, Auger Electron Spectroscopy of Alloy Surfaces, LBL-3742, March 1975.

3. Steven L. Bernasek, Molecular Beam Scattering Studies of Energy Transfer and Chemical Reaction on Well Characterized Platinum Surfaces (Ph.D. Thesis) LBL-3505, March 1975.

4. N. Garcia, L. L. Kesmodel, J. Solana and N. Cabrera, New Interpretation of Electron Diffraction Data for Al in Terms of Lennard-Jones Type Surface State Resonances, LBL-3764, March 1975.

5. Chin-An Chang and Wigbert J. Siekhaus, Enhanced Crystallinity of Low Temperature Deposited Silicon Films on Graphite Substrates, LBL-3795, April 1975.

6. Wigbert Siekhaus, Interface Phenomena in Solar Cells, LBL-3923, May 1975.

7. Christoph O. Steinbruchel, On the Interpretation of Adsorption and Desorption Kinetics Experiments, LBL-3796, May 1975.

8. James G. Crump, Mean Square Displacement of Surface Atoms on the Silicon (111) Crystal Face (M.S. Thesis) LBL-3575, March 1975.

9. S. H. Overbury and G. A. Somorjai, The Surface Composition of the Silver-Gold System by Auger Electron Spectroscopy, LBL-3925, May 1975.

10. Chin-An Chang and Wigbert J. Siekhaus, Enhanced Crystallinity of Low Temperatures Deposited Silicon Films on Graphite Substrate, LBL-3946, July 1975.

11. B. E. Nieuwenhuys, Adsorption of Noble Gases on Metals, LBL-3963, July 1975.

12. J. L. Gland and G. A. Somorjai, Low-Energy Electron Diffraction and Work Function Studies of Adsorbed Organic Monolayers on the (100) and (111) Crystal Face of Platinum, LBL-3799, April 1975.

13. D. I. Hagen and G. A. Somorjai, The Effect of Gold on Hydrogenolysis, Isomerization and Dehydrocyclization Reactions on Polycrystalline Platinum and Iridium Foils, LBL-4104, Aug. 1975.

14. Y. W. Tsang and L. M. Falicov, Steric Properties of the Transition-Metal Ions on Stepped Surfaces, LBL-4540, Sept. 1975.

15. G. A. Somorjai, The Application of Low Energy Electron Diffraction in Contact Catalytic Reactions, LBL-3920, May 1975.

16. Chin-An Chang, Dopant Gas Effect on Silicon Chemical Vapor Depositions. A Surface Potential Model, LBL-3938, June 1975.

17. G. A. Somorjai and D. W. Blakely, On the Mechanism of Catalysis of Hydrocarbon Reactions by Platinum Surfaces, LBL-4121, Aug. 1975.

18. S. T. Ceyer, R. J. Gale, S. L. Bernasek and G. A. Somorjai, Scattering of a Thermal Helium Beam from High-Miller Index (Stepped) Platinum Crystal Surfaces, LBL-4169, Sept. 1975.

19. L. E. Firment and G. A. Somorjai, The Surface Structures of Vapor-Grown Ice and Napthalene Crystals Studied by Low-Energy Electron Diffraction, LBL-4154, Sept. 1975.

20. D. W. Blakely and G. A. Somorjai, The Dehydrogenation and Hydrogenolysis of Cyclohexane and Cyclohexene on Stepped (High Miller Index) Platinum Surfaces, LBL-3976, Aug. 1975.

21. D. I. Hagen, B. E. Nieuwenhuys, G. Rovida and G. A. Somorjai, Low-Energy Electron Diffraction, Auger Electron Spectroscopy and Thermal Desorption Studies of Chemisorbed CO and O_2 on the (111) and Stepped {6(111)×(100)} Iridium Surfaces, LBL-4527, Nov. 1975.

22. J. C. Buchholz and G. A. Somorjai, The Structure of Adsorbed Gas Monolayers, LBL-4191, Nov. 1975.

23. G. A. Somorjai, Reactions on Single Crystal Surfaces, LBL-4187, Nov. 1975.

f. Nuclear Magnetic Resonance*

Alexander Pines, Principal Investigator

1. NMR LINE-BROADENING BY SLOWING DOWN OF SPIN FLUCTUATIONS

Alexander Pines

The phenomenon of motional narrowing is very common in magnetic resonance. Starting from a rigid solid in which the resonance lines are broadened by static magnetic interactions between the spins, the sample is heated and, as rapid thermal molecular reorientation and translations ensue, the lines narrow until high resolution spectra typical of isotropic fluids are observed. An interesting fact, shown by van Vleck is that there is another form of motional narrowing that may be thought of as occurring entirely in spin space without thermal motion. This can occur if there are exchange interactions that commute with the magnetization operator but not with the perturbation interaction responsible for the line broadening. The exchange induces rapid "flip-flops" of nuclear spins that can average away the broadening interactions if the exchange is strong enough.

As a particular example of considerable current interest, consider the case of the ^{109}Ag resonance in AgF first observed by Abragam and Winter. The line is unusually narrow for a solid and this is explained by the rapid decoupling of ^{109}Ag-^{19}F dipolar interactions by the ^{19}F-^{19}F dipolar couplings. The effect is marked since $\gamma_F \gg \gamma_{Ag}$ and the qualitative analogy with thermal motional narrowing is evident. To date, however, the analogy has not been complete. Whereas in the case of classical motional narrowing the rate of fluctuations can be controlled and the full regime from rigid to motionally narrowed can be covered by variation of temperature, no such control has been exercised over spin fluctuations in AgF. In particular, if it were possible to eliminate the ^{19}F-^{19}F coupling, Abragam has predicted that the ^{109}Ag resonance should broaden, allowing the full rigid lineshape to be observed in analogy to thermal cooling.

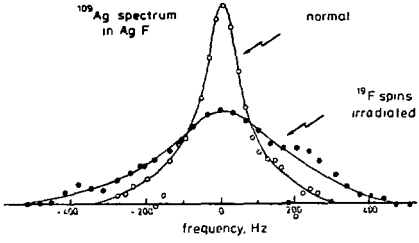

Fig. 1. Silver (^{109}Ag) resonance line at 4.2 Mhz in polycrystalline AgF with and without irradiation of the ^{19}F spins. Irradiation of the ^{19}F spins is performed with an rf field of 14 G close to the magic angle in their rotating frame. The scaling factor, cos θ_I has been taken into account in drawing the frequency scale. (XBL 767-8900)

We have demonstrated for the first time a completion of the analogy between spin and thermal fluctuations by selectively reducing the ^{19}F spin fluctuations. Figure 1 shows the observed behavior. When the ^{19}F spins in a sample of polycrystalline AgF are irradiated with a strong radiofrequency field such that the effective field in the rotating frame is close to the magic angle, the ^{19}F-^{19}F dipolar interactions are reduced and the ^{109}Ag resonance is indeed observed to broaden. A continuous variation of the spin fluctuation rate between the limiting cases of extreme narrowing and rigid is at the experimenter's

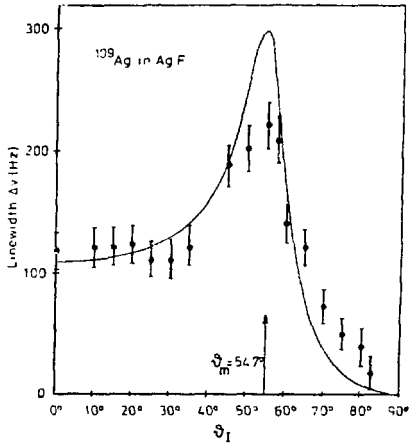

Fig. 2. Calculated and experimental excess half width $\Delta\nu = \delta/\pi$ of ^{109}Ag in polycrystalline AgF at 4.2 Mhz under irradiation of the ^{19}F spins with an rf field of 14 G at the angle θ_I in their rotating frame. The experimental excess half width has been obtained by deconvolution of the experimental spectra with the totally fluorine decoupled ($\theta_I = \pi/2$) silver resonance line. (XBL 767-8899)

control. Figure 2 shows the linewidth of the ^{109}Ag resonance as the ^{109}F irradiation frequency is varied. θ_I is the effective angle of the rotating field in the rotating frame.

Using this control of spin fluctuations, we are currently measuring spin correlation functions.

*The work described here was partly supported by the National Science Foundation.

*Work done in collaboration with M. Mehring, Institute of Physics, University of Dortmund, West Germany.

2. NEW APPROACH TO PROTON NMR IN SOLIDS*

A. Pines, D. J. Ruben and S. Vega

To obtain high resolution proton nmr spectra, an appealing idea would be to immerse the protons in a bath of deuterium nuclei thus rendering them isotopically dilute. The solid state ^{1}H high resolution spectrum could then be created by deuterium spin-decoupling. This has been used to observe ^{1}H dipolar spectra in selectively deuterated molecules dissolved in liquid crystals by Meiboom and co-workers. Why then, has this not been attempted to date in solids? In order to appreciate the difficulty, let us examine the situation depicted schematically in Fig. 1. The

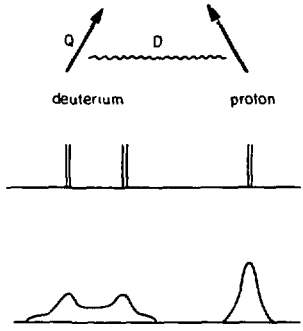

Fig. 1. Deuterium and proton spins interacting via magnetic dipolar D. The deuterium resonance is broadened severely by electric quadrupolar interaction Q. (XBL 756-6460)

^{1}H linewidth is dominated by dipolar coupling to the deuterium. Imagine that we apply at the deuterium frequency a rotating field of intensity ω_1 (in angular frequency units). The criterion for spin-decoupling is that the rate of transitions between the deuterium magnetic sublevels induced by ω_1 must be comparable to the dipolar coupling. If the quadrupolar splittings were absent, this rate would be proportional to ω_1^2, so this means:

$$\omega_1^2 \sim D^2 \quad , \tag{1}$$

an easily attainable experimental situation. However, with the quadrupolar splitting $Q/2\pi \approx 200$ kHz $\gg D/2\pi$, the criterion for decoupling is that we need to "cover" the spectral width of the deuterium:

$$\omega_1^2 \sim Q^2 \quad , \tag{2}$$

i.e., a rotating field of $H_1 \approx 300$ Gauss, which is quite simply prohibitive.

Let us consider, however the "forbidden" transition $m = 1 \rightarrow -1$ which can occur by a double-quantum process at the unshifted frequency ω_0 as shown in Fig. 2. We can provide a simple but illustrative argument to assess this effect. The

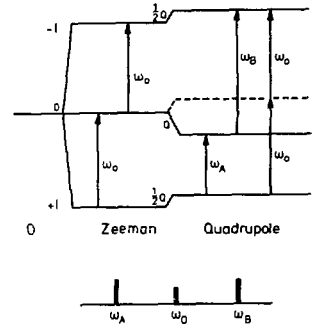

Fig. 2. Allowed single quantum (ω_A,ω_B) and double quantum transitions (ω_0) for deuterium nucleus in an axially symmetric field gradient. Spin-decoupling can be induced by the direct $1 \rightarrow -1$ transition since $m = 0$ induces no magnetic dipolar broadening. (XBL 7511-7627)

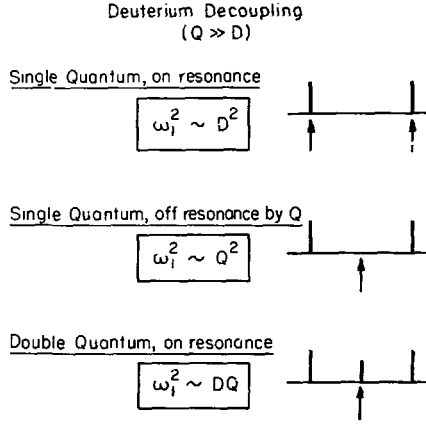

Fig. 3. Conditions for spin decoupling of spin-1 nuclei such as deuterium. D is the dipolar coupling to another nucleus and Q is the quadrupolar broadening. (XBL 756-6458)

probability for the double-quantum transition is easily calculated by second order perturbation theory:

$$W \sim \frac{\omega_1^4 |\langle 1|I_x|0\rangle|^4}{(\omega_0 - \omega_A)^2} \sim \frac{\omega_1^4}{Q^2} \tag{3}$$

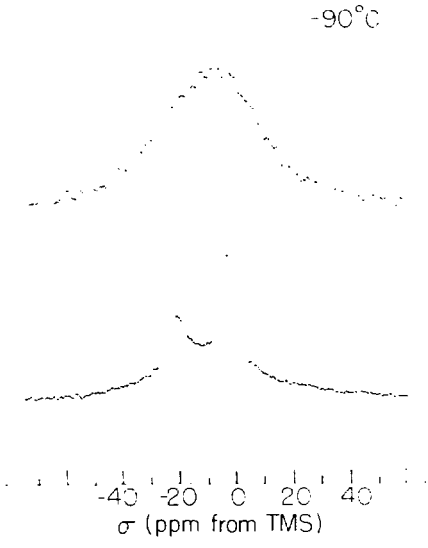

Fig. 4. Nmr spectra of ~ 1% residual protons in deuterated solid acetic acid. The top is the normal Fourier transform spectrum and the bottom one is obtained by spin-decoupling the deuterium through double-quantum transitions. (XBL 758-6991)

where ω_A is the allowed transition frequency for $m = -1 \rightarrow 0$. Employing again the spin-decoupling condition $W \approx D^2$ we find we need:

$$\omega_1^2 \approx QD \ . \qquad (4)$$

Thus the required power depends only linearly on Q and the power required by (4) is indeed accessible in our laboratory. The decoupling conditions are summarized in Fig. 3.

Figure 4 demonstrates the first application of this approach to the ~1% residual protons in deuterated acetic acid. As shown in Fig. 5 this is actually composed from a narrow line (methyl) and a broad line (carboxyl) showing a large anisotropy of the proton magnetic shielding. On spin-decoupling of the deuterium by double-quantum transitions the two lines from the methyl and carboxyl protons are resolved. This technique can now be used to study magnetic shielding and proton motion in solids.

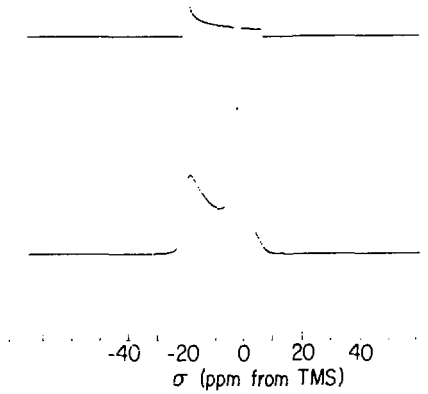

Fig. 5. Theoretically synthesized proton nmr lineshape for solid acetic acid, showing (top) a narrow line (methyl) and a broad axially symmetric powder line (carboxyl). Lower spectrum is after convolution with Gaussian and agrees with the experimental. (XBL 7512-9225)

3. FOURIER TRANSFORM MULTIPLE-QUANTUM NMR

A. Pines, S. Vega and T. W. Shattuck

All recent developments in high resolution solid state nmr have been carried out on nuclei with spin-1/2, i.e., proton, carbon-13, nitrogen-15, fluorine-19, silicon-29, phosphorus-31 and silver-109. Although it would be valuable to extend these experiments to nuclei with spin-1 and higher, no such attempts have been made. As a particularly relevant example, consider deuterium. By isotopically labeling large molecules with deuterium we could learn about local structure and motion; this has not been accessible to date.

Figure 1 demonstrates the difficulty. The deuterium spin-1 nucleus has an electric quadrupole moment and this causes a large broadening due to interactions with local electric fields in the solid. The broadening is of the order of 100 kHz whereas the resolution is of the order of 100 Hz. The spectrum derives from the allowed transitions between the magnetic sublevels $m = 1 \rightarrow 0$ and $0 \rightarrow -1$.

---

* Work done in collaboration with M. Mehring, Institute of Physics, University of Dortmund, West Germany.

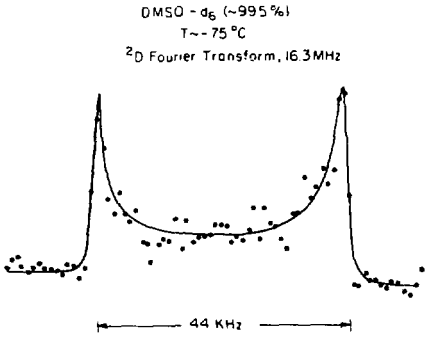

Fig. 1. Deuterium nmr spectrum of dimethylsulfoxide (DMSO)-d_6 showing the extremely large quadrupolar broadening. Only the center section of the spectrum is shown. (XBL 756-6464)

We have introduced a new technique involving direct double-quantum excitation $m = 1 \rightarrow -1$ as shown in Fig. 2. The coherence of superposition between states ± 1 which we label $\langle Q(t) \rangle$ decays as:

$$\langle Q(t) \rangle = f(t) \cos 2\delta\omega t \qquad (1)$$

where $\delta\omega$ is the resonance offset of the irradiating field. Thus the decay of (1) does not contain the quadrupole broadening, and yields on Fourier transformation a high resolution spectrum.

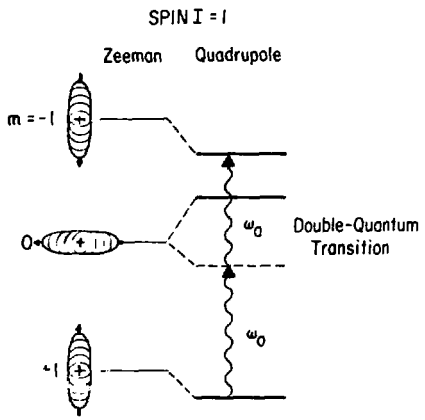

Fig. 2. Preparation of coherent superposition between studies ± 1 by double-quantum transition at ω_0. (XBL 767-8898)

Figure 3 demonstrates the application of this technique to 10% deuterium labeled oxalic acid. The decay of double quantum coherence for the carboxyl deuterium while proton decoupling yields a frequency of 20 ppm at a quadrupolar splitting of 16KHz, the first measurement of a deuterium magnetic shielding anisotropy.

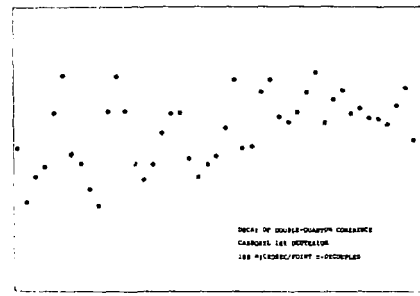

Fig. 3. Decay of coherence between $m = \pm 1$ levels in deuterium after preparation by a double-quantum 90° pulse. The sample was a single crystal of 10% deuterated oxalic acid and the carboxyl deuterons were observed. (XBL 767-8901)

The effect is analogous in many ways to coherent Raman Scattering and we have developed a full quantum mechanical formalism to account for the observations. We are also applying this novel technique to problems of deuterium evironment in labeled materials.

4. CARBON-13 MAGNETIC SHIELDING TENSORS IN ORGANOMETALLIC COMPOUNDS

A. Pines and D. E. Wemmer

We have shown previously that the orientation of the magnetic shielding tensor reflects to a large degree the local symmetry of the electronic wave function. This should be extremely valuable in studying the changes that occur when organic molecules bond to surfaces or to metals.

As a model for such studies we have measured the first magnetic shielding tensors for ^{13}C in organometallic compounds. As an example, consider the case of decamethyl-ferrocene, the fully methylated derivative of ferrocene. Usually, to obtain the magnetic shielding tensor, which is an anisotropic quantity, it is necessary to work with single crystals at several orientations. We have eliminated this substantial requirement by studying the spectra at two temperatures with different molecular motion in a polycrystalline sample.

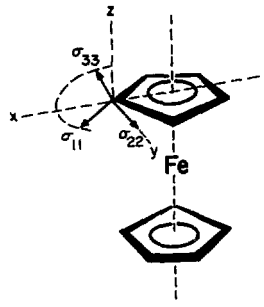

Fig. 1. Orientation of the magnetic shielding tensor σ in decamethylferrocene. The tensor axes are tilted by 20° and the direction of heaviest magnetic shielding σ_{33} is not perpendicular to the π-model plane as in isolated aromatic molecules. (XBL 7512-9194)

Figure 1 shows the orientation of the tensor thus obtained. The induced magnetic moment by the electrons is highest when the magnetic field is along σ_{11} and lowest when the field is along σ_{33}. If the fragment were an isolated cyclopentadienyl axion, σ_{33} would be exactly perpendicular to the ring planes. Thus the tilt in σ_{33} is induced by Fe^{2+} ion. Using this we can now study in detail the distortions in molecular and electronic structure induced by the nearby metal ion. A large series of compounds has been studied with different metals and ligands.

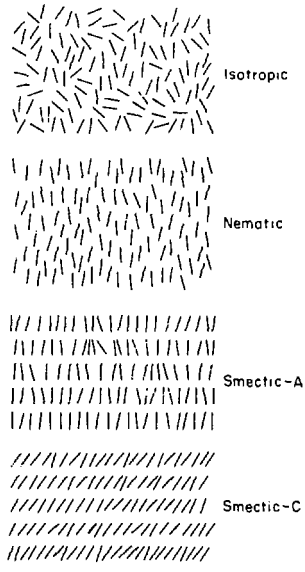

Fig. 1. Some of the higher temperature liquid crystal phases. (XBL 748-7063)

5. MOLECULAR ORDER IN NEMATIC LIQUID CRYSTALS

A. Pines, D. J. Ruben and A. Höhener

Liquid crystals are composed of long rod-like molecules. They exist in a number of phases, of which the common high temperature forms are shown in Fig. 1. As seen, there exist different types of long range orientational and translational order. The study of these materials is important since they serve as lubricants, for displays, and as models for phase transitions and biological membranes.

We previously made a preliminary study of the effect of molecular end chains on the order in the nematic phase. This order can be partially characterized by the parameter:

$$S = \frac{1}{2}\ (3\cos^2\theta - 1) \qquad (1)$$

where θ is the angle between the molecular axis and the director, the local average direction of the molecular axis. For $S = 1$, the molecules are perfectly ordered; for $S = 0$ the phase is completely isotropic. We have investigated with our new high field spectrometer the order S in a

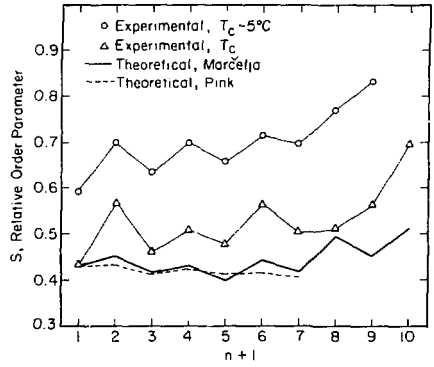

Fig. 2. Dependence of the microscopic nematic order parameter on the number of carbons (n+1) in the end chains of liquid crystal molecules. The theoretical lines are from mean-field calculations. The "even-odd" zig-zig shows the alternating stabilizing and destabilizing effects of carbon-carbon segments on the nematic interactions. (XBL 7512-9220)

homologous series of nematic molecules C_nH_{2n+1} - (CORE) - C_nH_{2n+1} where (CORE) depicts a semi rigid aromatic core, with n = 1 to 10. Figure 2 shows the results for an alkoxyazoxybenzene series; a marked "even-odd" effect is obtained in agreement with birefringence measurements by Shen. Thus the end chains affect substantially the properties of the anisotropic phase. Comparison with existing theories show that they underestimate the effects.

Thus we can determine a great deal about local microscopic effects in these phases. Our studies are being extended to other series and phases and to dynamical investigation of molecular conformational, rotational and diffusive motions.

6. ROTATIONAL ORDER IN THE SMECTIC-C PHASE

A. Pines and A. Höhener

One of the important low temperature liquid crystal phases is the smectic-C. From X-ray studies, it is known that this derives from the smectic-A by a tilt of the molecules in the layers. The microscopic molecular nature of this phase is still a controversial question and is of great interest since it can teach us about the molecular forces that cause the condensation into the various phases.

A microscopic theory due to McMillan proposes that the mechanism for the tilting is derived from the interactions between electric dipoles on the molecules as shown in Fig. 1. This would require that the molecules freeze in their rotation about the long axes, unlike the smectic-A phase. This property of rotational ordering has been the subject of several investigations.

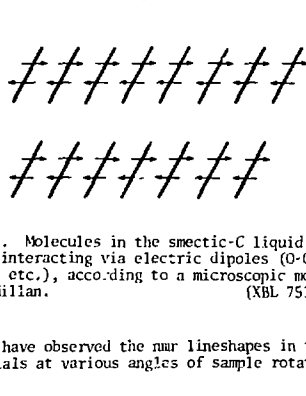

Fig. 1. Molecules in the smectic-C liquid crystal phase interacting via electric dipoles (O-C, N-C bonds, etc.), according to a microscopic model of McMillan. (XBL 751-5436)

We have observed the nmr lineshapes in two materials at various angles of sample rotation after cooling of samples into the smectic-C phase. The lineshapes are inconsistent with high rotational order of the molecules in the smectic-C phase. Our conclusions are in agreement with those of Luz and Meiboom and opposite to those of Doane and co-workers. It therefore appears to us that forces other than electric dipole are inducing the smectic-C tilt.

7. SYMMETRY OF MOLECULAR MOTION IN SOLIDS

A. Pines and D. E. Wemmer

A perennial and difficult question in the study of molecular studies has been that of the mode of molecular motion. In particular, one expects the potential binding rotational motion in the solid state to differ substantially from that in liquid or gaseous environments. Thus, rotational diffusion is usually assumed for fluids whereas transitions between discrete potential minima are more likely in a solid. Clearly, it is not simple to investigate experimentally the mode of motion in the solid since most observable properties are likely to differ very little between the different cases of motion.

One set of properties that differentiates between modes of motion are the time-correlation functions:

$$G_{\ell m}(\tau) = \langle T_{\ell m}(0)\ T_{\ell -m}(\tau)\rangle \qquad (1)$$

where $T_{\ell m}$ are components of spherical tensors of rank ℓ, which are related to our normal observables, e.g., dipole moment (ℓ=1), quadrupole moment (ℓ=2), magnetic shielding tensor (ℓ=2), etc., and $\langle\rangle$ denotes an ensemble average. Although magnetic resonance is normally a powerful microscopic tool, the $G_{\ell m}(\tau)$ in (1) cannot normally be extracted in full from experiments, and only a small number of points can be provided by relaxation studies. Thus, even though the different modes of motion yield different $G_{\ell m}(\tau)$, it has not been possible to use magnetic resonance to resolve this, and other approaches such as Raman scattering for direct measurement of (1) are also difficult.

By studying the nmr lineshapes at the onset of motion, we have been able to establish precisely the local symmetry of the potential determining the motion. Figure 1 shows an example for this in decamethyl-ferrocene exhibiting a five-fold potential. The three calculated lineshapes are for three ratios of the potential for $2\pi/5$ and $4\pi/5$ molecular jumps. The types of jumps are shown in Fig. 2. The best agreement with experiment (the lowest curve) is for a large ratio of the above potentials. Thus the lineshape is extremely

Fig. 1. Nmr powder lineshapes for ^{13}C in decamethyl-ferrocene. Top three are from theoretical calculations assuming a) $W_{12} \ll W_{13}$, (b) $W_{12} = W_{13}$, (c) $W_{12} \gg W_{13}$, where W_{12} is the probability of a $2\pi/5$ jump of the five-fold ring and W_{13} for a $4\pi/5$ jump, (d) is the experimental line. (XBL 7511-9418)

sensitive to the symmetry of local potentials and is being used to study short-range order and hindering potentials in condensed phases.

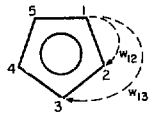

Fig. 2. Possible jumps ($2\pi/5$ and $4\pi/5$) of relevance in lineshapes of ferrocene. (XBL 7512-9191)

8. PROTON DYNAMICS IN ICE

A. Pines, D. E. Wemmer and D. J. Ruben

The nature of proton motion in ice-I has been intensively studied, since it is thought to be responsible for dielectric relaxation, diffusion and spin-relaxation. We have been able to determine for the first time the exact nature of the symmetry governing the mobility of the protons and to separate out the dynamics of reorientational motion from other types of motion. The information derived from these studies is being used to examine the nature of relaxation in ice and the effects of various impurities. Figure 1 shows the temperature dependence of ^1H spectra in heavy

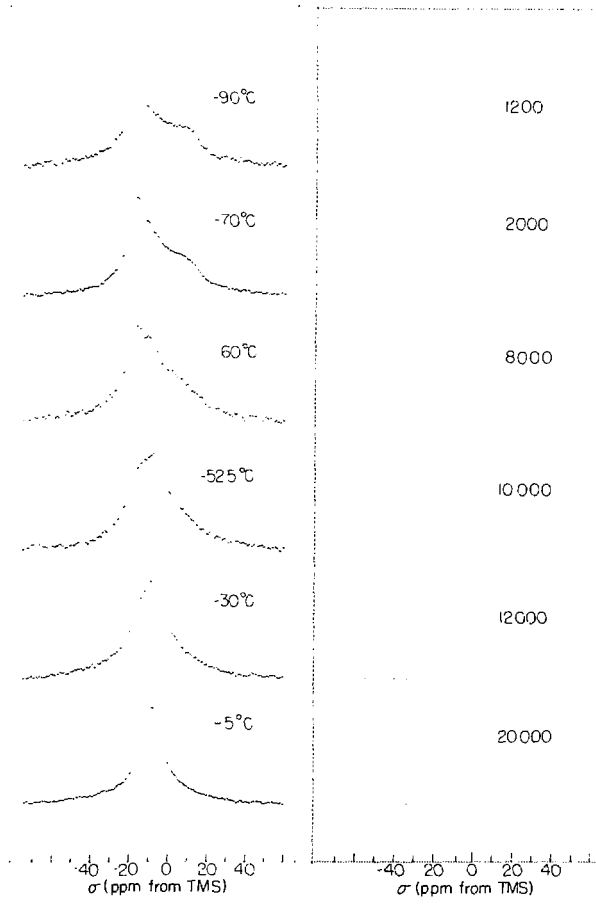

Fig. 1. Temperature dependence of proton nmr lineshapes in heavy ice-I. At left are experimental spectra obtained by decoupling the deuterium through double-quantum transitions. At right are calculated curves assuming the proton undergoes a move in tetrahedral symmetry. The numbers are proton jump rates in sec^{-1}. (XBL 7510-7416A)

ice-I obtained by decoupling the 99% deuterium nuclei by double-quantum transitions. At right are the theoretical spectra calculated for a model of proton motion in a tetrahedral potential. The agreement is virtually perfect; it can be explained by an effective rotation of the water molecules (low energy Slater configurations) in ice by migration of defects, as in Fig. 2. A possible defect causing this rotation is a Bjerrum fault shown in Fig. 3.

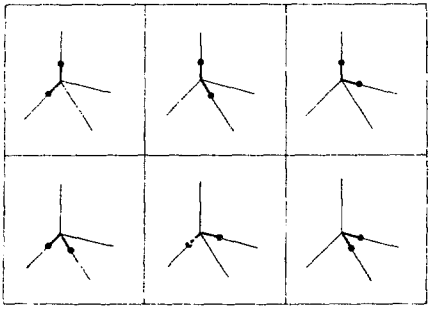

Fig. 2. Pseudorotation of water "molecules" (low energy Slater configurations for protons in hydrogen bonds) in ice-I. (XBL 759-8288)

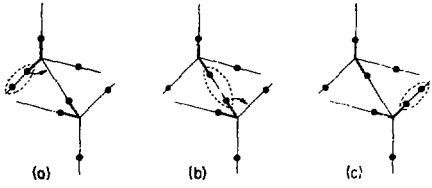

Fig. 3. Migration of a Bjerrum fault (two protons in one hydrogen bond), a mechanism for water reorientation in ice-I. (XBL 759-8287)

Other models of motional symmetry do not agree with the experiments and diffusional motion of protons has no effect. Thus, the technique is uniquely sensitive to reorientational motion. The activation barrier of ~ 4 kcal/mole for proton motion derives from the use of impure samples. Studies on pure heavy ice will be undertaken to complement the work of Lowe and others.

9. COMPOSITION AND STRUCTURE OF COAL AND OIL SHALE

A. Pines and D. E. Wemmer

Coal and oil shale are potentially important fuel and petrochemical sources: One of the principal problems in research on these materials has been the lack of simple and straightforward methods for their analysis. The usually useful information provided by classical nmr for fluids is handicapped by the low resolution obtained in immobile solids such as coal and oil shale.

We have opened the way for a solution to this problem by resolving with strong proton decoupling at high magnetic field the aliphatic aromatic carbon-13 signals, allowing for the first time a direct in situ determination of the aromatic/aliphatic carbon ratio. This quantity is of importance in assessing the usefulness of these materials.

As an example, we have studied the ^{13}C nmr spectra of samples of Bruceton coal provided by J. Larsen and E. W. Kuemmerle in Tennessee. Figure 1 depicts spectra using our techniques which show the first resolution of the two gross types of carbon in the raw material, aliphatic and aromatic. The sample was subsequently treated by the Tennessee group to enhance the aliphatic/

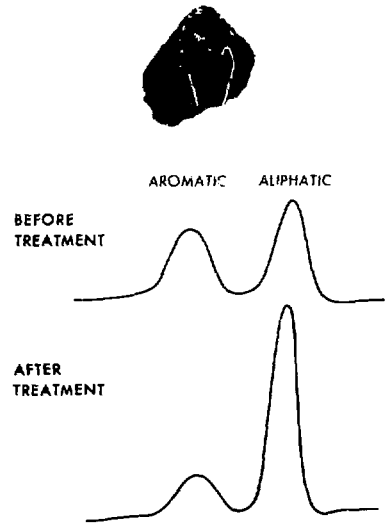

Fig. 1. Carbon-13 nmr spectra of coal after proton enhancement and spin-decoupling. Samples from Larsen and Kuemmerle in Tennessee. Proton frequency 185 MHz. (XBB 761-86) & (XBL 761-2018)

aromatic ratio and our lower spectrum indicates directly and simply that the ratio has indeed grown dramatically. Similar work is being done on other samples of coal and oil shale from various sources including oil companies and the Bureau of Mines.

We are currently building a high speed sample rotor for magic-angle spinning. This, together with our radiofrequency techniques, will allow much higher resolution and a complete determination of the carbon types and structure in these materials. In addition, by relaxation and diffusion measurements we will be able to study the mobility of molecules in these phase.

10. HIGH FIELD NUCLEAR MAGNETIC DOUBLE RESONANCE SPECTROMETER

A. Pines, D. J. Ruben and D. Wilkinson

We have completed and have fully operational a high field double resonance spectrometer. A schematic diagram is shown in Fig. 1. The device operates at 185 MHz for protons and has unprecedented sensitivity for detection of low frequency nuclei. It has been used for our novel experiments on carbon-13 and deuterium.

The probe for this device is equipped with high voltage components, with a goniometer for studying anisotropic properties of crystals and liquid crystals, and with accurate temperature control for temperatures between -160°C and 200°C. It is designed for the geometry of a superconducting solenoid.

Radiofrequency amplitude and phase is under control of an on-line computer through a homebuilt pulse programmer. The computer also handles data acquisition, complex Fourier transformation and storage.

Amplifiers are commercial radio amateur transmitters for the low frequencies and a homebuilt cavity tuned anode device for the 185 MHz. The spectrometer is currently being fitted with a high speed turbine rotor to allow high resolution in polycrystalline samples.

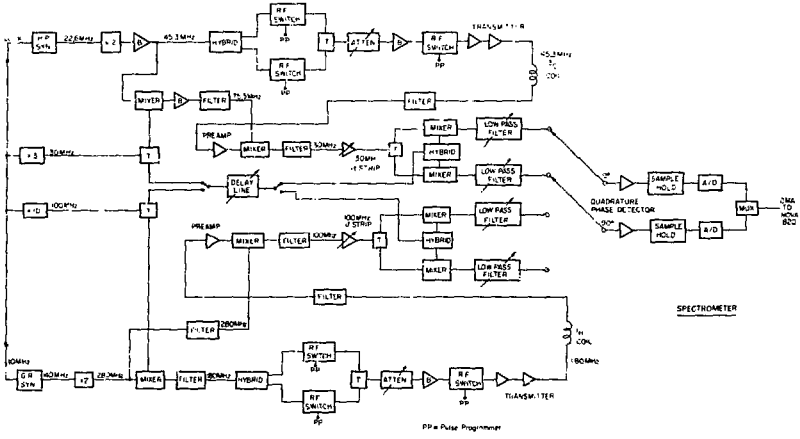

Fig. 1. Schematic diagram of high field nuclear magnetic double resonance spectrometer. (XBL 755-4959)

11. NUCLEAR MAGNETIC ISOTOPE EFFECT

A. Pines, S. Vega and S. Bustamente

Isotopes differ in nuclear mass and this results in a large number of phenomena classified as isotope effects. For example, there are isotope shifts of optical absorption lines, kinetic isotope effects inducing a change in the rate of chemical processes due to the isotope mass difference and isotope effects on transport properties. These phenomena have formed the basis for most modern approaches to isotope enrichment.

We have been interested in the fact that isotopes differ not only in mass but also in nuclear spin and have asked whether the spin can have a detectable effect on chemical reactions. At first sight, this appears highly unlikely since chemical bond energies are of the order of kilocalories/mole whereas spin magnet energies are of the order of milli-calories/mole. Thus, classically, any spin effects should be negligible. However, in quantum mechanics new forces arise due to the Pauli exclusion principle, namely that the total wavefunction must be antisymmetric with respect to exchange of identical fermions. This indicates that large effects of spin may be possible.

We have investigated this by studying the differential effect of ^{12}C (spin 0) and ^{13}C (spin 1/2) on the recombination of radicals in the following photochemical reaction:

$$\text{(I) } R\text{-}C = N = N \xrightarrow{h\nu} \text{(II) } R\text{-}C\text{: (triplet)} \xrightarrow{R'\text{-}C\text{-}H}$$

$$\text{(III) } R\text{-}HC\cdot \quad \cdot C\text{=}R' \longrightarrow \text{(IV) } R\text{-}HC\text{-}C\text{-}R'$$

previously studied in great detail by Closs. Figure 1 shows the nmr proton CIDNP (chemically induced dynamic nuclear polarization) of IV from photochemical decomposition of I enriched to 30% ^{13}C. The spectrum shows absorption and emission peaks due to ^{12}C and ^{13}C in the product (IV) and an enrichment of ~ 35% is calculated for ^{13}C. This is shown by studying the theoretical spectra calculated for no enrichment, 35% ^{13}C, and a higher enrichment as shown in Fig. 2. Only the second spectrum is in agreement with observation.

Thus, the effect appears to be present and we are currently in the process of determining it directly by analytical chemistry.

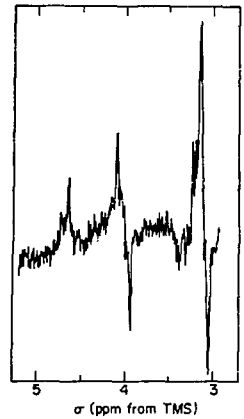

Fig. 1. Proton CIDNP spectrum obtained during 5200 Å irradiation of ^{13}C diphenyldiazomethane. The left peak is a ^{13}C satellite of the middle 2. The absorption and emission lines tell us that the reaction derives from a triplet carbene and allows us to determine the ^{13}C toluene hyperfine constant and enrichment. (XBL 7512-9221)

Fig. 2. Theoretical proton CIDNP for the reaction in Fig. 1: (a) ^{13}C hyperfine = 0, no ^{13}C enrichment; (b) ^{13}C hyperfine = 30 G, ~ 15% enrichment from 30% to 35% ^{13}C; (c) ^{13}C hyperfine > 30 G, > 15% enrichment. The best agreement with experiment appears to be (b). (XBL 7512-9224)

12. RESEARCH PLANS FOR CALENDAR YEAR 1976

Alexander Pines

1. Study of molecular ordering and motion in the low temperature smectic liquid crystal phases. This work will be expanded by employing our new deuterium resonance techniques. Extension of our work to homologous series of smectics.

2. Extension of our work on symmetry of molecular motion to other potentials. Details of motion

and short range order will be studied in molecular crystals and organometallic compounds.

3. Direct detection of the nuclear magnetic isotope effect by analytical chemical techniques. Investigation of other photochemical reactions in magnetic fields and evaluation of their potential for magnetic isotope discrimination.

4. Application of our new multiple-quantum techniques to the study of magnetic shielding of deuterium. This will also be used to study hydrogen bonding. Extension of the multiple-quantum ideas to other nuclear isotopes.

5. Implementation of a new high speed rotor in our probe to obtain high resolution nmr spectra in noncrystalline materials. These will be used to study in detail the composition and structure of coal and oil shale.

13. 1975 PUBLICATIONS AND REPORTS

Alexander Pines and Associates

Journals

1. J. J. Chang, R. G. Griffin and A. Pines, Carbon-13 Chemical Shielding Tensors in Ammonium Hydrogen Malonate, J. Chem. Phys. 62, 4923 (1975) (LBL-3518).

2. J. J. Chang, A. Pines, J. J. Fripiat and H. A. Resing, Qualitative Analysis of Chemisorbed Molecular Species via ^{13}C NMR, Surface Science 47, 661 (1975) (LBL-3721).

3. R. G. Griffin, A. Pines, S. Pausak and J. S. Waugh, ^{13}C Chemical Shielding Tensors in Oxalic Acid, Oxalic Acid Dihydrate and Diammonium Oxalate, J. Chem. Phys. 63, 1267 (1975)

4. R. G. Griffin, A. Pines and J. S. Waugh, Observation of C^{13}-N^{14} Dipolar Couplings in Single Crystals of Glycine, J. Chem. Phys. 63, 3676 (1975).

5. A. Pines, Applications of Novel NMR Techniques to Solids and Liquid Crystals, Proceedings of the Second Specialized Colloque Ampere, Budapest, Hungary, August, 1975, invited talk (LBL-4505).

Lectures

1. A. Pines, NMR Studies of Macroscopic Structure and Dynamics in Solid and Liquid Crystals, Gordon Conference on Magnetic Resonance, Holderness School, New Hampshire, June 1975, invited talk.

2. A. Pines, NMR Studies of Ordered Fluids and Disordered Solids, Third International Meeting on NMR Spectroscopy, St. Andrews, Scotland, July 1975, invited talk.

3. M. Mehring, G. Sinning and A. Pines, Spin-Decoupling in Solids, Third International Meeting on NMR Spectroscopy, St. Andrews, Scotland, July 1975, invited talk.

4. A. Pines, NMR Characterization of Partially Ordered Materials, Gordon Conference on Analytical Chemistry, New Hampton School, New Hampshire, August 1975, invited talk.

5. M. Mehring, G. Sinning, A. Pines and T. W. Shattuck, Dynamics of Heteronuclear Coupling and Decoupling in Solids, Second Specialized Colloque Ampere, Budapest, Hungary, August 1975.

6. Chemical Physics Colloquium, California Institute of Technology, Pasadena, California, January 1975.

7. IBM Research Laboratory, San Jose, California, January 1975.

8. Nuclear Magnetic Resonance Seminar, University of Dortmund, West Germany, March 1975.

9. Chemistry Department, University of New York, Stony Brook, New York, March 1975.

10. Quantum Optics and Resonance Seminar, University of California, Berkeley, May 1975.

11. Chemistry Department, University of Southampton, England, August 1975.

12. Institute Seminar, Weizmann Institute of Science, Rehovot, September 1975.

13. Biophysics Center, University of Basel, Switzerland, October 1975.

14. Molecular Physics Division, Max Planck Institute, Heidelberg, West Germany, October 1975.

15. Chemistry Department, University of California, Berkeley, November 1975.

LBL Reports

1. A. Pines, D. J. Ruben, S. Vega and M. Mehring, New Approach to High Resolution Proton NMR in Solids: Deuterium Spin-Decoupling by Multiple-Quantum Transitions, LBL-4525.

2. M. Mehring, G. Sinning and A. Pines, NMR Line-Broadening in Solids by Slowing Down of Spin Fluctuations, LBL-4546.

A. RADIATION AND SEPARATIONS RESEARCH

1. RADIATION SCIENCES

a. Photochemistry of Materials in the Stratosphere

Harold Johnston, Principal Investigator

1. EXPERIMENTAL STUDIES

a. Photolysis of the Nitrate Free Radical (NO_3) and Rate Constants Involving Dinitrogen Pentoxide (N_2O_5).*

Richard Graham

At room temperature under ordinary laboratory conditions, dinitrogen pentoxide is in rapid equilibrium with nitrogen dioxide and the nitrate free radical

$$N_2O_5 \rightleftharpoons NO_2 + NO_3$$

Dinitrogen pentoxide is rapidly formed from ozone and nitrogen dioxide

$$2\ NO_2 + O_3 = N_2O_5 + O_2$$

Dinitrogen pentoxide slowly catalyzes the decomposition of ozone

$$2\ O_3 \xrightarrow{N_2O_5} 3\ O_2$$

and it rapidly reacts with nitric oxide

$$NO + N_2O_5 \rightarrow 3\ NO_2$$

Ultraviolet radiation decomposes N_2O_5 to the lower oxides of nitrogen

$$2\ N_2O_5 + U.V. \rightarrow 4\ NO_2 + O_2$$

dinitrogen pentoxide undergoes a slow, irreversible decomposition

$$2\ N_2O_5 \rightarrow 4\ NO_2 + O_2$$

The interactions of NO, NO_2, O_3, and N_2O_5 involve seven elementary chemical reactions (six of which include NO_3 as either reactant or product) and several photochemical reactions. In a series of studies Richard Graham re-determined the rate constants for the six reactions involving NO_3, and he obtained preliminary results on the wave-length dependent photolysis of NO_3. From the values of these rate constants one can calculate the rate of interconversion of NO_2 and N_2O_5 in the stratosphere. At the low temperatures, low partial pressures, and intense ultraviolet radiation field of the middle stratosphere, the half time for interconversion of NO_2 and N_2O_5 is about a day or two. This rate is slower in the low stratosphere and higher in the upper stratosphere. Thus it happens that a substantial fraction of NO_x (NO and NO_2) is converted to N_2O_5 during the night and returned to the form NO_2 and NO during the day. For the polar night and adjacent high latitude winter conditions, virtually all NO and NO_2 is converted to N_2O_5. Thus on a global scale, N_2O_5 is an important, reversible, reservoir for the active oxides of nitrogen.

*Supported in part by the National Science Foundation.

b. Development of a Ground-Based Method to Monitor Stratospheric Nitrogen Dioxide.*

Peter Connell and David Johnston

A. W. Brewer and co-workers (Nature 246, 129, 1973) and Noxon and co-workers (Science 189, 547, 1975) have used spectroscopic methods based on absorption of visible light, to measure the concentration of nitrogen dioxide in the stratosphere and in the troposphere. We are developing a related method that gives more detailed information than these methods and may be able to follow in more detail the reactions of NO_2 in the stratosphere. We collect light with an eight-inch cassegrain telescope, use a small astronomical spectrograph, measure light intensity simultaneously in 500 wavelength channels with an optical multichannel analyzer, and analyze data with a minicomputer. By measuring in quick succession sunlight scattered from the zenith sky and directly transmitted sunlight, one can, in principle, infer the vertical distribution of NO_2 as a function of time. The method is being developed by theoretical, laboratory, and field tests.

*Supported in part by the National Science Foundation.

c. Absorption Spectrum of Nitrous Oxide

Gary Selwyn

The ultraviolet absorption spectrum of nitrous oxide (N_2O) was studied, with especial emphasis on the long-wavelength peak, which had been reported in the literature. It was found that the long-wavelength absorption (280-350 nm) did not exist in pure N_2O at one atmosphere pressure and at room temperature. Thus there is no photolysis of nitrous oxide in the troposphere. This simple measurement has fairly far-reaching atmospheric implications. It tends to confirm Junge's [J. Geophys. Res. 76, 8145 (1971)] position that

nitrous oxide must have a short (10 year not 100 year) atmospheric residence time, and thus there must be some large unknown source and some large unknown sink for nitrous oxide in the troposphere. It becomes a matter of considerable geochemical importance to identify these large unknown sources and sinks.

d. Effect of Nitrogen Fertilizer on Stratospheric Ozone

Harold S. Johnston

In 1971-72 Boeing Aircraft Company spokeman were quoted as saying: "Blame the farmers; don't blame us." The context was the discussion of the reduction of stratospheric ozone by human activities that produced stratospheric oxides of nitrogen. In nature, stratospheric nitric oxide (NO) is produced from nitrous oxide (N_2O) and singlet oxygen atoms, stratospheric nitrous oxide is transported from the troposphere by turbulent diffusion, and tropospheric nitrous oxide is produced by bacterial denitrification of nitrate in soils and in the ocean. Thus farmers adding artificial nitrogen fertilizers to the soil would be expected to increase tropospheric nitrous oxide and later reduce stratospheric ozone. At that time, however, many people (including Boeing authors) denied that the oxides of nitrogen (natural or artificial) had any effect on stratospheric ozone.

During the period 1971-75, the Department of Transportation conducted and coordinated an extensive study of the stratosphere, stratospheric ozone, atmospheric oxides of nitrogen, and related matters. These findings were published in 1975, both as Department of Transportation reports and as a National Academy of Sciences Report (Department of Transportation's Report of Findings of the Climatic Impact Assessment Program (DOT-TST-75-50), Washington, D.C., March 1975, National Academy of Sciences - National Research Council, Washington, D.C., April 1, 1975). These studies confirmed that the natural oxides of nitrogen play a dominant role in balancing stratospheric ozone and that nitrous oxide is the principal source of stratospheric NO_x. Furthermore, these studies agreed doubling stratospheric NO_x or N_2O would reduce ozone by 20 percent. Although this subject had been discussed from time to time by Crutzen (1972, 1974), the year 1973-75 was an appropriate time to re-open the question about the effect of nitrogen fertilizers on stratospheric ozone.

During 1974-75 there have been several discussions of this topic (Crutzen; McElroy; Johnston). The crux of the matter is that human fixation of nitrogen (fertilizer, combustion, etc.) is a large fraction (about 25 percent) of the recognized natural fixation of nitrogen (Delwiche, 1970); and the manufacture of nitrogen fertilizer is increasing exponentially with a very large future growth anticipated. When human activity (more or less) doubles a vital natural ingredient, then one must give thought to global consequences, perhaps delayed in appearance. Human activity is on the threshold of doubling the global natural fixation of nitrogen. If human activity should double tropospheric nitrous oxide, it would almost certainly reduce stratospheric ozone by about 20 percent. However, there are major recognized uncertainties in this problem: 1. The average delay time between nitrogen fixation and denitrification. 2. The role of the oceans in fixing nitrogen and in producing nitrous oxide. 3. The unknown sources and sinks of tropospheric nitrous oxide. 4. The actual global rate of fixation of nitrogen. These recognized uncertainties confer a factor of 10 uncertainty on the magnitude of the reduction of stratospheric ozone by a given level of human fixation of nitrogen. However, at the current rate of growth of chemical fertilizers, a factor of 10 is picked up in 25 years. The question may not be whether or not this is a serious problem; the question may be whether this will be a desperately serious problem in the year 2025 or the year 2050.

2. RESEARCH PLANS FOR CALENDER YEAR 1976

We plan to continue to develop a ground-based, spectroscopic method to study the vertical distribution of nitrogen dioxide in the stratosphere and troposphere. The goal of this work is to develop a method that could be used (by others) to monitor atmospheric nitrogen dioxide, and also we hope to measure the diurnal photochemical reactions of stratospheric nitrogen dioxide.

We are obtaining a high-intensity, variable wave-length, flash-driven laser to study primary photochemical reactions of ozone, nitrogen dioxide, chlorine dioxide, and the nitrate free radical NO_3. The purpose of this work is to obtain new or improved values of the rate constants for elementary reactions that are important in the atmosphere. We have underway studies of the photolysis of ozone to produce singlet oxygen atoms, and a molecular modulation study of the HOO free radical.

In collaboration with Professor Yuan Lee, we are developing molecular beam sources that can be used in Lee's apparatus to study certain radical-radical reactions. Over a period of many years, kineticists have been unable to obtain rate constants for some radical-radical reactions that are of considerable importance in atmospheric problems, and also in problems of combustion. Especially important examples are $HO + HOO \rightarrow H_2O + O_2$ and $O + HOO \rightarrow HO + O_2$. Mathematical modeling of both atmospheric reactions and combustion systems is severely limited by lack of satisfactory rate constants for these and other related elementary reactions.

3. 1975 PUBLICATIONS AND REPORTS

Harold S. Johnston and Associates

Journals and Books

1. J. W. Birks, S. D. Gabelnick, and H. S. Johnston, Chemiluminescence of IF in the Gas Phase Reaction of I_2 with F_2, Journal of Molecular Spectroscopy 57, 23 (1976) (LBL-3562).

2. J. W. Birks, H. S. Johnston, and H. F. Schaefer, Journal of Chemical Physics 63, 1741 (1975) (LBL-3753).

3. H. S. Johnston, Ground-Level Effects of Supersonic Transports in the Stratosphere, Accounts of Chemical Research 8, 289 (1975) (LBL-3564).

4. H. S. Johnston, Pollution of the Stratosphere, Annual Reviews of Physical Chemistry 26, 315 (1975) (LBL-3743).

5. H. S. Johnston, Global Ozone Balance in the Natural Stratosphere, Review of Geophysics and Space Physics 13, 637-649 (1975) (LBL-3756).

6. H. S. Johnston and G. Whitten, Chemical Reactions in the Atmosphere as Studied by the Method of Instantaneous Rates, reprinted from International Journal of Chemical Kinetics, Symposium No. 1, 1975, Proceedings of the Symposium on Chemical Kinetics Data for the Upper and Lower Atmosphere, John Wiley and Sons, Inc., pp. 1-26, 1975.

7. H. S. Johnston and G. Selwyn, New Cross Sections for the Absorption of Near Ultraviolet Radiation by Nitrous Oxide, (N_2O), Geophysical Research Letters 2, 549 (1975) (LBL-4168).

Presented Papers

1. H. S. Johnston, Pollution of the Stratosphere, Radiological and Chemical Physics Contractors' Meeting, Stanford Research Institute, Menlo Park, California, January 27-28, 1975.

2. H. S. Johnston, Pollution of the Stratosphere, Seminar, Argonne National Laboratories, Argonne, Illinois, February 7, 1975.

3. H. S. Johnston, Pollution of the Stratosphere, University of Chicago, Chicago, Illinois, February 10, 1975.

4. H. S. Johnston, Pollution of the Stratosphere, University of Illinois at Chicago Circle, Chicago, Illinois, February 11, 1975.

5. H. S. Johnston, Pollution of the Stratosphere, University of California-Santa Barbara, Santa Barbara, California, February 19, 1975.

6. H. S. Johnston, Pollution of the Stratosphere, California Polytechnic State University, San Luis, Obispo, February 27, 1975.

7. H. S. Johnston, Pollution of the Stratosphere, Local Section, American Chemical Society, Modesto, California, April 3, 1975.

8. H. S. Johnston, Pollution of the Stratosphere, Baylor University, Waco, Texas, April 17, 1975.

9. H. S. Johnston, Pollution of the Stratosphere, Stratosphere Physics and Chemistry Workshop, Goddard Space Flight Center, Greenbelt, Maryland, May 28-30, 1975.

10. H. S. Johnston, Pollution of the Stratosphere, Seminar, Stanford University, Stanford, California, July 30, 1975.

11. H. S. Johnston, Pollution of the Stratosphere, University of Southern Mississippi, Hattiesburg, Mississippi, September 24, 1975.

12. H. S. Johnston, Pollution of the Stratosphere, The University of South Dakota, Vermillion, South Dakota, October 27, 1975.

13. H. S. Johnston, Pollution of the Stratosphere, The University of Northern Colorado, Greeley, Colorado, October 28, 1975.

14. H. S. Johnston, Pollution of the Stratosphere, Sandia Laboratory, Albuquerque, New Mexico, October 29, 1975.

15. H. S. Johnston, Pollution of the Stratosphere, Sandia Laboratory, Livermore, California, October 30, 1975.

16. H. S. Johnston, Pollution of the Stratosphere, Rice University, Houston, Texas, November 19, 1975.

17. H. S. Johnston, Pollution of the Stratosphere, California Institute of Technology, Pasadena, California, December 11, 1975.

LBL Reports

1. Richard Alan Graham, The Photochemistry of NO_3 and the Kinetics of the N_2O_5-O_3, (Ph.D. Thesis) LBL-4147, Nov. 1975.

b. Radiation Chemistry

Warren M. Garrison, Principal Investigator

1. RADIOLYSIS OF SOLIDS AND LIQUIDS WITH HEAVY-ION BEAMS AT LOW FLUX DENSITIES*

M. E. Jayko, T.-L. Tung, G. P. Welch, and W. M. Garrison

A modification of the external beam-optics of the LBL 88-inch cyclotron now makes it practical to use cyclotron radiations in the detailed study of the effects of linear energy transfer (LET) in the radiation chemistry of solid and liquid systems at dosages and dose-rates comparable to those employed in conventional x-ray studies. The modification involves passing the focused beam through a pair of "beam-sweeping" magnets so that a circular target area of up to 10 cm in diameter can be uniformly irradiated with beams in the nanoampere range. Beam current is measured in the vacuum pipe with a secondary emission monitor that consists of two aluminum foils 6.4 μm thick at a separation of 12.7 mm. The upstream foil is maintained at -70 V while the downstream one is connected to a capacitor box and a feed-back type electrometer. The monitor is calibrated against a Faraday cup which is located in a magnetic field of 500 gauss.

As a check on dosimetry we have measured Fe^{3+} production in Fricke chemical dosimeter (.01 NFe^{2+} in 0.8 NH_2SO_4, air saturated) for several different beams. The data are summarized in Table 1. With a 1-nA beam uniformly distributed over the target area, the dose-rate to the irradiated volume corresponds to ~ 5×10^{18} eV/g min. Under these conditions no mechanical mixing of the solution is required.

Table 1. Ferric ion yields in the heavy-particle irradiation of the Fricke dosimeter.[a]

Radiation	Energy	$G(Fe^{3+})$[b]
He^{2+}	34	8.3
	34	(8.3)[c]
Be^{4+}	91	6.5
Ce^{6+}	102	5.2
	102	(5.0)[c]
Ne^{10+}	206	4.8

[a] .01 NFe^{2+} in 0.8 NH_2SO_4, air saturated.

[b] G represents the number of product species formed per 100 eV absorbed energy.

[c] Numbers in parenthesis are literature values obtained at high flux densities with mechanical stirring (e.g., J. Am. Chem. Soc. 79, 1565 (1975)).

*Abstracted from Biochem. Biophys. Res. Commun., in press.

2. EFFECTS OF LINEAR ENERGY TRANSFER (LET) IN THE HEAVY-ION RADIOLYSIS OF SOLID GLYCINE*

T.-L. Tung, G. P. Welch, H. A. Sokol, W. Bennett-Corniea and W. M. Garrison

The low flux facility described above has been used in the radiation-chemical study of solid glycine using beams of H^+, He^{2+}, Be^{5+}, C^{6+}, and Ne^{10+} at energies of ~ 10 MeV/nucleon. These particles have the same velocity and hence the profile of the radial energy deposition by secondary electrons along each of the particle tracks is essentially the same.[1] However, the linear energy transfer (LET) increases as a function of Z^2 as defined by the Bethe formulation.

Solid glycine was chosen for this preliminary heavy-ion study because the chemical action of γ-rays (low LET) on this system has been well defined in previous work at this laboratory and elsewhere[2] with γ-rays, the radiation induced step

$$NH_3^+CH_2COO^- \longrightarrow NH_3^+\dot{C}HCOO + H^+ + e^- \qquad (1)$$

is followed by the dissociative electron-capture reaction

$$e^- + NH_3^+CH_2COO^- \rightarrow NH_3 + \dot{C}H_2COO^- \qquad (2)$$

The long lived radicals produced in steps 1, 2 disproportionate on dissolution of the irradiated solid in O_2-free water to give acetic acid and iminoacetic acid.

$$NH_3^+\dot{C}HCOO^- + CH_2COO^- \rightarrow NH_2^+ = CHCOO^- + CH_3COO^- \qquad (3)$$

The latter then hydrolyzes spontaneously to give ammonia and glyoxylic acid. The observed stoichiometry for γ-rays corresponds to $G(NH_3) \approx 5 = G(CHOCOOH) + G(CH_3COOH)$; $G(CHOCOOH) \approx G(CH_3COOH) \approx 2.5$. Product yields obtained with the heavy-ion beams are compared in Figs. 1a and 1b with the γ-ray data.

We find in Fig. 1a that the product yields resulting from the charge-separation reactions (1 - 3) decrease with increasing LET and then tend to level off at LET values above ~ 10 eV/A. These results are in good agreement with the theoretical predictions that there is an equi-partition of energy between knock-on collisions and glancing collisions in the interaction of the heavy-ions with electrons along the track of the primary particle. We also find in Fig. 1b that processes in addition to reactions (1 - 3) become increasingly important with increasing LET. These processes are associated with chemistry within the core and are now being investigated in detail.

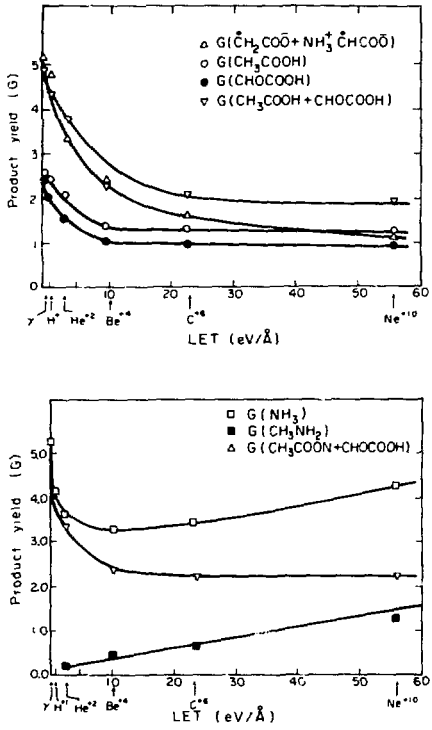

Fig. 1. Product yields as a function of LET in the heavy-ion radiolysis of solid glycine. (XBL 7511-9506 & XBL 7511-9505)

3. RESEARCH PLANS FOR CALENDAR YEAR 1976

Warren M. Garrison and Associates

Studies of LET effects in the radiolysis of biochemical systems with heavy-ion beams from the 88-inch cyclotron will continue. Both solid state and aqueous systems will be investigated. The glycine work will be extended to firmly establish the radiation-chemical processes involved both in the core and in the penumbra of heavy-ion tracks. Other compounds such as the N-acyl amino acids and the oligopeptides will also be investigated. Work on the measurement of radical and molecular product yields in water under heavy-ion radiolysis will be expanded. We are hopeful that heavy-ion radiolysis will be expanded, and we are hopeful that heavy-ion beams from the Bevalac will soon be available at sufficient intensities to permit radiation chemical studies of the above systems at energies in the 1000 MeV/nucleon range.

4. 1975 PUBLICATIONS AND REPORTS

Warren M. Garrison and Associates

LBL Reports

1. M. E. Jayk[illegible]. -L. Tung, G. P. Welch and W. M. Garrison, Methodology in the Radiolysis of Biochemical Compounds with Cyclotron Beams at Low Flux Densities, LBL-4098, Aug. 1975.

---

*Abstract of paper presented at the First Chemical Congress of the North American Continent, Mexico City, November 30 - December 5, 1975.

1. A. Chatterjee, H. D. Maccabee and C. A. Tobias, Radiation Res. 54, 479 (1973).
2. W. M. Garrison, "Current Topics in Radiation Research", Vol. IV (1968).

B. CHEMICAL AND GEOPHYSICAL ENERGY

1. CHEMICAL ENERGY

a. Formation of Oxyacids of Sulfur from SO_2

Robert E. Connick, Principal Investigator

1. THE CHEMISTRY OF SULFUR DIOXIDE AND RELATED COMPOUNDS

a. Aqueous Solutions of Sulfur Dioxide

Eckart von Deuster and Ron Chelsky

Since its inception in the summer of 1975 this project has been mainly devoted to developing the use of Raman spectra for detecting and measuring quantitatively the concentrations of sulfur-containing species in aqueous solutions. Considerable difficulty has been experienced in getting reproducible intensities, primarily because of limitations in the construction of the Raman spectrograph available to us. The first effort is being directed to the measurement of the equilibrium.

$$2HSO_3^- = H_2O + S_2O_5^=$$

There are two widely differing values in the literature for this important equilibrium constant, one published just this year. The equilibrium is difficult to measure because appreciable amounts of $S_2O_5^=$ are formed only at ca. 1 M HSO_3^- and higher. It is hoped that the Raman spectra of the two species will provide a more reliable measure of their concentrations than the ultra-violet spectra used in the previous measurements. In addition to the above species, Raman spectra have been obtained for a number of other sulfur containing species of importance in SO_2 solutions. Already they have indicated *qualitatively* the *disproportionation* of HSO_3^- solutions standing at room temperature for a number of days in the absence of oxygen.

b. The Reaction of SO_2 with Ammonia

Beat Mayer, Lyel Peter, Lunet McComber, and William Milliken

Preliminary experiments have been run on the reaction of NH_3 with SO_2, a reaction which has important environmental consequences for the atmosphere.[1,2] Although a number of studies have been made near room temperature and higher, it was of interest to trap the reactants together at low temperatures, and then let them react by slowly warming the mixture. At room temperature, the gas phase reaction yields a brown gas which quickly condenses as a red-brown solid[3] which is known to contain a mixture of ill identified species, several of which probably contain S-N bonds. In the presence of water, the main product is $(NH_4)_2S_2O_5$ or $(NH_4)_2SO_3$, depending on the ratio of materials.[4] We have observed the reaction under three different conditions: a) in rare gas matrices containing NH_3:SO_2 in ratios between 1:10 and 10:1 and with corresponding matrix ratios of 0:1000. Furthermore, the influence of water and D_2O traces in the ratio 0-10 was studied. Matrices were N_2 and Kr. b) Similar experiments were conducted in solids condensed at 20°K or 76°K, without matrix; and c) sealed pyrex tubes 0.8 cm outer diameter and 10 cm long, containing SO_2 and NH_3, were prepared by condensing the vapors at 76°K from a vacuum line in the desired sequence. Highly purified gas, as well as artificially moistened gases were used. The course of the reaction and the reaction products depend on temperature and pressure. In all matrix experiments, a white solid is formed which sublimes below -50°C in the high vacuum system without leaving traceable reaction products. The same holds for slowly codeposited gases without matrix. In sealed tubes, a slow reaction is observed at about -50°C, i.e., just below the melting point of the reactants. Upon melting, the reaction proceeds very rapidly. If excess NH_3 is present, a flaky white solid is formed which is partly *soluble in the excess liquid* NH_3. Divers *and* Ogawa[5] prepared the same material by reaction in organic solvents, and called the product $(NH_4)SO_2NH_2$, ammonium amido sulfurous acid. If excess SO_2 is present, a red solid forms, which is quite soluble in liquid SO_2 forming a yellow solution which Goehring[6] identified as yellow $NH(SONH_2)_2$, imido disulfinic acid. Above about 40°C, the flaky white solid turns red. This material might contain the ammonium salt of imide disulfonic acid, $N(SO_2NH_4)_3$ (Sander [7]; the red solid sublimes, but eventually reacts, forming an orange crystalline substance which is stable under dry N_2. All the above mentioned N-S compounds have been only identified by molecular weight and elemental analysis. We have recorded Raman spectra of all these substances and mixtures in situ. Raman spectra have been found useful for following the reaction conditions and for determining the number of end products that are formed. It is our goal to determine the identity of products and to assign the various Raman frequencies to the proper vibrational modes with the *help of* ^{34}S *and* ^{18}O. *This work will also help* the interpretation of thermodynamic measurements[8] which have been reported for solids of unknown composition.

1. R. J. Carlson, Science 184, 156 (1974).
2. E. McLaren, A. J. Yencha, J. M. Kushmir and V. A. Mohnen, Tellus 26, 291 (1974).
3. R. Boebermeier, J. Chem. & Phys. 47, 119 (1826).
4. A. Fock and K. Klüss, *Ber. 22*, 3149 (1890).
5. E. Diver and M. Ogawa, J. Chem. Soc. London 16, 104 (1900).

6. M. Becke-Goehring, Z. Anorg. Allg. Chem. 264, 48 (1951).
7. G. Jander, H. Knoll, H. Imming, Z. Anorg. Allg. Chem. 232, 229 (1937).
8. R. Landreth, R. G. dePena and J. Heikren, J. Phys. Chem. 79, 1785 (1975).

2. RESEARCH PLANS FOR CALENDAR YEAR 1976

Robert E. Connick

The chemistry of sulfur dioxide is of critical importance because of the large amounts presently being released into the atmosphere from power plants and the even larger amounts that will have to be dealt with in the future as more high-sulfur coal and oil are consumed. Currently the most effective way to remove SO_2 from stack gases is the wet limestone process which involves the absorption of the SO_2 from the gas phase into an aqueous limestone slurry. Considerable difficulties have been encountered in the development of this process (and others), in part because the chemistry of the process is not clearly understood. Sulfur dioxide absorbed in a solution of low acidity can form HSO_3^-, $S_2O_5^=$ and $SO_3^=$. In addition it can disproportionate to higher and lower oxidation states at a finite rate and it can be oxidized by oxygen to higher oxidation states. We propose to study these reactions, both as regards equilibria and rates, in order to lay a firm foundation for further process development by others. Studies will be completed on the HSO_3^- - $S_2O_5^=$ equilibrium. A completely uncharacterized yellow species formed at high HSO_3^- - SO_2 concentrations will be investigated and its formula determined. The products and the kinetics of the decomposition of SO_2 - HSO_3^- - $SO_3^=$ solutions will be studied. Oxidation of SO_2 solutions by oxygen will be investigated. Raman spectra will be used in these studies, but, where applicable, absorption spectroscopy and other physical methods of measurement will also be employed.

The reaction of NH_3 with SO_2 is important to the fate of SO_2 released into the atmosphere. The infrared and Raman data already obtained at low temperatures will be analyzed and further experiments performed to establish the course of the reaction under these conditions.

b. Synthetic and Physical Chemistry

William L. Jolly, Principal Investigator

1. X-RAY PHOTOELECTRON SPECTROSCOPY*

a. The Correlation of Vibrational Broadening of Core Lines in X-Ray Photoelectron Spectra with Valence Bond Resonance Structures+

William L. Jolly and Theodore F. Schaaf

Franck-Condon vibrational excitation contributes importantly to core photo-line broadening in molecules. In general, the photoelectric process yields a molecule-ion in which the nuclei are not in their equilibrium positions. The more strained geometry of the core-hole ion can be represented as an ordinary chemical species by applying the equivalent cores approximation. Then simple rules of classical valence bond theory can be used to predict changes in the weighting of resonance structures and corresponding changes in bond orders. Thus qualitative changes in relative linewidths can be predicted.

For example, the equivalent-cores representations of the fluorine 1s hole states of CF_4 and CH_3F are, respectively,

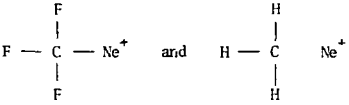

In the case of CF_3Ne^+, one expects considerable π bonding in the C-F bonds, corresponding to significant contributions from "no-bond" resonance structures of the following type:

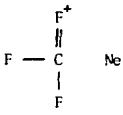

Inasmuch as the CF_3^+ ion would be expected to be a planar triangular species with relatively short C-F bonds, one predicts that the tetrahedral core-hole ion of CF_4 is formed in a highly strained state, yielding a broad line. In the case of CH_3Ne^+ no π bonding can occur, and so the core-hole ion of CH_3F is not formed in as strained a configuration.

*The X-ray photoelectron spectroscopic work was largely supported by a National Science Foundation grant.

+Abstracted from Chem. Phys. Letters 33, 254 (1975).

b. Evidence for Hyperconjugation from an X-Ray Photoelectron Spectroscopic Study of Isoelectronic Compounds*

Steven C. Avanzino, William L. Jolly, Marc S. Lazarus, Winfield B. Perry, Richard R. Rietz, and Theodore F. Schaaf

The shifts in core electron binding energies of oxygen, chlorine, and carbon atoms in some gaseous isoelectronic isostructural compounds can be readily explained in terms of simple trends in atomic charges. However the fluorine 1s binding energies for some fluoro compounds of silicon, phosphorus, sulfur, and chlorine show unusual shifts that suggest that hyperconjugation is important in the bonding of these compounds.

We have measured atomic core electron binding energies for several series of isoelectronic, isostructural compounds in the gas phase. Isoelectronic compounds were chosen for study because of the probability that the nature of the bonding in such compounds changes in a fairly systematic way with changes in the atomic numbers of the atoms in a given series of compounds. A core binding energy can be accurately represented as a linear function of three quantities: the atomic charge, the electrostatic potential due to the other atoms of the molecule, and the electronic relaxation energy. To a good approximation, the electronic relaxation energy for an atom of a particular element in a series of isoelectronic, isostructural compounds can be assumed to be constant. Therefore chemical shifts in binding energy can be ascribed to changes in atomic charge and changes in potential. We made minimal use of estimated atomic charges in our interpretations; hence our conclusions are relatively free of the weaknesses and assumptions of theoretical methods for estimating atomic charges.

Consider the five series of isoelectronic compounds listed in Table 1. In the first four series, halogen atoms or methyl groups are replaced stepwise with oxygen atoms as the atomic number of the central atom is increased stepwise. The last series of compounds may be looked upon as the compounds generated by the stepwise transfer of protons from one of the fluorine nuclei of SiF_4 to the silicon nucleus of that molecule. We believe it is reasonable to assume that, on progressing down through any one of the five series, the charge of the central atom increases. This increase in charge, coupled with the decrease in size, of the central atom would be expected to cause increased electron withdrawal from a given type of ligand atom. Hence the increase in the charge of the central

atom is probably responsible for the observed corresponding increase in the oxygen, chlorine, and carbon binding energies within each series.

Notice, however, that the fluorine 1s binding energies do not follow the simple predicted trend. In both the fourth and fifth series, the fluorine 1s binding energies increase to a maximum value and then decrease. We believe that the increase between SiF_4 and POF_3 is caused by the dominating effect of the increased positive charge and electronegativity of the central atom. The decrease in fluorine binding energy between SO_2F_2 and ClO_3F and between POF_3 and SNF_3 is apparently due to an increase in the negative charge of the fluorine atoms. This increase in negative charge tends to decrease the binding energy; clearly this effect is greater than and opposed to the effect of the increase in potential caused by the increase in positive charge on the central atom.

We believe that the increase in the negative charge of the fluorine atoms is due to the dominating effect of a large increase in the extent of hyperconjugation. Hyperconjugation (sometimes called "no-bond resonance") corresponds to the contribution of resonance structures of the types shown below.

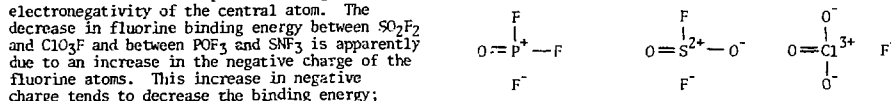

*Abstracted from Inorg. Chem. 14, 1595 (1975).

Table 1. Oxygen 1s, chlorine $2p_{3/2}$, carbon 1s, and fluorine 1s binding energies.

	E_B, eV							
Compound	O 1s		Cl $2p_{3/2}$		C 1s		F 1s	
$TiCl_4$			205.77	0.16				
$VOCl_3$	538.73	0.16	205.93	0.08				
CrO_2Cl_2	538.89	0.54	206.01	1.27				
MnO_3Cl	539.43		207.28					
$SiCl_4$			206.77	0.39				
$POCl_3$	537.80	1.54	207.16	0.16				
SO_2Cl_2	539.34		207.32					
$Si(CH_3)_4$					289.61	0.96		
$P(CH_3)_3O$	535.88	1.79			290.57	1.01		
$S(CH_3)_2O_2$	537.57				291.58			
SiF_4							694.56	0.8
POF_3	538.9	1.4					695.4	0.0
SO_2F_2	540.3	0.8					695.4	-1.2
ClO_3F	541.1						694.2	
SiF_4							694.56	0.8
POF_3							695.4	-0.4
SNF_3							695.0	

c. An X-Ray Photoelectron Spectroscopic Study of Charge Distributions in Tetracovalent Compounds of Nitrogen and Phosphorus*

Winfield B. Perry, Theodore F. Schaaf, and William L. Jolly

The bonding in four-coordinate compounds of nitrogen and phosphorus can be represented by I. However, because

(I)

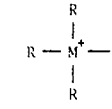

these compounds generally have short M-X bond lengths and high M-X stretching frequencies, multiple bond character has been postulated for the M-X bonds. Such multiple bonding can be explained by hyperconjugation, i.e., no-bond resonance, II. When the central atom is phosphorus, however, it is conceivable that the phosphorus 3d orbitals

(II)

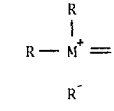

may significantly participate in the bonding. In this case, a resonance structure having no formal charges, such as III, would be appropriate. The latter structure implies $p\pi \rightarrow d\pi$ bonding between the central phosphorus atom and the peripheral X ligand.

(III)

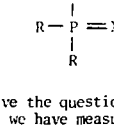

To help resolve the question of the bonding in these compounds, we have measured the core binding energies of the following tetracovalent compounds: $N(CH_3)_3BH_3$, $N(CH_3)_3O$, $P(CH_3)_3BH_3$, $P(CH_3)_3CH_2$, $P(CH_3)_3NH$, $P(CH_3)_3O$, $P(CH_3)_3S$, $POCl_3$, and $PSCl_3$. We have also measured binding energies for the simpler compounds $N(CH_3)_3$, $P(CH_3)_3$, PCl_3, NH_3, and PH_3. We have interpreted the chemical shifts qualitatively using simple electronegativity concepts and quantitatively using results from extended Hückel theory (EHT) and CNDO/2 molecular orbital calculations.

Although direct evidence for or against the presence of multiple bonding in these compounds was not obtained, certain conclusions may be inferred from our data. If the phosphorus 3d orbitals of the phosphorus compounds participate in $p\pi \rightarrow d\pi$ bonding, these interactions would be expected to increase the electron density of the phosphorus atoms at the expense of the formally charged peripheral atoms, X. Because we were able to obtain good correlations of the core binding energies of phosphorus and the X atoms by three different methods, all of which neglected or minimized $p\pi \rightarrow d\pi$ interactions, the following conclusion seems reasonable. Either the d orbitals are of comparable importance in determining the charge distributions of all of phosphorus compounds, including PH_3, $P(CH_3)_3$, and PCl_3, or they do not strongly affect the charge distributions of any of the compounds studied. We believe the latter hypothesis is correct.

Certain specific data also argue against d orbital bonding. The B 1s and O 1s binding energies of the compounds $M(CH_3)_3BH$ and $M(CH_3)_3O$ are lower when M = P than when M = N. This result indicates that the BH_3 and O groups have a greater negative charge in the phosphorus compounds than in the nitrogen compounds, in agreement with simple electronegativity predictions. This behavior is inconsistent with the presence of appreciable $p\pi \rightarrow d\pi$ bonding in the phosphorus compounds.

*Abstracted from J. Am. Chem. Soc. 97, 4889 (1975).

d. An X-Ray Photoelectron Spectroscopic Study of Volatile Vanadium Compounds*

Richard R. Rietz, Theodore F. Schaaf, and William L. Jolly

The CNDO/BW electronegativity equalization procedure for calculating atomic charges has been successfully used, in conjunction with the point-charge potential equation, to correlate core electron binding energies for a wide range of simple organic and inorganic compounds. The method has been parameterized for transition metal compounds and has been used to a limited extent for such compounds, but no systematic study has been made of the applicability of the

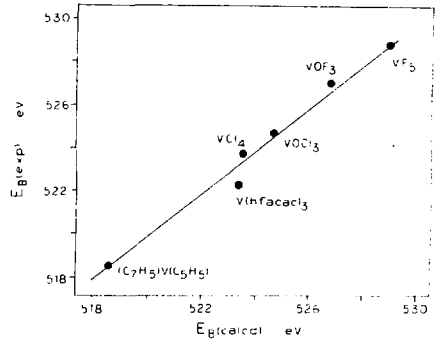

Fig. 1. Plot of experimental vanadium $2p_{3/2}$ binding energies versus binding energies calculated by the "transition-state" point charge potential equation. Standard deviation, 0.46 eV; correlation coefficient, 0.992. (XBL 755-6304)

method outside the main-group elements. In this study we measured gas-phase core electron binding energies for nine vanadium compounds and we drew conclusions about the nature of the bonding in these compounds from the data. This work was the first gas-phase XPS study of a series of compounds of a transition metal covering a wide range of metal oxidation states.

Vanadium $2p_{3/2}$ binding energies were correlated using CHELEQ atomic charges and the "transition state" point charge potential equation. Excellent correlation was obtained for six compounds which are well represented by single valence bond structures. A plot of experimental vs calculated binding energies for these compounds shown in Fig. 1. In the case of the other three compounds (i.e., $(\pi\text{-}C_5H_5)V(CO)_4$, $(\pi\text{-}C_7H_7)V(CO)_3$, and $V(CO)_6$), information regarding the relative contributions of various resonance structures and the importance of back-bonding was obtained by comparison of experimental and calculated binding energies. The data indicate stronger back-bonding to the CO ligands than to the C_5H_5 and C_7H_7 ligands.

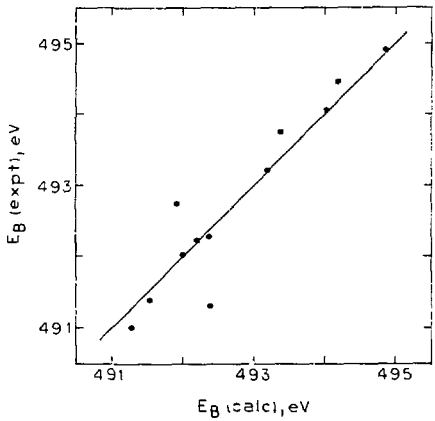

Fig. 2. Plot of E_B(expt) vs E_B(calc) for tin $3d_{5/2}$ binding energies for the following compounds: (1) $Sn_2(CH_3)_6$, (2) $(C_4H_9)_3SnOCH_3$, (3) $Sn(CH_3)_4$, (4) $(CH_3)_3SnI$, (5) $(CH_3)_3SnBr$, (6) $(CH_3)_3SnCl$, (7) SnH_4, (8) $(CH_3)_2SnCl_2$, (9) SnI_4, (10) CH_3SnCl_3, (11) $SnBr_4$, (12) $SnCl_4$.
(XBL 755-6358)

*Abstracted from Inorg. Chem. 14, 2818 (1975).

e. An X-Ray Photoelectron Spectroscopy Study of Volatile Tin Compounds*

Steven C. Avanzino and William L. Jolly

Core-level x-ray photoelectron spectra of fifteen compounds of tin have been measured in the gas phase. The measured binding energies are given in Table 2. The tin binding energies span

Table 2. Experimental binding energies.

Compound	E_B(eV)			ΔE_B(eV)
	Sn $3d_{5/2}$	C 1s	Cl $2p_{3/2}$	(Sn $3d_{5/2}$ - Sn $4d_{5/2}$)
SnH_4	492.74			460.97
$Sn(CH_3)_4$	491.38	289.47		461.03
$Sn_2(CH_3)_6$	491.01	289.27		460.85
$(CH_3)_3SnCl$	492.27	289.92	204.43	460.85
$(CH_3)_2SnCl_2$	493.21	290.42	204.96	460.84
CH_3SnCl_3	494.06	290.98	205.52	460.92
$SnCl_4$	494.92		206.19	460.85
$SnBr_4$	494.46			460.93
SnI_4	493.75			
$(CH_3)_3SnBr$	492.23	289.89		460.78
$(CH_3)_3SnI$	492.02	289.81		460.80
$(C_4H_9)_3SnOCH_3$	491.31			
$(CH_3)_3SnMn(CO)_5$	491.16			461.01
$Sn(NO_3)_4$	495.36			
$Sn\{N[Si(CH_3)_3]_2\}_2$	491.93	289.36		

a range of 4.4 eV and are well correlated by the "transition-state" point-charge potential model equation using atomic charges calculated by the CHELEQ electronegativity equalization method. A plot of experimental vs calculated binding energies is shown in Fig. 2. As expected, the empirically determined parameter k for tin is smaller than the k values obtained in previous work for carbon, silicon, and germanium. For $Sn(NO_3)_4$ and $Sn\{N[Si(CH_3)_3]_2\}_2$, the bonding can be described as a weighted average of several resonance structures. In these cases the binding energy data were used in conjunction with the CHELEQ method to determine the resonance structure weightings.

*A full description of this research will soon appear in the Journal of Electron Spectroscopy and Related Phenomena.

2. BORON HYDRIDE CHEMISTRY

a. Kinetics of the Reaction of Ammonium Ion with Hydroborate Ion in Liquid Ammonia*

Thomas S. Briggs and William L. Jolly

We have studied the kinetics of the following reaction in liquid ammonia from 25 to 45°:

$$NH_4^+ + BH_4^- \rightarrow H_2 + BH_3NH_3$$

In addition to obtaining rate constants and a heat of activation, we have determined the effect of ionic strength from μ = 0.01 M to μ = 1.92 M and have identified the principal product as BH_3NH_3.

From $\log[(P_\infty - P)/P_\infty]$ vs time plots, the reaction was found to be first order in both NH_4^+ and BH_4^-. The second order rate constants calculated from the slopes of such plots for various temperatures are given in Table 1. A log k vs 1/T plot of the data gave a least-squares heat of activation of 38.5 ± 0.6 kcal/mol. Our data may be compared with those of Gardiner and Collat,[1] who studied the aqueous reaction of NH_4^+ with BH_4^-. They obtained a rate constant of 2.4×10^{-4} M^{-1} sec^{-1} at μ = 1 and 25° and a heat of activation of 23 ± 2 kcal/mol. at μ = 0.5. The higher rate constant and lower activation energy of the aqueous reaction may be due to the participation, in the aqueous reaction, of water molecules hydrogen bonded to the ammonium ion. A Grotthuss-type proton transfer such as the following may be involved:

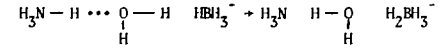

Because hydrogen bonding is relatively unimportant in liquid ammonia, the analogous mechanism in liquid ammonia is unlikely.

Table 1. Rate constants in liquid ammonia at μ = 0.9.

Temperature, °C	k (M^{-1} sec^{-1})
25	5.88×10^{-6}
30	1.79×10^{-5}
35	5.04×10^{-5}
40	1.43×10^{-4}
42	2.17×10^{-4}
45	3.40×10^{-4}

The Bronsted-Bjerrum method for correlating rate constants with ionic strength was shown to be consistent with our data.

*Abstracted from Inorg. Chem. 14, 2267 (1975).

1. J. A. Gardiner and J. W. Collat, J. Amer. Chem. Soc. 87, 1692 (1965).

b. A Study of the Hydroxyhydroborate Ion

Janice W. Reed and William L. Jolly

We have shown that, in aqueous solution, BH_3OH^- is a more powerful reducing reagent than BH_4^-. It will reduce organic functional groups that are not reduced by BH_4^-. Ethyl benzoate is nearly quantitatively reduced to benzyl alcohol by BH_3OH^- under appropriate conditions. Several organic co-solvents were used in the reaction mixtures to improve the miscibility of the ester and BH_3OH^- in the aqueous reaction mixtures. It was found that by using CH_3CN as co-solvent, the best yield of benzyl alcohol, 91%, was achieved in 43-48 hours at 0° at a pH of 11.90. The molar ratio of BH_3OH^- to ethyl benzoate was 10:1. Nitrobenzene was reduced to aniline in yields of 85% in 5 hours at 6° and pH 11.80. Again CH_3CN was used as co-solvent. The molar ratio of BH_3OH^- to nitrobenzene was 4:1. Benzonitrile was reduced to benzylamine producing yields of 85% in 16 hours at 25° and between the pH's of 12.30 and 12.50. The molar ratio of BH_3OH^- to benzonitrile was 10:1.

3. GERMANIUM CHEMISTRY

Duck J. Yang and William L. Jolly

Some germanium compounds have properties that are very different from those of the analogous carbon compounds. Thus, although aqueous acetic

acid and acetate ion are very stable, GeH_3COOH and its conjugate base undergo the following decomposition reactions:

$$GeH_3COOH \xrightarrow{\text{acid soln.}} \frac{1}{x}(GeH_2)_x'' + CO + H_2O$$

$$GeH_3CO_2^- + OH^- \xrightarrow[\text{mildly alkaline soln.}]{\text{hot neutral or}} GeH_4 + CO_3^{2-}$$

$$GeH_3CO_2^- + 3OH^- \xrightarrow[\text{alkaline soln.}]{\text{hot strongly}} 4H_2 + GeO_3^{2-} + CO_3^{2-}$$

In our study of this system during the last year, we have shown that the first reaction follows the rate law

$$-d(GeH_3COOH)/dt = k_1(H^+)(GeH_3COOH)$$

and has an activation energy of 16 kcal/mol. We have shown that the third reaction is first order in both $GeH_3CO_2^-$ and OH^- and has an activation energy of 22 kcal/mol. The third reaction involves the formation of an intermediate brown precipitate which may be $Ge(OH)_2$ or a polymer akin to "$(GeH_2)_x$".

4. RESEARCH PLANS FOR CALENDAR YEAR 1976

William L. Jolly

a. X-Ray Photoelectron Spectroscopy

The following projects are nearing completion, and the results will soon be ready for publication: (i) a study of π bonding in cyclophosphazenes, (ii) core binding energies of some metal β-diketonates and α-diketones in the vapor phase, and (iii) π-donor relaxation in the oxygen 1s ionization of carbonyl compounds.

We have initiated a study of the relative backbonding abilities of various metals in a series of cyclopentadienyl compounds of formula $M(C_5H_5)_2$. So far, the data suggest that charge transfer from the metal d orbitals is relatively unimportant in these compounds. Our measurements should be extended to other metals and to other aromatic ligands. By studying compounds of the type $(\pi\text{-}C_5H_5)\,Mn(CO)_{3-x}(L)_x$ and $(\pi\text{-}C_5H_5)Co(CO)_{2-x}(L)_x$, where L can be a backbonding ligand such as PF_3, $P(OR)_3$, PR_3, etc., it should be possible to determine whether the C_5H_5 group actually engages in significant backbonding.

We plan to study the modes of coordination of ligands (such as CO, C_7H_8, C_7H_7, and C_8H_8) in various complexes to elucidate the XPS spectra of such molecules adsorbed on catalyst surfaces.

We propose that a four-parameter function, $aF + bR$, be used to correlate core binding energy shifts. The parameters a and b would be used to characterize binding energy shifts in a particular class of compounds, and the parameters F and R would characterize substituent groups. We plan to evaluate the parameters by a least-squares analysis of binding energy data.

b. Boron Hydride Chemistry

A preliminary study indicates that the pyrolysis of NH_3BH_3 in an ammonia atmosphere yields the new compound $BH(NH_2)_2$. We plan to isolate the material in pure form and to determine its physical and chemical properties.

The kinetics of the hydrolysis of aqueous solutions of BH_3OH^- will be studied. The results will be significant with respect to the use of such solutions in synthetic reductions.

c. Germanium Chemistry

The structures of "$Ge(OH)_2$" (an amorphous material precipitated from aqueous solution) is unknown. It may be a polymer containing Ge-H bonds, and may be related to the amorphous material "$(GeH_2)_x$" formed in the decomposition of many germanium hydride species. We plan to investigate the structures of compounds of this type.

We hope to prepare transition metal coordination compounds containing the groups GeH_3–, GeH_3CO–, and GeH_3CO_2– to permit comparison with the carbon analogs.

d. Nitrogen Chemistry

Nitrosyl cyanide (ONCN) is a blue gas which, according to our preliminary studies, decomposes in the dark as follows:

$$3ONCN \rightarrow N_2 + N_2O + CO_2 + (CN)_2$$

We shall use ^{15}N-labelled material ($ONC^{15}N$), combined with mass spectrometry, to clarify the mechanism of the decomposition reaction. The compound has interest as a possible means for simultaneously adding NO and CN groups to a transition metal complex.

5. 1975 PUBLICATIONS AND REPORTS

William L. Jolly and Associates

Journals

1. W. L. Jolly, Science 187, 340 (1975); Book Review: "Electrons in Fluids," Springer-Verlag, 1973.

2. W. L. Jolly and T. F. Schaaf, The Correlation of Vibrational Broadening of Core Lines in X-Ray Photoelectron Spectra with Valence Bond Resonance Structures, Chem. Phys. Letters 33, 254 (1975) (LBL-3598).

3. S. Avanzino, W. L. Jolly, M. S. Lazarus, W. B. Perry, R. R. Rietz, and T. F. Schaaf, Evidence for Hyperconjugation from an X-Ray Photoelectron Spectroscopic Study of Isoelectronic Compounds, Inorg. Chem. 14, 1595 (1975)(LBL-3502).

4. W. B. Perry, T. F. Schaaf and W. L. Jolly, An X-Ray Photoelectron Spectroscopic Study of Charge Distributions in Tetracovalent Compounds of Nitrogen and Phosphorus, J. Amer. Chem. Soc. 97, 4899 (1975) (LBL-351).

5. S. Avanzino and W. L. Jolly, An X-Ray Photoelectron Spectroscopy Study of Volatile Tin Compounds, J. Electron Spectrosc. Relat. Phenom. 7, 000 (1975) (LBL-3932).

6. T. S. Briggs and W. L. Jolly, Kinetics of the Reaction of Ammonium Ion with Hydroborate Ion in Liquid Ammonia, Inorg. Chem. 14, 2267 (1975) (LBL-3769).

7. R. R. Rietz, T. F. Schaaf and W. L. Jolly, An X-Ray Photoelectron Spectroscopic Study of Volatile Vanadium Compounds, Inorg. Chem. 14, 2818 (1975) (LBL-3918).

Papers Presented

1. W. L. Jolly, An X-Ray Photoelectron Spectroscopic Study of Some Isoelectronic Compounds, Symposium on Photoelectron Spectroscopy, ACS Natl. Meeting, April 1975, Philadelphia, Pa.

2. T. F. Schaaf and W. L. Jolly, Effects of Chemical Structure on Relaxation Energies in X-Ray Photoelectron Spectroscopy, Symposium at Regional ACS Meeting, Hawaii, June 1975.

3. S. C. Avanzino and W. L. Jolly, X-Ray Photoelectron Spectroscopy Study of Tin Compounds, Symposium at Regional ACS Meeting, Hawaii, June 1975.

4. W. L. Jolly, Core Electrons and Chemistry, Calif. State University, Long Beach, Calif., Nov. 1975.

c. Electromechanical Systems

John Newman, Principal Investigator

1. ROTATING RING-DISK ELECTRODES

Peter Pierini and John Newman

Rotating-ring-disk electrodes are becoming common research tools. Thus computational procedures to explain the behavior of these devices were developed for situations in which electrode kinetics and concentration variations are important.[1] Methods presented by Newman[2] for potential distributions and concentration variations were used. Data for the ferro-ferri cyanide redox couple[3,4] taken on a sectioned electrode operated potentiostatically below the limiting current was well represented by the theory and the kinetic model developed by Pierini, Appel and Newman.[5] Calculations were also done explaining anomalous diffusion coefficients measured with a ring electrode operated at the limiting current and a zero net current to the disk, by a current distribution on the disk. Collection efficiencies for various modes of electrode operation were also computed.

---

1. Peter Pierini and John Newman, LBL Report No. LBL-4549 (December 1975).
2. John Newman, The Fundamental Principles of Current Distribution and Mass Transport in Electrochemical Cells, in Electroanalytical Chemistry, Vol. 6, A. J. Bard, editor (Marcel Dekker, New York, 1973), p. 187.
3. W. H. Smyrl and J. Newman, J. Electrochem. Soc. 119, 212 (1972).
4. W. H. Smyrl, private communication (January 1975).
5. P. Pierini, P. Appel and J. Newman, LBL Report No. LBL-3715 (February 1975).

2. CURRENT DISTRIBUTION ON A DISK ELECTRODE FOR REDOX REACTIONS

Peter Pierini, Peter Appel and John Newman

Current and concentration distributions on a rotating disk electrode were computed for a general surface reaction where the product concentration must be included in the analysis. The possibility of multiple or side reactions was excluded but the results do apply to multi-component reactions. Attention was further restricted to the case in which the effects of migration on the reactants and products could be suppressed by a supporting electrolyte. Equations were developed and implemented to determine the concentration variation of the supporting electrolyte, extending Newman's original analysis[1] to an arbitrary number of components.[2]

---

1. J. Newman, Electrochemical Systems, (Prentice-Hall, 1973), pp. 359-364.
2. P. Pierini, P. Appel and J. Newman, LBL Report No. LBL-3715 (February 1975).

3. THE DEPOSITION OF COPPER FROM AN AQUEOUS SALT SOLUTION CONTAINING IRON AND COPPER CHLORIDE COMPLEX IONS

Ralph White, Jim Trainham, and John Newman

A desire to limit the environmental pollution associated with the commonly practiced technique of leaching copper from its ore with sulfuric acid has interest in a little-used copper ore refining technique. The technique uses a concentrated aqueous salt solution as a leaching agent. One stream that exists in this process contains iron and copper complexed with chloride. It may be economically desirable to design an electrochemical cell to remove the copper from this stream directly rather than first removing the iron, as is often done now. We are conducting a feasibility study to determine if such an electrochemical cell could be designed.

4. THE FLUID MOTION GENERATED BY A ROTATING DISK: A COMPARISON OF SOLUTION TECHNIQUES

Ralph White, Charles M. Mohr, Jr., Peter Fedkiw and John Newman

The set of coupled, nonlinear, ordinary differential equations for the fluid motion of a rotating disk which arise from von Kármán's transformation to the Navier-Stokes equation were solved by an extension of Cochran's method and by five different numerical techniques.[1,2]

The results of the extension of Cochran's method are the most accurate values available for the characteristic parameters, a, b, A, B, and α. The values are:

$$a = 0.51023262 ,$$
$$b = -0.61592201 ,$$
$$A = 0.92486353 ,$$
$$B = 1.20221175 , \text{ and}$$
$$\alpha = 0.88447411 .$$

The five numerical techniques used to solve the set of governing equations with appropriate boundary conditions are:

1) Simultaneous solution, as a boundary-value problem, of the coupled, linearized equations by the method developed by Newman.[3]

2) Two techniques of extending the above method to order accuracy h^4, where h is the mesh interval.

3) A decoupling by improper linearization. In an iteration cycle, the equations are solved one by one and not simultaneously.

4) A "shoot-and-correct" method with Runge-Kutta integration.

This study indicates that Newman's method is the most convenient, reliable, and direct solution technique.

1. R. White, C. M. Mohr, Jr., P. Fedkiw and J. Newman, LBL-3910 (1975).
2. R. White, C. M. Mohr, Jr., LBL-4161 (1975).
3. J. Newman, IEC Fund. 7, 514-517 (1968); UCRL-17739 (August 1967).

5. CREEPING FLOW THROUGH A PERIODICALLY CONSTRICTED TUBE

Peter Fedkiw and John Newman

Work has begun on microscopically modeling the mass transfer characteristics in a porous packed bed reactor with creeping flow. The flow channels are envisioned as a grid of periodically constricted tubes. This idea was developed by Payatakes, et al.[1] The Nusslet numbers for this geometry will be calculated.

1. A. C. Payatakes, Chi Tien, R. M. Turian, AIChE J., Vol. 19, No. 1, 58-76 (1973).

6. MULTIPHASE EQUILIBRIA IN SYSTEMS CONTAINING WATER, HYDROCARBONS AND VOLATILE WEAK ELECTROLYTES*

Thomas J. Edwards, Toshikatsu Hakuta, John Newman and John M. Prausnitz

The vapor-liquid equilibria behavior of volatile weak electrolytes plays an important part in the proper design of pollution-abatement processes in industrial complexes.[1] A thermodynamic framework has been formulated[2] which calculates the equilibrium compositions of aqueous systems containing one or more of the volatile weak electrolytes – ammonia, carbon dioxide, and hydrogen sulfide. The present model is valid from 0 - 100°C and for low solute concentrations. Projected processes (coal-gasification and liquefaction), however, demand that the present temperature and composition ranges must be extended to higher values.

Due to the scarcity of available data, an apparatus has been constructed allowing the sampling and analysis of a three-phase system (vapor, hydrocarbon, and aqueous) containing these weak electrolytes up to 175°C and 30 atmospheres. The results of these experiments will be used in a new, improved theoretical model of the system. Equations are used to describe the activity of weak electrolytes in concentrated solutions which are in agreement with Pitzer's work[3] on strong electrolytes.

*This work supported by the National Science Foundation. T.H. is supported by the Science and Technology Agency of Japan.

1. M. R. Beychok, Aqueous Wastes from Petroleum and Petrochemical Plants, (John Wiley & Sons, London, 1967).
2. T. J. Edwards, J. Newman and J. M. Prausnitz, AIChE J., 21, 248 (1975).
3. K. S. Pitzer, J. of Phys. Chem. 77, 268 (1973).

7. MAXIMUM EFFECTIVE CAPACITY IN AN OHMICALLY LIMITED POROUS ELECTRODE*

William Tiedemann and John Newman

A model based on ohmic considerations was developed[1] for optimizing the performance of porous electrodes. Equations were developed which predict the optimum electrode porosity and thickness as a function of the solution and solid phase conductivities, specific charge capacity, separator conductivity and thickness, current density, and the allowable ohmic loss. Treatment of the porous LiAl electrode was presented as an example.

*Work supported by Globe-Union, Inc., Corporate Applied Research Group, Milwaukee, WI 53201.

1. J. Newman and W. Tiedemann, J. Electrochem. Soc. 122, 1482-1485 (1975).

8. PRIMARY RESISTANCES FOR RING-DISK ELECTRODES

Joseph J. Miksis, Jr. and John Newman

A system consisting of a disk electrode, a concentric ring electrode, and a large counterelectrode at infinity has three independent resistance values describing the primary potential difference between any two electrodes when current is passed between any two electrodes.[1,2] These resistance values were calculated and are presented as dimensionless correlations as functions of the ratios of radii of the disk and ring in Figs. 1-3.

1. J. J. Miksis, Jr., M.S. Thesis, LBL-4537 (November 1975).
2. J. J. Miksis, Jr. and J. Newman, LBL-4106 (July 1975).

9. MASS TRANSFER TO A ROTATING DISK IN TRANSITION FLOW

Charles M. Mohr, Jr. and John Newman

An experimental study of mass-transfer to a rotating disk electrode has been employed to determine an empirical correlation for the mass-transfer rate in the Reynolds number regime lying between simple laminar and turbulent flows.[1,2] This domain, apparently characterized by a regular vortex pattern, was found to extend from a Reynolds number of 2.0×10^5 to approximately 3.0×10^5. The resultant correlation for the average transfer rate, in terms of dimensionless Nusselt, Reynolds, and Schmidt numbers, is

$$Nu = 0.89 \times 10^5 Re^{-1/2} Sc^{1/3} + 9.7 \times 10^{-15} Re^3 Sc^{1/3} .$$

1. C. M. Mohr, Jr., Ph.D. Thesis, LBL-3913 (October 1975).
2. C. M. Mohr, Jr. and J. Newman, LBL-4145 (August 1975).

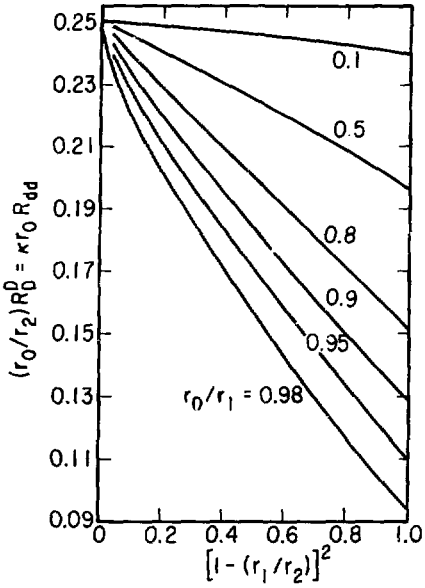

Fig. 1. Correlation of the disk resistance.
(XBL 757-6825)

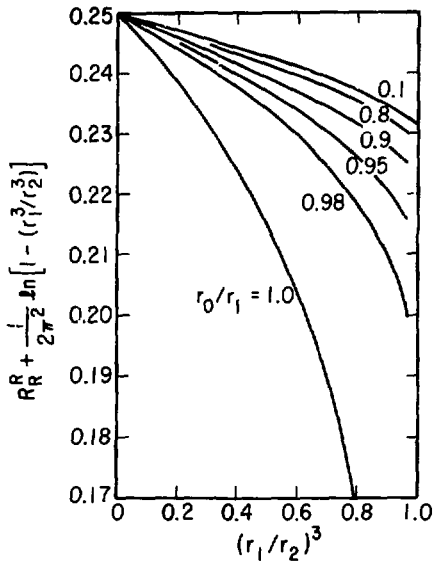

Fig. 3. Correlation of the ring resistance.
(XBL 757-6827)

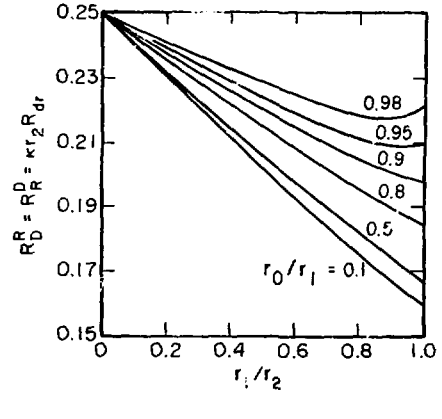

Fig. 2. Correlation of the interaction resistance.
(XBL 757-6826)

10. THE EFFECT OF SURFACTANT ON THE INTERFACIAL VELOCITY OF A BUBBLE OR DROP

M. Douglas LeVan and John Newman

Stream functions were derived for a spherical droplet in creeping flow with an arbitrary surface tension gradient at its interface. The stream functions are used to show that the interfacial velocity is retarded near the rear of the droplet when a trace of surfactant is present in the continuous phase and surface aging is controlled by diffusion. The effect on terminal velocity was also evaluated.

11. ELECTROCHEMICAL REMOVAL OF SILVER IONS FROM PHOTOGRAPHIC FIXING SOLUTIONS USING A POROUS FLOW-THROUGH ELECTRODE*

John Van Zee and John Newman

Silver ions were removed from a simulated photographic fixing solution by using a porous flow-through electrode. A feed of 1000 mg/ℓ of silver was reduced to less than 1 mg/ℓ in a 5.5 cm thick bed and to less than 10 mg/ℓ in a 4.0 cm thick bed. The flow rate in both cases was 22 cm^3/min across a superficial area of 61 cm^2. Side reactions reduced the current efficiency to 45% at these low product

concentrations. Optimization of incremental power costs and recovered silver suggests that further reduction of silver concentration is economical.

---

*Work supported by the University of California.

12. CURRENT AND POTENTIAL DISTRIBUTIONS IN PLATING CORROSION SYSTEMS

William H. Smyrl and John Newman

The numerical determination of current and potential distributions for plating corrosion systems has been accomplished. The distributions depend on characteristic parameters for the disk anode and surrounding plane cathode and also reveal that each of the electrodes influence the other due to their proximity. The results were applied to an array of disks and it was found that the corrosion potential of the system is a *linear function of the* area ratio of anode to cathode. This may be contrasted to the *logarithmic* dependence found when ohmic effects are neglected.

13. INTEGRAL TEST FOR CONSISTENCY OF VAPOR-LIQUID EQUILIBRIUM DATA

John Newman

This test can be used over a restricted range of composition, is essentially independent of the values used for the vapor pressures of the pure components, and avoids any differentiation of experimental data.[1]

---

1. J. Newman, LBL-3954 (June 1975).

14. ENGINEERING ANALYSIS OF SHAPE CHANGE IN ZINC SECONDARY ELECTRODES*

King W. Choi, Drannan Hamby, Douglas N. Bennion, and John Newman

Shape change, the redistribution of active material over the surface of the zinc electrode as a result of cell cycling, is caused by convective flows driven primarily by membrane pumping effects. A mathematical model is formulated on the basis of the above hypothesis for the zinc-silver oxide secondary cell. The model yields numerical predictions of material redistribution and fluid flow rates which can be compared to experiment. The results suggest that shape change can be eliminated if the convective flow in the zinc electrode compartment *parallel to the electrode surface is* stopped.

Data on zinc-silver oxide secondary cells are used to evaluate the convective flow hypothesis on the cause of shape change in zinc electrodes. Two cell designs have been used. A cell with flooded, vented electrodes which allows normal convective flow has been used to study fluid flow rates and material redistribution under convective conditions. A second cell, designed to minimize convective flow in the zinc electrode compartment has been used to study material redistribution under conditions of limited convective flow. Experimental results are presented which are supportive of the convective flow hypothesis.

---

*Work supported by the U.S. Air Force, Air Force Systems Command.

15. REMOVAL OF HEAVY METALS IN VERY DILUTE SOLUTION USING POROUS FLOW-THROUGH ELECTRODE REACTORS

James A. Trainham and John Newman

Three metal ions in particular are being considered: Cd^{++}, Hg^{++}, and Pb^{++}. Preliminary results on the removal of Hg^{++} ion from brine solutions has been quite successful. A feed concentration of 4 mg/ℓ has been reduced to less than 10 ppb.

Problems have been anticipated with hydrogen evolution in the removal of Pb^{++} and Cd^{++} ions and suitable electrode materials which will reduce this problem are being tried.

A criteria for determining the lowest attainable concentration in a porous electrode reactor has been developed and was discussed at the annual meeting of the AIChE.

16. CURRENT DISTRIBUTIONS BELOW THE LIMITING CURRENT IN POROUS FLOW-THROUGH ELECTRODE REACTORS

James A. Trainham and John Newman

A computer program is being developed which *models the behavior of a porous flow-through* electrode reactor operating below the limiting current. The program incorporates side reactions which will allow an optimization of the current density versus the current efficiency. The program forms the basis for the design and optimization of single and multiple reactor systems.

17. RESEARCH PLANS FOR CALENDAR YEAR 1976

John Newman and Associates

The dissolution rate of cadmium hydroxide from cadmium will be measured by utilizing a rotating ring-disk electrode. The nickel-cadmium battery will be modeled. Experimental investigations of mass transfer in turbulent flow with ring-disk systems will be developed. Fluid flow near the *equator of a rotating sphere will be further* investigated numerically. Modeling of the periodically constricted tube will be continued. Analysis of an iron rotating disk under passivation kinetics will be initiated.

18. 1975 PUBLICATIONS AND REPORTS

John Newman and Associates

Journals

*1. Hugo A. Massaldi, John Newman and C. Judson King, "Maximum Droplet Growth When Cooling a Saturated Solution", Chem. Eng. Sci. 30, 363-366 (1975).

2. Charles M. Mohr, Jr. and John Newman, "Mass Transfer to an Eccentric Rotating Disk Electrode", J. Electrochem. Soc. 122, 928-931 (1975) (LBL-2717).

*3. John Newman and William Tiedemann, "Maximum Effective Capacity in an Ohmically Limited Porous Electrode", J. Electrochem. Soc. 122, 1482-1485 (1975).

*4. Thomas J. Edwards, John M. Prausnitz and John Newman, "Thermodynamics of Aqueous Solutions Containing Volatile Weak Electrolytes", AIChE J. 21, 248-259 (1975).

5. John Newman and William Tiedemann, "Porous Electrode Theory with Battery Applications", AIChE J. 21, 25-41 (1975) (LBL-3117).

*6. John Newman and William Tiedemann, "Double Layer Capacity Determination of Porous Electrodes", J. Electrochem. Soc. 122, 70-74 (1975).

Papers Presented

1. "Engineering Analysis of Shape Change in Zinc Secondary Electrodes." II. *Experimental* (with King W. Choi, Dranman Hamby and Douglas N. Bennion, Hamby presenting the paper). General Session of the Battery Division at the Dallas meeting of the Electrochemical Society, October 9, 1975.

2. "Analysis of Porous Electrodes with Sparingly Soluble Reactants." III. Short Time Transients (with Hiram Gu and Douglas N. Bennion, who presented the paper). General Session of the Battery Division at the Dallas meeting of the Electrochemical Society, October 9, 1975.

3. "Removal of Lead Ions from Dilute Solutions Using Porous Flow-Through Electrode Reactors" (with J. A. Trainham, who presented the paper). Symposium on Electochemical Methods in Water Pollution Control at the Los Angeles meeting of the American Institute of Chemical Engineers, November 20, 1975.

4. "Primary Resistances for Ring-Disk Electrodes," Lecture at the Laboratorie Physique des Liquides et Electrochemie, University of Paris VI, September 11, 1975.

5. "Mass Transfer in the Transitional Region on a Rotating Disk," Lecture at the Technical Chemistry Colloquium, Swiss Federal Institute of Technology, Zurich, September 16, 1975.

6. "Engineering Analysis of Shape Change in Zinc Secondary Electrodes." I. (with King W. Choi, Dranman Hamby, and Douglas N. Bennion, who presented the paper). General Session of the Battery Division at the Dallas meeting of the Electrochemical Society, October 9, 1975.

LBL Reports

1. Ralph White, Charles M. Mohr, Peter Fedkiw and John Newman, "The Fluid Motion Generated by a Rotating Disk: A Comparison of Solution Techniques", LBL-3910 (November 1975).

2. Joseph John Miksis, Jr., "Primary Resistances for Ring-Disk Electrodes", M.S. Thesis, LBL-4557 (November 1975).

3. Peter Pierini, Peter Appel and John Newman, "Current Distribution on a Disk Electrode for Redox Reactions", LBL-3715 (February 1975).

4. Peter W. Appel and John Newman, "Application of the Limiting-Current Method to Mass Transfer in Packed Beds at Very Low Reynolds Numbers", LBL-4517 (November 1975).

5. Charles M. Mohr, Jr., "Mass Transfer in Rotating Electrode Systems", Ph.D. Thesis, LBL-3913 (October 1975).

6. Ralph White, Charles M. Mohr, Jr. and John Newman, "The Fluid Motion Due to a Rotating Disk", LBL-4161 (August 1975).

7. Charles M. Mohr, Jr. and John Newman, "Mass Transfer to a Rotating Disk in Transition Flow", LBL-4145 (August 1975).

8. Joseph J. Miksis, Jr. and John Newman, "Primary Resistance for Ring-Disk Electrodes", LBL-4106 (July 1975).

9. John Newman, "Integral Test for Consistency of Vapor-Liquid Equilibrium Data", LBL-3964 (June 1975).

---

*Not funded by MMRD.

d. High Energy Oxidizers and Heavy Element Chemistry

Neil Bartlett, Principal Investigator

1. PREPARATION OF GRAPHITE FLUOROSULFATE AND BORON NITRIDE FLUOROSULFATE

Neil Bartlett, Richard E. Largiani and Kevin Leary

Graphite and graphitic boron nitride each interact spontaneously with high purity peroxydisulfuryldifluoride, $S_2O_6F_2$ at room temperature (~ 20°C). The $S_2O_6F_2$ is prepared in the high purity, desirable for this synthesis, by the sequence of reactions: $SeF_2 + 2HOSO_2F \rightarrow 2HF + Se(OSO_2F)_2$; $Se(OSO_2F)_2 + Se + S_2O_6F_2$. The $S_2O_6F_2$ is in equilibrium with the SO_3F radical which has a high electron affinity. As SO_3F^- is incorporated into the graphite or boron nitride, there is an accompanying swelling which occurs along the c_o axis of each of the hexagonal symmetry materials. The limiting composition at ordinary temperatures appears to be $C_{12}SO_3F$ (at least for pyrolytic graphite) but for the BN, case may be as high as $(BN)_4SO_3F$. These salts are blue and are good conductors of electricity.

The boron nitride salt represents the first example of such a derivative of graphitic boron nitride. Although many graphite salts have been described over the years few claims have been advanced for intercalation compounds of BN and those few have been contested.[1] This difference in behavior of graphite and BN could have signified a difference in the bonding in the two materials. Indeed it has been argued that the bonding in the BN sheet involves only single BN bonds.[2]

X-ray powder photographs indicate that the graphite and boron nitride salt analogues are isomorphous and are hexagonal. It appears that the interatomic distances within the graphite or boron nitride sheets do not change since a_o is in each case a simple numerical relative of a_o for the parent material. There is considerable expansion along c_o. For $C_{12}SO_3F$ and its boron nitride analogue the X-ray powder photographs indicate that c_o is ~ 8 Å or a simple multiple of that value. This is in harmony with the intercalation of a single layer of approximately tetrahedral SO_3F^- ions between each pair of adjacent graphite or boron nitride sheets. The inter-sheet spacing for graphite is 3.35 Å and for BN is 3.33 Å.

Some observations which we have made indicate that the oxidation of the BN and the graphite occurs in stages as previously described for other graphite salts.[1]

1. W. Rudorff, Advances in Inorganic and Radiochemistry 1, 261 (1958).

2. "Comprehensive Inorganic Chemistry", J. C. Bailar et al. eds., Pergamon Press, Oxford 1973, Vol. 1, p. 918.

2. INTERACTION OF O_2^+ WITH Cl_2

Neil Bartlett and Richard Biargioni

The earlier findings of Richardson[1] have been confirmed but no decisive characterization of the purple adduct of O_2^+ and Cl_2 has yet been achieved.

1. T. J. Richardson, Ph.D. Thesis, U.C. Berkeley, 1974, LBL-3183.

3. SUBSTITUTED UF_6 COMPOUNDS

Konrad Seppelt and Neil Bartlett

The compound $U(OTeF_5)_6$ has been prepared[1] by the following routes:

$$UF_6 + 2B(OTeF_5)_3 \rightarrow U(OTeF_5)_6 + 2BF_3$$

$$UF_6 + 6F_5SiOTeF_5 \rightarrow U(OTeF_5)_6 + 6SiF_4$$

It is a yellow crystalline solid, m.p. 160°C, which sublimes in vacuo to yield well formed crystals. A crystal structure has been completed[2] and this shows the solid to be a close packed assembly of $U(OTeF_5)_6$ units. The U atom in $U(OTeF_5)_6$ is octahedrally coordinated in oxygen atoms and each Te atoms has an approximately octahedral coordination in the five F ligands and the oxygen atom. The U-O-Te angle is 170°. In spite of the ligand crowding about the U atom the compound hydrolyses readily in moist air.

Efforts to isolate other pure compounds in the series $F_xU(OTeF_5)_{6-x}$ always resulted in mixtures, in our hands. ^{19}F NMR spectra of the orange liquids produced by mixing UF_6 with less of the $OTeF_5$ containing reagent than necessary to bring about full substitution of the UF_6 F-ligands always gave evidence of mixtures. The $OTeF_5$ groups are identified by their characteristic AB_4 spectrum which are seen ~ +50 ppm from $CFCl_3$ as standard. The F ligands bound to uranium are located between -750 and -820 ppm ($CFCl_3$ standard) and such a region is shown in Fig. 1. In all cases, 12 lines

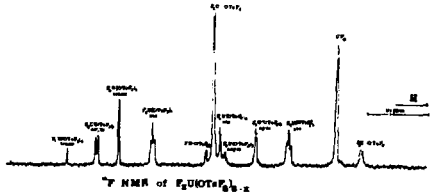

Fig. 1. ^{19}F chemical shifts (relative to $CFCl_3$) for F bonded to uranium in the series $F_xU(OTeF_5)_{6-x}$ (XBL 753-6004)

TABLE 1. ^{19}F NMR data of the compounds $F_xU(OTeF_5)_{6-x}$. Only uranium bonding fluorine atoms are listed, 56.4 MHz, $CFCl_3$ standard.

		ppm	J_{AB} (Hz)
UF_6		-764.0	--
F_5U - $OTeF_5$	AB_4	A: -759.5; B_4: -785.7	9
cis - $F_4U(OTeF_5)_2$	A_2B_2	A_2: -772.5; B_2: -796.4	14
trans - $F_4U(OTeF_5)_2$		-802.4	--
sym - $F_3U(OTeF_5)_3$		-778.3	--
asym - $F_3U(OTeF_5)_3$	AB_2	A: -783.7; B_2: -806.2	22
cis - $F_2U(OTeF_5)_4$		-784.5	--
trans - $F_2U(OTeF_5)_4$		-811.4	--
$FU(OTeF_5)_5$		-787.0	--
$U(OTeF_5)_6$		--	--

were observed in this region. The strong line at -764 ppm is due to UF_6. The other lines are assigned as indicated in Fig. 1. On the basis of these assignments, which are tabulated in Table 1, the correlation shown in Fig. 2, of chemical shift of F bonded to U, against the total number of uranium - bonded F atoms, was derived. Evidently all compounds $F_xU(OTeF_5)_{6-x}$ occur. Moreover, the line intensities in the ^{19}F NMR spectra indicated that the occurrence of cis and trans isomers of $F_4U(OTeF_5)_2$, symmetric and asymmetric $F_3U(OTeF_5)_3$ and cis and trans $F_2U(OTeF_5)_4$ is essentially as anticipated on the basis of chance replacement of the UF_6 F ligands.

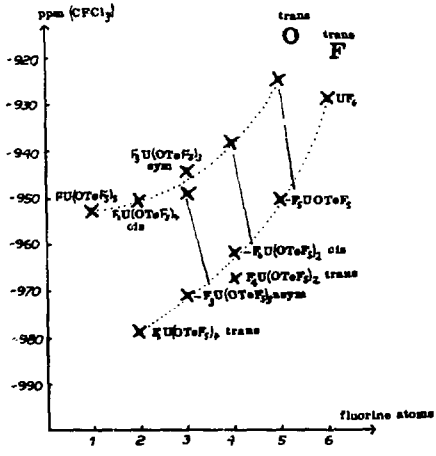

Fig. 2. Correlation of the chemical shift of the uranium bonded fluorine against the total number of uranium bonded fluorine atoms. The resonances are found on two lines: fluorine atoms standing trans to another fluorine atom are on the lower line, fluorine atoms in trans position to an $OTeF_5$ groups are found on the upper line. (XBL 753-6000)

---

1. K. Seppelt, Covalent Compounds of Uranium, Chemische Berichte, in press. LBL-3991.

2. K. Seppelt, L. K. Templeton, D. H. Templeton and N. Bartlett, to be published.

4. RESEARCH PLANS FOR CALENDAR YEAR 1976

Neil Bartlett

Delocalized-Electron Solids. Graphite and boron nitride salts will be further investigated. Special attention will be given to the oxidation of well oriented graphite and BN samples. The dependence of the properties upon the composition and structure will be studied. The oxidation of anthracene, borazines, carboranes and other aromatics to yield salts of the aromatic cations, Aromatic$^+X^-$, (with $X = SO_3F^-$, AsF_6^-) will also be attempted since the electron distribution in such cations should provide insight into the electron delocalization in the more extended systems.

Electrochemistry. The anodic oxidation of SO_3F^- and RuF_6^- will be studied. Simultaneously an effort will be made to exploit graphite salts such as $C_{12}^+SO_3F^-$ as anode materials.

Further Studies of O_2^+ Salts. The O_2^+, Cl_2 adduct will be further studied. This probably involves a novel Lewis acid-Lewis base interaction in which π^*

electrons of Cl_2 are donated to the empty π^* orbital of O_2^+. The O_2F radical molecule may exist at ordinary temperatures and efforts will be made to generate it in ponderable amounts. Coordination of O_2^+ salts by crown ethers may provide for dissolution of the O_2^+ salts in ether solvents.

5. 1975 PUBLICATIONS AND REPORTS

Neil Bartlett and Associates

Journals and Books

1. A. H. Cockett, K. C. Smith, N. Bartlett and F. O. Sladky, The Chemistry of the Monatomic Gases", Pergamon Press, Oxford (1975), 330 pages.

2. Neil Bartlett, Argo, "Enciclopedia della Chimica", USES Edizioni Scientifiche Firenze, (19) Vol. II, pp. 127-131.

3. Neil Bartlett, Cripto, "Enciclopedia della Chimica", USES Edizioni Scientifiche Firenze, (19) Vol. IV, pp. 128-132.

LBL Reports

1. Neil Bartlett and Kevin Leary, Quinquevalent Gold Salts, LBL-4166. (Accepted for publication in the issue of "Revue de Chimie Minérale", dedicated to Professor Wilhelm Klemm.)

2. Neil Bartlett, Boris Zemva and Lionell Graham, LBL-4195. (Accepted for publication in the issue of "Journal of Fluorine Chemistry", dedicated to Professor George H. Cady.)

3. Kevin M. Leary, Simple and Complex Fluorides of Gold and Palladium, (Ph.D. Thesis), LBL-3746, (May 1975).

Invited Lectures

1. "The Chemistry of O_2^+", at the University of Victoria, Victoria, B.C., Canada, on February 7, 1975; and Simon Fraser University, Burnaby, B.C., Canada, on April 30, 1975.

2. "A New MF_4 (M= Rh, Ir, Pd, Pt) Structure Type and Its Relationship to MF_5, MF_3 and MF_2 Structures", at the Symposium on Solid-State Chemistry of Fluorides and Oxyfluorides at the 169th American Chem. Soc. Meeting in Philadelphia, April 9, 1975.

3. "Noble-Gas Chemistry and Its Significance", Phi Lambda Upsilon Award Address, the University of Nebraska, Lincoln, Nebraska, October 16, 1975.

4. "Superoxidizers – From O_2^+ Salts to $C_6F_6^+$ Salts", Chemistry Department, University of Nebraska, Lincoln, Nebraska, October 17, 1975.

C. MOLECULAR AND ATOMIC SCIENCES

I. CHEMICAL PHYSICS

a. Energy Transfer Processes in Organic Solids

Charles B. Harris, Principal Investigator

1. EMISSION AND REFLECTANCE SPECTROSCOPY OF AROMATIC HYDROCARBONS ADSORBED ON CATALYTIC METAL SURFACES*

Antonio R. Gallo, Charles B. Harris and Mary Jane Shultz

The study of surface phenomena and the interaction of molecules adsorbed on surfaces has received much attention. Various tools have been developed to probe surface properties. These include Low Energy Electron Diffraction (LEED), Auger Electron Spectroscopy (AES), Photoelectron Emission Spectroscopy, and Multiple Reflection Infrared Absorption Spectroscopy. Areas of interest include the mechanism of adsorption, the identification of adsorbed species and their chemistry, the determination of the geometry of the adsorbed molecules, and the study of the nature and strength of the forces involved.

In the past year we have developed a UHV system that incorporates LEED, AES and quadrupole mass spectroscopy that is capable of operating over a large temperature range. The system will be used to develop phosphorescence and reflection spectroscopy of molecules adsorbed on single crystal oriented metal surfaces. It is the purpose of this program (1) to develop and adapt the methods of reflectance, fluorescence and phosphorescence spectroscopy to aromatic and azaaromatic hydrocarbons adsorbed as monolayers (or less) on a variety of transition metal and alloy surfaces; (2) to develop optically detected magnetic resonance (ODMR) as a technique for studying the molecular and electronic structure of these molecules adsorbed on catalytic surfaces; and (3) to apply the powerful methods of phosphorescence microwave double resonance (PMDR) to surface studies to determine what explicit changes in the molecular geometry, electronic structure, the radiative and radiationless decay channels occur upon adsorption to transition metal and alloy surfaces. These studies will also be correlated with the existing data obtained principally through LEED and AES. The investigation will start with the (111) and (100) surfaces of nickel and the nickel High Miller index faces, characterized by stepped surfaces, and then will be extended to other transition metal and alloy surfaces. A detailed comparison of the molecular and electronic structure of aromatic hydrocarbons on different transition metal surfaces and the correlation of this information to catalysis is an important aspect of this program.

Because of the sensitivity of optical detection, as few as 10^4 molecules in a sample can be investigated. This makes it ideal as a new tool for surface investigations. Preliminary calculations on aromatic hydrocarbons indicate that the emission spectra can be obtained on as few as 10^6 to 10^8 molecules per mm^2. Monolayer coverage for these molecules is 10^{11} molecules per mm^2. We expect that measurements of a 0.1% coverage will yield a good signal-to-noise ratio.

In the past year we have combined both UHV and cryogenic technologies and built an ultrahigh vacuum chamber, with a liquid nitrogen heat shield and a liquid helium cooled sample tip (cf. Figs. 1 and 2) to be used in these studies. We should be able to achieve a base pressure of 10^{-11} Torr over a sample temperature range from 2°K to 450°K.

In designing the equipment for the experiments, we have considered the explicit angular dependence of the radiation field on the sample. Consider a near normal incident beam of light, for example, impinging on an isotropic organic monolayer or thin film adsorbed on a metal, and the associated reflected beam. These beams will interfere to form a standing wave with an electric field of zero to the first order at the surface. This is

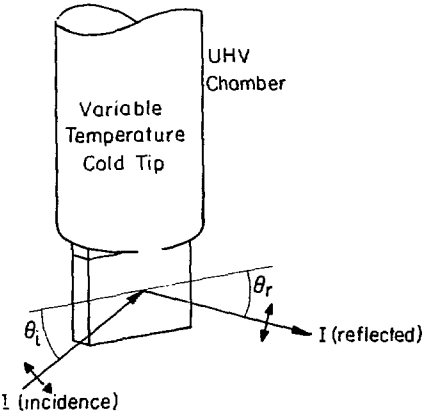

Fig. 1. Schematic of cold tip and sample orientation relative to plane of incident light. (XBL 762-6381)

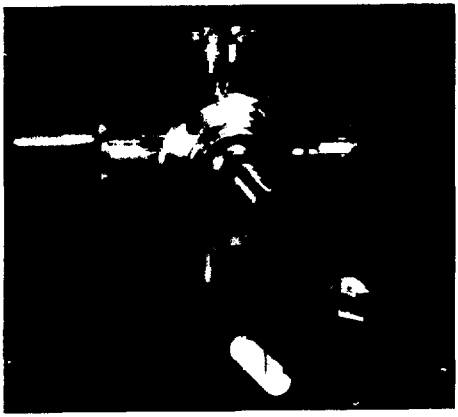

Fig. 2. Cold tip assembly with a nickel crystal sample. (XBB 764-3531)

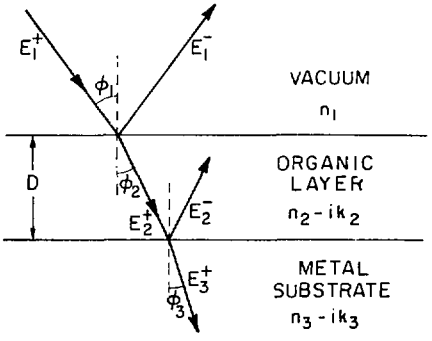

Fig. 3. Schematic of the model system used to calculate relative absorption of adlayer on a metal substrate showing electric field amplitudes and optical constants of the isotropic layers. (XBL 761-6323)

due to a 180° phase shift of the incident wave upon reflection. As a consequence, it would seem that molecules absorbed on the surface would be difficult to detect by optical methods. Such is not the case when grazing incidence geometries are considered.

This can be seen by writing expressions for propagating electromagnetic waves in the isotropic media shown in Fig. 3. The E's are mathematical sums of all waves which are traveling in the directions shown in each medium. By imposing boundary conditions on both E and H in the wave equations, one obtains a set of coupled equations in the E's in terms of two parameters, α and β. These are as follows:

$$(1)\quad (\cos\phi_1)(E_1^+ + E_1^-) = [(\alpha_2\cos\phi_2)/(n_2 - ik_2)][E_2^+ + E_2^-]$$

$$(2)\quad n_1(E_1^+ - E_1^-) = (n_2 - ik_2)(E_2^+ - E_2^-)$$

$$(3)\quad \{E_2^+ \exp[(-2\pi D/\lambda)(\beta_2 + i\alpha_2\cos\phi_2)] + E_2^- \exp[(2\pi D/\lambda)(\beta_2 + i\alpha_2\cos\phi_2)]\}$$
$$\times [(\alpha_2\cos\phi_2 - i\beta_2)/(n_2 - ik_2)] =$$
$$\{E_3^+ \exp[(-2\pi D/\lambda)(\beta_3 + i\alpha_3\cos\phi_3)]\}[(\alpha_3\cos\phi_3 - i\beta_3)/(n_3 - ik_3)]$$

$$(4)\quad \{\exp[(-2\pi D/\lambda)(\beta_2 + i\alpha_2\cos\phi_2)]E_2^+ - \exp[(2\pi D/\lambda)(\beta_2 + i\alpha_2\cos\phi_2)]E_2^-\}$$
$$\times (n_2 - ik_2) = \exp[(-2\pi D/\lambda)(\beta_3 + i\alpha_3\cos\phi_3)]E_3^+(n_3 - ik_3)$$

where

$$\alpha_j = n_1\sin\phi_1/\sin\phi_j \quad (j = 2,3); \quad \alpha_j^2 - \beta_j^2 = n_j^2 - k_j^2;$$

$$\beta_j = n_j k_j/\alpha_j\cos\phi_j \ .$$

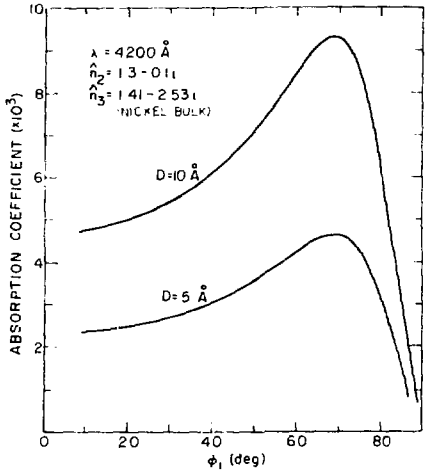

Fig. 4. Calculated relative absorption versus angle of incidence for a weakly allowed electronic transition. (XBL 761-6325)

The important quantities are not the amplitudes but rather the ratio of the intensity of the reflected beam versus the incident beam. This is given by the ratio of the modulus square of the E's, i.e., $R = |E_1^-|^2/|E_1^+|^2$. A convenient form is the absorption factor $A = (R^0 - R)/R^0$, where R^0 is the reflectance of the system when the organic layer is not absorbing, i.e., $k_2 = 0$. Although the equations are complex, they are easily solved by computer iteration procedures for a given set of optical parameters.

The results of these calculations are important insofar as they define the experimental geometry for any particular experiment. Typical plots of absorption factor versus angle of incidence are shown in Figs. 4 and 5 for a nickel metal substrate with an absorbed organic layer having optical constants typical of weakly allowed electronic transition (Fig. 4) and/or moderately strong infrared transition (Fig. 5). We note that there is a marked change of optimum angle of incidence for the two wavelengths.

*Partially supported by NSF.

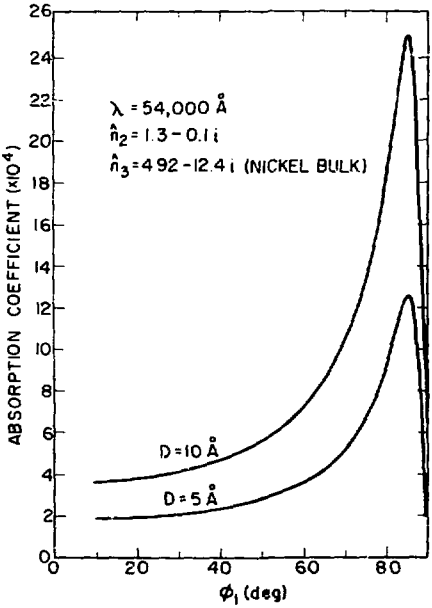

Fig. 5. Calculated relative absorption versus angle of incidence for a strongly allowed infrared transition. (XBL 761-6324)

2. THE USE OF THERMAL MODULATION SPECTROSCOPY IN THE STUDY OF ENERGY TRANSFER PROCESSES IN CRYSTALS

Alan R. Burns, Charles B. Harris and Marc E. Tarrasch

By utilizing the technique of controlled heat pulses in molecular solids, the phenomena of phonon-induced trap-to-trap excitation migration and spin-lattice relaxation processes in excited states are being studied. Heat pulses have long been used in investigations dealing with second sound propagation in liquid and solid helium. The distinct advantage of the pulse method over conventional steady state temperature experiments lies in the temporal and spatial resolution of the detected thermal modulation.

Small single crystal samples are placed in thermal contact with a thin film nichrome resistor that has been vacuum evaporated on a polished quartz substrate (cf. Fig. 1). Short duration (μsec to msec) current pulses are applied to the resistor, resulting in the generation of a wide band of high frequency phonons centered ar und kT_1/h, where T_1 is the temperature of the thin film. The theoretical basis for the experiments has been derived starting from the Stephan-Boltzmann equation for blackbody radiation:

$$I^2R_H/A = (2\ ^5k^4/5h^3C_1^2)(T_1^4 - T_2^4) , \qquad (1)$$

from which the temperature of the thin film can be calculated. In the above equation, I is the current through the thin film resistance R_H having an effective area A, C_1 is the velocity of sound

EXPERIMENTAL APPARATUS FOR MICROWAVE-HEAT PULSE MULTIPLE RESONANCE

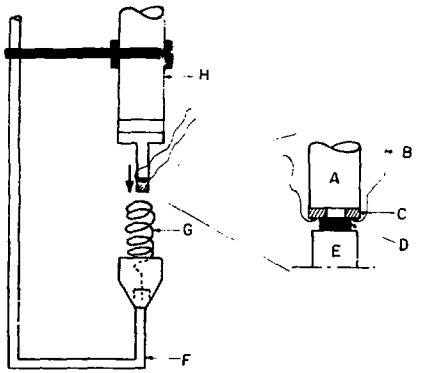

A	Quartz substrate	E	Crystal
B	Cu leads	F	50 Ω microwave line
C	Gold (thin film)	G	Slow wave helix
D	50 Ω Nichrome (thin film)	H	Support

Fig. 1. Apparatus for heat pulse experiment. (XBL 761-6343)

in the thin film, and T_2 is the ambient bath temperature.

When the product of the phonon Bose-Einstein distribution and the density of states for both the thin film heater and the crystal is integrated over the area of the crystal-heater interface, one obtains an expression for the net flux of phonons of frequency ν propagating into the crystal sample:

$$N(\nu) = A(2\pi\nu^2/C_1^2)\Gamma\{[\exp(h\nu/kT_1) + 1]^{-1} - [\exp(h\nu/kT_2) + 1]^{-1}\} \quad (2)$$

The phonon transmission coefficient Γ is an integral function of the relative densities and acoustic velocities of the crystal and the heater. In this expression, the crystal is assumed to be at the bath temperature T_2. When Eq. (2) is integrated over all frequencies greater than that required to delocalize a "trap" state, but less than the Debye cut-off of the thin film, the phonon flux for this frequency range can be calculated as a function of the heater temperature. From Eq. (1) and the integrated form of Eq. (2), one can calculate the phonon flux as a function of the power dissipated in the heater and the ambient bath temperature. The calculated phonon

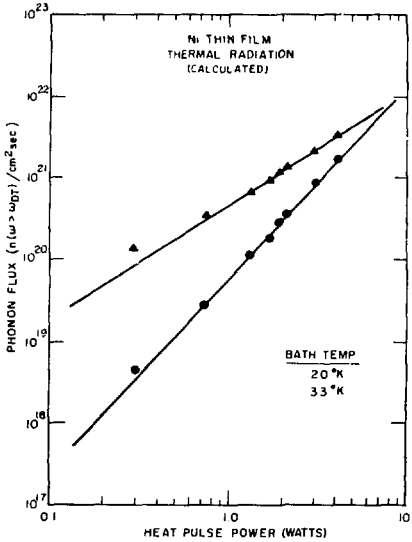

Fig. 2. The calculated phonon flux vs heat pulse power for phonons having energies greater than 22 cm^{-1}. (XBL 761-6204)

flux for the range between 22 cm^{-1} and 307 cm^{-1} (the cutoff for nickel films) is shown in Fig. 2.

a. Thermal Modulation of Trap and Exciton Phosphorescence

At temperatures below the λ point of liquid helium (2.17°K), there exists a non-Boltzmann distribution of excited states partitioned among the exciton band and the multiple traps in a crystal of d_2-TCB. At temperatures above the λ point, the partitioning approaches a Boltzmann distribution. It is expected that the thermal modulation of the two different relative population distributions of the trap and the exciton states will induce different changes in the respective phosphorescence intensities. This can be seen in Figs. 3 and 4. In these experiments, a shutter is placed in front of the detection monochromater so that the dark current of the photomultiplier can be determined. This is followed by the opening of the shutter which gives the steady state level of the phosphorescence intensity emitted from each state. This method allows one to estimate the subsequent modulation depth or percent change in phosphorescence intensity induced by the heat pulse. The peak of the modulation for each state was measured as a function of heat pulse power in the non-Boltzmann region (Fig. 5) and the Boltzmann region (Fig. 6). It is evident that the nature and the extent of the heat pulse-induced delocalization of trap states can be controlled

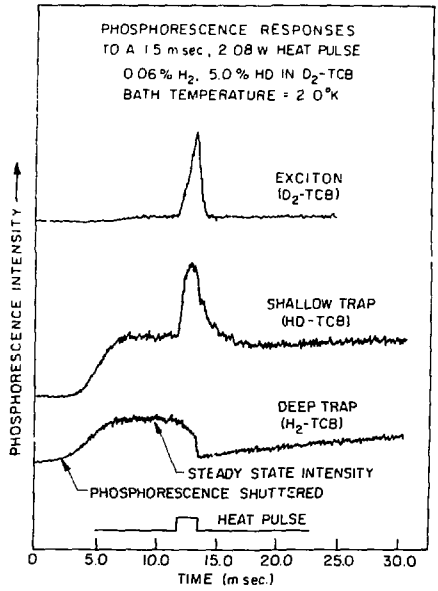

Fig. 3. The thermal modulation of trap and exciton phosphorescence for the mixed isotopic 1,2,4,5-tetrachlorobenzene (TCB) crystals in the non-Boltzmann temperature region (2.0°K).
(XBL 761-6206)

by the amount of input power, and hence one can extract relative phonon cross-sections for promotion to the exciton band.

h. Thermal Modulation of Triplet State Spin-Sublevel Populations

If a trap is present far below the exciton band, phonon-assisted promotion to the band states becomes energetically prohibitive at low temperatures. In these cases the thermal modulation of the non-Boltzmann spin distribution among the excited triplet state sublevels becomes possible to detect. The results presented in Figs. 7 and 8 depict the thermal modulation of the h_2-TCB trap state which lies 1456 cm^{-1} below the band states of durene. The population redistribution of the spin sublevels upon application of a heat pulse can be analyzed in terms of the rapid increase in the rate of phonon-assisted spin lattice relaxation.

c. Kinetics of Heat Pulse Induced Energy Migration and Spin Lattice Relaxation

Optically detected spin locking and adiabatic demagnetization experiments have yielded kinetic information on the absolute promotion rate of localized excited state populations into the delocalized exciton bands in one-dimensional exciton conductors. Work is now in progress that will provide more information regarding the phonon multiplicities of those interactions that result in delocalization and migration. These experiments involve the application of a heat pulse at a specific time during the course of the microwave pulse sequences. Since the phonon flux through the crystal is a function of the heat pulse power, it is possible to obtain more detailed kinetic data on the promotion and migration rates induced by the heat pulse. Preliminary spin locking heat pulse experiments have been completed on the h_2-TCB in durene system. In this case, only spin lattice relaxation, induced by the heat pulse, is expected to lead to the decay of the spin locked ensemble. As is shown by the preliminary data in Fig. 9, there is a decrease in the lifetime of the spin locked ensemble as the heat pulse power is increased.

d. Heat Pulse Transmission in Molecular Crystals

The thermal rise time of the thin film heater is expected to be less than 10^{-8} sec, since phonon-electron interactions in metals are very rapid. However, the thermal response time of

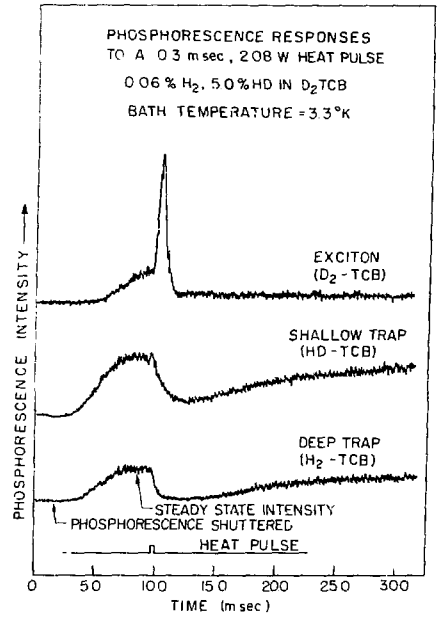

Fig. 4. The thermal modulation of trap and exciton phosphorescence for the mixed isotopic TCB crystal in the Boltzmann temperature region.
(XBL 761-6205)

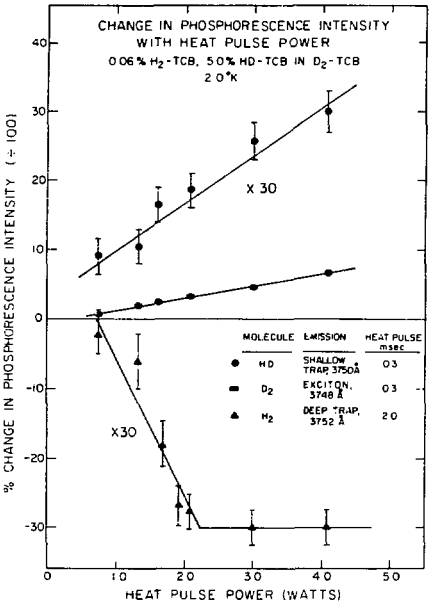

Fig. 5. Modulation depths of trap and exciton phosphorescence intensity in the non-Boltzmann temperature region as a function of heat pulse power. (XBL 761-6213)

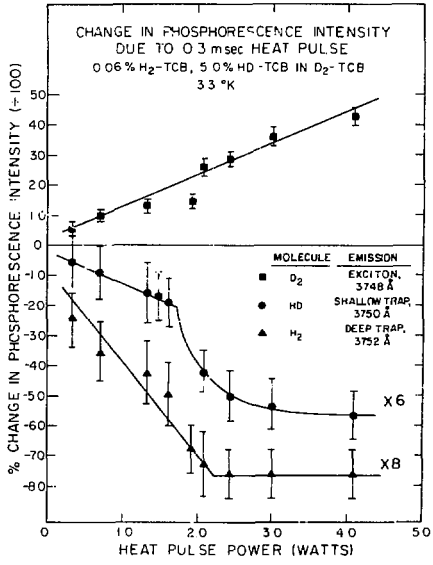

Fig. 6. Modulation depths of trap and exciton phosphorescence intensity in the Boltzmann temperature region as a function of heat pulse power. (XBL 761-6212)

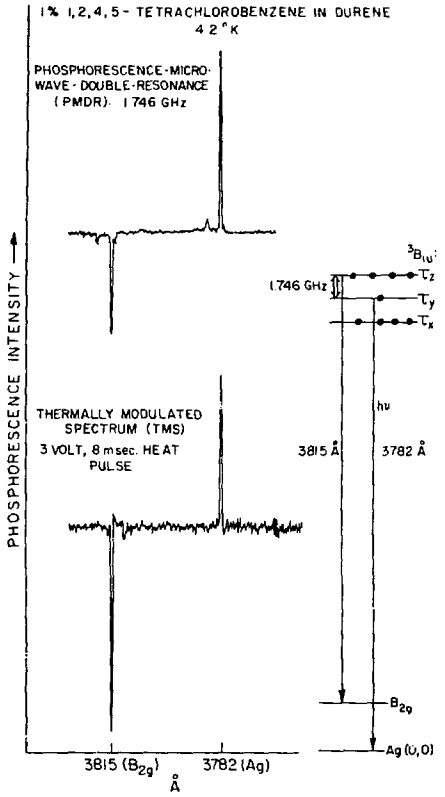

Fig. 7. Phase-detected thermal modulation and microwave-induced changes (PMDR) in phosphorescence intensity for h_2-TCB in durene. The initial non-Boltzmann spin distribution of the h_2-TCB triplet state in zero field is depicted at the right. Upon application of a heat pulse, the spin distribution in all three sublevels is thermally equalized, thus there is a decrease in emission from the τ_z sublevel (b_{2g}) and a concurrent increase in the emission from the τ_y sublevel (a_g). The microwave field simply inverts the τ_y and τ_z populations (π pulse), so the phosphorescence changes differ quantitatively but not qualitatively from the thermally modulated spectrum. (XBL 761-6214)

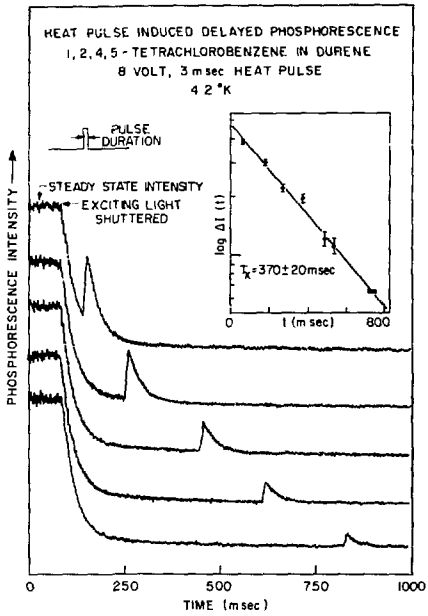

Fig. 8. Measurement of the lifetime of the long-lived or "dark" τ_x sublevel by way of heat pulse-induced delayed phosphorescence. In this experiment, the exciting light was shuttered, so that the beginning of each trace corresponds to the steady state light intensity at the origin (a_g). The exciting light is then turned off; thus one sees a rapid decay of light emitted from the "fast" τ_y sublevel and the much slower decay from the τ_x sublevel. At delay times corresponding to multiple lifetimes of the τ_y sublevel, a heat pulse is triggered. The amount of population left in the slow τ_x sublevel is then rapidly equalized among all three sublevels, resulting in a jump in the emission intensity (ΔI) from the τ_y sublevel. The insert shows that the jump in light intensity vs the heat pulse delay time yields the lifetime (T_x) of the τ_x sublevel. (XBL 761-6203)

the crystal sample and/or the bath temperature is expected to be much slower because of such factors as the thermal boundary resistance at the crystal/heater interface, the inherent thermal conductivity of the crystal, and heat losses to the helium bath. It is important therefore that some of these features be experimentally determined. To this end, work is now in progress using a fast (< 10^{-8} sec) and sensitive semiconductor thin film germanium bolometer. The heat pulse-induced response of the bolometer will be correlated with the observed phosphorescence changes, the calculated phonon fluxes, and film temperatures. The optically detected phosphorescence changes can be used to measure the average time scale of the thermal modulation process. The rapidity of the bolometer response time and the location of the bolometer with respect to the crystal surface opposite that in contact with

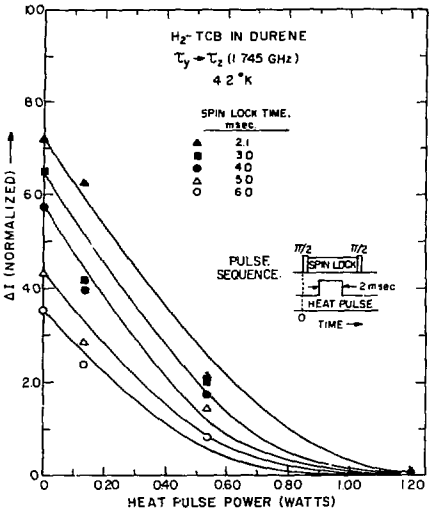

Fig. 9. Phosphorescence intensity changes following the final probe pulse ($\pi/2$) of spin locking heat pulse experiment as a function of heat pulse power. The decrease in the light change ΔI is associated with a greater loss of spin coherence. (XBL 761-6211)

the heater film will provide a different temporal resolution of the modulation as well as a spatial resolution of the heat pulse. With such experiments, one can measure the instantaneous temperature rise associated with the gradual rise of the bath temperature after Boltzmann equilibrium has been achieved in the phonon states.

3. COHERENT ENERGY TRANSFER IN SOLIDS: DETERMINATION OF AVERAGE COHERENCE LENGTH ON ONE-DIMENSIONAL SYSTEMS USING TUNABLE DYE LASERS*

Charles B. Harris, Robert M. Shelby and Ahmed H. Zewail

The coherent nature of energy propagation in molecular crystals at low temperatures was studied via the time-resolved phosphorescence response of the crystal to short optical pulses obtained from a nitrogen laser-pumped tunable dye laser. The information obtained from these measurements reflects the nature of triplet exciton-phonon interactions and the dynamics of exciton-trap equilibria. We have applied these techniques to two systems, 1,2,4,5-tetrachlorobenzene (TCB) and 1,4-dibromonaphthalene (DBN), which exhibit one-dimensional triplet exciton band structure. In the DBN system the presence of multiple localized states helped in exploring the many

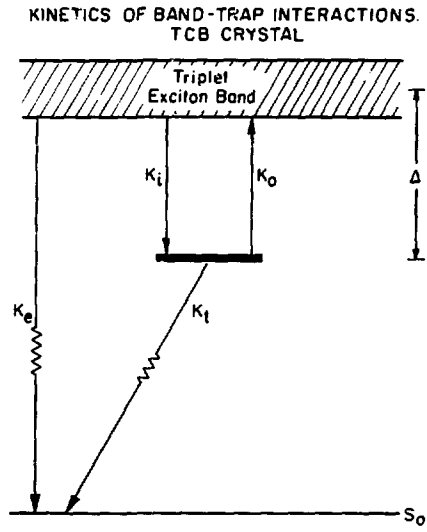

Fig. 1. Kinetic model for a coupled system of one trap and a one-dimensional triplet exciton band. K_i and K_o are the trapping and detrapping rate constants respectively, while K_e and K_t are rate constants for decay to the ground state of the exciton and trap levels respectively. (XBL 757-6635)

routes of communication between the band and traps which must be understood in order to further elucidate the nature of coherence in this system. However, the complexity of this system does not allow an unequivocal demonstration of coherence at this time. Such is not the case, however, with the simpler TCB system. In this case, only one trap is interacting with the band, and the bandwidth ($\sim 1\ cm^{-1}$) is small compared to the trap depth ($21.3\ cm^{-1}$). This allows the dynamics to be described by a simple kinetic model, and a minimum triplet exciton coherence length can be estimated.

The TCB system is represented schematically in Fig. 1, which shows the various pathways for the population and depopulation of the band and trap levels. The phosphorescence response resulting from laser excitation of the exciton band is shown in Figs. 2 and 3 at two different temperatures. By fitting the kinetic equations which we schematically represented in Fig. 1 to such measurements over a range of temperatures from 1.2°K to 4.2°K, we were able to estimate the value of K_i, the trapping rate constant. The data and fit to the theoretical model is shown in Figs. 4, 5, 6 and 7. Together with the knowledge of the trap concentration and some simplifying assumptions, this enabled us to obtain for the first time a minimum coherence length for

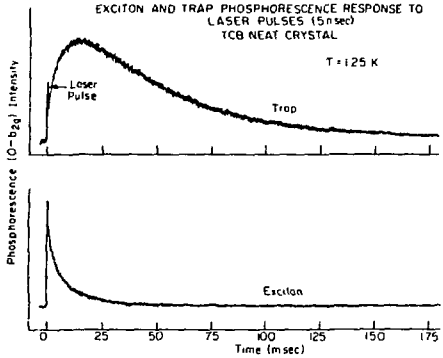

Fig. 2. Phosphorescence response of neat TCB to pulsed laser excitation in the low temperature/ slow detrapping regime. Note that the exciton decay and trap build-up rates are similar. (XBL 757-6639)

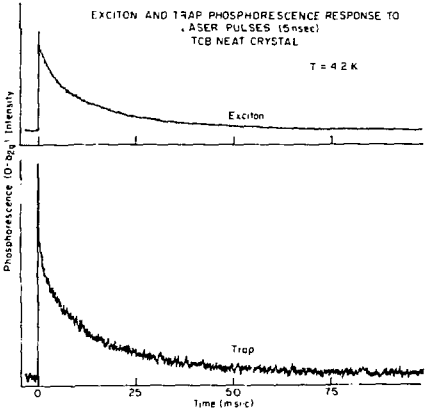

Fig. 3. Phosphorescence response of neat TCB to pulsed laser excitation in the high temperature/ fast detrapping regime. Note that the exciton and trap decay at the same rate and no trap population build-up is observed. (XBL 757-6640)

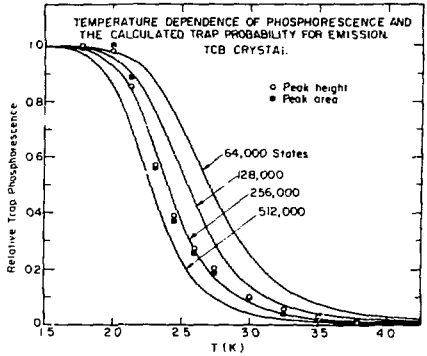

Fig. 4. Temperature dependence of steady state phosphorescence emission of the x-trap origin of neat TCB crystal. The solid curves were calculated for different values of the exciton chain length by assuming a Boltzmann distribution of population among the band and trap states. The bandwidth was taken as 1 cm^{-1} and trap depth as 21.3 cm^{-1}. (XBL 757-6638)

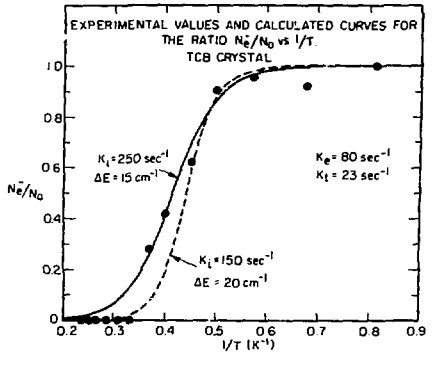

Fig. 5. Calculated fits to the experimental data for the fraction of exciton population which decays with a rate constant equal to the trap population build-up rate constant, α_-. The solid curve corresponds to the best fit for N_e^-/N_0, and gives the values of K_0 vs 1/T shown in Fig. 6. The dotted curve corresponds to values of K_0 obtained from the plot of α_- vs 1/T (see Fig. 7). (XBL 757-6641)

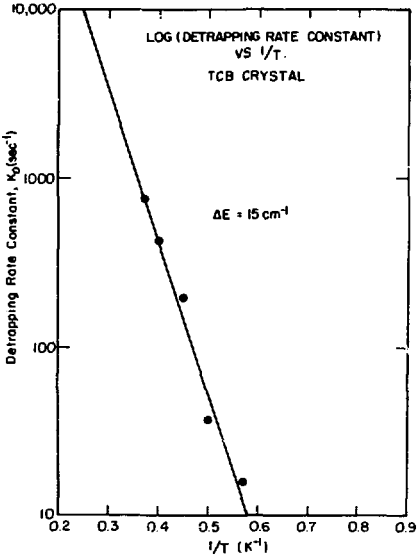

Fig. 6. Detrapping rate constant vs 1/T obtained from the solid curve in Fig. 5 and calculations based on the kinetic model. ΔE represents the energy difference between the trap level and the intermediate which is assumed to be active in mediating phonon-assisted detrapping. (XBL 757-6642)

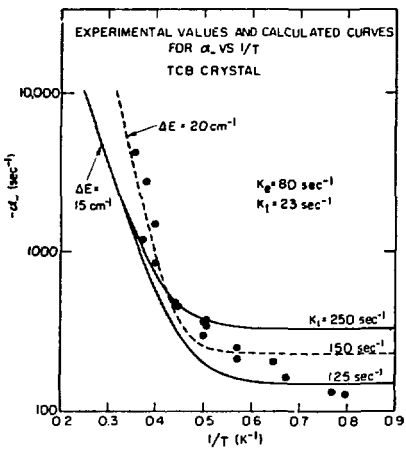

Fig. 7. Calculated fits to the data for α_-, the trap population build-up rate vs 1/T. The solid curves were calculated from the model equation using the values of K_D vs 1/T from Fig. 6. The curve for K_1 = 125 sec^{-1} corresponds to $K_t = K_e$ = 23 sec^{-1} rather than the values shown in the figure. The dotted curve is the best fit to α_-, and the corresponding values of K_D vs 1/T were used to calculate the dotted curve in Fig. 5. These latter calculations give a value of ΔE of 20 cm^{-1}. (XBL 757-6643)

excitons in molecular crystals at low temperatures: $\ell_{min} \geq 700$ Å = 186 molecules. This value of the measured coherence length indicates that exciton-phonon plays an important role in shortening the coherence length for very long linear chains.

*Partially supported by NSF.

4. ENERGY TRANSFER BETWEEN MULTIPLE LOCALIZED STATES IN MOLECULAR SOLIDS STUDIED BY ZEROFIELD OPTICALLY DETECTED MAGNETIC RESONANCE

Charles B. Harris, Alan M. Nishimura and Ahmed H. Zewail

Energy transfer in crystalline media, although complex, can be classified into two broad categories that are determined by the nature of the systems between which energy transfer is taking place. If the transfer involves two or more different systems, the roles of the various systems in the energy transfer process are dictated by their respective zero point energies and charge distributions, in addition to their relative concentrations and locations in the crystal. A typical example would be relatively low concentration guest molecules (acceptors) receiving excitation from a high concentration host molecule, or perhaps from another low concentration guest molecule (donor). A second possibility exists, in which the donor and acceptor molecules are identical species. This could arise either from transfer between various lattice defects in a pure crystal or in the dimer states of a quest in a host crystal. In the case of two neighboring guest molecules, i.e., a dimer, energy transfer not only depends on the host properties but also on the local symmetry of the pair in the host lattice and the magnitude of the resonance interaction between the molecules. In both categories, the possible pathways for energy transfer certainly depend on the geometrics of the molecules in the lattice.

In an attempt to understand the rather complex processes of molecular energy transfer, one would like to choose as simple a system as possible.

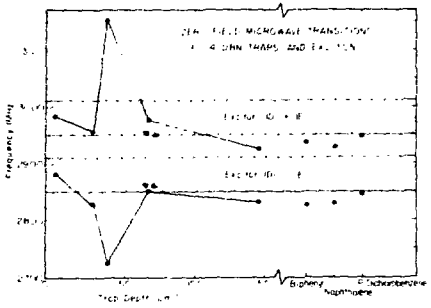

Fig. 1. Zero field microwave transitions of 1,4-dibromonaphthalene traps and exciton. The exciton resonances together with the error are represented by the dashed areas. The two points represented by solid triangles are the monomer and dimer frequencies. B represents biphenyl, D represents dichlorobenzene, and N represents naphthalene. (XBL 745-6407A)

In view of the strong influences of geometry on energy transfer, various investigators have naturally gravitated to the study of one-dimensional host bands with the intent that this would be the simplest of systems that contains all of the phenomena of interest. Using the knowledge gained from this situation, one could then apply it to understand the dynamics of multidimensional energy migration in both the coherent and incoherent limits. Further, the manifestations of these migration processes in both optical and EPR spectra could answer many questions pertaining to the dynamics of spin interactions between traps and excitons. The triplet band of 1,4-dibromonaphthalene (DBN) has been shown to approximate a one-dimensional system quite well. In addition, the pair structure in isotopically mixed crystals has been identified from both optical and EPR spectra. For these reasons, a systematic study by double resonance spectroscopy of the localized states of DBN, both as a dilute guest in host crystal and as a trap in the neat crystal, was undertaken.

The kinetic parameters associated with the various "localized" triplet states have been determined. These include the relative inter-system crossing rates, the relative radiative rates from the spin states to the electronic and vibronic origins, and the total depletion rates from the individual spin sublevels. The results of these studies indicate that the correlation of the magnetic structure of trap states and the energy difference between traps and a host band is not straightforward, even for one-dimensional systems (see Fig. 1). Moreover, these results imply that spin exchange and equilibrium between traps and band states can severely influence the dynamics of energy migration and must be incorporated into any temperature dependent line shape analysis of the exciton transitions, particularly for DBN because of the similarity in trap and exciton EPR frequencies.

5. DIRECT AND INDIRECT ENERGY TRANSFER IN ONE-DIMENSIONAL SOLIDS

Charles B. Harris, Mark T. Lewellyn and Ahmed H. Zewail

A full understanding of the mechanisms and pathways for energy transport in real molecular crystals can only be obtained by considering the important effects of lattice imperfections such as dislocations, impurities, and other types of energy traps. Both optical and magnetic resonance studies have shown that excitations are transferred among different trap sites by at least two distinct processes. The first involves the direct exchange of energy between trap sites via a virtual coupling with the host states while the second is an indirect pathway involving the decay into delocalized host states (exciton band), migration in the band, and retrapping. These processes are illustrated in Fig. 1 for the excited triplet state of an one-dimensional, isotopically mixed 1,2,4,5-tetrachlorobenzene (TCB) crystal.

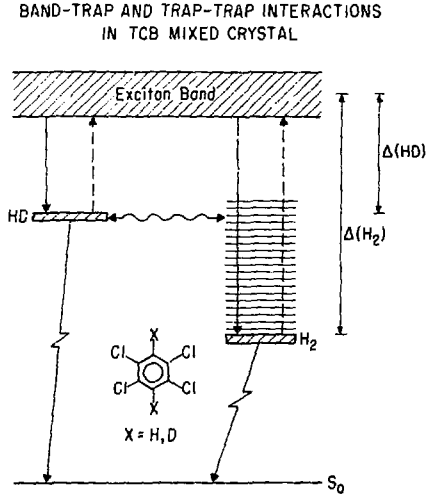

Fig. 1. A schematic for the structure of the excited triplet state of isotopic TCB crystals. Δ is the trap depth, and H_2 or HD refer to the different isotopic species. The solid arrows represent emission to the ground state or trapping to trap sites; emission of the exciton to the ground state is not shown. The dotted arrows represent detrapping processes to the band and the wiggly double-arrowed line represents the communication between traps via a "direct" mechanism. (XBL 753-1397)

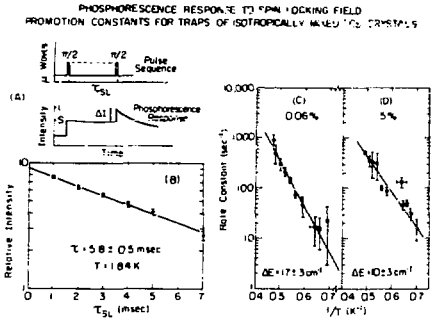

Fig. 2. (A) A schematic for the spin locking pulse sequence and the hypothetical phosphorescence response. (B) A typical decay of a spin locked triplet state spin ensemble of the 0.06% h_2 crystal. (C) and (D) show plots of the promotion rate constant vs 1/T for the 0.06% and 5% crystals, respectively. The ΔE values associated with the promotion processes approximate the h_2 (22 cm^{-1}) and hd (11 cm^{-1}) trap depths. (XBL 755-1405)

Details of trap-to-trap energy transfer in isotopically mixed crystals of TCB have been studied using a variety of techniques including pulsed electron spin coherence experiments and steady state luminescence studies. These experimental tools were utilized to investigate the effects of temperature and trap concentration on excitation transfer between monoprotonated (hd) and perprotonated (h_2) traps in perdeuterated TCB host crystals at low temperatures (< 2.2°K). Optically detected spin locking experiments yielded kinetic information on the absolute promotion rates of excited state population out of the h_2 traps to higher energy hd traps and host d_2 states.

By examining the temperature dependence of the promotion rate constants (see Fig. 2), it has been determined that in crystals containing low h_2 trap concentrations (0.06%) promotion is predominantly to the band states of the host, favoring an indirect exchange mechanism, while in crystals containing higher h_2 trap concentrations (5%) promotion is predominantly to hd trap states, indicating a direct exchange mechanism.

Application of these experimental techniques to other one-dimensional systems is currently being investigated.

6. ENERGY TRANSFER DYNAMICS IN SUBSTITUTIONALLY DISORDERED SOLIDS USING A TUNABLE DYE LASER

Charles B. Harris and Dirk A. Zwemer

Many solids are characterized by structural and/or substitutional disorder on the molecular level. Energy transport in these systems is particularly dependent on such disorder and often shows sharp discontinuities in the region of a critical impurity concentration, intermolecular spacing, or temperature. A much studied example would be electrical conduction in amorphous semiconductors at the limits of theoretical tractability. Our approach has been to investigate the details of the migration of electronic excitation in disordered molecular solids, where advantage can be taken of the "one-dimensional conduction" properties of certain organic compounds.

One system studied was a mixture of perproto(h_2)- and perdeutero(d_2)-1,2,4,5-tetrachlorobenzene (TCB) with an additional low concentration impurity, pyrazine. In such an isotopic mixture the crystal structure and chemical properties remain constant along the molecular chains and only the differences in energy of the first excited triplet electronic states of the three randomly distributed species (see Fig. 1) define a disordered potential surface. The energy partitioning between h_2-TCB and pyrazine, which are energy "traps" with respect to the d_2-TCB exciton band, reflects the ability of the triplet exciton to migrate between h_2-TCB traps.

Briefly, the triplet exciton can either be localized on a h_2-TCB molecule, or travel to another such molecule, by two processes: (i) thermally activated promotion into the delocalized energy levels of neighboring d_2-TCB molecules, or (ii) by direct quantum-mechanical tunneling through intervening molecules to another trap. After some average number of these jumps, the triplet exciton will finally reach a pyrazine molecule, which being at much lower energy traps it completely until it decays back to the ground state. If the migration is sufficiently rapid that most of the excitation reaches a pyrazine molecule within the triplet state lifetime, the phosphorescent emission observed will be predominantly that of pyrazine, even though the pyrazine concentration is orders of magnitude smaller than that of h_2-TCB. The experimentally adjustable parameter is the average distance between h_2-TCB localized wave-functions, which is

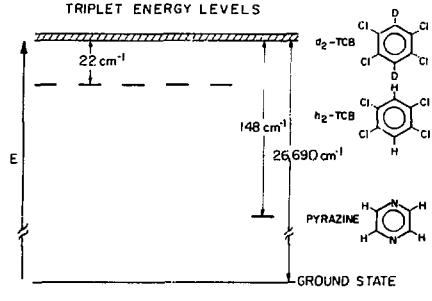

Fig. 1. Energy levels of first excited triplet states in three component mixed crystals. (XBL 761-6327)

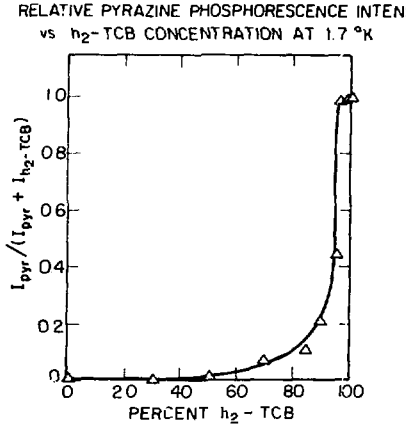

Fig. 2. Experimental dependence of relative supertrap phosphorescence on h_2-TCB concentration. Phosphorescent states excited directly with dye laser tuned to h_2-TCB triplet origin. Intensities of h_2-TCB and pyrazine were integrated over first 150 Å of spectra. (XBL 761-6326)

Tunneling Times

Barrier Size (# d_2-TCB molecules)	β_n (cm^{-1})	τ (sec)
1	3.9×10^{-3}	2.14×10^{-9}
2	5.1×10^{-5}	1.64×10^{-7}
3	6.7×10^{-7}	1.24×10^{-5}

$$\beta_n = \beta\left(\frac{\beta}{\Delta}\right)^n \qquad \tau = \frac{h}{4\beta_n},$$

β = nearest neighbor interaction energy

Δ = barrier height

Fig. 3. Interaction energies and exciton tunneling times between localized h_2-TCB bands assuming resonant transfer. Exciton lifetime is 23×10^{-3} sec. (XBL 761-6340)

controlled by varying the concentration of h_2- and d_2-TCB in a series of mixed crystals.

The excited triplet state is prepared with a nitrogen-pumped narrow line tunable dye laser. This has several advantages over conventional broadband illumination. First, a single energy level can be selectively excited so that energy transfer pathways can be unequivocally identified.

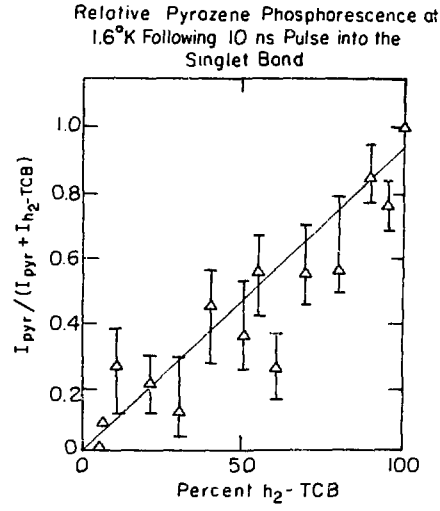

Fig. 4. Experimental dependence of relative supertrap phosphorescence on h_2-TCB concentration. Triplet phosphorescent states were prepared by excitation of singlet states with broadband illumination centered at 2800 Å. (XBL 761-6342)

Second, the high power densities available allow the molecule to be excited directly into the triplet state in spite of the low transition moment. Consequently, effects from migration within the singlet band are eliminated along with high local exciton densities which can lead to trap saturation, biexcitonic annihilation, and other non-linear effects. Third, the ten nanosecond duration of the dye laser pulses allows additional information on the exciton migration rate to be extracted from the time-resolved phosphorescence measurements, which have been taken down to the microsecond range with transient digitizer and signal averaging equipment.

In order to separate thermally-activated processes from direct transfer, the first experiments were done at 1.7°K. In a classical one-dimensional conductor, appreciable pyrazine phosphorescence should not appear until h_2-TCB concentration reaches the limit of 100%. Experimentally, a steep rise between 90% and 100% (see Fig. 2) indicates that barriers of two or three d_2-TCB molecules are the rate-determining features of the substitutionally disordered one-dimensional system for a 23 msec triplet lifetime. Figure 3 lists the appropriate tunneling times for a given barrier in these systems. At these high h_2-TCB concentrations, we must consider long-range intermolecular tunneling interactions to explain the data. The data also permits us to set upper limits on the translational inequivalent interaction between molecules on different linear chains.

Energy transfer in the triplet manifold is considerably different than in the singlet. This can be seen from Fig. 4 which demonstrates that the singlet bands for the proto and deutero species are amalgamated and hence one obtains a linear dependence in emission with concentration in the h_2 species.

7. STUDIES OF NONRADIATIVE DECAY OF ENERGY FROM IMPURITY STATES INTO DELOCALIZED BAND STATES IN SOLIDS USING OPTICALLY DETECTED ELECTRON SPIN COHERENCE*

Henry C. Brenner, John C. Brock and Charles B. Harris

The efficiency of energy transfer in solids is limited largely by the interaction of mobile excitons with crystalline impurities and dislocations that provide localized "trap" states for the excitation. Once trapped, however, an excitation can be thermally promoted to the exciton band where it can decay to the ground state, "retrap" at the same impurity site, or delocalize and migrate to another impurity site. The efficiency of this last process is expected to depend on the density of states in the exciton band (inversely proportional to the impurity concentration) as well as the lattice temperature.

Quantitatively, the probability per unit time of a localized state $|\tau\rangle$ interacting with a single phonon $P(\varepsilon)$ of energy ε and decaying into a specific band state $|k\rangle$ via an intermediate state $|\tau_i\rangle$ having energy E_i is given to the second order by

$$K_{k\varepsilon} = \pi/\hbar \langle n(\varepsilon)\rangle_T |\langle \tau P(\varepsilon)|H_{TP}|\tau_i P(\varepsilon - E_i)\rangle|^2 \quad (1)$$

$$\times \quad \tau_i P(\varepsilon - E_i)|H_{Ti}|kP(\varepsilon - E_i)\rangle|^2 \rho(E_i)$$

The term $\langle n(\varepsilon)\rangle_T |\langle \tau P(\varepsilon)|H_{TP}|\tau_i P(\varepsilon - E_i)\rangle|^2$ gives the probability for creating the intermediate τ_i. $\langle n(\varepsilon)\rangle_T$ is the average number of phonons having energy ε at temperature T given by the Planck distribution function times $\rho(\varepsilon)$, which is the density of phonon states as given by the phonon dispersion. The radiationless decay into the exciton manifold of k states at an energy E_i above the localized state is given by

$$|\langle \tau_i P(\varepsilon - E_i)|H_{Ti}|kP(\varepsilon - E_i)\rangle|^2 \rho(E_i) \quad (2)$$

where $\rho(E_i)$ is the exciton density of states function evaluated at E_i.

The total probability per unit time for the phonon-assisted promotion of a localized state to the exciton band, K_p, is obtained by summing over all phonons with energy $\varepsilon \geq E_i$ and then

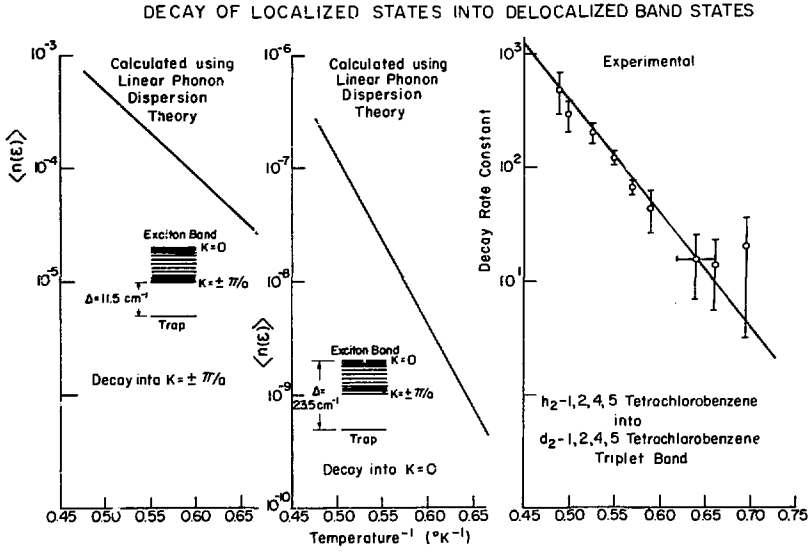

Fig. 1. Comparison of theory and experiment.
(XBL 762-6389)

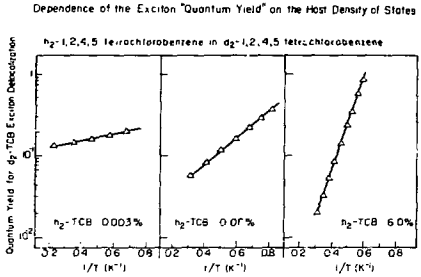

Fig. 2. Quantum features of the quantum yield for excitation delocalization upon thermal promotion of localized impurity states as a function of temperature and impurity concentration. The ordinates for 0.003% and 6% crystals are not the same. (XBL 761-6328)

summing over all intermediate states $|\tau_i)$ which have energies E_i equal to the energies of the band k states, i.e.,

$$K_p = \sum_k \sum_{\varepsilon \geq E_i} K_{k\varepsilon} \qquad (3)$$

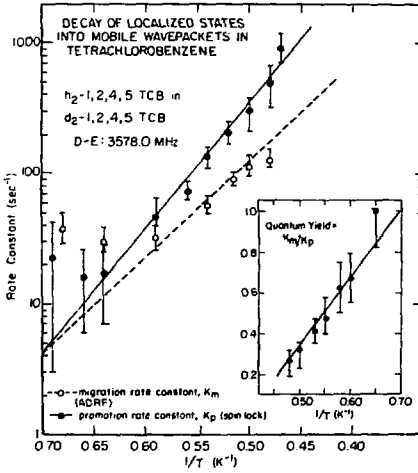

Fig. 3. Experimentally measured values of the rate constants for promotion of h_2-TCB localized trap states in d_2-TCB to the d_2-TCB exciton band (solid circles), and for h_2-TCB trap-to-trap migration (open circles). The rate constants K_p and K_m were measured versus temperature by means of optically detected spin locking and adiabatic demagnetization in the rotating frame, respectively. (XBL 745-6410)

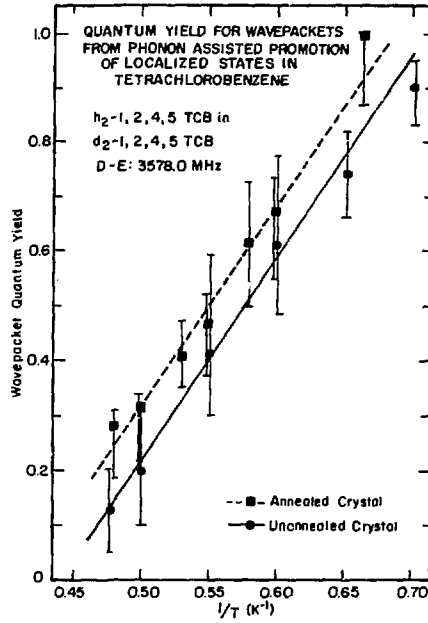

Fig. 4. Quantum yield for h_2-TCB trap-to-trap migration in d_2-TCB. The quantum yield given by the ratio of the migration rate constant to the promotion rate constant represents the fraction of trap spins which migrate to other traps after promotion to the exciton band. (XBL 745-6409)

At low temperatures, however, the phonon distribution function will weight the values of $K_{k\varepsilon}$ so that K_p will effectively represent detrapping to a relatively narrow range of k states whose energies are nearest the trap state.

In order for detrapping to occur, ε must be at least equal to Δ, the energy difference between the localized state and the exciton band. At liquid helium temperatures, kT is much less than Δ in this system, so that one can approximate $\langle n(\varepsilon)\rangle_T$ by $\rho(\varepsilon)\exp(-\varepsilon/kT)$. Figure 1 shows the calculated values for Eq. (3) in the narrow band limit for two different bands. It is seen that to a good approximation the data is in substantial agreement with theory (cf. Fig. 1).

Using optically detected spin locking, we have measured the rate constant for thermal promotion of localized states as a function of temperature and impurity concentration. This information is correlated with data obtained from optically detected adiabatic demagnetization in the rotating frame, a technique which provides information on the rate constant k_m for trap-to-

trap energy migration, to determine a quantum yield for the delocalization of excitations upon thermal promotion.

The qualitative features of the dependence of the quantum yield on temperature and concentration have been determined and are presented in Fig. 2. A more quantitative investigation of the concentration dependence is currently in progress, a study requiring a more detailed interpretation of both the spin locking and adiabatic demagnetization experiments. Results for a single concentration, based on a simplified interpretation of the data are presented in Figs. 3 and 4. From this data we can conclude that as the temperature increases, the retrapping of the exciton to the same lattice site increases, because the coherence of the exciton is rapidly destroyed.

*Partially supported by NSF.

8. ENERGY EXCHANGE BETWEEN MOLECULES IN COHERENT STATES*

Henry C. Brenner, John C. Brock and Charles B. Harris

A theoretical treatment of the effect of energy exchange between molecules in non-equivalent orientations (cf. Fig. 1) has been undertaken in order to study the effect of such excitation transfer on the properties of an ensemble of coherently coupled multilevel systems. The development has revealed that the magnitude of the effect on the ensemble's coherent component depends not only on the relative orientations of the molecules involved in the transfer, but also on the phase of the coherent superposition state, a result of some importance if the exchange rate is large compared to the inverse coherence time.

Application of this treatment to the problem of exchange among excited triplet states in substitutionally disordered molecular crystals has led to a prediction of the additional loss of the optically detected coherent component produced in spin locking, free induction decay, and spin echoes due to non-equivalent transfer of triplet excitations.

This work not only permits a more quantitative interpretation of spin coherence in excited triplet states experiments, but also provides a basis for understanding the effect of various relaxation phenomena on the induced coherent component in a laser media.

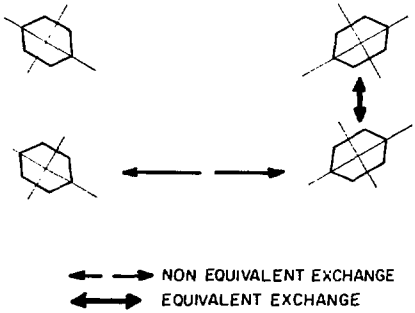

Fig. 1. Resonant energy exchange routes between coherently coupled molecules. (XBL 761-6329)

9. ENERGY MIGRATION IN ONE-DIMENSIONAL MOLECULAR SOLIDS

Charles B. Harris and Mark T. Lewellyn

Optical and pulsed microwave--optical double resonance spectroscopic techniques have been used to great advantage in detailing the nature of energy migration in one-dimensional, isotopically mixed crystal systems such as 1,2,4,5-tetrachlorobenzene. These techniques are being extended to other one-dimensional systems.

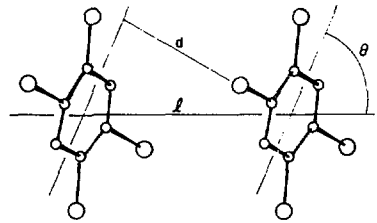

Fig. 1. Structural parameters for one-dimensional organic exciton conductors. (XBL 762-6580)

Table 1. One dimensional exciton systems.

	d	ℓ	θ
1,2,4,5 tetrachlorobenzene	3.86	3.53	66°
1,2,4,5 tetrabromobenzene	4.02	3.66	66°
1,3,5 trichlorobenzene	3.82	3.45	65°
1,3,5 tribromobenzene	4.08	3.58	62°
1,4 dichlorobenzene	3.99	3.60	65°
1,4 dibromobenzene	4.10	3.56	59°
1,4 dibromonaphthalene	4.09	3.70	65°
pyrazine	3.82	3.63	71°
pyrimidine	3.81	3.58	70°
1,3,5 triazine	3.64	3.64	90°

In Table 1 we list some of the systems which should exhibit one-dimensional exciton conduction. In Fig. 1, the one-dimensional structure of 1,2,4,5-tetrachlorobenzene is illustrated along with parameters associated with the structural homologues in Table 1. Pyrimidine is particularly interesting because of the large one-dimensional exchange interaction between the translationally equivalent molecules. Studies of this system are of special interest since the crystal structure of pyrimidine leads to the formation of two distinct, one-dimensional, excitonic systems.

The experimental aspects of this project, which are still in the initial stage, have involved the synthetic preparation of isotopically mixed pyrimidine crystals as well as the spectroscopic studies mentioned above.

10. STUDIES OF ENERGY TRANSFER PROCESSES AND ELECTRON-HOLE PAIR RECOMBINATION RATES IN SOLIDS AND SEMICONDUCTORS USING PICOSECOND SPECTROSCOPY

Charles B. Harris, Robert M. Shelby and Ahmed H. Zewail

The study of many aspects of energy transfer, in particular those related to radiationless transitions or involving vibrational energy transfer and relaxation, is complicated by the extremely short (10^{-9} to 10^{-12} sec) time scales involved. The technique of picosecond laser spectroscopy, although presenting considerable instrumental difficulties, circumvents the poorer time resolution of more conventional techniques through the use of mode-locked lasers as sources of ultra-short pulses of high intensity, coherent light. These pulses are used to excite the system, and then to spectroscopically monitor the state of the system at some time following excitation, thus reflecting the time evolution of the system in the interim.

Specifically, it has been shown that it is possible to produce coherent vibrational excitation of organic molecules in the liquid phase using the phenomenon of stimulated Raman scattering. The decay of both the coherence and the vibrationally excited population itself can then be monitored via the intensity of the coherent and incoherent anti-stokes scattering, respectively, of probing pulses of light. We have constructed a mode-locked Nd-glass laser, and using pulse selection and laser amplification techniques, are initiating a series of experiments with two basic goals in mind: (i) to study vibrational energy relaxation and vibrational energy transfer in solids, and (ii) to study the dynamics of electron-hole pair recombination in large band gap semiconductors. The aim of the latter experiments is to understand the relationship of surface band bending and electron-hole pair recombination rates to the physics of the photoelectrolysis of H_2O at semiconductor surfaces.

11. RESEARCH PLANS FOR CALENDAR YEAR 1976

Charles B. Harris

a. Energy Transfer from Organic Monolayers to Metal and Semiconductor Surfaces

The objectives of this program are to determine the mechanisms for redistributing the energy in photoexcited molecules into the surface states of metals and semiconductors, with the ultimate goal of understanding and developing materials useful in the surface photoelectrolysis and for obtaining high conversion of photoenergy into carriers in semiconductors.

b. The Use of Triplet States in Organic Solids as a Probe of the Molecular and Electronic Structure of Adsorbed Molecules on Surfaces

It is the purpose of this program to continue to develop and adapt the methods of emission and reflectance spectroscopy to aromatic and azaaromatic hydrocarbons adsorbed on transition metal, alloy, and organic surfaces, and to develop optically detected magnetic resonance as a technique for characterizing change induced in the molecular and electronic structure of these molecules by physi- and chemiadsorption. In particular, we are initiating a series of experiments to elucidate the bonding of a variety of aromatic hydrocarbons to the Ni(111) and Pt(111) surface. It is our intent to develop reflectance spectroscopy as a tool (i) to measure chemiadsorption bond energies on specific sites of the metal surfaces, (ii) to determine which molecular orbitals of the aromatic hydrocarbon participate in bonding to the surface, and (iii) to determine what the orientation of the adsorbed molecule is relative to the surface plane. It should be noted that we are six months ahead of schedule at this time. Last year we anticipated completion of the instrumentation late in 1976 and had not planned on simultaneously initiating the theoretical program.

c. Picosecond Studies of the Photoelectrolysis of H_2O on Semiconductor Surfaces

We are initiating a series of combined laser-surface experiments to elucidate the mechanism for the photoelectrolysis of H_2O to H_2 on O_2 on TiO_2 surfaces. In particular, we want (i) to determine the role of band bending present at different single crystal TiO_2 surfaces to the photoelectrolysis process, (ii) to locate the active site for photoelectrolysis of H_2O, and (iii) to measure electron diffusion rates from the surface to the bulk as a function of the position of the pinned Fermi levels to quantitatively relate the photo yield of O_2 and H_2 to the Fermi level and the electron-hole recombination rates.

d. Energy Transfer in Organic Solids

We will continue to develop techniques and methods for understanding exciton migration and energy transfer mechanisms in organic solids. We will also begin looking at organic surface states utilizing our UHV equipment and our picosecond laser facility.

12. 1975 PUBLICATIONS AND REPORTS

Charles B. Harris and Associates

Journals

1. W. G. Breiland, H. C. Brenner and C. B. Harris, Coherence in Multilevel Systems. I. The Optical Detection of Coherence in Excited States and Its Application to Phosphorescent Triplet States in Zero Field, J. Chem. Phys. 62, 3458 (1975) (LBL-2739).

2. A. H. Zewail and C. B. Harris, Coherence in Electronically Excited Dimers. II. Theory and Its Relationship to Exciton Dynamics, Phys. Rev. B 11, 935 (1975) (LBL-2734).

3. A. H. Zewail and C. B. Harris, Coherence in Electronically Excited Dimers. III. The Observation of Coherence in Dimers Using Optically Detected Electron Spin Resonance in Zero Field and Its Relationship to Coherence in One-Dimensional Excitons, Phys. Rev. B 11, 952 (1974) (LBL-3139).

4. H. C. Brenner, J. C. Brock, M. D. Fayer and C. B. Harris, Direct Measurement of the Quantum Yield for the Creation of Mobile Excitons from Localized States Using Optically Detected Electron Spin Coherence, Chem. Phys. Lett. 33, 471 (1975) (LBL-3560).

5. M. T. Lewellyn, A. H. Zewail and C. B. Harris, Energy Transfer in One-Dimensional Molecular Crystals: Direct and Indirect Energy Exchange in the Non-Boltzmann Regime, J. Chem. Phys. 63, 3687 (1975) (LBL-3195).

6. A. M. Nishimura, A. H. Zewail and C. B. Harris, Zerofield Optically Detected Magnetic Resonance of Multiple Localized States in 1,4-Dibromonaphthalene Crystals, J. Chem. Phys. 63, 1919 (1975) (LBL-3170).

7. H. Schüch and C. B. Harris, Optically Detected Spin Locking of Zero Field Electronic Triplet States and Cross Relaxation in the Rotating Frame, Z. Naturforsch. 30a, 361 (1975) (LBL-4918).

8. A. H. Zewail, Coherence in the Excited States of Multidimensional Systems: Dimer and Exciton Dynamics in Crystalline Phenazine, Chem. Phys. Lett. 33, 46 (1975) (LBL-3521).

9. C. B. Harris, Coherent Spectroscopy in Excited States, Proceedings of Arab Physical Society Conf. on Chemical Physics, Damascus, Syria, October 1975 (LBL-4183).

10. C. B. Harris and M. J. Buckley, Optical Detection of Nuclear Quadrupole Interactions in Excited Triplet States (book chapter), in Advances in Nuclear Quadrupole Resonance, Vol. II, edited by J.A.S. Smith, pub. by Heyden & Son, London, 1975 (LBL-3716).

11. C. B. Harris, The Feasibility and Advantages of Off-Resonance Lasers in Chemically Reacting Systems, in Lasers in Physical Chemistry and Biophysics, edited by J. Joussot-Dubien, Elsevier Pub., Amsterdam, 1975 (LBL-3916).

Papers Presented

1. C. B. Harris, 27th International Meeting of the Société de Chimie Physique, Paris, France, June 1975.

2. C. B. Harris, Arab Physical Society Conference on Chemical Physics, Damascus, Syria, October 1975.

LBL Reports

1. William George Breiland, Coherence in Multilevel Systems (Ph.D. Thesis), LBL-3917, July 1975.

2. W. G. Breiland, M. D. Fayer and C. B. Harris, Coherence in Multilevel Systems. II. Description of a Multilevel System as Two Levels in Contact with a Population Reservoir, LBL-3111.

3. R. M. Shelby, A. H. Zewail and C. B. Harris, Coherent Energy Migration in Solids: Determination of Average Coherence Length in One-Dimensional Systems Using Tunable Dye Lasers, LBL-3948.

b. Nuclear Magnetic Resonance Studies

Robert E. Connick, Principal Investigator

1. NUCLEAR MAGNETIC RESONANCE STUDIES OF HYDRATED METAL IONS

a. Effect on Water Lability of Partial Complexing of Nickel Ion by Iminodiacetate Ion

Thomas V. Rowland

The nickel iminodiacetate complex has two geometrically different

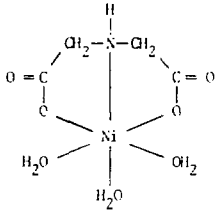

types of water, i.e., one type trans to the nitrogen and the other cis to the nitrogen, with the latter twice as abundant as the former. Nuclear magnetic resonance linewidth and chemical shift measurements of oxygen-17 in the bulk water were made from 0° to 140°C in order to determine the rates of exchange of the bound waters. Two distinct rates were found: one slow exchange site with $k_{25}° = 5.3 \times 10^4$ sec^{-1} and two equivalent fast exchanging sites with $k_{25}° = 2.4 \times 10^5$ sec^{-1}. Consideration of the data and comparison with water exchange rates for other systems leads to the conclusion that bond strain about the coordinated nitrogen, which is partially relieved by the elimination of one of the two waters cis to the nitrogen, is the most important factor in producing the greater rate of exchange from the cis positions. These results are in agreement with earlier studies on the water exchange from the nickel nitrilotriacetate complex and serve to establish the importance of bond strain of coordinated ligands in labilizing neighboring positions on metal ions. The studies were extended to the bis iminodiacetate complex of nickel ion to yield approximate values for the fraction of the time one acetate arm is dissociated and the rate of water exchange at such a "dissociated" position.

b. The Rate of Exchange of Water Molecules from the Second Coordination Sphere of Chromic Ion

William L. Earl

Although estimates and limits have been set on the rate at which waters in the second coordination sphere of metal ions exchange with waters further out, now actual measurements have been made. In the present study the values of the longitudinal and transverse relaxation times and the chemical shift of oxygen-17 in aqueous solutions of chromic ion were determined from ca. 10° to 100°C. From the data was calculated an average lifetime of 1.0×10^{-10} sec for a water molecule in the second coordination sphere of chromic ion. This lifetime is appreciably longer than the calculated lifetime for self diffusion in pure water and consequently must reflect the electrostatic attraction between the charge on the Cr^{3+} and the dipole moment of the water molecules.

c. The Lifetime of Water Molecules in the First Coordination Sphere of Europous Ion

Professor Thomas H. Norris of Oregon State Univ.

In a continuing program to determine lifetimes of water in the first coordination sphere of metal ions, the rare earth bivalent ion Eu^{2+} was investigated. While most rare earth ions are not amenable to such studies by nuclear magnetic resonance because of their extremely short electronic relaxation times, gadolinium in the +3 oxidation state is an exception since its half filled f orbitals yield no electronic orbital angular momentum. Europous ion, with the same electronic structure, therefore seemed a logical candidate. After considerable difficulties with the absolute exclusion of oxygen from the system and the establishment of acidity conditions where the oxidation by hydrogen ion was not too serious, measurements were made of line widths and chemical shifts from ca. 0° to 80°C. Using unpublished ESR data for Eu^{2+} obtained by Myers and Pratt, it appears that scalar coupling interrupted by chemical exchange is the principal mechanism of NMR relaxation of oxygen-17 of the water. The data are still being calculated but it is evident that the water exchange on Eu^{2+} is extremely rapid.

d. Computer Modeling of Exchange Reactions on Metal Ions

Robert E. Connick and Berni Alder of the Lawrence Livermore Laboratory

Attention has been focused on establishing in two dimensions the rigor of the method being used to sample rare events statistically. Since exchange with a high activation energy becomes very improbable, it is not possible to have the computer track the particles until a significant number of events occurs. Instead one particle is held in a ring around the center particle and allowed to equilibrate, when it is suddenly released and followed forward and backward in time. If the particle is near the activated complex, it has a reasonable chance of making a net crossing of the reaction barrier. The detailed motions of all particles can be followed for such an event on the computer. In addition the ratio of collisions on the outer wall to inner wall of the particle confined in the ring can be obtained for a series of just touching rings ranging from the central particle to the position of the activated complex. The continued product of these ratios gives the probability of finding the particle at the position of the activated complex. Runs are being made at relatively low activation energy to make sure that

the data obtained from the ring calculations agree with those from straighforward tracking of the particles with no rings present.

2. RESEARCH PLANS FOR CALENDAR YEAR 1976

Robert E. Connick

This research is directed toward the understanding of reactions of metal ions in solution where a ligand attached to the metal ion is replaced by another ligand. Such reactions commonly occur in chemical processes and are frequently of importance in biological systems. The iminodiacetate complex of nickel ion has been investigated in sufficient detail to yield the rates of water exchange for the two geometrically different water sites, with the conclusion that bond strain in ... amino acid ligand labilizes the waters cis to the nitrogen. Studies of the bis complex gave rough values for the fraction of the time an acetate arm is dissociated from the nickel and for the lifetime of waters coordinated at such sites. An attempt will be made to measure the rate at which the two oxygens of a carboxylate group of the bis complex interchange their positions from nickel coordinated to noncoordinated. In addition it is hoped that the present controversy in the literature over the identification of the NMR spectra of the two bis-isomers can be resolved and the rate of isomerization measured. Nuclear magnetic resonance measurements of oxygen-17 on water exchange rates will be made on the symmetrical and unsymmetrical ethylenediamine diacetate complex of nickel ion to yield further information on the bond strain effects and carboxylate labilizing effect since the data presently available cannot be used to resolve these effects unambiguously.

Work on the computer simulation of ligand exchange reactions will be continued. Once the method for sampling rare events is proven, the computations will be extended to three dimensions. One of the biggest problems in such calculations is knowing what data to ask the computer to record. While this was adequately resolved in two dimensions, going to the next higher dimension raises many new questions which will have to be answered.

3. 1975 PUBLICATIONS AND REPORTS

Robert E. Connick and Associates

LBL Reports

1. Thomas V. Rowland, Oxygen-17 NMR Studies of the Rate of Water Exchange from Partially Complexed Nickel Ion, Ph.D. Thesis, LBL-3122, October 1975.

2. William L. Earl, Oxygen-17 Nuclear Magnetic Resonance Studies of the Second Coordination Sphere of Chromium (III) in Aqueous Solution, Ph.D. Thesis, LBL-3712, November 1975.

c. Electron Paramagnetic Resonance

Rollie J. Myers, Principal Investigator

1. MAGNETIC INTERACTIONS FOR Cu^{2+}-Cu^{2+} and Ni^{2+}-Ni^{2+} PAIRS IN $ZnSeO_4 \cdot 6H_2O$

Michael R. St. John and Rollie J. Myers

In our previous studies we determined the magnetic exchange interactions between the $Ni(H_2O)_6^{2+}$ ions in α-$NiSO_4 \cdot 6H_2O$ and other ions such as Cu^{2+} and V^{2+} substituted into this lattice. Since each ion is surrounded by a variety of neighbors the total interaction is the sum of many interactions. However, with our molecular field model we can satisfactorily solve for the net exchange interaction between the Ni^{2+} and a variety of ions.

All of our calculations are based upon a pairwise model in which we assume that the largest exchange interactions come from hydrogen bonded nearest neighbors. In order to check this assumption we have substituted sufficient Cu^{2+} and Ni^{2+} into the isostructural $ZnSeO_4 \cdot 6H_2O$ to give a reasonable number of Cu^{2+}-Cu^{2+} and Ni^{2+}-Ni^{2+} pairs.

The resulting electron paramagnetic resonance spectra are quite complex. In addition to various types of weak pair spectra there are also intense single ion spectra. The various pair spectra result from the fact that there are four ions per unit cell and this gives both similar and dissimilar pairs, each with its own set of coordinates relative to the magnetic field axis. Despite these difficulties we have solved for the isotropic exchange parameter for both pairs. Our values do indicate that next nearest neighbor exchange is only about 20% of nearest neighbor exchange. However, it seems most likely that they are of the opposite sign so that the actual nearest neighbor interaction is at least 25% greater in α-$NiSO_4 \cdot 6H_2O$ than our simple molecular field model would indicate.

Recently, inorganic chemists have synthesized a number of transition metal complexes which contain closely coordinated metal pairs. The techniques that we have developed for the pairs in $ZnSeO_4 \cdot 6H_2O$ should be directly applicable to these pair complexes which are model compounds for homogeneous catalysis.

2. MAGNETIC RESONANCE STUDIES OF CATALYTIC COORDINATION SITES IN FERRITIN

Duane L. Lindner and Rollie J. Myers

Our use of electron paramagnetic resonance of transition metal ions to study the structure and function of the iron storage protein, ferritin, has continued. As noted last year we have observed the presence of an Fe(III) binding site on the protein distinct from the iron storage sites. This site is probably of importance to the catalytic functions of the protein during iron uptake and during iron mobilization. We have succeeded in replacing the iron with Cu^{2+} and VO^{2+} in an attempt to probe the structure of the site. Under conditions of proper pH and in the presence of imidazole, the Cu^{2+} EPR spectrum shows splittings due to nitrogenous ligands. Computer simulation of this spectrum reveals that there are four nitrogen nuclei of the coordination sphere of the copper ion. A study of the copper content of the protein as a function of pH and the knowledge that the N-terminal amino acid is acetylated shows the copper to be bound by histidine residues, as well as coordinating one or two imidazole molecules. The spectrum of VO^{2+} bound to the apoprotein is also consistent with bonding by two or three histidine residues. A study of Mn^{2+} binding to apoferritin indicates that while there are two different sites on the protein where this ion binds, neither of them binds it very strongly and from the number of such sites available, neither of these can be identified with the Cu^{2+} binding site.

We have been attempting to study the kinetics of iron mobilization in the presence of Cu^{2+} ion order to confirm the location of the Cu^{2+} binding site relative to an Fe^{2+} binding site.

3. ELECTRON PARAMAGNETIC RESONANCE SPECTRA OF BINUCLEAR FULVALENE COMPLEXES

Michael R. St. John and Rollie J. Myers

Professor James C. Smart, a synthetic inorganic chemist in the Department of Chemistry at Berkeley, has supplied us with some samples of recently prepared bis(fulvalene)dinickel complexes. These complexes were prepared as possible catalysts for the reaction of CO with H_2.

The samples supplied had the general formulae of $Ni_2(C_{10}H_8)_2^{z+}$, where z was 0, 1 and 2. Since the fulvalene is best represented as a dianion this corresponds for the nickel to $(3d)^8$-$(3d)^8$, $(3d)^8$-$(3d)^7$, and $(3d)^7$-$(3d)^7$ pairs. We examined powders of these materials near room temperature at 77K and if necessary at 4.2K. The most distinct electron paramagnetic resonance spectrum in these samples was observed at 4.2K for the $(3d)^8$-$(3d)^7$ material. A very similar spectrum was observed at 77K in the $(3d)^7$-$(3d)^7$ material. None of these spectra have been assigned and further work will have to be done to work out the exchange parameters and energy levels of these complexes.

4. DYNAMIC NUCLEAR POLARIZATION MEASUREMENT FOR AQUEOUS SOLUTIONS OF Cu^{2+} and VO^{2+}

Randall B. Wilson and Rollie J. Myers

During this past year we have assembled a dynamic nuclear polarization spectrometer to operate at 9 GHz. It is a flow design similar to our previous 3 GHz apparatus. With this spectrometer and with 20 watts of microwave power we have been able to observe a 50% polarization of the proton resonance of a dilute solution of VO^{2+} in water.

The purpose of this apparatus is to measure the spin-lattice relaxation sites for Cu^{2+} in aqueous solution at the higher field. Our previous work on Cu^{2+} at 3 GHz indicated that T_1 was quite a bit longer than T_2 for Cu^{2+} in water. Our old results were a little inaccurate and we want to establish the real accuracy of this observation at 9 GHz. The relative sizes of T_1 and T_2 is very much determined by the exact relaxation mechanism, and despite the fact that several papers have been written on this subject, the spin relaxation of Cu^{2+} is still uncertain.

5. RESEARCH PLANS FOR CALENDAR YEAR 1976

Rollie J. Myers

A number of transition metal-containing complexes have been found to be important in homogeneous catalysis. During this year we plan to spend most of our effort in a study of recently synthesized complexes that show promise as catalysts for reactions of CO with H_2. Particular attention will be paid to binuclear complexes containing two transition metals per molecule. Complexes containing more than one transition metal site can have rather subtle oxidation states and coordination properties. These properties make them excellent candidates for catalysts. Our recent methods developed for the electron paramagnetic resonance of transition metal pairs should be directly applicable to these complexes. A series of bis(fulvalene)dimetal complexes have been prepared in Berkeley with a variety of oxidation levels, and we will study the oxidation states and coordination of the transition metals in these complexes using electron paramagnetic resonance. For complexes that are diamagnetic we will use a multi-nuclear magnetic resonance approach, studying the signals from C-13, Co-59, Mn-55, or other nuclei.

There is current interest in two catalyzed reactions involving CO. They are:

$$CO + 2H_2 \rightarrow CH_3OH$$

and

$$3CO + 2H_2O \rightarrow CH_3OH + 2CO_2 .$$

The first reaction can be catalyzed fairly easily although efficient homogeneous catalysts have not yet been found. The second reaction is far more difficult, although the starting reactants are much more reasonable from the energy viewpoint. The final product, methanol, has been predicted to be a very useful fuel and it is volatile enough to be directly used in ordinary gasoline engines.

We also plan to finish our work on the iron storage protein, ferritin. Our primary interest is in the location and coordination of the Fe^{2+} at the "active site" where a catalyzed oxidation to Fe^{3+} is presumed to occur. In addition, we plan to make some dynamic nuclear polarization measurements in aqueous solutions of Cu^{2+} and establish its spin-lattice relaxation times in solution.

6. 1975 PUBLICATIONS AND REPORTS

Rollie J. Myers and Associates

LBL Reports

1. M. R. St. John and R. J. Myers, Electron Paramagnetic Resonance Spectra of Ions Substituted into Transition-Metal Ion Lattices (article accepted by Phys. Rev.), LBL-4165, Sept 1975.

2. M. R. St. John, The Electron Paramagnetic Resonance of Ions Substituted in Paramagnetic Transition Metals Metal Ion Hosts (Ph.D. Thesis), LBL-4185, Nov. 1975.

3. R. C. Wilson and R. J. Myers, Electron Paramagnetic Resonance Spectrum and Spin Relaxation for $Ti(H_2O)_6^{3+}$ in Aqueous Solution and Frozen Glass (article accepted by J. Chem. Phys.), LBL-4189, Oct. 1975.

4. R. C. Wilson, Electron Paramagnetic Resonance Studies of the Relaxation of Copper(II), Titanium(III), and Vanadyl Ions in Solution (Ph.D. Thesis), LBL-4162, Dec. 1975.

d. Physical Chemistry with Emphasis on Thermodynamic Properties

Kenneth S. Pitzer, Principal Investigator

1. QUANTUM CHEMISTRY FOR HEAVY ATOMS

Kenneth S. Pitzer and Yoon S. Lee

Considerable progress was made in the development of a sound yet feasible quantum mechanical theory for heavy atoms, ions, and molecules containing such atoms. In progressing from light atoms to heavy atoms one confronts not only the great increase in number of inner electrons but also the need to use relativistic quantum theory at least for electronic motion near the nucleus of a heavy atom. In building a foundation for a quantum chemistry for heavy atoms we obtained results which were reported in three short papers.

In order to help elucidate the effect of the 4f shell of electrons, Hartree-Fock (HF) calculations were made for the pseudo-atoms corresponding to Hf, Re, Au, Hg, Tl, Pb, and Bi without 4f electrons and with atomic numbers reduced by 14. The orbital energies for these pseudo-atoms are compared with those from HF and relativistic (DHF) calculations for the same atoms. It is found that the relativisitc effect and that of the 4f shell are of comparable magnitude and both are larger for 6s than for 5d or 6p electrons. (Paul S. Bagus, of IBM Research Laboratory, San Jose, participated in this portion of the research.)

In order to determine the effectiveness of a Dirac orbital for bonding in either a metal or a covalent compound, one may examine the angular function for each large component and its capacity to overlap the corresponding function on adjacent atoms. Alternatively, one may determine the appropriate functions for the very strong electric fields arising in bonding situations. Bethe and Salpeter[1] show that for strong electric fields m_ℓ and m_s replace j and m_j as the good quantum numbers. From the more detailed consideration of the angular functions,[2,3] one finds that relativistic s orbitals are appropriate for bonding. But a molecular orbital based on $p_{1/2}$ atomic orbitals is 1/3 σ bonding and 2/3 π antibonding on the basis of the large components. To obtain full σ-bonding character the combination $(1/3\ p_{1/2} + 2/3\ p_{3/2})$ must be taken. The best simple approximation for chemical bonding with p orbitals is to adopt valence states with weighted average $(1/3\ p_{1/2} + 2/3\ p_{3/2})$ energies. Similarly for bonding with d orbitals the $(2/5\ d_{3/2} + 3/5\ d_{5/2})$ average energies are appropriate while for s electrons the relativistic orbital energies may be used directly. These energies are best taken from the calculations of Desclaux.[4]

On the basis just described it was found that elements 112 and 114 should be volatile and relatively inert chemically. Specific estimates are made for the free energies of formation of various compounds. Our results are generally similar to those of Keller, et al,[5] for 114 but differ sharply from any earlier estimates for 112. These estimates should be useful in efforts to separate these elements should they be produced or be thought to exist naturally.

Another application of these concepts of bonding orbitals and promotion energies was made to the fluorides of radon and element 112. It was shown that these might well be ionic $M^{++}F^-_2$ compounds rather than molecular compounds analogous to XeF_2. The very limited data[6] concerning radon fluoride contrasts with the properties of xenon fluoride and seems to support the ionic picture.

1. H. A. Bethe and E. E. Salpeter, Quantum Mechanics of One and Two-Electron Atoms (Academic, New York, 1957).
2. R. E. Powell, J. Chem. Educ. 45, 558 (1968).
3. J. Oreg and G. Malli, J. Chem. Phys. 61, 4349 (1974).
4. J. P. Desclaux, At. Data Nucl. Data Tables 12, 311 (1973).
5. O. L. Keller, Jr., J. L. Burnett, T. A. Carlson, and C. W. Nestor, Jr., J. Phys. Chem. 74, 1127 (1970).
6. L. Stein, Science 168, 362 (1970).

2. OXYGEN-CATALYZED NUCLEAR-SPIN-SPECIES EFFECTS IN THE HEAT CAPACITY OF CH_4

Gerald J. Vogt and Kenneth S. Pitzer

The marked anomaly in the heat capacity of CH_4 shown in Fig. 1 near 0.8K has been found to be

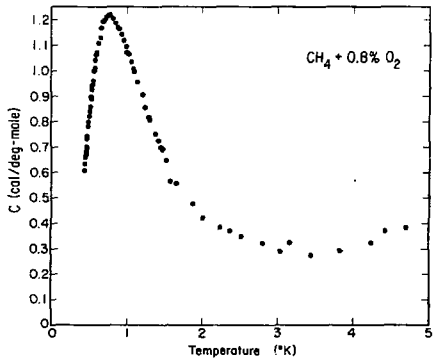

Fig. 1. The heat capacity of methane catalyzed for spin-species conversion. (XBL 756-6533)

quite consistent with the theory proposed by Kataoka, Okada, and Yamamoto. On this basis three-fourths of the CH_4 molecules are on sites of symmetry D_{2d} and are strongly ordered with respect to rotation. The lowest state for spin-

species T is expected to be about 1.9K in energy above the ground state which is for species A. We find this separation to be 1.951K on the basis of the heat capacity below 1.5K. The remaining one fourth of the molecules are orientationally disordered on sites of symmetry O_h and their rotational states are much more widely spaced in energy. Also the lowest states for the spin-species E are at higher energy. The interpretation of our heat capacity values above 1K in terms of the appropriate array of levels is progressing and should be completed soon.

1. Y. Kataoka, K. Okada, and Y. Yamamoto, Chem. Phys. Letters 19, 365 (1973).

3. THEORY OF MOLECULAR OXYGEN IN A METHANE LATTICE AND THE SPIN-SPIN INTERACTION

Janice J. Kim and Kenneth S. Pitzer

In order to help interpret the experimental results for solid CH_4 with O_2 impurity, a theoretical investigation was carried out concerning the quantum energy levels of an O_2 molecule placed in a vacancy in a CH_4 lattice. The oxygen molecule was described as undergoing hindered rotation in a cubic field. The Kramers dipole-dipole interaction between the two unpaired electrons in O_2 was included. Also considered was the mechanism of spin-species conversion of CH_4 by interaction with oxygen. The probability of various transitions was calculated approximately.

4. SOLUTIONS OF ELECTROLYTES: THERMAL PROPERTIES AT HIGH TEMPERATURES

Leonard F. Silvester and Kenneth S. Pitzer

The development of equations for the enthalpy and heat capacity of aqueous sodium chloride to 300°C (as well as for the activity and osmotic coefficients) is nearly complete. The resulting equations fit the very extensive array of experimental data of all types substantially within experimental error. For example, if the activity and osmotic coefficient data are fitted separately at each temperature by equations that fit almost perfectly where data are very precise, the standard deviation at all temperatures is 0.003. This is a fair indication of experimental error. When the single equation is fitted at all temperatures the standard deviation increases only to 0.005. The standard deviations for the single equation are 3.5 kcal/mole for the enthalpy data and 1 kcal/mole deg for the heat capacity.

Since geothermal brines are largely sodium chloride, these results are of great interest in dealing with geothermal power systems based on liquid brines. A report appropriate for this area of application is nearly completed. (This activity was also supported by the geothermal energy and geoscience programs at LBL.)

5. SOLUTIONS OF ELECTROLYTES: WEAK ELECTROLYTES

Kenneth S. Pitzer and Leonard F. Silvester

Equations previously developed and widely applied to the thermodynamic properties of strong electrolytes are extended to solutions involving a dissociation equilibrium. Excellent agreement is obtained with the data for pure phosphoric acid to 6M and for phosphate buffer solutions. The parameters of the strong electrolyte components of the buffer solutions are taken from other work, and the remaining parameters for H^+, $H_2PO_4^-$, and H_3PO_4 are evaluated including a pK of 2.146. The present method avoids ambiguities which formerly arose in treating weak acids with as small pK as this.

6. RESEARCH PLANS FOR CALENDAR YEAR 1976

Kenneth S. Pitzer

The development of a quantum chemistry for heavy atoms will proceed toward more detailed and quantitative calculations. It is expected, at this point, that the best approach will follow the pseudopotential pattern. This approach has been particularly fruitful for solid state calculations on a nonrelativistic basis. The chemically fundamental calculations of bond energies in molecules (or lattice energies in crystals) are somewhat more demanding than many calculations of solid-state interest, but the pseudopotential approach still seems most promising. Relativistic effects will reflect themselves in a different pseudopotential for $P_{1/2}$ as compared to that for $P_{3/2}$ orbitals (and for $d_{3/2}$ vs $d_{5/2}$, etc.), as well as in the absolute magnitude of the potentials in all cases. Initial applications will include cases where anomalous species appear for heavy elements such as Hg_2^{++}, Bi^+, UO_2^{++}, etc.

The work on the thermodynamics of electrolytes will emphasize high temperature properties and be directed to mixed electrolytes as well as to the pure electrolytes, other than NaCl, which are important in geochemical and geothermal brines.

7. 1975 PUBLICATIONS AND REPORTS

Kenneth S. Pitzer and Associates

Journals and Books

1. Kenneth S. Pitzer, Thermodynamics of Electrolytes. V. Effects of Higher Order Electrostatic Terms, J. Soln. Chem. 4, 349 (1975) (LBL-3105).

2. Lawrence S. Bernstein and Kenneth S. Pitzer, Electric Field Deflection of Molecules with Large Amplitude Motions, J. Chem. Phys. 62, 2530 (1975) (LBL-3526).

3. Paul S. Bagus, Yoon S. Lee and Kenneth S. Pitzer, Effects of Relativity and of the Lanthanide Contraction on the Atoms from Hafnium to Bismuth, Chem. Phys. Lett. 33, 408 (1975) (LBL-3787).

4. Kenneth S. Pitzer, Are Elements 112, 114, and 118 Relatively Inert Gases? J. Chem. Phys. 63, 1032 (1975) (LBL-3795).

5. Kenneth S. Pitzer, Fluorides of Radon and Element 118, J. Chem. Soc. Chem. Comm. (1975) 760 (LBL-3942).

6. Kenneth S. Pitzer and Lawrence S. Bernstein, Molecular Structure of XeF_6, J. Chem. Phys. 63, 3849 (1975) (LBL-3934).

7. Gerald J. Vegt and Kenneth S. Pitzer, Spin Species Conversion and the Heat Capacity of Solid Methane near 1K, J. Chem. Phys. 63, 3667 (1975) (LBL-3949).

8. Lawrence S. Bernstein, Janice J. Kim, Kenneth S. Pitzer, Stanley Abramowitz and Ira W. Levin, Potential Function for the ν_7 Vibration of Phosphorus Pentafluoride, J. Chem. Phys. 62, 3671 (1975) (LBL-3790).

9. Interview with Kenneth Pitzer by David Ridgway, J. Chem. Educ. 52, 219 (1975).

LBL Reports

1. Janice J. Kim, Topics in Physical Chemistry: Magnetic Properties of Oxygen, Mixed Electrolyte Solutions, and Pseudorotation in MX_5 Molecules, LBL-3955 (Ph.D. Thesis), Oct. 1975.

2. Kenneth S. Pitzer and Leonard F. Silvester, Thermodynamics of Electrolytes. VI. Weak Electrolytes including H_3PO_4, LBL-4520, (submitted to J. Soln. Chem.), Dec. 1975.

e. Chemical Dynamic Studies

Bruce H. Mahan, Principal Investigator

1. MICROSCOPIC REVERSIBILITY AND DETAILED BALANCE*

In this paper it is shown how the time reversal invariance of the laws of classical mechanics leads to a simple relation between the cross section of a collision process and its microscopic reverse. Assumption of a Boltzmann distribution of translational energies, and averaging of the microscopic collision rate over this distribution then produces the relation

$$k_{12} = k_{21}\left(\frac{\mu_2}{\mu_1}\right)^{3/2} \exp(-\Delta E_{21}/kT)$$

between the rate constant k_{12} of a forward process, and the rate constant for its reverse. Here μ_1 and μ_2 are the reduced masses of reactants and products. If the internal states of the reactants and products are also populated according to the Boltzmann distribution, then one obtains

$$\frac{k_{for}}{k_{rev}} = \frac{Q_p}{Q_r} e^{-\Delta E_o/kT} = K(T) \quad .$$

That is, the ratio of the conventional rate constants for the forward and reverse reactions is equal to the ratio of the partition functions Q_p and Q_r for products and reactants, multiplied by a Boltzmann factor of the zero point energy difference. This in turn is equal to the conventional equilibrium constant. This work is primarily pedagogical, but draws heavily on concepts that have been sharpened through research on collision phenomena.

*Abstracted from J. Chem. Ed. 52, 299 (1975), and LBL-3197.

2. THE $N^+ - H_2$ REACTION

Bruce H. Mahan and Walter E. Ruska

In previous work,[1,2] the dynamics of the reaction $N^+(N_2,H)NH^+$ have been investigated at low and intermediate initial relative collision energies. Electronic state correlation diagrams indicated that at low energies, the reaction should proceed on a potential energy surface which connects to the deep potential well associated with the stable NH_2^+ molecule ion. Experimental evidence was obtained in support of this prediction. The correlation diagrams also indicated that at high energies, the reaction should proceed diabatically on a $^3A_2$ surface, and that this surface should be essentially flat, with no deep wells or prominent barriers. Since the $N^+(H_2,H)NH^+$ reaction is very nearly thermoneutral, its dynamics at high energy should resemble those found for the $O^+(H_2,H)OH^+$ reaction.[3]

We have measured the energy and angular distributions of the products of collisions of N^+ with H_2, HD, and D_2 at initial relative energies above 7 eV. The findings are consistent with our predictions as outlined above. The $N^+ - HD$ case is particularly revealing. The NH^+ product is scattered predominantly in the forward direction near the peak associated with spectator stripping, while the ND^+ is almost exclusively scattered at large angles. In the $N^+ - D_2$ reaction, the spectator stripping peak disappears entirely when product at this velocity is unstable with respect to dissociation, and does not move to a higher velocity in the small angle reaction. On the basis of these findings, it appears that the retention of small angle reactive scattering at high initial relative energies occurs only when the reaction is exoergic, and the potential energy surface displays product repulsion.

1. E. A. Gislason, C. W. Tsao, B. H. Mahan, and A. S. Werner, J. Chem. Phys. 54, 3897 (1971).
2. J. A. Fair and B. H. Mahan, J. Chem. Phys. 62, 515 (1975).
3. K. T. Gillen, B. H. Mahan, and J. S. Winn, J. Chem. Phys. 59, 6380 (1973).

3. SPECTROSCOPY OF GASEOUS IONS

Richard Davis, Frederick Grieman, Bruce H. Mahan, and Ralph Terkowitz

We have completed construction of an apparatus designed to obtain the electronic spectra of gaseous ions by a laser induced fluorescence method. Ions are trapped in a mass selective manner by combined radiofrequency and static potentials applied to the electrodes of a three-dimensional quadrupole trap. The ions are then irradiated with a pulse of light from a tunable dye laser, and the fluorescence so induced is detected with a photomultiplier. After each pulse sequence, the ions are driven from the trap, and their number measured so that the fluorescence signal can be normalized. The pulse sequence is repeated at each wavelength until a satisfactory fluorescent signal has accumulated.

A number of important problems in connection with the experiment have been solved in the past year. Background radiation from the filament of the electron gun used to produce the ions has been effectively eliminated by optical baffling which permits the passage of electrons. The quadrupole trap resolution and general performance has been brought to a satisfactory level. Scattered light from the laser that reaches the photomultiplier has been greatly diminished but continues to be a problem. So far, fluorescence of stable molecules and electron impact induced emission of ions has been observed, but no ion fluorescence has been detected.

4. LOW ENERGY ION BEAM APPARATUS

James A. Farrar and Bruce H. Mahan

We have nearly completed construction of a new crossed ion-neutral beam apparatus which is intended for investigations of ion-molecule reaction dynamics at laboratory energies below 10 eV. The ion source is designed to be flexible so as to be able to produce a variety of ions conveniently. Mass analysis of the projectile ions is performed magnetically with the ions at higher energies, and is followed by a retarding lens chain which brings the ions to the desired laboratory energy. The whole ion source and analysis chain can be maintained at a high temperature so as to promote clean surfaces and minimize loss of intensity due to stray surface charges. The neutral beam source is a version of the supersonic nozzle which leads to an intense neutral beam of well defined energy. The detection train employs a 90° electrostatic ion energy analyzer and quadrupole mass filter enclosed in a chamber that is separately pumped. The path in the detection train is short so that losses of product signal by extraneous scattering are minimized.

5. RESEARCH PLANS FOR CALENDAR YEAR 1976

Bruce H. Mahan

Our immediate plans are to continue to establish the connection between the nature of potential energy surfaces and reaction dynamics by completing the study of the N^+-H_2 reaction, and examining the C^+-H_2 reaction at high energies. When the low energy beam apparatus comes into operation, we shall investigate the dynamics of reactions which are important in the ionosphere, such as

$$O^+ + N_2 \rightarrow NO^+ + N$$

$$N^+ + O_2 \rightarrow NO^+ + O \quad .$$

The high energy beam apparatus will eventually be used to study energy loss processes in the collisions of protons and deuterons with atmospheric molecules. During 1976, it should be possible to make the first attempts to obtain the spectra of gaseous ions with our laser induced fluorescence apparatus. If these experiments are successful, we shall concentrate on obtaining information concerning the electronic, vibrational, and rotational energy levels of small molecular ions.

6. 1975 PUBLICATIONS AND REPORTS

Bruce H. Mahan and Associates

Journals and Books

1. Bruce H. Mahan, Microscopic Reversibility and Detailed Balance, J. Chem. Ed. 52, 299 (1975) (LBL-3197).

2. Bruce H. Mahan, An Analysis of Direct Ion-Molecule Reactions, in "Interactions Between Ions and Molecules", P. Ausloos, editor (Plenum Publishing Co., New York, 1975) (LBL-3155).

3. Bruce M. Mahan, Electronic Structure and Chemical Dynamics, Accounts Chem. Res. 8, 55 (1975) (LBL-3525).

4. James A. Fair and Bruce H. Mahan, Dynamics of the Reaction of N^+ with H_2. II. Reactive Scattering at Relative Energies Below 5 eV, J. Chem. Phys. 62, 515 (1975) (LBL-3501).

5. Bruce H. Mahan, University Chemistry, 3rd edition (Addison-Wesley Pub. Co., 1975).

f. Theory of Low Energy Atomic and Molecular Collisions

William H. Miller, Principal Investigator

1. QUANTUM MECHANICAL TRANSITION STATE THEORY*

Sally Chapman, Bruce C. Garrett, and William H. Miller

Classical transition state theory provides an excellent description of the threshold region of chemical reactions which have an activation barrier. Figure 1, for example, shows the comparison of classical transition state theory to a classical trajectory calculation (the exact result within the realm of classical mechanics) for the $H + H_2 \rightarrow H_2 + H$ reaction in three dimensional space. The agreement is almost exact for energies up to 0.4 eV above the barrier height and is only 10% in error at 1 eV above the barrier height.

Quantum effects are important in the threshold region, however, so that a quantum mechanical version of transition state theory is required to describe real chemical reactions. The conventional quantum mechanical version of transition state theory works poorly in the threshold region, however, because it assumes that the Hamiltonian is separable about the saddle point. To have a quantitative theory one must apply transition state theory quantum mechanically and without approximating the Hamiltonian by a separable one.

A formal definition of such a quantum mechanical version of transition state theory has been given,[1] and its evaluation has been carried out using semiclassical approximations. The rate constant for reaction is given in this semiclassical limit of the theory by

$$k = (2\pi\hbar Q_a)^{-1} \int_0^\infty dE\, e^{-\beta E} N(E) \quad , \quad (1)$$

where Q_a is the usual partition function for reactants; the function N(E) is given by

$$N(E) = \sum_{n=0} \frac{1}{1+e^{2\theta(E_n)}} \quad , \quad (2)$$

where E_n is defined as the root of the equation

$$E_n = E - (n+\tfrac{1}{2})\hbar\omega(E_n) \quad . \quad (3)$$

The functions $\theta(E)$ and $\omega(E)$ are the classical action and stability frequency, respectively, for the periodic classical trajectory with energy E on the inverted potential energy surface, and they replace the "barrier penetration integral" (the exponent of the tunneling probability) and the vibrational frequency of the "activated complex" which appear in conventional transition state theory.

Figure 2 shows the function N(E) given by Eq. (2), compared to the exact result of quantum scattering theory, for a collinear version of the $H + H_2$ reaction. The good agreement over many orders of magnitude indicates that our basic hypothesis is correct, i.e., that transition state theory does describe the threshold of reactions accurately if the separability approximation is removed.

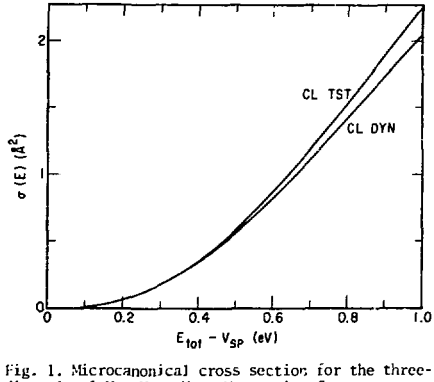

Fig. 1. Microcanonical cross section for the three-dimensional $H + H_2 \rightarrow H_2 + H$ reaction from a (microcanonical) classical trajectory calculation (CL DYN) and (microcanonical) classical transition state theory (CL TST), as a function of total energy above the saddle point of the potential energy surface. (XBL 7410-7518)

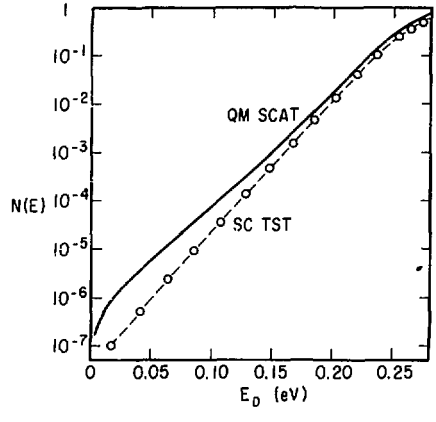

Fig. 2. N(E) as a function of initial translational energy E_o ($E = E_o + \varepsilon_{v=0}^{H_2}$). (XBL 751-5660)

*Abstracted from J. Am. Chem. Soc. 97, 892 (1975); J. Chem. Phys. 62, 1899 (1975); and J. Chem. Phys. 63, 2710 (1975). (Supported in part by the National Science Foundation.)

1. W. H. Miller, J. Chem. Phys. 61, 1823 (1974).

2. SEMICLASSICAL EIGENVALUES FOR MULTI-DIMENSIONAL SYSTEMS*

Sally Chapman, Bruce C. Garrett, and William H. Miller

We have shown that the semiclassical quantum condition resulting from periodic orbit theory is

$$\Phi(E) - \Phi'(E) \sum_{i=1}^{f-1} \hbar\omega_i(E) \left(n_i + \frac{1}{2}\right) = 2\pi\hbar\left(n_f + \frac{1}{2}\right) \quad , \quad (1)$$

where $\Phi(E)$ is the classical action along the periodic orbit with energy E, $\{\omega_i\}$ are the f-1 stability frequencies for the system with f degrees of freedom, and $\{n_i\}$, i=1,..., f are integers. Although this clarifies and corrects some earlier inconsistencies in periodic orbit theory, the approach itself is limited in that it implicitly assumes that most of the energy is in just one degree of freedom.

A more satisfactory approach is Born's formulation[1] that considers the classical Hamiltonian first in terms of some "zeroth order" action-angle variables $\underline{n}$ and $\underline{q}$,

$$H(\underline{n},\underline{q}) = H_0(\underline{n}) + V(\underline{n},\underline{q}) \quad , \quad (2)$$

where H_0 is a reference (i.e., separable) Hamiltonian and V is a nonseparable interaction which precludes the action variables $\underline{n} = \{n_i,q_i\}$ from being constants of the motion. The task is then to construct a canonical transformation from the variables $(\underline{n},\underline{q})$ to the "good" action-angle variables $(\underline{N},\underline{Q})$ such that the total Hamiltonian depends only on the action variables $\{N_i\}$,

$$H(\underline{N},\underline{Q}) \equiv E(\underline{N}) \quad . \quad (3)$$

The actions $\{N_i\}$ are then constants of the motion and semiclassical eigenvalues are given by Eq. (2) with the $\{N_i\}$ required to be integers.

We have found a way actually to carry out Born's canonical transformation non-perturbatively (i.e., numerically) and have applied the relavant equations to the following two-dimensional system:

$$H(p_x,p_y,x,y) = \tfrac{1}{2} m(p_x^2 + p_y^2) + \tfrac{1}{2} m(\omega_x^2 x^2 + \omega_y^2 y^2) + \lambda x(y^2 + \eta x^2) \quad , \quad (4)$$

where λ and η constants.

Figure 1 shows a comparison of the semiclassical and exact quantum mechanical eigenvalues for the lowest three states, as a function of the non-separable strength parameters. One sees that the agreement is quite good, even when the eigenvalue is very near the dissociation limit (shown by the dotted lines).

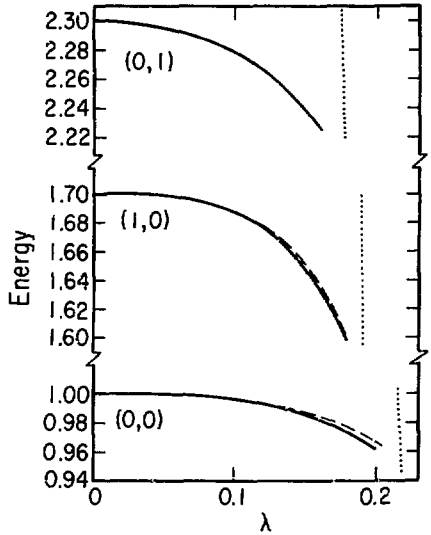

Fig. 1. Semiclassical (dashed line) and exact quantum (solid line) eigenvalues for the three lowest states of the system specified by Eq. (4), with $\omega_1 = 0.7$, $\omega_2 = 1.3$, and $\eta = -\lambda$. The dotted line is the position of a saddle point of the potential surface as a function of λ.

(XBL 757-6717)

*Abstracted from J. Chem. 63, 996 (1975) and LBL-3990. (Supported in part by the National Science Foundation.)

1. M. Born, The Mechanics of the Atom, Ungar, N.Y., 1960.

3. COOLING OF THE 6 CM AND 2 CM DOUBLETS OF INTERSTELLAR H_2CO BY COLLISION*

B. J. Garrison, W. A. Lester, Jr.,† and W. H. Miller

The $1_{11} \rightarrow 1_{10}$ transition of formaldehyde is seen in absorption against the 2.7°K cosmic background radiation in cool interstellar dust clouds, indicating that the lower state (1_{11}) has a population greater than would be expected if

the system were in equilibrium with the background radiation.[1,2] Townes and Cheung[3] have noted that since the 2_{12} state spontaneously decays (via a dipole-allowed transition) to the 1_{11} state, collisional excitation which favors the 2_{12} over the 2_{11} state could produce the observed "cooling" (i.e., enhancement of the population of the 1_{11} state). They further argue[3] that since the 2_{12} state corresponds to the rotational angular momentum being predominantly about the axis perpendicular to the plane of the molecule, collisional excitation of formaldehyde from a j=1 state to a j=2 state should indeed be preferentially to the 2_{12} state.

To test this hypothesis of a "collisional pump", a completely ab initio calculation has been carried out. A potential energy surface,[4] including electron correlation, was calculated for H_2CO-He, rotational cross sections were determined by solving the coupled channel Schrödinger equations, and steady-state populations of the various rotational levels of H_2CO were computed by solving the appropriate kinetic equations (including radiative processes). The background radiation temperature was assumed to be 2.7°K, and the kinetic (i.e., translational) temperature was varied between 5°K and 20°K.

Excitation temperatures for the 1_{11}-1_{10} (T_{12}) and 2_{12}-2_{11} (T_{34}) levels are shown in Fig. 1. (The "excitation temperature" T_{12}, for example, is simply the temperature which, inserted into the Boltzmann expression, gives the steady state population ratio of the 1_{11} and 1_{10} levels.) In the limit of no collisions (i.e., no He, $n \to 0$), the excitation temperatures approach that of the background radiation, 2.7°K, while in the limit of high density (rapid collisions) they approach the kinetic temperature T_K. For intermediate densities, however, one does see the cooling effect, excitation temperatures below that of the background radiation.

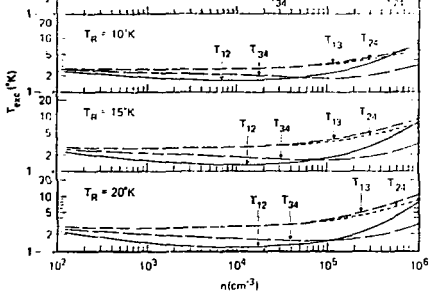

Fig. 1. Excitation temperatures for the 1_{11}-1_{10} (T_{12}) and 2_{12}-2_{11} (T_{34}) levels as a function of He density at selected kinetic temperatures T_K.
(XBL 768-10076)

Our results, therefore, support the collisional mechanism as the source of the cooling.

---

*Abstracted from Astrophys. J. Lett. 200, L175 (1975). (Supported in part by the National Science Foundation and by the Office of Naval Research.)

†Non-LBL personnel.

1. P. Palmer, B. Zuckerman, D. Buhl, and L. E. Snyder, Astrophys. J. 156, L147 (1969).
2. N. J. Evans, G. Morris, T. Sato, and B. Zuckerman, in preparation.
3. C. H. Townes and A. C. Cheung, Astrophys. J. 157, L103 (1969).
4. B. J. Garrison, W. A. Lester, Jr., and H. F. Schaefer III, J. Chem. Phys. 63, 1449 (1975).

4. SEMICLASSICAL DESCRIPTION OF DIFFRACTION IN ELASTIC SCATTERING*

George E. Zahr and William H. Miller

Semiclassical theory has had notable success in describing many of the quantum effects in elastic scattering--interference effects, the rainbow effect, glory oscillations, etc. Diffraction from a purely repulsive potential had been thought to lie outside the realm of a semiclassical description, but the present work shows this not to be the case.

In the usual semiclassical approximation to the partial wave sum for the scattering amplitude,

$$f(\theta) = \frac{1}{2ik} \sum_{\ell=0}^{\infty} (2\ell+1)\, P_\ell(\cos\theta)\, e^{2i\eta_\ell} , \qquad (1)$$

the values of ℓ which contribute within the stationary phase approximation are those which satisfy the classical relation

$$\Theta(\ell) = \pm\, \theta , \qquad (2)$$

where $\Theta(\ell) \equiv 2\eta'(\ell)$ is the classical deflection function. If the potential is purely repulsive, the $\Theta(\ell)$ is positive for all ℓ so that there is only one value of ℓ which satisfies Eq. (2); i.e., there is no value of ℓ which satisfies

$$\Theta(\ell) = -\theta . \qquad (3)$$

With only one value of ℓ contributing to the partial wave sum there is no interference structure in the cross section

$$\sigma(\theta) = |f(\theta)|^2 . \qquad (4)$$

On more thoughtful analysis, however, one finds that Eq. (3) does have solutions for complex values of ℓ. When this is taken into account the amplitude has two terms--from the two stationary phase values of ℓ, one real and one complex--so that there is now an interference structure predicted by Eq. (4).

Figure 1 shows how our theory works for a simple test case. The solid line is the exact quantum mechanical differential cross section and the dashed line the result of our semiclassical theory, while the dotted line (with no interference structure) is the result of the conventional approach.

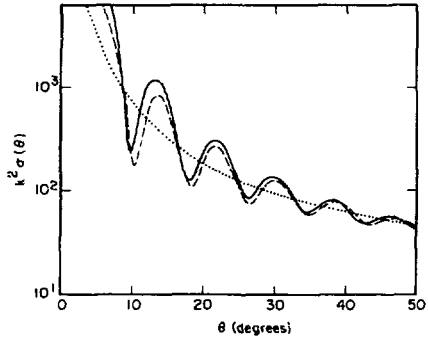

Fig. 1. Comparison of the quantum mechanical differential cross section (solid line) with that given by the present semiclassical theory (dashed line) and the conventional semiclassical approach (dotted line). (XLB 7412-7810)

*Abstracted from Mol. Phys. 30, 951 (1975). (Supported in part by the National Science Foundation.)

5. SEMICLASSICAL THEORY OF ATOMIC SCATTERING FROM SOLID SURFACES*

R. I. Masel,† R. P. Merrill,† and W. H. Miller

Diffraction of atoms (or molecules) from crystal surfaces is ideally described by "classical S-matrix" theory, a general semiclassical approach that combines classical dynamics and quantum mechanical superposition in a consistent theory. We have used it to analyze measurements of helium atom diffraction from the tungsten 112 surface and thus determine the potential function which characterizes the He-W(112) interaction. Figure 1 shows the calculated diffraction intensity compared to the experimental results.

To verify the accuracy of the semiclassical theory we have applied it to a simple model problem, a hard sinusoidal corrogated surface (i.e., bumpy in one direction but smooth in the other), and have also calculated the exact quantum mechanical results for the problem. If z is the direction perpendicular to the surface, the model is defined explicitly by the potential function

$$V(x,y,z) = 0, \quad z > D(x)$$
$$+\infty, \quad z < D(x) \ , \qquad (1)$$

where

$$D(x) = aH \sin(x/a) \quad ;$$

H is the "roughness" of the surface and "a" a length parameter.

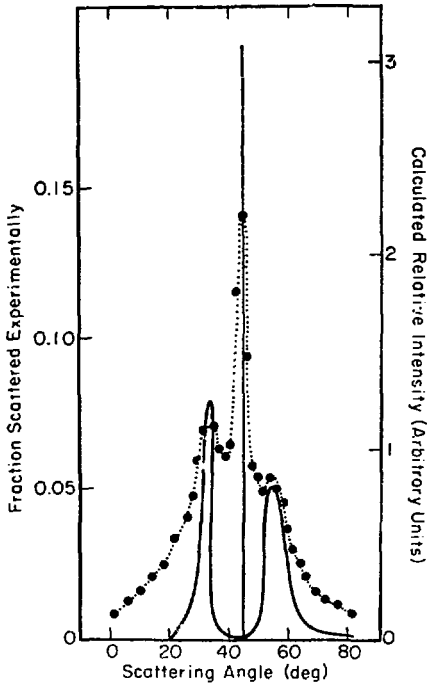

Fig. 1. Helium atom diffraction from tungsten 112, solid line is the calculated (theoretical) result and the dots are the experimental measurement. (XBL 768-10078)

A number of semiclassical and quantum mechanical results have been calculated for the model defined by Eq. (1), and there is in general excellent agreement between the two. Figure 2, for example, shows the intensity of the specular diffraction peak as a function of energy, for the (exact) quantum mechanical calculation and the semiclassical one. The agreement is within a few percent over the entire energy range.

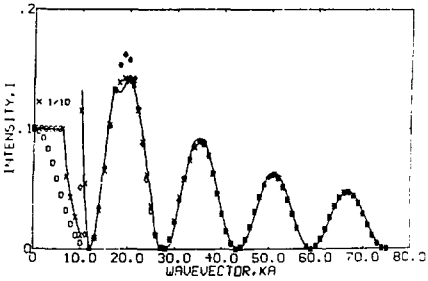

Fig. 2. Specular intensity as a function of the reduced wave vector $\kappa \equiv ka$. (XBL 768-10077)

---

*Abstracted from J. Chem. Phys. 63, 996 (1975) and Phys. Rev. B. 12, 5545 (1975). (Supported in part by the National Science Foundation.)

†Non-LBL personnel.

6. RESEARCH PLANS FOR CALENDAR YEAR 1976.

William H. Miller

We have recently made considerable progress toward solving an old, classic problem--determining the semiclassical eigenvalues of a non-separable, multi-dimensional system. The most direct application of this is to the vibrational spectrum of simple polyatomic molecules. Since the simple normal mode approximation breaks down for highly excited states--which are probed nowadays with intense laser sources--this theory may provide the framework for analyzing highly excited vibrational states. Initial application is planned for the vibrational spectrum of H_2O.

A topic closely related to that above is unimolecular isomerization or decomposition of molecules highly excited either by collisions (i.e., thermally) or by light (i.e., photochemically). The semiclassical eigenvalue analysis that we have developed can provide a great deal of insight into unimolecular dynamics. One of the applications of some current interest is the isomerization of hydrogen isocyanide

$$HNC \rightarrow HCN .$$

HNC is not stable under laboratory conditions--but has been observed in interstellar space--and one would like to understand this on the basis of its unimolecular dynamics.

For several years we have been interested in Penning ionization by metastable helium

$$He^* + A \rightarrow He + A^+ + e^-$$
$$\rightarrow HeA^+ + e^- ,$$

where A is an atom with an ionization potential less than the excitation energy (~ 20 eV) of He*. Work is planned to study in some detail collisional ionization of a diatomic molecule, for which a greater variety of products is possible:

$$He^* + AB \rightarrow He + AB^+ + e^-$$
$$\rightarrow HeAB^+ + e^-$$
$$\rightarrow HeA^+ + B + e^-$$
$$\rightarrow HeB^+ + A + e^-$$
$$\rightarrow He + A^+ + B + e^-$$
$$\rightarrow He + A + B^+ + e^- .$$

Plans are to compute the potential energy surface and autoionization rate for the He^*-A-B system and then to carry out the scattering calculation using classical trajectories (along which autoionization is allowed to take place with the appropriate probability).

7. 1975 PUBLICATIONS AND REPORTS

William H. Miller and Associates

Journals

1. G. E. Zahr, R. K. Preston, and W. H. Miller, Theoretical Treatment of Quenching in $O(^1D) + N_2$ Collisions, J. Chem. Phys. 62, 1127 (1975) (LBL-3192).

2. S. Chapman, S. M. Hornstein, and W. H. Miller, Accuracy of Transition State Theory for the Threshold of Chemical Reactions with Activation Energy: Collinear and Three-Dimensional $H + H_2$, J. Am. Chem. Soc. 97, 892 (1975) (LBL-3504).

3. W. H. Miller, Semiclassical Limit of Quantum Mechanical Transition State Theory for Non-Separable Systems, J. Chem. Phys. 62, 1899 (1975) (LBL-3541).

4. W. H. Miller, The Classical S-Matrix in Molecular Collisions, Advances in Chemical Physics 30, 77 (1975) (LBL-2521).

5. W. H. Miller, Semiclassical Quantization of Non-Separable Systems: A New Look at Periodic Orbit Theory, J. Chem. Phys. 63, 996 (1975) (LBL-3763).

6. W. H. Miller, Path Integral Representation of the Reaction Rate Constant in Quantum Mechanical Transition State Theory, J. Chem. Phys. 63, 1166 (1975) (LBL-3788).

7. R. N. Porter, L. M. Raff, and W. H. Miller, Quasiclassical Selection of Initial Coordinates and Momenta for a Rotating Morse Oscillator, J. Chem. Phys. 63, 2214 (1975)(LBL-4559).

8. G. E. Zahr and W. H. Miller, Semiclassical Theory of Diffraction in Elastic Scattering, Mol. Phys. 50, 951 (1975) (LBL-3545).

9. S. Chapman, B. C. Garrett, and W. H. Miller, Semiclassical Transition State Theory for Non-Separable Systems: Application to the Collinear H + H_2 Reaction, J. Chem. Phys. 63, 2710 (1975) (LBL-3591).

*10. F. T. Smith, D. L. Huestis, D. Mukherjee, and W. H. Miller, Semiclassical Perturbation Scattering by a Rigid Dipole, Phys. Rev. Lett. 35, 1073 (1975)

11. B. J. Garrison, W. A. Lester, and W. H. Miller, Cooling of the 6 cm and 2 cm Doublets of Interstellar H_2CO by Collision: An Accurate Quantum Mechanical Calculation, Astrophys. J. 200, L175 (1975) (LBL-3972).

*12. R. I. Masel, R. P. Merrill, and W. H. Miller, Quantum Scattering from a Sinusoidal Hard-Wall--Atomic Diffraction from Solid Surfaces, Phys. Rev. B, 12, 5545 (1975).

Papers Presented

1. W. H. Miller, "Semiclassical Methods in Inelastic and Reactive Scattering", IIIrd International Workshop on Gross Properties of Nuclei and Nuclear Excitations, Hirschegg, Austria, January 13-18, 1975.

2. S. Chapman, B. Garrett, and W. Miller, "Semiclassical Transition State Theory for Non-Separable Systems: Application to the Collinear H + H_2 Reaction", IXth International Conference on the Physics of Electronic and Atomic Collisions, Seattle, July 24-30, 1975.

3. A. P. Hickman, A. D. Isaacson, and W. H. Miller, "New Method for Calculating Widths for Penning Ionization", IXth International Conference on the Physics of Electronic and Atomic Collisions, Seattle, July 24-30, 1975.

4. W. H. Miller, "Semiclassical Theory of Electronically Non-Adiabatic Processes in Molecular Collisions", Workshop on Potential Energy Surfaces and Non-Adiabatic Phenomena, Orsay, France, July 6 - August 31, 1975.

LBL Reports

1. Andrew Wesley Raczkowski, Vibrational Inelasticity in H_2 Collisions with He and Li^+, (Ph.D. Thesis), LBL-3798, Sept. 1975.

2. Barbara Jane Garrison, Cooling of Interstellar Formaldehyde by Collision with Helium: An Accurate Quantum Mechanical Calculation, (Ph.D. Thesis), LBL-3940, Aug. 1975.

3. A. P. Hickman, A. D. Isaacson and W. H. Miller, Calculation of Autoionization State of He and H^-, Chem. Phys. Lett., LBL-3971, July 1975.

4. S. Chapman, B. C. Garrett and W. H. Miller, Semiclassical Eigenvalues for Non-Separable Systems: Non-Perturbative Solution of the Hamilton-Jacobi Equation in Action-Angle Variables, J. Chem. Phys., LBL-3990, July 1975.

5. R. I. Masel, R. P. Merrill and W. H. Miller, Semiclassical Theories and Quantum Hardwall Calculations of Atom Surface Scattering, J. Vac. Sci. Tech., LBL-4553, Oct. 1975.

6. W. H. Miller, Semiclassical Eigenvalues for Irregular Spectra, J. Chem. Phys., LBL-4561, Dec. 1975.

g. Photoelectron Spectroscopy

David A. Shirley, Principal Investigator

Introduction. This program transferred from Nuclear Chemistry during Divisional reorganization, so a brief history will be given. In 1958 the principal investigator joined Lawrence Berkeley Laboratory, and a project was built involving hyperfine interactions studied with nuclear radiations. In 1966 the first x-ray photoelectron spectroscopy program in the United States was begun in this project. The photoelectron spectroscopy program has broadened in scope to include solid-state, molecular, and atomic studies, while the hyperfine interactions work is being phased out. The reports below are grouped in several general interest areas.

A. Band Structure and Surface Physics (Reports 1 - 5)
B. Many-Electron and Correlation Effects (Reports 6 - 12)
C. Electronic Binding Energies of Elements 1 - 30. (Report 13)
D. Molecular Orbital Studies (Reports 14 - 17)
E. Hyperfine Structure (Reports 18 - 21)

1. CROSS SECTION AND SURFACE EFFECTS IN SOFT X-RAY PHOTOEMISSION FROM Cu AND Ag VALENCE BANDS

J. Stöhr, F. R. McFeely, G. Apai, P. Wehner, and D. A. Shirley

Photoelectron spectroscopy is the technique of choice to study the total electronic valence-band density of states in solids. Until recently, however, this technique has been severely inhibited by the lack of suitable variable-energy photon sources. Synchrotron radiation can provide such a source. In the United States the Stanford Synchrotron Radiation Project (SSRP), on the SPEAR ring at SLAC, is uniquely capable of producing variable-energy photon beams in the entire 50 - 250 eV range and in sufficient intensity for photoemission studies. Here we report such studies on Cu (3d) and Ag (4d) valence bands (VB) in the photon energy range 50 - 175 eV. Experiments were carried out on polycrystalline samples that were produced by in situ evaporation of the metals under a vacuum of $\sim 10^{-9}$ Torr. The photoelectrons were detected by a cylindrical mirror analyzer operated in the retarding mode (constant resolution of 0.3 eV). Experimental results for Cu are shown in Fig. 1. Common features of all spectra are the three peaks at ~2.3 eV, ~3.4 eV, and ~4.5 eV binding energy (BE) relative to the Fermi level. The most distinct changes in the shape of the VB spectra occur between 50 and 70 eV. While the peak positions remain essentially unshifted the relative intensities of the two high BE peaks increase with photon energy. Above 70 eV this trend continues in a less spectacular way, resulting in a slightly broader overall structure which at the highest energies approaches the spectrum observed with Al Kα (hν = 1486 eV) radiation.[1]

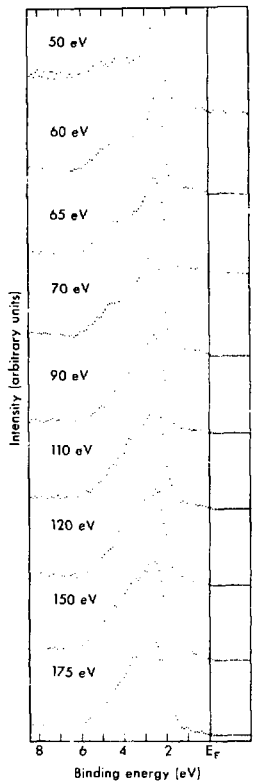

Fig. 1. Photoemission from the 3d valence band of polycrystalline Cu as a function of photon energy. (XBL 761-2005)

Figure 2 shows the photoelectron energy distribution (PED) for Ag. The spectra basically consist of two peaks at ~4.8 eV and ~6.4 eV BE relative to the Fermi level. As is the case in Cu, the peak positions remain unshifted with energy and only the relative peak heights change. The most prominent changes occur between 110 and 130 eV, where the peak heights are inverted relative to the higher and lower photon energy range. Simultaneously the inelastic background on the high BE side increases and at hν = 130 eV another smaller broad peak at ~9 eV BE becomes apparent. We have analyzed the observed changes

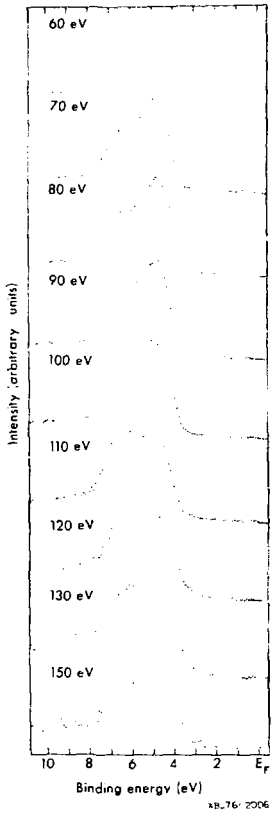

Fig. 2. Photoemission from the 4d valence band of polycrystalline Ag as a function of photon energy. (XBL 761-2006)

in the shape of the PED's of Cu by the following model of photoemission. The calculation of the PED's consists of a k-space integration over all initial and final states between which a transition can occur (conservation of energy and momentum) where each transition is weighted by the square of the transition matrix element. The initial state eigenvalues and eigenfunctions were obtained from a linear combination of atomic orbitals (LCAO) band structure calculation.[2] The final state was described by an orthogonalized plane wave (OPW) and the eigenvalues were calculated from a free electron model.[3]

The results of such a calculation are displayed in Fig. 3a. When compared to the experimental PED's in Fig. 3b, it is seen that reasonable agreement exists for $h\nu < 70$ eV and $h\nu \geq 120$ eV. The observed PED's are not reproduced well around $h\nu = 90$ eV. It should be pointed out, however, that our calculation predicts essentially constant line positions (3 peak structure) over the entire energy range, in complete agreement with experiment. In Fig. 3c we show the results of a calculation that assumes momentum broadening in the final state. The listed values for the parameter B represent a measure of the broadening in percent; i.e., $B = 100\ \Delta q_i/|\vec{q}|$ (i=x,y,z) where $\vec{q}$ is the final state momentum. The PED's calculated with this model show good agreement with experiment. The peak structure, which is seen to be too pronounced in our calculated spectra, arises entirely from the initial state band structure rather than from the transition matrix elements.

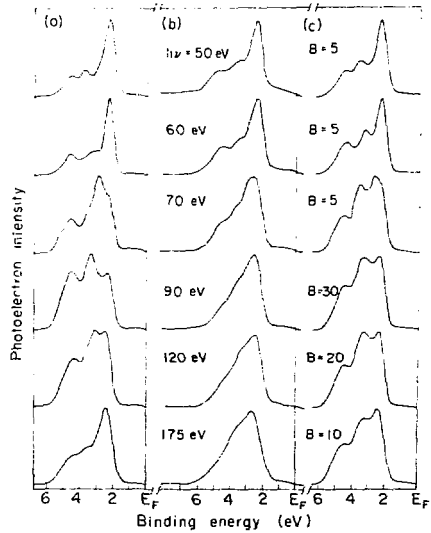

Fig. 3. a) PED calculation for Cu assuming k-conservation (direct transitions), b) Experimental results for Cu. The original data shown in Fig. 1 were corrected for their inelastic background. c) PED calculation for Cu assuming k-broadening in the final state. The broadening factors B are discussed in the text.
(XBL 761-2110)

Momentum broadening in the final state may arise from a minimum in the photoelectron mean free path. Figure 4 shows a plot of the electron mean free path versus its kinetic energy as taken from Ref. 4. As has been discussed by Feibelman and Eastman[5] such inelastic damping in the final state, which restricts the source region of the

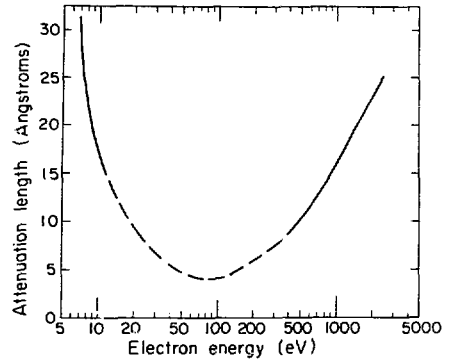

Fig. 4. Photoelectron mean free path versus its kinetic energy. The dotted line indicates an average for various materials (compare Ref. 4). (XBL 7212-4882)

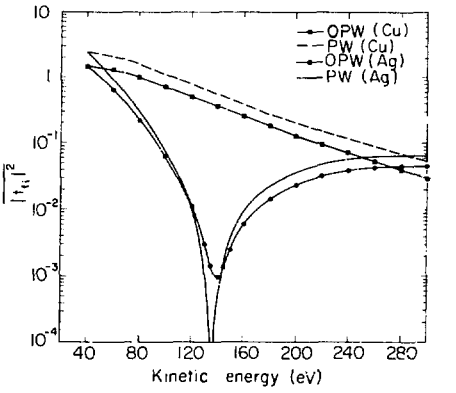

Fig. 5. Square of the radial transition matrix element

$$\overline{(|t_{fj}|^2)}$$

for Cu (3d) and Ag (4d) as a function of the kinetic energy of the photoelectron. PW means plane wave, OPW means orthogonalized plane wave final state. (XBL 761-2106)

photocurrent near the surface, results in an uncertainty or spread of the final-state momentum component perpendicular to the surface. The magnitude of the broadening factors in Fig. 3c indicates that the region of highest surface sensitivity occurs around hν = 90 eV or at a kinetic energy (E_{kin} = hν - work function - binding energy) of about 80 eV, which agrees remarkably well with the minimum of the curve in Fig. 4. On the other hand, the observed changes in the PED's for hν < 70 eV are predicted correctly by the direct transition model. The observed changes in peak intensities in this region can therefore be attributed to cross-section effects. In the case of Cu, the radial part of the transition matrix element is a monotonically decreasing function of energy (Fig. 5) and can therefore not be responsible for the observed changes. The angular part, however, is sensitively dependent on which final state can be reached at a given photon energy. We believe that this part of the matrix element gives rise to the observed effects.

The case of Ag is more complex. The inversion of the peak intensities in the range 110 - 130 eV may be attributed in part to the increasing inelastic high BE tail in this energy range. The broad additional peak at ~9 eV BE, which slowly develops in the region 110 - 130 eV, is thought to arise from plasmons. Its absence in all other spectra seems to point to a maximum in the electron - plasmon scattering in this energy range. Because of the high surface sensitivity in this photon energy region, surface plasmon excitation is thought to be mainly responsible for the enchanced inelastic background. At 130 eV one deduces a value of 3.8 ± 0.5 eV for the separation of the broad peak at ~9 eV from the middle of the 4d structure. This value is in good agreement with the values 3.6 eV and 3.9 eV which were previously found for the surface and bulk plasmon frequencies.[7] Finally, we point out another possible reason why the high BE peak in Ag is more pronounced in the 110 - 130 eV range than is the low BE peak. From Fig. 5 it is seen that for Ag the radial dipole element varies much more strongly with energy than it does for Cu and has a minimum at about 140 eV. At first, the minimum in 4d cross section tends to emphasize the relative intensity in the inelastic tail. Secondly, the slope of the curve in Fig. 5 is steepest for E_{kin} > 100 eV; and in this range there is a considerable change in cross section even over an energy interval of 3 eV, which corresponds to the peak separation in the Ag valence band. Thus in this range the high BE peak will always have a slightly larger cross section than the low BE peak. Although this is also true for E_{kin} < 100 eV there are effects of the angular matrix element in this regime (e.g., in Cu) which might compensate for the radial matrix element effect. On the other hand for E_{kin} > 130 eV the radial dipole matrix element favors the low BE peak.

In conclusion, photoemission experiments in the range 50 - 200 eV reveal several new phenomena which are not observed in conventional ultraviolet (hν < 40 eV) or x-ray (hν ~ 1 keV) spectroscopy. For Cu, we have pointed out a close connection between surface effects and effects that arise from the angular dipole matrix element. For Ag, cross-section effects deriving from the radial matrix element are found to be important. Independently, the high surface sensitivity in

the region studied allows us to observe inelastic electron loss structure that is not seen at other photon energies.

1. See, for examples, G. K. Wertheim, D. N. E. Buchanan, N. V. Smith, and M. M. Traum, Phys. Lett. 49A, 191 (1974).
2. L. Hodges, H. Ehrenreich, and N. D. Lang, Phys. Rev. 152, 505 (1966).
3. L. Pincherle, Electronic Energy Bands in Solids, (MacDonald, London, 1971) pp. 104 - 108.
4. C. R. Brundle, Surface Science 48, 99 (1975).
5. P. J. Feibelman and D. E. Eastman, Phys. Rev. B 10, 4932 (1974).
6. C. J. Powell, Surface Science 44, 29 (1974) and references therein.
7. H. Raether, Springer Tracts in Modern Physics 38, 84 (1965).

2. DIRECTIONAL ANISOTROPY IN PHOTOEMISSION FROM VALENCE BANDS OF Cu AND Au CRYSTALS USING 32-280 eV SYNCHROTRON RADIATION

J. Stöhr, F. R. McFeely, G. Apai, P. Wehner, R. S. Williams, and D. A. Shirley

Angle-resolved photoemission from single crystals had not been observed until recently when spectra were reported in the ultraviolet (UPS)[1,2] and x-ray (XPS)[3] range of photoemission. We have made the first investigation of this kind in the intermediate energy range 32 eV - 280 eV.

Using the first six 8-hour shifts dedicated to synchrotron radiation on the SPEAR ring at SLAC (as contrasted to running in a parasitic mode on high-energy physics experiments), we have studied the valence bands of copper and gold single crystals, obtaining angle-resolved photoemission energy distributions (PED) of electrons emitted along the [100] and [111] directions. Dramatic differences were found between the two directions and strong variations with energy were observed even at photon energies above 100 eV.

In copper (Fig. 1), several distinct trends were apparent. The 4s bands, between the Fermi energy and 2 eV binding energy, are strongest at $h\nu$ = 65 eV in the [111] direction but at $h\nu$ = 110 eV in the [100] direction. A 3d band feature at 4 eV binding energy in the [100] spectrum shows a broad resonance in intensity, peaking near $h\nu$ = 110 eV.

Gold showed similar behavior. Maximal 6s band intensity was observed at $h\nu$ = 40 eV in the [111] direction with a possible broad maximum at higher energy in the [100] direction (Fig. 2). A 5d-band feature at 6 eV binding energy in the [100] spectrum shows a resonance in intensity at $h\nu$ = 100 eV. In the [111] spectrum, a peak at this energy (6 eV) is very intense at $h\nu$ = 130 eV, the highest photon energy studied.

The spectra obtained here in an angle-resolved mode from single crystals exhibit considerably

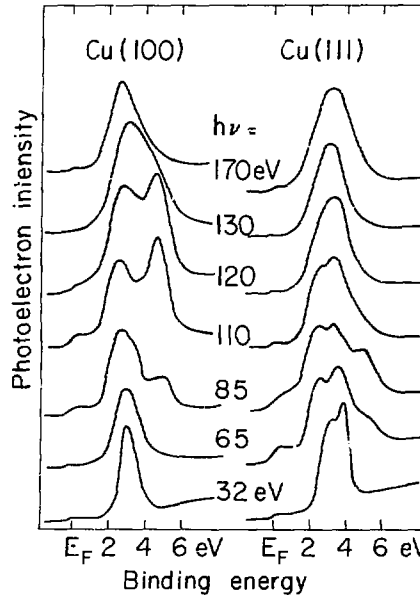

Fig. 1. Valence-band photoemission spectra of a copper single crystal in the [100] and [111] directions, using variable-energy synchrotron radiation from the SPEAR storage ring. Only 30% of the spectra taken are shown. (XBL 761-2111)

more structure and variation of structure than the angle-integrated spectra studied in the previous report. The difference between angle integrated photoemission (AIP) and angle resolved photoemission (ARP) arises from two macroscopic sources: (1) the direction of the photon $\vec{E}$ vector relative to the crystalline axes, and (2) the position of the detector relative to the crystalline axes.

For AIP from polycrystalline samples, the polarization of the incident photons has no effect because all crystalline orientations relative to the electric field vector occur with equal probability. For ARP from single crystals, there is only one orientation of the $\vec{E}$ vector with respect to the crystalline axes, and polarization has to be taken into account. Having mentioned the presence of polarization effects in ARP, we devote our attention exclusively to point (2) because we feel that this is the more important and interesting aspect. We shall assume that the incident light is unpolarized. For AIP from polycrystalline samples, the position of the detector determines only the total measured intensity. Spectra measured for various detector positions are identical (apart from possible changes caused by surface effects at low take-off angles).

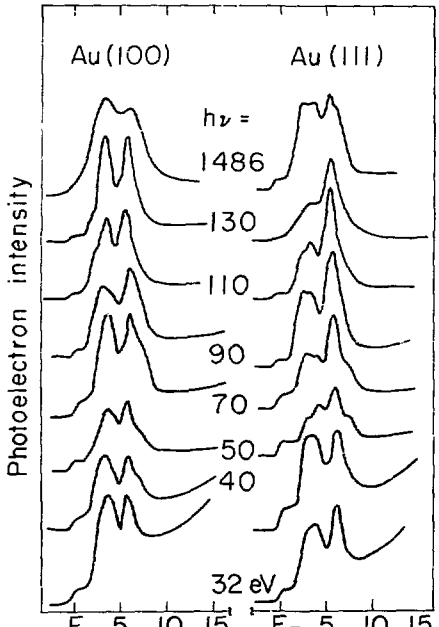

Fig. 2. Valence band photoemission spectra of a gold single crystal in the [100] and [111] directions, using variable-energy synchrotron radiation from the SPEAR storage ring. The peak at 6 eV in the higher-energy [111] spectra may be a surface state. (XBL 761-2112)

In this case one can envision the photoeffect in the following way. Whenever a transition from an initial state to a final state in the Brillouin Zone (BZ) of the crystal is allowed (energy and momentum conservation) it can be assumed that the photoelectron is detected. The PED is then determined by all possible excitations (sum over the BZ) and the detection process does not need to be considered explicitly. The spectrum measured in ARP, however, also depends on the detector position relative to the crystalline axes. In this case not all the allowed transitions are sampled, but only those where the photoelectron momentum vector points into the detector. As a result, a much smaller fraction of initial and final states in the BZ is sampled, which leads to more structure in the PED's. The spectral changes with photon energy are more pronounced for ARP for the same reason.

Because our ARP studies are very sensitive to the initial and final state band structure, they can in a sense be compared to photoemission studies in the UPS regime. Here the number of available final states is so small that strong modulation effects in the spectral shapes are observed even for polycrystalline samples. However, at the photon energies studied in this investigation, additional information may be obtained as compared to the UPS regime, a fact which has already been mentioned in the previous paper[4] dealing with photoemission from polycrystalline samples. Because of its better resolved structure, ARP actually should be more sensitive to the various effects mentioned in Ref. 4.

Finally we mention another unique advantage of using synchrotron radiation for studies of the present kind. While photoemission from valence bands is dependent on both the initial and final densities of states (for an important exception see Ref. 3) one may use the tunability of synchrotron radiation to excite photoelectrons from core levels into the same final state region. In this way, final state effects, which include diffraction effects of the outgoing electrons,[5] may be sorted out. Experiments of this kind have not been carried out but will certainly be attacked in the near future.

1. N. V. Smith and M. M. Traum, Phys. Rev. B 11, 2087 (1975).
2. P. O. Nilsson and L. Ilver, Solid State Comm. 17, 667 (1975).
3. F. R. McFeely, J. Stöhr, G. Apai, P. S. Wehner, and D. A. Shirley, submitted for publication and in the following report.
4. J. Stöhr, F. R. McFeely, G. Apai, P. S. Wehner, and D. A. Shirley in the previous report.
5. A. Liebsch, Phys. Rev. Lett. 32, 1203 (1974).

3. d-ORBITAL DIRECTED PHOTOEMISSION FROM SILVER AND GOLD

F. R. McFeely, J. Stöhr, G. Apai, P. S. Wehner, and D. A. Shirley

A new angular distribution effect in photoelectron spectroscopy, completely overlooked until now, has been predicted theoretically and confirmed experimentally. The effect is an essential consequence of the fact that a d shell provides two distinct irreducible representations of the cubic group: t_{2g} ($\Gamma_{25'}$) and e_g(Γ_{12}). By selecting photoelectrons emitted along the (100) axis or the (111) axis of a single crystal, it is possible to observed photoemission separately from e_g or t_{2g} states, respectively.

To develop a physical understanding of the effect, consider the ligand-field-theory limit, in which the crystal momentum is neglected. Photoemission is governed by a matrix element of the approximate form

$$\langle e^{i\vec{q}\cdot\vec{r}} \; |\vec{p}| \; \phi(d) \rangle \, ,$$

where $\phi(d)$ is the initial-state, one-electron wave function, $e^{i\vec{q}\cdot\vec{r}}$ represents the final continuum state of the photoelectron, and $\vec{p}$ is the one-electron momentum operator. This matrix element vanishes for $\phi(d) = d_{xy}$, d_{yz}, or d_{zx} (the t_{2g} orbitals) and electron emission in the (100) and crystallographically equivalent directions, as can be shown by direct calculation. Thus photoemission in the (100) direction selects the e_g states, which have nonzero matrix elements. The opposite is true for the (111) direction, along which the e_g elements vanish and the t_{2g} states are selected.

For many crystalline materials (e.g., metals) the crystal momentum must be explicitly included in the calculation. This is true for silver and gold, which were used as experimental test cases. The effect still persists, as can be shown by expanding the initial band state wave functions in the tight-binding formalism; i.e., in a t_{2g}, e_g basis.[1] Provided that the photon energy is relatively high, so that the $\vec{k}$-conservation is readily satisfied, all regions of the Brillouin Zone are sampled. The valence-band spectra in the (100) and (111) directions are then just proportional respectively to the e_g and t_{2g} projections of the total valence bands, integrated over the entire Brillouin Zone.

Results for gold and silver are shown in Fig. 1. In each case the top panel shows the valence-band (100) photoemission spectrum obtained from a single crystal specimen in ultrahigh vacuum (8×10^{-10} Torr), using monochromatized Al Kα radiation. The corresponding e_g projection of the d bands is shown as the third panel. The second and fourth panels show the (111) spectrum and the corresponding t_{2g} projection. The fifth panel shows the valence bands on a common energy scale.[1,2]

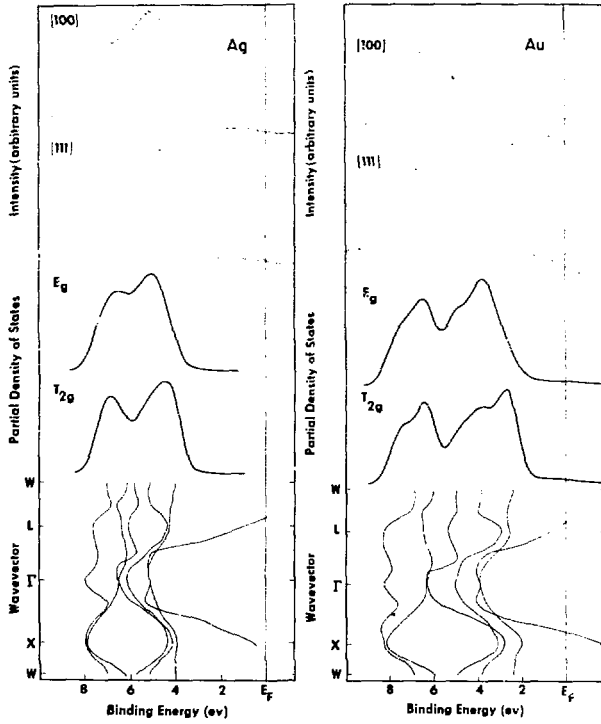

Fig. 1. X-ray photoemission spectra along (100) and (111) axes, partial e_g and t_{2g} state densities, and band structures of silver (left) and gold (right). (XBL 7510-4149 & XBL 7510-4148)

Two obvious anisotropy effects are present in both metals: (1) the higher binding-energy (E_B) peak is relatively less intense in the {100} spectrum, because of less e_g character; and (2) the lower-E_B peak has relatively less intensity on the low-E_B side. This follows because the top occupied band has t_{2g} character at the L, K, and X points in the Brillouin Zone. The existence of this anisotropy and the close correspondence with theory establish d-orbital directed photoemission as a real effect, previously overlooked.

This effect should be ubiquitous in d-orbital photoemission. It should be present in the valence bands of other transition metals, and in some (e.g., platinum) it may be more pronounced than in silver or gold. Because it is a symmetry effect, it should appear at all photon energies. Remeasurement of XPS spectra of all transition metals studied to date using oriented single crystals may therefore be expected to yield useful new information about the valence bands. Even more distinctive effects are predicted in transition-metal complexes, for which the t_{2g} and e_g orbitals are resolved in energy. There will also be diagnostic applications to orientational problems in absorbates on single crystals of catalytically active metals. It may be possible to determine the e_g vs. t_{2g} nature of adsorbate-substrate bonding in catalytic systems through d-orbital directed photoemission. Further work is under way.

1. H. Ehrenreich and L. Hodges, Methods in Computational Physics 8, 149 (1968).
2. N. V. Smith, Phys. Rev. B3, 1862 (1971).

4. THE EFFECT OF SPIN-ORBIT COUPLING ON THE VALENCE BAND DENSITY OF STATES OF LEAD

F. R. McFeely, L. Ley, S. P. Kowalczyk, and D. A. Shirley

The electronic structure of metallic lead has been the subject of numerous experimental studies, mostly concerned with the elucidation of the Fermi surface. Naturally, the ultimate aim of these experiments is to provide the information necessary to construct a band structure which will explain the Fermi surface, optical spectra, photoemission spectra, and other electronic properties. Unfortunately, the difficulties involved in the calculation of a full relativistic band structure have apparently served to deter extensive first-principles calculations of the lead band structure and density of states. In an earlier paper, Ley et al.[1] reported a high-resolution x-ray photoemission (XPS) spectrum of the lead valence bands, and tentatively interpreted the two-peak structure at the top of the valence band as the result of spin-orbit splitting of the p bands. Recently, however, Breeze[2] has asserted, on the basis of a non-relativistic LCAO calculation, that the XPS splitting is instead simply the result of a crystal-field interaction. We have reexamined the origins of this feature of the XPS spectrum by means of parameterized, tight-binding, band-structure calculations; spin-orbit coupling was systematically included and excluded. We have shown that the inclusion of spin-orbit coupling is essential to the understanding of the XPS, optical, and Fermi surface measurements.

Figure 1 shows the XPS spectrum obtained by Ley et al.[1] using a Hewlett-Packard 5950A electron spectrometer that employed monochromatized Al Kα radiation (1486.6 eV). We note again the important features in the spectrum: s-like and p-like bands split by ~2.5 eV, a splitting of 1.8 eV in the p-like bands, and a total occupied p-bandwidth of ~3.5 eV.

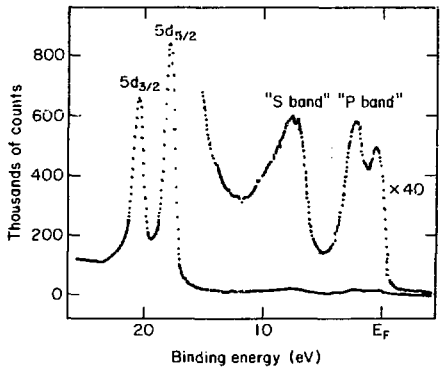

Fig. 1. X ray photoemission spectrum of the Pb valence band region from Ref. 1. (CBL 752-2325)

The tight-binding band structure calculations used to simulate the XPS spectrum are quite simple. The method consists of using tight-binding Bloch functions of the form

$$\phi^n_K(r) = N^{-1/2} \sum_{\ell} e^{iK\cdot\ell}\, U^n(r - \ell)$$

as basis functions, when $U^n(r - \ell)$ is an atomic function centered at site ℓ. In these calculations a basis of one s- and three p-functions (p_x,p_y,p_z) for each spin were used. All nearest-neighbor interactions were included, and two second-nearest-neighbor interactions of the form s-s and p-p were treated. Mixing between s and p basis functions was treated only in nearest neighbors. The largest second-nearest-neighbor integral in the final parameterization was a factor of 6 smaller than the smallest nearest-neighbor term; thus the inclusion of third-nearest-neighbor interactions would have only a negligible effect. The neglect of s-center terms was undoubtedly of greater importance. Using this method, the spin-orbit interaction is expressed in terms of

the atomic spin-orbit matrix elements. We performed two sets of calculations, one with the atomic value of the spin orbit coupling constant (ξ = 0.905) and one neglecting this term in the Hamiltonian. The XPS spectra were simulated by calculating the density of states below the Fermi level, and broadening the resulting function with a 0.7 eV FWHM Gaussian instrumental response function. The importance of the spin-orbit term in the XPS spectrum is evident in Fig. 2, where

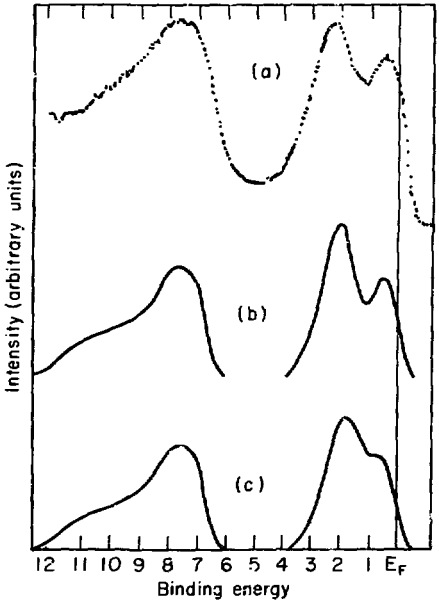

Fig. 2. (a) XPS valence band spectrum; (b) calculated spectrum with spin-orbit coupling; (c) calculated spectrum without spin-orbit coupling. (XBL 752-2524)

it leads to a superior fit to the experiment. In comparing the two band structures with the results of Fermi surface[3] and optical[4,5] data the band structure with ξ = 0.905 eV gave reasonable agreement with experiment while the band structure with ξ = 0 did not.

1. L. Ley, R. A. Pollak, S. P. Kowalczyk, and D. A. Shirley, Phys. Lett. 41A, 429 (1972).
2. A. Breeze, Solid State Comm. 14, 595 (1974).
3. J. R. Anderson and A. V. Gold, Phys. Rev. 139, A1459 (1965).
4. H. G. Liljenvall, A. G. Mathewson, and H. P. Myers, Phil. Mag. 22, 243 (1970).
5. A. G. Mathewson, H. P. Myers, and P. O. Nilsson, Phys. Status Solidi (b) 57, K31 (1973).

5. A HIGH-RESOLUTION X-RAY PHOTOEMISSION STUDY OF THE TOTAL VALENCE-BAND DENSITIES OF STATES OF GaSe AND BiI_3

S. P. Kowalczyk, L. Ley, F. R. McFeely, and D. A. Shirley

The physical properties of layered-structure compounds exhibit considerable anisotropy; this anisotropy is attributed to the strong intra-layer bonding as compared to the relatively weak van der Waals-type bonding between adjacent layers. These interesting properties have led to much interest in these materials because of their many possible applications such as in switching and memory devices. We have recently used high resolution x-ray photoelectron spectroscopy (XPS) to obtain the total valence-band density of states spectra for two semiconducting layered compounds, GaSe and BiI_3. In an earlier comprehensive study of the valence band spectra of III-V, II-VI, and alkali halide compounds, we demonstrated that XPS yields direct and detailed information about the occupied densities of states in solids.[1]

The experimental spectra for GaSe and BiI_3, obtained under ultra-high vacuum conditions from freshly cleaved single crystals, are shown in Figs. 1 and 2, respectively. Both spectra exhibit a characteristic three-peak structure. From previous work on other materials,[1] we know that the lowest peak (feature G in GaSe and D in BiI_3) has essentially anion "s" character, the middle peak (E in GaSe and B in BiI_3) cation "s" character, and that the uppermost peak (features C, B, and A in GaSe and A' and A in BiI_3) is mostly "p-like". There have been several band structure calculations for GaSe. Both a calculation based on a two-dimensional tight-binding scheme (TB)[2] and a three-dimensional empirical pseudopotential method (EPM) calculation[3] show qualitative agreement with our experimental results, but both leave much to be desired in terms of peak positions and bandwidths (see

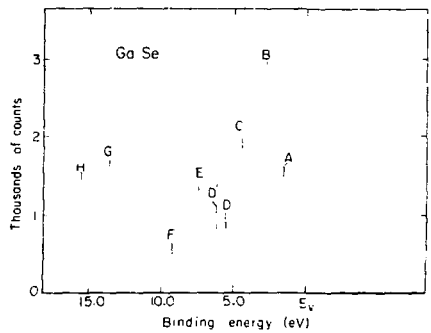

Fig. 1. Valence-band XPS spectrum of GaSe. (XBL 752-2404)

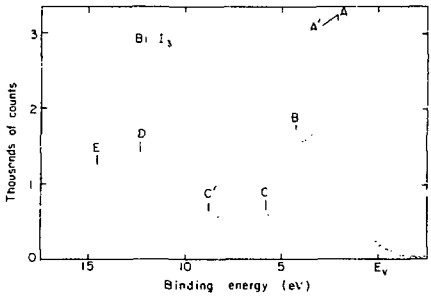

Fig. 2. Valence-band XPS spectrum of BiI_3. (XBL 752-2403)

Table 1). Charge densities derived from the EPM calculation show the interesting result that while the bonding in this compound is predominately covalent, there is a significant ionic component to the Ga-Se bond. Application of the recently proposed XPS scale of ionicity,[4] which is based on the measured "s-band" splitting, to our GaSe results, confirms Schlüter's observation.

Table 1. Comparison of energies (eV) of characteristic features in the valence band spectra from XPS, with EPM and tight binding calculations for GaSe

Feature	XPS[a]	Theory EPM[b]	TB[c]
A	1.56(10)	(-0.5)	—
B	2.89(10)	0.8	1.4
C	4.38(10)	2.1	1.8
D	5.0(3)	2.3	2.8
D'	6.0(3)	-3.0	3.2
E	7.23(10)	6.4	~5.5
F	9.0(2)	6.7	6.5
G	14.15(15)	-13.0	-13.0
H	16.0(4)	13.6	13.6
Ga $3d_{3/2,5/2}$[d]	19.39(10)	—	—
Se $3d_{5/2}$[d]	54.19(10)	—	—
Se $3d_{3/2}$[d]	54.82(10)	—	—

[a] This work (relative to the top of the valence band).
[b] Reference 3
[c] Reference 2
[d] This peak exhibits characteristic energy losses at 7.2(3) and 16.0(2)eV.

For BiI_3, neither band structure calculations nor any previous measurement of the valence band density of states exist. Our results for BiI_3 are summarized in Table 2. Comparison of these results with EPM calculations for the layered compound PbI_2[5], which should have some similarities to BiI_3, indicate that there exist problems with the theoretical results similar to the GaSe case. Using the observed "s-band" splitting to derive an ionicity indicates that the bonding in BiI_3 is more ionic than in GaSe.

Table 2. Comparison of energies (eV) of characteristic features in the XPS valence band spectrum of BiI_3

Feature	Energy[a]
A	1.68(8)
A'	2.07(8)
B	3.97(14)
C	5.63(8)
C'	8.64(8)
D	12.11(10)
E	14.17(40)
Bi $5d_{5/2}$[b]	24.99(8)
Bi $5d_{3/2}$[b]	28.39(8)
I $4d_{5/2}$[b]	48.43(8)
I $4d_{3/2}$[b]	50.11(8)

[a] This work (relative to the top of the valence band).
[b] This peak exhibits characteristic energy losses at 6.0(2) and 15.6(2)eV.

These measurements set narrow limits on the position and widths of the valence bands of GaSe and BiI_3; they were used to test theoretical studies on layered materials. The calculations were shown to be in need of further refinements.

1. L. Ley, R. A. Pollak, F. R. McFeely, S. P. Kowalczyk, and D. A. Shirley, Phys. Rev. B 9, 600 (1974); S. P. Kowalczyk, F. R. McFeely, L. Ley, R. A. Pollak, and D. A. Shirley, Phys. Rev. B 9, 3573 (1974).
2. F. Bassani and G. P. Parravicini, Nuovo Cimento B 50, 95 (1967).
3. M. Schlüter, ibid. B13, 313 (1973).
4. S. P. Kowalczyk, L. Ley, F. R. McFeely, and D. A. Shirley, J. Chem. Phys. 61, 2850 (1974).
5. I. CH. Schlüter, and M. Schlüter, Phys. Rev. B 9, 1652 (1974).

6. THEORY OF THE NEON 1s CORRELATION PEAK INTENSITIES

R. L. Martin and D. A. Shirley

Photoelectron spectroscopy (PES) is now a well-established technique for studying the electronic structure of atoms, molecules, and solids. Thus far, its advantage over other spectroscopic methods has been due to the fact that the most intense peaks in a PES spectrum generally have a one-to-one correspondence with the primary ionic states of the system and hence, via Koopmans' Theorem, the orbital structure of the ground state.

Associated with each strong peak there are also usually several weaker satellite peaks which arise through excitation of higher-energy final states of the ion. Earlier work in our laboratory on the HF molecule suggested that electron correlation in the ground state played an important role in determining satellite intensities. With this in mind, we decided to examine a better characterized experimental case (and a somewhat more tractable theoretical one): the Ne 1s orbital satellite spectrum.

The most intense peaks in the Ne 1s spectrum are based on the configurations $1s^1 2s^2 2p^6$, $1s^1 2s^2 2p^5 3p$, $1s^1 2s^2 2p^5 4p$, and $1s^1 2s^2 2p^5 5p$. There are seven states of ^2S symmetry which arise from these configurations -- the last three configurations give rise to two ^2S functions apiece due to the presence of three unpaired spins; that is:

$$\Phi_1(np) = (2s^2 2p^5 np(^3S),\ 1s)\ ^2S$$

$$\Phi_2(np) = (2s^2 2p^5 np(^1S),\ 1s)\ ^2S. \qquad (1)$$

The actual excited states can be written as a linear combination of such "configuration state functions"; that is:

$$\Psi_i(N-1) = \sum_j c_{ij} \Phi_j(N-1). \qquad (2)$$

A similar "CI" expansion can be used for the ground state, and typical configuration state functions which may mix with the Hartree-Fock configuration $1s^2 2s^2 2p^6$ will have the form $1s^2 2s^2 2p^5 3p$, $1s^2 2s^2 2p^4 3p^2$, etc.

For our purposes, a good approximation of the effective intensity of a given ionic state is given by

$$I_j \propto |(\Psi_j(N-1) | \Psi_i^{-1s}(N-1))|^2 \qquad (3)$$

The notation $\Psi_i^{-1s}(N-1)$ refers to the fact that we must delete the column containing the 1s electron and the row containing electron N from every Slater determinant in the initial-state expansion. The intensity is thus determined by the projection of a "frozen-orbital"-like primary hole state onto the exact eigenstates of the ion. This overlap will be large for the primary hole state and smaller, but non-zero, for the excited ionic states.

There are two main sources of intensity for the final states; one arises from configuration mixing in the ionic manifold, and one from CI in the initial state. To make this clearer, let us imagine we could suppress the exchange interaction between the Ne 1s electron and the valence electrons in the Ne^+ 1s hole states; the two $1s2s^2 2p^5 np$ (^2S) states would be replaced by $(2p^5 np)$ ^1S and ^3S states. The former would be very similar to the $1s^2 2s^2 2p^5 np$ (^1S) excited state in atomic neon(the ^3S state also has an analog in atomic neon, but it is not admixed into the ground state). Similar 1:1 correspondence would obtain between the other configurations in the Ne and Ne^+(1s hole) manifolds with the 1s exchange splitting removed; this is depicted in Fig. 1 (left side).

Configuration interaction generates correlated eigenstates as shown in Fig. 1 (right side). We describe these eigenstates by coefficients as shown, and note that these have magnitudes

$$a_0,\ a_0',\ b_0',\ \ldots \sim 1$$

$$a_1,\ a_1',\ b_1',\ \ldots \sim 0.1$$

There are four contributions to the intensity-determining overlap integrals. Path A (Fig. 1) is the largest term, and is of effective intensity

$$I_A \sim |a_0 a_0'|^2 \sim 1$$

where, for this example, we take the overlap integrals to be one or zero. It connects the main configuration in the ground state and the primary hole state. Path C connects the ground state with the correlation states. If the ground state were not correlated (i.e., $a_n = 0$ for all $n \neq 0$), then B would be the only mechanism for reaching correlation states and their intensities would be

$$I_B \sim |a_0 b_1'|^2 \sim 0.01 .$$

Initial-state configuration interaction provides a new avenue for populating final states: it introduces path C. It also provides a mechanism for populating satellites that do not have the correct symmetry to mix with the main hole state (although this is not obvious in our example). The satellites arising in this case have been the subject of experimental study in our group and will be discussed elsewhere.

Within a purely computational vein, our problem is now to obtain wavefunctions for the ground state and all ionic states of interest. A full description of the techniques used is available in the original report;[1] here we simply note that we first determined a CI wavefunction for the final states and computed the relative intensities of the satellites using the Hartree-Fock ground state wavefunction of neon. We refer to this as Calculation 1. It gave the intensities shown in the topmost "spectrum" of Fig. 2. These are to be compared to the experimental results[2] in the lowermost graph. This approach predicts only approximately one-half of the experimental intensity. Viewed in terms of our simple model this is to be expected -- we must bring path C into play. Calculation 2 therefore included single and double excitations from the Hartree-Fock configuration into a virtual space that did not include any diffuse Rydberg orbitals. Although this calculation recovered 55% of the Ne(^1S) L-shell correlation energy (0.33 au), it did not improve the intensities. Therefore, in Calculation 3 we included also single and double excitations into Rydberg-like 3s and 3p orbitals. As Fig. 2 shows, the results were dramatic; the intensities of the 3p(upper) and 5p(lower) peaks were more than doubled to near the experimental values. The remainder of Fig. 2 shows that this improvement also is obtained for the other states as we successively include the pertinent Rydberg orbitals in the ground state CI wavefunction. It seems safe to conclude on the basis of these calculations that the correct theoretical intensities of a given satellite can be calculated if that state is adequately represented in the configurations that describe the initial state (via path C), but that only about one-half the experimental intensity is predicted otherwise (path B).

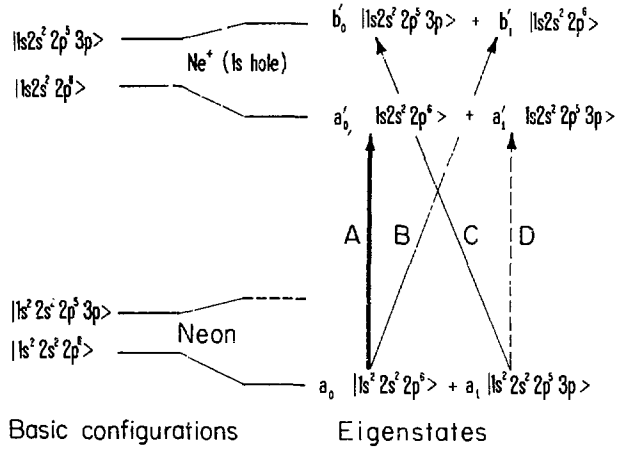

Fig. 1. Simple model to illustrate the effect of initial-state configuration interaction on correlation-peak intensities in Ne 1s photoemission (not to scale). With 1s exchange suppressed, the Ne^+(1s hole) configuration manifold would closely resemble the ground-state manifold (left). Introducing configuration interaction, this 1:1 correspondence would also obtain for the eigen-states (right), and $a_0 \sim a'_0$, $a_1 \sim a'_1$, etc. The main peak arises primarily from path A. Paths B and C arise because the two configurations "look for themselves" in the correlation state. They are of roughly equal strength, but the dashed path (D) is weak. (XBL 759-4146)

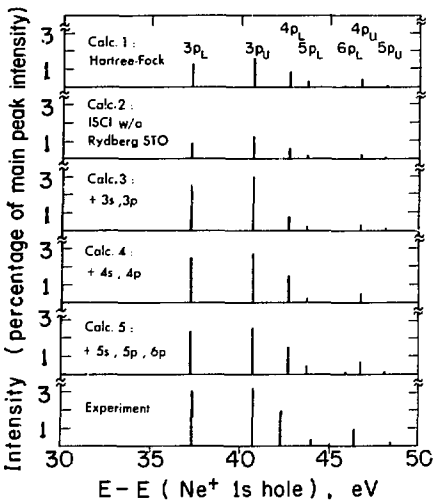

Fig. 2. Bar diagram of the 2p→np peak intensities for eight correlation states of Ne^+ (1s hole). As in text, calculation 1 is Hartree-Fock in the initial state. Calculation 2 includes correlation, but with no double-electron excitation into the Rydberg orbitals. Calculations 3, 4, and 5 include double excitation into the (3s,3p), (3s,3p,4s,4p), and (3s,3p,4s,4p,5s,5p,6p) orbitals, respectively. The calculated energies have been shifted upward by 0.8 eV to facilitate comparison with experiment.

This prototype calculation on neon has shown for the first time that quantitative satellite intensities are accessible within the framework of the overlap approximation embodied in Eq. 1. We should point out that while the relative intensities of the satellites in neon are only a few percent, certain transition metal complexes (e.g. CoCl2) exhibit core-level satellites which are ca. 60% of the main peak. The "spontaneous interconfiguration fluctuation" of recent interest in mixed-valence rare-earth compounds is another example of the breakdown of simple one-electron models and points to the need for a more general description of the initial state. Clearly, photoelectron spectra can be very sensitive probes of the details of electron correlation in the ground state, and such spectra possess the potential of yielding rather direct information about the electronic structure and reactivity of many chemically interesting systems.

---

1. R. L. Martin and D. A. Shirley, LBL-4556, submitted to Phys. Rev. A.
2. U. Gelius, J. Electr. Spectr. and Rel. Phenomena 5, 985 (1974).

7. THEORETICAL NEON PHOTOIONIZATION CROSS-SECTIONS

R. S. Williams and D. A. Shirley

In seeking to understand the relationship between the electronic structure of free atoms and experimental photoelectron spectra, several theoretical models of the photoemission process were investigated. The photoelectron cross sections of the Ne 1s, 2s, and 2p shells were evaluated for photon energies ranging from threshold for the different levels to 2000 eV. These calculated cross sections were then compared to experimental determinations of Ne photoemission cross sections. The models used may be divided into one-electron and many-electron pictures.

The one-electron models assume that in photoemission an electron in a bound state of an atom absorbs a photon and is raised to the continuum without disturbing the remaining electrons of the system. This is essentially equivalent to the Koopman's Theorem assumption that the ionization energy of an atomic shell is equal to the Hartree-Fock energy for the shell. The photoemission cross sections were calculated using plane waves, orthogonalized plane wave and numerically generated Hartree-Fock continuum functions (calculated in the field of the Koopman's Theorem or unrelaxed ion) as successive approximations to the continuum state of the photoemitted electron.

The many-electron models recognize that creating a hole in an electronic shell of an atom by a photoemission process perturbs the remaining bound electrons of the system. These remaining electrons relax to shield the hole from the atomic nucleus, thus altering the form of the bound one-electron orbitals. Since the bound one-electron orbitals of the initial and final states no longer belong to the same orthonormal set, additional terms appear in the transition matrix element which are not present in the one-electron picture. The initial and final states used for these calculations were the single-configuration ground state $1s^2 2s^2 2p^6$; ^1S for the Ne atom and single-configuration states for the $Ne^+ + e^-$ systems $1s^1 2s^2 2p^6 \varepsilon p$; ^1P, $1s^2 2s^1 2p^6 \varepsilon p$; ^1P; $1s^2 2s^2 2p^5 \varepsilon s$; ^1P, and $1s^2 2s^2 2p^5 \varepsilon d$; ^1P. The continuum functions utilized were plane waves, orthogonalized plane waves, and numerical Hartree-Fock continuum functions generated in the field of the relaxed ion.

The calculations proved to be very sensitive to the continuum functions. Plane waves and orthogonalized plane waves yielded very poor results in both the one-electron and many-electron pictures. The Hartree-Fock continuum functions yielded nearly identical results for Ne 2s and 2p photoionization in the one electron and many electron pictures; this is expected since relaxation due to ionization from the 2s and 2p orbitals is quite small. The agreement with experimental results was within 15% except for values at threshhold. For Ne 1s ionization, relaxation is much greater and this is reflected in the calculated cross sections. The many-electron model with a Hartree-Fock continuum function agrees with experimental determinations within 5%, while the one-electron model yields cross sections about 12% too high.

8. SATELLITE STRUCTURE IN THE UV PHOTOEMISSION SPECTRA OF ATOMIC Zn, Cd, Hg, Ca, Sr, and Ba

S. Süzer, S.-T. Lee, and D. A. Shirley

Photoelectron spectra of atomic Zn, Cd, Hg, Ca, Sr, and Ba were observed using HeI radiation at 21.21 eV (except in the case of Ba where NeI was used). The spectra were taken at high temperatures and are shown in Figs. 1 and 2. Figure 1 also shows the ^2D lines of Zn, Cd, and Hg taken with HeII radiation (40.8 eV). The ground states of these Group II-A and Group II-B atoms have configurations ns^2, and a considerable amount of configuration mixing is expected between this and the near-degenerate np^2, $(n-1)d^2$ and for Ba the $(n-2)f^2$ configurations. Upon photoelectron emission there is no further mixing of the resultant configurations np, etc., with the primary final ionic state ($ns\ ^2S_{1/2}$); hence we might expect to see satellites corresponding to ($np\ ^2P_{1/2,3/2}$), ($n'd\ ^2D_{3/2,5/2}$) and ($n''f\ ^2F_{5/2,7/2}$) states, and other less intense higher final states. We have observed these satellites in intensities up to 22% of the main line in the photoemission spectra. They were attributed to configuration mixing in the initial states of these atoms. Thus photoelectron spectroscopy provides a unique new method of studying electron correlation by direct observation of configuration interaction.

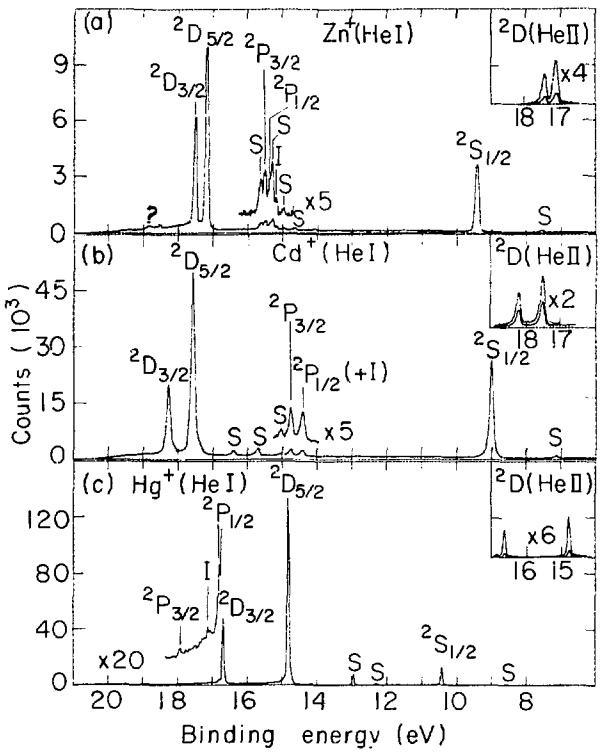

Fig. 1. Photoemission spectra of a) Zn vapor at 380°C, b) Cd vapor at 290°C, C) Hg vapor at 55°C using 21.21 eV HeI radiation and ^{2}D lines from HeII radiation at 40.8 eV at the upper right corner taken in the same runs. Lines marked "S" arise from tne HeI 23.08 and 23.74 eV radiation, and lines marked "I" are inelastic loss peaks. (XBL 7512-9907)

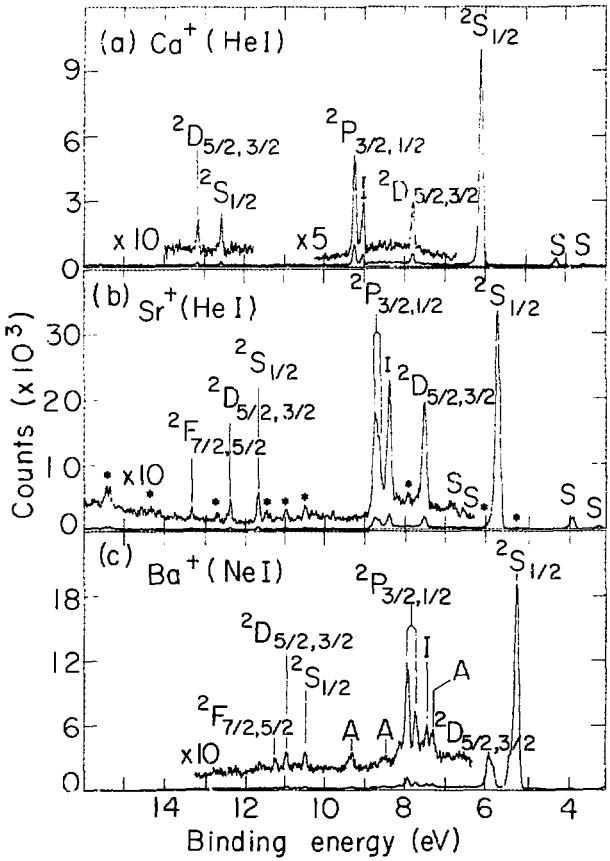

Fig. 2. Photoemission spectra of a) Ca vapor at 740°C, b) Sr vapor at 650°C using 21.21 eV HeI radiation, and c) Ba vapor at 700°C using 16.85 eV NeI radiation. Lines marked "S" arise from the HeI 23.08 eV radiation, lines marked "I" are inelastic loss peaks, and lines marked "A" are Auger lines. Asterisks in the Sr spectra lines indicate the Ba (HeI) impurity lines. (XBL 7512-9598)

9. RELATIVISTIC AND CORRELATION EFFECTS IN THE 21.2 eV PHOTOEMISSION SPECTRUM OF ATOMIC LEAD*

S. Süzer, M. S. Banna, and D. A. Shirley

Photoelectron spectra of atomic lead in the 700 - 806°C range were obtained, using HeI radiation (21.21 eV) and a special high-temperature cell. Large relativistic effects force the Pb ground state ($6s^2 6p^2; {}^3P_0$) to be mostly $6s^2\ 6p^2_{1/2}$, as opposed to the 1:2 ratio of

$$6p^2_{1/2} \quad \text{to} \quad 6p^2_{3/2}$$

expected in L-S coupling. This is observed in the line intensities of $Pb^+(6s^2 6p; {}^2P_{1/2})$ and $Pb^+(6s^2 6p; {}^2P_{3/2})$ final states which give the ratio as 1.000: 0.071, a figure in very good agreement with the RHF calculated ratio of 1.000: 0.081. Figure 1 shows the spectra and Table 1 summarizes the results. Several other final states with intensities of about 5% were observed which would be inaccessible from the s^2p^2 configuration. Their presence is attributed to the ground state of Pb being admixed with configurations of $6s^26d^2$ and $6s6p^26d$.

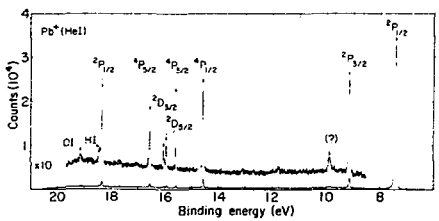

Fig. 1. Photoemission spectrum of Pb vapor at 715°C using 21.21 eV HeI radiation. Lines marked HI and OI arise from HI 10.199 eV and OI 9.493 radiation, respectively. (XBL 754-2733)

Table 1. States of Pb+ observed in photoemission from Pb vapor

Final states	Relative intensity[a]	Binding energy, eV[b]	Energy from optical data, eV[c]
$6s^2 6p\ {}^2P_{1/2}$	1.000	7.42(1)	7.415
$\quad {}^2P_{3/2}$	0.071(5)	9.16(1)	9.160
$6s6p^2\ {}^4P_{1/2}$	0.075(5)	14.59(1)	14.593
$\quad {}^4P_{3/2}$	0.024(5)	15.61(1)	15.611
$\quad {}^4P_{5/2}$	0.040(5)	16.57(1)	16.576
$6s6p^2\ {}^2P_{1/2}$	0.110(5)	18.35(1)	18.353
$6s^26d\ {}^2D_{5/2}$	0.022(5)	15.97(1)	15.963
$\quad {}^2D_{3/2}$	0.019(5)	16.06(1)	16.059
(?)[d]	0.014(5)	9.85(1)	—

[a] Relative areas divided by their kinetic energies to correct for the spectrometer efficiency.

[b] This work. Values given are averages of three runs. Errors in last place are given parenthetically. The Xe lines at 12.130 eV and 13.436 eV and the Ar lines at 15.759 eV and 15.937 eV are used for calibration.

[c] Reference 1.

[d] Not identified.

When the Pb spectrum was taken at 765°C several strong inelastic loss peaks appeared; Table 2 summarizes the results. All of the five peaks observed are interpreted to result from electron impact excitation of neutral Pb by photoelectrons emitted in exciting the $^2P_{1/2}$ line, at a kinetic energy of 13.80(1) eV.

*Abstracted from J. Chem. Phys. 63, 3473 (1975).

1. C. E. Moore, Natl. Bur. Stand. (U.S.) Circ. 467, Vol. 3 (1962).

Table 2. Inelastic loss peaks observed in neutral Pb

Peak	Transition from the ground state	Relative intensity[a]	Excitation energy, eV[b]	Energy from optical data, eV[c]
0	$6s^2 6p^2\ {}^3P_0$[d]	—	—	—
1	$6s^2 6p^2\ {}^3P_1$	1	0.97(1)	0.960
2	$6s^2 6p^2\ {}^3P_2$	4±0.5	1.32(1)	1.320
3	$6s^2 6p(^2P_{1/2})7s$ $\quad {}^3P_1^0$	4±0.5	4.37(1)	4.374
4	$6s^2 6p(^2P_{1/2})6d$ $\quad {}^3D_2^0$ $\quad {}^3D_1^0$	4±0.5	5.71(1)	5.709 5.710
5	$6s6p^2$[e]	16±1	10.52(2)	—

[a] Areas divided by their kinetic energies, relative to peak 1.

[b] Values given are averages of two runs. The Pb^+ lines from Table 1 are used for energy calibration.

[c] Reference 1.

[d] Zero loss line (i.e., the main peak).

[e] Assignment is tentative as explained in the text.

10. AUTOIONIZATION IN THE PHOTOELECTRON SPECTRUM OF Ba

S.-T. Lee, S. Süzer, E. Matthias, and D. A. Shirley

The photoelectron spectrum of Ba vapor was measured using both HeI and NeI radiation. The spectra are displayed in Fig. 1, with the peak assignments labelled. Our HeI spectrum as well as others[1,2] showed a number of excited-state peaks of Ba^+ with intensities comparable to that of the 6s state. Moreover, above the double ionization threshold of Ba (15.215 eV), three intense peaks were detected. By contrast, in the NeI spectrum of Ba the peak intensities of the excited states are much weaker and the satellite structure is less extensive.

Within the independent-electron approximation, the observed excited Ba^+ states are forbidden, and above the Ba^{++} threshold discrete peaks are not to be expected. The satellite structure in the NeI spectrum can be attributed to configuration interaction in the initial state. However, the rich satellite structure in the HeI spectrum is due to autoionization, which constitutes the major source for the single and double ionization. It appears that a highly excited state of Ba e.g., one of the $5p^56s^2$ (nd or ns) ^1P states, absorbs the HeI (21.22 eV) radiation resonantly.

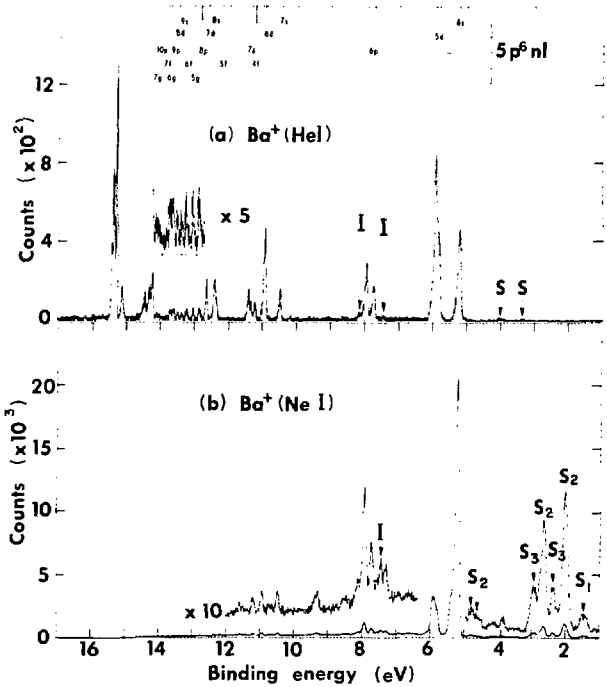

Fig. 1. (a) HeI photoelectron spectrum of Ba. (b) NeI photoelectron spectrum of Ba. In both spectra the peaks marked I are due to inelastically scattered electrons from the intense peaks in exciting the neutral Ba to the lowest ^1P state, i.e., $5p^6 6s^2(^1S) \rightarrow 5p^6 6s6p(^1P)$. Those marked S are due to excitations by the satellite lines of HeI and NeI radiation. Unidentified peaks in the NeI spectrum may be due to excitation by NeII radiation. (XBL 759-4143)

This state mixes, through configuration interaction, with a number of continuum states of the types: $Ba^{++}(5p^6)(\varepsilon l c' l')$, $Ba^+(5p^5 nln'l')(\varepsilon l'')$, and $Ba^+(5p^6 nl)(\varepsilon l')$. The oscillator strength of the resonant transition will be shared among these continuum states. Resonant absorption and autoionization gives rise to the various features observed in the HeI photoelectron spectrum. The three peaks above Ba^{++} threshold are reached from $Ba^+(5p^5 nln'l')(\varepsilon l'')$, but a two-step autoionization-Auger process.

---

1. B. Brehm and K. Höfler, Int. J. Mass. Spectrom. Ion Phys. 17, 371 (1975).
2. H. Hotop and D. Mahr, J. Phys. B. Atom. Molec. Phys. 8, L301 (1975), and private communication.

11. K-SHELL CORRELATION-STATE SPECTRA IN FORMAMIDE

B. E. Mills and D. A. Shirley

Core-level photoemission spectra consist of a main line plus satellite peaks at higher binding energies. These peaks arise from direct photoelectric transitions to states of the same symmetry as that of the main hole state. All these states -- main state plus satellites -- are eigenvectors formed via configuration mixing from simple configurations: hence the term "correlation states".

This prototypical study, with 1s holes on carbon, nitrogen, and oxygen, shows that $\pi \rightarrow \pi^*$ excitations are differentially stabilized according to the location of the 1s hole. Upon 1s ionization, each MO is stabilized in proportion to its population on the ionized atom. Thus, for example, the initial states (π_1 and π_2) in nitrogen would be stabilized by a N 1s hole while the final π_3^* state would be relatively unaffected. This would increase binding energy of the $\pi_2 \rightarrow \pi_3^*$ and $\pi_1 \rightarrow \pi_3^*$ correlation states relative to the main N 1s as compared to the same states for carbon and oxygen. Similar arguments can be made in the other cases. Figure 1 presents these experimentally observed effects along with the predictions of Basch. There is remarkable qualitative agreement, indicating that correlation-state spectra can be used to determine the responses of individual MOs to "test charges" -- 1s holes -- on individual atoms.

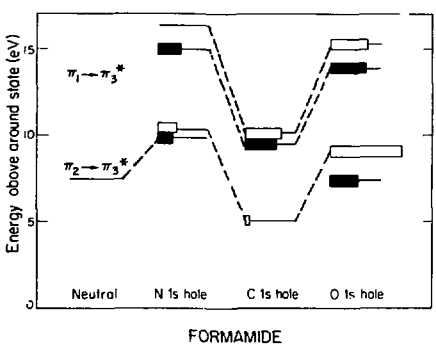

Fig. 1. Systematic variations of the $\pi_2 \rightarrow \pi_3^*$ and $\pi_1 \rightarrow \pi_3^*$ excitation energies and intensities in gaseous formamide. Where available, intensities are denoted by (horizontal) lengths of wide bars; open figures denote calculated values, filled figures denote experimental results. The low excitation energies accompanying C 1s ionization are attributed to the stabilization of the π_3^* orbital by the (positive) core holes; the high energies accompanying N 1s, to the stabilization of the π_1 and π_2. (XBL 7511-9554)

12. FURTHER STUDIES OF THE CORE BINDING ENERGY PROTON AFFINITY CORRELATION IN MOLECULES

B. E. Mills, R. L. Martin, and D. A. Shirley

X-ray photoelectron spectroscopy can provide a positive probe at a reactive atom, elucidating the fundamental effect of molecular structure on basicity and thus on reactivity in general. Core-level binding-energy shifts were measured for O1s levels in alcohols, ethers, acids, aldehydes, esters, and acetone; N1s levels in ammonia and aliphatic amines, P2p levels in phosphine and its methyl derivatives, and S2p levels in H_2S and its methyl derivatives. A total of 46 compounds were studied. The core-level shifts correlated well with gas-phase proton affinities, thereby extending and supporting earlier results of Martin and Shirley, Davis and Rabalais, and Carroll, Smith, and Thomas. In the amines, for which the data are most precise, a good correlation was observed for all 16 molecules taken together. On a finer scale, each series of amines (primary, secondary, tertiary) showed a linear correlation, while ammonia and its methyl derivatives showed a linear correlation with different slopes (Fig. 1).

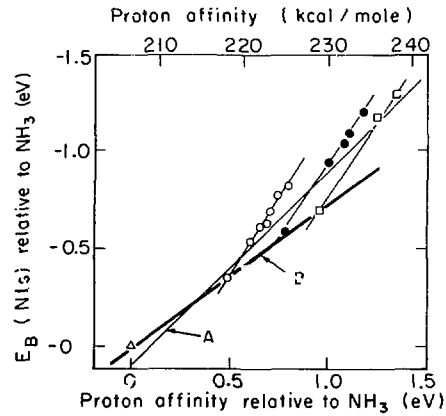

Fig. 1. Nitrogen 1s binding energies versus proton affinities for a series of aliphatic amines, using ammonia (triangle) as a reference. Primary amines are shown as open circles, secondary amines as filled circles, and tertiary amines as squares. Line A, drawn through all the data, has slope unity. Line B (ΔE_B (N1s) = -0.73 ΔPA) passes through ammonia and its methyl derivatives. The other lines (ΔE_B (N1s) = -1.5 ΔPA) show the linear variations within each series (primary, secondary, tertiary). Changes in local bonding at the nitrogen site between series (line B) effect the IP by angle change, rehydridization, etc.; the E_B is sensitive only to a change in the average potential. Within a series, however, induction in the initial state and polarization in the final state will effect E_B more strongly than IP. This accounts for the differences in the slopes of the lines. (XBL 756-3297)

These two correlations are interpreted as responses of the system to long-range effects and to changes in the local bonds, respectively. Similar behavior was observed in the single-bonded oxygen compounds. Excellent linear correlations were observed in the compounds of the third period elements phosphorus (ΔE_B = -0.6ΔPA) and sulfur (ΔE_B = -1.0ΔPA). Differences in the slopes were tentatively attributed to more pronounced changes in nuclear position on protonation of the phosphines. Analysis of the oxygen data supports the conclusion of Carroll et al. that protonation of carboxyl groups occurs on the keto oxygen. These results suggest that core level shifts can be used to predict proton affinities.

13. TABLE OF CORE-ELECTRON BINDING ENERGIES

D. A. Shirley, R. L. Martin, S. P. Kowalczyk, F. R. McFeely, and L. Ley

The recent discovery[1] that core-level electronic binding energies are systematically several eV lower in conducting solids that in free atoms necessitates a new tabulation of atomic energy levels. Previous tabulations[2] were drawn up without regard to whether the data were taken on free atoms or solids, and serious discrepancies are found when these tabulations are compared with theoretical binding energies.

The most common type of systematic error is caused by combining optical data for valence orbitals in atoms with x-ray data for core levels in metals, then comparing the results with either core-level binding energies measured directly by photoelectron spectroscopy on metals or with theoretical binding energies for free atoms. Solid-state effects render the photoelectron values systematically lower than the calculated atomic binding energies, while the values derived from x-ray and optical data are not rigorously comparable to binding energies in either atoms or metals.

We have, therefore, prepared a new table of binding energies which explicitly takes into account the differences between atomic data and data obtained on samples in the "standard" state, usually the metallic state. New values of core-level binding energies for Sc, Ti, V, Cr, Mn, Fe, Co, and Ni were measured by x-ray photoemission under ultra-high vacuum conditions. These were combined with other photoemission, optical, and x-ray data to compile binding energy values for the first 30 elements, both as free atoms and in their standard states. Comparisons of these values with theory were also made. This table is available in the original report.[3]

From an empirical point of view, most core-level binding energies in the first 30 elements are now known to within errors of 0.1 eV. For the 1s, 2s, and 2p levels of transition-metal atoms, x-ray energy shifts from metals to atoms may increase this error to ~4 eV. Because previous compilations did not take into account the difference between E_B values for free atoms and the standard state, they were in some cases in doubt by amounts up to the difference between the two, i.e., by up to 18 eV, in either E_B(atom) or E_B(metal).

The largest contributions to the change in the core-level binding energy in going from a free atom to a metal appear to arise through screening of the vacant orbital via extra-atomic relaxation of the metal's valence electrons, an increase in the repulsive potential experienced by core electrons in metals, and (in the transition series) changes in electron configurators.[1,4] These effects combine to make E_B(metal) less than E_B(atom) for all core levels.

The success of extra-atomic relaxation energy estimates[1] has led us to make theoretical estimates of core-level binding energies in metals by correcting theoretical free-atom binding energies for solid-state effects using a model described earlier.[1] Specifically, we have used the relation

$$E_B^V(\text{solid, theo}) = E_B(\text{atom, theo}) - \tfrac{1}{5} F^0(i,s).$$

Here $F^0(i,s)$ is a Coulomb integral between core level i and the screening orbital s, and the binding energy for the solid is referenced to the vacuum level and not the Fermi energy. There is in general very good agreement between the experimental and theoretical atomic binding energies. The first case is the Li(1s) level, for which the binding energy is 64.8 eV in the gas phase and 57.2 eV in the metal. The respective theoretical values are 64.8 and 60.5 eV. In other cases the absolute values of E_B may be reproduced very well by theory (e.g., for the Na(1s) case, E_B(atom) = 1079.1(9) eV, E_B(metal) = 1074.0(1) eV, compared with theoretical values of 1079 and 1075 eV, respectively), or they may not (e.g., 4 eV error in the K 1s case). Differences between the E_B(atom) and E_B(metal) are always present; however, they always have the expected sign and their magnitudes tend to follow quite closely the values predicted by the (1/5)F^0 estimate described above.

In conclusion, the results of this work provide very strong evidence that atomic binding energies are sufficiently well known experimentally and understood theoretically to necessitate that a clear distinction be made between the atomic state and the metallic state in future discussions of binding energy. When this distinction is made, the size of the solid-state shift and its sensitivity to electronic structure hold forth promise of its value in the elucidation of various electronic structure problems in metals.

---

1. D. A. Shirley, Chem. Phys. Lett. 16, 220 (1972); L. Ley, S. P. Kowalczyk, F. R. McFeely, R. A. Pollack, and D. A. Shirley, Phys. Rev. B8, 2392 (1973); P. H. Citrin and D. R. Hamann, Chem. Phys. Lett. 22, 301 (1973).
2. J. A. Bearden and A. F. Burr, Rev. Mod. Phys. 39, 125 (1967); K. Siegbahn et al., ESCA -- Atomic Molecular, and Solid-state Structure by Means of Electron Spectroscopy, Nova Acta

Regional Soc. Sci. Upsaliensa Ser. IV, Vol. 20 (1967); W. Lotz, J. Opt. Soc. Am. 58, 915 (1958); 60, 206 (1970).
3. D. A. Shirley, R. L. Martin, S. P. Kowalczyk, F. R. McFeely, and L. Ley, LBL Report 4065 (1975).
4. R. E. Watson, M. L. Perlman, and Jan Herbst, Phys. Rev. B, XXX (1976).

14. SODIUM ANODES FOR X-RAY PHOTOEMISSION STUDIES

M. S. Banna* and D. A. Shirley

As photoelectron spectroscopists turn their attention increasingly to synchrotron radiation sources to obtain variable energy and highly monochromatic radiation, it is important not to neglect the development of laboratory x-ray line sources. Because unconventional anode materials provide high photon fluxes at certain energies, many experiments can be performed in the laboratory, rather than at a synchrotron facility.

Sodium is the lightest metal that can be expected to produce sharp $K\alpha_{12}$ radiation. The linewidth should be significantly smaller than in heavier metals (~0.4 eV), and the NaKα line falls at a convenient energy of 1040 eV. The chemical reactivity of sodium has prevented its use as an anode material in the past, but anode preparation in vacuo has provided a source of NaKα radiation sufficiently intense for photoelectron spectroscopy. A sodium charge was loaded into holes on the cathode block near the filament of a standard x-ray tube in the Berkeley iron-free photoelectron spectrometer. When the filament was heated, the sodium charge was flashed onto a copper anode, producing a sodium anode which lasted for 24 hours.

The NaKα x-ray spectrum was studied by photoelectron spectroscopy, using the neon 1s line. A spectrum is shown in Fig. 1. A least-squares fit yielded the following satellites (positions, intensities) relative to the main $K\alpha_{12}$ peak: Kα' (4.00 eV, 0.02), $K\alpha_3$ (7.00 eV, 0.12), $K\alpha_4$ (8.52 eV, 0.094). Analysis of high-resolution spectra yielded an upper limit of 0.42 eV FWHM for the $NaK\alpha_{12}$ line.

Several test cases were used[1] to assess the value of the $NaK\alpha_{12}$ line for molecular photoelectron spectroscopy. For example, Fig. 2 shows the carbon 1s spectrum of methane, previously studied in detail with monochromatized AlKα x-rays by Gelius et al[2], who were able to obtain both the ratios and energy separations of the three vibrational levels under the main peak. Using their intensity ratios in our fitting procedures, we obtained separations of 0.43(2) eV and 0.41(7) eV between the vibrational levels in order of increasing binding energy; these values are in excellent agreement with the monochromatized x-ray value of 0.43(2) eV obtained by Gelius et al. Lorentzians constrained to have equal linewidth were used to fit the composite peak. While the monochromatic source of Gelius et al. gives appreciably better resolution of the vibrational components in CH_4, the spectrum shown in Fig. 2 is distinctly superior to results obtained

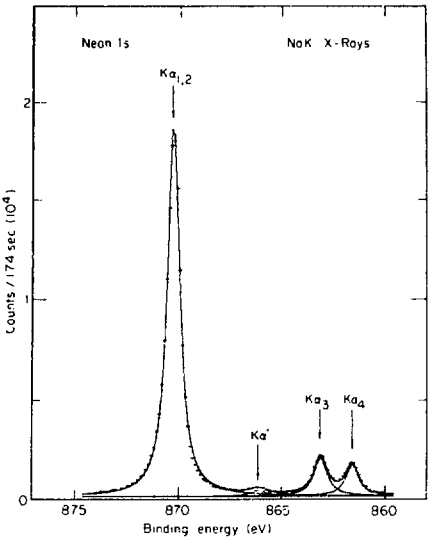

Fig. 1. Neon 1s photoemission spectrum and neighboring satellites; taken with $NaK\alpha_{12}$ x-rays. Linewidths are: $K\alpha_{12}$ peak, 0.68(1) eV; Kα', 0.9(2) eV; $K\alpha_3$, 0.76(4) eV; and $K\alpha_4$, 0.77(5) eV. (XBL 751-2128)

heretofore with other characteristic x-rays. We note that the asymmetry in the composite peak is obvious by visual inspection, and the ability of these data to yield the correct separations in the least-squares fit reinforces this observation. We believe that with a better spectrometer it would be possible to achieve considerably better resolution of the three C1s components in the $CH_4(NaK\alpha_{12})$ spectrum.

Many applications of the NaKα line are likely, particularly as ultrahigh vacuum spectrometers for surface studies become commonplace. This pilot study has established both that sodium is tractable as an anode material and that the gain in resolution with sodium anodes is worth the additional effort.

*Present address: Department of Chemistry, University of British Columbia, Vancouver, B.C.

1. M. S. Banna and D. A. Shirley, LBL-3491, to be published in J. Electron Spectr. and Related Phenomena.
2. U. Gelius, S. Svensson, H. Siegbahn, E. Basilier, A. Å. Faxälv, and K. Siegbahn, Chem. Phys. Lett. 28, 1 (1974).

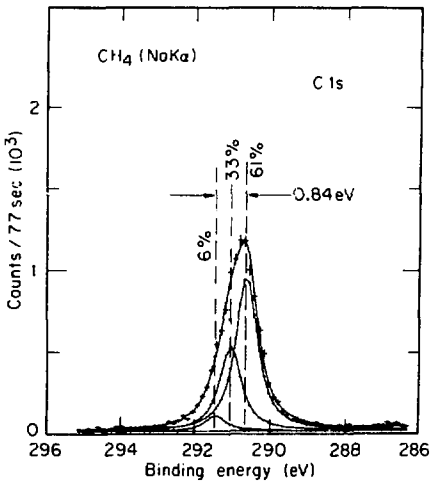

Fig. 2. Carbon 1s photoemission spectrum of methane, taken with $NaK\alpha_{1,2}$ x-rays. Counts were obtained at increments of 0.15 eV. Three Lorentzians of equal FWHM were used in the fit. (The linewidth of each was determined to be 0.65(2) eV.) Derived separations are 0.43(2) eV and 0.41(7) eV, in order of increasing binding energy. (XBL 751-2129)

15. PHOTOELECTRON SPECTROSCOPY OF SECOND-ROW DIATOMIC MOLECULES AT 132.3 eV

M. S. Banna and D. A. Shirley

Photoelectron spectroscopy has been hindered historically by a lack of suitable photon sources at energies between the hard UV range, which extends up to the 40.8 eV resonant $2p_{3/2}$ - 1s transition in He^+, and the soft x-ray range. The latter now extends down to 1040 eV (see above), the energy of the $NaK\alpha_{1,2}$ transition. Although intermediate-energy photon sources are desirable for many reasons, the most important single need arises in surface physics and chemistry. As Fig. 1 shows, the characteristic electron mean free path in a metal is shortest (~ 5Å), and the surface sensitivity of photoelectron spectroscopy therefore greatest, for electron kinetic energies of ~100 eV. With the goal in mind of developing a sensitive surface probe, we have designed and built an yttrium anode, following the pioneering work of M. Krause[1], and used the 132.3 eV yttrium $M\zeta$ x-ray to study molecular orbitals in gaseous N_2, O_2, CO, and C_2H_4--molecules that are commonly studied as adsorbates.[2]

A reliable yttrium anode was made by press-fitting an yttrium disc into a copper cup of slightly smaller diameter; the copper cup could

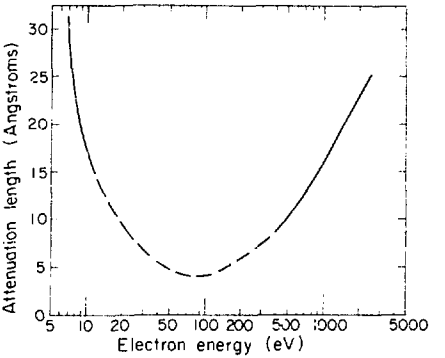

Fig. 1. The "universal" curve, derived from data on heavy metals, for electron attenuation length versus kinetic energy. Maximum surface sensitivity of photoemission falls in the 100 eV range. (XBL 7212-4882)

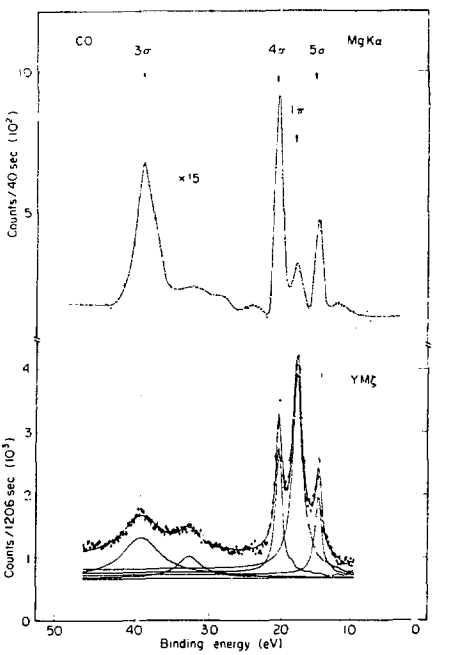

Fig. 2. Molecular-orbital photoemission spectra of CO taken with $MgK\alpha$ x-rays (1253.6 eV) and with $YM\zeta$ x-rays. (132.3 eV) (XBL 751-2122)

be directly water-cooled. Formvar windows of 20 μgm cm^{-2} thickness allowed the YMζ photons to pass, while maintaining a vacuum seal between the x-ray tube and sample chamber. The anode was biased positive to keep electrons from the window, which was also thermally shielded from the filament.

The resolution and intensities obtained in molecular photoelectron spectra excited by the YMζ line are entirely adequate for studying molecules as adsorbates in submonolayer coverages. Furthermore, the changes in relative intensities of molecular-orbital peaks, compared to those found with higher-energy MgKα source (1253.6 eV), definitively assign the atomic-orbital composition of the molecular orbitals. Thus, the spectra of CO (Fig. 2), together with the knowledge that $\sigma(2s)/\sigma(2p)$ increases by an order of magnitude from 10^{-2} eV to 10^{3} eV photon energy, establish the 2s character of the 3σ orbital, the 2p character of 1Π, and the s-p mixing in 5σ, the carbon lone pair.

1. M. O. Krause, Chem. Phys. Lett. 10, 65 (1971).
2. M. S. Banna and D. A. Shirley, LBL-3479 (to be published in J. Electr. Spectroscopy and Related Phenomena).

16. MOLECULAR PHOTOELECTRON SPECTROSCOPY AT 132.3 eV: THE SECOND-ROW HYDRIDES

M. S. Banna and D. A. Shirley

The 10-electron second-row hydrides HF, H_2O, NH_3, CH_4 comprise an instructive series for the study of electronic properties in the 1-10 eV energy range. On this scale some subtleties of molecular geometry are blurred over, and these hydrides can be regarded as being derived from atomic neon by moving 1-4 protons from the nucleus to the atomic periphery. The attendant reduction in strength of the central potential is manifest particularly in the variation of orbital binding energies, as well as other properties.

Photoelectron spectroscopy is an ideal technique for studying the quasiatomic character of trends in orbital binding energies along this series. By the use of the ultra-soft (132.3 eV) yttrium Mζ x-ray[1] together with soft (1253.6 eV) MgKα x-rays, it is also possible to determine the atomic-orbital composition of the molecular orbitals. A study of this type was carried out,[2] yielding the binding energies and peak intensities summarized graphically in Fig. 1.

Trends in the 2s - 2σ - $2a_1$ orbital properties follow from the 2s character of the 2σ and $2a_1$ orbitals, while the atomic-orbital composition of other molecular orbitals leads to characteristic intensity changes from MgKα to YMζ energies. Thus comparison of the neon and HF spectra shows that the peak labeled 1Π is in fact 2p-like, while the 3σ orbital has mixed 2s and 2p parentage. It is now possible to draw a complete set of orbital correlation diagrams from empirical binding energies and to determine in which orbitals the bond energy resides. For example Fig. 2, constructed in this way, shows the importance of the $2a_1$ orbital to the bond strength of methane.

1. M. O. Krause, Chem. Phys. Lett. 10, 65 (1971).
2. M. S. Banna and D. A. Shirley, LBL-3478 (J. Chem. Phys., to be published).

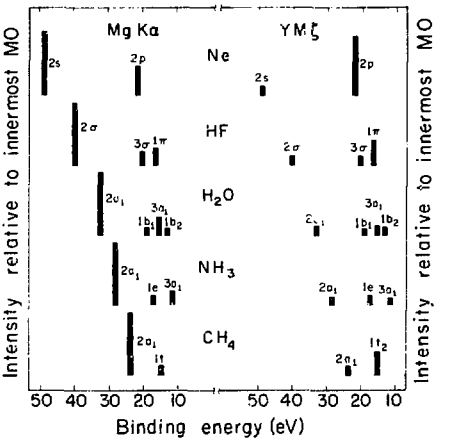

Fig. 1. Schematic of relative photoelectron peak areas and binding energies obtained from the experimental spectra of the second-row hydrides and neon with MgKα and YMζ x-rays. To facilitate comparison, the innermost MO intensities are shown equal for the entire series at each of the two exciting photon energies. (XBL 754-2699)

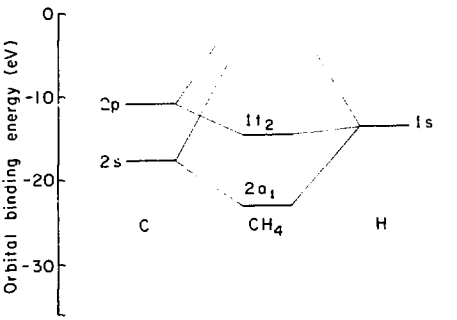

Fig. 2. An orbital correlation diagram for CH_4, using binding energies in C, H, and CH_4. Note lowering in energy of $2a_1$ orbital. (XBL 754-2698)

17. MOLECULAR PHOTOELECTRON SPECTROSCOPY AT 132.3 eV: ORBITAL INTENSITIES IN THE FLUORINATED METHANES

M. S. Banna and D. A. Shirley

In the development of molecular photoelectron spectroscopy using the 132.3 eV YMζ line, it is important to ascertain the extent to which relative peak intensities directly mirror atomic-orbital composition. To this end experiments were carried out on the fluorinated methanes.[1]

The data were analyzed using the Gelius model[2], in which the photoelectric cross section of molecular orbital i is given approximately as

$$\sigma_i(\text{mo}) \approx \sum_j P_{ij}\, \sigma_j(\text{AO}) \qquad (1)$$

Here σ_j is the photoelectric cross section of atomic orbital j, and P_{ij} is the population of that orbital in molecular orbital i. The model ignores cross terms that arise due to overlap. It is credible in the high-energy limit, but its accuracy at $h\nu = 132.3$ eV would be difficult to predict theoretically.

Results are set out in Table 1. In some cases energy separations were taken from earlier work.[3] Empirical atomic cross-section ratios were derived from orbital intensities in HF, CH_4, and CH_3F. Intensity ratios are given relative to the $4a_1$ orbital. Theoretical intensities were calculated using Eq. (1) together with ab initio wave functions given by Snyder and Basch.[4] Both gross and net atomic populations were used.

Table 1. Relative molecular orbital binding energies and intensity ratios for the fluorinated methanes. Energies are in eV.

Molecule	MO		I (YMζ) exp	I_G^a(YMζ)	I_N(YMζ)[b]
CH_3F	$3a_1$	38.41	1.	1.	1.
→	$4a_1$	23.48(6)	.4 (1)	.30	0.39
	$5a_1$	17.55(8)	.9 (1)	1.04	1.00
	$1e$	16.88(8)	1.2 (1)	1.05	1.78
	$2e$	13.35(6)	1.52(4)	1.30	1.56
CH_2F_2	$3a_1$	40.13	≈1.5	1.55	1.50
	$2b_1$	38.70	≈1.5	1.65	1.72
→	$4a_1$	23.86(3)	1.	1.	1.
	$1b_2$	--	--	1.41	1.25
	$5a_1$	19.31(3)	1.13(4)	1.74	1.61
	$3b_1$	18.71(3)	1.81(4)	1.95	1.91
	$1a_2$	15.69(5)	2.5 (1)	2.55	2.47
	$4b_1$	15.19(5)	1.5 (2)	2.29	2.55
	$6a_1$	14.90(5)	1.1 (2)	1.74	1.98
	$2b_2$	13.16(4)	1.02(6)	1.12	1.45
CHF_3	$3a_1$	47.0	--	1.	1.
	$2e$	39.15	2.17(7)	2.12	2.41
→	$4a_1$	24.38(3)	.52(9)	.88	0.97
	$5a_1$	20.89(3)	.76(7)	1.02	1.00
	$3e$	20.39(3)	1.41(7)	2.52	2.66
	$4e$	17.38(3)	2.35(8)	3.02	3.42
	$5e$	16.00(4)	2.3 (1)	2.98	3.59
	$1a_2$	15.30(4)	1.8 (1)	1.53	1.89
	$6a_1$	14.60(4)	.6 (2)	.92	1.28
CH_4	$3a_1$	43.81	1.	1.	1.
	$2t_2$	40.30	2.06(7)	3.16	3.73
→	$4a_1$	25.11(2)	.61(6)	1.14	1.10
	$1t_2$	22.21(3)	2.46(6)	3.69	4.09
	$5a_1$	18.55(3)	2.09(7)	3.07	3.53
	$4t_2$	17.48(3)	3.32(7)	4.42	5.49
	$1t_1$	16.28(3)	3.66(6)	4.61	5.96

[a] Based on gross populations

[b] Based on net populations

The intensities agree amazingly well with the simple theory, with very few exceptions. They give no basis for choice between net and gross population. We conclude that photoelectron spectroscopy at 132.3 eV has real diagnostic potential in studying molecular orbitals.

1. M. S. Banna and D. A. Shirley, Chem. Phys. Lett. 33, 441 (1975).
2. U. Gelius in Electron Spectroscopy, D. A. Shirley, ed., (North-Holland, Amsterdam, 1972) 311.
3. M. S. Banna, B. E. Mills, D. W. Davis, and D. A. Shirley, J. Chem. Phys. 61, 4780 (1974).
4. L. C. Snyder and H. Basch, Molecular Wave Functions and Properties, (John Wiley & Sons, New York, 1972).

18. RARE-EARTH VALENCE STATE STUDIES OF THE SERIES RIn_3 AND RSn_3 DERIVED FROM QUADRUPOLE COUPLING CONSTANTS

G. P. Schwartz* and D. A. Shirley

Discussions of the electronic structures of metals usually begin by partitioning the lattice into positively-charged ion cores plus itinerant valence electrons. For many metals this separation is a computational shortcut rather than an experimentally observable feature, but in the rare-earth metals and their compounds the "valence state" has a more exact meaning. The 4f electrons are sufficiently localized to be assigned unambiguously to the ion cores, which then have charges of +3 or, sometimes, +2. Considerable theoretical and experimental attention has recently been focused on the question of non-integral rare-earth valence and valence-state changes induced by pressure and temperature. Most of the cases studied to date have been rare-earth chalcogenides which have insulating or semi-metallic properties, but potentially interesting metallic cases have also been known for some time.

Early studies of the susceptibility and lattice constants of the rare-earth series RIn_3 indicated that Yb was in a lower valence state (presumably +2) than the other rare earths. The large increase in susceptibility noted on cooling to liquid helium temperatures was taken as an indication that the valence of Yb had changed from +2 to +3. In the RSn_3 series, $EuSn_3$ and $YbSn_3$ both appear with divalent rare earths, while $CeSn_3$ is trivalent at room temperature and originally was thought to become quadrivalent at helium temperatures. These early conclusions were disputed through later Mössbauer studies, but a consistent picture for the combined In and Sn series has not been published to date.

The RIn_3 and RSn_3 intermetallics crystallize in the FCC $AuCu_3$ structure, which places the In or Sn at a site with tetragonal symmetry. The non-cubic nature of this site leads to a non-vanishing, axially-symmetric electric field gradient q that is highly sensitive to changes in the surrounding rare-earth valence state. According to a simple point-charge model, q should scale as Z'/r^3, where

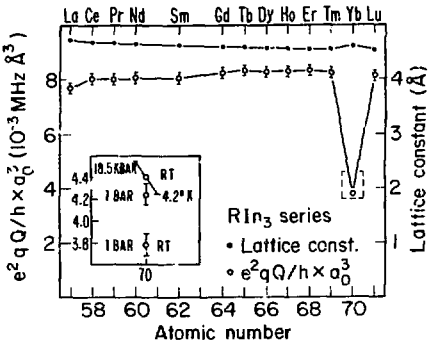

Fig. 1. Lattice constants and quadrupole coupling data for RIn_3 compounds plotted against atomic number. Inset shows variations for $YbIn_3$ with temperature and pressure changes. (XBL 758-3708)

Z' is an effective charge. The functional form of this dependence leads to a great sensitivity advantage of field gradients as opposed to lattice constants for determining valence states.

In this work radioactive ^{111}In was substituted into the In or Sn lattice sites of those RIn_3 and RSn_3 compounds that are stable at room temperature. Quadrupole coupling constants e^2qQ/h were determined by time-differential perturbed angular correlations in the 247 KeV state of ^{111}Cd following the electron-capture decay of ^{111}In. These were multiplied by a_o^3, where a_o is the lattice constant of each RIn_3 or RSn_3 compound, to form the product $(e^2qQ/h)a_o^3$; this latter should vary directly as Z'.

Figure 1 shows that Z' in the RIn_3 lattice is essentially constant for 12 rare earths, but dramatically lower for $YbIn_3$. This is interpreted as indicating a +2 valence state for Yb. The inset shows little change in $(e^2qQ/h)a_o^3$ at high pressure and at low temperature, indicating that the valence state does not change. The RSn_3 compounds showed similar behavior. Both $EuSn_3$ and $YbSn_3$ have divalent rare earths, while in $CeSn_3$ the cerium atoms are trivalent, as are La, Pr, Nd, Sm, and Gd in their respective compounds.

---

*Present address. Bell Telephone Laboratories, Murray Hill, NJ.

19. MEASUREMENT OF ZERO-POINT SPIN DEVIATIONS, PRESSURE-INDUCED HYPERFINE FIELD SHIFTS, AND SUBLATTICE MAGNETIZATIONS USING PERTURBED ANGULAR CORRELATIONS

H. H. Rinneberg, G. P. Schwartz, and D. A. Shirley

Time-differential perturbed angular correlation (TDPAC) of γ-rays has been applied increasingly to study solid-state properties. In most cases quadrupole interactions have been measured to infer the electric field gradient produced by the lattice at the site of the radioactive nucleus.[1] Recently, the well-known γ-γ cascade of ^{111m}Cd has been used to determine magnetic hyperfine fields at the impurity in Cd-doped antiferromagnetic insulators.[2] The observed internal fields have been discussed considering overlap and charge-transfer effects of the neighboring anions.

The purpose of this work was to use the PAC technique to probe properties of the magnetic lattice itself. The zero-point spin deviations in the doped two-dimensional Heisenberg-like antiferromagnets K_2NiF_4/Cd and Rb_2MnF_4/Cd were measured. The temperature dependences of the hyperfine fields in $RbMnF_3$/Cd and MnF_2/Cd yielded the temperature dependence of the sublattice magnetization next to the impurity. Finally we report the pressure dependence of the internal field in MnS/Cd.

Zero-point spin deviation, like zero-point motion, is a quantum-mechanical effect. It arises because the spins in a magnetic lattice cannot be aligned perfectly parallel. Rather, there is a deviation, Δ, such that

$$\langle S_z \rangle = S(1-\Delta)$$

In a three-dimensional antiferromagnetic lattice, theory predicts $\Delta_3 \sim 0.08$; while for the two-dimensional case the predicted value is larger: $\Delta_2 \sim 0.20$. By studying the supertransferred hyperfine fields[3] at Cd nuclei in the perovskites $KNiF_3$ and $RbMnF_3$ and the layered fluorides K_2NiF_4 and Rb_2MnF_4, and assuming the same spin transfer through each Ni-F-Cd and Mn-F-Cd path, it was possible to derive

$$\Delta_2(K_2NiF_4/Cd) = 0.26 \pm 0.10$$

$$\Delta_2(Rb_2MnF_4/Cd) = 0.25 \pm 0.10$$

if $\Delta_3 = 0.08$ was assumed in each case. These values are somewhat higher than the values $\Delta_2 = 0.17 - 0.20$ obtained from ENDOR and NMR studies, but they provide good qualitative confirmation of large Δ_2 values by a new, independent method.

The temperature dependence of the hyperfine field strength at a solute in a magnetic lattice helps set limits on the mechanism that create the field. For Cd in antiferromagnetic MnF_2 and $RbMnF_3$, the induced hyperfine field fell off slightly faster with temperature than the measured or inferred sublattice magnetization. At 30°K, for example, the hyperfine field at Cd in MnF_2 has fallen off 2% more than the ^{19}F NMR frequency in pure MnF_2, the agreement with a 1.5% decrease in the NMR frequency for ^{19}F next to (diamagnetic) Zn impurities.[3] Figure 1 shows the temperature trends.

When ^{111}Cd-doped MnS at 4.2°K is subjected to high pressures, the Mn-S bonds are shortened, thus increasing the strength at the exchange integral

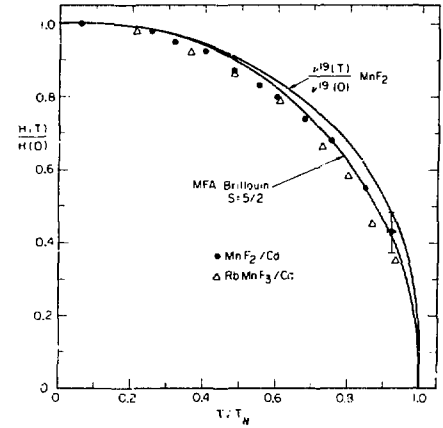

Fig. 1. Reduced temperature/hyperfine field plot for Cd-doped MnF_2 and $RbMnF_3$. (XBL 751-2075)

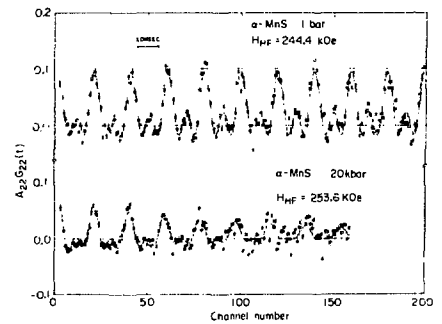

Fig. 2. Time spectrum of ^{111}Cd-doped MnS at 1 bar and 20 kbar. The solid line is a least-squares fit to a pure magnetic interaction in polycrystalline material. The time calibration is 0.888 ns/channel. (XBL 751-2078)

between $Mn3d_\sigma$ orbitals and $S3p_\sigma$ orbitals. The supertransferred hyperfine field at ^{111}Cd nuclei was predicted to increase by 4.3% at 20 kbar if in fact spin transfer through σ orbitals was responsible for this field. Figure 2 shows the time-dependent PAC spectrum. The experimental increase was 3.8 ± 0.8%, thus confirming this mechanism.

1. H. Haas and D. A. Shirley, J. Chem. Phys. 58, 3339 (1973).
2. H. H. Rinneberg and D. A. Shirley, Phys. Rev. Lett. 30, 1147 (1973).
3. M. Butler, V. Jaccarino, N. Kaplan, and H. J. Guggenheim, Phys. Rev. B 1, 3058 (1970).

20. BETA-DECAY ASYMMETRY FROM THE DECAYS OF ORIENTED ^{52}Mn AND ^{60}Co*

S. T.-C. Hung,† K. S. Krane,‡ and D. A. Shirley

In recent years numerous experimental studies have been made to search for evidence of parity (P) and time-reversal (T) violation in nuclei. Although no direct evidence for T violation has yet been obtained, indirect evidence results from the observation of CP-violation in the K_0 decay, and there is speculation as to whether this effect arises from T violation in weak or electromagnetic interactions. In the case of allowed beta decay, T violation would be manifest as a complex phase of the ratio of Fermi to Gamow-Teller amplitudes, y. Furthermore, because the size of the T-violating observable is proportional to $y/(1 + y^2)$, it is advisable to choose a case for investigation in which there is reasonable interference between the F and GT terms. Previous determinations of y in ^{52}Mn have not been in good agreement, and the possibility that a large value of y might make ^{52}Mn a favorable candidate for an investigation of T violation in beta decay prompted the present research.

The F/GT ratio y may be determined from a measurement of the directional asymmetry of beta particles relative to an axis of nuclear polarization. We have investigated the beta decay of ^{52}Mn by observing the asymmetry of positrons emitted from ^{52}Mn oriented at low temperatures. The ^{52}Mn nuclei were polarized in an iron lattice and cooled to 0.008°K by thermal contact with an adiabatically demagnetized paramagnetic salt. The positron asymmetry was determined by means of two independent techniques: the positrons were detected directly by using high-purity germanium detectors and indirectly by using NaI detectors to observe the annihilation gamma rays. These two techniques yielded a consistent result for the asymmetry, corresponding for this allowed decay to a ratio of the Fermi to Gamow-Teller matrix elements of $y = C_V M_F / C_A M_{GT} = -0.144 \pm 0.006$. An auxiliary experiment on ^{60}Co gave a beta asymmetry $A = -0.971 \pm 0.034$, in excellent agreement with the theoretical value of -1 expected for maximal parity violation.

This value of y is substantially larger than any of the seven values previously reported by other workers, which disagreed among themselves.* We are confident that our value is correct, however, because it is a much more direct measurement,

because the experimental design was superior, and because the larger asymmetry was obvious even by visual inspection of the raw data. Because the Fermi/Gamow-Teller ratio is so large, we conclude that ^{52}Mn would be an excellent candidate for an experimental test of time-reversal invariance in weak interactions.

*A detailed discussion, with references, appears in LBL-3488.

21. NUCLEAR ORIENTATION OF 2.3-d GOLD-198m

H.-E. Mahnke, G. Kaindl, F. Bacon, and D. A. Shirley

The magnetic hyperfine interaction of the $T_{1/2}$ = 2.3-d high-spin isomeric state of ^{198}Au has been measured in host metals of iron and nickel at temperatures down to 4 mK using the thermal-equilibrium nuclear-orientation technique. The resulting value for the magnetic moment, μ = (+) 5.55±0.35 n.m., strongly supports an interpretation of this state as a

$$[\pi h_{11/2};\ \nu i_{13/2}]\ 12^-$$

configuration analogous to ^{196m}Au and ^{200m}Au. The observed gamma-ray anisotropies are in agreement with the recently proposed decay scheme of ^{198m}Au; for the E2/M1-mixing ratio of the 204-keV gamma transition they result in a value of δ = -0.10±0.05.

22. RESEARCH PLANS FOR CALENDAR YEAR 1976

David A. Shirley and Associates

This will be a year of building and of exploratory research. Photoelectron spectroscopy (PES) has evolved into a reliable laboratory tool for characterizing one-electron properties of atoms, molecules, and solids using standard laboratory photon sources at fixed energies. Many valuable applications of PES to new materials can be expected in the future. The real frontiers of PES, however, involve the development of more sophisticated methods for the qualitative study of new phenomena. Our research efforts will be directed at the following goals of this nature.

The Stanford Synchrotron Radiation Project (SSRP) affords a unique, convenient facility for doing exploratory research with continuously tunable photon energies in the range 30 - 1000 eV. Initial experiments with copper and gold single crystals have shown a dramatic energy-dependent directional anisotropy in the d-band PES spectrum. This effect will be studied in detail. A complete analysis of the effect should answer certain fundamental questions about photoemission in solids.

Surface properties will be investigated. An attempt will be made to determine definitively the effect of the surface on binding energies, plasmon spectra, densities of states, and magnetic moments. Stepped surfaces will also be studied.

The new Berkeley Magnetic Photoelectron Spectrometer will be completed and tested. Plans are underway to use this high-efficiency, high-resolution machine to study PES spectra of exotic species, such as van der Waals' molecules, in molecular beams; this will be done in collaboration with Y. T. Lee.

High-temperature atomic and (later) molecular species will be studied to elucidate electron-correlation effects. Ultraviolet PES will be used, possibly at SSRP. Gas-phase core-level binding energies and time-dependent phenomena may also be studied at SSRP.

23. 1975 PUBLICATIONS AND REPORTS

David A. Shirley and Associates

Journals and Books

1. D. A. Shirley, X-ray Photoemission and Surface Structure, J. Vac. Sci. Technol. 12, 280 (1975).

2. W. J. Pardee, G. D. Mahan, D. E. Eastman, R. A. Pollak, L. Ley, F. R. McFeely, S. P. Kowalczyk, and D. A. Shirley, Analysis of Surface- and Bulk-Plasmon Contributions to X-ray Photoemission Spectra, Phys. Rev. B11, 3614 (1975).

3. M. S. Banna and D. A. Shirley, Molecular Photoelectron Spectroscopy at 132.3 eV. Methane, the Fluorinated Methanes, and Hydrogen Fluoride, Chem. Phys. Letters 33, 441 (1975).

4. D. A. Shirley, A Summary of the International Conference on Hyperfine Interactions Studied by Nuclear Reactions and Decay, Physica Scripta 11, 244 (1974).

5. D. A. Shirley, Hyperfine Interactions and ESCA Data, Physica Scripta 11, 117 (1974).

6. H.-E. Mahnke, G. Kaindl, F. Bacon, and D. A. Shirley, Nuclear Orientation of 2.3-d ^{198m}Au, Nuclear Physics A247, 195 (1975).

7. T. S. Chou, K. S. Krane, and D. A. Shirley, Nuclear-Orientation Measurements of Parity Admixture in the 501 - keV Gamma Transition in ^{180}Hf^m, Phys. Rev. C12, 286 (1975).

8. S. Süzer, M. S. Banna, and D. A. Shirley, Relativistic and Correlation Effects in the 21.2-eV Photoemission Spectrum of Atomic Lead, J. Chem. Phys. 63, 3473 (1975).

9. S. P. Kowalczyk, F. R. McFeely, L. Ley, and D. A. Shirley, Multiplet Splitting of X-ray Photoemission Spectra of Core Levels in Magnetic Metals, 20th Annual Conf. on Magnetism and Magnetic Materials, AIP Conf. Proc. 24, 207 (1975).

10. S. P. Kowalczyk, L. Ley, F. R. McFeely, and D. A. Shirley, A High-Resolution X-ray Photoemission Study of the Total Valence-Band Densities of States of GaSe and BiI_3, Sol. St. Comm. 17, 463 (1975).

11. M. S. Banna and D. A. Shirley, Molecular Photoelectron Spectroscopy at 132.3 eV. The Second-row Hydrides, J. Chem. Phys. 63, 4759 (1975).

Invited Talks

1. D. A. Shirley, Harvard-MIT Physical Chemistry Seminar (March 6).

2. R. L. Martin, Philadelphia Meeting, American Chemistry Society (April 8).

3. D. A. Shirley, IBM Research Laboratories, Yorktown Heights (April 10).

4. D. A. Shirley, Physics Departmental Colloquium, UC Berkeley (April 16).

5. D. A. Shirley, Georgia Tech Chemistry Department: Dupont Lecturer (May 8).

6. D. A. Shirley, Chemistry Department, UCSD (May 13).

7. D. A. Shirley, XXVth Congress of IUPAC, Jerusalem, Israel: Main Section Lecturer on Molecular Structure (July 7).

8. D. A. Shirley, Faraday Discussion, Vancouver, B.C.: (July 15).

9. D. A. Shirley, Tenth Annual Conference, Microbeam Analysis Society, Las Vegas, Nev. (August 15).

10. D. A. Shirley, Chemistry Colloquium, Purdue University (September 25).

11. D. A. Shirley, Physical Chemistry Seminar, UC Berkeley (October 7).

LBL Reports

1. B. E. Mills, R. L. Martin, and D. A. Shirley, Further Studies of the Core Binding Energy-Proton Affinity Correlation in Molecules, LBL-4057, June 1975.

2. F. R. McFeely, J. Stöhr, G. Apai, P. S. Wehner, and D. A. Shirley, D-Orbital Directed Photoemission from Silver and Gold, LBL-4325.

3. H. H. Rinneberg, G. P. Schwartz, and D. A. Shirley, Measurement of Spin Deviations, Pressure-Induced Hyperfine-Field Shifts, and Sublattice Magnetizations Using Perturbed Angular Correlations, LBL-4538.

4. G. P. Schwartz and D. A. Shirley, Rare-Earth Valence State Studies of the Series RIn_3 and RSn_3 Derived from Quadrupole Coupling Constants, LBL-4539.

5. B. E. Mills and D. A. Shirley, K-Shell Correlation-State Spectra in Formamide, LBL-4534.

6. S. P. Kowalczyk, L. Ley, F. R. McFeely, R. L. Martin, and D. A. Shirley, Relaxation and Final-State Structure in XPS of Atoms, Molecules, and Solids, LBL-3476.

7. S. T.-C. Hung, K. S. Krane, and D. A. Shirley, Beta-Decay Asymmetry from the Decays of Oriented ^{52}Mn and ^{60}Co, LBL-3488.

8. R. L. Martin and D. A. Shirley, Many-Electron Theory of Photoemission, LBL-3467.

9. R. L. Martin and D. A. Shirley, Theory of Core-Level Photoemission Correlation State Spectra, LBL-3468.

10. R. L. Martin, B. E. Mills, and D. A. Shirley, Fluorine 1s Correlation States in the Photoionization of Hydrogen Fluoride: Experiment and Theory, LBL-3469.

11. M. S. Banna and D. A. Shirley, Molecular Photoelectron Spectroscopy at 132.3 eV: N_2, CO, C_2H_4, and O_2, LBL-3479.

12. M. S. Banna and D. A. Shirley, On the Use of Yttrium and Sodium Anodes in Photoelectron Spectroscopy, LBL-3491.

13. Muhammad Salim Banna, Gas Phase Photoemission with Soft ($NaK\alpha$, $MgK\alpha$) and Ultrasoft ($YM\zeta$) X-ray Sources, (Ph.D. Thesis) LBL-3473.

14. Gary Paul Schwartz, Applications of Time-Differential Perturbed Angular Correlations to the Study of Solids (Ph.D. Thesis) LBL-4056.

h. Crossed Molecular Beams

Yuan T. Lee, Principle Investigator

1. ENERGETICS AND DYNAMICS OF THE FORMATION OF TRIHALOGEN MOLECULES

James J. Valentini and Michael J. Coggiola

Crossed molecular beam techniques have been used to study the endoergic reactions between F_2 and I_2, ICl, or HI. All three reactions produce the trihalogen (or pseudotrihalogen):

$$F_2 + I_2 \rightarrow FII + F \quad (1)$$

$$F_2 + ICl \rightarrow FICl + F \quad (2)$$

$$F_2 + HI \rightarrow FIH + F \quad (3)$$

The results of this experiment strongly suggest that the observed products in reactions (2) and (3) are indeed FICl and FIH with the F atom attached to I but not Cl or H, as ICIF or IHF. Figure 1 shows the threshold behavior of the formation of I_2F, ClIF and HIF products as the relative kinetic energy between F_2 and I_2, ICl, or HI is varied. From the observed threshold and the dissociation energies of F_2, I_2, ICl, and HI, lower bounds on the stability (with respect to the free atoms) of these triatomic species can be established as 69, 81, and 90 kcal/mole, respectively. Figure 2 is a schematic diagram of the reaction energetics for one of the systems, $F_2 + I_2$. Similar diagrams can be constructed for the F_2 + ICl and F_2 + HI systems.

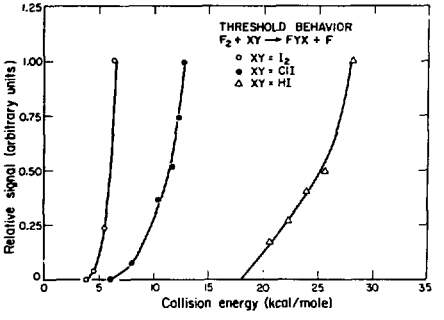

Fig. 1. Energy dependence of the relative total cross sections for the reactions: (○) $F_2 + I_2$; (●) F_2 + ICl; (Δ) F_2 + HI. (XBL 7510-8537)

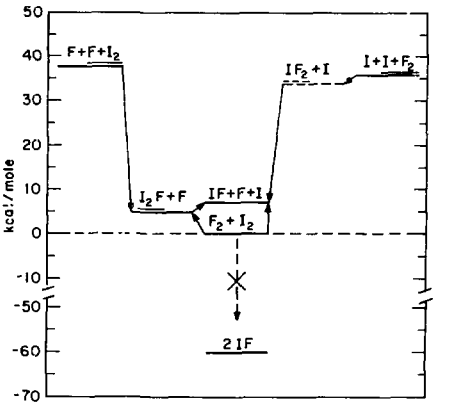

Fig. 2. Schematic diagram of the reaction energetics for $F_2 + I_2$. (XBL 753-2541)

For the systems $F_2 + I_2$ and F_2 + ICl, the reactions

$$F_2 + I_2 \rightarrow IF + I + F \quad (4)$$

$$F_2 + ICl \rightarrow IF + Cl + F \quad (5)$$

are also energetically allowed at the collision energies used in these experiments. IF was observed in both reactive systems. Figure 3 shows the angular distributions of the reactively scattered I_2F and IF products formed from $F_2 + I_2$ at collision energies of 12.6 and 18.7 kcal/mole. The IF distribution was obtained by subtraction of a fraction of the I_2F distribution from the measured IF signal. This subtraction is necessary to correct for IF produced from I_2F in the electron bombardment ionizer of the detector.

These results indicate that reaction (5) does not proceed via a four-center mechanism, as shown by the energy schematic in Fig. 2. Such a mechanism is exoergic by more than 60 kcal/mole. If even a small fraction of this energy appeared as product translation, the IF angular distribution would be much broader. Also, since the four-center reaction produces two identical molecules, the product distribution would have forward-backward symmetry in the center-of-mass coordinate system, and be roughly symmetric about the center-of-mass (c.m.) angle in the laboratory system under our experimental conditions.

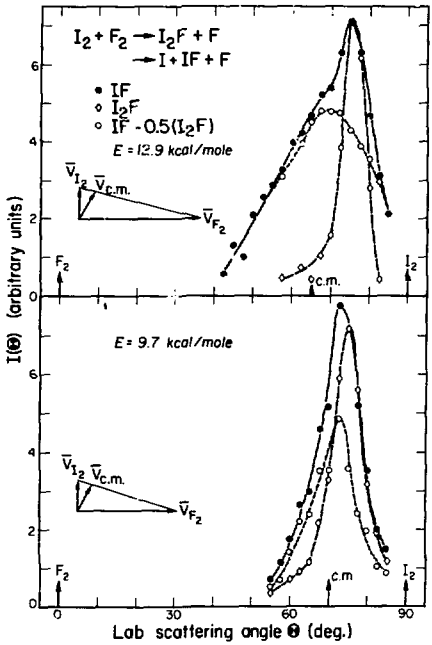

Fig. 3. Angular distributions of reactively scattered I_2F and IF products formed from $F_2 + I_2$ at collision energies of 12.6 and 18.7 kcal/mole. The IF distribution (solid line) was obtained by subtraction of a fraction of the I_2F distribution (dot-dashed line) from the measured (dashed line) IF signal. The appropriate Newton diagrams are shown for each collision energy. (XBL 7510-8536)

2. INTRAMOLECULAR ENERGY TRANSFER IN CHEMICALLY ACTIVATED COMPLEXES

Richard Buss and Michael Coggiola

Intramolecular energy transfer in long-live reaction complexes can be studied for some reactions, with crossed molecular beams. The effectiveness of this method depends on the reaction energetics as well as favorable kinematics relations. The reaction of chlorine atoms with bromo-olefins to produce chloro-olefins has several advantages. The detachment of bromine from the radical intermediate is known to proceed with negligible potential barrier. Thus no complication is added to the analysis regarding redistribution of energy in the exit channel. In addition, the exoergicity (about 12 kcal) is sufficiently small that the intermediate radical can be produced with energy only moderately above the chemical activation energy. We have begun a study of the extent of energy randomization in the chemically activated complex with the reaction of chlorine atoms and vinyl bromide (C_2H_3Br). A supersonic jet of chlorine atoms is produced from Cl_2 by thermal dissociation in a graphite oven at temperature about 1700K. The vinyl bromide beam is produced from a nozzle source at room temperature.

Angular distributions of product have been obtained for three collision energies by seeding the Cl in various inert carrier gases. The product intensity was determined at each angle by monitoring mass 62 (C_2H_3Cl) with a quadrupole mass spectrometer.

Preliminary results indicate that the magnitude of product translational energies are somewhat higher than what one would expect from a statistical theory.

We have begun velocity analysis of the product using a cross-correlation time of flight method. The product translational energy distribution will then be compared with that predicted by various models to ascertain whether internal energy is being redistributed in a statistical fashion.

3. INTERACTION POTENTIAL BETWEEN Cl and Xe: EVIDENCE OF INNER "CHEMICAL" WELL

Christopher Becker and James J. Valentini

The interaction potentials between open shell atoms or molecules and closed shell atoms or molecules play very important roles in chemical processes. For example, the understandings of a termolecular reaction, Cl + Cl + Xe → Cl_2 + Xe, or the atomic mechanism of HI formation; I + H_2 + I → 2HI, will not be possible without precise information on Xe + Cl and H_2 + I interaction potentials. However, the nature of the forces operating on electronic open shell-closed shell systems in presently obscure. Especially, it is not clear to what extent chemical forces are operating in these systems. Recently, a class of "van der Waals complexes" (e.g., ArClF, ArHCl) have been proposed to have characteristics of chemical bonding. The careful investigation of the open shell atom to rare gas atom interaction may prove to be a basis for understanding of weak "chemical bonding" in these systems.

In this experiment, the potential for ground state Cl + Xe is examined via crossed molecular beam measurements of differential elastic cross sections ($\sigma(\theta)$) for three different collision energies (E). The Ar + Xe system has also been studied for comparison. The angular distributions of ^{35}Cl (or ^{40}Ar) were measured in these experiments. The usual heavier rare gas scattering structures, namely rainbow and supernumerary rainbows were resolved in the Ar + Xe data. However, the Cl + Xe data displays a new oscillatory structure qualitatively different from the rare gas pair.

For a given E and potential V(r), the $\sigma(\theta)$ can be calculated by semiclassical scattering theory. By varying the parameters of an analytic form we attempt to find a best fit to the experimental results. In this way a flexible form of V(r) was used for Ar + Xe and r_{min} and the well depth determined to within 5%.

Unlike the easily explainable rare gas system, the analysis of the $\sigma(\theta)$ of ^{35}Cl is more complex. Preliminary fits of the data for E of ~2.4 and 6.1 kcal/mole using Lennard-Jones (N,6) potentials suggested two very different potentials for each E. Careful examination of the $\sigma(\theta)$ has led to the conclusion that a chemical well coexists in this system with a van der Waals region. This inner well is 2 to 3 times deeper than the van der Waals well and has perhaps more than an angstrom smaller r_{min} than for Ar + Xe. Recent spectroscopic data on Xe Cl analyzed by Tellinghuisen et al., has also pointed to a well depth about twice that for Ar + Xe. The vibrational level spacings were observed to be very different from normal diatomic molecules, supporting the conclusion that this potential has an unusual shape.

We remark that, as yet, unanalyzed earlier scattering data for F + Ar also shows an analogous interference pattern as does the D_2 + I system, which may have an incomplete analysis. Recent data for Cl + HI also show these informative oscillations. Further work is needed to elucidate the transition from a van der Waals to a chemical bonding region.

4. INTERACTIONS AND REACTIONS OF ELECTRONICALLY EXCITED ATOMS

Andrew Wang

The phenomenon of Penning ionization has received extensive attention in recent years. The interaction between the helium metastable atom with other rare gas atoms has, in particular, commanded a great deal of research effort. A favorite prototype in many of these studies is the reaction

$$He\ (^3S) + Ar \rightarrow \begin{matrix} HeAr^+ + e^- \\ Ar^+ + e^- + He \end{matrix}$$

Yet, notwithstanding the wealth of information available on this system, a very important and much sought after datum, namely the $He(^3S)$ + Ar potential, remains beleaguered by uncertainties. This system is quite suitable for crossed molecular beam studies: it having been established that Penning ionization by the metastable atom takes place only at small impact parameters, it follows that only the large ample region of the differential cross section is affected, leaving the information on the real part of the potential contained in the small angle measurements undisturbed. Previous studies employing crossed beams here however failed to produce a potential that harmonizes with all the available data, especially the total cross section results. We have therefore decided to make another attempt to arrest the indeterminateness in the potential parameters. Differential cross section measurements were taken at two temperatures, 300K and 650K, and a MMSV potential form was used to fit the data. The resulting potential, which consists of a real and an imaginary part, agrees very well with the total cross section measurements of Niehaus et al. It also compares favorably with the recent more refined results of Haberland et al.

Pursuing the same line of inquiry into the nature of the Penning process has led us to measure also the differential cross section for the reaction He(T/S) + D_2. We have made the measurements at three temperatures for both He(T + S) + D_2 and He (T) + D_2. This should enable us to unequivocally establish the potentials for He (T) + D_2 and He (S) + D_2. The ratio of associative ionization to Penning ionization has also been obtained as a function of the relative kinetic energy. Our results are currently being analyzed.

The advent of the dye laser with its impressive tuneability has spot-lighted another class of highly excited states, namely the Rydberg states. We are planning to make total collisional ionization cross section measurements for selectively produced high Rydberg states of He and other atoms as a function of relative kinetic energies. As such, a nitrogen-pumped dye laser system as well as a flashlamp dye laser are currently being assembled and tested. The tuneable dye laser will be used for the excitation of a beam of metastable rare gas atoms into high Rydberg state.

5. PHOTOIONIZATION CROSSED MOLECULAR BEAMS APPARATUS

Cheuk-Yiu Ng

The photoionization crossed molecular beams apparatus is constructed to combine the photoionization mass spectrometry and molecular beam techniques to study ion-molecule reactions and photoionization threshold behavior of atoms and molecules, at a photon energy lying between 5 eV to 25 eV. With a supersonic beam production system, it is possible to obtain a gas jet with well defined kinetic energy and full relaxation of internal degrees of freedom, and still maintain relatively high sample density. The full relaxation of internal degrees of freedom is essential in the study of photoionization threshold of polyatomic molecule. On the other hand, photoionization using highly monochromatic VUV photons provides very fine control of ionizing energies, which makes it the best method to prepare known internally excited atomic and molecular ions. These attractive features not only enable this machine to re-examine the photoionization efficiency curves from which more accurate structural and thermochemical data will be derived, and also to study ion-molecule reaction with known internal and kinetic energies. The arrangement of this apparatus is also suited for the investigation of radical molecules produced by chemical reactions in collision regions. The machine is essentially a chamber with two

independent beam production systems coupled to a dispersed windowless vacuum UV source. In addition, a quadrupole mass spectrometer, an electrostatic photoelectron energy analyzer and a photon detector which will give information on the mass of the product ions, internal state of the ions, and photon intensities respectively simultaneously during the progress of the experiment.

One of the systems we are going to look at in the near future is the reaction between hydrogen molecule ions at different vibrational excited states with helium to look for resonance structure in reactive scattering. An examples of photo-ionization efficiency curves, we will re-examine some polyatomic molecules such as CO_2, and SF_6. It is expected that from fully relaxed molecules, better information on the photoionization threshold and structure of molecule ions as well as other thermochemical data could be derived. Various components of this machine is now under careful testing. This program is carried out with the collaboration of Professor Mahan's group.

6. MEASUREMENT OF THE INELASTICITY OF RARE GAS ATOM-MOLECULE COLLISIONS

Randolph Sparks

A novel detector for our crossed molecular beam apparatus, which will allow measurement of particle flight times with a resolution previously unachievable, has been constructed in our laboratory. With this new detector, we hope to resolve inelastic effects in the collisions of rare gas atoms with simple molecules which have previously been seen only very poorly or not at all. The increased resolution of the detector is due to the possibility of a drastic reduction of the size of the region in which the critical measurement process takes place. In our standard ion-counting detection system, the incident beam is first modulated by a cross-correlation chopping wheel. After chopping, the beam travels approximately 17 cm to an ionizer. Ionization is necessary to allow quadrupole mass selection and scintillation particle detection. Once the particle is ionized, it is attracted by strong accelerating fields, and takes an insignificant additional amount of time to reach the ion-counting system. Since the ionization may occur anywhere within the length of the ionizer (~2 cm) the error in the effective total flight path (~17 cm) is large, thus resulting in very poor energy resolution of the scattered product. The critical measurement process occurs in the ionizer.

In the new detector, the problem of ion-gun length is eliminated entirely, while the effective total flight path is lengthened. The new detector consists of a cross-correlation chopping wheel, followed by a Weiss-type electron gun, again located approximately 17 cm behind the chopping wheel. A Johnson electron multiplier is located approximately 30 cm beyond the Weiss gun. The object is to excite the incoming particles to metastable electronic states by electron impact in the gun, a process which results in negligible longitudinal momentum change. Then the charged particles are removed by deflection fields. Finally, the signal is observed from the electrons ejected by the metastables when they collide with the front surface of the electron multiplier. Since, in this measurement scheme, the critical measurement process occurs at a surface, the detector, nominally, has infinite resolution. Our ability to measure time thus becomes the limiting factor. However, since we can measure the time intervals to a greater precision than we can define the initial velocity of our molecular beams, the resolution of the experiment becomes limited by our ability to control the initial conditions of the system, not by our ability to measure the relevant parameters. The limitation of the detector is that it requires one to study systems that can form high energy ($\geq$ 4 eV) metastable states. Rare gas atoms are the most convenient.

The detector will initially be used to measure the inelasticity of collisions of rare gas atoms with the simple triatomics N_2O and CO_2. These systems have previously been studied by our group using the old detection system. It is expected that the greatly increased resolution of the new detection system will yield much greater insight into the mechanisms of the collisional excitation of rotational and vibrational states of molecules.

7. RESEARCH PLANS FOR CALENDAR YEAR 1976

Yuan T. Lee

Interaction potentials between open shell atoms and closed shell atoms or molecules will be investigated in great detail. We hope to thoroughly understand the nature of weak "chemical" interaction in these systems during the next year. The understanding of termolecular recombination processes and the structure of "van der Waals molecules" will not be possible without this information. Special attention will be paid to rare gas-halogen atom interactions. Rare gas halide laser is one of the most powerful visible lasers under development. The development and improvement of rare gas halide laser urgently requires detailed information of interaction potentials of these systems.

Reaction dynamics of selectively excited atoms and molecules is another area we will make some major effort. Especially, chemistry of atoms in high Rydberg states, reactions of vibrationally excited molecule ions (with Mahan's group) and the reaction dynamics of vibrational - rotational state selected HF molecules by laser excitation. The understanding of the role played by internal excitation in promoting chemical reactions will be very useful in the development of effective laser isotope separation schemes. This information is also indispensable for the advancement of the modern theory of chemical kinetics.

Reactions between radical atoms and radical molecules will be studied with a special interest in chemiluminescence in visible region. In addition to the reactions of such radicals as

CH_3, I_2F and XeF, we will gradually shift our attention to those free radicals with atmospheric importance, i.e., HO_2, OH etc (with Johnston's group). Other reactions related to atmospheric chemistry which will be pursued immediately are reactions of oxygen atoms and ozene. $O_3 + Cl$ is one of such an example.

8. 1975 PUBLICATIONS AND REPORTS

Yuan T. Lee and Associates

Journals and Abstracts

1. J. M. Farrar and Y. T. Lee, Crossed Molecular Beam Study of F + CH_3I, J. Chem. Phys. 63, 3639 (1975) (LBL-4002).

2. Y. T. Lee, Molecular Beam Chemistry of Fluorine Containing Radicals, Abstract of paper 169th ACS National Meeting, Pennsylvania, Phys. 59, (1975) (LBL-4008A).

3. Michael J. Coggiola, James J. Valentini, and Y. T. Lee, Reactive Scattering of F_2 and I_2, Electronic and Atomic Collisions, IX ICPEAC Ed. by Risley and Geballe 1, 347, (1975) (LBL-4005A).

4. R. J. Gordon, D. S. Y. Hsu, Y. T. Lee, and D. R. Herschbach, Detection of Hydrogen Atom Beams by Stimulated Surface Ionization, J. Chem. Phys. 63, 5056 (1975).

Presentations

1. Y. T. Lee, Molecular Beam Chemical Kinetics, Lawrence Livermore Laboratory, Jan. 12, 1975.

2. Y. T. Lee, Energetics and Dynamics of Elementary Chemical Reactions, California Institute of Technology, Feb. 19, 1975.

3. Y. T. Lee, Studies in Chemical Dynamics (Plenary Lecture), Annual Conference on Mass Spectrometry and Allied Topics, Houston, Texas May 1975.

4. Y. T. Lee, Radical Chemistry by Molecular Beams Method, Stanford Research Institute, Oct. 16, 1975.

5. Y. T. Lee, Formation and Decomposition of Radical Molecules, University of California Davis, Oct. 28, 1975.

6. Y. T. Lee, The Formation and Decay of Radical Molecules, Richard Wolfgang Symposium in Chemistry, Yale University, Nov. 13-14, 1975.

LBL Reports

1. A. L. J. Burgmans, J. M. Farrar, and Y. T. Lee, Attractive Well of He-He from He^3-He^4 Differential Elastic Scattering Measurements, submitted to J. Chem. Phys., LBL-4072, July 1975.

2. James J. Valentini, M. J. Coggiola, and Y. T. Lee, If Bond Strength in HF, ClF, and HF, submitted to the J. Am. Chem. Soc., as a letter to the editor, LBL 4502, Oct. 1975.

3. M. J. Coggiola, James J. Valentini, and Y. T. Lee, Molecular Beam Study of $F_2 + I_2$, submitted to International Journal of Chemical Kinetics, LBL-4515, Oct. 1975.

i. Potential Energy Surfaces for Chemical Reactions

Henry F. Schaefer III, Principal Investigator

1. METAL CLUSTERS, CHEMISORPTION, AND SURFACE CHEMISTRY*

Charles W. Bauschlicher, Jr., and Henry F. Schaefer III

The critical importance of catalysis in meeting the world's near-term energy needs has created a tremendous surge of interest in surface chemistry. Until recently, theory has played only a limited role in the development of surface chemistry. However during the past five years, quantitative molecular orbital theories have been used to provide considerable insight into the properties of small metal clusters and the nature of the chemisorptive bond. However, most of these theoretical studies have employed semi-empirical methods, subject to well-documented deficiencies. During the past year we have nearly completed the first definitive ab initio study of chemisorption. The system considered was chemisorption of atomic hydrogen by the (0001) surface of beryllium metal. The surface was modeled by metal clusters as large as Be_{22}, which is seen in Fig. 1.

Among the more important questions addressed theoretically have been (a) the convergence of metal cluster properties to the analogous properties of the infinite metal surface, (b) the nature of and number of surface atoms participating in the chemisorptive bond, and (c) the energetics and structures of various plausible sites (on the surface) for chemisorption. The most significant of these results are summarized in Table 1, where it is seen that three sites are about equally favored for chemisorption, while the fourth (the directly overhead site) is somewhat less so.

*Abstracted from J. Chem. Phys. 62, 4815 (1975), LBL-4518, LBL-4516, and LBL-4573.

2. PHOTOCHEMICAL FORMATION, PROPERTIES, AND REACTIONS OF THE METHYLENE RADICAL*

Charles W. Bauschlicher, Jr., Clifford E. Dykstra, James W. Meadows, and Henry F. Schaefer III

One of the most characteristic features of the photochemistry of ketene is a dependence on the wavelength of the absorbed radiation. Both triplet and singlet methylene appear to be formed at wavelengths less than 3700 Å, but the triplet fraction reported varies from 26% at 2139 Å to 75% at 3660 Å. Since the first excited state ($a\,^3\Pi$) of the CO molecule is relatively high-lying (48,000 cm^{-1}), spin conservation requires that triplet and singlet methylene originate, respectively, with excited triplet and singlet states of ketene. Thus the nature and positions of the excited electronic states of ketene are expected to play a crucial role in any satisfactory

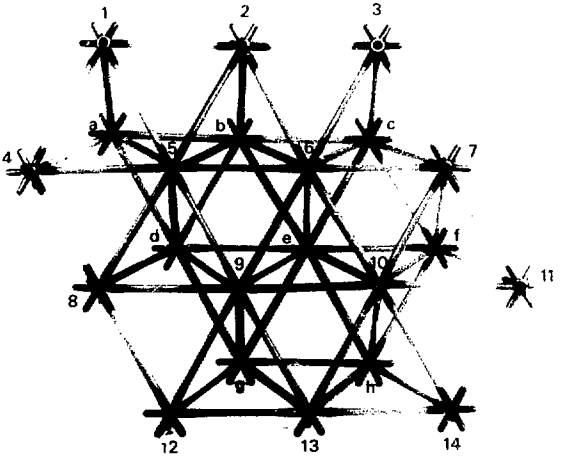

Fig. 1. Model of the Be_{22} cluster in the present theoretical study. The distance between adjacent atoms within a layer is 2.2866 Å, while that between adjacent atoms in different layers is 2.2255 Å. Surface atoms are labelled by the numbers 1-14, while second-layer atoms are labelled by the letters a-h. (XBB 7512-8737A)

Table 1. Models of the chemisorption of atomic hydrogen by the (0001) surface of beryllium metal. The cluster notation $Be_{10}(7,3)$ implies a model with seven atoms for the surface layer and three atoms for the second layer. Bond distances r_e are in Å and chemisorptive bond energies D_e in kcal/mole.

Open Site			Eclipsed Site			Bond Midpoint Site			Directly Overhead Site		
Model	r_e	D_e	Model	r_e	D_e	Model	r_e	D_e	Model	r_e	D_e
$Be_3(3,0)$	1.25	19.1	$Be_4(3,1)$	1.24	28.7	$Be_4(4,0)$	1.26	70.1	$Be_1(1,0)$	1.42	46.4
$Be_5(4,1)$	1.02	23.2	$Be_5(4,1)$	1.15	30.1	$Be_5(4,1)$	1.14	32.4	$Be_7(7,0)$	1.43	71.3
$Be_6(6,0)$	1.18	47.3	$Be_7(6,1)$	1.11	40.8	$Be_{10}(10,0)$	1.17	45.3	$Be_{10}(7,3)$	1.43	27.3
$Be_6(3,3)$	1.11	55.3	$Be_{13}(10,3)$[a]	0.90	57.2	$Be_{13}(10,3)$	1.05	44.8	$Be_{13}(10,3)$	1.41	31.1
$Be_9(6,3)$	1.13	50.2		0.94	58.3	$Be_{22}(14,8)$	1.04	53.4	$Be_{22}(14,8)$	1.39	31.4
$Be_{13}(10,3)$	0.99	39.0	$Be_{22}(14,8)$	0.97	51.9						
$Be_{22}(14,8)$	0.94	55.1									

[a] Two distinct $Be_{13}(10,3)$ clusters were studied.

understanding of the photo-decomposition of ketene. Vertical excitations of eighteen excited electronic states have been investigated theoretically. For eight of the low-lying states of ketene, equilibrium geometries have been predicted, and the resulting energy level diagram is shown in Fig. 1.

Ab initio electronic structure theory has also been applied to the insertion reaction of singlet methylene with molecular hydrogen. Since the molecular orbital descriptions of $CH_2(^1A_1) + H_2$ and CH_4 differ by two electrons, the least motion approach considered here is forbidden in the sense of Woodward and Hoffmann. Electron correlation was explicitly taken into account via configuration interaction (CI). The CI included all singly- and doubly-excited configurations (a total of 1192) with respect to three reference configurations. A primary goal was the location of the saddle point or transition state geometry

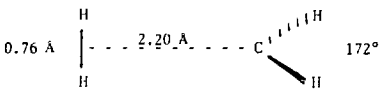

This stationary point on the potential energy surface lies 26.7 kcal/mole above separated $CH_2(^1A_1) + H_2$. The portion of the minimum energy path near the saddle point has been obtained by following the gradient of the potential energy in the direction of most negative curvature. The electronic structure at the transition state is compared with that of the reactants and product

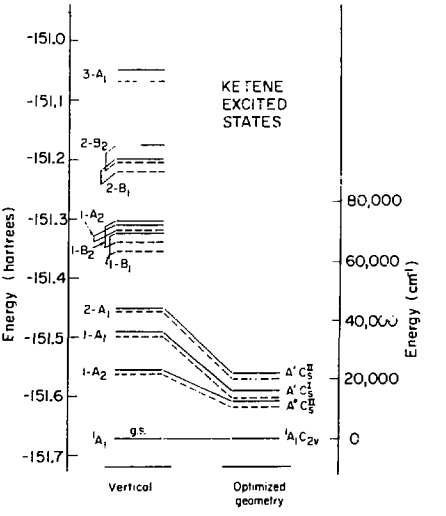

Fig. 1. Ketene excited states. Dotted lines represent triplet states and solid lines represent singlets. The vertical excitation energies are all for the same geometry, namely that of the $^1A_1$ ground state. The optimized results refer to geometries separately determined for each state, and the reduced symmetry and corresponding state designations are shown. (XBL 757-4445)

in terms of the natural orbitals resulting from the wave functions. A section of the potential energy surface is seen in Fig. 2.

The transition states and barrier heights for the reactions $CH_2(^3B_1) + H_2 \rightarrow CH_3 + H$ and $CH_2(^3B_1) + CH_4 \rightarrow CH_3 + CH_3$ have been predicted using nonempirical electronic structure theory. Our earlier work on the $CH_2(^3B_1) + H_2$ reaction has been extended by (a) the addition of polarization functions to the earlier double zeta basis set, and (b) the consideration of five additional degrees of freedom in the potential surface. The earlier conclusions remain essentially unchanged: the transition state occurs for a C_{2v} structure and the barrier height is ~15 kcal/mole. For the methane abstraction reaction a barrier height ~7 kcal/mole higher was found, implying that neither reaction should occur to a significant degree at room temperature. This conclusion is consistent with the BEBO calculations of Carr but in disagreement with the MINDO predictions of Dewar.

Finally, we have made a detailed study of the singlet-triplet electronic energy separation in methylene and silylene. Very large basis sets of contracted gaussian functions were employed. For CH_2, the factors leading to a reasonable (9 kcal/mole) value of the $^3B_1 - {}^1A_1$ energy separation are examined. For SiH_2, the $^1A_1$ state is predicted to lie below the $^3B_1$ state by ~ 10 kcal/mole.

*Abstracted from LBL-4027, LBL-4092, LBL-4320, and LBL-4529.

3. RESEARCH PLANS FOR CALENDAR YEAR 1976

Henry F. Schaefer III

Chemisorption of a wide variety of molecules (CO, N_2, C_2H_2, C_2H_4, etc.) on Li and Be metal surfaces will be studied in detail. In addition model theoretical studies of the bonding of transition metal (e.g., Mn, Fe, Co, Ni) atoms and clusters with the organic molecules acetylene and ethylene will be initiated. These studies should play an extremely important role in our developing understanding of simple catalytic processes.

The laser related reaction $F + H_2 \rightarrow HF + H$ will be revisited in 1976 at a much higher level of theory than previously attainable. This reaction is of special interest since it is one of the very few for which careful experiments (including resolution of the HF vibrational energy distribution) may be compared with theoretical treatments of the potential surface and dynamics. Very large scale configuration interaction will be carried out, with a special eye to the importance of three-electron correlation effects near the saddle point. Two other reactions to be studied by ab initio methods are the isoelectronic $O + C_2H_4$ and $CH_2 + C_2H_4$ systems. The resulting potential energy surfaces should allow us to discuss in general the reactions of oxygen atoms and methylene with olefins.

An important theoretical development now being vigorously pursued is the Theory of Self-Consistent Electron Pairs. This new theory avoids many of the difficult aspects of existing methods for the treatment of electron correlation in

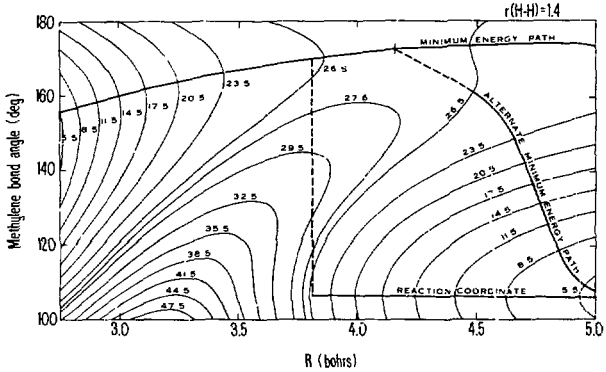

Fig. 2. Contour map (with r(H-H) = 1.4) used to illustrate several types of pathways for the singlet methylene insertion reaction. Note that access to the alternate minimum energy path requires less than 0.1 kcal/mole. (XBL 755-2894)

molecules. It holds the promise of reducing the correlation problem (i.e., the instantaneous repulsions of pairs of electrons) to a complexity comparable to ordinary Hartree-Fock procedures. Since the method has only been developed during the past six months and tested for LiH, much work remains to be done, especially concerning the extension to open-shell systems of the type our research usually concerns.

4. 1975 PUBLICATIONS AND REPORTS

Henry F. Schaefer III and Associates

Journals

1. Henry F. Schaefer III, Potential Energy Surfaces and Methylene Reactions, Chemistry in Britain 11, 227 (1975).

2. Clifford E. Dykstra, Peter K. Pearson, and Henry F. Schaefer III, Electronic Structure of Nitrenes. LiN, the Simplest Ionic Species, J. Am. Chem. Soc. 97, 2321 (1975) (LBL-2983).

3. Gretchen M. Schwenzer, Henry F. Schaefer III and Charles F. Bender, Excited Electronic States of HNC, Hydrogen Isocyanide, J. Chem. Phys. 63, 569 (1975) (LBL-2985).

4. Gretchen M. Schwenzer and Henry F. Schaefer III, The Hypervalent Molecules Sulfurane (SH_4) and Persulfurane (SH_6), J. Am. Chem. Soc. 97, 1393 (1975) (LBL-3421).

5. Peter K. Pearson, Henry F. Schaefer III and Ulf Wahlgren, Potential Energy Surface for the Model Unimolecular Reaction HNC → HCN, J. Chem. Phys. 62, 350 (1975) (LBL-3402).

6. Per Siegbahn and Henry F. Schaefer III, Potential Energy Surfaces for H + Li_2 → LiH + Li. Ground State Surface from Large Scale Configuration Interaction, J. Chem. Phys. 62, 3488 (1975) (LBL-3403).

7. Charles F. Bender, Barbara J. Garrison and Henry F. Schaefer III, A Critical Test of Semi-empirical FH_2 Potential Energy Surfaces: The Barrier Height for H + FH → HF + H, J. Chem. Phys. 62, 1188 (1975) (LBL-3432).

8. Charles W. Bauschlicher Jr., Dean H. Liskow, Charles F. Bender, and Henry F. Schaefer III, Model Studies of Chemisorption. Interaction Between Atomic Hydrogen and Beryllium Clusters, J. Chem. Phys. 62, 4815 (1975) (LBL-3465).

9. Clifford E. Dykstra and Henry F. Schaefer III, Electronic Structure of Dicarbonyls: The Ground State of Glyoxal, J. Am. Chem. Soc. 97, 7210 (1975) (LBL-4017).

10. Robert R. Lucchese and Henry F. Schaefer III, Charge-Transfer complexes. NH_3-F_2, NH_3-Cl_2, NH_3-ClF, $N(CH_3)_3$-F_2, $N(CH_3)_3$-Cl_2, and $N(CH_3)_3$-ClF, J. Am. Chem. Soc. 97, 7205 (1975) (LBL-3471).

11. Paul S. Bagus, Bowen Liu, Dean H. Liskow, and Henry F. Schaefer III, Electron Correlation and the Reality of XeF_2, J. Am. Chem. Soc. 97, 7216 (1975) (LBL-3482).

12. Gretchen M. Schwenzer, Charles F. Bender and Henry F. Schaefer III, Confirmation of the Discrepancy Between Theory and Experiment for the $\tilde{B}\ ^1A''$ State of HCN, Chem. Phys. Letters 36, 179 (1975) (LBL -3486).

13. Barbara J. Garrison, William A. Lester, Jr., and Henry F. Schaefer III, A Hartree-Fock Interaction Potential Between a Rigid Asymmetric Top and a Spherical Atom: (H_2CO, He), J. Chem. Phys. 63, 1449 (1975) (LBL-3493).

14. Leo Radom and Henry F. Schaefer III, Theoretical Predictions of the Molecular Structure of Sulphur Tetrafluoride, Aust. J. Chem. 28, 2069 (1975).

15. David R. Yarkony and Henry F. Schaefer III, The Acetyl Cation and its Geometrical Isomers, J. Chem. Phys. 63, 4317 (1975) (LBL-3497).

16. David R. Yarkony and Henry F. Schaefer III, Multiplet Splittings in the Photoelectron Spectra of Organic Radicals: Trimethylenemethane, Chem. Phys. Letters 35, 291 (1975) (LBL-4011).

17. John W. Birks, Harold S. Johnston and Henry F. Schaefer III, Ne-H-H Potential Energy Surface Including Electron Correlation, J. Chem. Phys. 63, 1741 (1975) (LBL-3753).

18. Dennis S. Marynick and Henry F. Schaefer III, Theoretical Studies of Metal-Phosphate Interactions. The Interaction of Li^+, Na^+, K^+, Be^{++}, Mg^{++}, Ca^{++} with $H_2PO_4^-$ and $(CH_3)_2PO_4^-$. Implications for Nucleic Acid Solvation, Proc. Natl. Acad. Sci. (USA) 72, 3794 (1975).

19. Barbara J. Garrison, William A. Lester, Jr., Per Siegbahn and Henry F. Schaefer III, Effect of Electron Correlation on the H_2CO-He Interaction Potential, J. Chem. Phys. 63, 4167 (1975) (LBL-4328).

20. Henry F. Schaefer III, Are Minicomputers Suitable for Large Scale Scientific Computation?, Proceedings of the Eleventh Annual IEEE Computer Society Conference, September, 1975.

Invited Lectures

1. Henry F. Schaefer III, Research School of Chemistry, Australian National University, Canberra, January, 1975.

2. Henry F. Schaefer III, Department of Chemistry, University of Western Australia, Perth, Australia, January, 1975.

3. Henry F. Schaefer III, Monash Chemical Society, Monash University, Melbourne, Australia, February, 1975.

4. Henry F. Schaefer III, Department of Theoretical Chemistry, University of Sydney, Sydney, Australia, February, 1975.

5. Henry F. Schaefer III, Department of Chemistry, University of Arizona, Tucson, Arizona, March, 1975.

6. Henry F. Schaefer III, Department of Chemistry, New Mexico State University, Las Cruces, New Mexico, March, 1975.

7. Henry F. Schaefer III, Theoretical Physics Colloquium, Los Alamos Scientific Laboratory, Los Alamos, New Mexico, March, 1975.

8. Henry F. Schaefer III, Department of Chemistry, Arizona State University, Tempe, Arizona, March, 1975.

9. Henry F. Schaefer III, Department of Chemistry, University of Oregon, Eugene, Oregon, April, 1975.

10. Henry F. Schaefer III, Department of Chemistry, University of California, Irvine, May, 1975.

11. Henry F. Schaefer III, Department of Chemistry, California Institute of Technology, Pasadena, May 1975.

12. Henry F. Schaefer III, Chemistry Division Colloquium, Argonne National Laboratory, Argonne, Illinois, July, 1975.

13. Henry F. Schaefer III, Department of Chemistry, Northwestern University, Evanston, Illinois, July, 1975.

14. Henry F. Schaefer III, Symposium "Are Big Machines Necessary?", Eleventh Annual IEEE Computer Society Conference, Washington, D.C., September, 1975.

15. Henry F. Schaefer III, Department of Chemistry, Carnegie-Mellon University, Pittsburgh, Pennsylvania, October, 1975.

16. Henry F. Schaefer III, Department of Chemistry, Pennsylvania State University, University Park, Pennsylvania, October, 1975.

17. Henry F. Schaefer III, Physical Chemistry Colloquium, University of California, Los Angeles, November, 1975.

18. Henry F. Schaefer III, Department of Chemistry, University of California, Davis, November, 1975.

LBL Reports

1. Clifford E. Dykstra and Henry F. Schaefer III, Electronic Structure of Dicarbonyls: Glyoxal Excited States, LBL-4017, April, 1975.

2. Charles W. Bauschlicher, Jr., Henry F. Schaefer III, and Charles F. Bender, The Least Motion Insertion Reaction $CH_2(^1A_1) + H_2 \rightarrow CH_4$: Theoretical Study of a Process Forbidden by Orbital Symmetry, LBL-4027, May, 1975.

3. Craig P. Baskin, Charles F. Bender, Robert R. Lucchese, Charles W. Bauschlicher, Jr., and Henry F. Schaefer III, Molecular Structure and Properties of CH_3BeF and CH_3MgF, LBL-4058, June, 1975.

4. Steven R. Ungemach and Henry F. Schaefer III, Molecular Structure of the $C\ell F_2$ and $C\ell F_4$ Radicals, LBL-4060, June, 1975.

5. David R. Yarkony and Henry F. Schaefer III, Self-Consistent-Field Wavefunctions Using a Symmetry-Restricted Annihilation of Single-Excitations Procedure, LBL-4073, July, 1975.

6. Clifford E. Dykstra and and Henry F. Schaefer III, Excited Electronic States of Ketene, LBL-4092, August, 1975.

7. Charles W. Bauschlicher, Jr., Charles F. Bender, Henry F. Schaefer III, and Paul S. Bagus, Chemisorption and the Properties of Metal Clusters, LBL-4516, November, 1975.

8. Charles W. Bauschlicher, Jr., Charles F. Bender, and Henry F. Schaefer III, Transition States for the Abstraction Reactions of Triplet Methylene with Hydrogen and Methane, LBL-4529, September, 1975.

9. Robert B. Brewington, Charles F. Bender and Henry F. Schaefer, Tetrahedral Be_4, LBL-4318, September, 1975.

10. James H. Meadows and Henry F. Schaefer III, Singlet-Triplet Separation in Methylene and Silylene, LBL-4320, October, 1975.

11. Charles W. Bauschlicher, Henry F. Schaefer III and Paul S. Bagus, A Realistic Cluster Model for Chemisorption, LBL-4573, December, 1975.

2. ATOMIC PHYSICS

a. Low Energy Atomic Physics

Howard A. Shugart, Principal Investigator

Introduction. The research activities of our group cover several areas including experimental and theoretical atomic physics, environmental monitoring through trace element detection, and energy conservation education. In basic research our goals included both measuring of atomic properties with sufficient accuracy for testing theoretical computations, and exploring atomic properties for developing new techniques and ideas. This year an important precision measurement on the $^3He^+$ ion has been reported. An accurate test of the foundations of quantum mechanics resolved a discrepancy which has existed for two years. The application of atomic and molecular absorption in carefully designed furnaces led to extremely sensitive detectors for monitoring Mercury, Cadmium, Lead, and NO_2 in environmental or medical samples. These developments and others are described in the summaries and publications which follow.

1. EXPERIMENTS ON STORED IONS

Michael H. Prior, Edmond C. Wang, and Randall D. Knight

Currently two experiments involving stored ions are in progress. The first makes use of a purely electrostatic ion trap to hold $^3He^+$ ions while a measurement of their hyperfine structure energy splitting, $\Delta\nu_2$, is made in the metastable 2s excited state. This is a precision measurement and the result to date has a fractional uncertainty of about 1.5×10^{-8} ($\Delta\nu_2$ = 1083.354979(15)MHz). This is 1/14 of the uncertainty achieved by an earlier ion beam technique. We compare our result with theory via the quantity $D_{21} \equiv 8\Delta\nu_2 - \Delta\nu_1$, where $\Delta\nu_1$ is the 1s hyperfine splitting. D_{21} is sensitive to terms in the theory of hydrogenic hyperfine structure which have a state dependence other than n^{-3} and in particular is very insensitive to difficult-to-evaluate nuclear structure effects. Our latest result shows a difference D_{21}(experiment) - D_{21}(theory) = 200 ± 120 Hz. It is interesting that this discrepancy is of the same size as the predicted next uncalculated quantum electrodynamic contribution to D_{21} (proportional to $\alpha(Z\alpha)^5\Delta\nu_1$). Radiative corrections to hydrogenic hyperfine structure of this high order have never before been required to reconcile experiment and theory.

The second experiment is one designed to measure the lifetime of the metastable $(1s2s)\,^3S_1$ state of Li^+. Theory predicts the lifetime of this He-like ion state to be about 50 sec. It decays by emission of a 200 Å magnetic dipole photon and we expect to determine the lifetime by counting these photons versus time while the ions are held inside a carefully constructed dynamic ion trap. Currently the ion trap is operating and being tested on N_2^+ ions. It appears to operate as designed and we expect soon to test it on Li^+ ions. The Li atomic beam injection system is 90% complete and we have on hand the necessary photon detectors and electronics to assemble the complete experiment. This is an important experiment because this lifetime has been measured with good precision (±5 to ±10%) only for He-like ions with $Z \geq 16$ where a departure from single exponential decay has been observed. This departure seems to increase with decreasing Z, which motivates our desire to do a 5 to 10% measurement at Z = 3.

2. TEST FOR PARITY VIOLATION IN WEAK NEUTRAL CURRENTS

Steve Chu, Eugene D. Commins, and Ralph Conti

The recent discovery of weak neutral currents in high energy neutrino interactions implies the existence of a weak electron-nucleon interaction which must coexist with the usual Coulomb interaction in atoms. If weak neutral currents violate parity (as ordinary weak currents do), the total atomic Hamiltonian is not parity-invariant, which implies that atomic energy states do not have exactly well-defined parity. One consequence is that photons emitted in transitions from unpolarized atomic states have a slight degree of circular polarization; alternatively there will be a slight circular-polarization-dependence for stimulated absorption.

This important and interesting effect may actually be of measureable size in certain cases. We are attempting to observe one of the most favorable cases, namely the forbidden magnetic dipole transition $6^2P_{1/2} - 7^2P_{1/2}$ (2927 Å) in thallium (Z = 81). Thallium vapor is contained in a fused-quartz cell at ~1000°K. The vapor is illuminated by 2927 Å radiation from a pulsed, flash-lamp pumped dye laser. Absorption is detected by observation of 5350 Å fluorescence emitted in the decay of $7^2P_{1/2}$ thallium atoms. So far we have succeeded in observing the $6^2P_{1/2} \rightarrow 7^2P_{1/2}$ forbidden transition in this manner when it is enhanced by application of a weak external electric field (Stark mixing). In spite of numerous subtle problems connected with this difficult experiment, progress is very encouraging and we are very optimistic about the possibility of observing parity violation, or at least of placing a useful upper limit on its existence.

3. THEORETICAL STUDIES OF ONE AND TWO ELECTRON IONS

Peter J. Mohr

The self-energy contribution to the Lamb shift $E(2S_{1/2}) - E(2P_{1/2})$ in a Coulomb potential has

been calculated to all orders in Zα for a wide range of Z. Improvement in the evaluation of the vacuum polarization contribution to the Lamb shift has been made. The results give a new theoretical value for the Lamb shift in hydrogen. In addition, these results have been combined with the other known contributions to make accurate theoretical predictions for the Lamb shift in hydrogenlike ions for Z in the range 2-30. This is an area of low energy tests of quantum electrodynamics which is actively being pursued by many experimental groups. Work on the evaluation of the self-energy contribution to the $2P_{3/2}$ state is in progress. This work is being done in an attempt to explain the discrepancy between theory and experiment for the Z dependence of the fine structure separation in high-Z atoms. Theoretical work, done in collaboration with H. Gould and R. Marrus, on the effect of the hyperfine interaction on lifetimes in high-Z heliumlike ions has been extended to the case of the 2^3P_0 state. A theoretical prediction for the effect of hyperfine interaction on the lifetime of the 2^3P_0 state has been made for Z in the range 9-29. Besides being of intrinsic physical interest, this effect is important in the interpretation of the data in certain beam-foil experiments. Work is in progress on a study of radiative corrections to the lifetime of the 2^3P_0 state in heliumlike ions. The lifetime of the state is sensitive to the Lamb shift, and a theoretical study is being made to determine if other radiative corrections are important. A reevaluation of the integrals associated with Zwanziger's calculation of the radiative corrections to the hyperfine difference $8\Delta\nu(2S_{1/2}) - \Delta\nu(1S_{1/2})$ has been made. The improvement in accuracy over the orginal calculation sharpens the comparison between quantum electrodynamics theory and the measurement of $\Delta\nu(2S_{1/2})$ in $^3He^+$ by Prior and Wang.

4. ENERGY CONSERVATION

Lee Schipper

During 1975 I spent a considerable amount of time continuing my research on galactic clusters and their statistics. This work included computing at LBL's computer center and in the Physics Department. I expect to finish this work in 1976.

Some of my work centered around Energy Conservation, in cooperation with the Energy and Environment Division of LBL and the Energy and Resources Group, UC Berkeley. I took part in LBL's "Energy Conservation Assessment Program," a study done for ERDA. I wrote several articles, including "Energy Conservation: Its Nature, Hidden Benefits, Hidden Barriers," to be published in 1976 in Energy Communications and "Raising the Productivity of Energy Use," to be published in 1976 in Annual Rev. of Energy. I taught in the LBL Summer course for teachers on energy conservation, gave several lectures to other groups on campus, and appeared in several "Citizen's Energy Workshops" on behalf of ERDA-SAN.

5. POLARIZATION CORRELATION EXPERIMENTS RELATED TO THE FOUNDATIONS OF QUANTUM THEORY

John F. Clauser

Several experiments have been performed which measure both the linear and circular polarization correlation of the two-photon system emitted by the $8^1P_1 \rightarrow 7^3S_1 \rightarrow 6^3P_0$ cascade of ^{202}Hg. The Hg atoms were excited by electron bombardment, and the photons were counted in coincidence after passing through quarter-wave plates and/or highly efficient pile-of-plates linear polarizers. The experiments tested the predictions of a generalization of Bell's inequality which applies for any alternative theory employing objectivity plus naive locality. The linear correlation data were found to violate this inequality, and thus helped to clarify the anomalous results found earlier by Holt and Pipkin at Harvard. The circular correlation magnitude was somewhat lower because of systematic errors in the quarter-wave plates. As a result it was not suitable for testing the above inequality. None the less it was useful for testing for the existence of "state vectors of the second kind" considered by Jauch and Selleri as a basic outgrowth of Furry's hypothesis.

6. FIFTH INTERNATIONAL CONFERENCE ON ATOMIC PHYSICS

Richard Marrus, Chairman

Members of the Atomic Physics Group are currently planning the arrangements and details for the Fifth International Conference on Atomic Physics which will be held in Berkeley on July 26-30, 1976. The University of California Department of Physics and the Lawrence Berkeley Laboratory will co-host the Conference, which will cover the most important developments in atomic physics since the last Conference in 1974. Most of the activity this year has been devoted to soliciting financial support for the conference, to planning the scientific program and to establishing communication with 1500 atomic physicists throughout the world. The response thus far is enthusiatic, and we expect an attendance of approximately 600 participants.

7. ATOMIC BEAM MAGNETIC RESONANCE

Ahsanul Huq, Atilla Ozmen and Howard Shugart

High precision atomic beam measurements provide important information for testing refined atomic theory and for establishing a reference base upon which other methods may rely. Our earlier measurement on the Helium (2^3S_1) g_J - factor helped resolve a discrepancy between a 1958 atomic beam measurements and a 1972 optical pumping determination which cast doubt on theoretical computations.

Our determination agreed with theory and the earlier experiment but disagreed with the optical pumping work. Just recently a new optical pumping determination has confirmed our value.

Although accurate computations of g_J - factors are available only for atoms of one, two or three electrons, several atomic theorists are interested in the accuracy of their methods when applied to many electron systems. Thus our 1974 $^5S_2$ g_J measurement in the oxygen atom finds agreement with theory to one part in 10^5 while our experimental value is known 20 times better. This situation forms reasonable testing ground for the development of better computational methods, which in turn benefit all atomic theory.

During 1975 we have been developing high temperature evaporators of carbon for use in a precision determination of the g_J in carbon's $^5S_2$ metastable state. In addition, we have developed an Auger detector to count these low-lying metastable states. The $^5S_2$ state in carbon is of interest because it has one fewer electron than a half-filled p-shell while the already measured $^5S_2$ state in oxygen has a half-filled p-shell plus one electron.

Following the work on carbon we plan to carry out a seven significant figure measurement on the lithium ground state g_J, since theory has now been completed to this accuracy and is in need of experimental testing.

8. ATOMIC ABSORPTION AND FLUORESCENCE

Tetsuo Hadeishi and Associates

With financial support from the National Science Foundation and the Energy and Environment Division we have extended the Isotope-shift Zeeman- effect Atomic Absorption (IZAA) spectrometer which was so successful with mercury to the analysis of cadmium and lead. This technique utilizes two optical components of the Zeeman split light source; one component monitors the resonant absorption and the other samples off resonant light losses that are caused by a process other than absorption by the element of interest. Mercury from biological samples (e.g., tuna fish, bovine liver, orchard leaves, etc.) may be assayed to ±10 parts per billion in this spectrometer when the sample is vaporized in a furnace at about 900°C. When small aqueous samples of lead or cadmium are vaporized in a carrier of hydrogen gas in an oven at 1100°C, the water vapor passes through the absorption cell in two or three seconds, while the lead or cadmium requires 30 to 60 seconds for passage (depending on the furnace temperature). The separation seems to be effective only if the metal salts momentarily stick to the walls of the furnace. As larger volumes of solution are used, the interaction with the walls becomes less. Negligible loss of cadmium occurs from 0.5 ml of solution, while lead losses occur with somewhat smaller volumes. Evaluation of the capabilities and limitations of this technique are in progress.

A second project is underway to develop an optical detector for NO_2 and NO using optical fluorescence from excitation by two Ar^+ laser lines. This technique should allow fine spatial and temporal resolution of reaction products in combustion phenomena. Such resolution has previously not been possible.

9. RESEARCH PLANS FOR CALENDAR YEAR 1976

Howard A. Shugart and Associates

a. Ion Trapping

We plan to complete work on the high precision measurement of the $2^2S_{1/2}$ $^9Be^+$ hyperfine structure. We plan to study the lifetime of the 2^3S_1 Li^+ metastable state because this determination is important in understanding an unexplained trend in lifetimes of much higher Z. We also plan to utilize laser excitation of trapped ions, a method which is being explored for its intrinsic value but which has application as a diagnostic probe in fusion plasmas.

b. Small Sample Detectors

We plan to evaluate the capabilities and limitations of our recently developed detectors for trace amounts of cadmium and lead. We also plan to pursue the development of a sensitive and fast method for the optical determination of NO_2 and NO in combustion environments containing turbulence and particulate contaminations. This work receives partial support from the N.S.F.

c. Energy Conservation Education

In conjunction with the Energy and Environment Division and the Energy and Resources Group, U.C. Berkeley, we intend to explore the quantitative aspects of Energy Resources, utilization and conservation. Participation in public education through publishing technical and popular articles and through personal appearances will be an important aspect of our program.

d. Weak Neutral Currents and Atomic Structure

The apparatus which was constructed last year will attempt to measure the possible influence of a weak electron-nucleon interaction on an atomic state. This equipment is now functioning and should provide either an observation of a mixed parity state or place an upper limit on its existence.

e. Theoretical Atomic Physics

We will extend and improve theoretical and computational techniques as they apply to one and two electron atoms of higher nuclear charge. In particular the Lamb shift of the $2P_{3/2}$ state in heavy hydrogenlike ions will be computed using recently developed methods which should greatly improve on previous estimates.

f. Atomic Beams

Very high precision measurements of the g_J factor of the most important states for comparison with theory are planned. In particular the $^5S_2$ metasable state in carbon and the $^2S_{1/2}$ ground state in lithium will be the center of attention during 1976.

g. Metastable Lifetimes

We will attempt to reproduce an unpublished measurement from our laboratory of the lifetime of the $^6S_{5/2}$ metastable state in nitrogen. This new measurement should eliminate suspicion of possible contamination in the earlier result. If atomic beam studies on $^5S_2$ carbon are successful, we will attempt a measurement of its lifetime.

h. Fifth International Conference on Atomic Physics

Our group will host the next International Conference on Atomic Physics to be held July 26-30, 1976. We expect about 600 participants representing every country actively engaged in atomic physics research. The extensive planning of the program, publications, and social events for the conference should ensure a productive and rewarding meeting.

10. 1975 PUBLICATIONS AND REPORTS

Howard A. Shugart and Associates

Journals and Books

1. P. J. Mohr, Lamb Shift in a Strong Coulomb Potential, Phys. Rev. Letters 34, 1050 (1975) (LBL-3641).

2. M. H. Prior and E. C. Wang, Hyperfine Structure of 2s $^3He^+$, Phys. Rev. Letters 35, 29 (1975) (LBL-3802).

3. R. Marrus, Studies of Hydrogen-like and Helium-like Ions of High Z, chapter for book on beam-foil spectroscopy (March 1975).

4. L. D. Commins, Weak Nuclear Interactions, McGraw-Hill Encyclopedia of Science and Technology, 4th edition (August 1975).

5. T. Hadeishi and R. D. McLaughlin, ETAA, a New Approach to Chemical Analysis, The American Laboratory (May 1975) (LBL-3259).

6. T. Hadeishi and R. D. McLaughlin, Isotope Zeeman Atomic Absorption: A New Approach to Chemical Analysis, The American Laboratory (August 1975).

7. B. D. Zak, B. Chang, and T. Hadeishi, Current Controlled Phase Retardation Plate, Applied Optics, 14, 1217 (1975).

Presented papers

1. R. Marrus and H. A. Gould, Radiative Decay in Helium-Like Krypton, Am. Phys. Soc., Knoxville Meeting, Bull. Am. Phys. Soc. 20, 818 (1975) (LBL-3815).

2. P. Mohr, Hyperfine Quenching of the 2^3P_0 State in Helium-like Ions, Fourth International Conference on Beam-Foil Spectroscopy, June 1975 (LBL-3858).

3. P. Mohr, Lamb Shift in Hydrogen-like Ions, Fourth International Conference on Beam-Foil Spectroscopy, June 1975 (LBL-3876).

4. H. Gould and R. Marrus, Lifetime of the 2^3S_1 State of Helium-like Ar^{+16} and Kr^{+34}, Am. Phys. Soc., New York Meeting, Feb. 1976 (LBL-4526).

5. D. A. Church, M. C. Michel, W. Kolbe, and T. Hadeishi, Beam-Foil Orientation of the He 4^1D_2 Level: Energy and Foil Angle Dependence, Am. Phys. Soc., Anaheim Meeting; Bull. Am. Phys. Soc. 20, 74 (1975) (LBL-3436).

6. D. A. Church, W. Kolbe, M. C. Michel and T. Hadeishi, Coherent Orientation and Hyperfine Decoupling in the 4^1D_2 State of Fast ^3He Atoms, Am. Phys. Soc., Atlanta Meeting; Bull. Am. Phys. Soc. 19, 1176 (1974) (LBL-3406).

7. W. A. Davis and R. Marrus, Radiative Decay of the 2^3P States of Helium-like Argon, Fourth International Conference on Beam-Foil Spectroscopy, Sept. 1975, (LBL-3890).

8. M. H. Prior and E. C. Wang, Hyperfine Structure of 2s $^3He^+$, Am. Phys. Soc., Tucson Meeting; Bull Am. Phys. Soc. 20, 1465 (1975) (LBL-4259).

9. W. A. Davis and R. Marrus, Radiative Decay of the 2^3P States of Helium-like Argon, Fourth International Conference on Beam-Foil Spectroscopy (Gatlinburg), Sept. 1975 (LBL-4258).

10. A. Ross-Bonney, A Few Comments on Interpreting Quantum Mechanics, Am. Phys. Soc., Pasadena Meeting; Bull. Am. Phys. Soc. 20, 1504 (1975).

11. H. Gould and R. Marrus, Radiative Decay and Fine Structure of the 2^3P_0 and the 2^3S_1 States of Helium-like Krypton (Kr XXXV), Spectroscopy of One and Two - Electron Ions at Medium Z.

12. P. J. Mohr, Lamb Shift in Hydrogen-like Ions, Fourth International Conference on Beam-Foil Spectroscopy and Heavy-Ion Atomic Physics Symposium, Sept. 1975 (LBL-3876).

13. P. J. Mohr, Hyperfine Quenching of the 2^3P_0 State in Helium-like Ions, Fourth International Conference on Beam-foil Spectroscopy and Heavy-Ion Atomic Physics Symposium, Sept. 1975 (LBL-3858).

14. R. D. McLaughlin and T. Hadeishi, Development of Multielement ETAA Capability, 11th Tokyo Conference on Applied Spectroscopy, Oct. 1975 (LBL-3298).

LBL Reports

1. D. Church, Electronic State Alignment, Orientation, and Coherence Produced by Beam-Foil Collisions, LBL-3276, July 1975.

2. T. Hadeishi and R. D. McLaughlin, ETAA Determination of Lead with Dual Chamber Furnace, LBL-4426, Nov. 1975.

3. L. Schipper, Explaining Energy: A Manual of

Non-style for the Energy Outsider Who Wants In! reprinted in final format, UCID 3663, June 1975.

4. L. Schipper, Energy Conseration: Its Nature, Hidden Benefits and Hidden Barriers, UCID 3725, LBL-3295, June 1975.

5. J. F. Clauser, Measurement of the Circular Polarization Correlation in Photons from an Atomic Cascade, LBL-4564, Dec. 1975.

6. J. F. Clauser, Experimental Investigation of a Polarization Correlation Anomaly, LBL-4518, Oct. 1975.

7. L. Schipper, Holidays, Gifts and the Energy Crisis, UCID 3707 Rev., Dec. 1975.

8. L. Schipper, Toward More Productive Energy Utilization, LBL-3299, Oct. 1975.

9. L. Schipper, The Energy Tax: Not a Bad Idea, Daily Californian, Jan 1975.

10. L. Schipper, Making Ends Meet in a Resource-Limited World, The Daily Californian, Feb. 1975.

11. L. Schipper, What is Good for G.M..., in the New York Times, May 1975.

12. L. Schipper, Energy Conservation: It Doesn't Mean Caves and Candles, San Diego Union, August 1975; Sacramento Bee, July 1975.

13. L. Schipper, Energy Wasted Says Expert, UC Clip Sheet, Sept. 1975.

b. Atomic Physics

Richard Marrus, Principal Investigator

1. STUDY OF THE DECAY $2^3S_1 \rightarrow 1^1S_0$ IN HELIUM-LIKE KRYPTON (Z = 36)

H. Gould and R. Marrus

During calendar 1975 observation was made of radiative decay from the 2^3S_1 state of two-electron Kr^{+34} (Z = 36). To our knowledge this is the highest Z two-electron system ever observed. A time-of-flight experiment yielded measurements of the transition rates A ($2^3P_0 \rightarrow 2^3S_1$) and A ($2^3S_1 \rightarrow 1^1S_0$). A preliminary publication has been issued (ref. 1). These measurements are significant because the measurement of A ($2^3S_1 \rightarrow 1^1S_0$) verifies the theory of relativistic magnetic dipole decay. This verification is important because the theory has been applied to interpretation of x-ray data on the solar corona and x-ray observations made in laboratory plasmas. The importance for plasma diagnostics lies in the fact that Gabriel and Jordan have shown that knowledge of the decay rate makes possible the determination of the electron density in plasmas from observation of the line intensity. This is of interest for both laboratory and astrophysical plasmas.

1. H. Gould and R. Marrus, Lifetime of the 2^3S_1 State of Helium-like Ar^{+16} and Kr^{+34}, submitted to the New York Meeting of the American Physical Society, Feb. 2-6, 1975 (LBL-4526 Abstract).

2. STUDY OF THE ULTRAVIOLET TRANSITIONS $2^3P_2 \rightarrow 2^3S_1$ AND $2^3P_0 \rightarrow 2^3S_1$ IN HELIUM-LIKE ARGON

W. A. Davis and R. Marrus

The indicated transitions are being studied with a normal-incidence Seya-Namioka spectrometer. The goal is to obtain precision lifetimes and wavelengths for these transitions. These measurements are of value for work on plasma diagnostics. As noted in the Barnett report, argon and other rare gases are often used for plasma diagnostics. In particular, the $2^3P \rightarrow 2^3S$ transitions can be used for ion temperature determination in a region of high electron temperature. Precise wavelength and lifetime information is important to these determinations.

3. LAMB SHIFTS IN THE N = 2 STATE OF HYDROGEN-LIKE ARGON (Z = 17)

H. Gould and R. Marrus

The goal of this experiment is to obtain a value for the Lamb Shift in the one-electron atom Ar^{+17} with an accuracy of 1% or better. At this level of accuracy it should be possible to see deviations from the $Z\alpha$ expansion and to decide between conflicting calculations of Mohr and Erickson. This will provide a new text of quantum electrodynamics.

During the calendar year substantial progress was made. Signals were observed for the first time and significant improvements made in signal to noise ratio. A simple, precise system to measure the beam velocity was installed and a magnetic field measuring system is now in place and in operation. The consistency of the measurements obtained so far leads us to anticipate that a 1% result will be obtained in calendar year 1976.

4. RADIATIVE DECAY OF THE 2^3P STATES OF HELIUM-LIKE ARGON

William A. Davis and Richard Marrus

We would like to report preliminary results on a measurement of the lifetimes and wavelengths of the allowed E1 decays from 2^3P states of helium-like Ar XVII. These decays are observed using a vacuum ultraviolet monochrometer to view the decay radiation of the transitions $2^3P_2 - 2^3S_1$ and $2^3P_0 - 2^3S_1$.

Previous studies of the 2^3P states of high Z (Z > 10) helium-like atoms have been mainly concerned with measuring lifetimes for the 2^3P_2 state. This state has been observed by viewing the M2 radiation emitted in the decay $2^3P_2 - 1^1S_0$, which for Z ≳ 18 becomes the dominant decay mode, exceeding the E1 mode, $2^3P_2 - 2^3S_1$.[1,2]

The M2 decay of the 2^3P_2 state was first observed in Ar XVII by Marrus and Schmieder,[3,4] and its lifetime was found to be 1.7(3) nsec. This measurement was complicated by the inability to resolve the M2 decay $2^3S_1 - 1^1S_0$ of 3104 eV from the M2 decay of 3126 eV using high resolution (~ 200 eV) Si(Li) detectors. Subsequent measurements have been made on S XV, Cl XVI, Ti XXI, V XXII, and Fe XXV by Cocke, et al.[5] and Gould, et al.[6] Cocke, et al., were able to resolve the M2 decay by making use of a doppler tuned spectrometer,[7] with a resolution of ~3 eV.

The 2^3P_0 state can normally only decay by E1 to the 2^3P_1 state, and as such has not been observed for Z > 10. For nuclei with hyperfine structure, the effect of mixing of the 2^3P_2 and 2^3P_0 states with the 2^3P_1 state (which in high Z atoms is quenched to the ground 1^1S_0 state by spin-orbit mixing with $^1P_1$ states) has been demonstrated in V XXXII.[6]

In our studies we are using a 1/2 meter Seya-Namioka Monochrometer, mounted with the entrance slit perpendicular to the beam line. The instrument views the decaying atoms at 90° from the beam line. The grating is a tripartite replica grating, coated with platinum, and most of our data has been taken with the slits at 200 microns, giving instrumental widths of 3.9 angstroms. The detector is a Bendix Continuous Dynode electron multiplier, operated in the pulse counting mode.

Presently we have been able to measure the lifetimes of the two states and are now working on an accurate wavelength measurement. Lifetime data was accumulated in the following manner.

The 2^3P_2 - 2^3S_1 and 2^3P_0 - 2^3S_1 wavelengths are calculated to be 559.8(17) and 662.3(20) angstroms, respectively.[8] After bending and focusing the 140 MeV Ar beam from the Lawrence Berkeley Laboratory super-HILAC, we collimated the beam through 1/4 inch collimators 12 feet apart. At this beam energy the acceptance angle of the monochrometer contributes 4.8 angstroms to the linewidth. Time-of-flight lifetimes were measured using a 49 ugm/cm^2 carbon foil mounted on a moveable track, and scaling counts while looking at fixed wavelength points in the background, 10 angstroms above and below the line center, as well as directly under the line center. The data points were normalized to the integrated beam current collected in a Faraday cup. With beam currents of 300 charge namp we observed count rates of ~3 counts per second.

Three separate lifetime measurements were made for the 2^3P_2 - 2^3S_1 decay, and two for the 2^3P_0 - 2^3S_1 decay. The data were analyzed by averaging the background count rates, subtracting them from the data, and fitting the resulting signal count rates to single exponentials.

For 2^3P_2 - 2^3S_1 we took eight data points over 9 cm. For 2^3P_0 - 2^3S_1 we took 13 data points over 17 cm. For the 2^3P_0 - 2^3S_1 decay, the five closest points to the foil do not lie on an exponential decay curve and had anomalously high count rates. The concave nature of the decay curve cannot be explained by cascading through the 2^3P_0 state. At this time we do not know how to account for this observation and these points are ignored in fitting the data. Fitting the last eight points with a single exponential we obtain the lifetime.

The results of these experiments are shown in Table 1 where for comparison calculated lifetimes are given, both including Lamb Shift effects, and neglecting them.[6] The quoted error includes the error in fitting the lifetimes, plus a 6% uncertainty in the beam energy. These errors are added algebraically. Other systematic errors are calculated to be well under 1%.

Table 1. Observed and predicted lifetimes (2^3P - 2^3S_1) of Ar XVII (nsec).

	2^3P_2 - 2^3S_1	2^3P_0 - 2^3S_1
Observed	1.62(8)	4.87(44)
Predicted without Lamb Shift	1.51(4)	4.70(12)
Predicted with Lamb Shift	1.52(4)	4.82(12)

5. RADIATIVE DECAY AND FINE STRUCTURE OF THE 2^3P_0 AND THE 2^3S_1 STATES OF HELIUM-LIKE KRYPTON (Kr XXXV)

Harvey Gould and Richard Marrus

Introduction

In this paper we report the measurement of the radiative lifetimes of the 2^3S_1 and 2^3P_0 states of the two-electron ion Kr XXXV. Our results for the 2^3P_0 lifetime enable us to infer a value for the 2^3S_1 - 2^3P_0 energy splitting, which is sufficient precision to be sensitive to the Lamb shift. The measurement of the 2^3S_1 lifetime in this system extends the range of lifetimes for which this transition has been measured (He I to Kr XXXV) to 4×10^{13}.

Theory: Radiative Decay from the n = 2 States of Helium-Like Krypton

Decay of the 2^1P_1 State. Of the six n = 2 states (Fig. 1), all but the 2^1P_1 are metastable against decays to the 1^1S_0 (ground) state. The 2^1P_1 state decays to the 1^1S_0 state by a fully allowed electric dipole transition (E1). The decay rate scales roughly as Z^4 and the lifetime in helium-like krypton is about 10^{-15} sec.

Decay of the 2^3P_1 State. To the extent that the total electron spin S is a good quantum number, E1 transitions from the 2^3P_1 state to the 1^1S_0 state are forbidden. In neutral helium, all of the 2^3P states, which are nearly degenerate, decay to the nearby 2^3S_1 state by E1 radiation with a lifetime of 10^{-7} sec.[1] At higher Z the spin spin-orbit and other relativistic effects cause substantial singlet-triplet mixing, and E1 transitions to the 1^1S_0 state become the dominant decay mode.[2] At Z = 36 the 2^3P_1 and 2 F states have comparable lifetimes.

Decay of the 2^3P_2 State. In addition to the E1 decay to the 2^3S_1 state, the 2^3P_2 state can decay to the 1^1S_0 state by a magnetic quadrupole (M2) transition. At low Z the E1 rate dominates, but the M2 rate[3] which scales roughly as Z becomes comparable at Z = 17. In helium-like krypton the decays are predominantly M2 and the lifetime is 10^{-11} sec.

1. R. H. Garstang, Publ. Astron. Soc. Pac. 81, 488 (1969).
2. G. W. F. Drake, Astrophys. J. 158, 119 (1969).
3. R. Marrus and R. W. Schmieder, Phys. Rev. Letters 25, 1689 (1970).
4. R. Marrus and R. W. Schmieder, Phys. Rev. A 5, 1160 (1972).
5. S XV, C. L. Cocke, B. Curnutte, and R. Randall, Phys. Rev. A 9, 1823 (1974). Cl XVI, C. L. Cocke, B. Curnutte, J. R. Macdonald, and R. Randall, Phys. Rev. A 9, 57 (1974).
6. V XXII, Fe XXV, H. Gould, R. Marrus and P. J. Mohr, Phys. Rev. Letters 33, 676 (1974). Ti XXI, H. Gould, Private communication.
7. R. W. Schmieder and R. Marrus, Nucl. Instr. Meth. 110, 459 (1973).
8. P. J. Mohr, private communication.

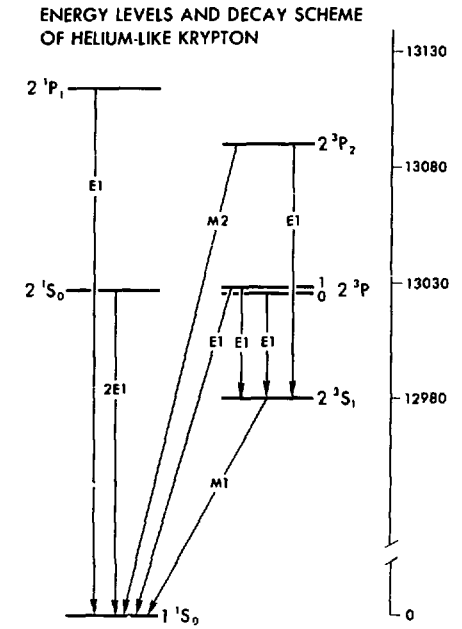

Fig. 1. Radiative decay of the n=2 states of helium-like krypton. The energy levels of the n=2 states are shown in the scale to the right of the figure (all units are 17 eV).
(XBL 759-3881)

Decay of the 2^1S_0 State. Conservation of angular momentum prohibits any single-photon transition from the 2^1S_0 state to the 1^1S_0 ground state. The 2^1S_0 state can, however, decay by the simultaneous emission of two electric-dipole photons (2E1), the same process which accounts for the decay of the $2^2S_{1/2}$ in hydrogen. The transition rate for helium-like atoms in the limit of high Z is[4] $A_{2E1}(2^1S_0) = 16.5\ (Z - \sigma)$,[6] where σ is a screening constant < 1. The lifetime of the 2^1S_0 state in helium-like krypton is about 3×10^{-11} sec.

Decay of the 2^3S_1 State. The dominant decay mode of the 2^3S_1 state is by magnetic-dipole decay (M1). However, it is only the relativistic contributions to the magnetic-moment operator which are nonvanishing. The nonrelativistic operator, $\vec{\mu} = -\mu_0(\vec{\ell} + 2\vec{s})$, has no radial dependence, and because of the orthogonality of the 1s and 2s wavefunctions, the matrix element, $\langle 1s|\vec{\mu}|2s\rangle$, is zero. In the relativistic theory the magnetic-moment operator has a radial dependence. Calculations to lowest order in αZ yields:

$$A_{M1}(^3S_1) = \frac{\pi}{3S}\alpha^9 Z^{10}\,\mathrm{Ry} = 2.5\times10^{-6}\ Z^{10}\ \mathrm{sec}^{-1} \quad (1)$$

Detailed calculations, that include the effects of electron-electron interactions have been carried out by several authors.[5] The numerical calculations of Johnson and Lin[6] yield a lifetime of 0.17 nsec for the 2^3S_1 state of helium-like krypton.

Decay of the 2^3P_0 State. In the absence of hyperfine structure effects of external fields, direct decay of the 2^3P_0 state to the 1^1S_0 state is very highly forbidden. All single-photon transitions to the 1^1S_0 state are forbidden by the conservation of angular momentum, while parity conservation forbids 2E1 and 2M1 transitions. The dominant decay process is E1 decay to the 2^3S_1 state, which subsequently decays by M1 to the ground state. The transition rate[7] for E1 decay $2^3P_0 - 2^3S_1$ is given by

$$A_{E1}(2^3P_0) = \alpha k^3 12(2\alpha)^{-2}[1 + 0.759Z^{-1} - 0.417(2\alpha)^2]^2 \quad (2)$$

in units of $m_e = c$ and $\hbar = 1$, and where k is the $2^3S_1 - 2^3P_0$ energy separation.

The $2^3S_1 - 2^3P_0$ Fine Structure in Helium-Like Krypton. The 2^3P_0 state arises purely from the coupling of the $1s_{1/2}$ and the $2p_{1/2}$ electrons, and contains no admixture of $2p_{3/2}$ as does the P_1 states. Similarly the 2^3S_1 arises entirely from the coupling of the $1s_{1/2}$ and the $2s_{1/2}$ electrons. In the hydrogenic approximation, where the $1s_{1/2}$ is a spectator electron, the (2^3S_1 and 2^3P_0) levels are degenerate in the absence of Lamb shift.

There are three important contributions to the $2^3S_1 - 2^3P_0$ fine structure: 1) a Coulomb interaction involving the charge distributions of the two electrons which scales as Z, 2) the interaction between the spin, magnetic, and dipole moments of the two electrons, which scales roughly as Z^3, accounts for about one-quarter of the energy separation at Z = 36, and 3) the Lamb shift.

The Lamb shift, which accounts for 2×10^{-5} of the $2^3S_1 - 2^3P_0$ splitting in neutral helium (Fig. 2) scales almost as fast as Z^4, and at Z = 36 is about 4% of the energy separation. With the 2^3P_0 lifetime dependent upon the cube of the energy separation, the presence of the Lamb shift changes the lifetime by roughly 12%. The Lamb shift makes the S state less tightly bound, decreases the $2^3S_1 - 2^3P_0$ fine structure separation, and thus increases the 2^3P_0 lifetime. For our calculations at high Z we have used the one-electron (hydrogenic) Lamb shift. The error in this approximation is mostly in ignoring the screening of the inner electron. The effect decreases the size of the Lamb shift, but at Z = 36 is small compared to the resolution of the experiment.

Experiment: Observation of the Decay of the 2^3S_1 State of Helium-Like Kr

The experiment was performed at the Lawrence Berkeley Laboratory's Super Heavy-Ion Linear

Table 1. Lifetimes of the metastable states (n=2) of helium-like ions.

Species	Z	$^3S_1$	$^3P_0$	$^1S_0$	$^3P_2$
He I	2	8×10^{3}	1×10^{-7}	2×10^{-2}	1×10^{-7}
Ne IX	10	9×10^{-5}	1×10^{-8}	1×10^{-7}	1×10^{-8}
Ar XVII	18	2×10^{-7}	4.5×10^{-9}	2.5×10^{-9}	1.5×10^{-9}
Kr XXXV	36	1.5×10^{-10}	1.6×10^{-9}	3×10^{-11}	1×10^{-11}
Decay Mode		M1	E1	3E1	M2+E1

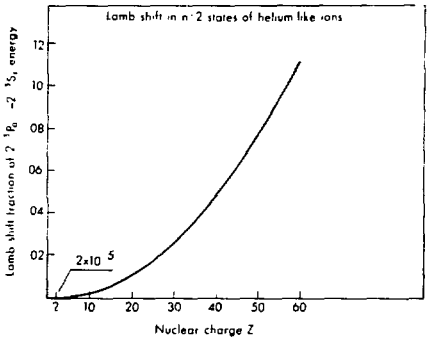

Fig. 2. Lamb shift as a fraction of the $2^3P_0 - 2^3S_1$ energy separation. (XBL 7510-8585)

Accelerator (Super HILAC). Helium-like Kr was produced by passing 4×10^9 cm/sec (714 MeV) beam of Kr^{86} through 350 μg/cm² foils of Be or C. The x-rays from the decays in flight of the 2^3S_1 state are observed by a pair of Si(Li) x-ray detectors located downstream from the foil (Fig. 3). As the foil-detector separation is increased by moving the foil on a track, the number of x-rays seen by the detectors decreases exponentially.

The beam is collected in a Faraday cup for normalization. Collimating slits in the beam insure that the beam collected in the Faraday cup has all been subject to view by the detectors. A system of collimators and baffles keeps scattered beams from striking the detectors or surfaces of the chamber in view of the detectors, as well as keeping the stripping foil out of the field of view of the detectors.

Identification of the radiative decays in helium-like Kr is based upon several factors: 1) the observation of a sizable fraction of Kr^{+34} emerging from the foil, 2) observation of x-rays from decays in flight and the determination that their energy corresponds to the $2^3S_1 - 1^1S_0$ transition that the x-ray energy was independent of foil detector separation, 4) observation of the compound decay $2^3P_0 \rightarrow 2^3S_1 \rightarrow 1^1S_0$, and 5) knowledge of the helium-like system[7,8] obtained from experiments on forbidden decays in helium-like systems for Z = 16 to 26.

Energy of the $2^3S_1 - 1^1S_0$ Transition

Figure 4(a) shows a semilogarithmic plot of the x-ray detector pulse-height spectra from the decay in flight of the 2^3S_1 state of helium-like Kr. The solitary peak in the middle of the graph is located at 12.89 keV. The 300 eV linewidth is due to the instrumental linewidth plus a small amount of Doppler broadening. The x-ray detectors were calibrated against the known K_α and K_β x-rays[9] obtained by fluorescence from compounds of Br, Sr, Mo, Cu, and Zn [Fig. 4(b)]. Both the data peaks and the calibration peaks were fit to the known detector lineshape of a Gaussian with a small leading exponential. A least-squares fit to the calibration spectra is shown in Fig. 5, and a summary of the energy determination is given in Table 2. The relation between the energy of the emitted photon ν_0 and the observed photon ν is given by

$$\nu = \nu_0[1 - \beta^2]^{1/2}\,[1 - \beta\cos\theta]^{-1}\,, \qquad (5)$$

where $\beta = v/c$ (v = velocity of the beam, c = speed of light). The quantity $[1 - \beta^2]^{1/2}$ is the relativistic Doppler shift referred to in Table 2. The major source of error in the energy determination is the uncertainty in the angle θ between the detectors and the beam.

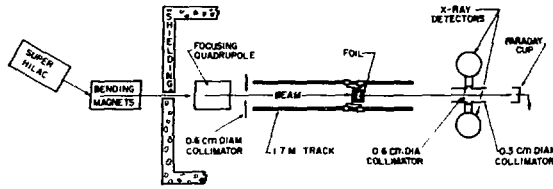

Fig. 3. Schematic diagram of the experimental apparatus. (XBL 737-878A)

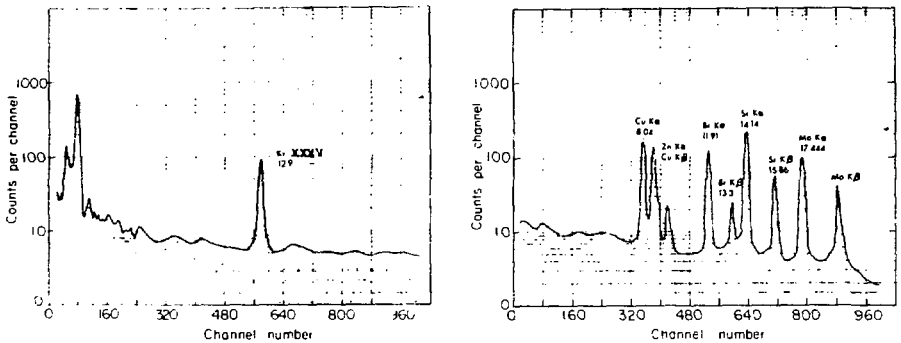

Fig. 4. (a) Observed pulse-height spectra with a foil detector separation of 6 cm. The peak at channel 580 is the 12.89 keV x-ray from the decay in flight of the 2^3S_1 state of helium-like Kr. The origin of the low-energy peaks has not been identified. (XBL 7510-8597)
(b) Calibration pulse-height spectra. (XBL 7510-8596)

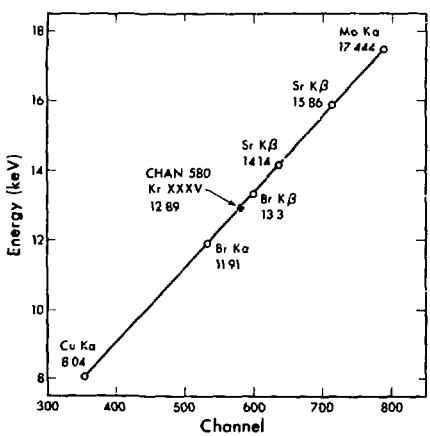

Fig. 5. Least-squares fit of the peaks used to determine the energy calibration. (XBL 759-3884)

Table 2. Kr XXXV 2^3S_1 - 1^1S_0 energy separation.

Experiment:		
Observed x-ray	= 12.893	
Relativistic Doppler shift correction (1.009)	= 13.009	
Peak uncertainty		0.010
Calibrated uncertainty		0.010
Alignment error (1.5°)		0.030
	13.009 ± 0.033 (1σ)	
Theory:		
Zα expansion (Doyle)	12.981	
$(Z\alpha)^6$ correction	0.007	
1s - 2s Lamb shift	-0.011	
	12.997	
Experiment - Theory =	0.032 ± 0.033 (1σ)	

Lifetime of the 2^3P_0 State

As the initial population of the 2^3S_1 state decays within a few cm of the foil and as there are no populated long-lived states other than the 2^3P_0 state, the entire population of the 2^3S_1 state at large distances is due to decays from the 2^3P_0 state. Furthermore, as the 2^3P_0 lifetime is an order of magnitude shorter than the 2^3P_0 lifetime, by monitoring the $2^3S_1 \rightarrow 1^1S_0$ x-ray transition we determine the 2^3P_0 lifetime. Figure 6 shows one of eight decay curves obtained in this experiment. For each of eight decay curves, observations were made over at least two decay lengths. Values of the lifetimes obtained by least-squares fits to these decay curves are shown in Fig. 7, along with the calculated lifetimes, both with and without the Lamb shift contribution to the energy separation.

Our result for the 2^3P_0 lifetime (corrected for 1% time dilation) is $(1.66 \pm 0.63) \times 10^{-9}$ sec, where the quoted error represents 2σ + 1% for uncertainty in the beam velocity. The value of the 2^3S_1 - 2^3P_0 fine structure separation obtained using Eq. (2) from measurement of the 2^3P_0 lifetime is 43.65 ± 0.55 eV. The theoretical energy, without the Lamb shift, using the nonrelativistic terms of Sanders and Scherr,[10] the relativistic corrections of Doyle,[11] and a Z^{-2} correction[12] to the Breit interaction (obtained by comparison of lower Z values of Accad, Pekeris, and Schiff[13]) is 45.48 eV. This is identical to the value obtained by Ermolaev and Jones, excluding relativistic corrections.[1] (Neither calculation includes corrections to order $\alpha^6 Z^5$ in the expansion of the Breit operator.) Including the Z = 36, n = 2 hydrogenic Lamb shift of 1.73 eV[12]

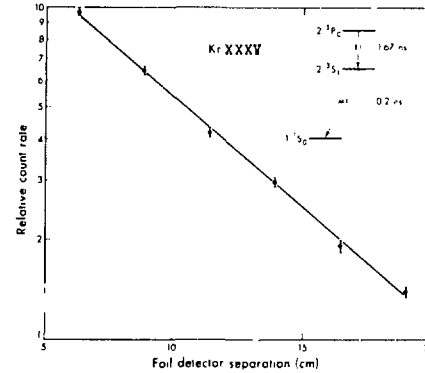

Fig. 6. Typical decay curve of 2^3P_0 - 2^3S_1 - 1^1S_0. (XBL 759-5885)

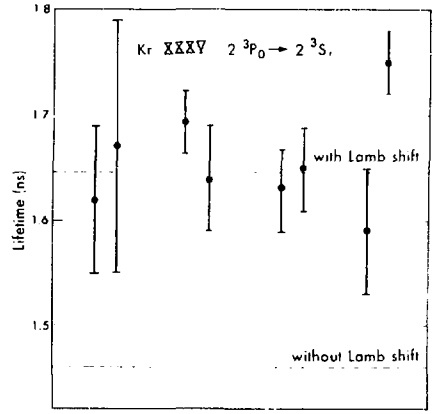

Fig. 7. Measured values of the 2^3P_0 lifetime as compared with theoretical lifetimes. The error bars are from the least-squares fit to the decay curves. (XBL 759-4038)

brings the theoretical 2^3S_1 - 2^3P_0 fine structure to 43.75 eV.

Lifetime of the 2^3S_1 State

By moving the stripping foil close to the x-ray detectors the decay of the initial population of the 2^3S_1 state is observed, and a decay curve of count-rate vs foil-detector separation is obtained. As there will be some cascades from the 2^3P_0 present, the decay curve (Fig. 8) was

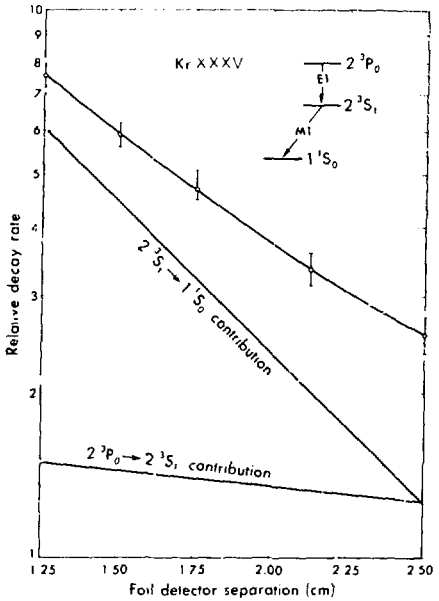

Fig. 8. Decay curve of the $2^3S_1 - 1^1S_0$. Due to cascading from the 2^3P_0 state, the curve was fit to a double exponential. The two exponentials are shown below the decay curve. (XBL 759-3885)

fit to a double exponential. The minimum foil detector separation was limited by the collimating system, hence the range of distances over which useful data could be obtained was somewhat restricted. Therefore, the fit to the double exponential was achieved by entering the 2^3P_0 lifetime as a constant, and computing 2^3S_1 lifetimes as a function of the 2^3P_0 lifetime (Fig. 9). As shown by the fits in Fig. 9, most of the count rate is from the decay of the initial population of the 2^3S_1 state and the extracted lifetime is insensitive to the exact 2^3P_0 lifetime. Again choosing $2\sigma + 1\%$ as the error, the measured 2^3S_1 lifetime in helium-like Kr is 0.20 ± 0.06 nsec, in agreement with the theoretical value of 0.17 nsec of Johnson and Lin.[6] A comparison of current experimental and theoretical lifetimes for the 2^3S_1 state of helium-like atoms is given in Fig. 10.

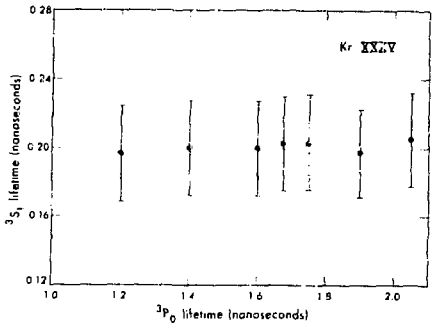

Fig. 9. Lifetime of the 2^3S_1 state as a function of the lifetime of the 2^3P_0 state cascading to the 2^3S_1 state. (XBL 759-3880)

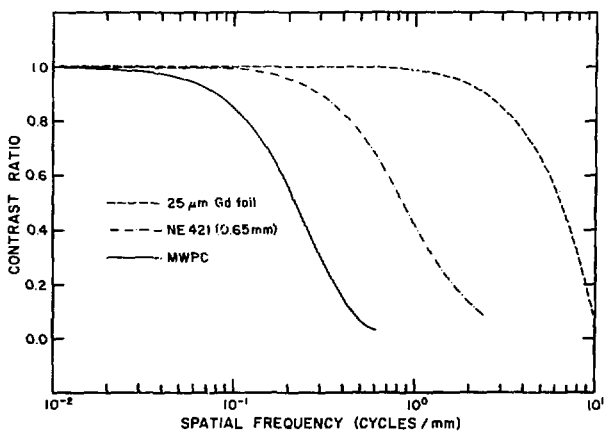

Fig. 10. Comparison of theoretical and experimental values of the 2^3S_1 lifetime for helium-like systems with $Z = 2$ to 36. (XBL 742-285)

Acknowledgements

We are again delighted to thank the operators and crew of the SuperHILAC whose skill and dedication make this work possible. We thank Douglas MacDonald for excellent engineering assistance and gratefully acknowledge the helpful conversations with Peter Mohr.

1. W. L. Wiese, M. W. Smith and B. M. Glennon, Atomic Transition Probabilities, NSRDS - NBS 4 (U.S. GPO, Washington, D.C., 1966), Vol. 1, p. 125.

2. G. W. F. Drake and A. Dalgarno, Astrophys. J. 157, 459 (1969).

3. R. H. Garstang, Publ. Astron. Soc. Pac. 81, 488 (1969), and G. W. F. Drake, Astrophys. J. 158, 119 (1969).

4. G. A. Victor and A. Dalgarno, Phys. Rev. Lett. 25, 1105 (1967).

5. G. Feinberg and J. Sucher, Phys. Rev. Lett. 26, 681 (1971); I. L. Beigman and U. I. Safronova, Zh. Eksp. Teor. Fiz. 60, 2045 (1970). [Sov. Phys.-JETP 33, 1102 (1971)]; G. W. F. Drake, Phys. Rev. A 5, 1979 (1972); S. Feneuilli and E. Koenig, C. R. Acad. Sci. Ser. B 274, 46 (1972); and G. W. F. Drake, Phys. Rev. A 3, 908 (1971).

6. W. R. Johnson and C. Lin, Phys. Rev. A 9, 1486 (1974).

7. H. Gould, R. Marrus and P. Mohr, Phys. Rev. Lett. 33, 676 (1974).

8. R. Marrus and R. W. Schmieder, Phys. Rev. A 5, 1160 (1972); R. W. Schmieder and R. Marrus, Phys. Rev. Lett. 32A, 431 (1970); H. Gould, R. Marrus and R. W. Schmieder, Phys. Rev. Lett. 31, 504 (1973); C. L. Cocke, B. Curnutte and R. Randall, Phys. Rev. Lett. 31, 507 (1973); C. L. Cocke, B. Curnutte, J. R. MacDonald, J. R. MacDonald, J. A. Bednar and R. Marrus, Phys. Rev. A 9, 2242 (1974); C. L. Cocke, B. Curnutte, J. R. MacDonald and R. Randall, Phys. Rev. A 9, 57 (1974); and J. A. Bednar, C. L. Cocke, B. Curnutte and R. Randall, Phys. Rev. A 11, 460 (1975).

9. J. A. Bearden, X-ray Wavelengths and X-ray Atomic Energy Levels, NSRDS-NBS 14 (U.S. GPO, Washington, D.C., 1967), pp 10 and 11.

10. F. C. Sanders and C. W. Scherr, Phys. Rev. 181, 84 (1969).

11. H. T. Doyle, in Advances in Atomic and Molecular Physics, edited by D. R. Bates and I. Esterman (Academic Press, New York, 1969), Vol. 5, p. 337.

12. P. Mohr, private communication (1975).

13. Y. Accad, C. L. Pekeris and B. Schiff, Phys. Rev. A 4, 516 (1971).

14. A. M. Ermolaev and M. Jones, J. Phys. B 7, 109 (1974).

A. LOW ENERGY NUCLEAR SCIENCE

1. HEAVY ELEMENT RESEARCH

a. Actinide and Lanthanide Chemistry

Norman M. Edelstein, Neil Bartlett, John G. Conway, Kenneth Raymond, Glenn T. Seaborg, Andrew Streitwieser, Jr., David H. Templeton, and Allan Zalkin, Principal Investigators

1. THE PREPARATION AND SPECTRAL PROPERTIES OF ACTINIDE (IV) HEXAIODOCOMPLEXES

D. Brown,* P. Lidster,* B. Whittaker,* and N. Edelstein

As part of a detailed investigation of the trends in bonding of $5f^1$ compounds, we have previously reported optical spectral data for octahedral compounds of the type $(NEt_4)_2PaX_6$ (X = F, Cl and Br). The trends in the ligand field parameters θ and Δ were explained qualitatively in terms of molecular orbital theory with large variations in σ bonding dominating the total ligand field splitting as the halide was varied, a feature which was also observed for certain hexhalogenouranates (V). Hexaiodo-complexes of tetravalent actinide elements have been extensively studied and the single protactinium (IV) complex reported, $(Ph_3MeAs)_2PaI_6$, was only prepared on a very small scale and its physical properties were not examined.

We report now the preparation of new hexaiodocomplexes. $(NEt_4)_2M^{IV}I_6$ (M^{IV} = Th, Pa, and U) and $(NMe_3Ph)_2M^{IV}I_6$ (M^{IV} = Pa and U) together with details of their i.r., Raman and (Pa and U only) solid state electronic spectra, and x-ray powder diffraction results. The ligand field and spin-orbit coupling constants derived from the electronic spectra of the hexaiodoprotactinates (IV) are compared with those available for other octahedral $5f^1$ compounds.

The hexaiodocomplexes crystallize when the appropriate tetraiodide and alkyl/aryl-ammonium iodide are mixed in anhydrous, oxygen-free methyl cyanide. The products are extremely sensitive towards moisture, and for small-scale preparations (e.g., 50 mg of PaI_4) it is essential to pass previously purified methyl cyanide down a column of fresh molecular sieves in order to ensure complete absence of water. They are moderately soluble in methyl cyanide and insoluble in isopentane. The addition of aqueous ammonia results in the formation of hydrous oxides, the characteristic black protactinium (IV) hydroxide turning white within a few minutes in the presence of oxygen.

I. R. and Raman Spectra

Two infrared-active fundamentals, ν_3 (t_{1u}) and ν_4 (t_{1u}), and three Raman-active fundamentals, ν_1 (a_{1g}), ν_2 (e_g), and ν_5 (t_{2g}) are predicted by group theory for regular octahedral molecules of the type MX_6 belonging to the point group O_h. The t_{2u} mode, ν_6, is totally forbidden. Comparison of our spectra for the hexaiodo-complexes with those for hexafluoro-, hexachloro-, and hexabromo-complexes of a variety of tetravalent actinide elements results in the assignments shown in Table 1.

Table 1. Partial x-ray powder diffraction data for $(NEt_4)_2PaI_6$.

$\sin^2\theta_{obs}$	I^a_{est}	$\sin^2\theta_{obs}$	I^a_{est}
0.0108	M+	0.0716	S
.0115	M-	.0772	M-
.0293	W-	.0788	M-
.0331	W--	.0826	M
.0426	M	.0853	M
.0451	M	.0959	M+
.0464	W-	.0974	W-
.0501	W	.0996	W
.0511	W	.1045	M+
.0521	W-	.1080	W
.0545	W-	.1122	W+
.0563	W-	.1143	W-
.0571	W-	.1171	W-
.0604	W	.1261	M+
.0622	W-	.1327	M+
.0644	W	.1386	W
.0666	W-	.1421	W
0.0689	W-	.1471	W
		0.1542	W-

[a] S, strong; M, medium; W, weak.

Electronic Spectra

The solid-state spectra obtained for $(NE_4)_2PaI_6$ are shown in Figs. 1 and 2 and that for $(NEt_4)_2UI_6$ at 85 K in Fig. 3. The last has not been interpreted and will not be discussed in detail.

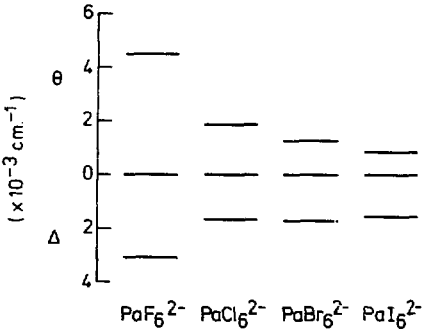

Fig. 1. The spectrum of $(NE_4)_2PaI_6$ at 300 K. (XBL 758-1888)

The measured band positions for $(NEt_4)_2PaI_6$ and $(NPhMe_3)_2PaI_6$ are provided in Table 2 together with assignments. The estimated accuracy of measurement is ± 10Å. Bands present in the spectra (Figs. 1 and 2) at ca 1.68μ are associated with transitions within the tetraethylammonium cation. No other bands were observed at higher wavenumbers. The spectra are similar to those we reported earlier for the octahedral hexahalogenoprotactinates (IV) $[(NEt_4)_2PaX_6$; X = F, Cl, and Br) and the optical absorption bands are similarly

Table 2. I.r. and Raman data for hexaiodo-complexes.

Compound	Colour	Observed Vibrational Modes (cm^{-1})			
		ν_1	ν_3	ν_4	ν_5
$(NEt_4)_2ThI_6$	White	131	143	c	68,50[c]
$(NEt_4)_2PaI_6$	Blue	a	143	c	a
$(NEt_4)_2UI_6$	Red	b	143	c	b

[a] not observed owing to fluorescence

[b] not observed owing to rapid decomposition of compound in laser beam

[c] discussed in the text.

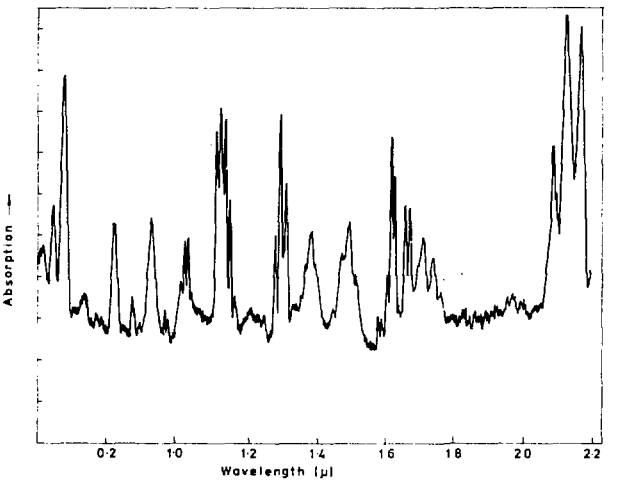

Fig. 2. The spectrum of $(NEt_4)_2PaI_6$ at 85 K. (XBL 758-1889)

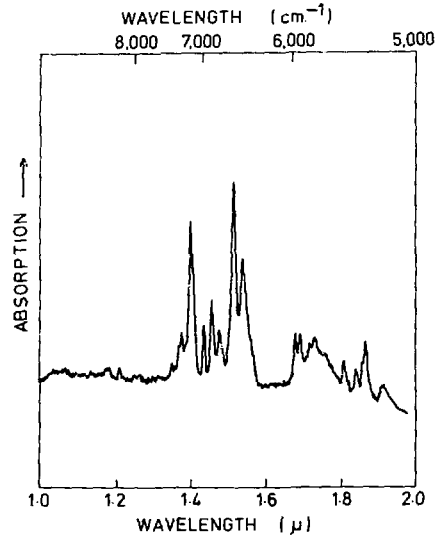

Fig. 3. The spectrum of $(NEt_4)_2UI_6$ at 85 K. (XBL 758-1890)

assigned to transitions from the Γ_7 ground level to the Γ_6, Γ_7' and Γ_8' states as indicated in Table 3.

The assignments at 85 K shown in Table 3 were used to fit the ligand field splittings, θ and Δ, and the spin-orbit coupling constant ζ; in order to have a check on these parameters the g value for PaI_6^{2-} was estimated at -1.15. The experimental and calculated values are compared in Table 4, and the θ and Δ values are compared with those for other hexahalogenoprotactinates (IV) in Fig. 4. The apparent increase in the spin-orbit coupling ' ant ζ through the series from the fluoride to the iodide complex should be treated with caution since the values obtained are strongly dependent on the g values estimated. Magnetic measurements are necessary on these compounds in order to determine accurate values of ζ.

The very marked decrease in θ and the relatively constant value of Δ across the series $PaF_6^{2-} \rightarrow PaI_6^{2-}$ (Fig. 4) reflects the progressive lowering in energy of the Γ_6 state relative to the Γ_8' and Γ_7' states. The Γ_7' state in fact increases very slightly in energy from $PaCl_6^{2-}$ to PaI_6^{2-}. As discussed previously, it can be shown for $5f^1$ compounds in octahedral symmetry that,

$$\theta \simeq (\alpha_\pi^2 + \alpha_\sigma^2 - \alpha_\pi'^2)\ (E_f - E_p)$$

and,

$$\Delta \simeq (\alpha_\pi'^2)\ (E_f - E_p) \qquad (1)$$

Table 3. Spectral results for the hexaiodoprotactinates. (IV)[a]

	$(NEt_4)_2PaI_6$						$(NMe_3Ph)_2PaI_6$					
	At 85K			At 300K			At 85K			At 300K		
	Band Position (cm^{-1})	Int.	Freq. (cm^{-1})	Band Position (cm^{-1})	Int.	Freq. (cm^{-1})	Band Position (cm^{-1})	Int.	Freq. (cm^{-1})	Band Position (cm^{-1})	Int.	Freq. (cm^{-1})
							7413	w	+420			
	7282	w	+298	7262	sh	+298	7315	w	+322			
	7138	m	+174	7145	m	+179	7143	m	+150	7143	m, br	+145
	7102	sh	+138									
Γ_7-Γ_6	6964	m	0	6964	w	0	6993	m	0	6998	vw	0
	6868	m	-96	6859	m	-105	6887	sh	-106			
	6770	m	-194	6780	m	-184	6840	m	-153	6840	m, br	-158
	6729	sh	-235				6752	w	-241			
	6601	m		6605	m		6627	m		6614	m, br	
Γ_7-Γ_8'	6502	m		6451	m		6494	m		6398	m, br	
	5534	w	+152	5525	m	+140	5540	w	+155	5540	m	+149
	5452	w	+50	5429	m	+44	5423	w	+38	5429	m	+38
Γ_7-Γ_7'	5382	sh	0	5385	m	0	5385	m	0	5391	m	0
	5359	m	-23	5362	m	-23	5362	m	-23	5371	m	-20
				5350	sh	-35	5333	sh	-107	5330	sh	-61
	5241	w,b	-141	5264	w	-141	5236	w, br	-149	5241	w	-150

[a] s, strong; m, medium; w, weak; br, broad; sh, shoulder.

Table 4. Calculated and experimental transition energies, ligand field parameters and spin-orbit coupling constants for hexaiodoprotactinates (IV).

Compound		Energy (cm^{-1})			Parameters (cm^{-1})			
		Γ_7-Γ_6	Γ_7-Γ_8'	Γ_7-Γ_7'	g	θ	Δ	ζ
$(NEt_4)_2PaI_6$	Calc.	7002	6497	5397	-1.142	832	1546	1542
	Exp.	6998	6506	5391	-1.150[a]			
$(NMe_3Ph)_2PaI_6$	Calc.	6973	6497	5399	-1.130	782	1592	1540
	Exp.	6964	6518	5385	-1.150[a]			

[a]Estimated value.

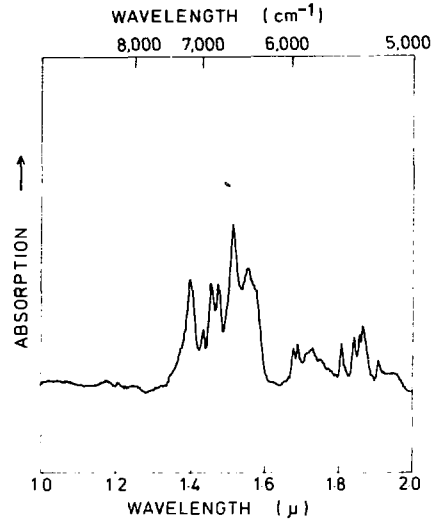

Fig. 4. Ligand field splittings θ and Δ for octahedral complexes of the type $(NEt_4)_2PaX_6$ (X = F, Cl, Br, and I). (XBL 758-1891)

where α_π and α_σ are ligand admixture coefficients for the t_{1u} state, α_π' is that for the t_{2u} state, and E_f and E_f' are the binding energies of the outer f metal ion electrons and the outer p shell ligand electrons, respectively. Thus, since θ changes much more rapidly than Δ for the hexahalogenoprotactinates (IV) (Fig. 4) and α_π and α_π' involve the same ligand orbital, changes in π bonding will have relatively little effect on θ but (Eq. 1) will directly effect Δ. It appears therefore that as the halide ion is changed from fluoride to iodide in the hexahalogenoprotactinates (IV), $(NEt_4)_2PaX_6$ (X = F to I), large changes in σ bonding occur while the π bonding is relatively unaffected.

2. RADIOPOLAROGRAPHY OF Am, Cm, Bk, Cf, Es, AND Fm

K. Samhoun* and F. David+

Introduction

The aim of this work is to determine the standard E^0III-0 or E^0II-0 electrode potentials for some transplutonium elements in aqueous solution, and to obtain information on the electrochemical properties of 5f elements. The standard electrode potentials are essential for the determination of some thermodynamic functions such as the enthalpy of formation $\Delta H_f(M^{3+})$. This function, combined with others, is used for correlation between 4f and 5f series, allowing predictions of some unknown data on the heavy actinide elements.

In this work the radiopolarography technique is applied to study Am, Cm, Bk, Cf, Es, and Fm. This technique permits a radiochemical determination of the half-wave E 1/2 potential, by studying the electrochemical behavior of the aquo-ion at the dropping mercury cathode.

Principle

When a radioisotope is .educed to the metallic state at the dropping mercury cathode, then the activity A collected in a given number of drops, where a given potential -E is imposed, is proportional to the number of reduced ions. This activity is thus proportional to the corresponding polarographic current. The radiopolarogram obtained by plotting A against -E should parallel the known current-potential curves.

For a controlled diffusion radiopolarographic wave the limiting activity A_d, measured in the mercury collected each θ seconds, could be calculated from the transformed Ilkovic equation:

$$A_d = 0.627 \times m^{2/3} \times t^{1/6} \times D^{1/2} \times \theta \times A_s$$

where A_s is the activity of 1 ml of the solution; and m, t, and D have their usual meanings and are expressed in $g \times s^{-1}$ respectively.

Provided A_d is measured with reasonably accuracy (~ 5%), the diffusion coefficient D can be calculated from the measured limiting activity of the radiopolarogram. The number n of electrons exchanged in the electrode process does not figure any more in the transformed Ilkovic equation. However, this number can be obtained from the slope (0.059/n) of the logarithmic analysis of the wave:

$$E = E\ 1/2 - \frac{0.059}{n} \log \frac{A}{A_d - A} .$$

In the case of a reversible electrode process ($\alpha = 1$), this slope should be 60 mV if $n = 1$, 30 mV if $n = 2$, and 20 mV if $n = 3$. It is understood that this slope is less steep if $\alpha < 1$ (quasireversible or irreversible electrode process).

The radioisotopes investigated are listed in column 1 of Table 1. Half-life and α energy of each one is reported in columns 2 and 3. The average of the amounts used in one experiment, expressed in nanograms and by concentration (mM/mℓ), are listed in columns 4 and 5, respectively.

Table 1. Radioisotopic investigation in this work.

M	T 1/2	Energy MeV	Nanogram	mM/mℓ
^{241}Am	433 y	5.49	15	2×10^{-8}
^{244}Cm	18.11 y	5.81	0.4	7×10^{-10}
^{249}Bk	314 d	β^-	0.27	3×10^{-10}
^{249}Cf	360 y	5.81	10	1.2×10^{-8}
^{254}Es	276 d	6.44	0.025	3×10^{-11}
^{255}Fm	20.1 h	7.02	3×10^{-15}	3×10^{-15}

The 20.1 hour ^{255}Fm was available in a mixture of ^{249}Cf- ^{254}-^{255}Es. ^{255}Fm was ~ 0.01% (by activity) in this mixture. The elution with 0.4 M α-hydroxyisobutyrate at pH 3.5 from Dowex cationic resin was applied to the "milking" of ^{255}Fm.

In order to insure a determination on these elements with equal precision, a mixture of two or three actinides is generally used in one experiment. An element for comparison is also added to the mixture; in our experiments the γ emitter ^{54}Mn was added. The radiopolarogram of Mn is used to check the normal functioning of the radiopolarogram.

Radiopolarograms of Am, Cm, Bk, Cf, and Fm were obtained with a good reproducibility (see Fig. 1). The standard deviation of the experimental points is less than 3%. The accuracy of the measured half-wave E 1/2 potentials is less than 3 mV. The experimental points obtained for Fm (Fig. 1) are less accurate because of the small amount of ^{255}Fm available.

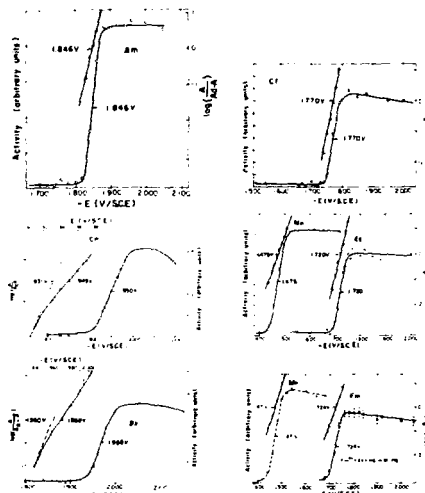

Fig. 1. Radiopolarograms of: Am, pH 2.0, LiCl 0.26M; Cm, pH 2.5, LiCl 0.10M; Bk, pH 2.5, LiCl 0.10M; Cf, pH 2.5, LiCl 0.10M; Es, pH 2.5, LiCl 0.10M; Fm, pH 2.5, LiCl 0.10M. (XBL 756-1634)

Mechanism of the Electrode Process

Am, Cm, Bk, Cf, Es. The slope of the curve $-E = f(\log A/A_d - A)$ was measured for each investigated element. Most of the measured slopes for Am, Cf, and Es lie within 25 ± 5 mV; this is consistent with the following electrochemical process:

$$M^{3+} + 3e + Hg \rightarrow M(Hg) .$$

The transfer coefficient α is estimated to vary between 0.7 and 1. This is characteristic of a "quasireversible" electrode process.

Table 2.

M	pH	$-(E\ 1/2)$ (volts)	n	α	$-(E\ 1/2)_{rev}$ (volts)	δE_3 (volts)	δE_2 (volts)	$-E^0_{III-0}$ (volts)	$-E^0_{II-0}$ (volts)
^{241}Am	2.0 - 2.2	1.598	3	0.78	1.594(5)	0.46	--	2.06	--
^{244}Cm	1.7 - 2.0	1.66	3	0.40	1.62 (1)	0.445	--	2.07	--
^{249}Bk	2.0 - 2.2	1.64	3	0.45	1.62 (1)	0.50	--	2.12	--
^{249}Cf	2.0 - 2.2	1.503	3	0.90	1.500(5)	0.51	--	2.01	--
^{254}Es	2.0 - 2.2	1.456	3	0.80	1.452(5)	0.53	--	1.98	--
^{255}Fm	2.5	1.474	2	0.90	1.474(6)	--	0.90	1.95	2.37

Fm. As with the preceding elements, the slope was found to be 29 ± 4 mV. The number of electrons exchanged in this case, according to α, could be two or three. However, the fact that the standard electrode E^0III - II of Fm is less negative than -1.15 V/NHE suggests that the Fm ion is in the divalent state at the dropping mercury cathode since the radiopolarographic wave is detected at -1.47 V/NHE. The following mechanism is therefore suggested:

$$Fm^{2+} + 2e + Hg \rightarrow Fm(Hg) .$$

In order to confirm this mechanism, study of the radiopolarogram behavior in the presence of a complex agent (lithium citrate) was undertaken. The calculated shift on the half-wave potential of Fm should be about 50 mV in the presence of 0.005 M lithium citrate, when the electrode process is $Fm^{2+} \rightarrow Fm^0$. This shift in the same conditions should be more than 200 mV if the electrode process is $Fm^{3+} \rightarrow Fm^0$. The measured shift confirmed $Fm^{2+} \rightarrow Fm^0$ mechanism.

Half-Wave Potentials and Standard Electrode Potentials

Frequently in polarography pH may affect the half-wave potential determination. Searching for the minimum value of E 1/2 at suitable pH, radiopolarograms of Am, Cm, Bk, Cf, and Es were obtained in several pH media (from pH 1.7 to 2.5). From the analysis of half-wave E 1/2 potentials measured for each of these elements, it appears that minimum values for Am, Cf, and Es are obtained with pH between 2 and 2.2. However, all measured E 1/2 beyond this range are more negative by only a few mV. In Table 2, column 2, the measured E 1/2 are listed for all investigated elements. In column 2 the corresponding pH is listed, and in columns 4 and 5 the number n of electrons and the transfer coefficient α, both obtained from the measured slope of $-E = f(\log A/A_0 - A)$. In column 6 the deduced $(E\ 1/2)_{rev}$ are tabulated and will be used for the standard electrode potential determination.

Since the mechanisms of the electrode process correspond to the reduction of the divalent or trivalent ion to the metallic state, the measured half-wave E 1/2 potentials include the energy of amalgamation. δE_3, for the trivalent ion or δE_2 for divalent ion, so that:

$$(E\ 1/2)_3 = \delta E_3 + E^0_{III - 0}$$

and

$$(E\ 1/2)_2 = \delta E_2 + E^0_{II - 0}$$

The energies of amalgamation of Bk, Cf, and Es are estimated by correlating the intra-series variation in δE_3 (known for Gd, Tb, Ho, and Lu) and deduced for Am and Cm from the standard electrode E^0III-0 potentials measured by Fuger et al. and our experimental half-wave E 1/2 potentials. Estimated values δE_3 are listed in column 7 of Table 2. The δE_2 of Fm is estimated (column 8) by interpolating the variation in known δE_2 of divalent elements Mg, Ca, Sr, Ba, Ra, Eu, and Yb with the corresponding radii of the divalent metals. Finally, E^0III-0 and E^0II-0 are listed in column 9 and 10.

*K. Samhoun, on leave from CNRS of Lebanon. Present address: Institut de Physique Nucleaire, Bat. 100 B. P. No. 1, 91406 Orsay, France.

*F. David, Institut de Physique Nucleaire, Bat. 100, B.P. No. 1, 91406 Orsay, France.

3. THE PHYSICAL PROPERTIES OF URANIUM(IV) DIETHYLAMIDE: CRYSTAL STRUCTURE, OPTICAL AND MAGNETIC PROPERTIES

J. Reynolds, A. Zalkin, D. H. Templeton, and N. Edelstein

The compound uranium(IV) diethyl amide, $U(N(C_2H_5)_2)_4$ was first synthesized by Gilman et al.[1] from the reaction of lithium diethylamide with

UCl_4 using diethyl ether as a solvent. After removal of the solvent the uranium amide was purified by distillation under vacuum and was obtained as an emerald-green liquid which crystallized at approximately 55°C. This material was extremely reactive to oxygen and water but proved useful as an intermediate for preparing uranium(IV) mercaptides and alkoxides. Bagnall and Yanir[2] have reacted uranium(IV) diethyl amide with CS_2, CO_2, and COS to achieve the insertion of these compounds into the uranium-nitrogen bond and the formation of the corresponding carbamates. Jamerson and Takats[3] reacted uranium(IV) diethylamide with two moles of cyclopentadiene to form $(\eta\text{-}C_5H_5)_2U[N(C_2H_5)_2]_2$ which appears to be an intermediate useful for the formation of compounds of the type $(\eta\text{-}C_5H_5)_2UX_2$. Because of the synthetic utility of uranium(IV) diethylamide and its known volatility we have investigated its structural and spectroscopic properties. We report in this paper the crystal structure of uranium(IV) diethylamide, its optical and proton magnetic resonance (pmr) spectra in various solvents, and its temperature-dependent magnetic susceptibility.

The crystal structure of uranium(IV) diethylamide, $U(N(C_2H_5)_2)_4$, was analyzed by single-crystal x-ray diffractometry. The material crystallizes in the monoclinic space group $P2_1/n$ with cell dimensions $a = 9.326$, $b = 17.785$, $c = 15.867$ Å, and $\beta = 108.45°$. With four formula units per unit cell the calculated density is 1.65 g/cm³. More than 2700 unique data were obtained by the omega-two-theta scan technique on a Picker FACS-1 diffractometer equipped with a molybdenum tube and a graphite monochromator. After the trial model had been found by the Patterson and Fourier methods, the 1809 data where $F^2 > 2\sigma(F^2)$ were used in the full-matrix-least-squares refinement of the structure parameters. All atoms, with the exception of hydrogen, were located, and the positional and anisotropic thermal parameters were refined by least squares. For the 1809 reflections the conventional R was reduced to 0.035 and the weighted R to 0.051.

The crystals consist of dimer molecules. As shown in Fig. 1, five nitrogen atoms form an approximate trigonal bipyramid about each uranium atom, and two of these groups share an edge to form the dimer. U-N distances are 2.46 and 2.57 Å for the bridging nitrogen atoms and 2.21, 2.22, and 2.24 Å for the others. The N-U-N and U-N-U angles for the bridge bonds are 74° and 106° respectively. The bond angles in the trigonal bipyramid are 116°, 118°, and 125° for the equatorial set, and 167° for the axial pair.

The proton magnetic resonance spectra of $U(NEt_2)_4$ in various solvents at ambient temperature are shown in Fig. 2. In each spectrum there are two peaks of approximate relative intensity 3:2. The smaller peak is assigned to the methylene protons and the larger peak to the methyl protons; in all four solvents the smaller peak is shifted to a greater extent than the larger peak. Gilman et al.,[1] have reported that $U(NEt_2)_4$ is monomeric in benzene so in this solvent (and pentane) the most probable structure in solution is tetrahedral. If we assume this hypothesis is correct then the large methylene proton shifts would be due to a fermi contact hyperfine interaction because the pseudo-contact term would vanish with this symmetry. However, the large upfield shifts observed in the ether solvents are probably due to pseudo-contact shifts because these solvents would be expected to coordinate to the metal ion and lower the symmetry. Nonetheless, we can not rule out a possible dimer-monomer equilibrium. Further studies are underway on the temperature dependence of the pmr spectra.

The optical and near ir spectra of $U(NEt_2)_4$ at room temperature and in various solvents are shown in Fig. 3 and the peak positions are reported in Table 1. As in the pmr data the spectra in benzene and hexane are very similar while the spectra in the ether solvents are markedly different. Again we attribute these spectral

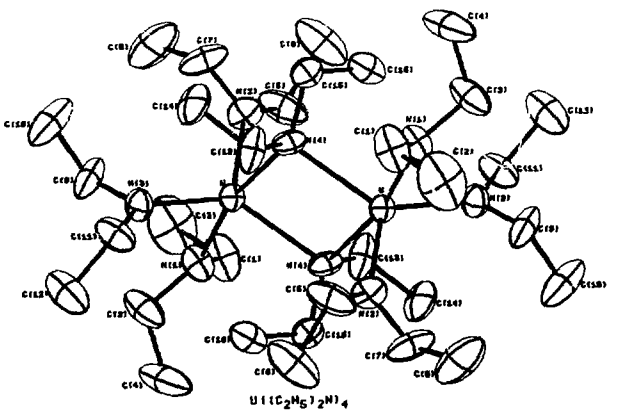

Fig. 1. Molecular structure of the uranium diethylamide dimer. (XBL 7512-9894)

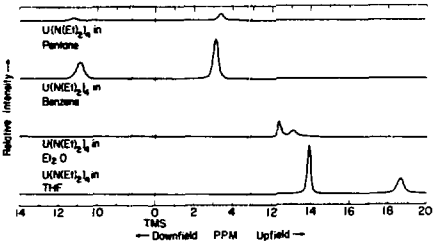

Fig. 2. Proton magnetic resonance of $U(NEt_2)_4$ in various solvents at room temperature. (XBL 7512-9946)

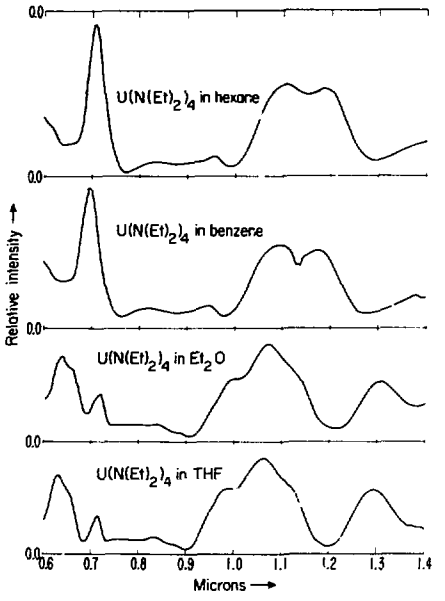

Fig. 3. Optical spectra of $U(NEt_2)_4$ in various solvents at room temperature. (XBL 7512-9945)

Table 1. Peak positions of $U(NEt_2)_4$ in various solvents (a).

Solvent	Peak 1	2	3	4	5	6
Hexane	0.704	a	b	1.104	1.188	b
Benzene	0.692	a	b	1.090	1.172	b
Diethylether	0.638	0.660	0.718	0.990	1.070	1.302
THF	0.630	0.653	0.715	0.985	1.061	1.287

[a] Peaks were not split into two components

[b] Peaks masked by solvent bands

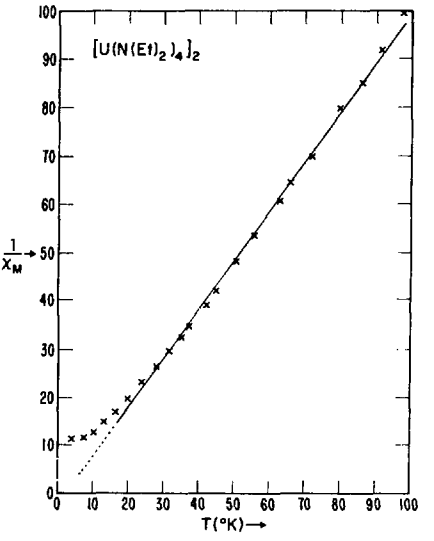

Fig. 4. Inverse susceptibility of $[U(NEt_2)_4]_2$ vs temperature. The straight line is the calculated inverse susceptibility in that temperature range with the parameters obtained from a least-square fit as given in the text. (XBL 7512-9944)

The inverse of the molar magnetic susceptibility of $[U(NEt_2)_4]_2$ in the temperature range 4.2°K - 100°K is shown in Fig. 4. At low temperatures ($T < 10$°K) the susceptibility becomes temperature independent. Above 20°K the susceptibility follows the Curie-Weiss law:

$$\chi_M = \frac{C}{T + \theta} \quad ,$$

with $C = 1.052$, ($\mu_{eff} = 2.81$ BM) and $\theta = 2.4$°K.

If we assume $[U(NEt_2)_4]_2$ to be a U^{4+} compound (Rn core, $5f^2$) with approximately C_{3v} crystal symmetry about the U^{4+} ion, then the ground L-S state will be a $^3H_4$ which will be split into three singlets and three doublets. The magnetic susceptibility appears to be due to a ground state singlet with a doublet state approximately 20 cm^{-1} higher in energy. The third crystal field state must be greater than 70 cm^{-1} from the ground state. It is interesting to note that there is no indication of magnetic ordering in this dimeric compound down to 4.2°K.

Although other Li amides besides the diethyl compound have reacted with UCl_4, only $U(NEt_2)_4$ has been isolated by sublimation. The unusual five-coordinate dimeric structure of this compound suggests that steric effects play the primary role in determining its stability. It appears that the -N-R (R = C_2H_5) group is small enough to allow coordination to stabilize the dimer but is large enough to prevent further coordination to a polymeric compound. R groups smaller than $-C_2H_5$ may cause the U compound to polymerize while larger R groups on the U ion may be too bulkly to form stable dimers and instead polymerize. The relatively low yield of $[U(NEt_2)_4]_2$ after sublimation (≤ 30% based on UCl_4) may be due to a competition between the dimerization and polymerization. Further work is in progress on the solution studies.

The crystal structure described here is the only example we know of uranium with five-coordination in the crystalline state. It is also a rare example of bridge-bonding of a uranium complex.

1. R. G. Jones, G. Karmas, G. A. Martin, Jr., and H. Gilman, J. Amer. Chem. Soc. 78, 4285 (1956).
2. K. W. Bagnall and D. Yanir, J. Inor. Nucl. Chem. 36, 777 (1974).
3. J. D. Jamerson and J. Takats, J. Organometal. Chem. 78, C23 (1974).

4. MAGNETIC SUSCEPTIBILITIES OF URANOCENES WITH HYDROCARBON SUBSTITUENTS AND THEIR ELECTRONIC GROUND STATES

N. Edelstein, A. Streitwieser, Jr., D. G. Morrell, and R. Walker

The successful syntheses of neutral cyclooctatetraene sandwich complexes with the first five tetravalent ions of the actinide series (Th^{4+} - Pu^{4+}) has generated much interest in the electronic structures of these compounds. The original impetus for the synthetic work came from the recognition that the highest filled orbitals of the cyclooctatetraene (COT) dianion (a 10 π electron system) and an f electron metal ion which could be involved in bonding were similar to the bonding orbitals of iron series bis cyclopentadienyl compounds except that the orbitals had one more node in rotating about the symmetry axis.[1] This qualitative picture was later supported by a molecular orbital calculation by Hayes and Edelstein[2] (HE) which showed considerable mixing of the ligand $\ell_z = \pm 2$ orbitals and the corresponding metal f-orbital. This calculation showed that the main feature of their electronic ground states was determined by the one electron antibonding metal-like orbitals occurring in two groups with the $\ell_z = \pm 1, \pm 3$ orbitals lying below the $\ell_z = \pm 2, 0$ orbitals. This ordering was reproduced with an effective crystalline field potential. By this method the results of the one-electron molecular orbital calculation were included in the diagonalization of the electrostatic, spin-orbit, and crystalline field matrices for the f^n systems of interest. The calculated ground state magnetic properties for $U(COT)_2$, $Np(COT)_2$, and $Pu(COT)_2$ were good agreement with the experimental results.

This calculation predicts Curie-Weiss behavior for the magnetic susceptibility of uranocene below ~ 300°K. The experimental evidence, however, indicates that the susceptibility becomes temperature independent below 10°K. It was suggested this deviation from the predicted behavior could be explained by a low symmetry crystalline field lifting the ground state degeneracy of the $J_z = \pm 3$ states which was imposed by the assumption of a C_8 molecular axis in the molecular orbital model.[2]

An alternative model has been proposed to explain the temperature dependence of the magnetic susceptibility of $U(COT)_2$ by Amberger et al.[3] In this model, which also assumes a C_8 symmetry axis, the lowest state for the ground J = 4 term is a singlet $J_z = 0$ level. The $J_z = \pm 1$ level is then placed 17 cm^{-1} above the ground state in order to reproduce the experimental susceptibility. A number of theoretical approaches were used in an attempt to verify this model. Values were also given for the crystalline field parameters which gave the optimal fit to the measured susceptibility.[3]

This alternative model seriously challenges the concept of the uranocenes as an aromatic f-electron organometallic series homologous to d-electron metallocenes. A distinction between those two models can be made by the study of the magnetic behavior of related organoactinide compounds. In this paper we present magnetic measurements on several substituted uranocenes. We also extend the calculations of Ref. 3 to include $Np(COT)_2$ and $Pu(COT)_2$. This work will demonstrate that at this time only the HE model is consistent with all of the data and supports Streitwieser's original concept.

The results of the measurements are summarized in Table 1. Typical graphs of the inverse susceptibility vs temperature for two compounds are shown in Figs. 1 and 2. The measured susceptibilities of the substituted uranocenes (Table 1 and earlier measurements) fall into two classes: one that shows a Curie-Weiss dependence in the temperature range measured, and another that follows the Curie-Weiss dependence down to approximately 10 - 20°K where the susceptibility becomes temperature independent.

We make the assumption that the gross electronic structure of uranocene and its substituted analogs are basically similar. The experimental evidence supports this assumption, for the optical spectra show only minor shifts from one compound to another and the ring proton magnetic resonance spectra of the various uranocenes occur in the same region. Furthermore, the empirical electronic magnetic moments are very similar. Therefore, we expect the model that explains the uranocene data should also hold as a first approximation for its substituted analogs even though the local symmetry is certainly lower in the latter compounds. The

Table 1. Magnetic properties of some substituted uranocenes.[a]

Compound	Temperature (°K)	μ_{eff} BM	θ (°K)
$[(CH_3)_4COT]_2U$	1.9 - 73.7	2.2 ± 0.2	11.3 ± 3
$[(C_6H_5)_4COT]_2U$	4.2 - 100	2.5 ± 0.1	6.7 ± 1
$[C_6H_5COT]_2U$	14 - 100	2.65± 0.2	12.2 ± 3
	< 8	TIP[c] (χ_M = 0.036 ± 0.001 emu)	

[a] $\chi_M = C/T + \theta$

[b] $\mu_{eff} = 2.84\sqrt{C}$ BM

[c] TIP = temperature independent paramagnetism

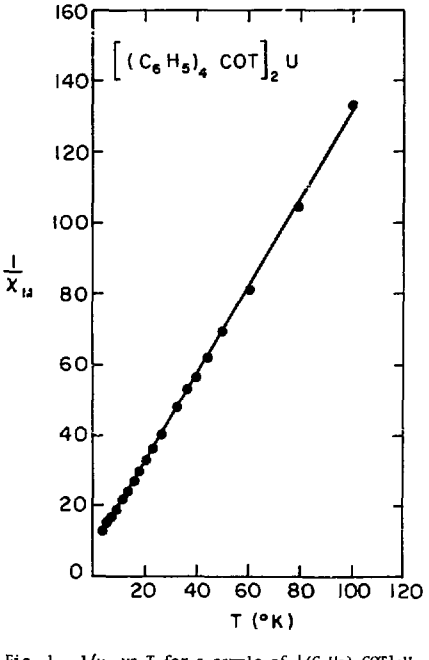

Fig. 1. $1/\chi_M$ vs T for a sample of $[(C_6H_5)_4COT]_2U$. The smooth line represents a least-square fit to the experimental data. (XBL 7511-9503)

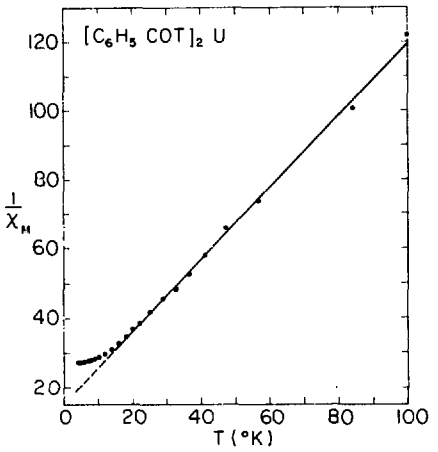

Fig. 2. $1/\chi_M$ vs T for a sample of $[C_6H_5COT]_2U$. The smooth line represents a least-square fit to the experimental data. (XBL 7511-9502)

ring substituents appear to have only minor effects on the electronic properties of these compounds.

The magnetic data presented earlier show Curie-Weiss behavior for two of the compounds over the entire temperature range. This type of magnetism is incompatible with the model given by Amberger et al.[3] which requires the $J_z = 0$ level to be the lowest crystalline field level.

We have extended the calculations of Ref. 3 to include $Np(COT)_2$ and $Pu(COT)_2$. We used their empirical crystalline field parameters with the spin orbit and electrostatic parameters described previously[2] to determine the ground state level structure and magnetic properties for these higher 2 actinide complexes. Since the complete f^2 basis set was not used in Ref. 3, we have slightly different crystalline field parameters. The results of the calculations are shown in Table 2 and the value of the crystalline field parameters are given in Table 3.

These calculations give the effective moment for $Np(COT)_2$ as 2.35 BM, in fair agreement with the experimental value of 1.8 BM. However, the ground state of $Pu(COT)_2$ is predicted to be the $J_z = \pm 4$ state which would be paramagnetic and follow the Curie-Weiss law. This prediction is in contradiction with the striking diamagnetic behavior of $Pu(COT)_2$ and shows again the inadequacies of the model of Amberger et al.

Table 2. Ground state energy levels and magnetic properties of $Ac(COT)_2$ compounds, Ac = U, Np, and Pu, predicted by the models of Amberger et al.[3]

$U(C_8H_8)_2$[a]			$U(C_8H_8)_2$[b]			$Np(C_8H_8)_2$[b]			$Pu(C_8H_8)_2$[b]		
J_z	E,cm^{-1}	$g_{\parallel}$	J_z	E,cm^{-1}	$g_{\parallel}$	J_z	E,cm^{-1}	$g_{\parallel}$	J_z	E,cm^{-1}	$g_{\parallel}$
0	0	--	0	0	0	±7/2	-2612.6	4.694	±4	-5901.7	4.552
±1	17	--	±1	19.1	0.654	±1/2	-2404.6	1.302[c]	±2	-3849.4	2.230
±2	200	--	±2	202.6	3.454	±5/2	-2011.3	3.802	±1	-3314.8	-0.427
±3	1535	--	±3	1537.5	6.380	±3/2	-1691.9	3.307	±3	-2287.3	5.835
±4	6600	--	±4	6779.3	9.098	±9/2	- 683.0	8.187	0	-1770.6	0

[a]Values given in Ref. 8

[b]This work $g_{\perp}$ = 0 unless noted

[c]$g_{\perp}$ = 2.972

Table 3. Values of the empirical crystalline field parameter.[a]

B_0^2	-11220.[b] cm^{-1}	-10356.4[c] cm^{-1}
B_0^4	-11408.[b] cm^{-1}	- 9936.0[c] cm^{-1}
B_0^6	-11680.[b] cm^{-1}	-14324.4[c] cm^{-1}

[a]Nomenclature as given in Ref. 6

[b]Parameters obtained by Amberger et al.[3] with an incomplete f^2 basis set.

[c]Parameters obtained in this work with the complete f^2 basis set.

1. A. Streitwieser, Jr. and U. Müller-Westerhoff, J. Amer. Chem. Soc. 90, 7364 (1968).

2. R. G. Hayes and N. Edelstein, J. Amer. Chem. Soc. 94, 8688 (1972).

3. H. D. Amberger, R. D. Fischer, and B. Kanellakopulos, Theor. Chim. Acta 37, 105 (1975).

5. σ- VS π-BOND ORGANOACTINIDES. THE SYNTHESIS AND STRUCTURAL ANALYSIS OF TRIS(η^5-CYCLOPENTADIENYL)-η^1-2 METHYLALLYLURANIUM(IV)*

Gordon W. Halstead, Edgar C. Baker, and Kenneth N. Raymond

The synthesis, characterization, and structural analysis of the title compound, $(C_5H_5)_3[CH_3C(CH_2)_2]U^{IV}$, is reported. The reaction of $U(C_5H_5)_3Cl$ with $Mg[CH_3C(CH_2)_2]Cl$ under inert atmosphere conditions at -78° in THF gives a high yield of the uranium allyl. Slow recrystallization gives dark red-brown crystals. The structure has been determined from three-dimensional x-ray diffraction data collected by counter methods. Three π-bonded η^5-cyclopentadienide rings are bonded to the uranium atom with an average bond distance of 2.74(1) Å. A σ-bonded η^3-methylallyl group completes the coordination sphere with a U-C bond length of 2.48(3) Å (see Fig. 1).

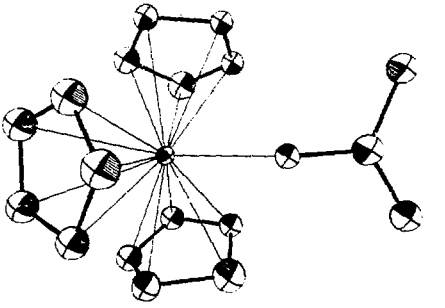

Fig. 1. The $U(C_5H_5)_3[CH_3C(CH_2)_2]$ molecule viewed with the 2-methylallyl group in the plane of the paper. Atoms are drawn at the 40% probability contour scale. (XBL 743-634)

The coordination geometry is a distorted tetrahedron with approximate C_{3v} symmetry. The average (center of cyclopentadienide ring)-U-(allyl carbon) bond angle is 100°. A σ-bonded ground state geometry vs the π-bonded geometry observed in $(C_5H_5)_4U$ is explained by the competition between the reorganization energy and the increase in coordinate bonds on going from the σ- to π-bonded complexes as shown in Fig. 2.

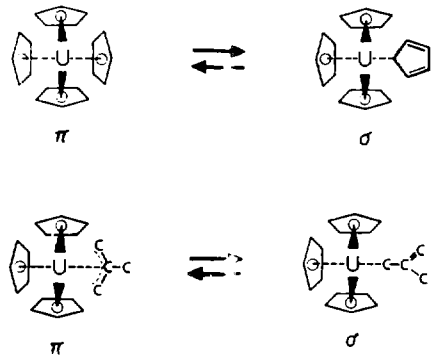

Fig. 2. Interconverion of $(\eta^5\text{-}C_5H_5)_4U$ to $(\eta^5\text{-}C_5H_5)_3(\eta^1\text{-}C_5H_5)U$ and of $(\eta^5\text{-}C_5H_5)_3[\eta^3\text{-}CH_3C(CH_2)_2]U$ to $(\eta^5\text{-}C_5H_5)_3[\eta^1\text{-}CH_3\text{-}C(CH_2)_2]U$. (XBL 7410-7927)

The crystals conform to space group $P2_12_12_1$ with a = 10.240(4); b = 8.737(4); c = 18.198(4) Å; Z = 4; and ρ_{calcd} = 1.99 g cm^{-3}. A total of 5470 reflections was collected of which 1698 independent reflections with $F^2 > 3\sigma(F^2)$ were used in the final refinement by full-matrix least-squares methods to give weighted and unweighted R factors of 6.4 and 6.5% respectively.

---

*Abstracted from J. Amer. Chem. Soc. 97, 5049 (1975). Partially supported by the National Science Foundation.

6. STRUCTURE OF A VOLATILE URANIUM FLUOROTELLURATE*

L. K. Templeton, D. H. Templeton, K. Seppelt, and N. Bartlett

An analysis by x-ray diffraction confirmed the constitution of $U(OTeF_5)_6$ and established its crystal and molecular structure. The preparation of the yellow crystals and their analysis by chemical and spectroscopic methods are described in another section of this report.[1] Because none of the diffraction patterns was of very high quality, a large number of crystals were examined by photographic or counter methods, and data sets were collected for two crystals with the diffractometer. The best data set, consisting of 780 independent reflections with $I > \sigma(I)$, was derived by averaging equivalent reflections in the full sphere out to $2\theta = 42°$. Correction factors for absorption, ranging from 1.2 to 2.5, were verified by measurements made at various azimuthal angles for several reflections. The structure was found by Fourier methods and refined by least squares to R = 0.06%, with anisotropic thermal parameters for all atoms except oxygen.

The crystals are monoclinic, space group C2/m, with cell dimensions a = 10.30(1), b = 16.61(2), c = 9.97(1) Å, and β = 114.14°. The molecular structure (Fig. 1) has uranium bonded in an

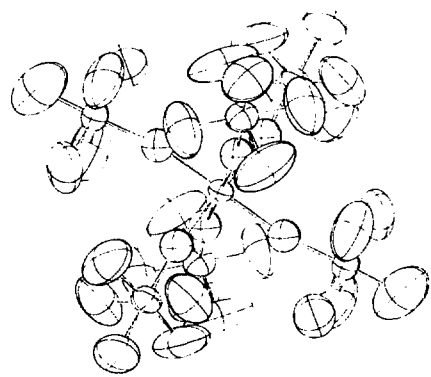

Fig. 1. Molecular structure. (XBL 7512-10075)

octahedral fashion to six oxygen atoms, while each tellurium atom has an oxygen and five fluorine atoms as octahedral neighbors. Average bond distances, not corrected for the substantial thermal motion, are U-O = 2.05, Te-O = 1.81, and Te-F = 1.69 Å. The bond angle at oxygen is 170° or 171°. The globular molecules pack in triangular fashion in layers (Fig. 2) which stack to give each molecule 10 nearest neighbors in a manner similar to the body-centered-tetragonal structure of protactinium metal. The weak bonding between these molecules is reflected in the volatility

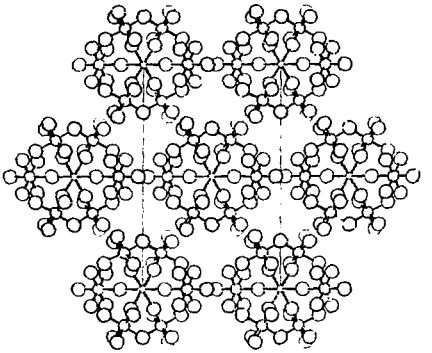

Fig. 2. Crystal structure: a axis horizontal, b axis vertical. (XBL 7512-10074)

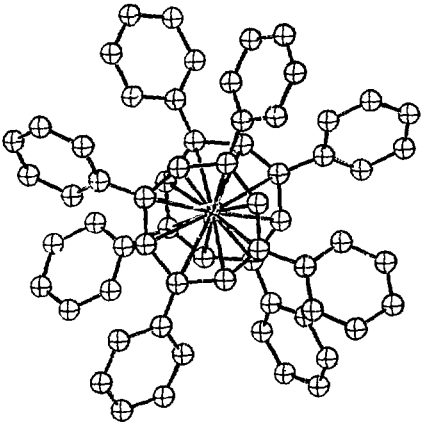

$U(C_8H_4(C_6H_5)_4)_2$

Fig. 1. Molecular structure of octaphenyluranocene. (XBL 7512-10072)

of the compound which in spite of its high molecular weight can be sublimed at 60°C.

1. (report being prepared by N. Bartlett)

7. MOLECULAR STRUCTURE AND DISORDER IN CRYSTALS OF OCTAPHENYLURANOCENE

L. K. Templeton and D. H. Templeton

Bis-π-(1,3,5,7-tetraphenylcyclooctatetraene) uranium, $U(C_8H_4(C_6H_5)_4)_2$, was prepared by Streitwieser and Walker[1] by reaction of UCl_4 with the dianion of 1,3,5,7-tetraphenylcyclooctatetraene. They sublimed it in vacuum to obtain tiny black crystals. A structure analysis of these crystals by the x-ray diffraction method confirmed that the material (Fig. 1) is a sandwich compound with the same uranium-carbon bond geometry as in unsubstituted uranocene.[2] The phenyl rings are tilted about 42° from the planes of the 8-rings and are interlocked in a manner which effectively shields the uranium atom from approaching molecules. This feature of the structure is presumed to explain the stability of this compound in air, in contrast to air-sensitive uranocene and its other known derivatives. X-ray diffraction measurements, which showed no significant change over a period of two months, gave the first quantitative data of the extent of this stability.

The crystals exhibit a remarkable type of molecular disorder which complicated the interpretation of the diffraction data. The diffraction patterns contain sharp reflections and diffuse streaks. The sharp features correspond to the orthorhombic symmetry Pccn with unit cell dimensions a = 24.84(3), b = 12.43(1), c = 7.587(6), and Z = 2; in this symmetry the two uranium atoms per unit cell must be distributed randomly over four equivalent positions. The carbon atoms, however, can be assigned positions without any disorder. This structure was refined to R = 0.088 for 723 independent reflections with $F > \sigma(F)$. The diffuse features show that the true structure is ordered in layers parallel with b and c, but the stacking of these layers in the a direction involves disorder of the uranium positions. The ideal ordered structure is described by the monoclinic symmetry P2/c for a cell with a = 24.86, b = 7.587, c = 27.78, β = 116.58, and Z = 4. The disorder can be described as polysynthetic twinning of this monoclinic structure with two orientations of the monoclinic c axis.

The explanation of the disorder in molecular terms is that the shape of the molecules permits them to stack in the direction of the orthorhombic c axis with parallel 8-rings and interlocking phenyl groups so that the space between molecules is almost the same as the space occupied by an uranium atom. These stacks of molecules are viewed end-on in Fig. 2. In this crystal the average of ring-to-ring distances in the molecule and between the molecules is 3.79 Å, while in the uranocene molecule[2] the ring-to-ring distance is 3.85 Å. Thus uranium atoms will fit in either position if carbon atoms are shifted about 0.06 Å, according to which side is occupied by uranium. This kind of partial disorder is commonplace in structures of metals and salts, but we do not know of an analogous molecular example.

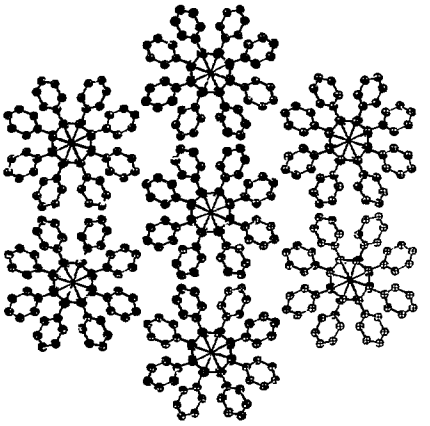

$U(C_8H_4(C_6H_5)_4)_2$

Fig. 2. Crystal structure of octaphenyluranocene, viewed down the orthorhombic c axis; a is horizontal and b vertical. (XBL 7512-10073)

1. A. Streitwieser and R. Walker, J. Organometallic Chem. 97, C41 (1975).
2. A. Avdeef, K. N. Raymond, K. O. Hodgson, and A. Zalkin, Inorg. Chem. 11, 1083 (1972).

8. POLAR HYDROGEN SCATTERING FACTORS IN X-RAY DIFFRACTION ANALYSIS*

A. J. Olson and D. H. Templeton

The standard least squares refinement of atomic positional and thermal parameters from x-ray diffraction data requires a scattering model for each of the atomic constituents of the crystallographic unit cell.

The customary model of a spherically symmetric atom is described by a scattering factor f which is a function of the magnitude of the diffraction vector h. A realistic description of a terminal hydrogen atom requires recognition that the electron density is not centered at the proton, nor is it spherically symmetric. Both the magnitude and phase of the complex form factor $|f|\exp(i\phi)$ are functions of $|h|$ and the angle between h and the bond direction. The form factor must be calculated separately for each atom in the primitive unit (or half of them in the centric case) since it is changed by rotation or reflection. Inversion gives the complex conjugate. The economy of retaining only real terms for half the atoms in the centric case is possible if ϕ is added to the argument $2\pi(hx+ky+\ell z)$ and if $|f|$ is used in place of the ordinary real f. With this method and neglect of df/dx in calculating $d|F|/dx$, we found that no change was required in our routine for calculating derivatives and solving the least squares equations.

Polar hydrogen form factors developed by Stewart et al.[1] have been applied to x-ray data from decaborane ($B_{10}H_{14}$) and sucrose ($C_{12}H_{22}O_{11}$). This application has yielded improvements over the spherical hydrogen model in the derived B-H, C-H, and O-H bond lengths as judged by comparison to the corresponding distances determined by neutron diffraction studies of the same molecules. The improvements have not been uniform between the different bonding types. Using this polar hydrogen model in x-ray refinements, the mean deviations from neutron bond lengths for B-H, C-H, and O-H were 0.019 Å, 0.043 Å, and 0.079 Å respectively. This trend can be explained by the fact that the model employed in all refinements was based upon hydrogen in the H_2 molecule. With increase in atomic number and electronegativity across the first row of the periodic chart, the bond to the hydrogen becomes increasingly more polar than the H-H bond in the hydrogen molecule. The thermal parameters resulting from these x-ray refinements also indicate varying applicability of the polar model of Stewart et al.

From this initial work, we recognized the necessity of employing hydrogen form factors that are dependent upon the bonded atom type. For this purpose, an ab initio method of modeling bond specific hydrogen electron density and producing polar hydrogen scattering factors was developed. Calculations involving several different wave function representations of the water molecule have been carried out using a variety of computational parameters. Oxygen-bonded hydrogen scattering factors have been generated from these molecular descriptions by appropriate estimation of the non-hydrogen electron density contribution in the vicinity of the proton, point by point subtraction, tail fitting, and subsequent Fourier inversion. In the methods outlined, computational parameters and pathways have been selected for use in these calculations. Also, certain minimum criteria for the selection wavefunctions have been established.

A summary of calculations has been reported and their results have been compared among themselves and with x-ray and neutron data on sucrose, descriptive of the O-H bond. The best table produced was generated from an extended Gaussian molecular water wave function and a matching masking function representing the oxygen density. It gives O-H x-ray bond lengths that are, on the average, only 0.005 Å shorter than the corresponding neutron-derived values. Thus the polarity of the hydrogen electron distribution is well described by this model. The thermal parameters derived using this table are on the average 0.48 $Å^2$ larger than the corresponding neutron values.

Although a comparison of these parameters is less reliable than the bond distance comparison, the discrepancy may indicate an inadequacy in the radial electron distribution of the model. A possible explanation may lie in the failure of the model to account for the additional diffuse character of the bonded hydrogen charge distribution imparted by the existence of intra- and inter-molecular hydrogen bonds in sucrose. Further tests of this table on data from non hydrogen-bonded molecular systems could answer this question.

*Abstracted from LBL-4530

1. R. F. Stewart, E. R. Davidson, and W. T. Simpson, J. Chem. Phys. 49, 2071 (1965).

9. STRUCTURES OF SODIUM URANYL FLUORIDE HYDRATES

J. R. Hauser, L. K. Templeton, and D. H. Templeton

We have been studying the phases that crystallize from concentrated aqueous solution of uranyl salts; the purpose is to extend our knowledge of the crystal chemistry of actinide elements and to gain a better understanding of the solubility behavior of uranium. Experiments with mixtures of sodium fluoride and uranyl nitrate have resulted in a variety of phases according to conditions which we have succeeded in reproducing only in part. Two of these phases, not previously reported to our knowledge, have been identified by crystal structure analysis as $Na_3(UO_2)_2F_7 \cdot 2H_2O$ and $Na_3(UO_2)_2F_7 \cdot 6H_2O$. Work continues to identify some other phases of unknown composition and to explore the conditions for their formation.

The dihydrate is monoclinic, space group C2/c, with cell dimensions a = 15.127, b = 6.926, c = 11.235 Å, and β = 94.77°. The hexahydrate is triclinic, space group P$\bar{1}$, with cell dimensions a = 7.177, b = 8.633, c = 7.000 Å, α = 113.28°, β = 104.92°, and γ = 77.88°. Both structures were determined by Fourier methods and refined by least squares. For the dihydrate, R = 0.022 for 2534 independent reflections included in the final refinement; for the hexahydrate, R = 0.024 for 2846 reflections. In difference maps we detected the hydrogen atoms for the dihydrate, and they were included in the calculations. For the hexahydrate the evidence for hydrogen positions was marginal, and they were neglected.

In both structures each uranium atom has neighbors at the corners of a pentagonal bipyramid: two oxygen atoms on the axis and five fluorine atoms around the pentagon. This geometry is the rule for other uranyl fluoride salts that have been studied. These bipyramids, however, are linked together by sharing corners, edges, or both in diverse ways, and the present structures (Figs. 1 and 2) are not the same as any other known examples.

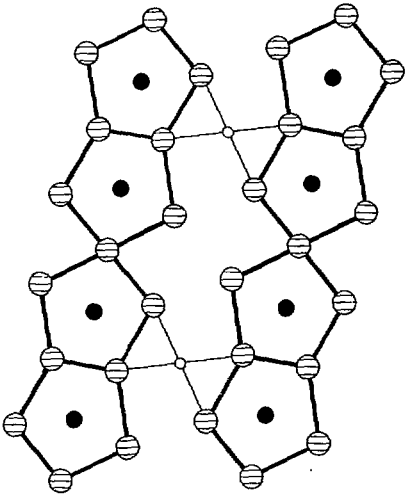

Fig. 1. Structure of $Na_3(UO_2)_2F_7 \cdot 2H_2O$. (XBL 764-1233)

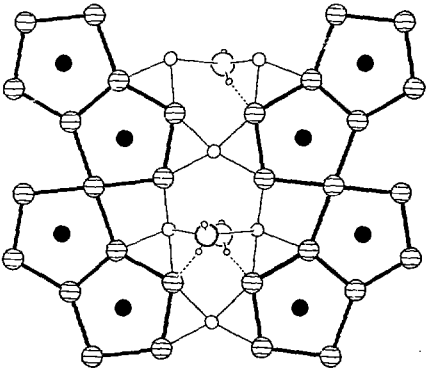

Fig. 2. Partial structure of $Na_3(UO_2)_2F_7 \cdot 6H_2O$. (XBL 764-1234)

10. ENERGY-LEVEL ANALYSIS OF Pm^{3+}:$LaCl_3$*

W. T. Carnall, Hannah Crosswhite, H. M. Crosswhite, and John G. Conway

A diagonalization of the matrices representing the combined atomic and crystal-field interactions

for the $4f^1$-configuration has provided the basis for interpreting the spectrum of Pm^{3+}:$LaCl_3$. Experimental data were drawn from the literature and were augmented by unpublished absorption and fluorescence results. A method of truncating the large matrices that are involved was developed and yielded results in excellent agreement with complete calculations. Fluorescence branching ratio calculations based on the Judd-Ofelt intensity theory were used to guide the interpretation of the fluorescence spectra.

11. INFRARED SPECTRA OF CURIUM, BERKELIUM, AND CALIFORNIUM

John G. Conway, Earl F. Worden, Jean Blaise, Pierre Camus, and Jean Verges

Infrared spectra of curium and berkelium in the region of 3700 to 1200 cm^{-1} were recorded on the high resolution Fourier Spectrometer located at the Laboratoire Aimé Cotton in Orsay, France. Each of the actinide materials was sealed in a quartz tube as the iodide and then evacuated. These tubes were then used as lamps in an electrodeless discharge cavity. The curium spectra have been analyzed and the report is in press (Spectrochemica Acta.).

The term analyses of Bk was fairly well along so it was possible to make a great number of assignments. The whole list contained 1225 lines of which 533 or 44% have been assigned to transitions within known levels of Bk I. There are 37 assignments to transitions of Bk II. This work also produced the interval between the ground level and the first level of the opposite parity. The ground state belongs to the $5f^9\ 7s^2$ configuration and the first level of the $5f^8 6d 7s^2$ is at 9141.113 cm^{-1}.

The analysis of the Cf spectra is underway.

12. ISOTOPE SHIFT IN THE CURIUM SPECTRUM

John G. Conway, George V. Shalimoff, and Earl F. Worden

The interpretation of the spectrum of Cm I is well advanced.[1] Extension of the analysis will be made only after new experimental results are produced. One experiment underway is the measurement of a great number of isotope shifts.

Two samples were available in the winter of 1974. The one which we refer to as ^{248}Cm contained the following mole ratios:

^{248}Cm - 54.6%

^{246}Cm - 16.4%

^{244}Cm - 27.1%

and the second called ^{245}Cm contained:

^{246}Cm - 21.44%

^{245}Cm - 23.12%

^{244}Cm - 54.96%

Electrodeless discharge lamps were made with the iodides of these samples. The spectra were photographed on the 30-ft Paschen-Runge spectrograph at the Argonne National Laboratory and the plates are being measured at Livermore. These data, together with a re-measurement of the plates containing ^{242}Cm - ^{244}Cm (Ref. 2), will give us a great amount of isotope shift data with which to extend the work on curium.

1. Earl F. Worden, John G. Conway, Energy Level Analysis of the First Spectrum of Curium, Cm I, UCRL No. 76921, J. Opt. Soc. Am. (accepted for publication).

2. John G. Conway, Ralph D. McLaughlin, J. Opt. Soc. Am. 46, 91-93 (1956).

13. SPECTRA OF EINSTEINIUM

John G. Conway, Earl F. Worden, W. Carnall, Ruth Sjoblom, H. M. Crosswhite, and M. Fred

The level analysis and a limited line list of Es were published in 1974.[1] At that time it was decided that a more complex list was needed to extend the work. A joint project was planned by scientists from LBL, ANL, and LBL for March, 1975.

Four different Es emission lamps were prepared in 2 weeks. Chemical recovery and purification of the Es were necessary between each lamp preparation. The first two lamps were not satisfactory as they contained great amounts of impurities. The third and fourth lamps were very good and we were able to photograph the Es spectrum from 2500 Å to 1μ. Zeeman spectra in the region of 2500 to 8900 Å were then obtained. The plates were left at Argonne to be measured.

The problem of observing the complete spectrum of Es, with its 21-day half-life, is so difficult it requires the efforts of a complete team of workers ready to do their part at any time of the day or night. It was only by combining the effort of workers from the three national laboratories that such a difficult spectroscopic problem could be undertaken.

In the year to come these plates will be measured and the analysis extended.

1. E. F. Worden, R. W. Lougheed, J. G. Conway, J. Opt. Soc. Am. 64, 77 (1974).

14. SPECTRA OF HIGHLY IONIZED ATOMS

J. G. Conway, G. W. Shalimoff, T. Hayhurst, S. P. Davis, S. Goldsmith, and C. H. H. Van Deurzen

We wish to mention several ongoing projects in the area of highly ionized spectra.

At the beginning of the year, S. Goldsmith built a power supply for a three-electrode triggered spark. This supply, together with a suitable discharge chamber, was tested on several elements. Spectra have been taken of Fe, Au, Cu, and Th. Recently, Fe and Th have been photographed on the 2-m grazing incidence spectrograph in the Space Science Laboratory. For this work a camera was designed and constructed. These plates are being used to evaluate the technical problems and shortly we will photograph other elements, varying the circuit parameters.

Standards have been a problem in the 10 - 500 Å region. In order to improve this situation and to extend the analysis of V(V) we have taken plates, using a sliding spark source, on the National Bureau of Standards grazing incidence spectrograph. These plates have been measured, but we are not satisfied with the standards. Some normal incidence plates also taken at NBS have been measured and additional lines have been identified on our plates so it has been possible to obtain a more accurate and consistent set of levels. These levels are now being used to calculate standards in the 10 - 500 Å region. We will use these calculated standards as internal standards and extend the accuracy of our measurements. This will not only give us a better and more completed description of V(V) but it will enable us to extend the analysis and provide us with an increased number of wavelength standards.

A few new levels have been identified in Th IV but the extension seems difficult. With this in mind we have used Hartree-Fock parameters to calculate the spectrum. Additional and as yet unlocated configurations have been included and the calculations are done with and without configuration interaction. This is giving us a better understanding of the problems in extending such an analysis. The same calculations will be used on the analyzed spectra of Sc III, Ti IV, V(V), and Cr VI.

Experiments on the Zeeman effect of U ions in a sliding spark source have been attempted. There is a very noticeable difference in the discharge with a change in the resulting spectra. This is being further investigated.

15. IONIZED SPECTRA OF GOLD*

S. Goldsmith, J. G. Conway, and S. P. Davis

By controlling the circuit parameters of a sliding spark discharge it is possible to vary the stages of ionization of a gaseous species and the spectra which are emitted. Using the conditions which favored the AuIII spectrum, we have photographed Au vapor in the region from 500 to 4500 Å. A study was also made of the series Pt I through Bi VI. In this series the systematics were studied and Au II was found to have several misidentified levels.[1]

In Au II the array $5d^86s \rightarrow 5d^76s6p$ was studied from an experimental and a theoretical viewpoint. The experimental scheme was determined, then using calculated Hartree-Fock parameters it was predicted. It was found that the Hartree-Fock parameters must be scaled. Some of the scaling factors were known from previous work, such as that done by R. Cowan of Los Alamos, who supplied us with his program and the first calculations for Au. When the parameters were derived from least square fitting of the experimental data, and these new parameters were used to calculate intensities, a greatly improved fit was obtained. We also gained insight into the scaling of the Hartree-Fock parameters.

A three-electrode, low-inductance spark source has been constructed and gold has been observed in the region of 500 to 1200 Å. This source should produce more highly ionized spectra. However, these spectra cannot adequately be studied and verified until observations are made in the 50 - 500 Å region. We are sure that higher ionization states are produced since in the sliding spark source we have found spectra of Au V.

---

*A paper presented to the Atomic Spectroscopy Symposium, September, 1975, National Bureau of Standards, Gaithersburg, Maryland.

1. Samuel Goldsmith and John G. Conway, LBL-4001, J. Opt. Soc. Am. 65, 1371 (1975).

16. RESEARCH PLANS FOR CALENDAR YEAR 1976

Norman M. Edelstein, Neil Bartlett, John G. Conway, Kenneth Raymond, Glenn T. Seaborg, Andrew Streitwieser, Jr., David H. Templeton, and Allan Zalkin

The basic purpose of this project is to study lanthanide and actinide materials in order to provide the basic knowledge necessary for their safe and economic utilization in present day and future technology.

This program will include studies of the preparation and physical and chemical properties of a variety of new gaseous, liquid, and solid phases. Synthesized compounds will be identified and characterized by x-ray diffraction, optical and vibrational spectroscopy, and by magnetic resonance and magnetic susceptibility techniques. Equilibrium constants for complex formation will be measured. Neutron diffraction studies will be done in cooperation with other laboratories.

From these complementary studies, new insights into the structural and chemical principles of

actinide compounds will be gained to imagine new bonding situations and to design new synthetic schemes to produce new materials.

A major aspect of our program is the design of sequestering agents for actinide ions which can engulf the ion and generate neutral or negatively charged complexes. The sequestering agents will have a very high specificity for actinide ions as well as large absolute formation constants with these ions. Such compounds may have use in the treatment of actinide poisoning or in new processing schemes for nuclear waste. A systematic application of various macrocyclic polydentate chelating agents containing such functional groups as hydroxamate and catecholate anions to the lower oxidation state actinide ions will be investigated. Reagents will be developed which can be used to extract the actinides from aqueous media.

The preparation of new organoactinide compounds and their characterization is of great chemical and perhaps industrial importance. The discovery of uranocene by Streitwieser and Müller-Westerhoff in 1968 has led to a renaissance of interest in these actinide organometallic compounds. Further synthetic efforts with substituted cyclooctatetraenes could produce uranocene-type compounds with substantially different properties. This work will be extended to higher Z actinides.

The preparation and physical studies of new inorganic actinide compounds and well-characterized actinide metals will continue. Studies on the optical spectra of free atoms and ions of the actinide series, and on actinide ions in crystals in collaboration with other ERDA laboratories will be pursued with special emphasis on highly ionized ions. The spectral analyses of the highly ionized ions is important to the understanding of the chemistry of these elements. For example, the ionization potentials and location of various electron configurations can be experimentally obtained by no other method.

17. 1975 PUBLICATIONS AND REPORTS

Norman M. Edelstein and Associates

Journals

1. N. Edelstein and D. G. Karraker, Comment on Electronic Structure of UF_6^- by M. Boring, J. H. Wood, and J. W. Moskowitz, J. Chem. Phys. 63, 2269 (1975).

*2. A. Streitwieser, Jr., and R. Walker, Bis-π-(1,3,5,7-tetraphenylcyclooctatetraene) uranium, an Air Stable Uranocene, J. Organometal. Chem. 97, C-41 (1975).

*3. G. W. Halstead, E. C. Baker, and K. N. Raymond, σ vs π-Bonded Organoactinides. The Synthesis and Structural Analysis of Tris (η^5-cyclopentadienyl)-η^1-2-methylallyluranium(IV), J. Amer. Chem. Soc. 97, 3049 (1975).

4. S. Goldsmith and J. G. Conway, An Analysis of the Configuration $5d^96p$ in Pt I through Bi VI, J. Opt. Soc. Am. 65, 1371 (1975).

Papers Presented

1. F. David, K. Samhoun, R. Guillaumont, and L. J. Nugent, Study of Some Thermodynamic Properties of 5f Elements, 4th International Transplutonium Element Symposium, Baden - Baden, Germany, September 13-17, 1975.

2. K. Samhoun and F. David, Radiopolarography of Am, Cm, Bk, Cf, Es, and Fm, 4th International Transplutonium Element Symposium, Baden - Baden, Germany, September 13-17, 1975.

3. D. K. Fujita, T. C. Parsons, N. Edelstein, M. Noé, and J. R. Peterson, The Magnetic Susceptibility of ^{244}Cm Metal and ^{249}Cf Metal, 4th International Transplutonium Element Symposium, Baden - Baden, Germany, September 13-17, 1975.

4. G. T. Seaborg, The Heaviest Transplutonium Elements, 4th International Transplutonium Element Symposium, Baden - Baden, Germany, September 13-17, 1975.

5. J. G. Conway, Spectroscopy of the Actinide Elements, Atomic Spectroscopy Symposium, National Bureau of Standards, Gaithersburg, Maryland, September 23-26, 1975.

6. E. F. Worden and J. G. Conway, Level Analysis of the First Spectrum of Curium, Cm I, Atomic Spectroscopy Symposium, National Bureau of Standards, Gaithersburg, Maryland, September 23-26, 1975.

7. S. Goldsmith and J. G. Conway, The Transition Array $5d^87s$ - $5d^76s6p$ in Au III, Atomic Spectroscopy Symposium, National Bureau of Standards, Geithersburg, Maryland, September 23-26, 1975.

8. D. H. Templeton, L. K. Templeton, J. R. Hauser, and A. Zalkin, Experimental Verification of Absorption Corrections in X-ray Diffraction, Acta. Crystallogr. A31, S219 (1975); Congress of International Union of Crystallography, Amsterdam, August, 1975.

LBL Reports

1. D. Brown, P. Lidster, B. Whittaker, and N. Edelstein, The Preparation and Spectral Properties of Actinide (IV) Hexaiodocomplexes, Inorg. Chem. (in press).

*2. N. Edelstein, A. Streitwieser, Jr., D. G. Morrell, and R. Walker, Magnetic Susceptibilities of Uranocenes with Hydrocarbon Substituents and Their Electronic Ground States, submitted to Inorg. Chem.

*3. A. Streitwieser, Jr., and C. B. Grant, Organoactinide Chemistry, a chapter for J. J. Katz and G. T. Seaborg, Editors, The Chemistry of the Actinide Elements, (in press).

*4. E. C. Baker, G. W. Halstead, and I. N. Raymond, The Structure and Bonding of 4f and 5f Series Organometallic Compounds, Structure Bonding 25 (in press).

5. K. Volz, A. Zalkin, and D. H. Templeton, Crystal and Molecular Structures of Thorium and Uranium Tetrakis (hexafluoroacetonylpyrazolide) Complexes, Inorg. Chem. (to be published).

6. J. G. Conway, J. Blaise, and J. Verges, The Infrared Spectrum of Curium - 244, Spectrochimica Acta (in press).

7. E. F. Worden and J. G. Conway, Energy Level Analysis of the First Spectrum of Curium, Cm I, J. Opt. Soc. Am. (in press).

8. J. G. Conway, E. F. Worden, J. Blaise, P. Camus, and J. Verges, The Infrared Spectrum of Berkelium - 249, submitted to Spectrochemica Acta.

9. J. G. Conway, E. F. Worden, J. Blaise, and J. Verges, The Infrared Spectrum of Californium - 249, submitted to Spectrochemical Acata.

10. W. T. Carnall, H. Crosswhite, H. M. Crosswhite, and J. G. Conway, Energy Level Analysis of Pm^{3+}: $LaCl_3$, submitted to J. Chem. Phys.

*Partially supported by the NSF.

I. LASER CONCEPTS

a. New Synthetic Methods in Actinide Chemistry for Volatile Materials

Norman M. Edelstein, Principal Investigator

1. STUDIES OF VOLATILE ACTINIDE COMPOUNDS

R. Rietz and N. Edelstein

We have begun a program to prepare, isolate, and characterize new compounds of the lanthanide and actinide elements. We are emphasizing the syntheses of new volatile materials.

We are reviewing recent synthetic advances in d-transition metal chemistry in order to apply these methods to the lanthanide and actinide series. We will explore promising synthetic routes to new actinide complexes and will investigate their properties by physical and spectroscopic techniques. High resolution spectroscopic studies of volatile compounds in the vapor phase will provide information on isotopic effects. We expect the results of this program will find important applications in isotope enrichment efforts, actinide separation technology, and biological research work.

Our recent research effort has been divided between two synthetic efforts. The first was an attempt to synthesize hexakis-(trifluoromethyl)-uranium(VI) by reaction of UCl_6 with trifluoromethyl radicals produced in a low-frequency rf discharge. We have also tried, unsucessfully, more conventional chemical methods to synthesize $U(CF_3)_6$. The second project we have begun involves the use of uranium hexachloride and uranium hexafluoride as percursors to uranium(VI) compounds. Many interesting and unexpected products have been identified but no new volatile materials have been discovered. One of our experiments has produced a new means to synthesize UCl_6 of exceptional purity. Details of our experiments follow.

a. Attempted Synthesis of $U(CF_3)_6$

Uranium hexachloride was reacted with trifluoromethyl radicals and the major volatile products identified. The CF_3 radicals were produced by homolytic cleavage of C_2F_6 in a 8.55 MHz rf discharge. The UCl_6 was positioned at various points in the plasma tail. In some experiments UCl_6 was heated from 60-100°C to sublime it through the plasma tail. The rf power, C_2F_6 pressure, and experimental duration were varied. In all the experiments, a major portion of the UCl_6 was recovered downstream from the plasma or in the first downstream trap. At high rf power levels a mirror formed in the reaction chamber. When UCl_6 was sublimed through the plasma tail a yellow-green glow was seen over the UCl_6. Reactions at room temperature produced no colors other than that of the CF_3 plasma itself. Some reactions left small amounts of non-volatile white or yellow-green residues.

The volatile products from above were separated by high vacuum fractional distillation. X-ray fluorescence tests using Mo Kα radiation showed that none of the volatile materials, aside from the recovered UCl_6, contained uranium. The freons produced were identified by their molecular weights, vapor pressures, infrared spectra, and ^{13}C and ^{19}F nmr spectra. In addition to C_2F_6, we recovered C_3F_8, C_4F_{10}, $C(CF_3)_4$, and a mixture of C_5 - C_6 fluorochlorocarbons.

Our second approach toward preparing $U(CF_3)_6$ involved the pseudohalogen-halogen exchange:

$$UF_6 + 2P(CF_3)_3 \rightarrow U(CF_3)_6 + 2PF_3$$

which might parallel the reported reaction:

$$UF_6 + 2PCl_3 \rightarrow UCl_6 + 2PF_3$$

Tris-(trifluoromethyl)phosphine was prepared and purified but it underwent no reaction with UF_6 in a stainless steel bomb in 4-1/2 hours at 20°C. Subsequently, the bomb was heated to 200°C for 8 hours, causing reaction of all the UF_6. The only uranium containing material recovered was UF_4, identified by its x-ray powder pattern. The volatile products, identified by vapor pressures and infrared spectra, contained varying amounts of unreacted $P(CF_3)_3$ as well as $(CF_3)_3PF_2$, $(CF_3)_2PF_3$, CF_3PF_4, PF_5, and traces of PF_3 and C_2F_6.

Subsequently the reported reaction ($UF_6 + 2PCl_3 \rightarrow UCl_6 + 2PF_3$) was reinvestigated and we found no UCl_6 or PF_3 as claimed. A number of phosphoranes were produced, i.e., PCl_3F_2, PCl_4F, PF_5 but only a nonvolatile uranium residue remained.

A third attempt to synthesize $U(CF_3)_6$ involved exchange with an element already in its highest oxidation state:

$$UCl_6 + 3Hg(CF_3)_2 \rightarrow U(CF_3)_6 + 3HgCl_2$$

Uranium hexachloride does not react with dry $Hg(CF_3)_2$ or with $Hg(CF_3)_2$ in $CFCl_3$ solution. These compounds did not react when heated together. Both reactants were easily separated and recovered by fractional sublimation.

b. Reactions of UCl_6 and UF_6

The volatile tungsten(VI) compound $W[N(CH_3)_2]_6$ has been reported. We have attempted to prepare an analogous uranium compound, $U[N(CH_3)_2]_6$.

The following reaction, which closely paralleled the tungsten work, was attempted.

$$UCl_6 + 6LiN(CH_3)_2 \rightarrow U[N(CH_3)_2]_6 + 6LiCl \downarrow$$

No volatile U compounds were found. The uranium was present in an unidentifiable grey powder.

Uranium hexachloride and $LiN(CH_3)_2$ did not react when mixed as the dry powders; however, they exploded violently when heated to 48°C under vacuum. A dark brown powder was formed, from which small amounts of dimethylamine and tetramethylhydrazine were identified. When n-pentane was condensed on dry UCl_6 and $LiN(CH_3)_2$, warmed to room temperature and stirred for one hour; an explosion occurred when the n-pentane was pumped off. These reactions are under investigation.

A monel vacuum line was fabricated to study reactions of UF_6.

We have explored the known halogen exchange reaction

$$UF_6 + 2BCl_3 \rightarrow UCl_6 + 2BF_3$$

using stainless steel bombs to produce gram amounts of UCl_6 in 25% yield. Although the yield is good, the UCl_6 sublimes with a red film that produces impurity lines in the x-ray powder pattern. We are currently trying to isolate and identify this impurity.

By analogy we tried the following reaction in an attempt to synthesize the known uranium(VI) alkoxides in one step,

$$UF_6 + 2B(OCH_3)_3 \rightarrow U(OCH_3)_6 + 2BF_3.$$

Trimethoxyboron and UF_6 did not react in 18 hours in a S.S. bomb. They were subsequently heated to 200°C for 3 days to produce a reaction. The only non-volatile product was UF_4, identified by its x-ray powder pattern. The major volatile products were dimethyl ether and a low volatility liquid. Molecular weight and mass spectral analysis showed the liquid to be a substituted boroxine:

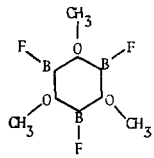

The following reaction was attempted to produce $U[N(CH_3)_2]_6$:

$$UF_6 + B[N(CH_3)_2]_3 \rightarrow U[N(CH_3)_2]_6 + 2BF_3$$

We synthesized $B[N(CH_3)_2]_3$ and this material was warmed from -196 with UF_6 in a S.S. bomb using $CFCl_3$ as a heat moderator. After 12 hours the only volatile products were $CFCl_3$ and excess $B[N(CH_3)_2]_3$. The $UF_6/B[N(CH_3)_2]_3$ ratio was 1/1. No BF_3 was present. The uranium-containing non-volatile grey powder did not sublime up to 250°C. The x-ray powder pattern of this material could not be identified. It is currently under study.

We have also attempted the methathesis route with UF_6:

$$UF_6 + 6LiNMe_2 \rightarrow U[N(CH_3)_2]_6 + 6LiCl \downarrow$$

These reactants were warmed from -196° in a S.S. bomb. The bomb was opened in one week. The only volatile products were traces of dimethyl amine, tetramethylhydrazine, and tetramethyltriazine; these being identified by infrared and mass spectra. The uranium was contained in a non-volatile green and white powder. Its chemical form has not been identified.

We are currently exploring the use of electropositive groups to extract fluorine from UF_6 according to the scheme:

$$UF_6 + 6(CH_3)_3SiR \rightarrow UR_6 + 6(CH_3)_3SiF$$

The first reaction tried was

$$UF_6 + 6(CH_3)_3SiCl \rightarrow UCl_6 + 6(CH_3)_3SiF.$$

This reaction was conducted in a S.S. bomb at 20° for 23 hours. At this time, the major volatile products were $(CH_3)_3SiF$, $(CH_3)_2SiF_2$, and excess $(CH_3)_3SiCl$. The uranium was contained in a brown residue. The black crystal subliming from this residue at 80° were identified as UCl_6 from their x-ray powder pattern. The non-volatile, air-stable grey residue was similarly identified as UF_4. This UCl_6 was free of the red coloration seen in the material prepared from UF_6 and BCl_3. Its powder pattern showed no spurious lines.

The second reaction tried was

$$UF_6 + 6(CH_3)_3SiOCH_3 \rightarrow U(OCH_3)_6 + 6(CH_3)_3SiF$$

This reaction was conducted in a S.S. bomb at 20° for 24 hours. At this time, the major volatile products were CH_3OCH_3, $(CH_3)_3SiF$, excess $(CH_3)_3SiOCH_3$, and a high boiling siloxide. The uranium was contained in a non-volatile red-brown powder. An x-ray powder pattern showed this material to be amorphous.

2. RESEARCH PLANS FOR CALENDAR YEAR 1976

Norman M. Edelstein

Our present efforts are directed toward syntheses and studies of new volatile uranium compounds that appear to be promising materials for new isotopic enrichment techniques. This chemical knowledge will benefit other more physically oriented isotope separation studies and may influence larger scale enrichment facility design.

a. Uranium Borohydrides

$U(BH_4)_4$ has been photolyzed to produce uranium atoms. $U(BH_4)_4$ is one of the most volatile

uranium(IV) compounds known, but it is hydrolytically unstable. $U(BH_4)_4$ is prepared from $Al(BH_4)_3$ and UF_4. $Al(BH_4)_3$ is an explosive, oxygen and water-sensitive material.

We shall attempt to make other uranium borohydrides that might be more hydrolytically stable at room temperature but could be heated slightly to produce a molecular vapor from which U atoms might be generated. Precedents from the d-transition metal complexes suggest that $U(B_3H_8)_4$, $U(B_5H_8)_4$, and $U(B_6H_9)_4$ molecules are possible. Experiments to synthesize these compounds have begun.

The substituted species $U(BH_4)_3(BH_3CH_3)$ and $U(BH_3CH_3)_4$ are of the same volatility as $U(BH_4)_4$ but are also hydrolytically unstable. We plan to replace the methyl groups with the more sterically hindered $-Si(CH_3)_3$ groups to form a more volatile but less chemically reactive species, e.g. $U[BH_3Si(CH_3)_3]_4$.

We will attempt to devise new and safer reactions to prepare $U(BH_4)_4$ utilizing the readily available materials UF_6, UCl_4, and uranium metal. We will convert the metal to UH_3 and attempt to hydroborate this to $U(BH_4)_4$. We have already found that $Al(BH_4)_3$ will not reduce UCl_6 to $U(BH_4)_4$. Presently, we are studying the chemical reactions of $U(BH_4)_4$ toward common substrates, e.g. amines, alcohols, alkoxides. Such basic chemical knowledge is essential if $U(BH_4)_4$ or any of its analogs are to be produced and handled safely and economically in large quantities.

b. Uranium Amides

The chemistry of $U[N(C_2H_5)_2]_4$ is currently under investigation in this laboratory. This volatile solid is extremely reactive toward oxidizing agents. The diethylamide ligands can easily be displaced in the presence of ligands containing protonic hydrogen atoms. Plans are being made to study the photolytic and thermal decomposition of this material; for it, too, may be another source of free uranium atoms.

We are presently trying several approaches toward producing new uranium amides that will be less oxygen-sensitive than $U[N(C_2H_5)_2]_4$ but more volatile. A recent x-ray crystal structure has supported the idea that $U[N(C_2H_5)_2]_4$ is prone to oxidative addition, particularly in its monomeric solution and gaseous configurations. (It is five-coordinate and dimeric in the solid.) We have exchanged some of the $-N(C_2H_5)_2$ ligands with the much bulkier $-N[Si(CH_3)_3]_2$ group, producing a new volatile uranium amide. Our present evidence suggests we have not completed the exchange to $U[N[Si(CH_3)_3]_2]_4$, the fully substituted product. We have also tried to produce this compound directly from UCl_4 and have obtained a second compound. Both of these materials are under active investigation. Our goal is to produce a near spherial molecule with all external C-H units shielding the uranium from chemical decomposition. In a similar fashion, we are attempting to prepare $U[N(CH_2CF_3)_2]_4$, thus using the $-CF_3$ groups not only as shielding for the metal but also to increase the volatility.

Attempts are also being made to synthesize uranium amides that resist oxidation because of their high oxidation states and saturation of their coordination spheres. We are attempting to synthesize $U(V)[N(C_2H_5)_2]_5$ and $U(VI)[N(CH_3)_2]_6$. Both of these molecules might be expected to be monomeric and quite volatile.

b. Selective Photochemistry

C. Bradley Moore, Principal Investigator

1. VIBRATIONALLY INDUCED PHOTOCHEMISTRY*

R. Glen MacDonald and C. Bradley Moore

The effect of enhancing chemical reactions by the addition of internal energy to the reactant species is the subject of great current interest. The study of vibrationally induced photochemistry is not only important from a theoretical point of view since it enables valuable information to be obtained about potential energy hypersurfaces, but also has important practical applications such as isotope separation and possibly chemical synthesis.

The reactions investigated so far have been[1]

$$HCl(v=2) + Br \xrightarrow{k_1} HCl(v=1) + Br \qquad (1)$$

$$\xrightarrow{k_2} HBr(v=0) + Cl$$

$$HCl(v=2) + O \xrightarrow{k_1} HCl(v=1) + O \qquad (2)$$

$$\xrightarrow{k_2} OH(v=0,1) + Cl$$

The HCl was excited directly to v = 2 by an optical parametric oscillator (OPO). Since the OPO is tunable with a bandwidth of ~0.005 cm^{-1} either species $H^{35}Cl$ or $H^{37}Cl$ may be excited to v = 2. The time dependence of HCl(v = 2) and (v = 1) was followed by monitoring the infrared fluorescence 2 → 1 and 1 → 0 of HCl. The 2 → 1 and 1 → 0 fluorescence may be separated using an HCl cold gas filter to absorb the 1 → 0 radiation. The population of HCl(v = 2) is directly proportional to the 2 → 1 fluorescence intensity. The reactions (1) and (2) were carried out in a fast flow system. The atoms were produced in a microwave discharge of the parent diatomic molecule and the atom concentration determined by an appropriate gas phase titration. The competition between k_1 and k_2 was determined by a fluorescence depletion technique. It was also possible to determine the total removal rate of HCl(v = 1) by these atoms.

Reaction (1) is approximately thermoneutral as written. From chemiluminescence studies of the reverse exothermic reaction (ΔH° = -15.5 kcal/mole) between unexcited Cl and HBr it is known that vibrationally excited HCl is produced. Microscopic reversibility would suggest that vibrational energy would be efficiently utilized in reaction (1). This was found to be the case. Reaction (2) is exothermic by 15.3 kcal/mole as written. The activation energy has been determined to be 5.9 kcal so that there is 9.4 kcal of vibrational energy in excess for reaction. It is expected that the reaction of HCl(v = 2) + O atoms would be much faster than the thermal rate constant. This was found to be the case. In both systems it was found that relaxation was the dominant path for removal of HCl(v = 2). The results are summarized in Table 1.

*Partially supported by U.S. Army

1. S. R. Leone, R. G. MacDonald and C. B. Moore, J. Chem. Phys. 63(11), 4735 (1975).

Table 1. Results for the relaxation and reaction of HCl(v = 2) by Br atoms and O atoms at 296°K.

Atom	k_1 Relaxation rate (cm^3 $molecule^{-1}$ sec^{-1})	k_2 Reaction rate (cm^3 $molecule^{-1}$ sec^{-1})	Reaction rate / Thermal rate
Br	$(1.4 \pm .21) \times 10^{-12}$	$(3^{+5}_{-3}) \times 10^{-13}$	10^{10}
O	$(4.1 \pm .32) \times 10^{-12}$	$(9 \pm 7) \times 10^{-13}$	$8.2 \pm 6.4 \times 10^{3}$

2. FORMALDEHYDE PHOTOCHEMISTRY

a. Appearance Rate, Vibrational Relaxation, and Energy Distribution of the CO Product*

Paul L. Houston and C. B. Moore

The mechanism of formaldehyde photochemistry has been investigated by monitoring the appearance rate, relative yield, and vibrational distribution of the CO photochemical product detected either by its infrared fluorescence or by its absorption of a cw CO laser. The energy levels of formaldehyde and its photolysis products are shown in Fig. 1. In the limit of low formaldehyde pressures, the CO product appears with a rate more than 100 times slower than the decay rate of the formaldehyde first excited singlet state. This fact indicates the presence of a long-lived intermediate state between S_1 and the molecular products, H_2 + CO. It is found that the appearance rate for CO is linearly proportional to the pressure of H_2CO, Fig. 2. Collision-induced CO production following 337.1 nm formaldehyde excitation occurs with appearance rates of 2.7×10^{-11} cm^3 molec^{-1} sec^{-1} for D_2CO and 4.7×10^{-11} cm^3 molec^{-1} sec^{-1} for H_2CO. After its production, CO(v = 1) relaxes to the ground vibrational state in collisions with D_2CO at a rate of 3.3×10^{-12} cm^3 molec^{-1} sec^{-1} and in collisions with H_2CO at a rate of 3.7×10^{-14} cm^3 molec^{-1} sec^{-1}. These rates have been confirmed by a separate measurement that monitors CO(v = 1) fluorescence following excitation with a Q-switched CO laser. The CO photolysis yield decreases with the addition of argon, but increases dramatically for 305.5 nm photolysis upon the addition of NO or O_2.

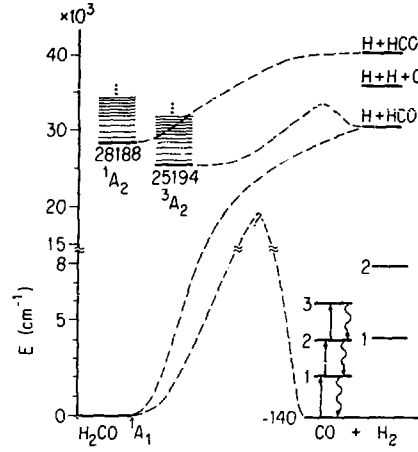

Fig. 1. Energy levels of formaldehyde and its photolysis products. (XBL 755-1435)

In addition, vibrational distributions of the CO product have been measured as a function of energy and vibrational level of the formaldehyde singlet state. The result is shown in Table 1. Although the amount of energy appearing in CO

Table 1. CO vibrational distributions.

λ (nm)	H_2CO Vibrational level	Product CO fraction v=0	1	2	3	4	5	6	Percent of Available E
347.2	4_0^3	.900	.100						0.7
337.1	$4_0^2 6_0^1$	.870	.110	.020					1.1
317.0	$2_0^2 4_0^3$	.731	.213	.049	.005	.002			2.3
314.5	$2_0^3 4_0^1$	.663	.195	.071	.032	.021	.012	.005	4.1
309.1	$2_0^1 6_0^1$, $2_0^2 4_0^3 6_0^1$	.607	.265	.092	.029	.005	.002		3.7
305.5	$2_0^3 4_0^3$	.661	.242	.058	.026	.009	.004		3.2
303.6	$2_0^4 4_0^1$	.571	.262	.103	.037	.015	.008	.004	4.5
295.0	$2_0^4 4_0^3$	.598	.255	.094	.034	.014	.005		3.9
294.0	$2_0^5 4_0^1$	.609	.264	.099	.024	.004			3.5

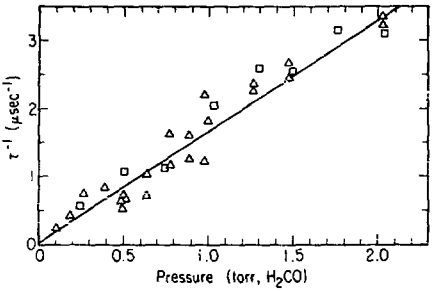

Fig. 2. Appearance rate of the CO product from H_2CO. Dissociation was at 357.1 nm. The triangles represent the appearance rates for CO(v = 1), while the squares represent the appearance rates for CO(v = 0). (XBL 755-1437)

vibrational modes increases with increasing excitation energy, the CO vibrational energy accounts for only between 0.7 and 4.5% of the energy available to the products at the measured dissociation wavelengths.

*Partially supported by NSF and U.S. Army.

b. Rotational Quantum Number Dependence of Radiationless Transition Rates in Formaldehyde*

A. P. Baronavski, Y. Haas and C. Bradley Moore

Two sets of measurements have revealed a striking dependence of the lifetime of the first excited singlet state of formaldehyde on rotational quantum number. This result is especially interesting since none of the theories proposed for the non-radiative decay of excited formaldehyde predict a variation with rotational excitation.[1] Table 1 shows the results of preliminary fluorescence lifetime measurements for the first excited singlet state of formaldehyde with one quantum of the out-of-plane bending vibration excited. There is no clear pattern to the variation of lifetime with J and K quantum numbers. It is not known whether the long decay is an isolated molecule phenomenon, or the result of collisions, or an experimental artifact. The pressure-tuned, N_2-pumped dye laser and Tektronix-PDP fast signal averaging system will be used to answer these questions. For higher vibrational levels where fluorescence lifetimes are too short to measure directly simultaneous fluorescence excitation and absorption spectra have been recorded using a tunable, high-resolution

Table 1. Observed lifetimes of single rotational states of $H_2{}^{12}CO$ in the 4_0^1 band.

Laser wavelength (nm)	τ_{short} (nsec)	τ_{long} (nsec)	Assignment J'	Assignment K_{-1}'
706.048	104.	889.	11	1
706.107	134.	1563.	1	1
706.129	100.	1435.	8	2
706.132	116.	610.	11	2
706.154	170.		16	4
706.180	121.	447.	2	1
706.195	178.	462.	3	1
706.213	164.	770.	18	2
706.220	104.	447.	4	1
706.244	108.	604.	5	1
706.269	128.	885.	13	2
706.290	116.	1124.	10	2
706.298	100.	1077.	12	0
706.313	61.	558.	7	0
706.320	108.	2105.	19	2
706.323	79.	541.	6	0
706.329	116.		8	1
704.281	137.		12	6
704.291	100.		20	8
704.302	113.		13	6

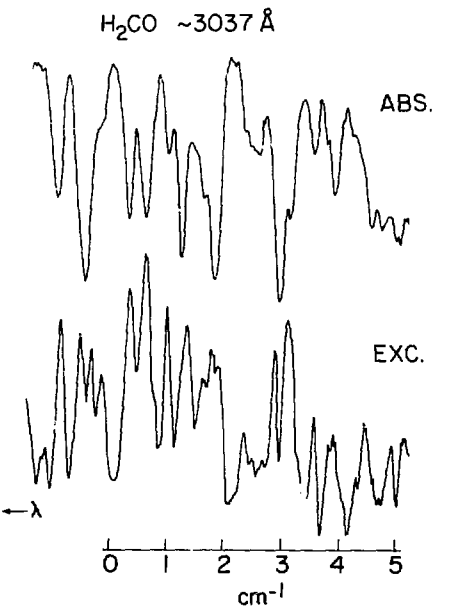

Fig. 1. Absorption and fluorescence excitation spectra of H_2CO near 3037 Å. Differences in relative intensity show variations in lifetime with rotational level. (XBL 764-1362)

ultraviolet laser. The ratio of fluorescence intensity to absorption strength is proportional to the radiative emission rate divided by non-radiative transition rate. Since radiative lifetimes are independent of rotational quantum number, the variations in the relative strengths of the two spectra (Fig. 1) demonstrate the dependence of the non-radiative transition rate on rotational quantum number. In these spectra as well, the variation of lifetime with J and K appears quite random.

These results point out another serious gap in our theoretical understanding of the radiationless processes in formaldehyde. Careful study of these phenomena is crucial to a understanding of the photochemical and photophysical processes in formaldehyde vapor.

*Partially supported by NSF

1. E. S. Yeung and C. B. Moore, J. Chem. Phys. 60, 2139 (1974).

3. FLUORESCENCE LIFETIMES OF NO_2*

Y. Haas, P. L. Houston, J. H. Clark and C. Bradley Moore (in collaboration with H. Rosen and P. Robrish, Energy and Environment Division, LBL)

Unravelling the exceedingly complex visible absorption and emission spectra of NO_2 is a problem in molecular spectroscopy that is only recently beginning to be solved.[1] The most widely accepted theoretical model[2] predicted that the prominent $K_a = 0$ lines of the $^2B_1$ state in the absorption spectrum of NO_2 would exhibit lifetimes on the order of 1 μsec.

In contrast with previous experiments and expectations, we have found[3] that the $K_a = 0$, $^2B_1$ lines near 454.8 nm do not have short lifetimes, but rather that they exhibit long collisionless lifetimes of 33 ± 4 μsec. To achieve this result, it was necessary to resolve the spectrum both in excitation (using a narrow-band, tunable dye laser) and in emission (using a 3/4 m monochromator). Thus we isolated the fluorescence specifically from the $K_a = 0$ states. An unambiguous assignment of the lines as $K_a = 0$, $^2B_1$ was obtained by comparison of the fluorescence excitation spectra with previously published work.[4] Figure 1 compares the lifetimes of the resolved fluorescence from the $K_a = 0$ lines with that of the unresolved, broadband fluorescence.

All the experimental evidence, including our excitation spectra, point to the $K_a = 0$, $^2B_1$ levels as unperturbed states. However, a lengthening of the lifetime by a factor of 30 is not compatible with essentially unperturbed states. Thus we conclude that the oscillator strength from which the lifetime near 1 μsec is calculated must be due to transitions to states other than $^2B_1$, most likely the $^2B_2$ state and that the lifetime measured in our experiments is the lifetime of the unperturbed $^2B_1$ electronic state.

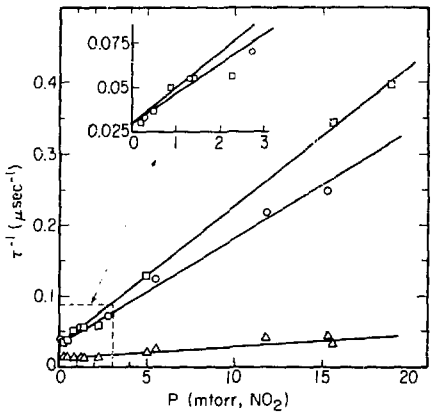

Fig. 1. Reciprocal lifetimes for NO_2 fluorescence as a function of pressure. The circles and squares are for resolved blue fluorescence excited by the Q(13) and Q(11) lines, respectively. The triangles are for the unresolved red fluorescence. The insert shows an expansion of the low-pressure region for the blue fluorescence. (XBL 755-1360)

*Partially supported by NSF

1. R. E. Smalley, B. L. Ramakrishna, D. H. Levy, and L. Wharton, J. Chem. Phys. 61, 4363 (1974). See also preprint: "The Fluorescence Excitation Spectrum of Rotationally Cooled NO_2," by R. E. Smalley, L. Wharton, and D. H. Levy.
2. A. E. Douglas, J. Chem. Phys. 45, 1007 (1966).
3. Y. Haas, et al., J. Chem. Phys. 63, 4195 (1975).
4. P. Robrish and H. Rosen, Lawrence Berkeley Laboratory Report LBL-3233.

4. LABORATORY FACILITIES

A. H. Kung and C. B. Moore

This program was initiated in January 1975 and the laboratory space completed in April 1975. Since then the following experimental systems have been set up or are in the process of being developed:

(1) A pressure-tuned, N_2-laser pumped dye laser is under construction which when completed will deliver radiation tunable from 3500 Å to 7100 Å with bandwidths of less than 1 GHz. By frequency doubling techniques the tuning range can be extended to 2600 Å and shorter. The output energy of the system will be in the order of 0.1 mJ to

0.5 mJ. It will be used to measure isotopic shifts and to study spectrally resolved excited state lifetimes, energy transfers and photochemical processes.

(2) A high average power Nd:YAG oscillator-amplifier chain with its first four harmonics will be used as a pump laser to obtain high power, high energy, narrow-band radiation throughout the visible and the ultraviolet. With the help of a $LiNbO_3$ optical parametric oscillator, broadly tunable radiation from 1.4 μm to 4.4 μm can also be obtained. The Nd:YAG laser system puts out energy in excess of 500 mJ at 1.06 μm and is expected to deliver tunable energy of as much as 20 mJ per pulse. This will improve the signal-to-noise ratio of our experiments greatly and make many new measurements possible. It will be especially valuable for kinetic spectroscopy studies of photochemical reaction products and possibly for multiphoton infrared dissociation studies.

(3) A commercial flash-lamp pumped dye laser has been installed. The laser has average output power of 0.5 W or better and is suitable for some photochemical and isotope separation experiments in the visible and near ultraviolet ranges.

(4) For data processing a Tektronix-PDP signal averaging system has been installed and is in operation. The system has a time resolution of 0.5 ns and is being used for signal averaging in all experiments.

(5) The above combination of facilities will enhance our experimental capability to a great extent. Additional equipment such as a high power carbon dioxide oscillator-amplifier system will permit multiple photon dissociation studies in the infrared. Photochemical processes in heavy molecules, related kinetics and multiphoton-multilevel processes can be observed and applications to separation of isotopes studied. A CW tunable dye laser will provide extremely high frequency resolution and will permit kinetic absorption spectroscopy of reaction intermediates and measurements of isotopic shifts and lineshapes under Doppler-free conditions. These instruments will be installed when additional funds become available.

5. RESEARCH PLANS FOR CALENDAR YEAR 1976

C. Bradley Moore

Vibrationally-Induced Photochemistry

The work on HCl(v = 2,1) will be extended to collisions with other reactive atoms such as Cl and H. Some studies will be made as a function of temperature to search for evidence of an activation energy. The new Nd:YAG pump laser may make it possible to extend these studies to higher vibrational levels and to other molecules. The rates of reactions which are exothermic for ground state reagents and are the microscopic reverse of vibrationally induced reactions will be measured. In this work the translational energy and rotational temperature of the reactants will be varied independently. These studies will complement molecular beam work on reactions of vibrationally excited molecules in Y. T. Lee's group.

Predissociation and Photochemistry of Formaldehyde

The initial work on rotational quantum number dependence of S_1 excited state lifetimes will be continued and extended to include measurements of pressure dependence, depolarization, and energy transfer. This requires completion of the N_2-pumped pressure-tuned dye laser in its final oscillator-amplifier configuration. Time resolved spectroscopy of the photolysis products of H_2CO will be extended to include H and HCO. A direct search for the spectrum of the unknown intermediate state or states in formaldehyde photolysis will be undertaken by infrared fluorescence and visible absorption spectroscopy. Photochemistry at very high pressures of foreign gas will be attempted. From this work we hope to be able to generate a complete picture of the photophysics and photochemistry of formaldehyde which will lead to quantitative theoretical work.

Chemical Reactions of Excited Electronic States

Initial studies will be of Cl_2^* + HBr HCl + ClBr and Br_2^* + olefins. In the former case a search for the fluorescence of ClBr in the visible and of HCl in the infrared will be undertaken. In the latter both kinetic spectroscopy and final chemical product analyses will be made. We are searching for an appropriate olefin which reacts directly with Br_2^* rather than inducing dissociation to Br atoms followed by free radical reactions and scrambling. If we are successful, a simple isotope separator for Br can be set up producing grams per day.

An expanded isotope separation program in MMRD at LBL has been proposed separately. This involves a joint effort with the groups of Lee, Shen and Winn. It will include in addition to the above work the program of Lee and a joint program on multiphoton infrared-induced dissociation.

6. 1975 PUBLICATIONS AND REPORTS

C. Bradley Moore and Associates

Journals and Conference Proceedings

1. R. G. MacDonald, I. W. M. Smith, F. J. Wodarczyk, and C. B. Moore, Vibrational Relaxation of HCl(v = 1) by Cl Atoms, J. Chem. Phys. 63, 2934 (1975).

2. K. Bergmann and C. B. Moore, Energy Dependence and Isotope Effect for the Total Reaction Rate of Cl + HI and Cl + HBr, J. Chem. Phys. 63, 643 (1975).

3. K. Bergmann, S. R. Leone, and C. B. Moore, Effect of Reagent Electronic Excitation on the Chemical Reaction $Br(^2P_{1/2,3/2})$ + HI, J. Chem.

Phys. 63, 4161 (1975) (Partially sponsered by NSF, and the U.S. Army, Research Office, Durham.)

4. J. Finzi and C. B. Moore, Relaxation of $CO_2(10^0 1)$, and $N_2O(10^0 1)$ Vibrational Levels by Near-Resonant V → V Energy Transfer, J. Chem. Phys. 63, 2285 (1975).

5. S. R. Leone, R. G. Macdonald, and C. B. Moore, Vibrational Relaxation and Photochemistry of HCl(v = 1,2) and Br Atoms, J. Chem. Phys. 63, 4735 (1975) (Partially sponsered by NSF and the U.S. Army Research Office Durham.).

6. J. H. Clark, Y. Haas, P. L. Houston, and C. B. Moore, Carbon Isotope Separation by Tunable-Laser Predissociation of Formaldehyde, Chem. Phys. Lett. 35, 82 (1975) (Sponsered by the University of California).

7. Y. Haas, P. L. Houston, H. Rosen, P. Robrish, and C. B. Moore, Long-lived $K_a = 0$, $^2B_1$ States of NO_2: A Direct Measurement Using a Tunable Dye Laser, J. Chem. Phys. 63, 4195 (1975) (Partially sponsered by NSF).

8. A. P. Baronavski, J. H. Clark, Y. Haas, P. L. Houston, and C. B. Moore, Photochemistry and Isotope Separation in Formaldehyde, Proceedings of the Second Laser Spectroscopy Conference, Megeve, France (1975). (Partially sponsered by NSF, U.S. Army Research Office, Durham, and the University of California.).

9. K. Bergmann, S. R. Leone and R. G. Macdonald, Vibrational Photochemistry, Proceedings of the 25th IUPAC Conference, Jerusalem, Israel (1975). (Partially sponsered by NSF, U.S. Army Research Office, Durham, and the University of California.)

10. C. B. Moore, Laser Photochemistry and Isotope Separation, Bull. Am. Phys. Soc. 20, 24 (1975).

Invited Lectures

1. Photochemistry of Formaldehyde, Seminar given at Stanford Research Institute.

2. Laser Isotope Separation, Stanford University Industrial Associates Laser Chemistry Symposium.

3. Laser Isotope Separation, Nuclear Chemistry Division Seminar at LBL.

4. Laser Isotope Separation, Nuclear Engineering Department Seminar, University of California, Berkeley.

5. Reaction and Relaxation in Halogen Atom Hydrogenhalide Collisions, Chemical Physics Seminar, University of Lausanne, Switzerland, June 20, 1975.

6. Photochemistry and Isotope Separation in Formaldehyde, Second International Laser Spectroscopy Conference, Megeve, France, June 25, 1975.

7. Chemical Kinetics, Isotope-selective Vibrational Photochemistry, and Isotope Separation by Photopredissociation. The International School of Quantum Electronics, Erice, Sicily, Italy, June 28, and July 8-9, 1975.

8. Vibrational Photochemistry, 25th International Union of Pure and Applied Chemistry, Jerusalem, Israel, July 11, 1975.

9. Reaction and Relaxation in Halogen Atom Hydrogenhalide Collisions, Seminar at Physics Institute, Polytechnic University, Milan, Italy September 19, 1975.

10. Reaction and Relaxation in Halogen Atom Hydrogen Halide Collisions, Physics Department, Technical University of Munich, Germany, September 26 1975.

11. Laser Isotope Separation, Physics Seminar, University of Kaiserslautern, Germany, September 29, 1975.

12. Laser Isotope Separation and Selective Photochemical Processes, General Colloquium of the Spectroscopy Institute of the Soviet Academy of Sciences, Moscow, Oct. 9, 1975.

13. Photophysique et Photochemie de Formaldehyde, Colloquium of Institute of Molecular Photophysics, University of Paris-Sud, Orsay, France, October 22, 1975.

14. Separation des Isotopes par Laser, A series of three special lectures to the French Commission d'Energie Atomique at Saclay, October 23, 1975 and November 18, 20 1975.

15. Photochemie et Relaxation Vibrationelle, Quantum Optics Seminar Ecole Polytechnique, Palaiseau, France, November 10, 1975.

16. Photochemie et Relaxation Vibrationelle, Colloquium of Molecular Photophysics Laboratory, Orsay, France, November 26, 1975.

17. Laser Isotope Separation, Avco Everett Research Laboratory, Everett, Mass., December 23, 1975.

LBL Reports

1. Jack Finzi, Vibrational Relaxation Studies in CO_2, N_2O, and H_2O Using a Tunable Infrared Laser, (Ph.D. Thesis) LBL- , June 1975. (Partially sponsered by NSF and the U.S. Air Force Office of Scientific Research.)

2. A. P. Baronavski, Photophysical and Photochemical Processes in Formaldehyde, (Ph.D. Thesis) LBL- , December 1975. (Partially sponsored by NSF.)

c. Isotope Separation

Yuan T. Lee, Principal Investigator

1. LASER ISOTOPE SEPARATION

Peter Schultz and Michael J. Coggiola

The method of laser isotope separation is primarily based on the change of physical and chemical properties of selectively excited atoms or molecules. Most of the approaches that have demonstrated certain degrees of success, such as multiphoton dissociation, selective ionization, selective chemical reactions and predissociation, could be considered as "high energy" approaches in which either chemical bond ruptures or electron removals are involved. Although some of these approaches may lead to a feasible, large scale separation scheme, they are usually more complicated due to secondary reactions, in addition to which the energy input in terms of laser photons is also quite high.

It seems to be possible to develop a "low energy" scheme, such that the change of physical property induced by single IR photon is sufficient to accomplish the separation process. The process we are investigating at present is a method based on a simple dissociation process of van der Waals' molecules in a molecular beam. When the vibrational motion of a molecule containing a desired isotope in a van der Waals' molecule is excited by an IR laser, the recoil velocity associated with vibrational to translational and rotational relaxation will send those molecules containing the desired isotope away from the beam.

We have constructed a new differentially pumped beam chamber for the production of a "clean" molecular beam containing desired van der Waals' molecules for this purpose. The first series of experiments that will be carried out in the very near future will be the separation of isotopic halogen molecules. By using a tuneable dye laser, isotopic halogen molecules in van der Waals' molecules such as XeCl, $XeBr_2$ can be excited. The vibrational energy of electronically excited halogen molecules in van der Waals' molecules is the only energy required for the separation. Electronic excitation is not required at all in this separation scheme. The availability of the tuneable dye laser makes it convenient to excite vibrational motion of halogen molecules through electronic excitation.

Energy transfer processes between atoms and molecules will be investigated through both high resolution velocity analysis and laser fluorescence state analysis. The process of intramolecular energy transfer will be further studied as a function of total excitation energies in chemically activated complexes. More and more effort will be made in the area of photon (laser)-molecular beam interactions, and photoelectron spectroscopy of beams of radicals or van der Waals' molecules (with Shirley's group); multi-photon excitation of vibrational energy levels (with Shen's group) are the areas in which the combination of molecular beams method and laser technology will give enormous advantages.

The effort in the laser isotope separation will be expanded in 1976. In addition to the decomposition of van der Waals' molecules in molecular beams, we will investigate the possibility of using selective condensation processes for effective isotope separation. This principle is based on the reduction of sticking coefficients of vibrationally excited molecules during the condensation processes.

Surface chemistry using molecular beam method is another area (with Somorjai's group) that will pick up lots of activities in 1976. A new improved beam-surface machine will be completed in the near future and the reactions on catalytic surfaces will be investigated in detail.

MATERIALS AND MOLECULAR RESEARCH DIVISION STAFF - 1975

Principal Investigators	Postdoctoral and Other Scientists	Graduate Students
Neil Bartlett	A. Cheetham *K. Seppelt	*R. Biagioni L. Graham K. Leary
Robert Bragg	*S. Justi	D. Baker S. Bose K. Danso S. Ho D. Morrow R. Saxena *L. Valero
Leo Brewer	L. Andrews R. Lamoreaux J. Wang W. Worrell	G. Bullard
John Clarke	*G. Donaldson *W. Goubau *G. Hawkins	T. Gamble G. Hoffer T. Hsiang *M. Ketchen J. Orthel M. Rappaport C. Tesche R. Voss N. Yeh
Marvin Cohen	*D. Bullett *M. Schluter *A. Simunek	*J. Chelikowsky *K. Ho S. Louie
Robert Connick	C. Meyer *T. Norris E. von Deuster	W. Earl K. Klotter T. Rowland
Lee Donaghey	A. Lin W. Worrell	T. Anderson *R. deBernardy-Sigoyer C. Figueroa *R. Gentile C. Manke *P. Sides S. Styer
Norman Edelstein J. Conway *K. Raymond *G. Seaborg *A. Streitweiser *D. Templeton	A. Avdeef J. Bucher A. Olson R. Reitz H. Ruben G. Shalimoff W. Wagner A. Zalkin	E. Baker *C. Berke *C. Grant G. Halstead J. Hauser T. Hayhurst *J. Hildebrand *W. Luke E. Price *W. Smith

Principal Investigators	Postdoctoral and Other Scientists	Graduate Students
Richard Fulrath	*V. Shumenko	D. Biswas S. Chandratreya J. Dih J. Dullea D. Mentley D. Miller V. Nagesh B. Powell D. Wang
Warren Garrison	W. Corniea M. Jayko M. Sokol T. Tung	
Charles Harr..	*H. Brenner Y. Yen A. Zewail	W. Breiland J. Brock A. Burns A. Gallo M. Lewellyn R. Shelby M. Tarrasch D. Zwemer
†Ralph Hultgren		
Harold Johnston	R. Graham *G. Whitten	P. Connell J. Girman R. Graham M. Kowalczyk D. Littlejohn F. Magnotta *B. Nordstrom J. Podolske G. Selwyn
William Jolly	C. Gin *J. Koepke *T. Schaaf	*S. Avanzino A. Bakke T. Briggs J. Illige J. Reed D. Yang
George Jur..	K. Kim	
Yuan Lee	M. Coggiola	C. Becker *R. Buss *S. Ceyer *C. Kahler *C. Ng *P. Schulz *S. Sibener R. Sparks *D. Trevor J. Valentini A. Wang
Bruce Mahan	J. Farrar	R. Davis F. Greiman W. Ruska R. Terkowitz
Richard Marrus	H. Gould	W. Davis

Principal Investigators	Postdoctoral and Other Scientists	Graduate Students
William Miller	*S. Chapman *A. Hickman *D. Knirk	J. Adams B. Garrett B. Garrison A. Isaacson A. Raczkowski C. Zahr
C. Bradley Moore		*C. Dasch *J. Finzi *F. Hovis *C. Mei *J. Wiesenfeld *M. Zughul
J. W. Morris, Jr.	K. Hanson *D. Huang *S. Jin C. Syn	M. Alavi S. Altintas K. Chang D. Grivas K. Hanson M. Hong S. Hwang M. Lee E. Pundarika J. Sanchez K. Walker S. Wen B. Whitaker
Rolf Muller	M. Sand	C. Chew J. Riggs M. Sand C. Smith
Rollie Myers		D. Lindner M. St. John R. Wilson
John Newman		P. Fedkiw C. Law *C. Mohr P. Pierini J. Trainham D. Ullman R. White
Donald Olander	M. Balooch D. Davis	R. De Paula D. Dooley K. Kim A. Machiels S. Shann C. Tsai R. Yang

Principal Investigators	Postdoctoral and Other Scientists	Graduate Students
Earl Parker	B. Francis	C. Atherton
Victor Zackay	N. Kennon	M. Bhat
	R. Lamoreaux	L. Brass
	A. Levy	M. Castro-Cedeño
	*A. Mukhopadhyay	R. Clark
	E. Plaza	J. Conn
	F. Ravitz	T. Darroudi
	*R. Ritchie	*W. Garrison
	G. Sheldon	G. Gettle
	J. Shively	G. Haddick
	W. Toutolmin	R. Horn
		J. Huang
		P. Joukoff
		N. Kar
		R. Kar
		D. Kleist
		G. Kohn
		T. Lechtenberg
		*A. Llopis
		D. McFadden
		Y. Mishima
		C. Mitchell
		R. Omer
		*M. Perra
		S. Singh
		*P. Spencer
		L. Thompson
		J. Wert
		E. Wylie
		M. Young
Joseph Pask	P. Dokko	*N. Cassens
	R. Langston	P. Dokko
	B. Wong	V. Draper
		G. Holmquist
		*C. Kramer
		*C. Marumo
		S. Risbud
		M. Sacks
		W. Snowden
		C. Tao
		S. Tso
		B. Wong
Norman Phillips	G. Brodale	W. Fogle
	E. Hornung	*F. Hermans
		B. Krusor
Milton Pickus	M. Dariel	M. Chen
	J. Wang	R. Ciardella
		G. Drago
		J. Granda
		K. Hemachalam
		J. Klein
		M. Malekzadeh
		D. Modi
		F. Reinel
Alexander Pines	*D. Ruben	*S. Allison
	A. Hohener	*M. Hoza
	S. Vega	*J. Murdoch
		T. Shattuck
		*L. Sterna
		C. Weitekamp
		D. Wemmer

Principal Investigators	Postdoctoral and Other Scientists	Graduate Students
Kenneth Pitzer	*L. Silvester	J. Kim Y. Lee P. Rogers G. Vogt
†Otto Redlich		
Paul Richards	*J. Claassen *Y. Taur D. Woody	R. Aurbach R. Bailey J. Bonomo *D. Lambert S. McBride N. Nishioka T. Shen D. Woody
Henry Schaefer		C. Bauschlicher *C. Dykstra *G. Schwenger *S. Ungemach *D. Yarkony
Alan Searcy	*A. Buchler D. Meschi P. Mohazzabi	T. Basu C. Chen T. Darroudi M. Huang G. Knutsen *S. Lim P. Mohazzabi
Y. Ron Shen	*J. Camassel *F. De Martini *K. Inoue *K. Miyano *A. Mysyrowicz A. Schmidt *J. Voitchovsky *R. Yu	D. Bethune T. Chiang *E. Hanson A. Jacobson S. Kohn R. Smith
David A. Shirley	W. Heppler S. Lee W. Matthias P. Young	G. Apai A. Ewing S. Kowalczyk R. Martin F. McFeely B. Mills *E. Poliakoff R. Rosenberg R. Streater P. Wehner *R. Williams
Howard Shugart *E. Commins	T. Hadeishi A. Huq P. Mohr M. Prior E. Wang	S. Chu R. Conti R. Knight D. Neuffer A. Ozmen L. Schipper

Principal Investigators	Postdoctoral and Other Scientists	Graduate Students
Gabor Somorjai	*L. Atanasoska R. Bastasz J. Bellier S. Bernasek J. Buchholz *C. Burggraf *C. Chang *W. Fink D. Hagen *T. Kaminska L. Kesmodel B. Nieuwenhuys *G. Rovida *M. Salmeron B. Sexton *W. Siekhaus C. Steinbruchel *T. Taylor *Y. Tsang *K. Yoshida	*D. Blakely S. Ceyer L. Firment *P. Hollins R. Johnson *J. Kleckner C. Megerle S. Overbury C. Smith P. Stair
Gareth Thomas	D. Clarke *J. Dutkiewicz *P. Karnthaler E. Ness *R. Sinclair O. Van der Biest *K. Westmacott	M. Carlson *Y. Chen *V. Dahmen F. Dizon G. Goeser R. Gronsky D. Howitt M. Kao J. Koo K. Kubarych R. Mishra B. Narasimha Rao M. Okada C. Wu M. Young
Charles Tobias	R. Atanasoski *T. Lengas *C. Vass *M. Yamashita	E. Carlson A. Kindler H. Law D. Munger R. Putt J. Riggs
Jack Washburn	*J. Grilhe *M. Guillen T. Kosel T. Peterson K. Seshan	B. Chin R. Drosd T. Huo *T. Kosel C. Lampert H. Mohamed T. Mowles T. Peterson K. Seshan A. Srivastava W. Wu

MMRD SUPPORT STAFF

C. Peterson - Business Officer

Administrative Staff

§S. Ashley - Staff Assistant Technical Reports
M. Janzen - Staff Assistant - Administration
E. Skrydlinski - Staff Assistant - Personnel
S. Stewart - Staff Assistant - Purchasing

Clerical and Secretarial Staff

L. Butters
G. Brazil
C. Davis
L. Fernander
N. Gearhart
C. Hacker
J. Hardin
ΔM. Herrington
§L. Hesleph
ΔE. Hoffer
B. Hosier
K. Janes
S. Jennings
D. Kaufman
M. Kell
K. Krushwitz
V. Lam
J. Lowrie
ΔD. Martin
R. McCollough
M. Ossa
E. Radmilovic
§A. Ramirez
B. Rancatore
M. Saarni
M. Schonborn
ΔC. Webb
A. Weightman
§J. Wolslegel
ΔE. Wright
C. Yoder

Technical Staff

§E. Edwards - Mechanical Coordinator
§D. Curtis - Electronics Coordinator

ΔC. Ackley
ΔR. Agnihotri
A. Bakke
§G. Baum
T. Bevan
ΔR. Botney
J. Boyer
ΔJ. Brown
§M. Brown
P. Bucksbaum
K. Carey
M. Carlson
ΔW. Carmichael
ΔR. Chelsky
H. Chen
J. Conn
D. Curtis
ΔP. Curtis
C. Cyders
ΔC. Deutscher
J. Dillon
G. Drago
ΔR. Drues
ΔE. Evans
J. Frease
L. Galovich
W. Giba
§G. Gordon
H. Harrell
R. Hauser
ΔP. Henerlau
P. Ho
ΔN. Hogan
J. Holthuis
ΔC. Ivy
J. Jacobsen
§L. Johnson
D. Johnston
D. Jurica
ΔT. Kane
ΔD. Kattenhorn
ΔN. King
D. Kleist
ΔT. Kommers
E. Kozak
ΔD. Kreitz
§D. Krieger
ΔD. Kronenberg
S. Lee
G. Lesh
§R. Lindberg
M. Lindley
ΔJ. Ling
§J. Liu
A. Ma
D. MacDonald
ΔJ. Marr
J. McClure
D. McFadden
ΔM. McKelvy
ΔG. Mikkelson
ΔB. Mulliken
§D. Newhart
A. O'Keefe
§G. Pelatowski
ΔL. Peter
C. Phillips
§B. Pope
R. Provance
L. Ison
J. Randall
ΔP. Reis
J. Reynolds
C. Ritter
ΔM. Robson
J. Shirley
B. Snyder
§P. Stagnaro
S. Strehl
S. Suzer
C. Thom
ΔE. Tobias
W. Toutolmin
W. Vandouris
L. Wachs
§P. Witherell
§W. Wong
ΔY. Yamazaki
P. Yarnold
M. Young

---

*Participant Status
†Emeritus
ΔNo longer with LBL
§LBL Support Staff

☆GPO – 789-634